Doctoral Dissertation
Doctoral Program in Civil and Environmental Engineering (38th Cycle)

Recovery of Critical and Strategic Raw Materials from mine waste: development of a methodology supported by international and Italian case studies

By

Gabriele Baldassarre
* * * * * *

Supervisor(s):
Prof. Paola Marini, Supervisor
Prof. Adriano Fiorucci, Co-Supervisor

Politecnico di Torino
2026

This thesis is licensed under a Creative Commons License, Attribution - Noncommercial - NoDerivative Works 4.0 International: see www.creativecommons.org. The text may be reproduced for non-commercial purposes, provided that credit is given to the original author.

I hereby declare that the contents and organisation of this dissertation* constitute my own original work and does not compromise in any way the rights of third parties, including those relating to the security of personal data.

Gabriele Baldassarre
2026

* This dissertation is presented in partial fulfilment of the requirements for **Ph.D. degree** in the Graduate School of Politecnico di Torino (ScuDo)

“If someone tells you it’s impossible, they’ve revealed their limits…not yours.”
Anonymous.

“Quando qualcuno ti dice che non si può fare, ricorda…è un riflesso dei suoi limiti, non dei tuoi.”
Anonimo.

Acknowledgments

It has been a long and challenging journey. I have tried to navigate the uncertainties of this path by keeping pure curiosity at the forefront and by developing alternative approaches whenever the work reached a bottleneck.

For this reason, I would like to acknowledge the many people who have helped me achieve this goal. I truly believe that everyone I encountered along the way has, in some form, left a mark on this journey.

First and foremost, I would like to thank my Supervisor, Prof. Paola Marini, for her constant support and trust throughout the development of this project, and for encouraging me to explore new environments to improve both my skills and the quality of my research. I am equally grateful to my co-supervisor, Prof. Adriano Fiorucci, for his wise suggestions, constructive discussions, and the many books he generously shared with me over these years.

A special thanks goes to the MIWATCH team colleagues in Brisbane, who welcomed me into their community, allowing me to learn extensively and to take part in incredible fieldwork and research experiences. I will always be grateful for the unforgettable memories of my time in Australia.

I would also like to thank all the scholars, experts, and students who enthusiastically contributed to the collection of information, curiosities, and field data across Italy, and who actively participated in some of the outcomes presented in this thesis.

To my colleagues in Turin, in the office and in the “saletta”, thank you for sharing the joys and challenges of our paths, for supporting one another, and for building a fair and supportive network that helped us navigate the storm. I wish you all the very best!

My deepest gratitude goes to my family, who carried the most demanding responsibility of supporting me through the emotional and practical ups and downs of this experience. This achievement would have been scarcely possible without your constant involvement and commitment to my choices.

Finally, thank you, Chanty, my everyday supporter, who has stood by my side with love and patience from the very first moments to the most demanding final stages. It is finally done!

This study was carried out within the MICS (Made in Italy – Circular and Sustainable) Extended Partnership and received funding from the European Union Next-GenerationEU (PIANO NAZIONALE DI RIPRESA E RESILIENZA (PNRR) – MISSIONE 4 COMPONENTE 2, INVESTIMENTO 1.3 – D.D. 1551.11-10-2022, PE00000004).

This manuscript reflects only the authors' views and opinions; neither the European Union nor the European Commission can be considered responsible for them.

Abstract

The increasing demand for critical raw materials driven by energy transition policies and technological development is posing important challenges to raw materials supplies in Europe and worldwide, while stimulating interest in alternative sources. Accordingly, abandoned and historical mine waste represents a promising secondary source to be considered. However, the assessment of their recovery potential for obtaining critical and strategic raw materials is often limited by data availability, partial characterisation, and the lack of large-scale applicable evaluation methodologies.

This Doctoral Thesis develops and applies a data-driven methodological approach for the assessment of mine waste deposits as potential secondary sources of valuable raw materials. In particular, the proposed methodology merges together information screening, site-specific characterisation, and laboratory-scale recovery trials, providing a structured pattern from preliminary evaluation to technical application of recovery solutions. International guiding case studies are included as procedural benchmarks, such as the Finnish national mine waste database for prioritisation of actions and characterisation methodologies applied on Kanmantoo mine (Australia) for secondary prospectivity of tailings materials.

The proposed framework is applied to selected Italian case studies (Traversella, Libiola and Fenice-Capanne), representing different historical mining districts, site characteristics and mine waste typologies. Site investigations, including sampling and geophysical surveys, were combined with geochemical and mineralogical analyses to assess the occurrence, distribution and concentration of critical minerals and elements. Subsequently, laboratory-scale recovery trials, including mineral processing and hydrometallurgical methods, are performed to preliminarily evaluate the technical feasibility of recovering critical and strategic elements while validating the assessment outcomes.

Results demonstrate that bulk geochemical characterisation should be coupled to detailed mineralogical and geometallurgical information for guiding the selection of applicable processing methodologies and for defining a recovery potential of critical and strategic raw materials from mine waste. Additionally, real-case applications proposed through the Italian case studies, confirm that mine waste may be recovered according to solutions tailored to the specific conditions of each site, such as mine waste type, materials characteristics and accessibility of the areas.

Overall, the proposed methodology describes a transferable scheme for supporting the evaluation of mine waste sites that could be implemented in wider protocols for developing data-driven protocols to assess potential exploitation of mine waste in Italy.

The outcomes of this Thesis could contribute to advancing sustainable approaches for mine waste valorisation according to circular economy principles and create opportunities for resource recovery and environmental restoration.

Contents

1. Introduction 1

1.1 Critical and strategic raw materials: a worldwide issue 2
1.2 European law framework for addressing a secure supply of raw materials: the role of extractive waste 7
1.3 Mining waste in Italy: background and regulatory actions 9
1.4 Mine waste as a possible source of CRMs and SRMs: classification and technical challenges for its recovery 13
1.4.1 Mine waste typologies 13
1.4.2 Technical solutions for mine waste and tailings recovery 15
1.5 Goal of the study 21
1.6 Thesis Outline 22

2. Methods 23

2.1 Mine waste database evaluation and individuation of prioritization actions 23
2.2 Methodology for site individuation, data collection, sampling and recovery trials: a multi-step approach 23
2.3 On-field methods 24
2.3.1 Sampling 24
2.3.2 Electrical Resistivity Tomography (ERT) 25
2.4 Mineralogical Characterisation 27
2.4.1 Optical Microscopy (OM) 27
2.4.2 Scanning Electron Microscopy (SEM-EDS) 27
2.4.3 Mineral Liberation Analyser (MLA) 28
2.4.4 X-Ray Powder Diffraction (XRPD) 29
2.5 Geochemical characterisation 30
2.5.1 Sample preparation procedure for geochemical analyses 30
2.5.2 Hand-held X-Ray Fluorescence (HH-XRF) 31

2.5.3 Induced Coupled Plasma Mass Spectroscopy (ICP-MS).....32
2.5.4 Induced Coupled Plasma Optical Emission Spectroscopy (ICP-OES) 34
2.5.5 Laser Ablation Induced Coupled Plasma Mass Spectroscopy (LA-ICP-MS) 35
2.6 Treatment methods 36
2.6.1 Physical treatments.....36
2.6.2 Particle Size Distribution (PSD) 36
2.6.3 Crushing and milling.....36
2.6.4 Magnetic Separation.....39
2.6.5 Gravity separation 40
2.6.6 Physical separation evaluation 41
2.6.7 Hydrometallurgical treatments.....42
2.6.8 Post-leaching metal recovery evaluation 44
2.7 Case-by-case applied methodology resume.....45
Part I. International examples of mine waste data organisation and collection for enhancing the recovery of mine waste and tailings 46
3. Data analysis for decision-making initiatives: the Finnish mine waste database 47
3.1 Preface 48
3.2 The GTK database for Finnish extractive waste facilities.....49
3.3 A novel tool for implementing Economic Importance into tailings quantity: The Economically Important – Equivalent Ton (t_{EIeq}).....51
3.3.1 Economic Importance (EI) evaluation method from the European Commission.....51
3.3.2 Definition and application of the t_{EIeq} unit 53
3.4 Economic value embedded in Finnish tailings 55
3.4.1 Proximity of smelter infrastructures to tailings sites.....57
3.5 Comparison of Economic Importance and Economic Value obtained data 61
3.6 Environmental Risk (ER) associated with tailings sites 62
3.7 A 3-D decision matrix for sites prioritisation according to their Economic Importance (EI), Economic Value (EV) and Environmental Risk (EV) 64
3.7.1 Application of the matrix 65

3.8 UNFC classification standard applied to the Otanmaki tailings site67
3.9 Final Remarks 69

4. Advanced strategies for data collection and secondary prospectivity of mine waste: the Kanmantoo, Australia, historical tailings storage facility characterisation campaign 71

4.1 Site description 72

4.1.1 Geological setting and historical mining activities 72
4.1.2 Mining and mineral processing history of the site 73
4.1.3 Available information on tailings and their associated critical metal potential 75

4.2 Sampling strategy 76
4.3 Chemical and mineralogical characterisation 79

4.3.1 Chemical characterisation results 79
4.3.2 Mineralogical characterisation 85

4.4 Geochemical considerations and critical metal tenor 96
4.5 Final Remarks 99

Part II. Potential recovery of mine waste: 3 Italian case studies 101

5. Case study 1: Traversella Mine, Piedmont, Italy 102

5.1 Site Description and Geological Setting 103

5.1.1 Historical mining activities in the area 104
5.1.2 Mine waste accumulation areas 106

5.2 Sampling strategy 108
5.3 Mineralogical and chemical characterisation 108

5.3.1 Bulk sample characterisation results 109
5.3.2 Geochemical, mineralogical and environmental considerations 115

5.4 Lab-scale processing trials 117

5.4.1 Crushing, grinding, and sieving 118
5.4.2 Feeding material characterisation – Size class 0.250-0.125 mm 118
5.4.3 Feeding material characterisation – Size Class < 0.125 mm 130
5.4.4 Test A – Dry magnetic separation using LIMS 133
5.4.5 Test B – Gravity separation using ST 135
5.4.6 Comparison of separation performances for Test A and Test B 137

5.4.7 Test C – Dry magnetic separation (LIMS) and gravity separation (ST) 139
5.4.8 Test D – Wet magnetic separation using WHIMS 142
5.5 Final Remarks 145
6. Case Study 2: Libiola Mine, Liguria, Italy 146
6.1 Site description 147
6.1.1 Geological setting and historical mining activities 147
6.1.2 Mine waste dumps 150
6.2 ERT geophysical survey results 154
6.2.1 Mine waste volume estimation results 158
6.3 Sampling strategy 159
6.4 Chemical and mineralogical characterisation 161
6.4.1 Chemical characterisation results 161
6.4.2 Mineralogical characterisation results 170
6.5 Geochemical, mineralogical and environmental considerations 172
6.6 Lab-scale processing trials 175
6.6.1 Chemical and mineralogical characterisation of samples before leaching 176
6.6.2 Leaching test results 176
6.7 Final remarks 181
7. Case Study 3: Fenice-Capanne, Tuscany, Italy 183
7.1 Site description 183
7.1.1 Geological setting and historical mining activities 183
7.1.2 Mine waste dumps and tailings storage facilities 187
7.2 Tailings and roasting samples 191
7.3 Chemical and mineralogical characterisation 191
7.3.1 Chemical characterisation results 191
7.3.2 Mineralogical characterisation results 197
7.4 Geohemical, mineralogical, and environmental considerations 198
7.5 Lab-scale processing trials 202
7.5.1 Sample characterisation before leaching 203
7.5.2 Leaching test results 208

7.6 Final Remarks 215

Part III. Conclusion and Future Developments 217

8. Conclusions 218

8.1 General aspects of the research 218
8.2 International reference examples and their methodological relevance 219
8.3 Methodological application on the Italian case studies 220
8.4 Limitations and future developments 222
8.5 Environmental restoration and resource recovery: a synergic action 222

References 223

A. Appendix A 253

A.1. Calculated tEI,eq values according to chemical assays reported in the METSO-GTK database 254
A.2. Calculated economic values in Finnish mine waste sites 261

B. Appendix B 265

B.1. List, depth and location of collected samples from old TSF, Kanmantoo 265

C. Appendix C 266

C.1. MLA modal mineralogy results for 0.250-0.125mm size class - Traversella 266
C.2. Matlab script for semi-automated liberation analysis based on SEM-BSE images 267
C.3. Image processing TD_BSE1 – 0.250-0.125mm size class - Traversella 276
C.4. Image TD_BSE2 - 0.250-0.125mm size class - Traversella 278
C.5. Image TD_BSE3 - 0.250-0.125mm size class - Traversella 280
C.6. XRPD Spectra – Output materialsTest A, Test B, Test C, Test D – Traversella 282

D. Appendix D 289

D.1. List and location of sampling points - Libiola 289
D.2. HH-XRF results from field survey – Libiola North, South and Margherita dumps (values in ppm) 290

D.3. ICP-MS results – Libiola North (LN), South (LS) and Margherita (LM) dumps (ALS ME-MS61 method) 296
D.4. ICP-MS results – Libiola North (LN), South (LS) and Margherita (LM) dumps (ALS ME-MS81 method) 300
D.5. XRPD quantitative analyses results (values in wt%) - Libiola 303
D.6. ICP-OES characterisation of leachate solutions and calculated R_{ICP} values - Libiola 304
D.7. HH-XRF characterisation of post-leaching solid residues and calculated R_{XRF} *values* - Libiola 305

E. Appendix E 306

E.1. HH-XRF results for Fenice Capanne Tailings and Roasting samples (values in ppm, ND: Not Detected) 307
E.2. ICP-MS results – Fenice-Capanne tailings and roastings samples (ALS ME-MS61 method) 311
E.3. ICP-MS results – Fenice-Capanne tailings and roastings samples (ALS ME-MS81 method) 314
E.4. XRPD quantitative analyses results (values in wt%) – Fenice-Capanne 316
E.5. MLA modal mineralogy results for sample FC15, Fenice-Capanne 317
E.6. ICP-OES characterisation of leachate solutions and calculated R_{ICP} values – Fenice-Capanne 318
E.7. HH-XRF characterisation of post-leaching solid residues and calculated R_{XRF} values – Fenice-Capanne 319

List of Tables

Table 1 - Lower LODa for SciAps X-555 running "Soil" acquisition program («SciAps.com», 2025) 32
Table 2 – Limit of Detection (LOD) range for ME-MS61 four-acid digestion ICP-MS method (ALS Global, 2025) 33
Table 3 - Limit of Detection (LOD) range for ME-MS81 lithium borate fusion ICP-MS method (ALS Global, 2025) 34
Table 4 - Summary of applied characterisation methods for each of the proposed case studies. PSD: Particle Size Distribution; ERT: Electrical Resistivity Tomography; OM: Optical Microscopy; SEM-EDS: Scanning Electron Microscopy with Energy-Dispersive Spectroscopy; MLA: Mineal Liberation Analysis; XRPD: X-Ray Powder Diffraction; HH-XRF: Hand-Held X-Ray Fluorescence; ICP-MS: Induced Coupled Plasma Mass Spectroscopy; ICP-OES: Induced Coupled Plasma Optical Emission Spectroscopy; LA-ICP-MS: Laser Ablation ICP-MS. 45
Table 5 – Selected mine waste sites (n = 22) from the GTK database in the study, with the reported quantities of tailings and waste rocks. 49
Table 6 - EI values calculated for 2023 by the European Commission. Adapted from European Commission, 2023 52
Table 7 – Calculated $t_{EI,eq}$ values according to chemical assays reported in the METSO-GTK database 54
Table 8 – Calculated economic value (EV) for selected Finnish tailings sites 56
Table 9 - Road distances between selected tailings sites in the Finnish mine waste database and smelter plants locations in Finland 58
Table 10 - Assigned environmental risk (ER) scores (Low, Mid, High) according to environmental impacts observed from the Finnish mine waste database. n.a.: not available. 62
Table 11 - Jenks classification ranges for assigning classes for EV and EI parameters calculated for tailings sites in the Finnish mine waste database 65
Table 12 - Prioritisation results after the application of the 3-D prototyped matrix for the Finnish tailings sites considered. *Red: Highly Recommended actions, Yellow: Recommended actions, Green: Programmable actions, Neg: Negligible actions. 66

Table 13 - Number of samples and maximum depth of bored drill holes in the old tailings storage facility of the Kanmantoo mine, Australia. 76
Table 14 - Summary statistics for selected elements measured in the old tailings storage facility, Kanmantoo mine, Australia (n = 38) (*: ME-MS81 method) 80
Table 15 - List of selected samples from old tailings storage facility of the Kanmantoo mine, Australia, for mineralogical characterisation (XRPD and MLA), according to rationales related to ICP-MS characterization. 85
Table 16 - Summary statistic for mineral phases abundance measured by quantitative XRPD for old tailings facility samples, Kanmantoo mine, Australia (n = 6). 86
Table 17 – Summary statistics for quantified mineral phases by MLA in samples from old tailings storage facility, Kanmantoo mine, Australia (n = 6). 88
Table 18 - Summary statistics for selected elements measured by LA-ICP-MS in garnet (n = 187) and pyrite (n = 15) found in samples from the old tailings storage facility of the Kanmantoo mine, Australia. 92
Table 19 – Correlation matrix for selected critical metals and trace elements measured in garnet minerals (n=187) in the old tailings storage facility of the Kanmantoo mine, Australia. (R values higher than 0.7 in **bold**).....93
Table 20 - Correlation matrix for selected critical metals and trace elements measured in pyrite minerals (n = 7) in the old tailings storage facility of the Kanmantoo mine, Australia. (R values higher than 0.7 in **bold**).....95
Table 21 - Summary for critical and strategic elements values measured by geochemical analyses compared to crustal abundance concentrations for the old tailings storage facility of the Kanmantoo mine, Australia (n = 38). (In **bold** concentrations > 1x time higher than the average abundance;*: Rudnick & Gao, 2014; [1]: not included in the Australian critical elements list; [2]: included in the Australian strategic elements list). 97
Table 22 - Summary for REEs values measured by geochemical analyses compared to crustal abundance concentrations for the old tailings storage facility of the Kanmantoo mine, Australia (n = 38). (*: Rudnick & Gao, 2014). 98
Table 23 - Mine waste dump names and positions according to on-site inspections in the Traversella mine area. 106
Table 24 - Identified mineral phases for the "Piano Svedesi" bulk sample, Traversella mine. 112
Table 25 - HH-XRF chemical assays for Piano Svedesi bulk sample, Traversella mine. 113

Table 26 - ICP-MS geochemical assays for Piano Svedesi bulk sample, Traversella mine (*: ALS ME-MS81 method) 114
Table 27 - Summary of processing trials performed on Piano Svedesi mine waste material, Traversella mine. 117
Table 28 - Weight fractions for the obtained size classes after crushing, milling, and sieving, of waste rock samples from Traversella mine. 118
Table 29 - XRPD mineral phases for 0.250-0.125 mm material obtained after comminution and sieving of waste rock samples from Traversella mine..... 119
Table 30 – Particle size distribution percentiles calculated from magnetite liberated free-grain size analysis for size class 0.250–0.125 mm material after comminution and sieving of mine waste rocks from Traversella mine 127
Table 31 - Particle size distribution percentiles calculated from magnetite and scheelite particle size distribution curves for the 0.250-0.125mm size class material after comminution and sieving of mine waste rocks from Traversella mine 127
Table 32 - Comparison of liberation grade and particle size distribution percentiles calculation for magnetite grains contained in the 0.250-0.125mm size class material obtained after comminution and sieving of mine waste rock samples from Traversella mine, according to the Matlab script processing of SEM-BSE images and MLA system 128
Table 33 - HH-XRF assays for the 0.250-0.125 mm size class material obtained after comminution and sieving of mine waste rock samples from Traversella mine 129
Table 34 - XRPD mineral phases for size class < 0.125 mm material obtained after comminution and sieving of mine waste rock samples from Traversella mine 130
Table 35 - HH-XRF assays for size class <0.125 mm obtained after comminution and sieving of mine waste rock samples from Traversella mine... 133
Table 36 - Yield, HH-XRF assays, and mineral phases identified by XRPD after separation Test A performed on waste rock samples from Traversella mine. 134
Table 37 - ER values for separation concentrates calculated after separation Test A performed on waste rock samples from Traversella mine. 135
Table 38 - Recovery rates for selected target elements calculated after separation Test A performed on waste rock samples from Traversella mine..... 135
Table 39 - Yield, HH-XRF assays, and mineral phases identified by XRPD after separation Test B performed on waste rock samples from Traversella mine. 136

Table 40 - ER values for separation concentrates calculated after separation Test B performed on waste rock samples from Traversella mine. 137
Table 41 - Recovery rates for selected target elements calculated after separation Test B performed on waste rock samples from Traversella mine.....137
Table 42 – Total yield (Y_{tot}), relative yield to LIMS (Y_{LIMS}) and ST (Y_{ST}), and HH-XRF assays after Test C performed on waste rock samples from Traversella mine. 140
Table 43 – ER values calculated after combined LIMS and ST separation Test C performed on waste rock samples from Traversella mine. 141
Table 44 – Recovery rates for selected target elements after separation Test C performed on waste rock samples from Traversella mine. 141
Table 45 - Yield, HH-XRF assays, and mineral phases identified by XRPD after separation Test D performed on waste rock samples from Traversella mine. 142
Table 46 - ER values calculated after separation Test D performed on waste rock samples from Traversella mine. 143
Table 47 - Recovery rates for selected target elements calculated after separation Test D performed on waste rock samples from Traversella mine. 143
Table 48 - Libiola mine waste dump positions and type description according to ISPRA national mine waste database (ISPRA, 2022) 151
Table 49 - Libiola mine waste dumps ERT data acquisition parameters.....154
Table 50 – Volume estimation resume for Libiola mine waste area, considering indicated and inferred volumes 158
Table 51 - Summary statistics for HH-XRF results for selected detected elements after field measurements on Libiola North and South mine waste dumps (n = 22). *The LOD/2 rule was applied to values below the detection limit.....161
Table 52 - HH-XRF results for major elements and selected minor elements from Libiola Margherita mine waste dump sample (LM1). 164
Table 53 - ICP-MS summary statistics for selected elements for Libiola North and South dumps (*ALS ME-MS81 method) 165
Table 54 - ICP-MS results for selected elements for Libiola Margherita mine waste dump sample LM1 (*: ALS ME-MS81 method). 166
Table 55 - Summary statistics for mean concentrations from ICP-MS analyses of critical and strategic metals from the Libiola North and South dumps compared to crustal abundance. In bold concentration at least 1x time higher than crustal abundance *(Rudnick & Gao, 2014) 173
Table 56 - Summary statistics for mean concentrations from ICP-MS analyses of base and valuable metals from the Libiola North and South dumps. In bold

concentration at least 10x times higher than crustal abundance *(Rudnick & Gao, 2014) 173
Table 57 – List of selected samples from Libiola mine waste and the batch testing time applied for each leaching test. 175
Table 58 - HH-XRF results for target elements and main detected minerals by XRPD on selected samples from Libiola mine waste dumps before leaching tests. 176
Table 59 – Fenice Capanne mine waste accumulation areas position and classification according to ISPRA national mine waste database (ISPRA, 2022) 188
Table 60 - Historical samples from Fenice Capanne mine waste accumulation areas considered in this study. 191
Table 61 - HH-XRF summary statistic for selected major and minor elements for Fenice Capanne tailings samples (n=11). *The LOD/2 rule was applied to values below the detection limit 192
Table 62 - HH-XRF results for major elements and selected minor elements from Fenice Capanne roasting sample FC20. 193
Table 63 - ICP-MS summary statistics for selected elements for Fenice Capanne tailings samples (n = 11). (*: ALS ME-MS81 method; [a]: Values exceeding upper LOD were considered without any modification) 194
Table 64 - ICP-MS results for selected elements for Fenice Capanne roastings dump sample FC20 (*: ALS ME-MS81 method) 195
Table 65 – Summary statistics for XRPD mineral phase abundances for Fenice Capanne tailings samples (n = 11). 197
Table 66 – Critical and strategic raw materials summary from ICP-MS values compared to crustal abundance concentrations for Fenice Capanne tailings and roasting samples. In bold concentration at least 1x time higher than the average abundance. * (Rudnick & Gao, 2014) 199
Table 67 – Crustal abundance comparison of base and valuable metals from Fenice Capanne tailings and roasting samples. In bold concentrations at least x10 times higher than average crustal abundance. *(Rudnick & Gao, 2014) 200
Table 68 - List of selected samples from Fenice Capanne tailings, leaching mode and leaching times applied. 202
Table 69 - P80 values for tailings samples from Fenice Capanne mine 203
Table 70 - HH-XRF results for target elements and main detected minerals by XRPD on selected samples from Fenice Capanne mine waste dumps before leaching tests 204

Table 71 - p80 values for metal-bearing minerals in Fenice Capanne tailings sample FC15 207
Table 72 - RXRF values and detected mineral phases from solid residues after glycine (max time) and sulphuric acid leaching performed on Fenice Capanne tailings samples. 213

List of Figures

Figure 1 - Countries having a CRM list (source: Zhang et al., 2023).....2
Figure 2 – Supply risk of relevant raw materials used in technologies related to crucial EU industrial sectors (source: Eurostat, EU Joint Research Centre).....4
Figure 3 – Map of the CRMs producing countries, showing market shares for the EU (source: European Commission, 2023) 5
Figure 4 - Materials demand forecast for selected raw materials for 2030 and 2050. (LDS: Low Demand Scenario, HDS: High Demand Scenario) (Source: EU Joint Research Center, 2023).....6
Figure 5 - European CRMs and SRMs 2023 list. (source: consilium.europa.eu).....6
Figure 6 – Thematic overview panel of the CRMA, showing main addressed topics and involved stakeholders (source: Hool et al., 2024) 8
Figure 7 - Number of active mines and extracted commodity between 1870 and 2020. MET: Base metals; ORO: Gold; B&F: Baryte and Fluorite; MCI: Ceramic and Industrial minerals; MDC: Cement-grade marl; CFB: Fossil fuels and Bitumen; TAG: Talc, Asbestos and Graphite; SSP: Halite and Potash; ZFO: Sulfur; ALT: Other commodities. (Source: https://www.miniereitaliane.it/).....9
Figure 8 - Map of mine waste facilities, classified according to environmental and sanitary risk (source: ISPRA, 2022) 11
Figure 9 - Degree of association between host metals and primary production of companion metals (source: Nassar et al., 2015).....13
Figure 10 - Traditional extraction process and related waste streams (source: Valenta et al., 2023).....14
Figure 11 - Flowsheet including different mineral processing technologies proposed for the recovery of CRMs from historical tailings in Sweden. (Source: Mulenshi et al., 2019) 16
Figure 12 - A conceptual flowsheet for extracting copper using glycine as a lixiviant (Source: Eksteen et al., 2017).....18
Figure 13 - Scheme of the bioleaching mechanisms on mine tailings substrate (Source: Nguyen et al., 2021) 19
Figure 14 – Phytomining mechanism using hyperaccumulator plants in metal rich soils (Source: Dhiman et al., 2024) 20

Figure 15 – Multi-step methodological scheme followed for the assessment of site selection, sampling, characterization and processing of mine waste case studies in Italy. 24
Figure 16 - Hand-scoop used during sampling campaigns (Photo credits: G. Baldassarre) 25
Figure 17 - Hand auger equipment used during tailings sampling campaign (Photo credits: G. Baldassarre) 25
Figure 18 - Electrode and cable detail during ERT data acquisition on the field (Photo credits: G. Baldassarre) 26
Figure 19 – 3-D printed moulds for SEM and GLE analyses 28
Figure 20 – Procedure for subsampling, crushing and micronisation of mine waste sample for geochemical analyses. 31
Figure 21 - Magutt CR25 laboratory jaw crusher 37
Figure 22 - Magutt M-10 laboratory jaw crusher 37
Figure 23 – Laboratory rod mill 38
Figure 24 - Retsch PM300 planetary ball mill 38
Figure 25 - Induced disk low-intensity magnetic separator, Davies Mod.45 .39
Figure 26 - Eriez Model L4 wet high-intensity magnetic separator 40
Figure 27 – Krupp Humbold-Wedag 1000x500 mm laboratory shaking table 41
Figure 28 - Experimental set-up used during leaching tests performed (Photo credits: G. Baldassarre) 43
Figure 29 - Map of selected mine waste site for the study. (source: Google satellite image) 50
Figure 30 – Total $t_{EI,eq}$ values for mine sites reporting more than 5Mt (top) and less than 5Mt (bottom) of tailings reported in the Finnish mine waste database 55
Figure 31 - Economic value for mine sites having more (top) and less than (bottom) 5Mt of tailings reported in the Finnish mine waste database 57
Figure 32 - Location of smelter facilities in Finland (source: Google satellite images) 58
Figure 33 - Radar plot for road distances between smelter plants in Finland and selected tailings sites in kilometres (km). 59
Figure 34 - Total Equivalent EI tons and Economic value for tailings sites having more than 5Mt (top) and less than 5Mt (bottom) of tailings selected in the Finnish mine waste database. 61
Figure 35 - 3-D Decision Matrix prototype for selecting priority action on tailings sites selected in the Finnish mine waste database. Grey: Negligible

actions; Green: Programmable actions; Yellow: Recommended actions; Red: Highly recommended actions; Black: Urgent actions 64
Figure 36 - The UNFC classification system with its three fundamental category definitions of environmental-socio-economic viability (E-axis), technical feasibility (F-axis), and the level of confidence (G-axis). (Source: United Nations, 2020) 68
Figure 37 - (a) Regional geological map of the Kanmantoo region, Australia (after Pollock et al., 2018) (b) Cu grades measured from exploration campaigns realised by Hillgrove Resources in the Kanmantoo area, Australia. (GABS = garnet-andalusite-biotite schist, source: Hillgrove Resources (2020)) 73
Figure 38 - Satellite view of the actual status of the Kanmantoo mine, Australia. Yellow: new tailings storage facility; Red: old tailings storage facility; Green: Giant Pit, currently exploited by underground operations; Orange: Waste rock dump produced by Giant Pit excavation; Blue: mineral processing plant. (source: Google satellite image, Coordinate system: WGS84) 74
Figure 39 - Drill holes and sampling positions performed in previous studies in the old TSF of the Kanmantoo mine, Australia (after Agnew, 1998) 75
Figure 40 - Old tailings storage facility view at the Kanmantoo mine, Australia, during sampling operations (Photo credits: F. Colombi and G. Baldassarre, 2024) 76
Figure 41 - Location of drill holes and sampling points in the old tailings storage facility, Kanmantoo mine, Australia. (source: Google satellite image, Coordinate system: WGS84) 77
Figure 42 - Recovered tailings material from old tailings storage facility (Hole KA07) in the Kanmantoo mine, Australia. Top left: Start of the hole, Bottom right: End of the hole (Photo credits: G. Baldassarre, 2024). 77
Figure 43 – Observed facies and colours of tailings material recovered from drill holes realized during sampling operations in the old TSF, Kanmnatoo mine, Australia (source: Colombi et al., 2024).....78
Figure 44 – Boxplot for selected elements assayed in the old tailings storage facility, Kanamntoo mine, Australia, according to the realised holes (n = 38) (source: Colombi et al., 2024) 79
Figure 45 - Downhole plot of ICP-MS data collected in the old tailings storage facility, Kanmantoo mine, Australia, for S (%), Fe (%), Cu (ppm), and Co (ppm) (source: Colombi et al., 2024).....81
Figure 46 - Downhole plot of ICP-MS data collected in the old tailings storage facility, Kanmantoo mine, Australia, for Al (%), Fe (%), Mn (ppm), Bi (ppm) LREE (ppm) and HREE (ppm) (source: Colombi et al., 2024).....82

Figure 47 - Spatial plots for selected elements across old tailings facility, Kanmantoo mine, Australia: (a) Cu; (b) Mn. (source: Google satellite image. Coordinate system: WGS84) 83
Figure 48 - Spatial plots for selected elements across the old tailings facility, Kanmantoo mine, Australia: (a) Co; (b) Bi (source: Google satellite image. Coordinate system: WGS84) 84
Figure 49 - Mineral phase abundance determined by XRPD of selected samples from the old tailings storage facility, Kanmantoo mine, Australia (n = 6) 86
Figure 50 - Modal mineralogy calculated from MLA data of old tailings facility samples, Kanmantoo mine, Australia (n = 6). 87
Figure 51 – Classified MLA mineralogy images for tailings samples from old tailings storage facility of the Kanmantoo mine, Australia: (a) sample KA35; (b) sample KA62. (after Colombi et al., 2024).....89
Figure 52 – Particle size distribution of selected minerals contained in analysed samples from old tailings facility of the Kanmantoo mine, Australia: (a) pyrite (n = 4); (b) garnet (n = 6); (c) Iron oxides (n = 6) (source: Colombi et al., 2024) 90
Figure 53 - Mineral associations for samples from the old tailings storage facility of the Kanmantoo mine, Australia: (a) pyrite (n = 4); (b) garnet (n = 6); (c) iron oxides (n = 6). (source: Colombi et al., 2024).....91
Figure 54 - LA-ICP-MS compositional pattern for garnet sample KA35_gnt-56 from old tailings storage facility of the Kanmantoo mine, Australia. (source: Colombi et al., 2024) 93
Figure 55 - Correlation diagram for elements having R >0.7 measured in garnet samples (n = 187) from the old tailings storage facility of the Kanmantoo mine, Australia (source: Colombi et al., 2024).....94
Figure 56 - LA-ICP-MS compositional pattern for pyrite sample KA62_py-02 from old tailings storage facility of the Kanmantoo mine, Australia. (source: Colombi et al., 2024) 94
Figure 57 - Correlation diagram for elements having R > 0.7 measured in pyrite samples (n = 7) from the old tailings storage facility of the Kanmantoo mine, Australia (source: Colombi et al., 2024).....95
Figure 58 - Spider plot showing geochemistry summary statistic for old tailings storage facility samples from the Kanmantoo mine, Australia, normalised to the average crustal abundance values (Rudnick & Gao, 2014). (source: Colombi et al., 2024) 96

Figure 59 - Geological map of the Traversella area (readapted from Nimis, 2014) 104
Figure 60 – (**a**) Position of potential mine waste area around Traversella mine (red line), Traversella mine's old processing plant (blue line), and position of proven mine waste dump piles (red diamonds); (**b**) NDVI soil coverage layer and mine waste areas dump positions (source: Google Satellite Image. Coordinate system: WGS84/UTM Zone 32N) 107
Figure 61 - (a) Photograph of "Piano Svedesi", Traversella mine, sampling point showing the 3 × 3 elements grid; (b) Zoomed photograph of sampling section #4 (source: Baldassarre et al., 2025) 108
Figure 62 – Detail of a waste rock fragment collected in "Piano Svedesi" waste rock dump site in the Traversella mine area (source: Baldassarre et al., 2025) 109
Figure 63 - Optical microscopy images of thin section in parallel transmitted light (PL) and cross-polarised light (XPL) from Traversella mine waste rock samples: (a) Thin Section #1, PL; (b) Thin Section #2, XPL; (c) Thin Section #2, PL; (d) Thin Section #2, XPL. Identified minerals: Ap – Apatite, Mag – Magnetite, Tlc – Talc, Chl – Chlorite, Lz – Lizardite. (source: Baldassarre et al., 2025) 110
Figure 64 – Optical microscopy images of thin sections in parallel transmitted light (PL) and cross-polarised light (XPL) from Traversella mine waste rock samples: (a) Thin Section #3, PL; (b) Thin Section #3, XPL. Identified minerals: Ap – apatite, Mag – magnetite, Tlc – talc, Chl – chlorite, Lz – lizardite, Mlc – malachite. (source: Baldassarre et al., 2025) 111
Figure 65 - XRPD spectrum for the bulk sample material sampled in Piano Svedesi area, Traversella mine. 112
Figure 66 - Spider-plot for the geochemical summary of Piano Svedesi samples, Traversella mine, normalized against average abundance of elements in the Earth's crust by Rudnick & Gao, 2014 115
Figure 67 - Spider plot comparing Piano Svedesi, Traversella mine, elemental concentration with the normalised metallic element limits established by Legislative Decree 152/2006. Green: elements exceeding Column A; Blue: elements exceeding Column B 116
Figure 68 - Size reduction procedure for obtaining size fractions suitable for lab-scale processing trials of waste rock samples from Traversella mine. 118
Figure 69 - XRPD spectrum for feeding material 0.250-0.125 mm size class obtained after comminution and sieving of waste rock samples from Traversella mine. 119

Figure 70 - (a) SEM-BSE image for sample 0.250-0.125mm obtained after comminution and sieving of waste rock samples from Traversella mine; (b) Mineralogy image for the same sample as determined by MLA.....120
Figure 71 – Modal mineralogy pie chart for size class 0.250-0.125 mm obtained after comminution and sieving of waste rock samples from Traversella mine. 121
Figure 72 - (a) SEM-BSE image from epoxy-mounted samples of 0.125–0.250 mm material obtained after comminution and sieving of waste rock samples from Traversella mine (yellow dot: pyrite grain; blue dot: magnetite grain; green dot: gangue mineral grain); (b) EDS spectrum and quantification for pyrite (yellow dot); (c) EDS spectrum and quantification for magnetite (blue dot); (d) EDS spectrum and quantification for silicate gangue mineral (green dot) (source: Baldassarre et al., 2025).....122
Figure 73 - Magnetite mineral association in the 0.250-0.125mm size class obtained after comminution and sieving of waste rock samples from Traversella mine. 123
Figure 74 - Scheelite mineral association in the 0.250-0.125mm size class obtained after comminution and sieving of waste rock samples from Traversella mine. 123
Figure 75 - (a) SEM-BSE image from epoxy-mounted samples of the size class 0.25–0.125 mm obtained after comminution and sieving of waste rock samples from Traversella mine; (b) binary mask for magnetite grains; and (c) binary mask for gangue minerals associated with magnetite grains. (source: Baldassarre et al., 2025).....124
Figure 76 - TD_BSE2 specimen BSE image of 0.250–0.125 mm material, obtained after comminution and sieving of waste rock samples from Traversella mine, with grain contours overlapping (green contours: magnetite; red contours: gangue) (source: Baldassarre et al., 2025).....125
Figure 77 - Liberation characteristics of magnetite in size class 0.250–0.125 mm material after comminution and sieving of mine waste rocks from Traversella mine obtained from BSE image fields TD_BSE1, TD_BSE2, and TD_BSE3, and average liberation values. (source: Baldassarre et al., 2025).....126
Figure 78 - Calculated particle size distribution curves for magnetite free-grains, according to their equivalent diameter from image analyses, for size class 0.250–0.125 mm material after comminution and sieving of mine waste rocks from Traversella mine (source: Baldassarre et al., 2025).....126

Figure 79 - Particle size distribution for magnetite and scheelite from the 0.250-0.125mm size class after comminution and sieving of mine waste rocks from Traversella mine.....127
Figure 80 - Liberation analysis for magnetite and scheelite grains contained in the 0.250-0.125mm size class material obtained after comminution and sieving of mine waste rock samples from Traversella mine.....128
Figure 81 – XRPD spectrum for size class < 0.125 mm material 0.250-0.125mm size class material obtained after comminution and sieving of mine waste rock samples from Traversella mine.....130
Figure 82 - (a) SEM-BSE image of scheelite grain from size class < 0.125 mm material obtained after comminution and sieving of mine waste rock samples from Traversella mine; (b) EDS Spectrum and quantitative chemical analysis (source: Baldassarre et al., 2025).....131
Figure 83 - (a) SEM-BSE image of a malachite grain from size class<0.125 mm obtained after comminution and sieving of mine waste rock samples from Traversella mine; (b) ESD spectrum and quantitative chemical analysis (source: Baldassarre et al., 2025).....132
Figure 84 – Separation Test A flowsheet: dry magnetic separation using LIMS on size class 0.250-0.125 mm material obtained after comminution and sieving of mine waste rock samples from Traversella mine.....134
Figure 85 – Separation Test B flowsheet, gravity separation using ST on size class 0.125-0.250 mm material obtained after comminution and sieving of mine waste rock samples from Traversella mine.....136
Figure 86 - Metal grade of target elements (Fe, W, Cu) plotted as a function of recovery rate of each output product after separation trials, Test A and Test B, performed on waste rock samples from Traversella mine. ER is reported only for values >1, assuming a reached concentration after separation. (source: Baldassarre et al., 2025) 138
Figure 87 - Test C flowsheet, combined dry magnetic and gravity separation using LIMS and ST on size class 0.125-0.250 mm material obtained after comminution and sieving of mine waste rock samples from Traversella mine...139
Figure 88 - Test D flowsheet, wet magnetic separation using WHIMS on size class <0.125 mm material obtained after comminution and sieving of mine waste rock samples from Traversella mine.....142
Figure 89 - Geological setting of the Libiola mine area, with details regarding local lithologies, surface water streams and villages (adapted and modified after Marescotti et al., 2003) 148

Figure 90 - Libiola Mine scheme, showing open pit area (dark pink) and underground works (adapted and modified after Marescotti et al, 2003).....149
Figure 91 - (a) Poorly sorted and eroded material from North mine waste dump, Libiola mine; (b) Detail of mine waste accumulation strata in the South dump, Libiola mine (Photo credits: G. Baldassarre, 2024) 150
Figure 92 - (Top) Position of mine waste in the Libiola mine area according to ISPRA database (ISPRA, 2022) (magenta stars), old pit area (blue line), and perimeter of mine waste dumps considered in this study (red line); (Bottom) NDVI soil coverage layer and considered mine waste areas (source: Google Satellite Image. Coordinate system: WGS84/UTM Zone 32N) 152
Figure 93 - (a) Panoramic view of North mine waste dump, Libiola mine; (b) Panoramic view of South mine waste dump, Libiola mine (Photo credits: G. Baldassarre, 2023(a), 2024 (b)) 153
Figure 94 - (Left) ERT lines location on the South mine waste dump, Libiola mine; (Right) ERT line realised on the North mine waste dump, Libiola mine (source: Google Satellite Image. Coordinate system: WGS84/UTM Zone 32N)155
Figure 95 – ERT1 2D resistivity inversion profile realised on the South mine waste dump, Libiola mine. (Pink line: evaluated mine waste boundary) (Image Courtesy: C.Colombero).....156
Figure 96 – ERT2 2D resistivity inversion profile realised on the South mine waste dump, Libiola mine. (Pink line: evaluated mine waste boundary) (Image courtesy: C. Colombero).....156
Figure 97 - ERT3 2D resistivity inversion profile realized on the North mine waste dump, Libiola mine. (Pink line: evaluated mine waste boundary; Black line: bedrock) (Image courtesy: C. Colombero) 157
Figure 98 - (a) HH-XRF field measurements, according to 3 identified sectors; (b) Sampling vertical trench showing the three sectors forming the total amount of material collected. Sampling point LN8, North mine waste dump, Libiola mine (Photo credits: G. Baldassarre, 2024).....159
Figure 99 - (Left) Sampling points location on the South and Margherita mine waste dumps, Libiola mine; (Right) Sampling points location on the North mine waste dump, Libiola mine (source: Google Satellite Image. Coordinate system: WGS84/UTM Zone 32N). 160
Figure 100 - (a) Comparison of HH-XRF and ICP-MS data for Cu considering the entire dataset of acquisitions of Libiola waste rock samples, (b) Data comparison for concentrations < 10,000 ppm; (c) Data comparison for concentrations > 10,000 ppm. Red line: x = y = ICP-MS values 167

Figure 101 - Comparison of HH-XRF and ICP-MS for selected element acquisitions regarding considered Libiola waste rock samples : (a) Ni, (b) Co, (c) Zn. Red line: x = y = ICP-MS values 168
Figure 102 - Quantitative XRPD mineralogical determination for selected samples from Libiola North dump (n = 7), South dump (n = 6), and Margherita dump (n = 1). (Data courtesy: C. Carbone and G. Specchia) 170
Figure 103 - Average mineral abundance for Libiola North dump, from XRPD data (Data courtesy:C.Carbone and G. Specchia).....171
Figure 104 - Average mineral abundance for Libiola South Dump from XRPD data (Data courtesy: C. Carbone and G. Specchia).....171
Figure 105 - Spider plot for the geochemical summary of Libiola North and South dumps samples, with mean values normalised against the average abundance of elements in the Earth's crust by Rudnick & Gao, 2014. 172
Figure 106 - Spider plot comparing Libiola North and South dumps mean elemental concentration with the normalised metallic element limits set by Legislative Decree 152/2006. Green: elements exceeding Column A; Blue: elements exceeding Column B. 174
Figure 107 - pH values variation over glycine leaching time for Libiola mine waste samples. 177
Figure 108 - R_{ICP} calculated values for Cu after glycine leaching (Gly) and sulphuric acid leaching (H_2SO_4), for each of the tested Libiola mine waste samples 178
Figure 109 - R_{ICP} values for Cu as a function of glycine leaching time for the tested Libiola mine waste samples.....178
Figure 110 - Comparison of R_{ICP} values for Fe, considering the maximum glycine leaching time and sulphuric acid leaching for Libiola mine waste samples. 179
Figure 111 - Comparison of R_{ICP} and R_{XRF} values for Cu, obtained after post-leaching characterization of Libiola mine waste samples 180
Figure 112 - Geological section sketch of the Fenice Capanne Lode. Legend: cl - Flysch; cv - Cavernous limestone; ev - Anhydrites; fi - Phyllites with anhydrite intercalations; BH - Exploration boreholes. (modified after Arisi Rota et al., 1971) 184
Figure 113 – "Linea 2000" flotation cells in the Fenice Capanne mineral processing plant (1984). (Photo credits: M. Gilli, 1984) 186
Figure 114 - "Linea 1000" grinding mills in the Fenice Capanne processing plant (1984). (Photo credits: M. Gilli, 1984) 187

Figure 115 - (Left) Position of mine waste accumulation areas around Fenice Capanne mine according to ISPRA database (ISPRA, 2022) and other authors (Benvenuti et al., 1999, Mascaro et al., 2001); (Right) NDVI soil coverage layer and considered mine waste areas (Source: Google Satellite Image. Coordinate System: Gauss Boaga West). 189
Figure 116 - Comparison of HH-XRF and ICP-MS assays of Fenice Capanne tailings samples for: (a) Cu, (b) As, (c) Pb, (d) Bi, (e) Zn, (f) Sb. Red line: x=y=ICP-MS values. 196
Figure 117 - Quantitative XRPD mineralogical determination for samples from Fenice Capanne accumulation areas (n = 12). 197
Figure 118 – Spider plot showing geochemistry summary statistic for Fenice Capanne tailings and roastings samples compared to the average crustal abundance values by Rudnick & Gao, 2014 198
Figure 119 – Spider plot comparing Fenice Capanne tailings and roasting elemental concentrations to the Italian Law Decree 152/2006 limit for soil contamination. Green: elements exceeding Column A; Blue: elements exceeding Column B. 201
Figure 120 - PSD of tailings sample from Fenice Capanne mine selected for leaching tests 203
Figure 121 - SEM BSE images of tailings sample from Fenice Capanne: (a) FC2 sample full frame BSE image; (b) BSE image of pyrite grain from sample FC2; (c) FC10 sample full frame BSE image; (d) BSE image of pyrite (brown dot) and sphalerite (blue dot) grains from sample FC15; (e) FC5 full frame BSE image, with a chalcopyrite grain (red circle). 205
Figure 122 - Modal mineralogy pie chart for Fenice Capanne tailings sample FC15 206
Figure 123 - Mineral association of metal-bearing minerals in Fenice Capanne tailings sample FC15 207
Figure 124 - Particle size distribution of metal-bearing minerals detected in Fenice Capanne tailings sample FC15 207
Figure 125 - pH values variation over glycine leaching time for Fenice Capanne tailings samples. 208
Figure 126 - R_{ICP} calculated values for Cu after glycine leaching (Gly) and sulphuric acid leaching (H_2SO_4), for each of the tested Fenice Capanne tailings sample. 209
Figure 127 - R_{ICP} calculated values for Zn after glycine leaching (Gly) and sulphuric acid leaching (H_2SO_4), for each of the tested Fenice Capanne tailings sample 210

Figure 128 -R_{ICP} values for Cu (top) and Zn (bottom) as a function of glycine leaching time for Fenice Capanne tailings samples.....211
Figure 129 - Comparison of R_{ICP} values for Fe, considering the maximum glycine leaching time and sulphuric acid leaching for the considered Fenice Capanne tailings samples.....212
Figure 130 - Comparison of R_{ICP} and R_{XRF} values for Cu (top) and Zn (bottom), obtained after post-leaching characterisation of Fenice Capanne tailings samples.....214

Chapter 1

1. Introduction

The demand for raw materials, driven by industrial development, ecological transition and digital transformation, is posing important challenges to raw materials supplies worldwide. Mining operations are facing significant challenges due to declining ore grades, increasing environmental constraints, geopolitical and social acceptance issues, raising the need for alternative, secure, and more sustainable sources of raw materials.

Mine waste, having originated from active or historical mining operations, can represent a potential secondary source of crucial minerals and metals. These anthropogenic materials could host a significant amount of raw materials that were not recoverable or were overlooked in past industrial activities, due to different economic, technological or geopolitical conditions. Additionally, mine waste accumulation could generate environmental contamination affecting relevant portions of land, highlighting the need for urgent remediation actions.

National and International law have introduced policies for mapping, characterising, and proposing actions for the recovery of critical elements from extractive waste materials. Mine wastes present specific and site-dependent conditions, requiring appropriate methodologies to identify, evaluate and assess potential recovery strategies.

In this Thesis, starting from relevant international examples and best- practice approaches, developed for mine waste data collection and comprehensive characterisation, a data-driven methodological procedure is designed and applied to selected case studies in Italy. The proposed approach aims to reduce existing knowledge gaps and support the identification of possible solutions for assessing the potential recovery of valuable elements from mine waste.

1.1 Critical and strategic raw materials: a worldwide issue

In modern society, technological development, industrial applications, ecological transition and digital transformation require a wide range of raw materials, metals and minerals. These materials are economically and technically essential for the production of renewable energy, e-mobility, and defence technologies, while at the same time, they are usually limited and unevenly distributed on the Earth's Crust (Hofmann, Hofmann, Hagelüken, & Hool, 2018). As a consequence, many of these raw materials are facing a high risk of supply disruption, limited substitution possibilities and leverage geopolitical tensions, becoming industrially and economically essential for many crucial industrial sectors in the world. (Lewicka, Guzik, & Galos, 2021; Maltais, Canales, & Larsen, 2026).

The concept of critical raw materials (CRMs) has been mainly discussed in the last few decades in the Global North of the planet, especially in North America, Europe, and Japan. The same definition of "criticality" showed different, but similar definitions in national and international regulations (Fojtíková, Pekarčíková, Sousedíková, Vaněk, & Dvořáček, 2025; Lewicka et al., 2021).

Different methodologies have been developed to assess and quantify the criticality of selected metals and minerals according to a specific economic and industrial background (Zhang, Bourdeau, Nwaila, & Ghorbani, 2023). Countries having a CRMs list are Australia, China, South Korea, Japan, the United Kingdom, Canada and the European Union, as reported in Figure 1 (Zhang et al., 2023).

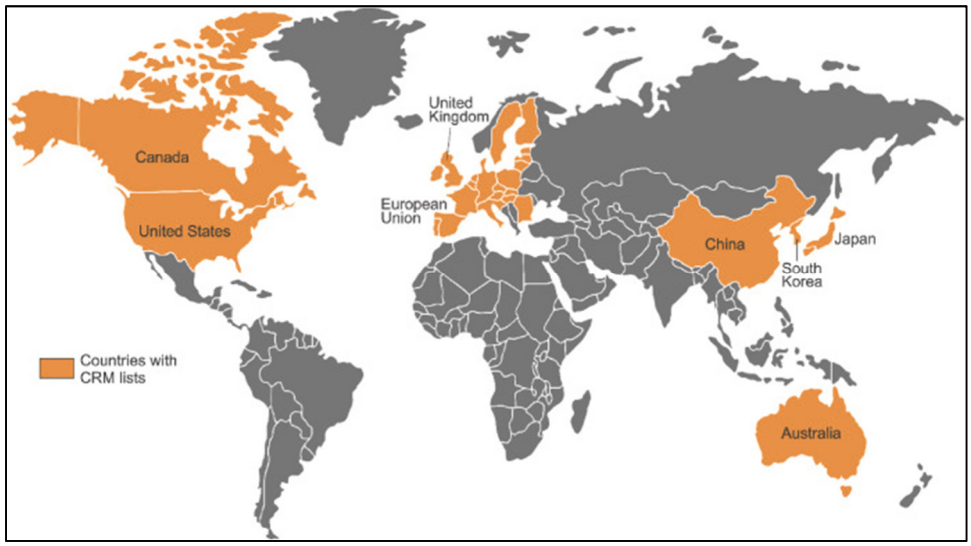


Figure 1 - Countries having a CRM list (source: Zhang et al., 2023)

Concerning Europe, the first initiative for defining a CRMs list was formulated in 2011, and the list has been updated every three years (2011, 2014, 2017, 2020, 2023), being the political institution having the longest series of criticality assessments (Zhang et al., 2023). A systematic methodology for defining the CRMs list was released in 2017 and continuously applied to the following updates (European Commission, Directorate General for Internal Market, Industry, Entrepreneurship, and SMEs).

According to this methodology, a raw material is defined as "critical" if it shows a high economic importance for the continental industry and whose supply is associated with high risk (Blengini et al., 2017). Furthermore, in 2023, "strategic raw materials" (SRMs) were defined as a subgroup of the CRMs list. The strategic importance was defined according to the relevance that a certain raw material had towards green and digital transition, defence and aerospace applications, according to different parameters, such as the type and quantity of technologies that require a certain raw material and the demand for strategic technologies foreseen on a global scale (European Union, 2025a).

Some authors agree on the assumption that CRMs and SRMs supply risk is only partially related to a physical scarcity, but is especially bound to different aspects, such as geopolitics, market strategy, circular performance, and governance actions (Arendt, Muhl, Bach, & Finkbeiner, 2020; Hool, Helbig, & Wierink, 2024; Montana et al., 2024). Additionally, supply risk for raw materials in Europe is also linked to some structural vulnerabilities that characterise its economic and industrial background (Figure 2).

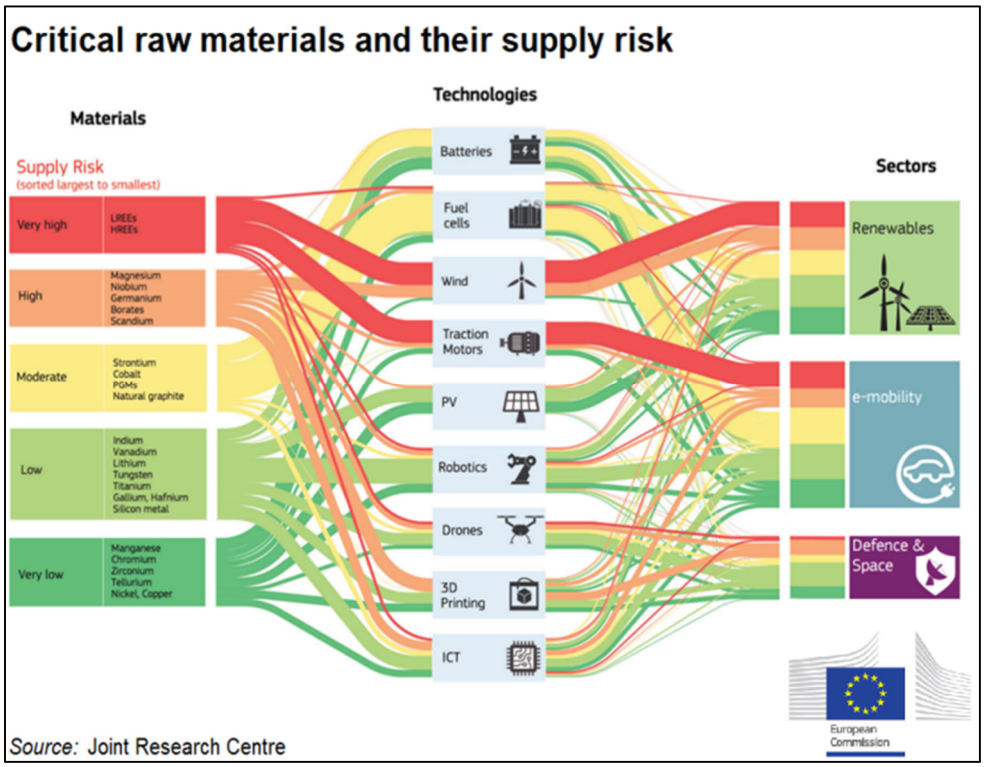


Figure 2 – Supply risk of relevant raw materials used in technologies related to crucial EU industrial sectors (source: Eurostat, EU Joint Research Centre)

For example, the EU industry imports most of the metals needed for its domestic industry, accounting for 25-30% of the global metal consumption, but this situation is weakly counterbalanced by new domestic supplies resulting from exploration, mining and processing (Arendt et al., 2020; Berthet et al., 2024). As a consequence, the limited extraction and processing capacity produced higher overall supply risk for many key raw materials (Kannan, Fleming, Hirwa, Castillo, & Eggert, 2025). Furthermore, the source of important raw materials is concentrated in a few supplier countries, which hold both production and processing technologies and could be associated with weak governance or trade measures used strategically (Hool et al., 2024; Zhang et al., 2023). In particular, China's dominant role in the primary processing and supply of some energy-transition materials (Figure 3), mainly used for green energy technologies, exposes the EU industries to operational bottlenecks and price volatilities for both supplies and final products (Rabe, Kostka, & Smith Stegen, 2017; Sesini, Zwickl-Bernhard, Münchmeyer, & Hobbs, 2025).

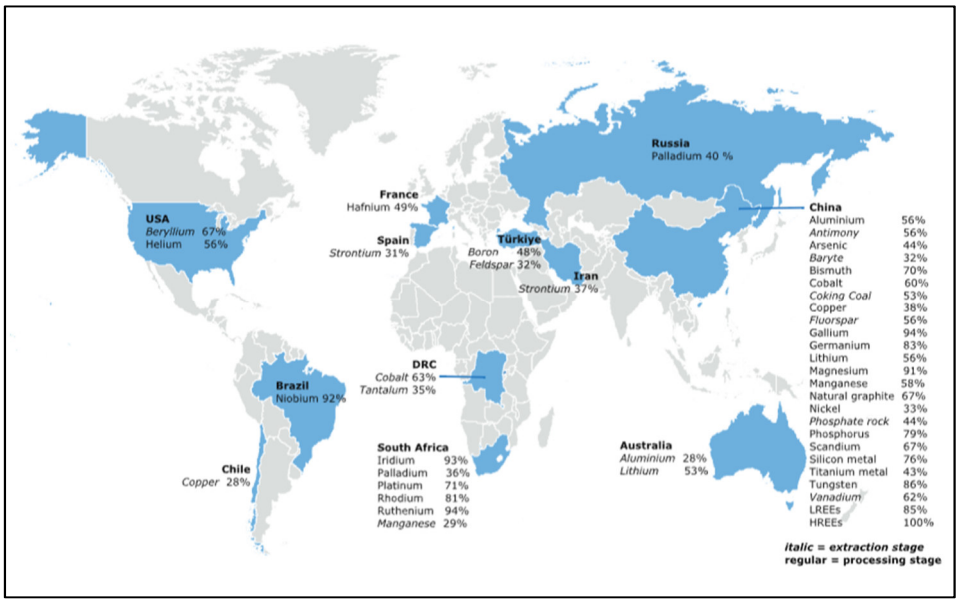


Figure 3 – Map of the CRMs producing countries, showing market shares for the EU (source: European Commission, 2023)

Additional variables that worsen the EU supply risk can also be found in the technology-driven demand growth, mainly imposed by challenging political goals introduced by recent EU policies, in particular the European Green Deal and the 2050 Long-Term Strategy for Climate Neutrality (European Commission, 2023; European Commission, 2019), which boosted the demand of certain CRMs and SRMs faster than the development of an alternative supply chains characterized by a lower risk (Figure 4). As a result, many materials rose in economic importance and criticality in a short period of time, triggering a narrow set of metals to become exceptionally critical (Feichtinger & Posch, 2025; Montana et al., 2024; Zhang et al., 2023). Challenges for the reduction of supply risk for certain raw materials are posed by recycling and substitution actions that could change the import mix. Still, the mitigation effect depends on the ability to create a high domestic collection of end-of-life products and scraps, processing capabilities and the reintroduction of these materials into the industrial value chain (Santillán-Saldivar et al., 2021). Nevertheless, for many CRMs, supply risk is challenging to mitigate due to low recycling rates and limited technical substitution options (Løvik, Hagelüken, & Wäger, 2018; Zhang et al., 2023).

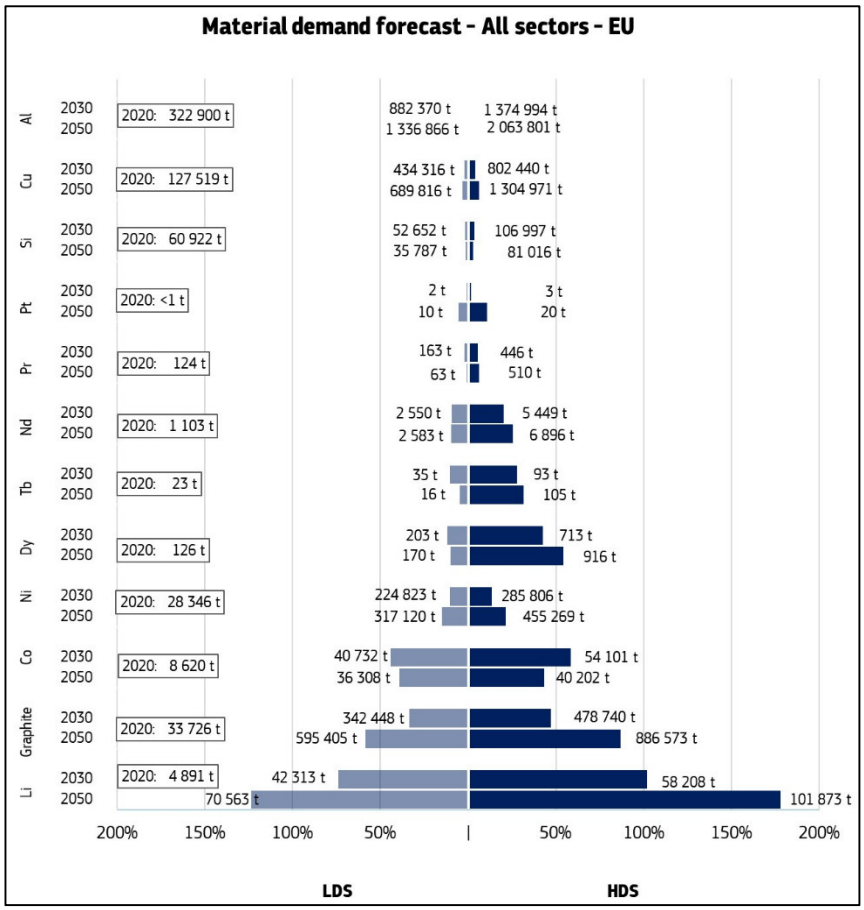


Figure 4 - Materials demand forecast for selected raw materials for 2030 and 2050. (LDS: Low Demand Scenario, HDS: High Demand Scenario) (Source: EU Joint Research Center, 2023)

According to the latest assessment completed in 2023, the European CRMs and SRMs list contains 32 CRMs and a subgroup of 17 SRMs (European Commission, 2023c), as reported in Figure 5.

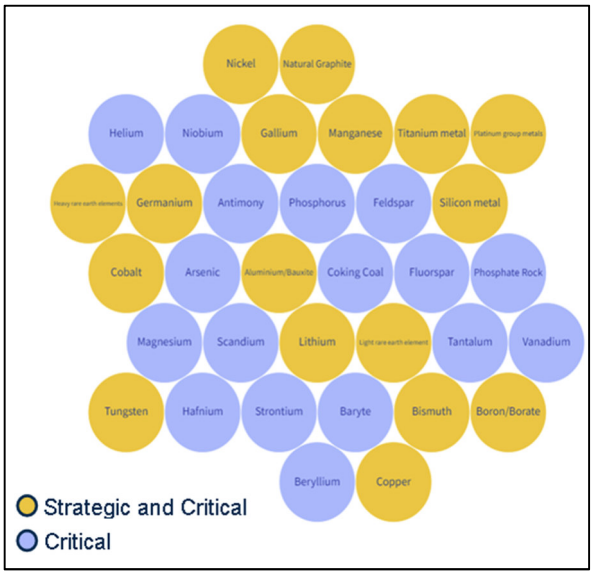


Figure 5 - European CRMs and SRMs 2023 list. (source: consilium.europa.eu)

1.2 European law framework for addressing a secure supply of raw materials: the role of extractive waste

The EU response to address the structural problem of the supply of CRMs and SRMs was formally introduced through the publication of the Critical Raw Materials Act (CRMA) in 2023 (European Commission, 2023b).

This new legal action aimed at creating a binding continental framework to achieve a secure and sustainable supply of CRMs and SRMs over a fixed time span by 2030 (Correia, Falck, & Komac, 2024; Hool et al., 2024). In particular, the CRMA defined clear objectives for an overall strengthening of the EU raw materials value chain, a diversification of imports to reduce the dependence on a single third country, an improvement in the monitoring and management of risks related to supply disruptions, and an increase in circular and sustainable practices for raw materials use.

Some quantitative benchmark targets were defined to specifically address the CRMs and SRMs continental supply issues. In particular, the Act requires achieving at least 10% of the annual consumption extracted from domestic sources, at least 40% of CRMs and SRMs processed within the EU, and obtaining 15% of the supply from domestic recycling. In addition, the annual sourcing of every single SRMs should be limited to 65% from a single third country (European Union, 2023). These defined targets are foreseen to be supported by a set of selected "strategic projects" focusing on extraction, processing and recycling of CRMs/SRMs, which can benefit from fast-track permitting and coordinated financing (Hool et al., 2024). The first list of approved strategic projects was released in 2025, identifying 47 proposals within the EU and 13 projects within partner countries (European Union, 2025b).

The scheme reported in Figure 6 summarises the main aspects introduced by the CRMA, the topic addressed by each article and the involved stakeholders for each stage, according to Hool et al. (2024).

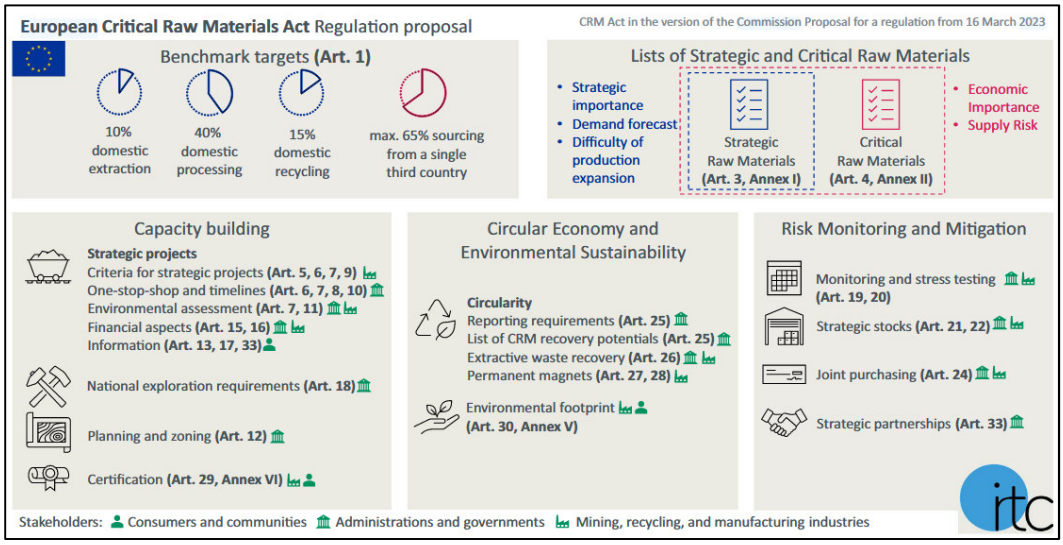


Figure 6 – Thematic overview panel of the CRMA, showing main addressed topics and involved stakeholders (source: Hool et al., 2024)

Among many innovative aspects introduced by the CRMA, the recovery of CRMs and SRMs from extractive waste was treated as a relevant feature for circularity and environmental sustainability and as a core pillar for introducing new possible raw materials streams in the continental industry.

In detail, Article 26 announced some obligations for mining operators and Member States for systematically assessing and evaluating the potential recovery of CRMs and SRMs in mining waste streams. Private operators are required to perform preliminary studies for the definition of presence, quantities and recovery possibility of CRMs in stored extractive waste and for waste material generated during exploitation operations. In parallel, Member States are mandated to create publicly available databases of closed and abandoned extractive waste facilities, including details such as location, surficial extent, waste volumes, the approximate quantities and concentrations of all raw materials potentially contained, and any other relevant information useful for enabling the recovery of CRMs and SRMs from waste materials. To provide these details, Member States were asked to undertake specific activities for all the closed waste facilities, including a comprehensive review of the permitting paperwork, representative geochemical sampling and, where potentially economically recoverable quantities of CRMs are indicated, a more detailed analysis such as exploratory drilling and core logging. Furthermore, a United Nations Framework Classification for Resource (UNFC) should be included and made public in the database (European Union, 2023).

1.3 Mining waste in Italy: background and regulatory actions

The mining industry in Italy has been characterised by significant historical industrial activity, particularly between the late 1800s and the first half of the 20th century. In detail, the temporal evolution of active mining sites in Italy, as shown in Figure 7, reached the highest number of active mining operations between the 1920s and the 1960s, recording a total of 1,231 active operations in 1945 (Dacquino, 2026).

Mining activity showed a constant increase in the number of operations until the 1950s, mainly sustained by base metals, sulphur, fossil fuels, cement-grade marl, and ceramic and industrial minerals extraction. In 1965, the mix of mined commodities was composed of 6 groups of commodities, such as base metals, Sulphur, talc and asbestos, halite and potash, ceramic and industrial minerals, fossil fuels and cement-grade marl. From this point, the number of sites had been constantly decreasing until reaching the historical minimum of the first decades of the 21st century. (Dacquino, 2026)

The most significant decrease was the abrupt cessation of base metals and sulphur operations in the 1970s, limiting the exploited commodities mainly to industrial and ceramic minerals and cement-grade marls, represented by 49 and 15 sites, respectively.

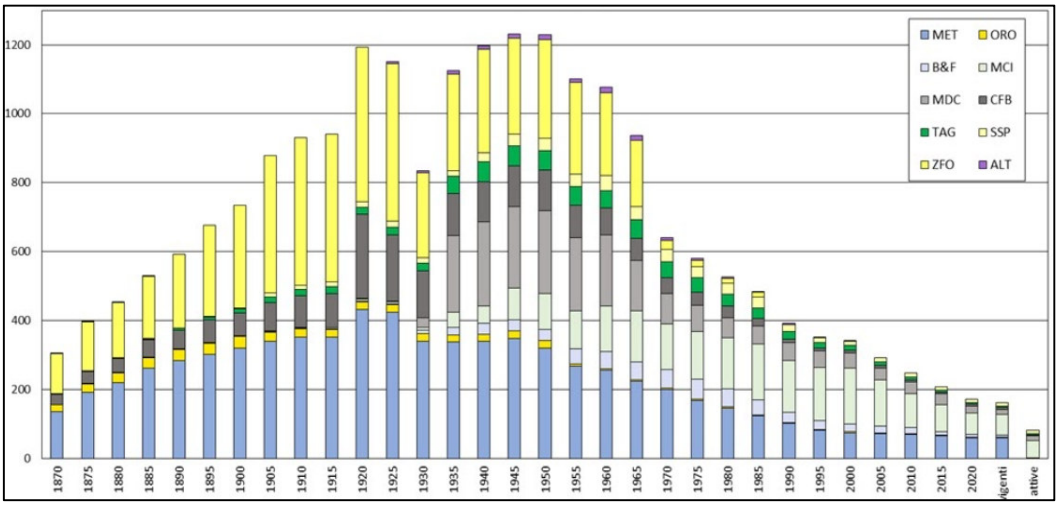


Figure 7 - Number of active mines and extracted commodity between 1870 and 2020. MET: Base metals; ORO: Gold; B&F: Baryte and Fluorite; MCI: Ceramic and Industrial minerals; MDC: Cement-grade marl; CFB: Fossil fuels and Bitumen; TAG: Talc, Asbestos and Graphite; SSP: Halite and Potash; ZFO: Sulfur; ALT: Other commodities. (Source: https://www.miniereitaliane.it/)

As previously described, the Italian mining industry faced a strongly declining phase starting from the 1970s in line with the European mining trends, due to competition from cheaper extra-European producers, technological changes, stricter environmental regulations, and social opposition to mining extraction. Additionally, obsolete mining techniques and low productivity made many Italian sites less competitive under new global market conditions, especially during the oil shocks period in the 1980s. As a consequence, by the 1990s, most of the base

metal mines in Italy were permanently closed (Aristone & Loreto, 2016; Pistolesi, 2024).

Most of the domestic mining extraction, until the present day, remained significant for construction materials, industrial and ceramic minerals, such as limestone, marl and clays (Luino et al., 2024). In fact, Italy was ranked as the second worldwide producer of feldspar and nepheline syenite, accounting for the 17% global production, while showing relevant extracted quantities of industrial sand, gravel, and dimension stones. By contrast, by 2024, mining operations targeting base metals have largely ceased (Abdale & Trimmer, 2023; Trimmer, 2024).

Many of the decommissioned Italian mining sites have been facing post-industrial challenges related to the long-term management of former mining areas, especially for environmental degradation due to abandoned mine sites and waste and difficult economic alternatives to promote a transition toward different businesses (Deiana & Giua, 2023).

According to the European Mine Waste Directive (2006/21/EC), the Italian Institute for Environmental Protection and Research, ISPRA (Istituto Superiore per la Protezione e la Ricerca Ambientale), has been updating national inventory of closed waste storage facilities, a census for abandoned structures potentially associated to severe negative effects on the environment, or which can pose ecotoxicological threat to human health. ISPRA published the last two updates of the inventory in 2017 and 2022 (Serra & Andrisani, 2017, 2022). In the most recent 2022 update, 583 mine waste sites were identified within the Italian territory. Regions having the largest number of mine waste facilities are Sardinia (209 sites), Lombardy (128 sites), Tuscany (76 sites), Piedmont (57 sites), and Liguria (25 sites), being associated with most of the collocation of historical mining districts (Figure 8).

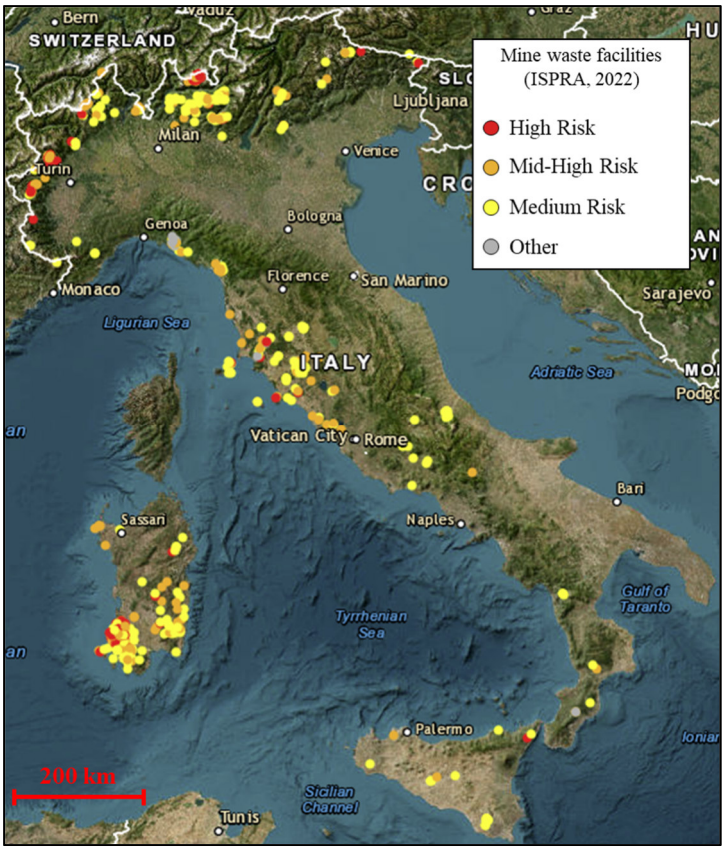


Figure 8 - Map of mine waste facilities, classified according to environmental and sanitary risk (source: ISPRA, 2022)

This database contains different types of information recovered by a variety of sources (research projects, reclamation actions, etc.), but it presents many regional differences. In general, the classification method has been principally developed for risk assessment, resulting in a lack of information about minerals and elements that could represent a potential recovery interest (Žibret et al., 2020).

The Italian mining industry is regulated by one of the most ancient regulatory frameworks in Europe, the Royal Decree n.1443, dating back to 1927, that regulates the classification of commodities and how mining licences are assigned. Following modifications (Law Decrees 112/1998), transferring to the regional authorities regulation roles for the mining sector, creating a different planning, heterogeneous datasets in terms of completeness and quality. This situation required the collection and gathering of data for creating a homogeneous national framework, and in particular, legislation pushes are recommended for legal reassessment of mine waste (Lucarini, Carta, Fumanti, Martarelli, & Serra, 2020; Lucarini, Fumanti, Martarelli, & Serra, 2023).

In this context, the CRMA can be considered the most impactful regulatory change that resulted in the approval of many new regulations and the financing of different initiatives in Italy for supporting actions for the recovery of raw materials from mine waste in the last few years. It enhanced the approval of the Law Decree n.84/2024 for introducing norms for the recovery of mineral resources from extractive waste, along with several initiatives for data collection,

creation of publicly available databases and the definition of a national exploration strategy for mineral exploration.

In July 2025, the National Exploration Programme (PNE) was released, including explicit actions aiming at mapping and characterising mine waste and tailings for the recovery of CRMs and SRMs (ISPRA, 2025b, 2025a). Within this framework, a set of working packages and actions, defined in the URBES (URBan mining and Extractive waste information System) project, has been planned for future years for mapping and characterising abandoned mine waste facilities with the goal of recovering secondary raw materials (ISPRA, 2025b).

1.4 Mine waste as a possible source of CRMs and SRMs: classification and technical challenges for its recovery

As primary sources become increasingly depleted and geopolitically constrained, attention on secondary sources, including mine waste and tailings, has been rising around the world and, as previously described, also in Europe. As reported by many authors, these materials could contain economically significant concentrations of CRMs and SRMs, such as rare earth elements (REEs), cobalt, antimony, copper and tungsten (De Oliveira, Silva, Morais, & Fernandes, 2025; Rosario-Beltré et al., 2023; Sarker, Haque, Bhuiyan, Bruckard, & Pramanik, 2022; Sedda, De Giudici, Fancello, Podda, & Naitza, 2023; Whitworth, Forbes, et al., 2022; Whitworth, Vaughan, et al., 2022).

Extractive waste could contain metals and minerals that may be overlooked in past industrial operations (Dold, 2020). Additionally, many of the raw materials included in the CRM's list are often found as companion metals, principally associated with a single host or with multiple hosts at varying rates (Nassar, Graedel, & Harper, 2015), as reported in Figure 9.

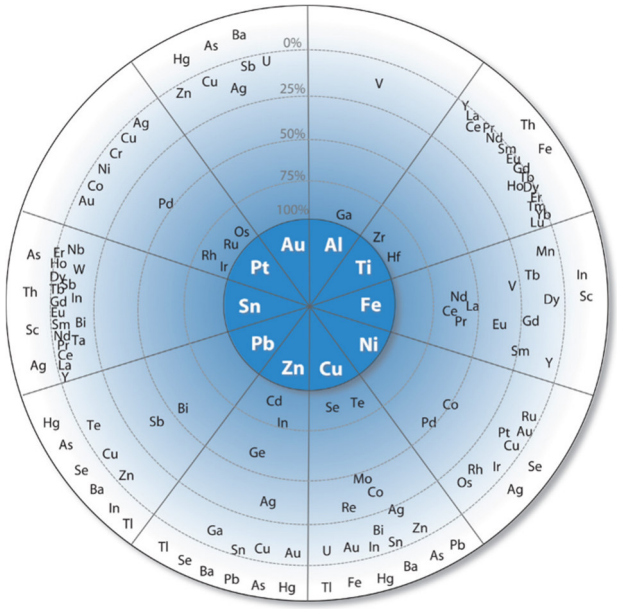


Figure 9 - Degree of association between host metals and primary production of companion metals (source: Nassar et al., 2015)

1.4.1 Mine waste typologies

Mine waste can be classified according to the stage of the process in which it is generated and its physical form. According to a process-based perspective, three main categories of mine waste are recognised in the literature: waste rock, tailings, and metallurgical waste, as reported in Figure 10.

Waste rocks are produced during mining operations performed both in open-pit and underground, and consist mainly of overburden rock or coarse and large fragments that are excavated through host rocks for accessing the ore body. Within this group, some distinction can be made between conventional "mine waste rock" and "pre-concentration waste rock", being the latter produced for upgrading the grade of commodities using pre-concentration processing technologies. In general, mine waste rocks are coarse-sized, usually dry and can differ in residual concentrations of metal and spatial distribution.

Processing wastes are produced during mineral beneficiation and are defined as "tailings". These materials are usually composed of finely ground residual ore minerals and non-economic rocks and process waters, disposed as a slurry in artificial impoundments. Furthermore, tailings can be sub-classified as "fine tailings" if produced as a by-product of conventional grinding-flotation processing, or as "coarse tailings" if discharged from coarse particle processing (e.g., coarse particle flotation), with overall grain size and water content being crucial parameters for possible recovery options.

By contrast, metallurgical wastes are generated during smelting, roasting and hydrometallurgical processing and can include slags, roasted or leached ores, and ashes. These wastes are often enriched in certain minor and critical metals (Valenta et al., 2023)

Overall, each of the aforementioned type of mining waste are characterized by highly variable chemical and physical properties and could contain sub-economic primary ore minerals, gangue minerals, secondary weathering products having particle sizes from fines in tailings to boulders in waste rocks and a wide range of textures and crystal structures (Valenta et al., 2023)

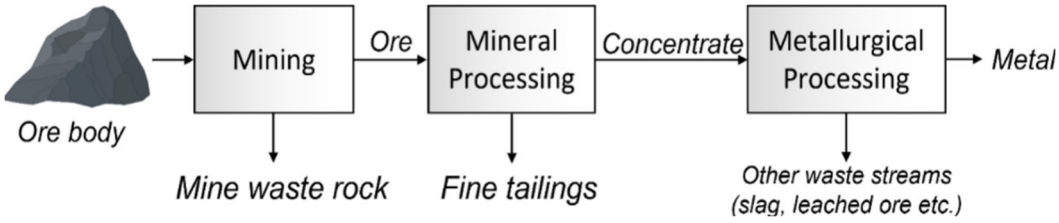


Figure 10 - Traditional extraction process and related waste streams (source: Valenta et al., 2023)

Along with general classification, mine waste could also be categorised based on its associated environmental risk and potential damage to soil and water. These impacts often arise from the deportment of heavy metals due to Acid Rock Drainage (ARD) and Acid Mine Drainage (AMD) phenomena, which are often observed in different types of mine wastes associated with sulphide-bearing ores (Colombi et al., 2025). As a consequence, environmental geochemical classifications are used to subdivide mine waste (waste rocks, tailings, etc.) into acid-forming categories, such as "potential acid-forming" (PAF), "non-acid-forming" (NAF), saline or metalliferous NAF and sometimes acid-consuming materials, according to specific procedures which consider sulfur content, neutralising capacity and leachate chemistry derived from static and kinetic tests

(Ait-Khouia, Benzaazoua, & Demers, 2021; Masindi et al., 2022; Parbhakar-Fox, Edraki, Walters, & Bradshaw, 2011; Parbhakar-Fox, Fox, Hill, Ferguson, & Maynard, 2018). Additionally, some authors suggest adding ecotoxicological and pollution indices to categorise particular PAF mine waste according to ecological risk (Ferri-Moreno et al., 2023).

1.4.2 Technical solutions for mine waste and tailings recovery

This wide range of chemical and physical characteristics typical of mine waste material entails many technical challenges for its recovery.

Marked spatial heterogeneity requires representative and systematic sampling campaigns, remote sensing, geophysical surveys and multi-modal characterisation to understand grades, spatial extension, and to build reliable resource models (Blannin, Frenzel, Tolosana-Delgado, & Gutzmer, 2022; Guglietta et al., 2020; Nascimento et al., 2023; Whitworth, Forbes, et al., 2022). In addition, detailed geochemical and mineralogical characterisation using different analytical methodologies, such as chemical assays and automated mineralogy, is strongly needed for screening recoverable minerals, critical elements-bearing minerals, along with grain size, liberation, association and metal deportment information (Jamieson, Walker, & Parsons, 2015; Whitworth, Forbes, et al., 2022).

Heterogeneity, fine granulometry, low metal grades, and surface alteration could make conventional mineral processing technologies difficult to apply. For example, weathering and exposure of mine waste to air and water oxidise mineral surfaces, making flotation less effective and requiring adapted or innovative mineral processing technologies for concentrating CRMs bearing minerals (Whitworth, Forbes, et al., 2022).

1.4.2.1 Physical treatments and mineral processing technologies

Mineral processing technologies are widely used for recovering CRMs from mine waste and tailings (Figure 11). Advanced comminution technologies, such as stirred mills, are used to enhance the liberation of valuable minerals from coarse to fine-grained mining waste or tailings; classification technologies, such as hydrocyclones, semi-inverted, and hybrid cyclones, are used for efficiently screening and generating size fractions suitable for direct recovery or further mineral separation steps (Whitworth, Forbes, et al., 2022).

Froth flotation is widely used for the recovery of residual sulphides and critical minerals, especially through advanced applications such as fluidised-bed and reactor-separator cells that can be adapted for coarse and very fine particles in mine waste and tailings. Non-selective flotation processes can also be used for obtaining a reducing potential acid-forming phenomena by recovering sulphides and sulfosalts from mine waste and tailings (Abaka-Wood, Zanin, Addai-Mensah, & Skinner, 2019b; Amar, Benzaazoua, Elghali, Hakkou, & Taha, 2022; Na, Eom, Yoo, & Diaz Alorro, 2024; Whitworth, Forbes, et al., 2022). Gravity separation technologies, including spirals, shaking tables, Falcon and Knelson concentrators,

were used for concentrating denser minerals, such as wolframite and scheelite, from historic mine waste (Das, Kundu, Dash, & Angadi, 2023; Han, Golev, & Edraki, 2021; Mulenshi, Khavari, Chelgani, & Rosenkranz, 2019).

Additionally, magnetic separation techniques, both in dry and wet conditions, were applied for the recovery of magnetic and paramagnetic minerals for the preconcentration of critical elements in magnetite-rich tailings and for the recovery of REEs minerals from mine waste (Abaka-Wood, Zanin, Addai-Mensah, & Skinner, 2019a; Mulenshi et al., 2019), while innovative sorting technologies are also applied to the recovery of valuable minerals from coarse waste rocks, like sensor-based sorters using X-ray transmission for detecting tungsten-bearing minerals, or to recover phosphate rock from gangue materials (Amar et al., 2023; TOMRA Mining, 2023).

In general, combined flowsheets composed of several physical processing units in sequence are needed to process mine waste and tailings for recovering valuable and critical minerals contained (Y. Li, Lv, Li, Zhou, & Qin, 2024).

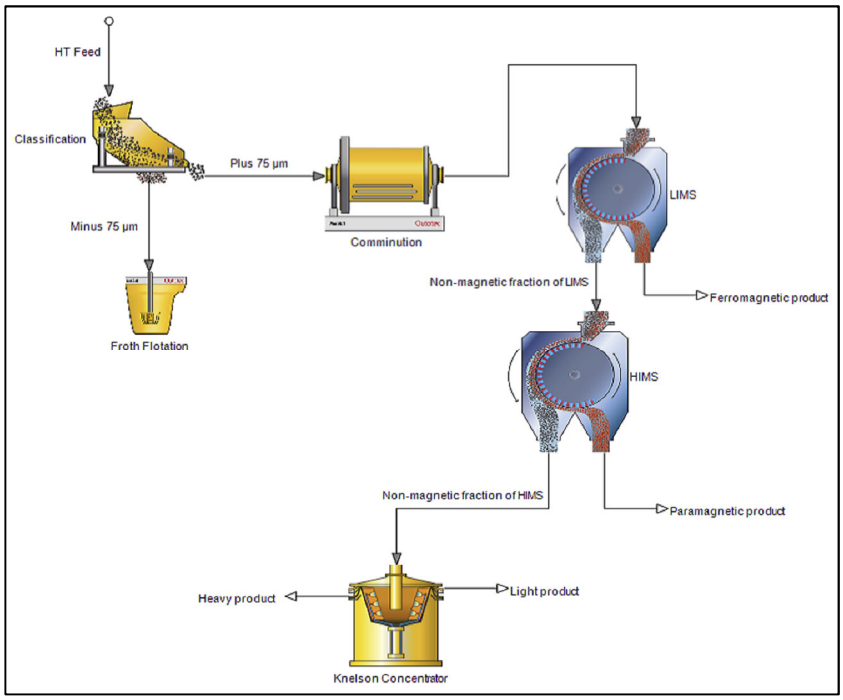


Figure 11 - Flowsheet including different mineral processing technologies proposed for the recovery of CRMs from historical tailings in Sweden. (Source: Mulenshi et al., 2019)

1.4.2.2 Hydrometallurgical processes using conventional and innovative lixiviants

Alternatively to mineral processing, extractive metallurgical approaches, such as hydrometallurgy, pyrometallurgy and electrometallurgy, can be applied for those cases in which physical processing solutions would be difficult to apply to mine waste and tailings.

In particular, hydrometallurgy processes are suitable for extracting metals from low-grade ores and secondary raw materials, and can be developed at a small scale to face site-specific conditions (Whitworth, Vaughan, et al., 2022).

Conventional practices consist of acid leaching procedures using, for example, sulphuric acid, chloridric acid or nitric acid, for dissolving and recovering Cu, Zn, Fe, Co and other metals, achieving recoveries above 90% from tailings (Maltrana & Morales, 2023). Conventional acid leaching is generally applied in different processing configurations, such as atmospheric leaching and pressure leaching. Atmospheric leaching is characterised by low operating temperatures and non-pressurised or open vessels. The most common configurations are through agitated tanks, heap leaching or vat leaching techniques. By contrast, pressure leaching uses high pressures and high temperatures for the solubilization of metals. Most common configurations include agitated tanks, columns or autoclaves and controlling pressure, oxidative and temperature according to the mineralogy of the material and the target metals involved. Acid leaching is often followed by solvent extraction, electrowinning, ion exchange or precipitation units for recovering valuable and critical metals from liquors, while controlling impurities and unwanted leached elements such as Fe. Pre-treatments, including grinding, sieving, and preliminary weak acid washing, are needed for increasing the surface area of the material and removing soluble compounds, and improving the performance of acid leaching processes (Maltrana & Morales, 2023). Sulphuric acid remains a widely used inorganic acid due to its low market prices, widespread availability and high dissolution capacity despite being highly corrosive, dangerous to transport and environmentally deleterious (Crane & Sapsford, 2018).

A wide range of innovative hydrometallurgical techniques and use of innovative lixiviants have been studied and developed for recovering critical metals from mine waste and tailings.

In this context, alternative and green reagents, like organic acids and amino acids, are facing a growing interest in the application to secondary raw materials due to their low toxicity, biodegradability and recyclability (Crane & Sapsford, 2018). Among others glycine has been extensively tested for its ability to selectively leach gold, copper and other valuable elements from waste. (Eksteen, Oraby, & Tanda, 2017; Jamett, Carrasco, Olmos, & Hernández, 2022; H. Li, Deng, Oraby, & Eksteen, 2023).

Glycine (NH_2CH_2COOH) is the simplest of the proteinogenic amino acids, being a non-toxic, non-volatile, biodegradable, low-cost and easily commercially available reagent (H. Li et al., 2023). In aqueous solutions, it can occur as protonated (Gly+) or deprotonated glycinate (Gly-), with the latter dominating in alkaline conditions and having strongly complexing characteristics. Under these conditions, glycine acts as a chelating ligand forming strong chemical complexes, called metal-glycinates, with many chalcophile metals, in particular Cu, Ni, Co and Zn. This enables a selective dissolution of these elements while suppressing the dissolution of other metals like Fe, Al, and Mg (Davoise & Méndez, 2025).

For mine waste or tailings recovery applications, glycine leaching is generally operated at a pH range between 9 and 11 using NaOH as pH modifier, ambient to moderate temperature, often in combination with oxidants such as oxygen or hydrogen peroxide to oxidise sulphides and release Cu^{2+} ions that can complexate with glycinates in the solution. Waste materials could need crushing or grinding for achieving suitable grain dimension and increased surface area, while improving overall dissolution of metals in the pulp (Barragán-Mantilla, Gascó, Almendros, & Méndez, 2024; Davoise & Méndez, 2025).

After leaching, Cu can be recovered from glycinate liquors by several routes, which also include the liberation of glycine for reagent recycling, being electrowinning after solvent extraction and acid strip, sulfides precipitation, chemical reduction using hydrazine, ion-exchange resins and direct electrodeposition for the production of high-purity Cu powders (Deng, Oraby, & Eksteen, 2020; Eksteen et al., 2017; H. Li et al., 2023; Mohammed, Bezuidenhout, Oraby, & Eksteen, 2024; Mokhlis, Drissi Daoudi, & Azzi, 2021).

Solid residues resulting from glycine leaching were proven to have phytostimulant potential and suitability for agronomical uses, highlighting options for environmental remediation for oxidised tailings material after glycine leaching processes (Barragán-Mantilla et al., 2024; Davoise & Méndez, 2025).

Although difficulties in process design and many aspects under scientific development, improvement in industrial research has provided potential full-scale glycine-based solutions applicable to mine waste and sub-economical materials for the sustainable recovery of valuable and critical elements (Figure 12) (Draslovka, 2025; Eksteen et al., 2017)

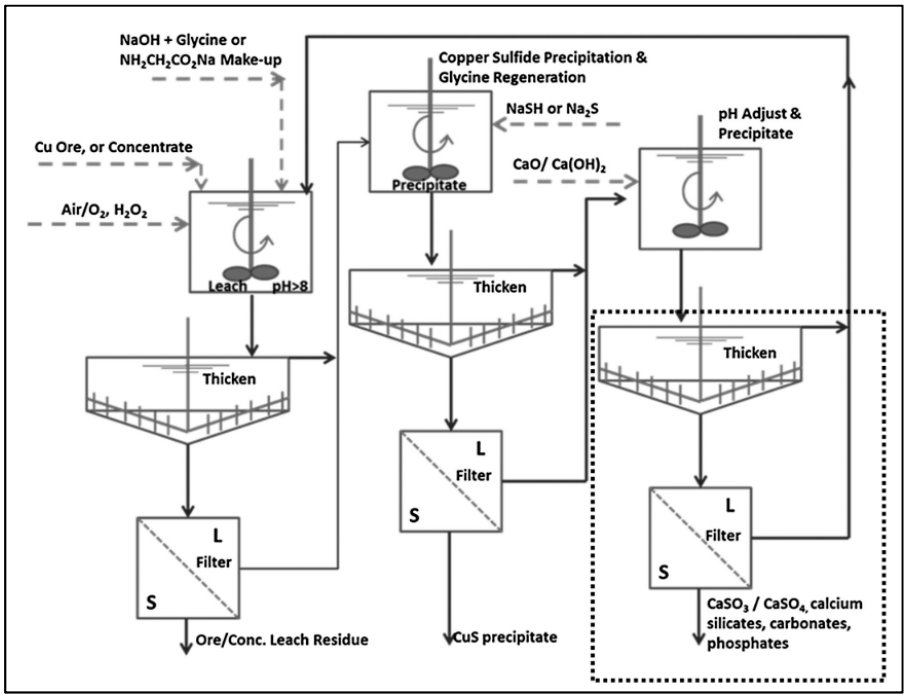


Figure 12 - A conceptual flowsheet for extracting copper using glycine as a lixiviant (Source: Eksteen et al., 2017)

1.4.2.3 Bio-leaching and phyto-mining approaches

Other innovative solutions for CRMs recovery options from extractive waste is represented by bio-leaching and phytomining.

Bio-leaching utilises bacteria and fungi to solubilise metals, such as Cu, Co, Ni, Zn and REEs, from tailings or mine waste, reaching relevant metal recoveries while reducing the environmental risk of the treated materials (Figure 13) (Fereydouni, Naseri, & Mousavi, 2025; Mäkinen, Salo, Khoshkhoo, Sundkvist, & Kinnunen, 2020; Roberto & Schippers, 2022). Additionally, bioleaching is a low-cost and environmentally friendly technology compared to traditional chemical extraction procedures (Nguyen, Won, Ha, Nguyen, & Kang, 2021), but for achieving relevant recovery of metals, many operational parameters need to be optimized, such as pH, temperature and aeration, while sequential or integrated hydrometallurgy schemes are often implemented for treating pregnant leach solutions. (Falagán, Grail, & Johnson, 2017; Fereydouni et al., 2025; Fomchenko & Muravyov, 2020; Riekkola-Vanhanen, 2013).

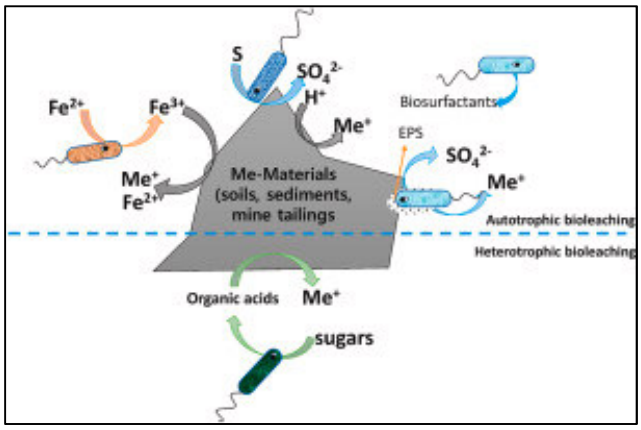


Figure 13 - Scheme of the bioleaching mechanisms on mine tailings substrate (Source: Nguyen et al., 2021)

Phytomining uses hyperaccumulator plants to take up valuable metals and metalloids from mining waste (Figure 14), resulting in the production of "bio-ore" that can be further treated for metallurgical recovery (Dhiman et al., 2024). Different approaches have been tried to provide engineered conditions to maximise plant uptakes, improving recovery of CRMs, while reducing the concentration of polluting elements from mine tailings. (Anawar, Hossain, Santa-Regina, Strezov, & Akter, 2019; Kikis, Thalassinos, & Antoniadis, 2024; Medina-Díaz, Lopez-Bellido, Alonso-Azcárate, Fernández-Morales, & Rodríguez, 2024; Remigio et al., 2020; Scotti, Silvani, Juárez, Godeas, & Ubaldini, 2022)

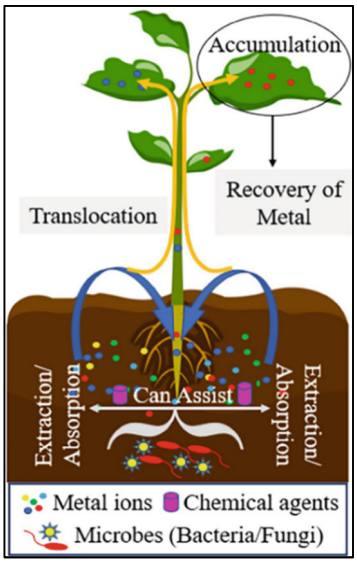


Figure 14 – Phytomining mechanism using hyperaccumulator plants in metal rich soils (Source: Dhiman et al., 2024)

In conclusion, many variables and complex technical factors should be considered when approaching the recovery of mine waste and tailings. In fact, despite significant research and development of innovative recovery approaches, mine waste valorisation projects often do not progress beyond laboratory or pilot scale, and full-scale success remains relegated to rare cases. The main reasons behind this high failure rate are related to limited commercial implementation due to economic and technical barriers linked with high capital costs, volatility of commodity prices, and difficulties in scaling up processes related to material heterogeneity and lack of characterisation data (Stander & Broadhurst, 2021). Additionally, regulatory challenges related to fragmented and unclear standards for products derived from waste, complex permitting processes and poor governamental incentivating policies further decrease the possibility of reaching success for the recovery of mine waste and tailings (Araya, Kraslawski, & Cisternas, 2020).

However, it is important to underline that circular economy practices are crucial for transforming extractive waste recovery from long-term liabilities into secondary sources. A holistic perspective is needed for addressing post recovery materials to different applications, such as geopolymers, cement, backfill materials, construction materials, and soil amendments for reducing the overall footprint of reprocessing operations and enhancing land rehabilitation.

1.5 Goal of the study

The overall aim of this study is to develop a reproducible methodological framework for the assessment of mining waste and tailings sites as potential secondary sources of CRMs and SRMs in the Italian context.

To support the definition of a reliable methodology, the work firstly focused on international top-notch examples, included in the dissertation as guiding case studies: in particular, the development of prioritisation procedures for mine waste sites indexed in the Finnish national mine waste database and assessment methodologies developed and applied in Australia. These examples represent the state of the art of mine waste data collection and provide a sound basis for defining methodological approaches.

Based on this, the research defined a data-driven methodological approach specifically designed for the Italian context, where abandoned and historical mine waste sites are characterised by heterogeneous and fragmented datasets. The objectives of the study include the collection of already available mine waste data, site sampling followed by detailed mineralogical and geochemical characterisation, and the evaluation, on a laboratory scale, of potential technically feasible approaches for recovery of possibly present CRMs and SRMs from different types of mine waste. The methodology is then applied to selected case studies to test its applicability and potential to deliver results in line with the main goal.

Ultimately, this study wants to provide a framework for supporting decisions and assisting institutions and possibly involved stakeholders in the identification, characterisation, and prioritisation of mine waste site having high potential for resource recovery, contributing to the implementation of circular economy principles within the extractive and raw materials sector.

1.6 Thesis Outline

This thesis is structured into eight chapters, organised to progressively introduce and describe the development of the study. The present introductory Chapter 1 served as a research background definition and introduced the aims and scope of the research. Chapter 2 presents the methods adopted in the study, describing the overall methodological approach defined, on-field methods for sampling and volume estimation, mineralogical and chemical characterisation, and physical and hydrometallurgical treatments methodologies applied in the proposed case studies.

The thesis is then divided into three main parts. Part I contains the international examples of mine waste management used as benchmark reference cases. In this section, Chapter 3 describes the definition of prioritisation actions extrapolated from a wide set of information available from the Finnish mine waste database, while Chapter 4 presents the advanced sampling and characterisation strategies applied to the old tailings storage facility of the Kanmantoo mine in Australia, illustrating a real-case application of top-notch procedures.

Part II is dedicated to the application of the defined methodological approach for the recovery of mine waste in three Italian case studies. Chapters 5,6, and 7 are dedicated to Traversella, Libiola and Fenice-Capanne mine waste sites, respectively. Each of these chapters contains site-specific geological setting, industrial history, mine waste characteristics, analytical results and interpretation, together with results of laboratory-scale recovery trials performed to evaluate technical feasibility to recover CRMs and SRMs from mine waste materials.

Finally, Part III is dedicated to the conclusions. Chapter 8 summarises the main findings of the research, future development and perspectives arising from the presented data.

Chapter 2

2. Methods

2.1 Mine waste database evaluation and individuation of prioritization actions

Data contained in the national mine waste database were elaborated for prioritisation of possible actions for the recovery of mine waste in the listed sites. This involved the introduction of a novel tool named the Economically Important Equivalent Ton (t_{EIeq}) and the comparison of the obtained data with economical value embedded in mine waste deposits and environmental risk related to each listed site.

This methodology is applied only in the case study focused on the Finnish mine waste database, more details describing the applied methodology are reported in ***Chapter 3.***

2.2 Methodology for site individuation, data collection, sampling and recovery trials: a multi-step approach

A multi-step approach was used for the selection of case studies in Italy. This methodology was introduced as a screening procedure for background definition, mapping, sampling, characterisation, treatment and recovery of mine waste from mine waste in Italy. The procedure was designed to achieve a schematic and reproducible method for studying and assessing the possibility of recovering valuable raw materials from mine waste based on theoretical and experimental data.

The proposed scheme included four phases, as graphically reported in Figure 15. More in detail, the first phase focused on the identification of the target sites according to relevant information collected from official or governmental public databases, industrial documents and scientific literature. After site selection, the second phase introduced the gathering of geographical and topographic information, resulting in the creation of a GIS model including satellite images of

the area. Normalised Difference Vegetation Index (NDVI) analyses were performed on multispectral satellite images to understand the soil coverage and the accessibility of the area, propedeutical for sampling campaign design. In the third phase, the sampling campaign is designed and realised. Representative samples were collected according to standard procedures, taking into account accessible and safe areas for operators and the best achievable representative sampling area. The fourth and final phase included a multi-modal chemical and mineralogical characterisation of the sampled waste materials for the identification and quantification of CRMs and SRMs, before proceeding to lab-scale processing tests for assessing the technical potential recovery of target elements or minerals present in the samples. The quality of processing methods applied was assessed in particular for the definition of the recovery efficiency.

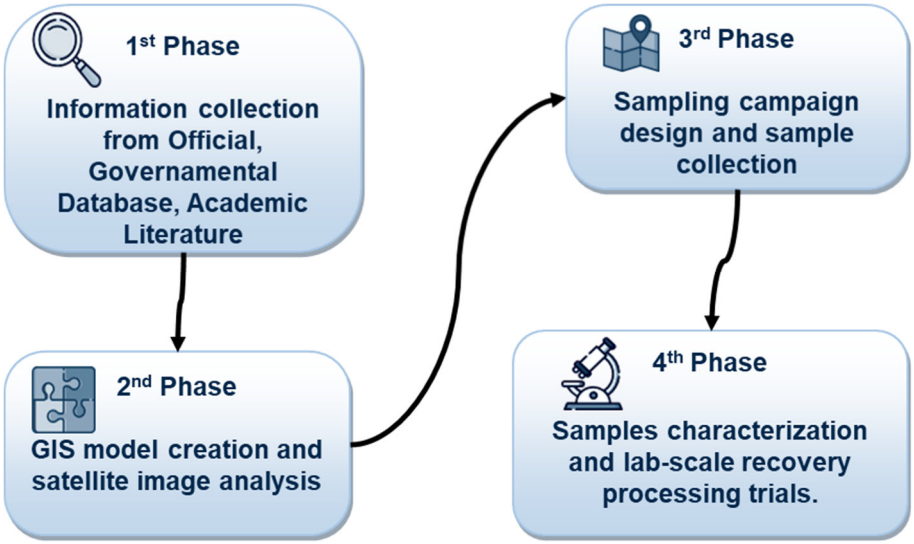


Figure 15 – Multi-step methodological scheme followed for the assessment of site selection, sampling, characterization and processing of mine waste case studies in Italy.

2.3 On-field methods

2.3.1 Sampling

Sampling was realised following different methodologies according to the characteristics of each of the considered sites. In general, grab sampling and hand augering were the principal sampling options used.

Grab sampling was realised using a hand scoop (Figure 16) for collecting loose mine waste material on field. The sampling was conducted following a grid covering the study area or as a point sampling according to the accessibility of the site. This methodology was mainly applied for waste rock sampling in the Traversella (***Chapter 5***) and Libiola (***Chapter 6***) case studies.



Figure 16 - Hand-scoop used during sampling campaigns (Photo credits: G. Baldassarre)

Hand augering sampling was realised for the sampling of tailings material. The equipment consisted of an auger handle, an auger bit and 1m screwable long extension rods (Figure 17). The augering procedure applied followed different reiteration steps, including: positioning the auger vertically over the hole location, pushing down and rotating the handle to penetrate the ground, applying 10-15 twists on the handle, and pulling up the augering equipment for sampling collection. Before the next push, the depth of the hole was measured, and an additional extensive rod was added in case of need.

This sampling methodology was used in the Kanmantoo case study (***Chapter 4***).



Figure 17 - Hand auger equipment used during tailings sampling campaign (Photo credits: G. Baldassarre)

The specific sampling strategy applied to each of the considered case study site is described in the reference paragraph.

2.3.2 Electrical Resistivity Tomography (ERT)

Direct current resistivity data were collected using the georesistivimeter Iris Syscal Pro, a 144-channel multi-node device having a 10-channel receiver and a 250W internal transmitter. Available cables had 2, 3, 5 or 10 m spacing options. Stainless steel and impermeable electrodes were used. Array configurations were the Wenner and Wenner-Schlmberger, using a pulse duration of 500ms. Each electrode position was recorded with a GPS receiver, and the final lines were imported into QGIS software.

Raw data were elaborated with ProsysIII software, obtaining 2D inversion resistivity profiles for further interpretation.

Field acquisition and data processing were realised under the guidance of Mr Diego Franco and Prof. Chiara Colombero, from the Geophysics Research Group, Politecnico di Torino, Italy.

Figure 18 shows an electrode during data acquisition related to the Libiola case study (***Chapter 6***), where ERT measurements were realised.



Figure 18 - Electrode and cable detail during ERT data acquisition on the field (Photo credits: G. Baldassarre)

2.3.2.1 Mine waste volume estimation

For the estimation of mine waste volumes, the thickness ranges obtained from ERT survey data interpretation were adopted as reference values.

To ensure consistency between the uncertainties associated with the investigated areas and the actual ERT surface coverage, the following volume classification criteria were applied:

- *Indicated volumes* were calculated for mine waste dumps directly measured through ERT surveys, with defined areal extents proven by field inspections;

- *Inferred volumes* were estimated using the ERT-derived thickness ranges as reference data. Areas corresponding to the indicated volumes were subtracted from the total extension areas indicated by the available literature.

This volume estimation was applied to the Libiola case study (***Chapter 6***)

2.4 Mineralogical Characterisation

2.4.1 Optical Microscopy (OM)

Optical microscopy (OM) was performed in the DIATI Multimodal Analysis Lab (Politecnico di Torino, Turin, Italy) on uncovered, polished 30 μm thick sections prepared from representative rock sample slices. A Leica Ortholux II POL-MK optical polarised-light microscope equipped with a DeltaPix camera for image acquisitions was used. Normal and polarised transmitted light modes were applied to identify the main mineralogical features of the considered samples.

Thin section observation was performed on the Traversella case study material (***Chapter 5***).

2.4.2 Scanning Electron Microscopy (SEM-EDS)

Scanning electron microscopy (SEM) analyses were performed in the DIATI Multimodal Analysis Lab (Politecnico di Torino, Turin, Italy) using a FEI QUANTA INSPECT 200LV microscope equipped with a tungsten filament and an Energy Dispersive Analysis X-Ray (EDS) detector. Measurements were taken in high-vacuum mode at 5.00 kV using a backscattered electron detector (BSED).

Alternatively, some SEM-EDS analyses were performed in the DISAT Metallurgy Lab (Politecnico di Torino, Alessandria, Italy – Scientific Coordinator: Prof. Marco Actis Grande, Scientific supervision during acquisitions: Dr Matteo Giardino) using a Zeiss EVO 15 microscope equipped with a W filament and an Oxford UltimMax 40 EDS detector. The measurements were performed at a voltage of 20 kV.

Samples were Au or carbon-coated before analyses for minimizing charging effects on the surface.

This method was applied in Traversella (***Chapter 5***) and Fenice-Capanne (***Chapter 7***) case studies.

2.4.2.1 Free Grain Size and Liberation Evaluation

Grain morphology and free-grain size assessment were evaluated using SEM-EDS BSE images. For this determination, approximately 3g of sample was embedded in epoxy resin using a trans-vertical, 3D-printed mould designed to minimise the effect of the gravitational settling of heavier grains (Figure 19). This mould was customised and optimised starting from Grant et al. (Grant, Goudie, Shaffer, & Sylvester, 2016). After a 48h curing period, the exposed surface was polished and gold-coated. SEM images were acquired in the BSE mode, covering different image fields. MATLAB R2024b software (The MathWorks Inc., 2024) and the Image Processing Toolbox plug-in (The MathWorks Inc.) were used for

the processing and analysis of the acquired BSE images. According to the preliminary investigation on single grains, two different binary masks were manually created using the Segment Anything Model function included in the Image Segmenter plug-in and run as input data. This script was designed to automatically calculate the grain-by-grain liberation of selected mineral grains according to overlapping ratios between valuable and associated gangue areas (***Appendix C.2***).

This method was used for the Traversella case study (***Chapter 5***).

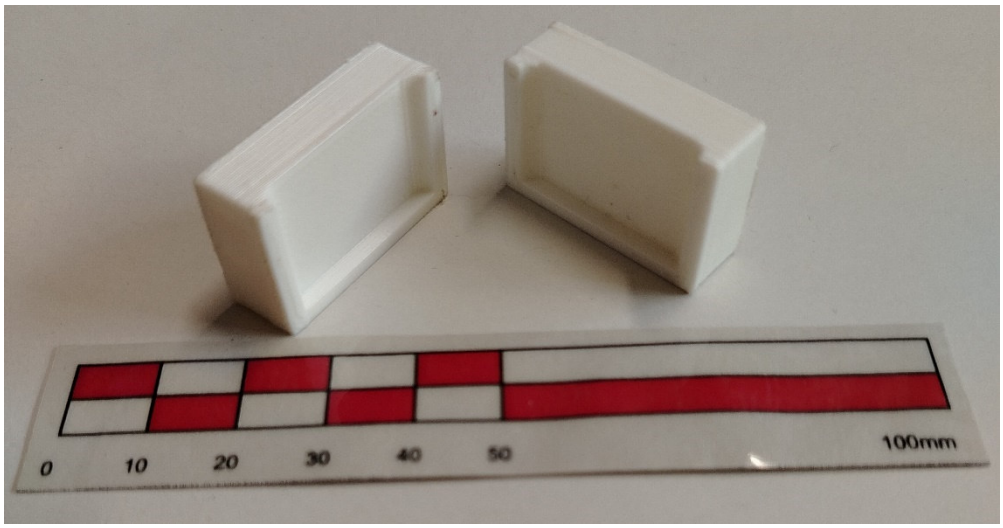


Figure 19 – 3-D printed moulds for SEM and GLE analyses

2.4.3 Mineral Liberation Analyser (MLA)

Automated mineralogy by Mineral Liberation Analysis (MLA) (Gu, 2003) was performed at the UQ-SMI MLA Laboratory (University of Queensland – Sustainable Minerals Institute, Brisbane, Australia – Facility Manager: Dr Gerda Gloy) using a FEI Quanta 600 MLA-FEG scanning electron microscopy equipped with two EDS probes. The X-Ray Backscattered Emission (XBSE) measurement mode was used to collect information on the relative abundance of minerals in the sample and identify the hosted elements.

Samples were prepared according to the vertical mounting method, consisting of mixing a representative portion of the sample in a mould with graphite powder and epoxy resin. The mixture was cured, sectioned and remounted in a 30mm round mould, then finely polished before carbon coating. A site-specific mineral reference library was developed for each sample, and the obatined data were processed using the Dataview software.

This method was used on selected samples from Kanmantoo (***Chapter 4***), Traversella (***Chapter 5***), and Fenice-Capanne (***Chapter 7***).

2.4.4 X-Ray Powder Diffraction (XRPD)

X-ray powder diffraction (XRPD) analysis was mainly performed in the DIATI Multimodal Analysis Lab (Politecnico di Torino, Turin, Italy) using a Rigaku SmartLab SE diffractometer, with CuKα radiation at 40 kV and 30 mA. The acquisition was performed in a 5–90° 2θ range, 0.02° step width, and 4°/min scan. The "*X-Ray Fluorescence (XRF) Reduction*" mode was enabled to mitigate the fluorescence effect of Fe-bearing minerals when contained in the samples (Omori, 2021a). Main mineral phases detection and qualitative analyses were performed using the ICDD PDF-5+ database (Kabekkodu, Dosen, & Blanton, 2024). The sample holder was filled using a side-loading technique to avoid preferred orientation effects (Omori, 2021b). Samples were hand-ground using an agatha mortar and pestle.

This equipment was used for the Traversella (***Chapter 5***) and Fenice-Capanne case studies (***Chapter 7***).

For the Libiola case study (***Chapter 6***), mine waste samples characterisation was performed in the Diffractometry Lab at DISTAV (University of Genoa, Genoa, Italy – Laboratory Coordinator and scientific supervision: Prof. Cristina Carbone) using a Philips PW1720 diffractometer equipped with a PW1080/81 goniometer, using a CoKα radiation at 40 kV and 20 mA. The acquisitions were performed in a 3–100° 2θ range, 0.02° step width, 1s/step count time, and 15 rpm sample rotation speed. Semi-quantitative analyses were performed in order to quantify the mineralogical phases contained in the material.

Regarding the Kanmantoo case study (***Chapter 4***), samples were analysed in the Sietronics Laboratory Services Pty laboratories (Mitchell, ACT, Australia) using a Bruker-AXS D8 XRD, with CuKα radiation at 40 kV and 25 mA. Acquisitions were performed in a 5-80° 2θ range, with a 0.02° step width and 91s/step count time. Identification of the detected mineral phases was carried out using the ICDD PDF-4+ database. Quantitative phase analysis was performed using SIROQUANTTM version 5 software. Samples were first hand-ground using a mortar and pestle. A sub-sample of 2g was split off and subsequently micronised using a McCrone ® mill using agata beads and ethanol, then dried. Each sample was then spiked with 20 wt% % corundum powder for the determination of amorphous phase content. The resulting powders were introduced in the sample holder by back-pressing.

2.5 Geochemical characterisation

2.5.1 Sample preparation procedure for geochemical analyses

To ensure homogenization and maintain the representativeness of the sampled material, the initial material was split and reduced according to the scheme shown in Figure 20. After drying for 12h at 40°C, approximately 10 kg of the collected material was first reduced using the coning and quartering technique to obtain representative subsamples of about 5 kg. This material was then subjected to a first stage of size reduction using a Magutt CR25 jaw crusher (see paragraph 2.6.3.1). The crushed output was further split with a riffle splitter, yielding a fraction of about 1–1.5 kg. This portion was subsequently processed with a smaller Magutt M10 jaw crusher (see paragraph 2.6.3.2). The particle size distribution was verified with a 6.3 mm aperture sieve to confirm a passing diameter P80 ≤ 6.3 mm. The resulting fraction was then further split with a riffle splitter to isolate a representative subsample of approximately 50–100 g. Finally, this material was pulverised in a planetary mill, producing a final pulp having P80 ≤ 75 µm.

This procedure was used for the case studies involving mine waste sampling, such as Traversella (***Chapter 5***) and Libiola (***Chapter 6***).

For tailings samples from Fenice-Capanne (***Chapter 7***), no micronisation was performed.

For the Kanmantoo (***Chapter 4***) sample pulps for geochemical analyses were prepared directly from field-sampled materials by ALS Laboratory, according to their internal standard procedure (ALS Global, 2025)

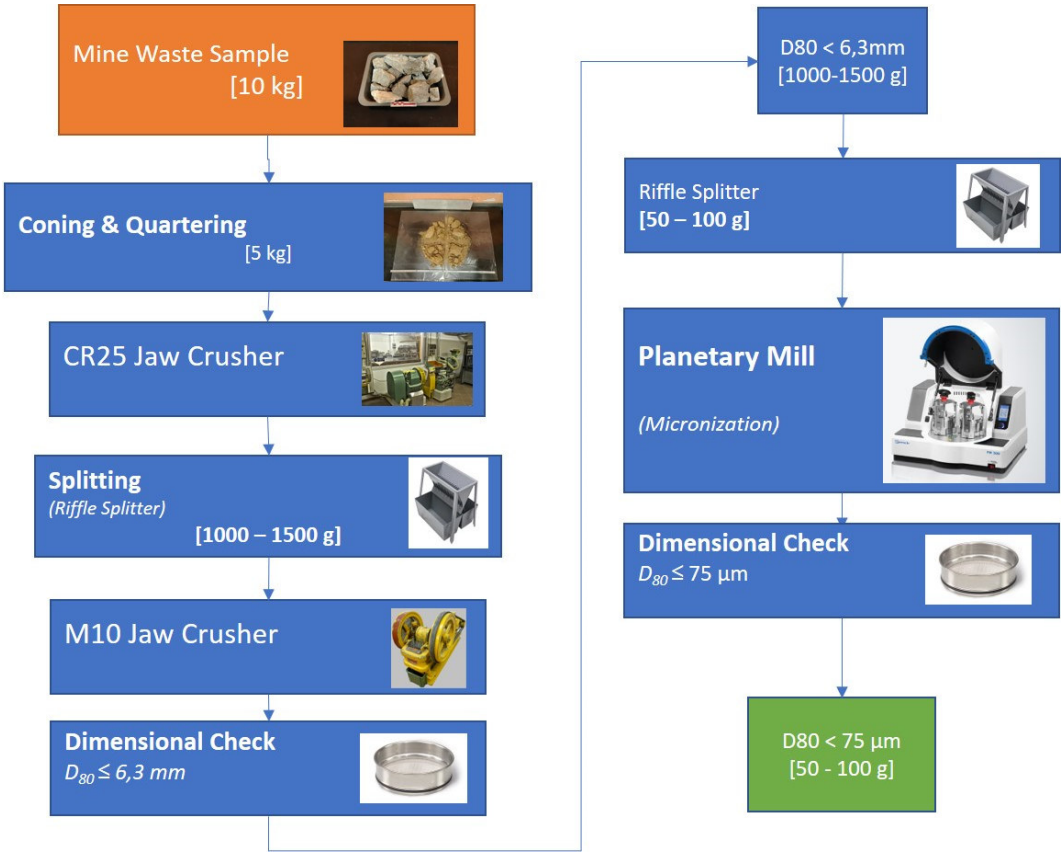


Figure 20 – Procedure for subsampling, crushing and micronisation of mine waste sample for geochemical analyses.

2.5.2 Hand-held X-Ray Fluorescence (HH-XRF)

Hand-held X-Ray Fluorescence spectroscopy (HH-XRF) was realised in the DIATI Multimodal Analysis Lab (Politecnico di Torino, Turin, Italy) using a SciAps X-555 hand-held XRF equipped with 5W, max 55 kV, 200 µA, Au anode X-ray generator and a 140-eV resolution 20 mm^2 drift detector. The equipment was operated with the proprietary measurement programs:

- *Mining*: using a Fundamental Parameter (FP) calibration applying two different tube emission beams at 39,78 kV and 9.91 kV with 30s exposition for both.
- *Soil*: using an Empirical Calibration (EC) having pre-acquired Certified Reference Materials from the factory, applying three different tube emissions beams at 54.66 kV, 39.78 kV, and 14.91 kV with 30s exposition for each mode.

The lower limit of detection (LOD) for the *Soil* program is listed in Table 1

Table 1 - Lower LODa for SciAps X-555 running "Soil" acquisition program («SciAps.com», 2025)

Element	**Au**	**Ag**	**As**	**Ba**	**Bi**	**Ca**	**Cd**	**Ce**	**Co**	**Cr**
Lower LOD (ppm)	1	2	1	27	1	50	3	15	9	2
Element	**Cu**	**Eu**	**Fe**	**Gd**	**Hg**	**La**	**Mn**	**Mo**	**Nb**	**Nd**
Lower LOD (ppm)	3	60	14	90	1	13	17	1	1	27
Element	**Ni**	**P**	**Pb**	**Pr**	**Rb**	**S**	**Sb**	**Se**	**Sm**	**Sn**
Lower LOD (ppm)	5	160	1	18	1	20	9	1	30	7
Element	**Sr**	**Ta**	**Te**	**Ti**	**Tl**	**U**	**V**	**W**	**Y**	**Zn**
Lower LOD (ppm)	1	15	5	3	2	1	1	10	1	2
Element	**Zr**									
Lower LOD (ppm)	1									

The measurement accuracy was periodically tested with external or internal reference materials. The powdered samples were introduced using a loose powder method in sample cells (Takahashi, 2015), and a portable docking station supported the gun in the laboratory setting.

HH-XRF acquisitions were performed on sampled and processed materials from Traversella (***Chapter 5***), Libiola (***Chapter 6***) and Fenice-Capanne (***Chapter 7***) case studies.

2.5.3 Induced Coupled Plasma Mass Spectroscopy (ICP-MS)

Inductively Coupled Plasma Mass Spectroscopy (ICP-MS) analyses were performed in the ALS Laboratories (Loughrea, Ireland or Adelaide, Australia). The analyses were performed according to two different sample digestion techniques:

- *Four-acid digestion (ALS ME-MS61 method)*: 1g of powdered sample was digested using a mixture of hydrochloric acid (HCl), nitric acid (HNO_3), hydrofluoric acid (HF), and perchloric acid ($HClO_4$) to achieve a near-total decomposition of the sample matrix. The digested

solution was analysed using an ICP-MS for quantifying major and trace elements. Elements considered and their LOD range are listed in Table 2.

- *Lithium borate fusion (ALS ME-MS81 method)*: 0.2g was mixed with a flux of lithium metaborate. The mixture was fused in a furnace to produce a molten bead that was dissolved in nitric acid before analysis. The solution was then analysed using ICP-MS to determine a suite of trace and rare earth elements. Elements considered and their LOD range are listed in Table 3.

Table 2 – Limit of Detection (LOD) range for ME-MS61 four-acid digestion ICP-MS method (ALS Global, 2025)

Element	**Ag (ppm)**	**Al (%)**	**As (ppm)**	**Ba (ppm)**	**Be (ppm)**	**Bi (ppm)**	**Ca (%)**	**Cd (ppm)**	**Ce (ppm)**	**Co (ppm)**
Lower LOD	0.01	0.01	0.2	10	0.05	0.01	0.01	0.02	0.01	0.01
Upper LOD	100	50	10,000	10000	1000	10000	50	1000	500	10000
Element	**Cr (ppm)**	**Cs (ppm)**	**Cu (ppm)**	**Fe (%)**	**Ga (ppm)**	**Ge (ppm)**	**Hf (ppm)**	**In (ppm)**	**K (%)**	**La (ppm)**
Lower LOD	1	0.05	0.2	0.01	0.05	0.05	0.1	0.005	0.01	0.5
Upper LOD	10000	500	10000	50	10000	500	500	500	10	10000
Element	**Li (ppm)**	**Mg (%)**	**Mn (ppm)**	**Mo (ppm)**	**Na (%)**	**Nb (ppm)**	**Ni (ppm)**	**P (ppm)**	**Pb (ppm)**	**Rb (ppm)**
Lower LOD	0.2	0.01	5	0.05	0.01	0.1	0.2	10	0.5	0.1
Upper LOD	10000	50	100000	10000	10	500	10000	10000	10000	10000
Element	**Re (ppm)**	**S (%)**	**Sb (ppm)**	**Sc (ppm)**	**Se (ppm)**	**Sn (ppm)**	**Sr (ppm)**	**Ta (ppm)**	**Te (ppm)**	**Th (ppm)**
Lower LOD	0.002	0.01	0.05	0.1	1	0.2	0.2	0.05	0.05	0.01
Upper LOD	50	10	10000	10000	1000	500	10,000	100	500	10000
Element	**Ti (%)**	**Tl (ppm)**	**U (ppm)**	**V (ppm)**	**W (ppm)**	**Y (ppm)**	**Zn (ppm)**	**Zr (ppm)**		

Lower LOD	0.005	0.02	0.1	1	0.1	0.1	2	0.5
Upper LOD	10	10000	10000	10000	10000	500	10000	500

Table 3 - Limit of Detection (LOD) range for ME-MS81 lithium borate fusion ICP-MS method (ALS Global, 2025)

Element	**Ba (ppm)**	**Ce (ppm)**	**Cr (ppm)**	**Cs (ppm)**	**Dy (ppm)**	**Er (ppm)**	**Eu (ppm)**	**Ga (ppm)**	**Gd (ppm)**	**Hf (ppm)**
Lower LOD	0.5	0.1	10	0.01	0.05	0.03	0.02	0.1	0.05	0.1
Upper LOD	10000	10000	10000	10000	1000	1000	1000	1000	1000	1000
Element	**Ho (ppm)**	**La (ppm)**	**Lu (ppm)**	**Nb (ppm)**	**Nd (ppm)**	**Pr (ppm)**	**Rb (ppm)**	**Sm (ppm)**	**Sn (ppm)**	**Sr (ppm)**
Lower LOD	0.01	0.1	0.01	0.1	0.1	0.02	0.2	0.03	1	0.1
Upper LOD	1000	1000	1000	2500	10000	1000	10000	1000	10000	10000
Element	**Ta (ppm)**	**Tb (ppm)**	**Th (ppm)**	**Tm (ppm)**	**U (ppm)**	**V (ppm)**	**W (ppm)**	**Y (ppm)**	**Yb (ppm)**	**Zr (ppm)**
Lower LOD	0.1	0.01	0.05	0.01	0.05	5	1	0.1	0.03	2
Upper LOD	2500	1000	1000	1000	1000	10000	10000	10000	1000	10000

2.5.4 Induced Coupled Plasma Optical Emission Spectroscopy (ICP-OES)

Induced Coupled Plasma Optical Emission Spectroscopy (ICP-OES) analyses were performed in the DISAT Metallurgy Laboratory (Politecnico di Torino, Alessandria, Italy) using a Perkin Elmer Optima 5300V spectrometer equipped with a cyclonic spray chamber and a Meinhard-type nebuliser. The RF generator power was set at 1300 W. The sample uptake rate was 1.00 mL/min. Each sample was analysed in triplicate to ensure reproducibility.

This method was used for the chemical determination of metal contents of leachate solutions obtained after hydrometallurgical reprocessing performed in the Libiola (***Chapter 6***) and Fenice-Capanne (***Chapter 7***) case studies.

2.5.5 Laser Ablation Induced Coupled Plasma Mass Spectroscopy (LA-ICP-MS)

Laser ablation analyses were carried out at the University of Adelaide using a RESOlution-SE laser platform, equipped with an ATL 193 nm excimer laser and S155 large-format sample cell, coupled to an Agilent 8900 quadrupole ICP-MS. The laser spot size used for mineral grains of interest was 24 μm, while 50 μm and 64 μm were used for GSD-1G and NIST1612 primary standard glasses, respectively. Data reduction was performed using the LADR, Norris Scientific, software package.

This method was applied on materials considered in the Kanmantoo case study (***Chapter 4***)

2.6 Treatment methods

2.6.1 Physical treatments

Crushing and grinding equipment were used to reduce the collected sub-sample dimensions and produce material suitable for lab-scale separation trials, aiming to recover mineral phases that host valuable elements. Separation processes were realised using a low-intensity magnetic field separator (LIMS) and a wet high-intensity magnetic separator (WHIMS). Moreover, gravity separation was performed using a shaking table (ST) to separate minerals according to their density. This sequence of size reduction and separation was intended to efficiently classify the sample material into fractions based on mineralogical and physical properties.

2.6.2 Particle Size Distribution (PSD)

Particle size distribution was realised using different combinations of sieves in wet and dry conditions, according to the main characteristics of the analysed material. In general, dry sieving was used for characterising the material after crushing or milling tests, using sieves having apertures of 0.250 mm and 0.125 mm, in the Traversella case study (***Chapter 5***).

Particle size analysis performed in wet conditions, using 0.300 mm, 0.250mm, 0.125mm, 0.075 mm, 0.053mm and 0.038mm sieves. Materials retained on each sieve were filtered, oven-dried at 40°C and weighed.

This was applied in the Fenice-Capanne case study (***Chapter 7***)

2.6.3 Crushing and milling

2.6.3.1 Magutt CR25 jaw crusher

Crushing operations were performed using a Loro & Parisini Magutt CR-25 laboratory jaw crusher (Figure 21) powered by a 4.5 kW electric motor operating at 440 rpm. The crusher was set to a closed-side setting (CSS) of 7.5 mm and an open-side setting (OSS) of 15 mm. The material exceeding the input size limit was crushed manually using a hammer.



Figure 21 - Magutt CR25 laboratory jaw crusher

2.6.3.2 Magutt M10 jaw crusher

For finer material crushing, a Loro & Parisini Magutt-M10 laboratory jaw crusher was used (Figure 22). This crusher was powered by a 0.6 kW electric engine running at a speed of 250 rpm. The selected CSS was 5 mm, with an OSS of 15 mm. The dimensions of the feed opening in the crushing chamber for the material to be processed are 100 × 60 mm, limiting the input material dimension to d < 40 mm.

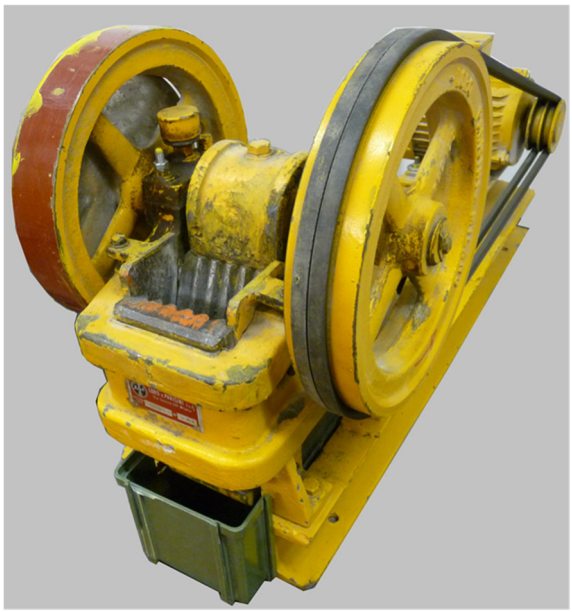


Figure 22 - Magutt M-10 laboratory jaw crusher

2.6.3.3 Laboratory rod mill

Mine waste material was milled using a lab-scale rod mill characterised by a drum measuring 193 mm in diameter and 267 mm in length, with 9 steel rods with a diameter of 8 mm. The mill was powered by a 0.45 kW electric motor. The drum was filled with 1 kg of material at a 30% volume/volume filling ratio, and grinding was performed for 7 min at a rotation speed of 50 rpm.

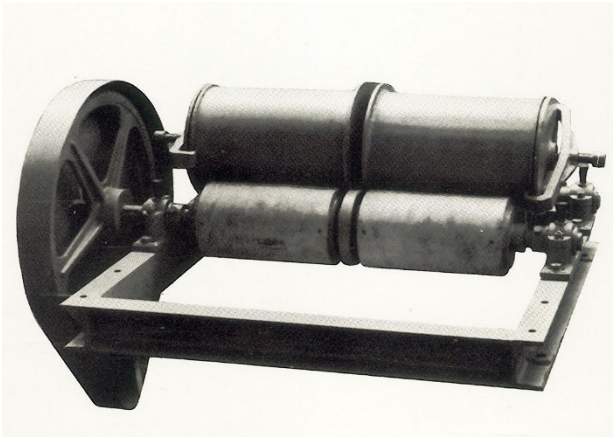


Figure 23 – Laboratory rod mill

2.6.3.4 Retsch PM 300 planetary ball mill

A Retsch PM300 ball mill (Figure 24) was used for the micronisation of the samples before geochemical analyses. Pulps were produced using zirconia-coated jars filled with 5 zirconia 30mm-diameter beads. The milling was performed at 350 rpm for 5 minutes. Quartz sand was used to clean the milling jar after each sample to avoid contamination of the samples.



Figure 24 - Retsch PM300 planetary ball mill

2.6.4 Magnetic Separation

2.6.4.1 Low-Intensity Magnetic Separator (LIMS)

Dry magnetic separation tests were conducted using a laboratory-scale induced disk low-intensity magnetic separator (LIMS), Davies Model 45 (Figure 25). The magnetic field was adjusted using the instrument's built-in finger-tip control for magnet gap adjustment and the rheostat to control the electromagnet's input current. Magnetic field intensity was measured with an MG-3002 portable AC/DC magnetic meter. The separation tests were conducted in two steps in series, using different magnetic field intensities of 0,20 T and 0,35 T at a mass rate of 1kg/h



Figure 25 - Induced disk low-intensity magnetic separator, Davies Mod.45

2.6.4.2 Wet High-Intensity Magnetic Separator (WHIMS)

Wet magnetic separation tests were conducted using an Eriez Model L-4 wet high-intensity magnetic separator (WHIMS) (Figure 26). The canister positioned between the electromagnetic coils contained a steel matrix with a 2 mm aperture size and 10 mm width. Magnetic field strength was adjusted using the instrument's rheostat to control the input current to the electromagnet. Magnetic field intensity was measured with an MG-3002 portable AC/DC magnetic meter. Separation tests were performed at magnetic field intensities of 0.80, 0.95, and 1.10 T. For each test, around 500g of material was introduced into 20 %wt pulp.

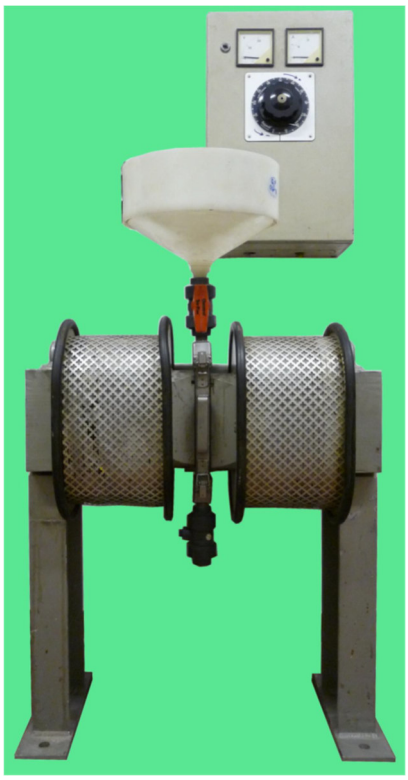


Figure 26 - Eriez Model L4 wet high-intensity magnetic separator

2.6.5 Gravity separation

2.6.5.1 Shaking Table (ST)

Gravity separation was performed using a Krupp Humboldt Wedag lab-scale shaking table (ST) with a rubber-coated surface measuring 1000 × 500 mm (Figure 27). The oscillation was generated by an eccentric mass driven by a 0.25 kW electric motor. The feeding material was introduced at a rate of 50 g/min, with a water discharge of 10 L/min and an inclination angle of 7°.



Figure 27 – Krupp Humbold-Wedag 1000x500 mm laboratory shaking table

2.6.6 Physical separation evaluation

To evaluate and compare the reprocessing outcomes, three key parameters were calculated for each test. Yield (Y), recovery (R), and enrichment ratio (ER), as defined by Wills et al. (Wills & Finch, 2015), were calculated according to the following formulas:

Equation 1 - Yield

$$Y\ (\%) = \frac{C}{F} \times 100$$

Equation 2 - Recovery

$$R\ (\%) = \frac{Cc}{Ff} \times\ 100$$

Equation 3 – Enrichment Ratio

$$ER = \frac{c}{f}$$

Where C represents the mass of the concentrate, and c indicates the grade of the concentrate. F represents the mass of the feed, and f the grade of the feed. The feed and concentrate grades were determined by HH-XRF acquisition.

2.6.7 Hydrometallurgical treatments

Hydrometallurgical treatments were performed on representative subsamples of material, which were previously crushed and milled or on bulk samples. The selected aliquot was 5g of material. Each sample was tested according to two different extraction solutions: one containing glycine and another containing sulphuric acid. This approach was tested on mine waste and tailings materials considered in the Libiola (***Chapter 6***) and in the Fenice-Capanne (***Chapter 7***) case studies.

2.6.7.1 Glycine alkaline leaching

The solution containing glycine was prepared with a concentration of 0.4M, dissolving 30.03g of solid glycine powder in 1l of distilled water. To this solution, 8g of pelletized NaOH were added to obtain a 0.3M solution.

From the obtained solution (glycine + NaOH), 99ml aliquots were transferred to a 100ml flask, and 1ml of H_2O_2 (30% v/v) was added to obtain a 1% v/v concentration of hydrogen peroxide and put in a 250ml beaker where 5g of the solid sample was added. This procedure was repeated for any of the treated samples.

The initial solution was characterised by a pH in the range of 9.90-9.95, and it was additionally modified using drops of a 10M NaOH solution until reaching pH 10. Following the initial pH tuning, the magnetic stir bar was introduced in the beaker, and the stirring system was activated.

Samples were stirred at 300 rpm speed, at room temperature (around 20-22°C) for leaching times of 0.5, 2, 4, 6, and 24 hours for all the samples, and until 168 hours (7days) for selected samples. pH measurement was repeated at the end of each leaching test, according to the selected stirring time.

At the end of the treatment, each sample was filtered on 420nm PTFE membranes in order to recover the leachate, while solid residues were oven-dried and recovered for further determinations. Leachate solutions were stored in HDPE bottles and acidified using 1.5ml of HNO_3 (65%) to avoid glycine complexes precipitation before ICP-OES analyses.

Figure 28 shows the laboratory setting used for the leaching tests.

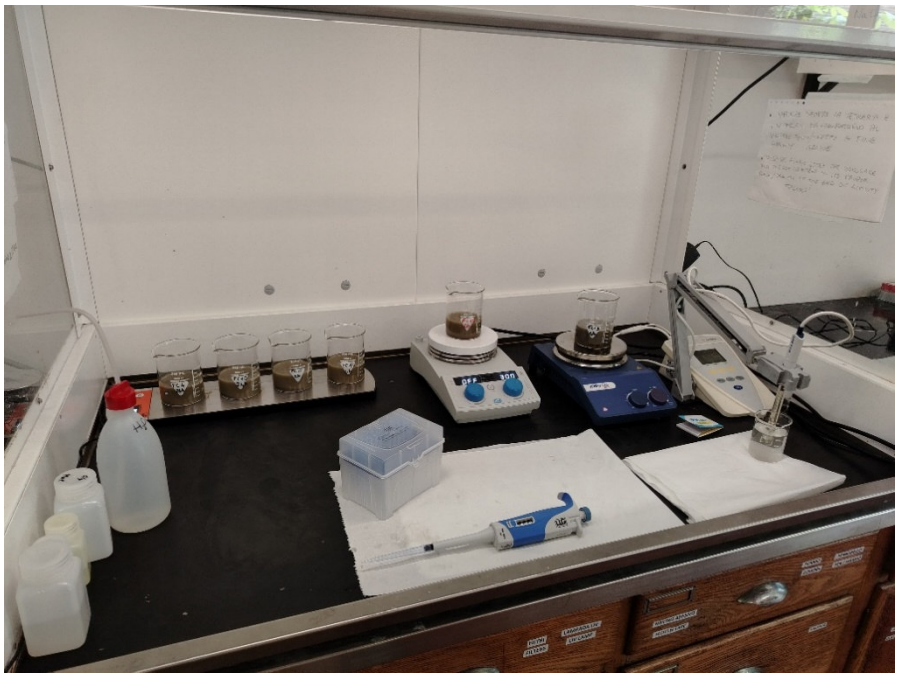


Figure 28 - Experimental set-up used during leaching tests performed (Photo credits: G. Baldassarre)

2.6.7.2 Sulphuric acid leaching

Sulphuric acid solution was prepared according to the parameters described by Sokić et al. (2019).

Each leaching solution was obtained by mixing 16.2 ml of H_2SO_4 (98% v/v) and 23 ml of H_2O_2 (30% v/v), and then making up the volume to 100 ml of distilled water. The obtained solution was 3M for both H_2SO_4 and H_2O_2.

5g of the solid sample was introduced into a 250ml beaker with the prepared leaching solution. The mix was magnetically stirred on a heating plate, controlling the temperature at 50°C with a thermocouple. The stirring time was 2 hours for each of the considered samples.

After leaching tests, each sample was filtered on 420nm PTFE membranes to recover the leachate, which was stored in HDPE bottles and sent to ICP-OES analyses. Solid residues were oven-dried and recovered for further determinations.

2.6.8 Post-leaching metal recovery evaluation

In order to evaluate the recovery of target metals, ICP-OES and HH-XRF analyses were performed on both the leachate solutions obtained and on solid residues remaining after leaching. R_{ICP} and R_{XRF} recovery rates were calculated according to the following equations:

Equation 4

$$R_{XRF}(\%) = \frac{f - r_{(t)}}{f} \cdot 100$$

Where f is the concentration of the metal in the feed material and $r_{(t)}$ is the concentration of the solid residue after leaching time t according to HH-XRF measurements.

Equation 5

$$R_{ICP}(\%) = \frac{m_{l\,(t)}}{m_f} \cdot 100$$

Where m_f is the mass of the metal in the feed material according to HH-XRF analyses, and $m_{l(t)}$ is the mass of the metal in the leachate solution after time t, measured by ICP-OES.

2.7 Case-by-case applied methodology resume

Considering the different peculiarities of each case study described in the previous paragraphs, a recapitulative table of the characterisation methods applied is listed in Table 4.

Table 4 - Summary of applied characterisation methods for each of the proposed case studies. PSD: Particle Size Distribution; ERT: Electrical Resistivity Tomography; OM: Optical Microscopy; SEM-EDS: Scanning Electron Microscopy with Energy-Dispersive Spectroscopy; MLA: Mineal Liberation Analysis; XRPD: X-Ray Powder Diffraction; HH-XRF: Hand-Held X-Ray Fluorescence; ICP-MS: Induced Coupled Plasma Mass Spectroscopy; ICP-OES: Induced Coupled Plasma Optical Emission Spectroscopy; LA-ICP-MS: Laser Ablation ICP-MS.

		Characterization Methods										Processing methods	
Case Study	Dataset elaboration	PSD	ERT	OM	SEM-EDS	MLA	XRPD	HH-XRF	ICP-MS	ICP-OES	LA-ICP-MS	Physical	Hydromet.
Finnish database (***Chapter 3***)	X	-	-	-	-	-	-	-	-	-	-	-	-
Kanmantoo (***Chapter 4***)	-	-	-	-	-	X	X	-	X	-	X	-	-
Traversella (***Chapter 5***)	-	X	-	X	X	X	X	X	X	-	-	X	X
Libiola (***Chapter 6***)	-	-	X	-	-	-	X	X	X	X	-	X	X
Fenice-Capanne (***Chapter 7***)	-	X	-	-	X	X	X	X	X	X	-	-	X

Part I. International examples of mine waste data organisation and collection for enhancing the recovery of mine waste and tailings

Chapter 3

3. Data analysis for decision-making initiatives: the Finnish mine waste database

Part of the work presented in this chapter has been previously published in:

Karlsson, T., Hokka, J., Kauppila, P.M., Tornivaara, A., Baldassarre, G., 2024. *Potential of critical raw materials in closed Finnish mine waste sites: a preliminary review*. In: Proceedings of the ICARD 2024 – 13th International Conference on Acid Rock Drainage, *Halifax, Nova Scotia, Canada. Canadian Institute of Mining, Metallurgy and Petroleum* (Karlsson, Hokka, Kauppila, Tornivaara, & Baldassarre, 2024)

3.1 Preface

This chapter presents a methodology designed to extract and analyse information from the GTK-METSO database, which contains data on the tonnages and grades of metals and CRMs in various mine waste sites across Finland.

An evaluation tool was designed to assess chemical data, total mine waste quantities, and criticality parameters from the GTK-METSO database. An artificial unit of measurement, the Economically Important – Equivalent Ton (t_{EIeq}), was introduced. It consisted of a mathematical weight assigned to the estimated tonnage of a specific commodity or mineral in the waste material, allowing a comparison with the economic value of the waste under the assumption of ideal processing with 100% recovery of the contained commodities.

This approach produced a ranking of mine sites based on a parameter that considered not only the potential economic value embedded in mine waste deposits considered, but also the weighted economic importance, according to EU parameters, of the contained raw materials. Furthermore, the proximity to smelter infrastructures was examined to account for the feasibility of transporting hypothetically processed mine tailings to a smelter or refining plant.

Finally, a 3-D decision matrix was designed for ranking the obtained Economic Importance, Environmental Risk, and Economic Value values calculated from each site and assigning potential actions.

3.2 The GTK database for Finnish extractive waste facilities

The main data source for this study was the extractive waste database accessed from GTK archives, including available datasets, projects, and publications related to mine waste. Main data have been gathered and collected in the GTK's METSO database (GTK, 2024). This database serves as a centralised repository for data on tailings and waste rock materials as potential secondary resources in Finland. This dataset included several information, such as site descriptions, historical production data, site locations, waste descriptions, geochemical and mineralogical analyses, and observed or measured environmental contamination.

Table 5 reports the closed Finnish mine sites that were considered in this study for assessing their potential to host significant quantities of critical raw materials and any related prioritisation actions. Figure 29 shows the location of the 22 sites considered.

Table 5 – Selected mine waste sites (n = 22) from the GTK database in the study, with the reported quantities of tailings and waste rocks.

Site	*Tailings (Mt)*	*Waste rocks (Mt)*
Pyhäsalmi	20.0	-
Hitura	15.0	5.5
Luikonlahti	14.3	-
Vihanti	13.7	-
Otanmäki	11.8	-
Rautuvaara	9.5	-
Kotalahti	9.4	-
Vuonos	9.0	4.6
Enonkoski	6.6	-
Hammaslahti	5.3	2.3
Hällinmäki	4.2	-
Virtasalmi	4.2	0.5
Raajärvi	2.9	-
Ylöjärvi	2.8	-
Aijala	2.0	-
Haveri	1.4	-
Orijärvi	1.0	-
Outokumpu	1.0	-
Mätäsvaara	1.0	-
Korsnäs	0.85	
Kylmäkoski	0.7	-
Makola	0.4	-

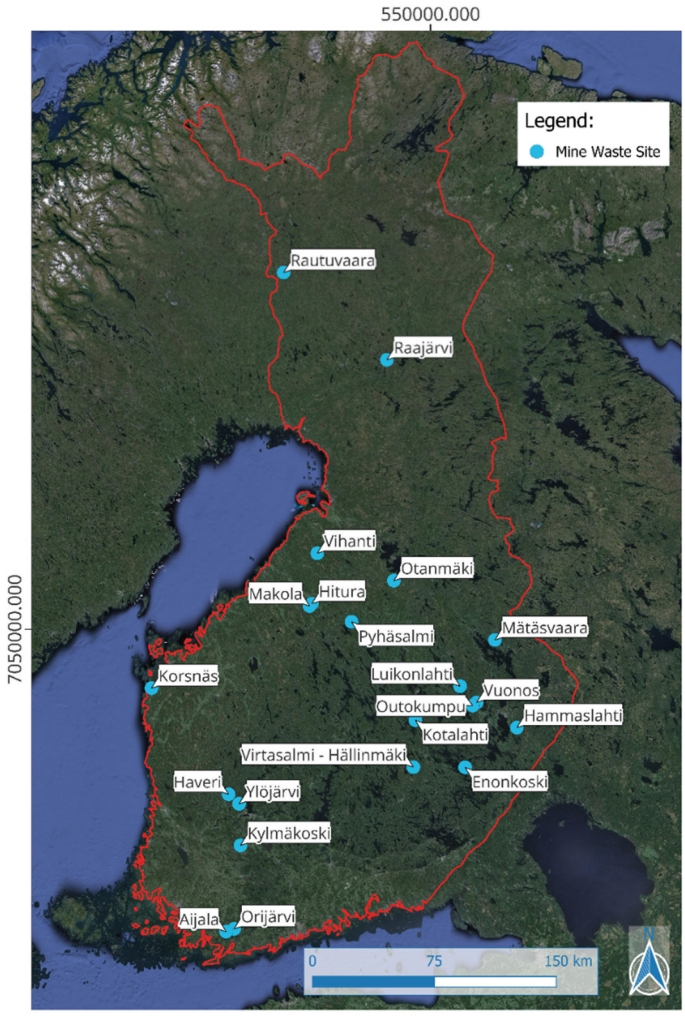


Figure 29 - Map of selected mine waste site for the study. (source: Google satellite image)

The available concentration of metals and critical elements reported in the database originated mainly from small-scale environmental studies conducted during the last decades by GTK and other autonomous authors. Many times, the values were obtained using aqua regia extraction for the determination of polluting metals, often overlooking the quantification of elements that are considered critical or valuable at present times.

The set of extractive waste sites (Table 5) included the most important closed mine sites in Finland, considering some minor exclusions.

All the sites reporting tailings materials were included, while sites containing only waste rock accumulations were not considered. The tailings sites are usually characterised by surface impoundments, containing most of the tailings' volume that was accumulated during processing operations. The small amount or absence of reported waste rock materials in the major closed mine sites is because most of the considered mines were operated by underground operations, and waste rock was returned as a backfill for the exploitation voids.

3.3 A novel tool for implementing Economic Importance into tailings quantity: The Economically Important – Equivalent Ton (t_{EIeq})

The viability of recovering commodities from mine tailings is typically assessed based on the economic value of the materials present and the technical feasibility for efficiently recovering the valuable fractions. As a consequence, market and regulatory needs must be matched in order to justify industrial revenue (Kinnunen, Karhu, Yli-Rantala, Kivikytö-Reponen, & Mäkinen, 2022).

Traditional evaluation practices, mainly focused on quantifying the economic value embedded in the waste materials, could bias considerations concerning resource recovery. As a result, raw materials that may have significant economic importance to the industry, even if correlated to lower economic value, may be overlooked during evaluation. The new proposed unit aims at assessing and quantifying the criticality and the economic relevance of commodities contained in mine waste materials, supporting a more holistic and complete evaluation for their recovery.

3.3.1 Economic Importance (EI) evaluation method from the European Commission

In 2023, the European Commission published the Final Report on Critical Raw Materials for the European Union (EU) (European Commission. Directorate General for Internal Market, Industry, Entrepreneurship and SMEs, 2023). This assessment evaluated the criticality of selected raw materials for the European economic system. The CRMs are defined as materials characterised by high economic importance and a high supply risk for the EU industry. Economic importance (EI) is estimated based on the added value by corresponding EU manufacturing sectors, adjusted by a substitution index. Supply risk (SR) is calculated considering supply concentration at both global and EU levels, weighted by a governance performance index and adjusted by recycling and substitution parameters. An assessed raw material is considered "critical" when it surpasses a defined threshold for both economic importance and supply risk (European Commission. Directorate General for Internal Market, Industry, Entrepreneurship and SMEs., 2017).

According to the EU methodology for establishing the EU list of CRMs (European Commission. Directorate General for Internal Market, Industry, Entrepreneurship and SMEs., 2017), the EI is defined by the following formula:

Equation 6 – Economic Importance as defined by EU methodology (European Commission, 2017)

$$EI = \sum_{s} (A_s \cdot Q_s) \cdot SI_{EI}$$

Where:

- EI: Economic Importance
- A_s: the share of end use of a raw material in a NACE (statistical classification of economic activities) Rev. 2 (2-digit level) sector;
- Q_s: the sector's VA (value added) at the NACE Rev. 2 (2-digit level);
- SI_{EI}: the substitution index of a raw material related to economic importance;
- *s* denotes the specific sector considered.

Table 6 reports the EI parameters for the assessed list of raw materials as published in the 2023 EU CRM assessment (European Commission, 2023c).

Table 6 - EI values calculated for 2023 by the European Commission. Adapted from European Commission, 2023

Commodity	Type	Economic Importance score (EI)
Aluminium/bauxite	*Mineral*	*5.8*
Antimony	*Metal*	*5.4*
Arsenic	*Metal*	*2.9*
Baryte	*Mineral*	*3.5*
Cadmium	*Metal*	*4.1*
Chromium	*Metal*	*7.2*
Cobalt	*Metal*	*6.8*
Copper	*Metal*	*4.0*
Gold	*Metal*	*2.4*
HREE (Eu)	*Metal*	*3.3*
Iron ore	*Mineral*	*7.2*
Lead	*Metal*	*4.2*
Limestone	*Mineral*	*3.6*
LREE (La)	*Metal*	*2.9*
Manganese	*Metal*	*6.9*
Molybdenum	*Metal*	*6.7*
Nickel	*Metal*	*5.7*
Phosphate rock	*Mineral*	*6.4*
Selenium	*Metal*	*4.8*
Silica	*Mineral*	*3.1*
Silver	*Metal*	*4.6*
Tin	*Metal*	*4.5*
Titanium	*Metal*	*5.4*
Tungsten	*Metal*	*8.7*
Vanadium	*Metal*	*3.9*
Zinc	*Metal*	*4.8*

3.3.2 Definition and application of the t_{EIeq} unit

To provide an additional indication of the economic importance of a commodity, a new unit was defined to assess the weighted economic importance of the commodities contained in a given amount of tailings. This unit, named Economically Important – Equivalent Ton ($t_{EI,\ eq}$), was defined by the following formula:

Equation 7 - Definition of the $t_{EI,eq}$ unit

$$t_{EI,eq,c} = Q_t \cdot C_c \cdot EI_c$$

Where:

- Q_t: total quantity of tailings reported, expressed in metric tons;
- C_c: concentration or assay of a selected commodity/material, expressed in parts per million (ppm);
- EI_c: Economic Importance parameter for the selected commodity/material reported in EC Critical Raw Materials Assessment (European Commission, Directorate General for Internal Market, Industry, Entrepreneurship and SMEs., 2023), expressed as a dimensionless coefficient.

To sum the overall amount of t_{EIeq} for a selected site, it is calculated by summing the contribution of each singular commodity considered for the selected site, according to the following equation:

Equation 8 – Total $t_{EI,eq}$ for a selected site

$$Total\ t_{EI,eq} = \sum_{i=1}^{n} t_{EI,eq,i}$$

According to Equation 7 and Equation 8, a total amount of t_{EIeq} was estimated for each mine waste site considered from the GTK METSO dataset by integrating tonnage information, chemical assays, and their corresponding economic importance.

Table 7 reports the details of partial and total values t_{EIeq} obtained for each of the selected sites. Full data are reported in ***Appendix A.1***.

For chemical assays, only records regarding critical metals, valuable elements and minerals were considered. Due to the lack of mineralogical data available, several commodities included in the EC Critical Raw Materials (CRM) assessment (European Commission, 2023c) were excluded from the evaluation.

Table 7 – Calculated $t_{EI,eq}$ values according to chemical assays reported in the METSO-GTK database

Mine Site	**Σ $t_{EI,eq}$**
Aijala	57,024
Hällinmäki	11,046
Korsnäs	28,125
Hitura	479,010
Pyhäsalmi	2,086,093
Luikonlahti	361,590
Enonkoski	156,783
Hammaslahti	35,056
Haveri	9,431
Kotalahti	200,867
Kylmäkoski	8,053
Makola	6,416
Mätäsvaara	3,814
Orijärvi	48,684
Otanmäki	11,245,400
Outokumpu	14,925
Raajärvi	2,107,641
Rautuvaara	147,213
Vihanti	220,946
Virtasalmi	11,404
Vuonos	421,012
Ylöjärvi	9,942

Figure 30 reports the considered sites ranked according to descending tailings quantities, being more than 5 Mt and less than 5Mt, respectively. In addition, the plots show the calculated total value of $t_{EI,eq}$ for each mine site considered.

According to the plotted data, some of the studied sites contained a significant amount of economically important commodities. Among sites that reported more than 5Mt of tailings, Otanmäki showed the highest value of 11.25 $Mt_{EI,\ eq}$, followed by Pyhäsalmi (2.09 $Mt_{EI,\ eq}$). In addition, for smaller sites (<5Mt of tailings), Raajärvi showed the highest value of economically important commodities of 2.11 $Mt_{EI,\ eq}$.

In general, large amounts of tailings did not directly correspond to high values of economically important tons of critical or valuable commodities. More in detail, the Pyhäsalmi and Raajärvi mine sites had similar values of total $t_{EI,eq}$, with 2.086 and 2.108 million equivalent tons (Mteieq) respectively. Despite this, the Pyhäsalmi site has 20 million tons (Mt) of tailings, whereas the Raajärvi site has only 2.9 Mt.

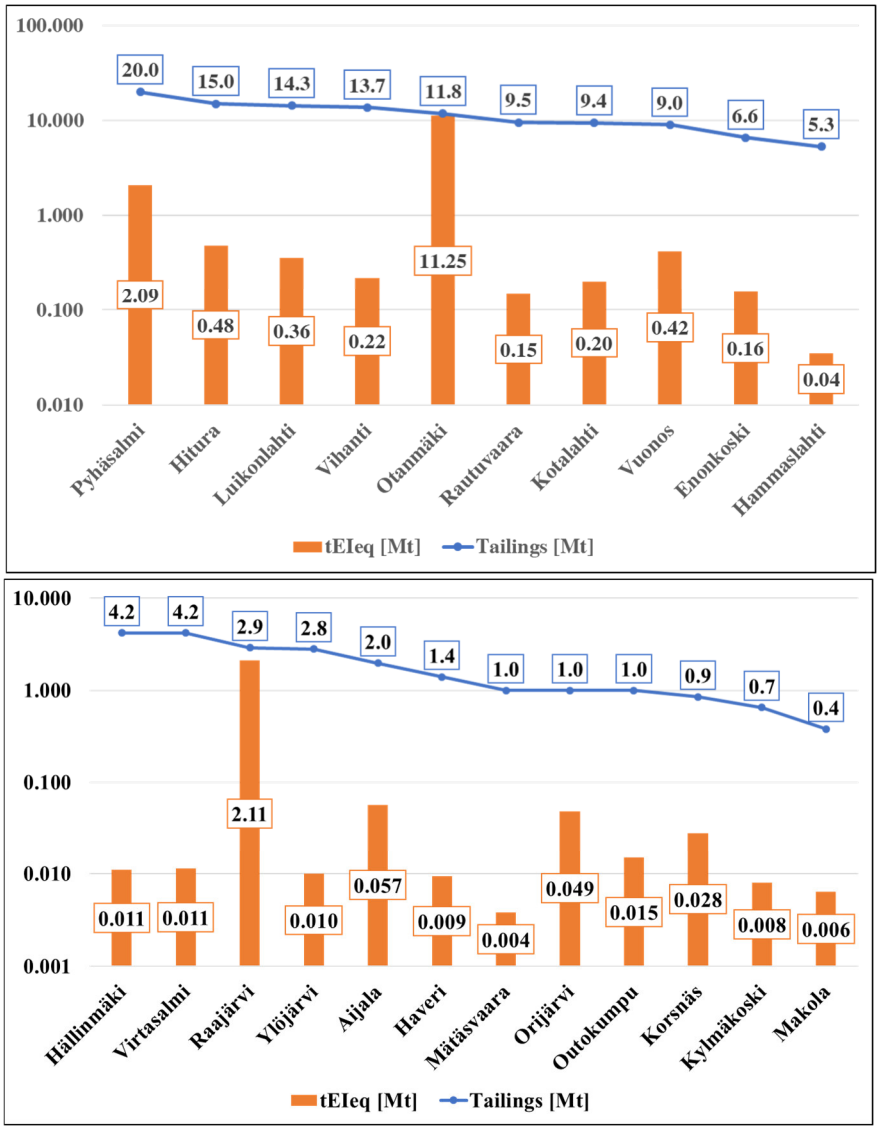


Figure 30 – Total $t_{EI,eq}$ values for mine sites reporting more than 5Mt (top) and less than 5Mt (bottom) of tailings reported in the Finnish mine waste database

3.4 Economic value embedded in Finnish tailings

The economic value (EV) contained in the considered mine sites in this study was estimated. It was assumed that the concentration of valuable elements from the METSO database accurately represents the entire volume of the waste material. A unit price was assigned to each commodity, derived from the average quotations recorded over recent years, as per the 2024 Mineral Commodity Summary (U. S. Geological Survey, 2024).

For each site, a resulting economic value was calculated by estimating the potential content in tons of each available element or mineral and multiplying this amount by the assigned value in US Dollars (US$).

Table 8 reports the economic evaluation performed for each of the selected sites. Full data are reported in ***Appendix A.2***.

Table 8 – Calculated economic value (EV) for selected Finnish tailings sites

Mine Site	*EV [MUS$]*
Aijala	51
Hällinmäki	31
Korsnäs	22
Hitura	1,242
Pyhäsalmi	708
Luikonlahti	755
Enonkoski	468
Hammaslahti	84
Haveri	125
Kotalahti	318
Kylmäkoski	21
Makola	29
Mätäsvaara	26
Orijärvi	58
Otanmäki	2,562
Outokumpu	44
Raajärvi	576
Rautuvaara	173
Vihanti	386
Virtasalmi	39
Vuonos	752
Ylöjärvi	42

Figure 31 reports economic values calculated for each site, for sites having more than 5Mt and less than 5Mt of tailings.

For sites having >5Mt materials, Otanmäki had the highest calculated economic value of 2,562 MUS$, followed by Hitura, showing 1,242 MUS$ estimated value. Among sites having less than 5Mt of tailings reported, Raajärvi and Haveri had the highest economic value, being 576 MUS$ and 125 MUS$, respectively.

Moreover, some sites, such as Otanmäki, Hitura and Raajärvi were characterised by relatively high economic values, even if associated with modest quantities of tailings, respectively 11.8 Mt, 15.0 Mt and 2.9 Mt. By contrast, Pyhäsalmi and Luikonlahti have significant amounts of tailings, respectively 20 Mt and 14.3 Mt, but their economic values appeared to be contained, being respectively 708 M US$ and 755 M US$.

The estimated economic value should be considered only as a general parameter, according to the generic estimation regarding the amounts of reported

tailings, the associated chemical assays, and assuming that a hypothetical 100% of possible extraction of valuable fractions was assumed.

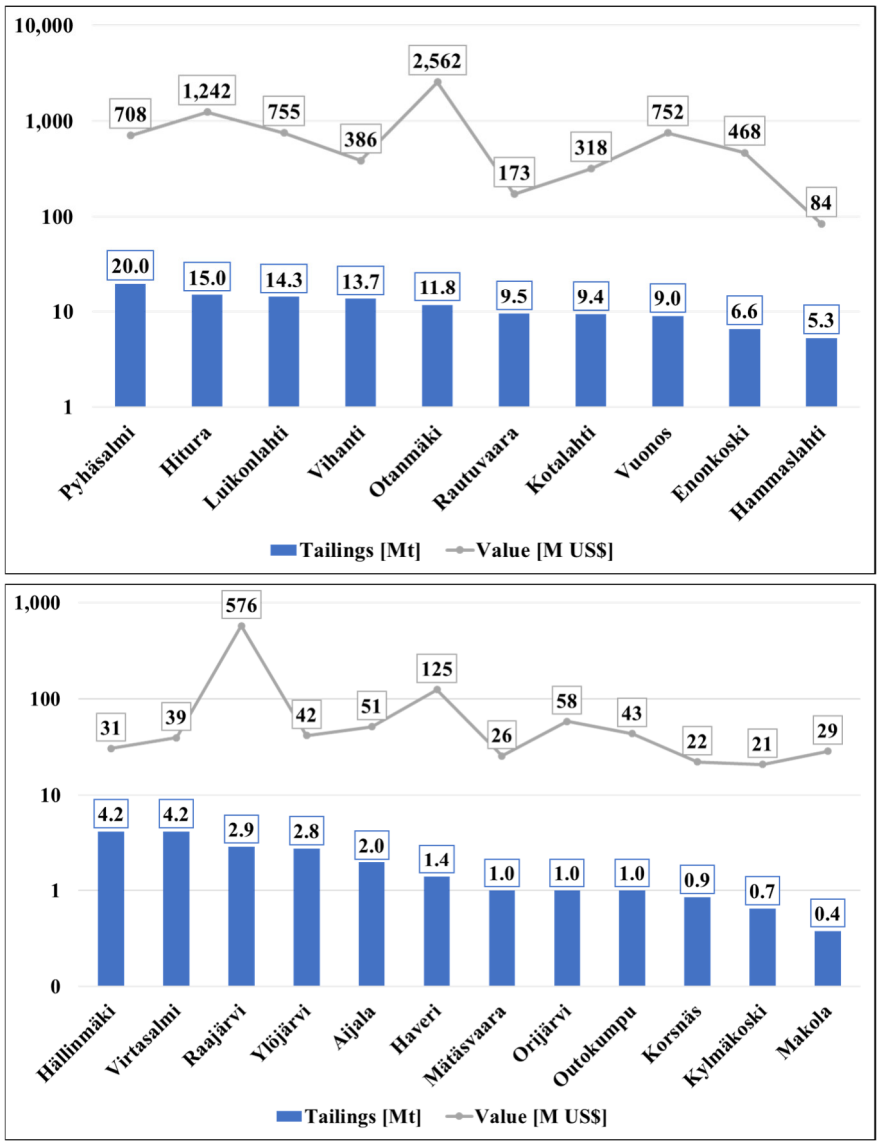


Figure 31 - Economic value for mine sites having more (top) and less than (bottom) 5Mt of tailings reported in the Finnish mine waste database

3.4.1 Proximity of smelter infrastructures to tailings sites

Distances between selected mine sites and active smelter plants in Finland were calculated to provide additional data for economic considerations.

Smelter facilities in Finland are three and are located in two locations (Figure 32): Kokkola (Central Ostrobothnia province) and Harjavalta (Satakunta province).

In Kokkola, the smelter plant operated by Boliden Group is specialised in zinc and sulfuric acid production (Boliden Group, 2025b). In Harjavalta, two smelters are active. They are operated by Norilsk Nickel Oy and Boliden Group, being primarily dedicated to the refinement and production of nickel, copper, silver,

gold, and sulfuric acid production (Boliden Group, 2025a; Norilsk Nickel Harjavalta Oy, 2025).



Figure 32 - Location of smelter facilities in Finland (source: Google satellite images)

The distances between the selected tailings sites and smelters were calculated using Google Earth's road distance estimation tool, considering the most convenient routes in terms of travel time. Table 9 reports the obtained distances of the selected mine waste sites and the smelter areas.

Table 9 - Road distances between selected tailings sites in the Finnish mine waste database and smelter plants locations in Finland

Site	*Distance from Kokkola [km]*	*Distance from Harjavalta [km]*
Aijala	*499*	*182*
Enonkoski	*436*	*491*
Hällinmäki	*359*	*385*
Hammaslahti	*458*	*533*
Haveri	*285*	*102*
Hitura	*111*	*410*
Korsnäs	*174*	*196*

Site	*Distance from Kokkola [km]*	*Distance from Harjavalta [km]*
Kotalahti	*324*	*394*
Kylmäkoski	*382*	*113*
Luikonlahti	*369*	*481*
Makola	*115*	*414*
Mätäsvaara	*396*	*566*
Orijärvi	*499*	*181*
Otanmäki	*220*	*519*
Outokumpu	*390*	*491*
Pyhäsalmi	*173*	*449*
Raajärvi	*475*	*809*
Rautuvaara	*543*	*878*
Vihanti	*140*	*453*
Virtasalmi	*359*	*385*
Vuonos	*397*	*498*
Ylöjärvi	*309*	*115*

According to the calculated distances, the Haveri site was the closest to the Harjavalta smelters, at a distance of 102 km. Kylmäkoski and Ylöjärvi were located 113 km and 115 km from Harjavalta, respectively. Furthermore, the Kokkola smelter was situated 111 km from the Hitura mine site, making it the closest processing facility for this mine site. Makola and Vihanti were 115 km and 140 km away from the Kokkola smelter, respectively. By contrast, the sites of Enonkoski, Hammaslahti, Raajärvi, and Rautuvaara were located more than 400 km from both smelter areas. The Rautuvaara site was the farthest, being 543 km from Kokkola and 878 km from Harjavalta.

Figure 33 shows a radar plot comparing the distances of each site from smelter plants locations.

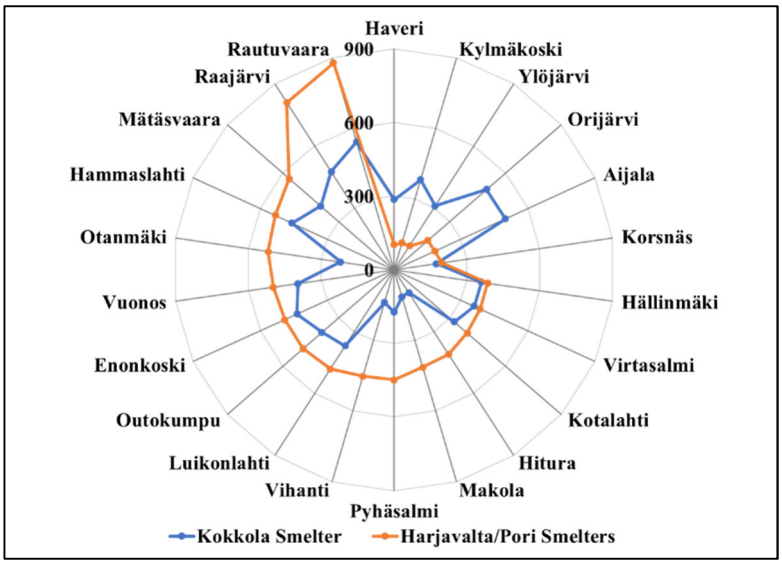


Figure 33 - Radar plot for road distances between smelter plants in Finland and selected tailings sites in kilometres (km).

Based on the calculated distances, a top five list of the closest sites to each smelter plant location was elaborated. The five closest sites to Kokkola smelter are:

1. Hitura (111 km);
2. Makola (115 km);
3. Vihanti (140 km);
4. Pyhäsalmi (173 km);
5. Korsnäs (174 km).

Similarly, the list of the five most proximate sites to Harjavalta smelters was arranged as follows:

1. Haveri (102 km);
2. Kylmäkoski (113 km);
3. Ylöjärvi (115 km);
4. Orijärvi (181 km);
5. Aijala (182 km);

To conclude, the Kokkola smelter is, on average, 337.0 km away from the selected mine waste sites, with all sites being within 600 km. By contrast, the Harjavalta smelters are, on average, 411.1 km away from the selected sites, with most sites being within 600 km, except for two being more than 800km away.

3.5 Comparison of Economic Importance and Economic Value obtained data

The data obtained from previous calculations regarding the newly introduced the total $t_{EI,eq}$ and total economic value were compared with each other. Additionally, the total amount of tailings was plotted together, as reported in Figure 34. This comparison aimed to understand the predominant parameter among the ones considered for a possible prioritisation of actions.

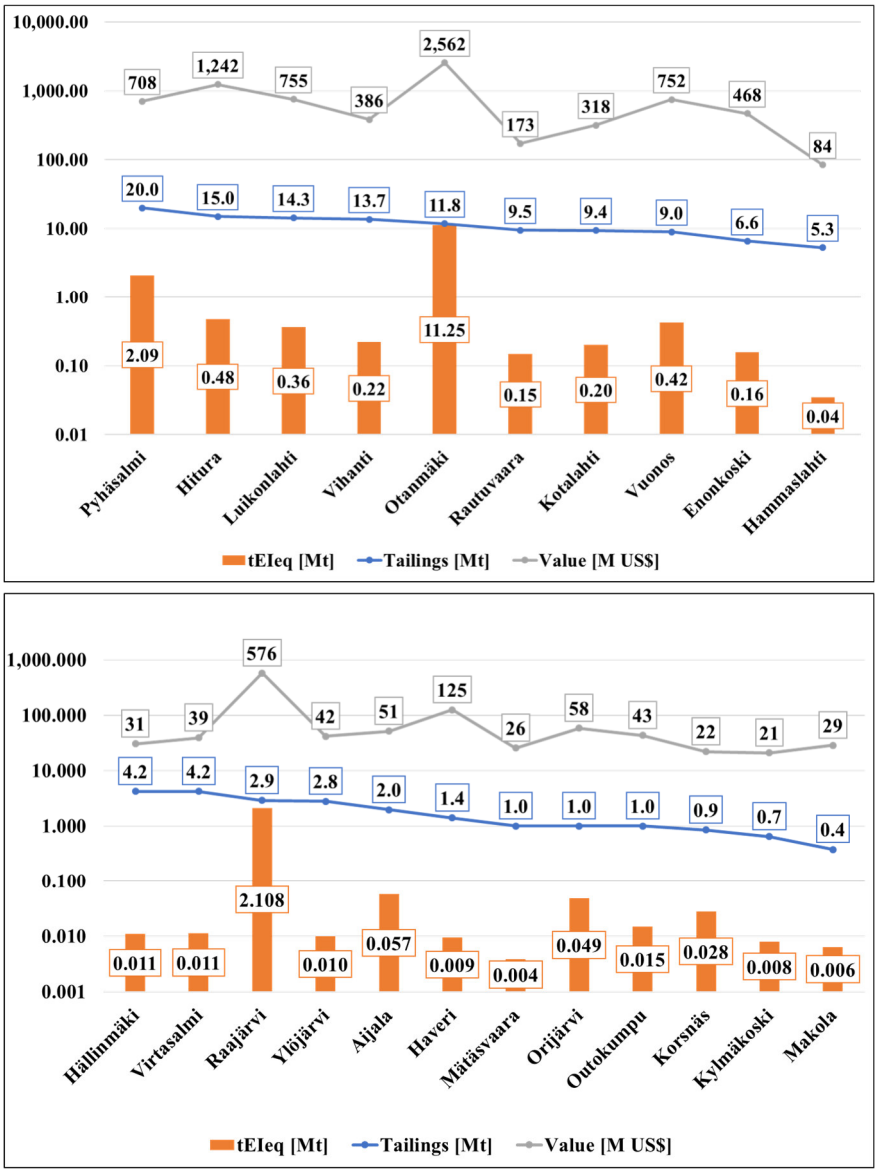


Figure 34 - Total Equivalent EI tons and Economic value for tailings sites having more than 5Mt (top) and less than 5Mt (bottom) of tailings selected in the Finnish mine waste database.

The Otanmäki site showed the highest EI (11.25 M $t_{EI,eq}$) and EV (2,562 MUS$) values associated with a consistent quantity of tailings (11.8 Mt). Furthermore, Pyhäsalmi and Hitura, being the sites with the highest reported

quantity of tailings, exhibited relevant EI and EV values. In particular, Pyhäsalmi had an EI of 2.09 $Mt_{EI,eq}$ associated with a modest EV of 708 MUS$, while Hitura showed a higher EV of 1,242 MUS$ and a limited EI value of 0.48 $Mt_{EI,eq}$. Additionally, Vuonos was characterised by a relevant EV of 752 MUS$, associated with contained EI of 0.42 $Mt_{EI,eq}$, and 4.0 Mt of tailings.

For sites being characterised by less than 5 Mt of tailings, Raajärvi showed the highest EI and a modest EV value, being 2.11 $Mt_{EI,eq}$ and 576 MUS$, respectively, with only 2.9 Mt of tailings. Other sites had, in general, EV lower than 100 MUS$ and EI never exceeding 0.06 $Mt_{EI,eq}$.

3.6 Environmental Risk (ER) associated with tailings sites

Environmental Risk (ER) associated with selected waste sites was considered as a crucial parameter for prioritisation and decision-making action within this study.

The GTK METSO database (GTK, 2024) contains, in most cases, observed environmental impacts or problems extrapolated from literature works or national reports. These impacts were gathered and ranked, as reported in Table 10. From each reported environmental problem, an ER qualitative score was assigned, according to three steps: Low, Mid and High. The ER scores were assigned arbitrarily, qualitatively grading the reported comment on environmental problems associated with each site. For sites for which no information was present in the database, no score was assigned.

These scores were needed to complete the input parameters for the 3-D decision matrix, which will be described in more detail in the following paragraphs.

Table 10 - Assigned environmental risk (ER) scores (Low, Mid, High) according to environmental impacts observed from the Finnish mine waste database. n.a.: not available.

Site name	*Affected environmental aspect(s)*	*Observation(s)*	***ER (assigned)***
Pyhäsalmi	*Air* *Habitat*	*Damaged vegetation* *Dusting* *Heavy metals in soil*	***High***
Hitura	*Air* *Surface waters*	*Alkaline seepage* *Dusting*	***Mid***
Luikonlahti	-	-	***Low***
Vihanti	*Radioactive emission* *Surface waters*	*Acid-generating tailings*	***High***
Otanmäki	*None*	*None*	***Low***
Rautuvaara	*Habitat* *Dust*	*Alteration of local fauna*	***Mid***
Kotalahti	*Acid drainage* *Surface waters*	*pH<4 seepages* *Heavy metals in water*	***High***
Vuonos	*Acid drainage*	*High S level*	***High***

Site name	*Affected environmental aspect(s)*	*Observation(s)*	***ER (assigned)***
Enonkoski	*n.a.*	*n.a.*	***n.a.***
Hammaslahti	*Acid drainage* *Surface waters*	*Acid waters* *Heavy metals in water* *Contaminated soil*	***High***
Hällinmäki	*None*	*None*	***Low***
Virtasalmi	*None*	*None*	***Low***
Raajärvi	*n.a.*	*n.a.*	***n.a.***
Ylöjärvi	*Acid drainage* *Surface waters* *Habitat* *Soil* *Air*	*Acid-generating tailings* *Heavy metals in water* *Dead vegetation* *Heavy metals in soil* *Dusting of tailings*	***High***
Aijala	*Air* *Habitat* *Sediments*	*Heavy metals in water* *Contaminated lake sediments*	***High***
Haveri	*Acid drainage* *Sediments* *Air*	*Acid-generating tailings* *Contaminated sediments* *Dusting of tailings* *Contaminated soil*	***High***
Orijärvi	*Acid drainage* *Surface waters* *Habitat*	*Acid-generating tailings* *Heavy metals in water* *Damaged fauna population*	***High***
Outokumpu	Acid drainage Groundwater Habitat	*Low pH groundwaters* *Heavy metals in groundwaters* *Damaged vegetation*	***High***
Mätäsvaara	Air	*Possible dusting*	***Low***
Korsnäs	*Radioactive emission* *Surface waters* *Sediments*	*Radioactive tailings* *Heavy metals in water* *Heavy metals in soils*	***High***
Kylmäkoski	*n.a.*	*n.a.*	***n.a.***
Makola	*n.a.*	*n.a.*	***n.a.***

According to the reported data, 11 sites reported a "*High*" assigned ER score. Most of the sites ranked with this comment reported several environmental impacts reported in the database, such as potential or observed acid drainage, contamination of surface waters or soils, and radioactive radiation. Furthermore, 2 sites were assigned a "*Mid*" ER score, being characterised by minor environmental aspects affected or impacted by deposited tailings in the site. To conclude, 5 sites were assigned with *"Low"* ER score, having no relevant impacts

reported in the database, while 4 sites showed no data or comments regarding environmental impacts in the consulted dataset.

3.7 A 3-D decision matrix for sites prioritisation according to their Economic Importance (EI), Economic Value (EV) and Environmental Risk (EV)

A 3-D decision matrix was designed and proposed to classify the selected sites in this study based on the assigned and calculated parameters describing Economic Importance, Economic Value, and environmental risk. This tool aims to facilitate a data-driven methodology for prioritising actions for the valorisation of mine sites with associated abandoned extraction waste facilities.

In Figure 35, a prototype of the matrix is reported. The X-axis represents the environmental risk (ER) level categorised into Low, Mid, and High. This descriptor was considered crucial for determining action prioritisation in case of an associated high environmental risk score.

The Y-axis represents the economic importance (EI) derived from the value of the Total $t_{EI,eq}$ divided into Low, Mid, and High categories. Finally, the Z-axis represents the economic value (EV) of the selected mine site, divided into three levels (Low, Mid, and High).

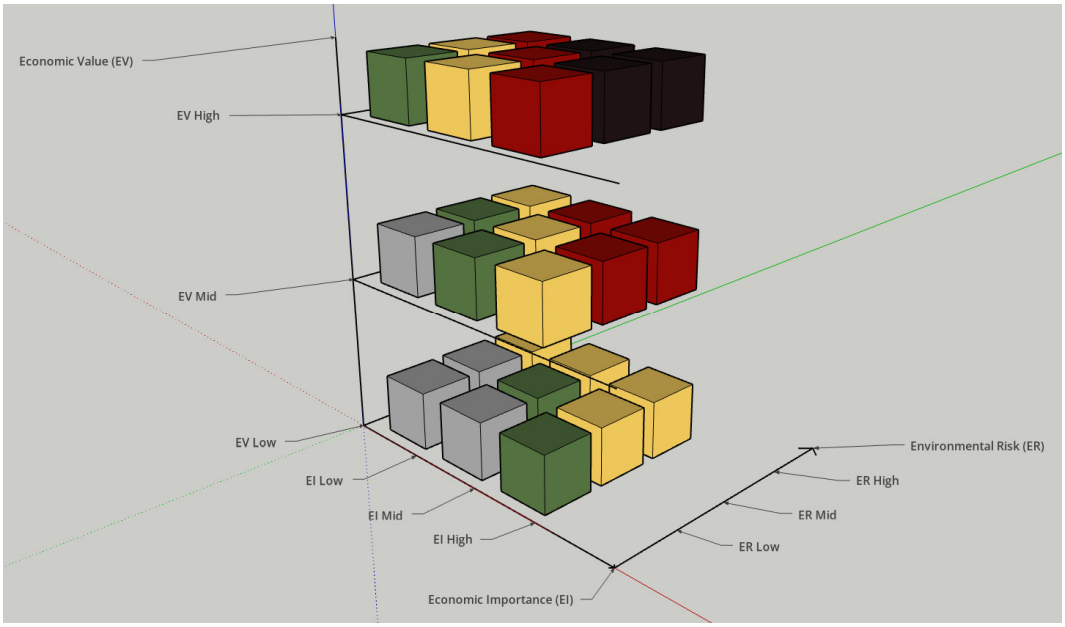


Figure 35 - 3-D Decision Matrix prototype for selecting priority action on tailings sites selected in the Finnish mine waste database. Grey: Negligible actions; Green: Programmable actions; Yellow: Recommended actions; Red: Highly recommended actions; Black: Urgent actions

In the reported prototyped 3-D matrix, a colour-based system was introduced to assign different outputs as recommended actions according to the different combinations of inputs. Each colour was assigned to a distinct degree of intervention considering three different levels of economic value, economic importance and environmental risks associated with each of the studied sites.

More in detail, grey boxes represent situations for which no immediate action was considered necessary according to the assessed input parameters. These scores may indicate low environmental risk linked with minimal economic value and importance, suggesting a lower priority for intervention.

Green boxes are assigned to scenarios where programmed actions could be advisable. The sites exhibiting this priority are characterised by low to mid environmental risk, mid to high economic importance, and low to mid economic values. In this scenario, planned and systematic interventions could be finalised for the assessment of a potential recovery of mine waste while monitoring environmental hazards related to the site.

Yellow boxes highlight a priority stage in which actions are recommended, underlining mid to high environmental risks, coupled with mid to high economic importance and variable economic value associated with the site. The sites being scored with this priority may necessitate targeted interventions, in particular regarding environmental restoration and monitoring, while potential recovery of mine waste should be considered a crucial possibility.

Red boxes are related to highly recommended actions, resulting in significant (Mid to High) environmental risks, economic importance, and economic value of the site. This could represent an urgent need for attention and the development of proactive measures for the site. Sites falling under this classification may require immediate intervention to prevent or mitigate severe environmental effects resulting from mine waste materials. Alternatively, the economic importance and value of the commodities embedded in the tailings could represent a viable opportunity to assess the possible recovery of metals or minerals from the tailings material.

Lastly, black boxes indicate a scoring linked to urgent actions. This is the most severe classification, for which a high economic value of the waste material is associated with mid to high economic importance and environmental risk. The sites being classified should be highly prioritised for developing actions to address environmental problems present in the site and explore possibilities to valorise the commodities embedded in tailings.

3.7.1 Application of the matrix

The proposed matrix was applied to the evaluation performed on the selected sites, according to economic importance, economic value and environmental risk.

Economic importance and economic value data were statistically binned according to the Jenks classification (Jenks, 1967) in order to obtain the needed charting levels. The results of this classification are reported in Table 11

Table 11 - Jenks classification ranges for assigning classes for EV and EI parameters calculated for tailings sites in the Finnish mine waste database

Parameter	Low	Mid	High
EV [MUS$]	*21 – 318*	*318 – 1,242*	*1,242 – 2,562*
EI [$Mt_{EI,eq}$]	*0.04 – 0.48*	*0.48 – 2.11*	*2.11 – 11.2*

According to the assigned EV and EI categories and merging the environmental risk scoring (Table 10), prioritisation colours were assigned to each site, as reported in Table 12. Multiple final options were assigned for those sites having not available data for the ER scoring.

*Table 12 - Prioritisation results after the application of the 3-D prototyped matrix for the Finnish tailings sites considered. *Red: Highly Recommended actions, Yellow: Recommended actions, Green: Programmable actions, Neg: Negligible actions.*

Site name	*EV*	*EI*	*ER*	Output block*
Pyhäsalmi	*Mid*	*Mid*	*High*	🔴
Hitura	*Mid*	*Low*	*Mid*	🟢
Luikonlahti	*Mid*	*Low*	*Low*	⚪
Vihanti	*Mid*	*Low*	*High*	🟡
Otanmäki	*High*	*High*	*Low*	🔴
Rautuvaara	*Low*	*Low*	*Mid*	⚪
Kotalahti	*Low*	*Low*	*High*	🟡
Vuonos	*Mid*	*Low*	*High*	🟡
Enonkoski	*Mid*	*Low*	*n.a.*	⚪🟢🟡
Hammaslahti	*Low*	*Low*	*High*	🟡
Hällinmäki	*Low*	*Low*	*Low*	⚪
Virtasalmi	*Low*	*Low*	*Low*	⚪
Raajärvi	*Mid*	*Mid*	*n.a.*	🟢🟡🔴
Ylöjärvi	*Low*	*Low*	*High*	🟡
Aijala	*Low*	*Low*	*High*	🟡
Haveri	*Low*	*Low*	*High*	🟡
Orijärvi	*Low*	*Low*	*High*	🟡
Outokumpu	*Low*	Low	*High*	🟡
Mätäsvaara	*Low*	Low	*Low*	⚪
Korsnäs	*Low*	*Low*	*High*	🟡
Kylmäkoski	*Low*	*Low*	*n.a.*	⚪🟡
Makola	*Low*	*Low*	*n.a.*	⚪🟡

According to the applied methodology, 2 sites were classified with “highly recommended actions”, 10 sites fell under the “recommended actions”, 1 was

characterised for “Programmable actions”, and 5 were assigned with “Negligible actions”. Moreover, 4 sites had a non-unique assigned output block, and no site was attributed with the black block, suggesting urgent actions.

More in detail, Pyhäsalmi and Otanmäki were the sites having the highest level of prioritisation, being assigned to a red output block. The Pyhäsalmi site was characterised by Mid EV and ER, while showing a high ER score. By contrast, Otanmäki showed a low ER associated with high EV and ER.

Sites showing “recommended actions” were mainly characterised by a high ER score and low EV and EI scores associated, indicating that these sites should be examined carefully for environmental restoration actions for which mine waste could act as an economical or strategic leverage.

3.8 UNFC classification standard applied to the Otanmaki tailings site

The UNFC code for resource and reserve classification is based on a three-dimensional scheme. This 3-D matrix is composed of three axes describing the categories used for the classification. In particular, each axis represents a specific category or main criteria (Figure 36): the E-axis represents the environmental-socio-economic viability, the F-axis the technical feasibility, and the G-axis the level of geological confidence (United Nations, 2020).

For each axis, the uncertainty is reduced moving from rate 4, the worst rating, to rate 1, representing the best rating. In practice, projects assigned with code numbers “E1, F1, G1” are classified as “viable projects” whether they are in production or in a near-production stage. Overall, the majority of the Finnish tailings sites, when considered as sources of secondary raw materials, would fall under the highest rates, being associated to very high uncertainties linked to poor details available in terms of geological confidence and technical feasibility.

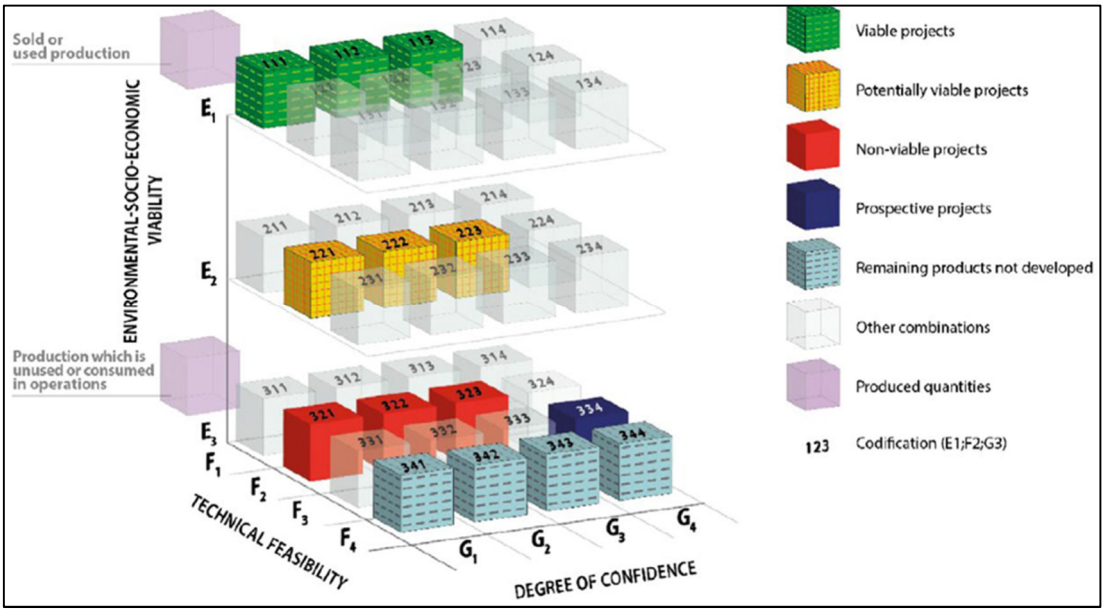


Figure 36 - The UNFC classification system with its three fundamental category definitions of environmental-socio-economic viability (E-axis), technical feasibility (F-axis), and the level of confidence (G-axis). (Source: United Nations, 2020)

The Otanmäki site was a Fe-V mine, currently owned and developed by Otanmäki Mine Oy. During its production lifespan (1953–1985), it produced around 25.5 Mt of run-of-mine material, associated with the deposition of around 9.8 Mt of tailings in a 1.45 km^2 basin (Otanmäki Mine Oy, 2025). Nowadays, the Otanmäki Mine Oy is developing a project for the reprocessing of this tailings material, targeting the recovery of about16% of ilmenite present in the waste material. The further recovery of about 1960 t of Co, 980 t of Cu and 1960 t of Ni assayed in the material was proven to be technically unfeasible and will not be considered in the final project. The Otanmäki tailings re-mining project is under development, and it is planned to start commercial operations in 2027 (Otanmäki Mine Oy, 2025).

According to the analyses performed in the previous paragraphs, this site appeared to be at the top of the prioritisation analyses among the sites considered.

Accordingly, the Otanmäki tailings site was assessed and classified according to the UNFC system, obtaining a scoring of E2, F2, G2 as reported by (Eerola, Solismaa, Karlsson, & Hokka, 2024). Additionally, further investigation was performed to improve the geological confidence associated with the site. Following a detailed exploration campaign and a block modelling of the basin, a G1 classification was proposed for the site, according to the UNFC guidelines (Leskelä, Hokka, & Karlsson, 2025).

The Otanmäki case showed that the recovery of low metal grades contained in extractive wastes may not be economically feasible, raising the need for a holistic extractive waste management, as proposed by Kinnunen et al. (2022), that should include a comprehensive evaluation of a wider range of potential valorisation opportunities.

3.9 Final Remarks

The Finnish mine waste database gathers different information about historical mine sites, including tailings quantities, metal assays, mineralogical and environmental information.

The work presented in this chapter proposed a complementary tool for assessing the prioritisation of sites for action, aiming at the recovery of critical raw materials from the mine waste of the 22 selected sites. The Economically Important – Equivalent Ton (t_{EIeq}) was introduced to calculate and quantify the economic importance of raw materials embedded in tailings, while the economic value was calculated according to commodity prices. Additionally, the distance of the selected sites from active smelter facilities was calculated for a more comprehensive analysis. From the calculated data, it was highlighted that economic importance and economic value could not be directly dependent in terms of expressed quantities, and also, a large amount of tailings could not represent the highest economic value. In more detail, the Otanmäki site showed the highest t_{EIeq} and economic value in the selected sites, followed by Pyhäsalmi and Hitura. However, the obtained data contains several uncertainties related to the quality of the chemical assays and the reported quantity of waste materials reported in the database, originating from collected literature. Additionally, environmental risk was evaluated and scored according to the information found in the database and implemented in the prioritisation analysis.

A 3-D decision matrix was designed and applied, offering a systematic way to visualise and prioritise mine sites according to their economic importance, economic value, and environmental risk. Two sites appeared to be in a situation for which action for evaluating potential recovery of raw materials was considered highly recommended. By contrast, the majority was considered to be in a condition for which actions are recommended, especially for the high environmental risk associated with mine waste.

In general, the methodology and unit developed in this chapter could provide a valuable first-pass screening tool for identifying and prioritising sites for potential CRM recovery, starting from a national mine waste database. As a result, focusing on the most promising sites could provide a more efficient planning of the source and action needed for reducing knowledge gaps and provide more data for understanding whether a potential recovery of critical raw material could be viable. The application of the UNFC classification system for those sites having a reduced variability in field data could enhance a clearer tool for attracting potential stakeholders in recovery actions.

To conclude, a well-organized database could provide crucial information for narrowing the attention to mine waste facilities having higher potential. Furthermore, considerations including several key parameters should be implemented, and many implications should be considered while shaping action for mine waste recovery. A holistic point of view should be preferred since action driven solely by profit could overlook solutions including environmental restoration or use of lower value raw material as a secondary product to be

reintroduced on circular industrial applications, as well as proper economic considerations related to historical metal prices trends and potential implications should be considered for a sounder prioritisation of sites.

Chapter 4

4. Advanced strategies for data collection and secondary prospectivity of mine waste: the Kanmantoo, Australia, historical tailings storage facility characterisation campaign

The work presented in this chapter has been previously published in:

Colombi, F.; Jackson, L.; Baldassarre, G.; Parbhakar-Fox, A. 2024. RB 2024/00036 Secondary prospectivity of South Australia's mine waste: Kanmantoo Cu, Au and Ag mine. Departmental Publication - Geological Survey Geoscience Publication. Government of South Australia. (Colombi, Jackson, Baldassarre, & Parbhakar-Fox, 2024).

4.1 Site description

4.1.1 Geological setting and historical mining activities

Kanmantoo mine is located about 44km southeast of the city of Adelaide, South Australia, and it is classified as a metasediment-hosted Cu-Au-Ag deposit located in the local Tapanappa Formation, as a part of the Cambrian Kanmantoo Group (Figure 37a).

This area is characterised by the presence of several orebodies (Figure 37b) having predominant mineralisations containing chalcopyrite, magnetite and pyrrhotite associated with minor presence of pyrite. (Seccombe, Spry, Both, Jones, & Schiller, 1985). The genesis of these ores has been debated in the literature, resulting in three proposed genetic models (Pollock et al., 2018):

- Syn-sedimentary: sulphide mineralisation was primarily formed by hydrothermal processes below or at the seafloor and the remobilised during later metamorphism (Belperio et al., 1998; Both, 1990; Burtt, 2008; Parker, 1986; Pollock et al., 2018; Seccombe et al., 1985; Spry, Schiller, & Both, 1988; Toteff, 1999; Verwoerd & Clergorn, 1975).

- Syn-metamorphic: the mineralisation generated during the peak of metamorphic phenomena (Burtt, 2008; Gum, 1998; Oliver, Dipple, Cartwright, & Schiller, 1998; Parker, 1986; Schiller, 2000; Solomon & Groves, 1994; Thomson, 1975).

- Post-peak metamorphism: the ore-bearing fluids originated from orogenic intrusive rocks, such as granite, in the final stage of the Delamerian Orogeny (Arbon, 2011; Focke, Schmidt Mumm, Tedesco, Seifert, & Bradey, 2009; Foden, Sandiford, Dougherty-Page, & Williams, 1999; Lyons, 2012; Schmidt Mumm, Tedesco, & Focke, 2009; Tedesco, 2009; Wilson, 2009).

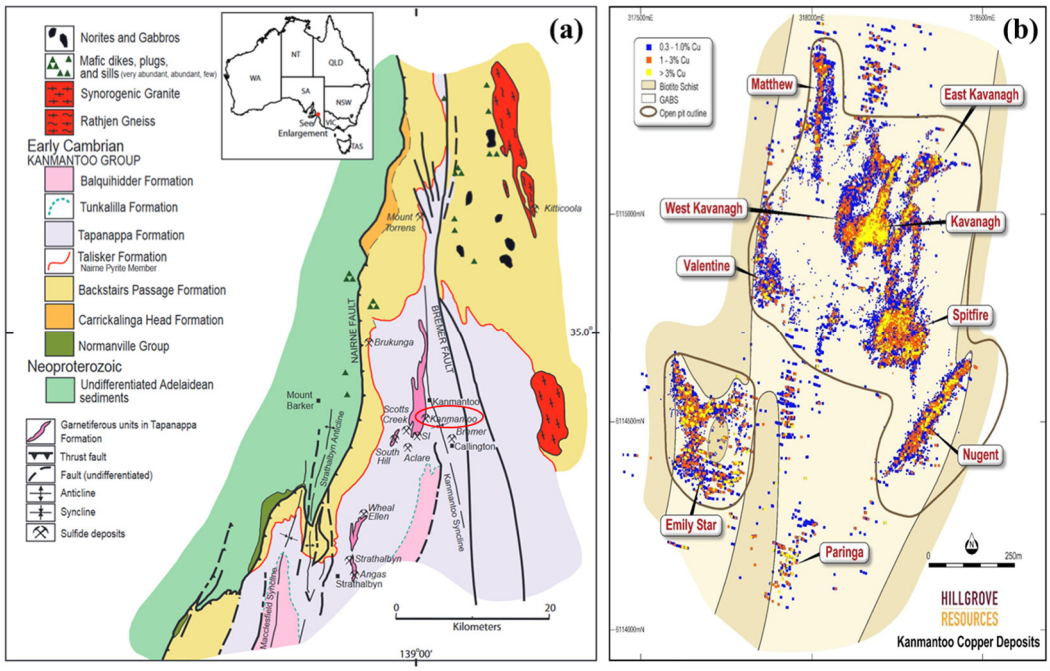


Figure 37 - (a) Regional geological map of the Kanmantoo region, Australia (after Pollock et al., 2018) (b) Cu grades measured from exploration campaigns realised by Hillgrove Resources in the Kanmantoo area, Australia. (GABS = garnet-andalusite-biotite schist, source: Hillgrove Resources (2020))

4.1.2 Mining and mineral processing history of the site

The first mining operation in the Kanmantoo area started in 1846 after preliminary explorations lasted several years, and developed until 1874 when exploitation was interrupted for economic reasons following a severe worldwide crisis of copper prices. Between the late 1800s and the early 1960s, intermittent prospecting initiatives took place in the area. A joint venture founded by two exploration companies, North Broken Hill Ltd and Hill South Ltd, led to the discovery of the main ore deposit in the Kanmantoo area in the late 1960s (Hillgrove Resources, 2020).

In 1970, the company Kanmantoo Mines Ltd started the exploitation by open pit methods of the Kavanagh deposit, retracing the ancient pits' outline. The mine produced in the first 6 years of activity 4.05 Mt of ore, having an average 1% Cu grade (Seccombe et al., 1985). At that time, the site was hosting an open pit, a mineral beneficiation plant, a waste rock dump and a tailings storage facility. In 1976, the works were interrupted due to falling copper prices (Hillgrove Resources, 2020).

During the 1980s, environmental restoration measures were implemented by covering about 65% of the surface occupied by the old tailings basin (1970-1976) with soil to promote the germination of indigenous and introduced vegetal species, such as grasses, shrubs, and trees (Agnew, 1998). Additionally, the old mineral processing plant area was repurposed for the installation of a fertiliser

manufacturing facility operated by Neutrog Australia Pty (Neutrog Australia Pty Ltd, 2025).

In 2003, Hillgrove Resources commenced a new exploration program in the Kanmantoo area, which led to a resumption of mining activities in 2010. Mining operations consisted of a main pit called “Giant Pit”, exploiting the Kavanagh deposit, and two additional pits, named Emily Star and Nugent, developed for the exploitation of smaller discovered orebodies. A new tailings storage facility was built overlapping the western edge of the old waste rock dumps left during the 1970s operations, while no actions were taken on the old tailings basin. The two minor pits were backfilled with produced waste rock once the extraction of the economically viable resources ceased. Subsequently, exploitation operations on the Giant pit ceased in May 2019 due to resource depletion.

The plant has been processing remaining run-of-mine stockpiles, concentrating mainly on Cu and Au, with accessory Ag minerals until 2021, when the design of underground operations for exploiting the deeper extension of the Kavanagh ore-body placed below the Giant pit commenced (Wallace, 2021). Underground mining began in May 2023, while commercial production was declared to commence in July 2024. Hillgrove Resources is targeting an annual production of 1.7 – 1.8 Mt by 2026, based on a total Mineral Resources of 19.3Mt of ore grading 0.77% Cu and containing 0.14 g/ton of Au. (Hillgrove Resources, 2025).

Figure 38 shows the actual configuration of the Kanmantoo mine site.

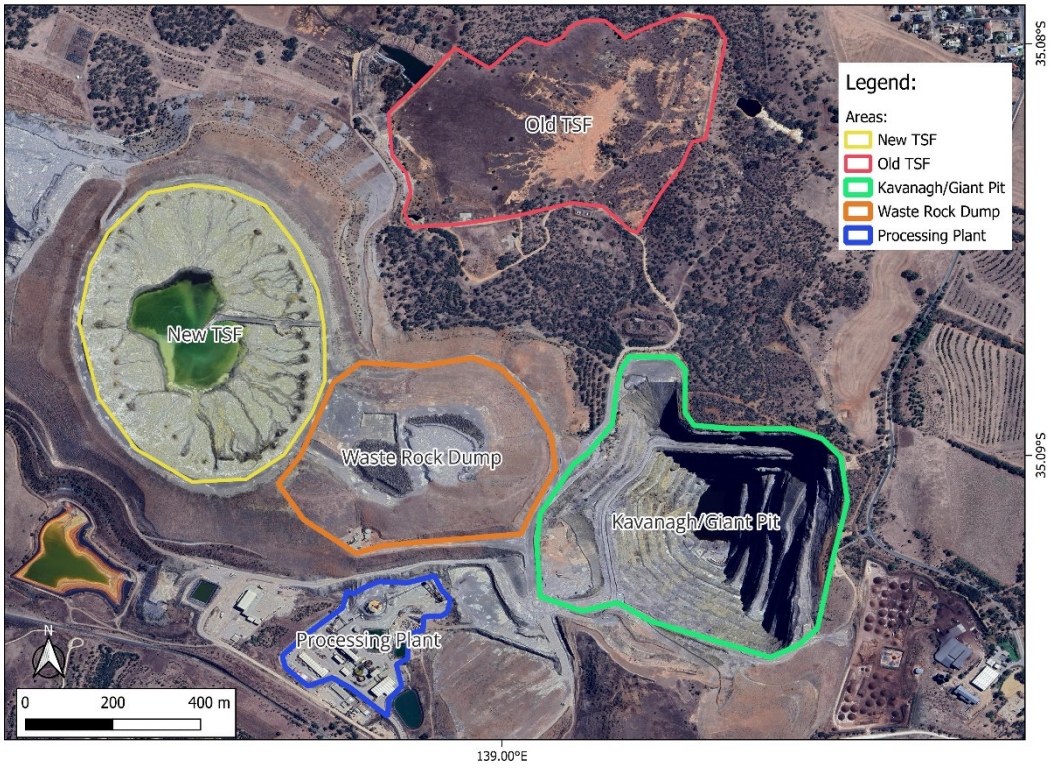


Figure 38 - Satellite view of the actual status of the Kanmantoo mine, Australia. Yellow: new tailings storage facility; Red: old tailings storage facility; Green: Giant Pit, currently exploited by underground operations; Orange: Waste rock dump produced by Giant Pit excavation; Blue: mineral processing plant. (source: Google satellite image, Coordinate system: WGS84)

4.1.3 Available information on tailings and their associated critical metal potential

The main source of geochemical and mineralogical information available regarding the old tailings storage facilities is represented by Agnew (1998). The author collected samples aimed at understanding the formation of hardpans on the tailings pond surface. The sampling campaign realised by Agnew (1998) consisted of four drill holes performed on the Old TSF surface, as shown in Figure 39.

Materials were collected at different depths for 3 holes, and were characterised in terms of geochemistry and mineralogy. Overall, at that time, the author reported that the dam was covered by deposited soil, occupying an area of about 192,000 m^2, and having a waste-to-ore ratio of 5:1. Moreover, materials were found to have a 60% fraction of fine sand and their mineralogy showed the presence of about 1% of pyrite, with main gangue minerals represented by quartz, muscovite, clinochlore, and almandine. pH values associated with tailings samples were between 3 and 5, while portable XRF analyses highlighted relevant concentrations of metals such as Cu, Zn, Zr, and Co (Agnew, 1998).

Additional environmental assessment and analyses of the old tailings basin were performed by Hillgrove Resources before the reactivation of mining activities in the early 2000s (Hillgrove Resources, 2020).

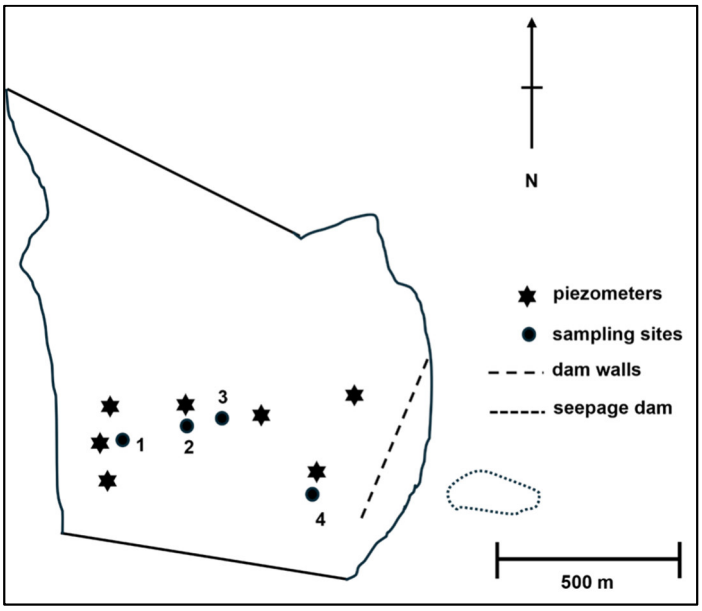


Figure 39 - Drill holes and sampling positions performed in previous studies in the old TSF of the Kanmantoo mine, Australia (after Agnew, 1998)

Critical mineral potential in the Kanmantoo area could be represented by the residual metal content potentially hosted in the tailings materials, but also from the country's host rock, being a garnet-andalusite-biotite schist, with a prevalent presence of almandine and pyrope minerals (Pollock et al., 2018). These minerals

were proposed to be a potential unconventional source of Sc and REEs (Klimpel, Bau, & Graupner, 2021). Previous studies (Hammerli, Spandler, & Oliver, 2016) studied the composition of non-mineralised metasediments belonging to the Kanmantoo Group, but Sc was not included in the analytical suite.

4.2 Sampling strategy

Sampling in the Kanmantoo site was realised by hand augering, targeting the old tailings storage facility (Figure 40).



Figure 40 - Old tailings storage facility view at the Kanmantoo mine, Australia, during sampling operations (Photo credits: F. Colombi and G. Baldassarre, 2024)

Five holes were drilled around the tailings basin to deliver a well-distributed coverage of the study area. In some cases, a mechanical hand drill was used for penetrating denser subsurface material present in the basin. As reported in Table 13, a total of 38 samples were collected, and the maximum depth reached by augering was 5.9 m in hole KA05. Figure 41 shows the location of drill holes in the old tailings storage facility. Full details on sample locations are available in ***Appendix B.1***.

Table 13 - Number of samples and maximum depth of bored drill holes in the old tailings storage facility of the Kanmantoo mine, Australia.

Hole ID	Number of samples	Max depth (m)
KA05	11	5.9
KA06	5	4.2
KA07	10	5.6
KA08	4	2.5
KA09	8	5.3

Total	**38**	**-**

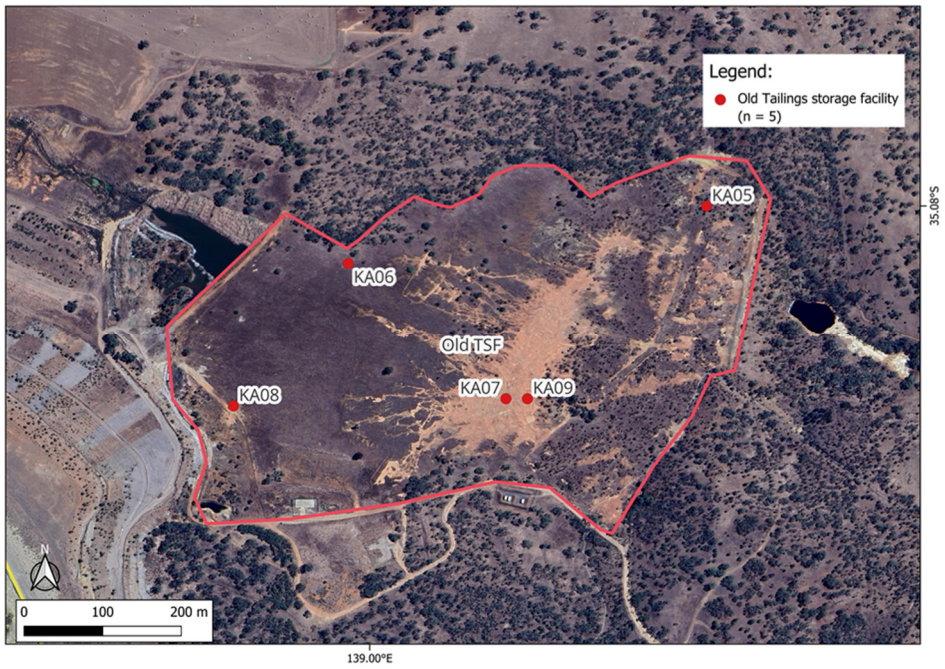


Figure 41 - Location of drill holes and sampling points in the old tailings storage facility, Kanmantoo mine, Australia. (source: Google satellite image, Coordinate system: WGS84)

During hand augering operations, samples were progressively recovered and placed on a plastic tarp (Figure 42), photographed, and observed to describe changing features with depth, such as stratigraphy and colour (Figure 43). The material recovered was sub-sampled according to different facies characteristics, then stored in plastic bags and labelled. For quality standards, certified reference materials were introduced in the sample set every 15 samples, along with duplicates, before shipment to the characterisation laboratory facilities.



Figure 42 - Recovered tailings material from old tailings storage facility (Hole KA07) in the Kanmantoo mine, Australia. Top left: Start of the hole, Bottom right: End of the hole (Photo credits: G. Baldassarre, 2024).

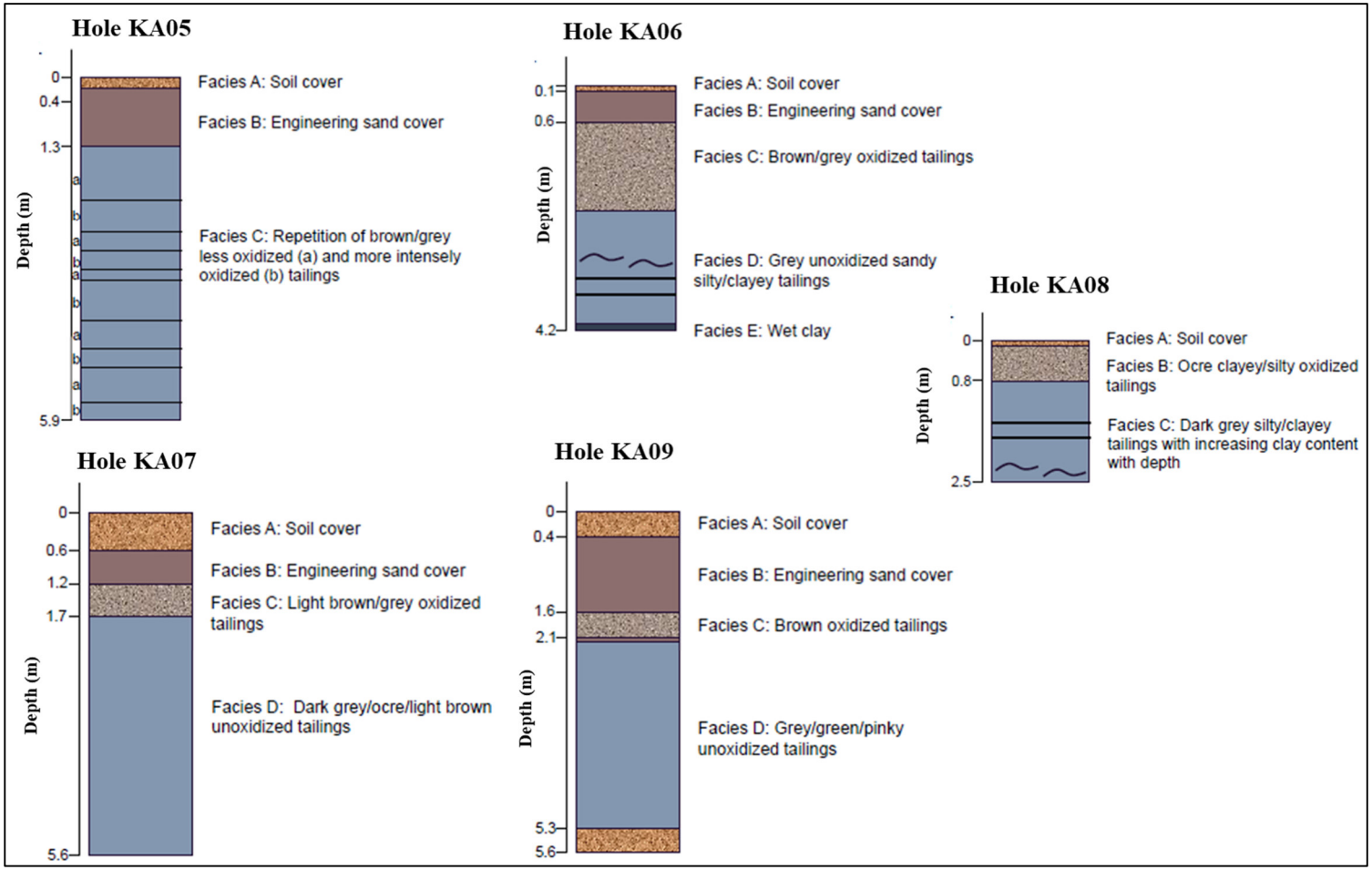


Figure 43 – Observed facies and colours of tailings material recovered from drill holes realized during sampling operations in the old TSF, Kanmnatoo mine, Australia (source: Colombi et al., 2024)

4.3 Chemical and mineralogical characterisation

The samples collected from the old tailings dam in the Kanmantoo were analysed to define chemical and mineralogical features according to the following methodologies:

- ICP-MS – (***Par. 2.5.3***)
- XRPD – (***Par. 2.4.4***)
- MLA – (***Par. 2.4.3***)
- LA-ICP-MS – (***Par. 2.5.5***)

After field collection, wet samples were oven-dried for 24h at 60°C. After drying, samples were crushed to 70% passing 2mm, then split and pulverised to a p85 of 75 µm. The pulverised portion of the bulk was used for ICP-MS and XRPD analyses, while the coarser crushing product (p70 = 2 mm) was used for MLA and LA-ICP-MS determinations.

4.3.1 Chemical characterisation results

4.3.1.1 ICP-MS characterisation methods

Chemical characterisation performed by ICP-MS showed that samples collected in the old tailings storage facilities are characterised by a relatively abundant concentration of metals such as Mn, Co, Cu, Bi, and Rb, as shown in Figure 44

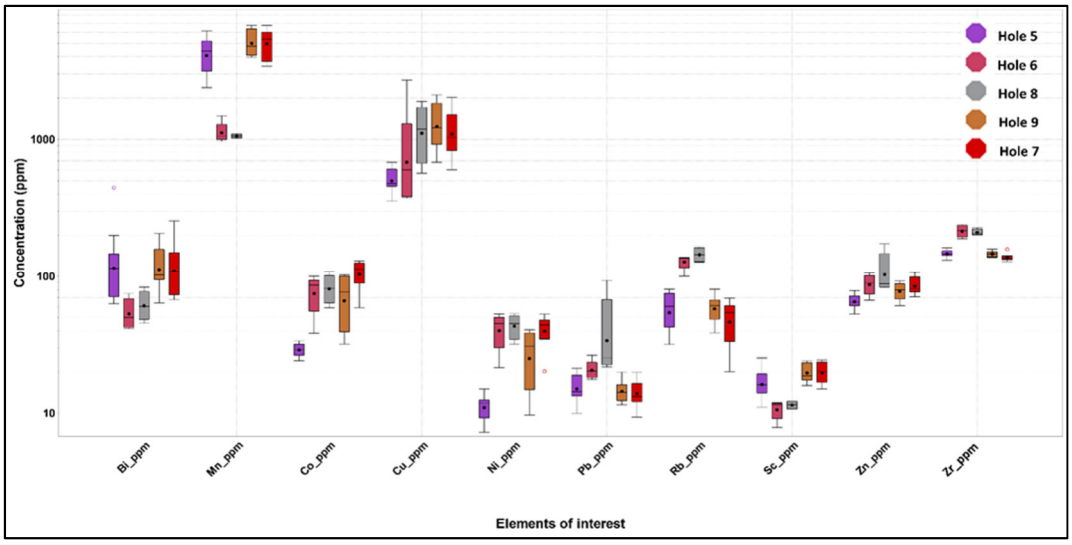


Figure 44 – Boxplot for selected elements assayed in the old tailings storage facility, Kanamntoo mine, Australia, according to the realised holes (n = 38) (source: Colombi et al., 2024)

More in detail, as reported in Table 14, Mn showed a mean assay of 3,902 ppm (min 973 ppm – max 6,730 ppm), Cu on average assayed 986 ppm (min 356 ppm – max 2,700 ppm), Bi had a mean concentration of 111 ppm (min 41 ppm –

max 447 ppm), while Co and Rb were measured in lower concentration, being on average 71 ppm (min 24 ppm – max 131 ppm) and 74 ppm (min 9.4 ppm – max 166 ppm). Moreover, LREEs and HREEs showed mean concentrations of 158 ppm (min 98ppm – max 279 ppm) and 76 ppm (min 33 ppm – max 128 ppm), respectively. Sc was found in trace concentration, assaying on average 17 ppm, ranging between a maximum of 25 ppm and a minimum of 7.9 ppm.

Table 14 - Summary statistics for selected elements measured in the old tailings storage facility, Kanmantoo mine, Australia (n = 38) (: ME-MS81 method)*

	Ag (ppm)	***Al (%)***	***As (ppm)***	***Bi (ppm)***	***Co (ppm)***	***Cu (ppm)***	***Fe (%)***	***In (ppm)***
Max	1.1	8	40	447	131	2,700	22	0.5
Min	0.3	5.2	0.8	41	24	356	9.8	0.2
Mean	0.7	6.8	3.1	111	71	986	16	0.3
Median	0.7	6.8	1.5	95	80	796	16	0.2
	Mg (ppm)	***Mn (ppm)***	***Ni (ppm)***	***P (ppm)***	***Pb (ppm)***	***Rb (ppm)***	***S (%)***	***Sc (ppm)***
Max	2.4	6,730	53	850	93	166	1.7	25
Min	0.9	973	7.3	450	9.4	20	0.2	7.9
Mean	1.3	3,902	30	568	18	74	0.8	17
Median	1.1	4,165	34	520	15	62	0.6	17
	Zn (ppm)	***Zr* (ppm)***	***∑LREE* (ppm)***	***∑HREE* (ppm)***				
Max	174	240	279	128				
Min	53	130	98	33				
Mean	81	161	158	76				
Median	78	147	144	78				

ICP-MS results were plotted against depth according to the realised drill holes during sampling operations. Figure 45 and Figure 46 show downhole plots reporting correlations of selected elements of interest for the old tailings storage facility.

In detail, Figure 45 reports the correlation between Fe, S, Cu, and Co with depth, highlighting a strong correlation of Cu with Fe and S according to the observed changing characteristics of the materials with depth. Similarly, Figure 46 shows the correlation of Fe, Al, Mn, Bi, LREEs and HREEs, in which Fe followed a similar trend with depth in association with Al, Mn, Bi and REEs, being the correlation of HREEs being stronger than that of LREEs.

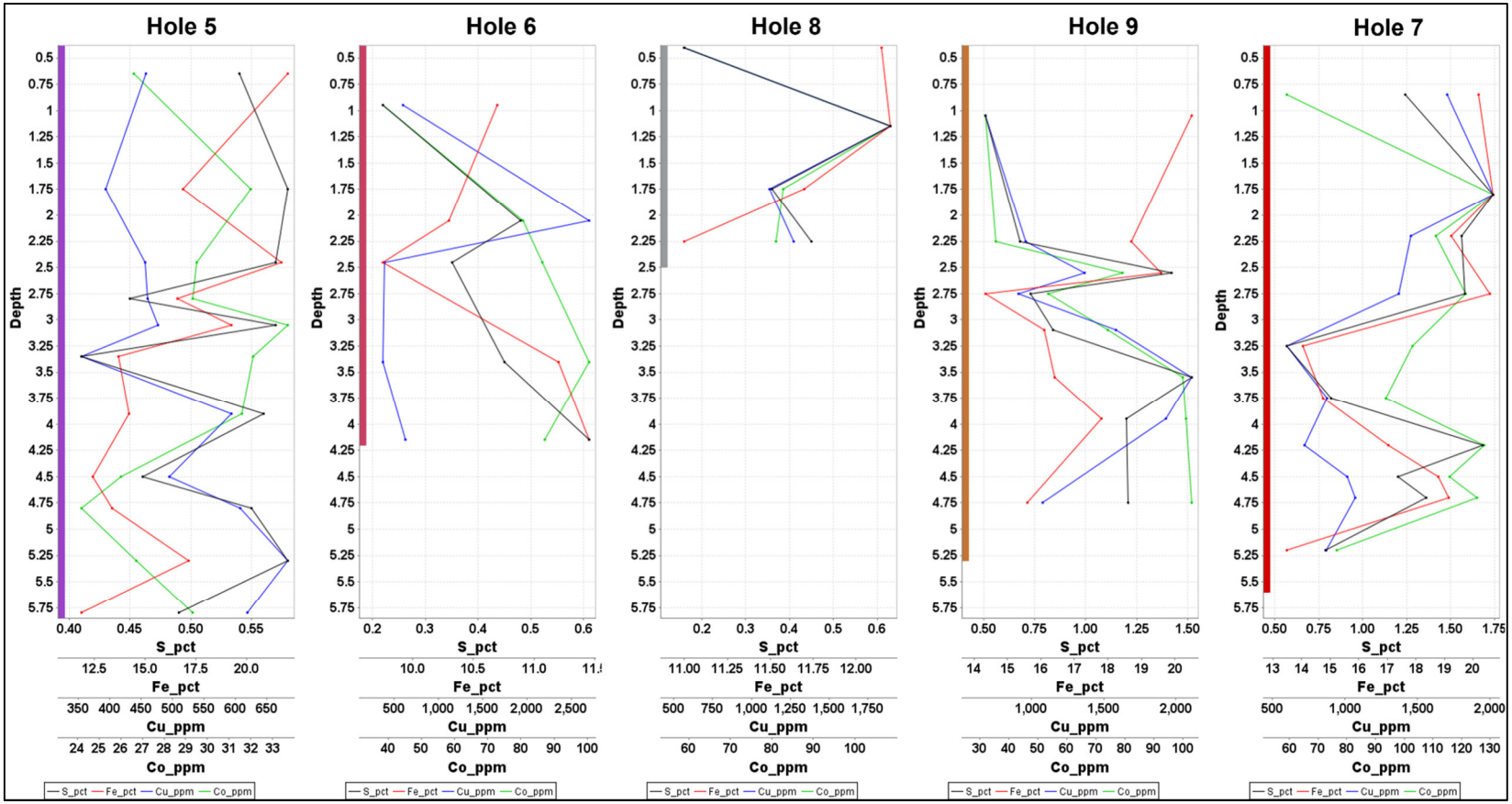


Figure 45 - Downhole plot of ICP-MS data collected in the old tailings storage facility, Kanmantoo mine, Australia, for S (%), Fe (%), Cu (ppm), and Co (ppm) (source: Colombi et al., 2024)

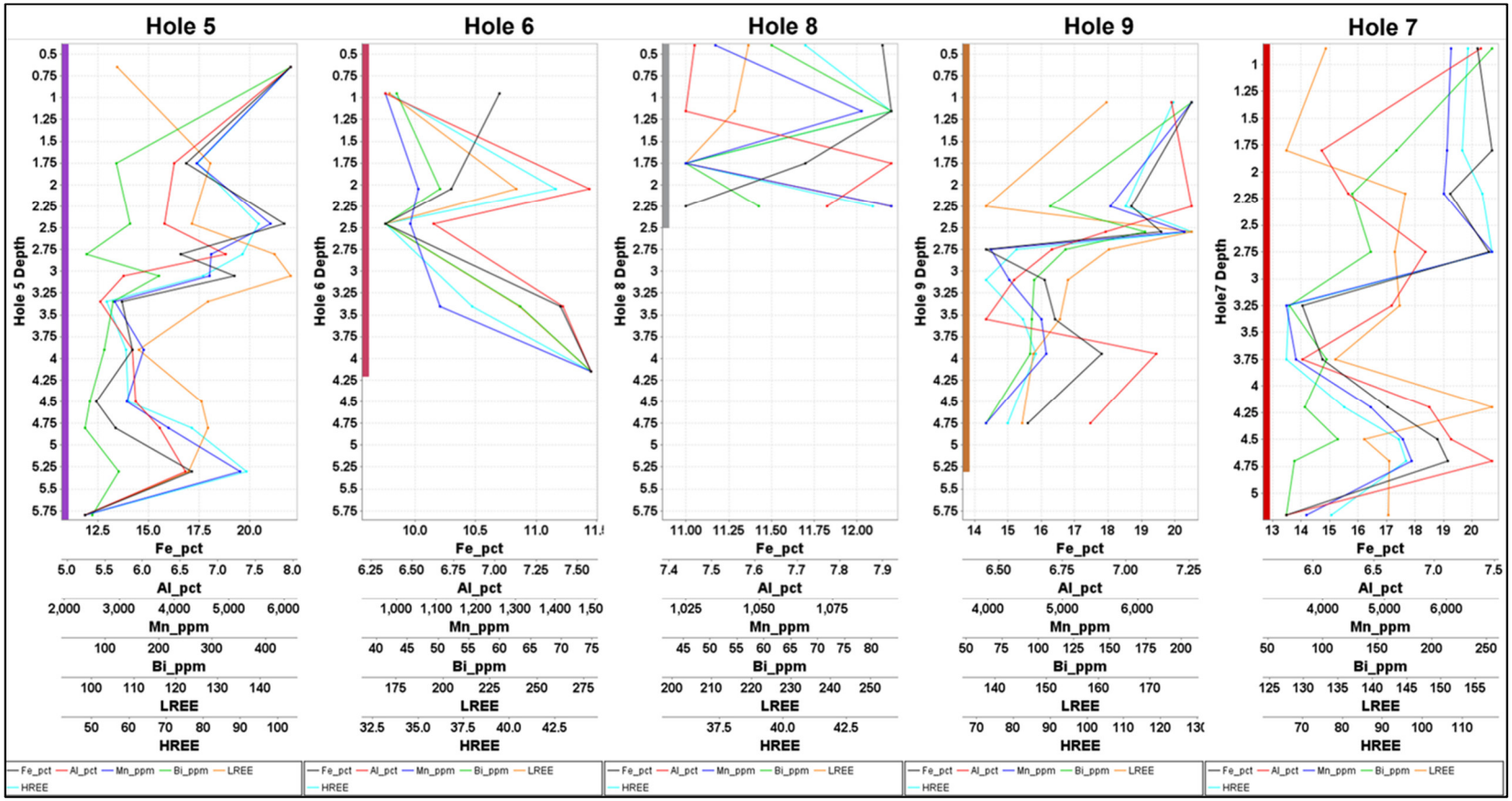


Figure 46 - Downhole plot of ICP-MS data collected in the old tailings storage facility, Kanmantoo mine, Australia, for Al (%), Fe (%), Mn (ppm), Bi (ppm) LREE (ppm) and HREE (ppm) (source: Colombi et al., 2024)

The obtained chemical data were spatially correlated with drill hole locations, as reported in the spatial plots in Figure 47a-b and Figure 48a-b.

Holes KA06, KA07, KA08, and KA09 hosted high Cu concentrations, in the range 1015 ppm − 2,700 ppm (Figure 47a), while Mn was assayed in relevant concentrations in holes KA05, KA07, and KA09, ranging 4.680 ppm − 6,730 ppm (Figure 47b). Additionally, Co showed the highest values (range 100 ppm – 131 ppm, Figure 48a) in holes KA06, KA07, KA08, and KA09, while Bi showed relevant values in the range 104 ppm – 447 ppm in holes KA05, KA07, and KA09 (Figure 48b).

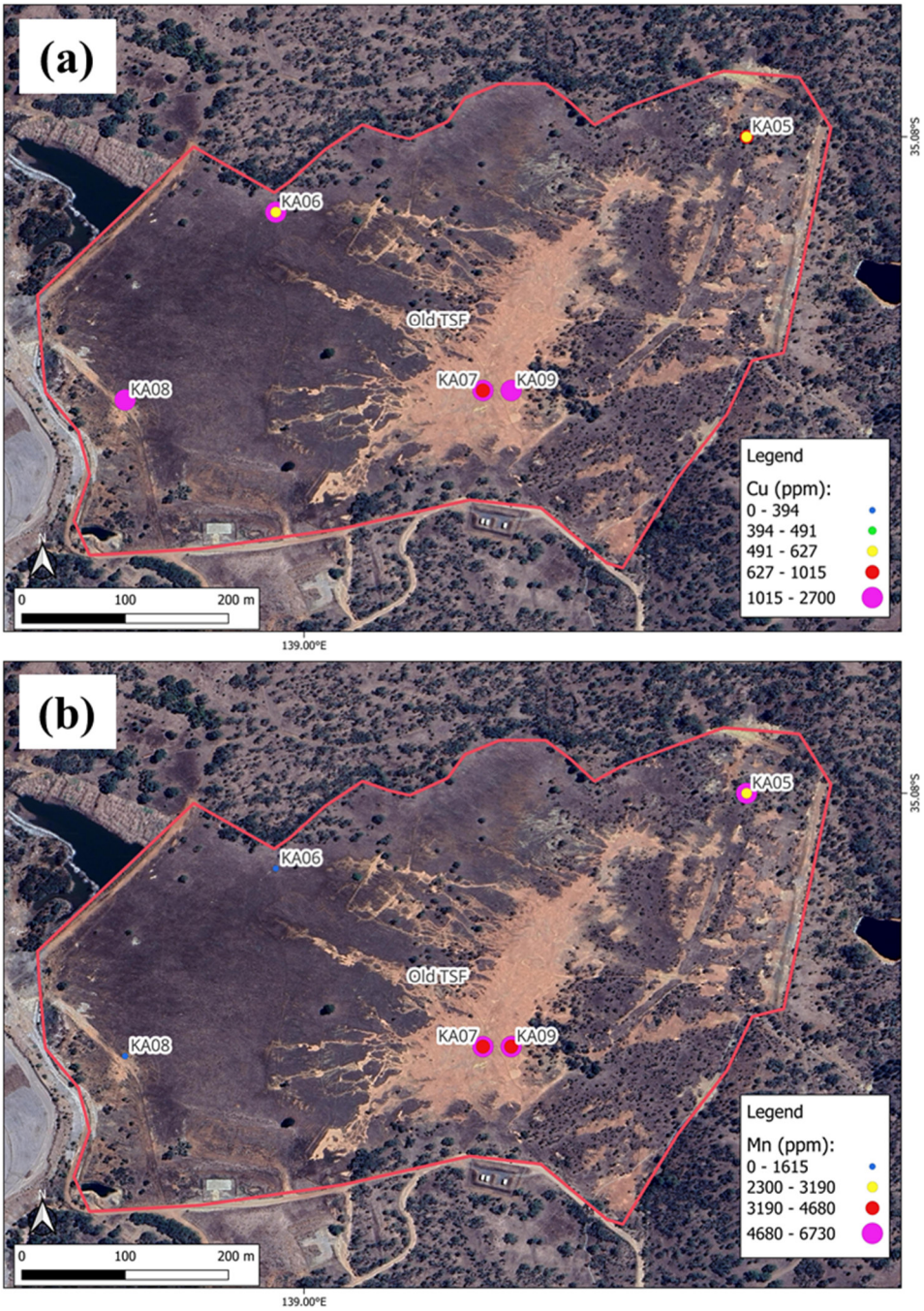


Figure 47 - Spatial plots for selected elements across old tailings facility, Kanmantoo mine, Australia: (a) Cu; (b) Mn. (source: Google satellite image. Coordinate system: WGS84)

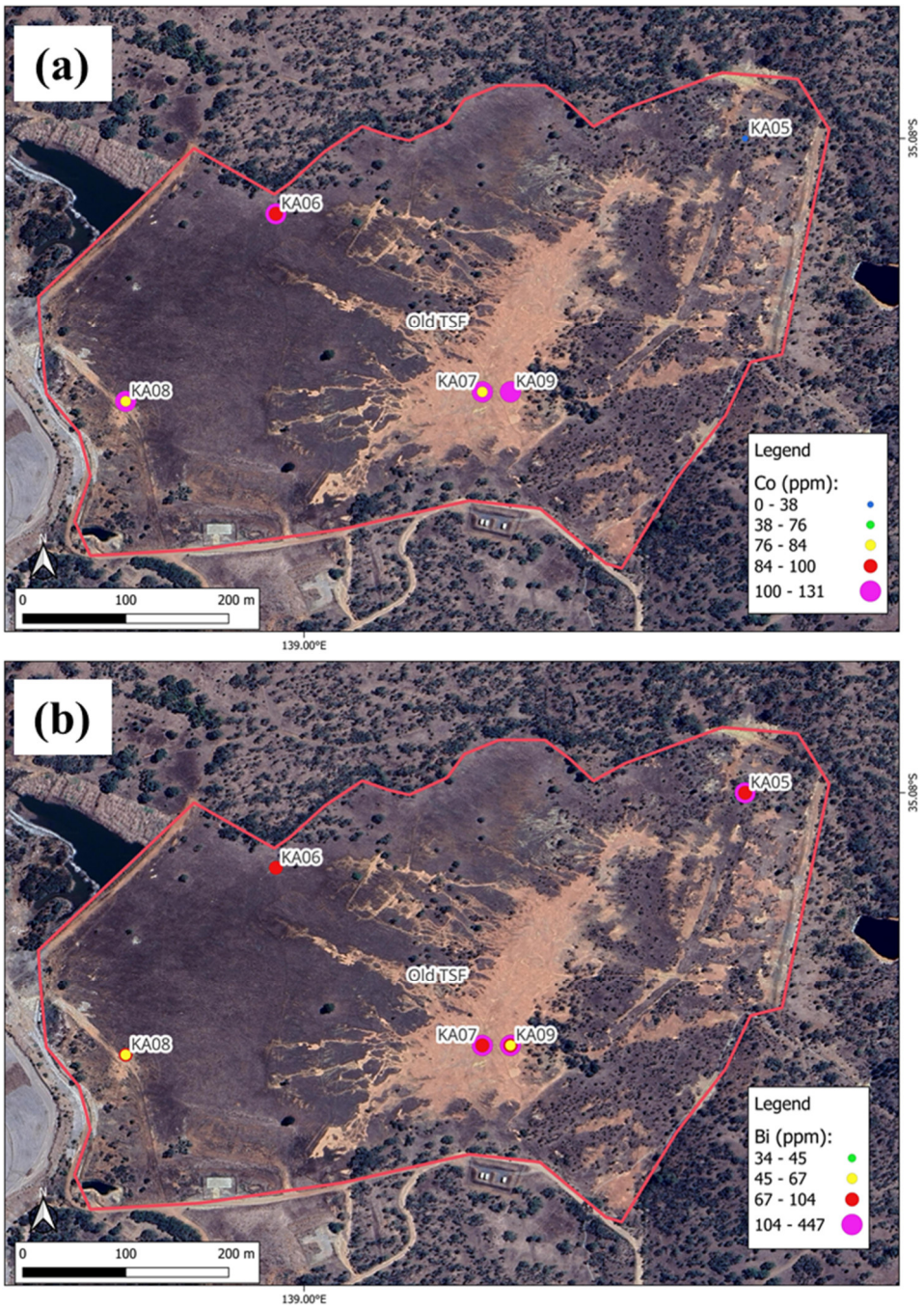


Figure 48 - Spatial plots for selected elements across the old tailings facility, Kanmantoo mine, Australia: (a) Co; (b) Bi (source: Google satellite image. Coordinate system: WGS84)

4.3.2 Mineralogical characterisation

Following chemical characterisation, a subset of samples was selected for further mineralogical investigation using XRPD and MLA, as reported in Table 15. Samples were selected according to observations related to ICP-MS collected values and aimed at characterising those samples that better represented geochemical trends related to key elements concentration, such as Ag, Bi, Co, S, Fe and Mn.

Table 15 - List of selected samples from old tailings storage facility of the Kanmantoo mine, Australia, for mineralogical characterisation (XRPD and MLA), according to rationales related to ICP-MS characterization.

Sample ID	***HoleID***	***Rationale***
KA33	KA05	High average Bi
KA35	KA05	Highest Ag and Fe with high Bi
KA51	KA07	Highest Co and S
KA53	KA07	Highest average Mn
KA62	KA08	High Ag, Co and Ni
KA65	KA09	High Bi and Mn

4.3.2.1 XRPD characterisation results

As reported in Figure 49 and Table 16, quantitative XRPD analyses realised on samples collected in the old tailings facility highlighted a mineralogy characterised by prevalent almandine and quartz phases, being on average 35.2 wt% (min 5 wt% − max 35.2 wt%) and 28.8 wt% (min 25 wt% − max 37 wt%), respectively. Additionally, other detected phases were biotite (9 wt%, min 1 wt% – max 17 wt%), and chlorite (5.7 wt%, min 4 wt% − max 11 wt%). Minor phases were represented by magnetite, muscovite-illite, andalusite, jarosite, staurolite, goethite, mixed-layer clay, pyrite, chalcocyanite and hematite. Amorphous content was estimated to be on average 12.2 wt%, ranging between a minimum content of 5 wt% and a maximum of 25 wt%. Complete XRPD data are reported in (Colombi et al., 2024).

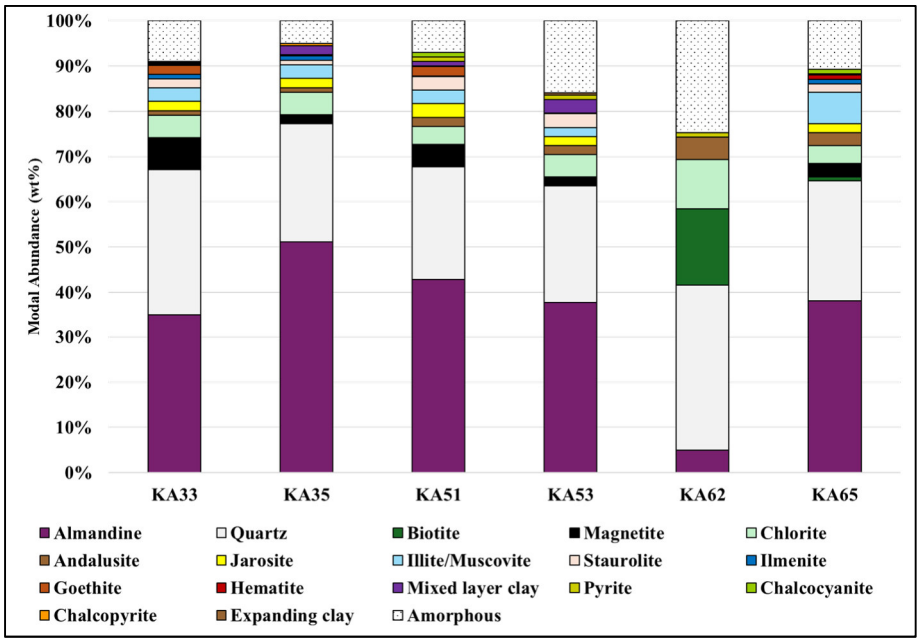


Figure 49 - Mineral phase abundance determined by XRPD of selected samples from the old tailings storage facility, Kanmantoo mine, Australia (n = 6)

Table 16 - Summary statistic for mineral phases abundance measured by quantitative XRPD for old tailings facility samples, Kanmantoo mine, Australia (n = 6).

Mineral Phase	***Min (%wt)***	***Max (wt%)***	***Mean (wt%)***	***Median (wt%)***
Almandine	5	51	35.2	38.5
Quartz	25	37	28.8	26.5
Biotite	1	17	9	9
Chlorite	4	11	5.7	5
Magnetite	2	7	3.8	3
Muscovite-Illite	2	7	3.6	3
Andalusite	1	5	2.3	2
Jarosite	2	3	2.2	2
Staurolite	1	3	2.2	2
Goethite	2	2	2	2
Mixed-layer clay	0.2	3	1.6	1.5
Pyrite	0.2	1	0.7	1
Chalcocyanite	0.2	1	0.7	1
Hematite	0.2	1	0.4	0.2
Amorphous phase	5	25	12.2	10

4.3.2.2 MLA results

Figure 50 and Table 17 report modal mineralogy data obtained after MLA analyses. Old tailings storage facility samples were mainly characterised by a relevant presence of garnet, having a modal abundance in the range of 8.2 wt% to 65.6 wt.%, with an average abundance of 45.1 wt.%. The second most abundat mineral is quartz with an average mass rate of 25.4 wt.% (min 15.2 wt% − max 35.2 wt%), followed by biotite (avg: 4.9 wt.%, min 0.2 wt% − max 25.5 wt%), silicate agglomerate (avg: 10.3 wt%, min 6.1 wt% − max 14.1 wt.%) and chlorite (avg: 2.3 wt%, min 0.3 wt% − max 11.1 wt %). Minor phases included andalusite, staurolite and Fe oxides, while were identified trace amounts of other minerals such as kaolinite-pyrophyllite, muscovite-illite, jarosite, ilmenite, pyrite, pyrrhotite and apatite. Complete data are reported in (Colombi et al., 2024).

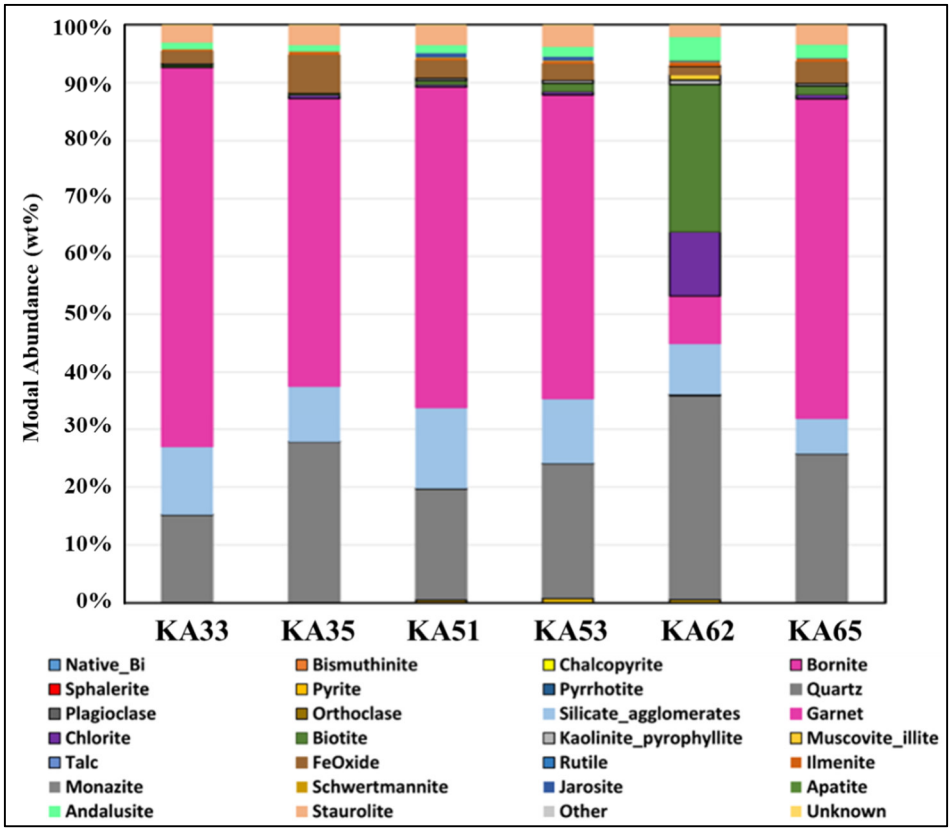


Figure 50 - Modal mineralogy calculated from MLA data of old tailings facility samples, Kanmantoo mine, Australia (n = 6).

Table 17 – Summary statistics for quantified mineral phases by MLA in samples from old tailings storage facility, Kanmantoo mine, Australia (n = 6).

Mineral Phase	***Min (%wt)***	***Max (wt%)***	***Mean (wt%)***	***Median (wt%)***
Garnet	8.2	65.6	45.1	53.9
Quartz	15.2	35.2	25.4	24.4
Biotite	0.2	25.5	4.9	1.1
Silicate agglomerate	6.1	14.1	10.3	10.5
Chlorite	0.3	11.1	2.3	0.6
Andalusite	1.1	4	2	1.5
Staurolite	1.9	3.6	3	3.2
Fe oxide	1.4	6.4	3.2	2.8
Kaolinite-pyrophyllite	0.2	0.8	0.4	0.4
Muscovite-Illite	0.1	1	0.3	0.2
Jarosite	b.d.l	0.8	0.3	0.1
Ilmenite	0.3	0.7	0.5	0.5
Pyrite	b.d.l	0.7	0.3	0.2
Pyrrhotite	b.d.l	0.3	0.1	0.1
Apatite	b.d.l	0.3	0.1	0.1
Schwertmannite	b.d.l	0.1	0.1	0.1
Plagioclase	b.d.l	0.2	0.1	0.1
Orthoclase	b.d.l	0.1	b.d.l	b.d.l

More in detail, Figure 51a shows a classified MLA image for the tailings sample KA62, whose mineralogical composition included quartz (35.2 wt%), biotite (25.5 wt.%), chlorite (11.1 wt%), silicate agglomerates (8.8 wt%), garnet (8.2 wt%), andalusite (4 wt%), staurolite (1.9 wt%) and Fe oxides (1.4 wt%). Minor mineralogical phases were represented by muscovite-illite (0.9 wt%), kaolinite-pyrophyllite (0.8 wt%), ilmenite (0.6 wt%), pyrite (0.5 wt%), apatite (0.3 wt%) and pyrrhotite (0.2 wt%).

Additionally, the sample KA35 classified MLA image is reported in Figure 51b, where main mineralogical phases included garnet (49.7 wt.%), quartz (27.8 wt.%), silicate agglomerates (9.7 wt.%), Fe oxides (6.4 wt.%), staurolite (3.3 wt.%) and andalusite (1.1 wt.%) with minor phases being represented by chlorite (0.6 wt.%), ilmenite (0.5wt.%) and kaolinite-pyrophyllite (0.2 wt.%).

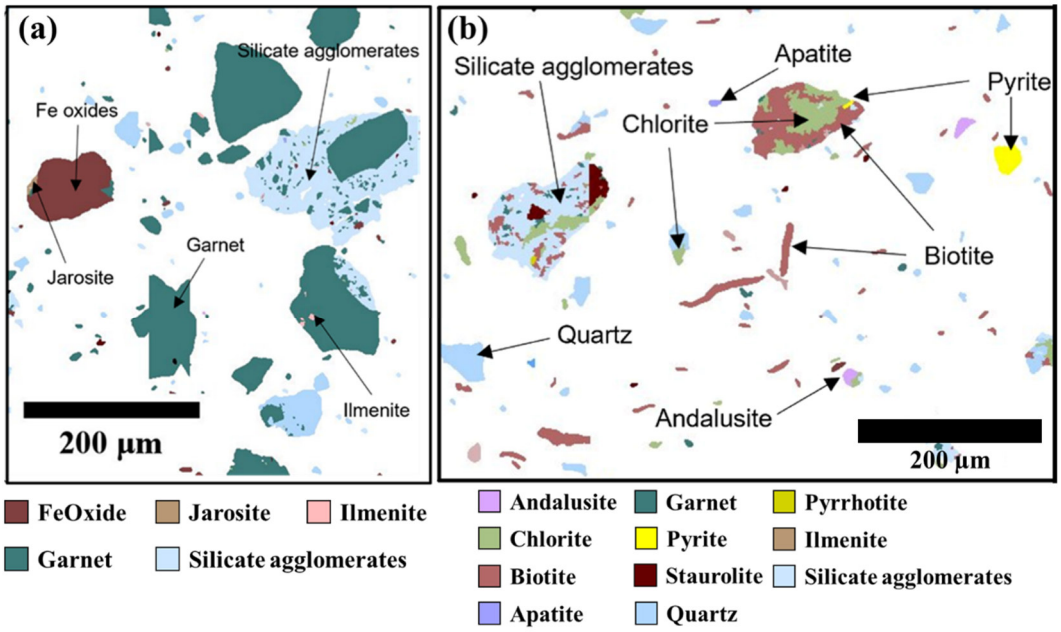


Figure 51 – Classified MLA mineralogy images for tailings samples from old tailings storage facility of the Kanmantoo mine, Australia: (a) sample KA35; (b) sample KA62. (after Colombi et al., 2024)

Garnet, pyrite, and iron oxides minerals identified using MLA modal mineralogy analyses were considered for further investigation, including the determination of their particle size distribution. Although pyrite was less abundant than garnet and iron oxides, it was likewise targeted due to its potential to contain critical elements.

Figure 52a-c shows the particle size distribution curves for garnet, pyrite and iron oxides detected in the samples from the old tailings storage facility. In detail, pyrite was characterised by a p80 ranging between 11 µm and 55 µm, and a narrower p50 of about 12µm (Figure 52a). Garnet minerals reported a p80 varying between 23µm and 83 µm, associated with a p50 of 11µm − 29µm (Figure 52b), while Iron oxides showed different dimensional features with a p80 diameter ranging between 25 µm to 41 µm and a p50 of 10.5 µm – 17 µm (Figure 52c).

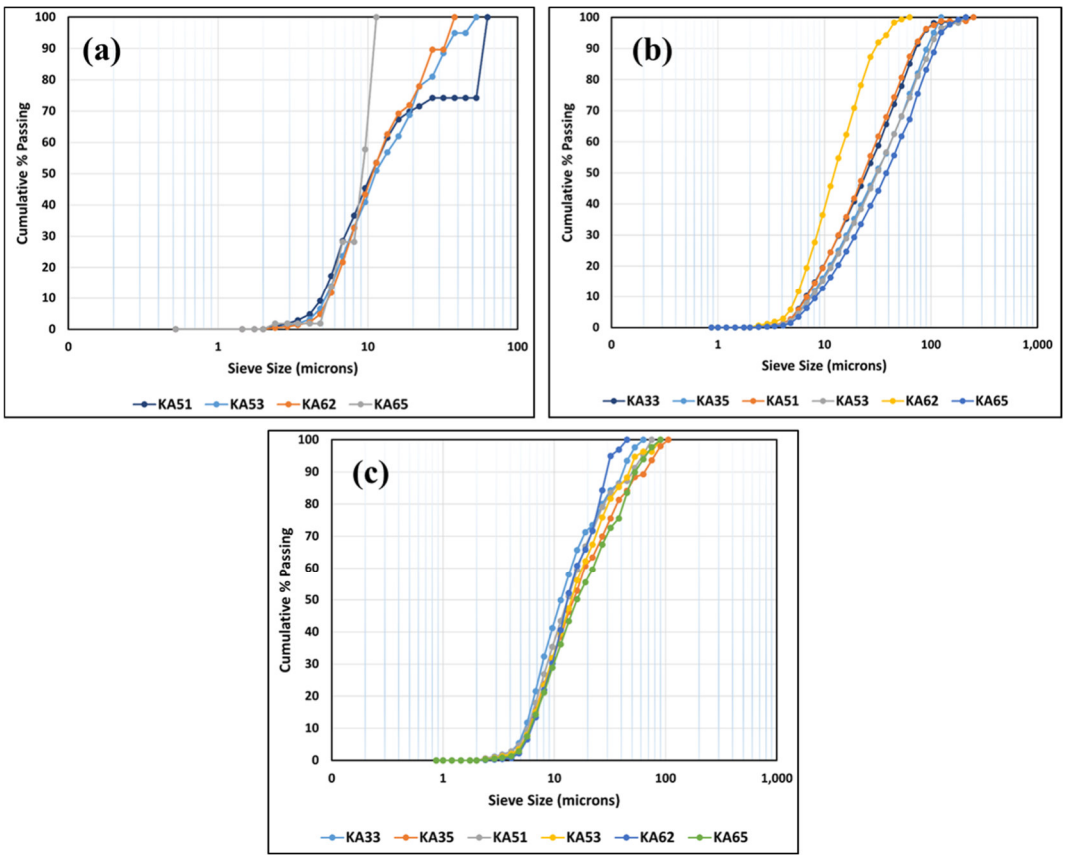


Figure 52 – Particle size distribution of selected minerals contained in analysed samples from old tailings facility of the Kanmantoo mine, Australia: (a) pyrite (n = 4); (b) garnet (n = 6); (c) Iron oxides (n = 6) (source: Colombi et al., 2024)

Pyrite, garnet, and iron oxides were mostly liberated, as shown in the mineral association graphs in Figure 53a-c. In detail, pyrite grains showed free surfaces for mass rates between 83 wt% and 97 wt%, and were mainly associated with silicate agglomerates and garnet (Figure 53a). Moreover, most of the garnet grains exhibited a free surface in the range 75 wt% − 83 wt%, and a prevalent association with quartz and silicate agglomerates (Figure 53b). Lastly, iron oxides had a relevant share of grains with free surface (76 wt% − 90 wt%), being mainly associated with garnet and silicate agglomerate and showing a residual association with quartz grains (Figure 53c).

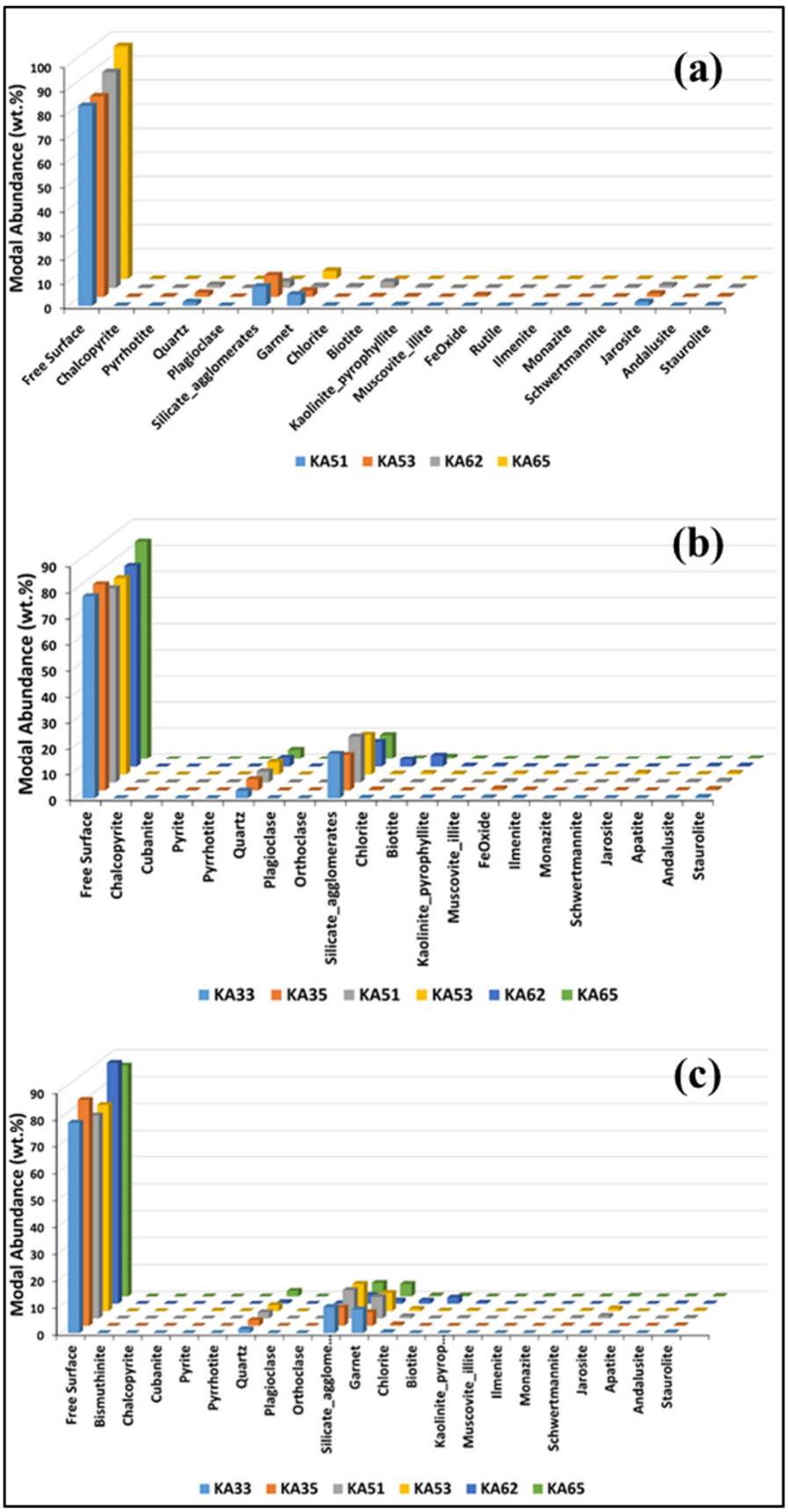


Figure 53 - Mineral associations for samples from the old tailings storage facility of the Kanmantoo mine, Australia: (a) pyrite (n = 4); (b) garnet (n = 6); (c) iron oxides (n = 6). (source: Colombi et al., 2024)

4.3.2.3 Mineral chemistry characterisation results (LA-ICP-MS)

Mineral chemistry of selected target minerals was investigated using the LA-ICP-MS methodology. In particular, garnet and pyrite grains from 3 tailings samples (KA35, KA53 and KA62) were assayed to describe the distribution of valuable and critical metals such as Bi, Co, Mn, Zr, Ti, LREEs and HREEs.

Realised mineral chemistry analyses indicated that garnet grains had the highest Mn concentration, showing mean values of 14,057 ppm, as reported in Table 18. In addition, garnet also hosted relevant average concentrations of Zr (22,328 ppm), Bi (23,115 ppm) and Ti (36,963 ppm) (Table 18).

Additionally, pyrite showed the highest concentrations of Cu (8,845 ppm), Ni (1,668 ppm) and Co (3,983 ppm), as shown in Table 18.

Iron oxide grains were not included in this investigation due to their small particle size, hindering reliable signal acquisition by LA-ICP-MS.

Table 18 - Summary statistics for selected elements measured by LA-ICP-MS in garnet (n = 187) and pyrite (n = 15) found in samples from the old tailings storage facility of the Kanmantoo mine, Australia.

	^{90}Zr (ppm)	^{209}Bi (ppm)	^{66}Zn (ppm)	^{65}Cu (ppm)	^{60}Ni (ppm)	^{59}Co (ppm)	^{49}Ti (ppm)	^{55}Mn (ppm)
Garnet (n = 187)								
Min	1.21	0.01	2.9	0.24	0.09	9.6	26.9	5,486
Max	22,328	23,115	52.4	801	30.7	96	36,963	49,927
Mean	623	592	19.1	70.1	3.9	38	3,163	14,057
Median	3	0.2	15.1	0.2	0.2	28	120	11,150
Pyrite (n = 15)								
Min	0.01	0.36	0.63	1.16	1.91	11.99	2	3.7
Max	5.3	123	24.5	8,445	1,668	3,983	639	135
Mean	1.1	19.4	5.6	946	772	2,236	135	39
Median	0.2	2.4	3.3	53	720	2,468	59.5	25

Figure 54 shows an example of the garnet sample KA35_gnt-56 compositional pattern collected during LA-ICP-MS analyses. This sample showed elevated concentrations of heavy elements, such as Zr (22,327 ppm), U (210 ppm), 70 ppm Th (70 ppm), and Hf (523 ppm). More in detail, the reported graph indicated that elements such as Bi, Hf, Th, Ti, U, and Zr were found as micro-inclusions, highlighted by their peak-shape patterns.

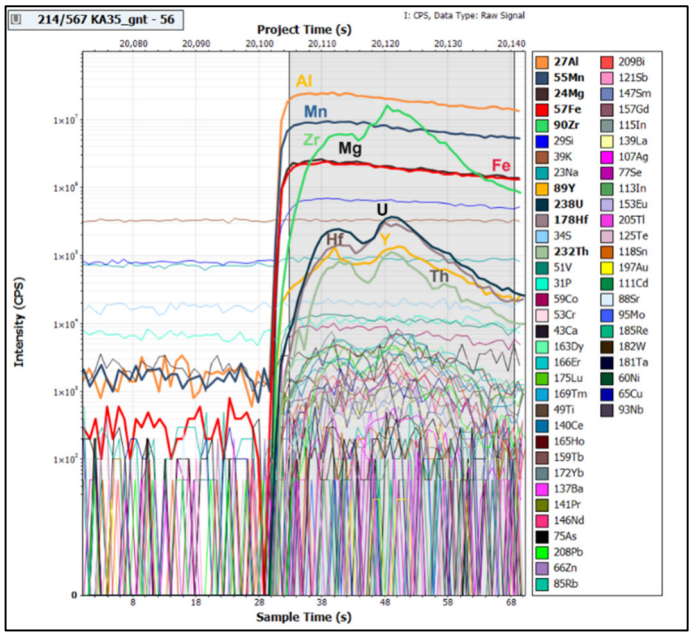


Figure 54 - LA-ICP-MS compositional pattern for garnet sample KA35_gnt-56 from old tailings storage facility of the Kanmantoo mine, Australia. (source: Colombi et al., 2024)

Table 19 shows the correlation matrix built for selected valuable and critical elements detected in garnet minerals measured by LA-ICP-MS. The analysed dataset revealed complex geochemical associations, especially regarding Pb with LREEs (La, Ce, Pr, Nd, Sm, and Eu) and some HREEs (Tb, Dy), as shown graphically in Figure 55.

*Table 19 – Correlation matrix for selected critical metals and trace elements measured in garnet minerals (n=187) in the old tailings storage facility of the Kanmantoo mine, Australia. (R values higher than 0.7 in **bold**)*

	^{27}Al	^{57}Fe	^{209}Bi	^{208}Pb	^{31}P	^{139}La	^{140}Ce	^{141}Pr	^{146}Nd	^{147}Sm	^{153}Eu	^{157}Gd	^{159}Tb	^{163}Dy
^{27}Al	1													
^{57}Fe	0.33	1												
^{209}Bi	-0.58	-0.23	1											
^{208}Pb	-0.16	-0.17	0.14	1										
^{31}P	-0.09	-0.32	0	0.43	1									
^{139}La	-0.03	-0.11	-0.05	**0.97**	0.4	1								
^{140}Ce	-0.04	-0.11	-0.04	**0.97**	0.4	**1**	1							
^{141}Pr	-0.02	-0.11	-0.06	**0.98**	0.4	**1**	**1**	1						
^{46}Nd	-0.04	-0.1	-0.04	**0.97**	0.4	**1**	**1**	**1**	1					
^{147}Sm	-0.06	-0.12	-0.02	**0.97**	0.41	**1**	**1**	**1**	**1**	1				
^{153}Eu	-0.06	-0.14	-0.03	**0.97**	0.4	**1**	**1**	**1**	**1**	**1**	1			
^{157}Gd	-0.07	-0.21	-0.04	**0.95**	0.46	**0.98**	**0.98**	**0.98**	**0.98**	**0.98**	**0.98**	1		
^{159}Tb	-0.1	-0.49	-0.07	0.5	0.52	0.56	0.54	0.54	0.51	0.52	0.55	0.68	1	
^{163}Dy	-0.09	-0.5	-0.07	0.08	0.42	0.11	0.09	0.09	0.08	0.1	0.13	0.29	**0.89**	1

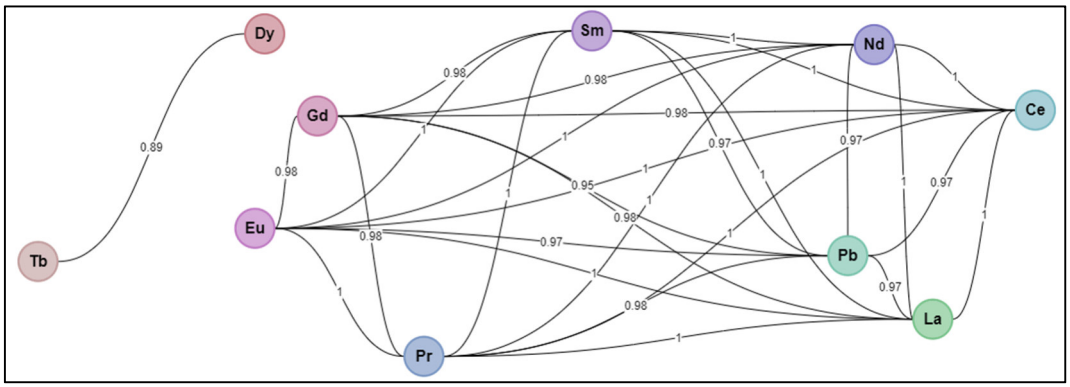


Figure 55 - Correlation diagram for elements having R >0.7 measured in garnet samples (n = 187) from the old tailings storage facility of the Kanmantoo mine, Australia (source: Colombi et al., 2024)

Compositional pattern graph, reported in Figure 56, for the pyrite sample KA62_py-02 minerals detected showed relevant concentration of Co (2,468 ppm), Ni (1,578 ppm), and Cu (1,802 ppm). These metals were detected throughout the mineral matrix of the analysed grain, while Ti showed a spike signal correlated to a moderate concentration of 640 ppm.

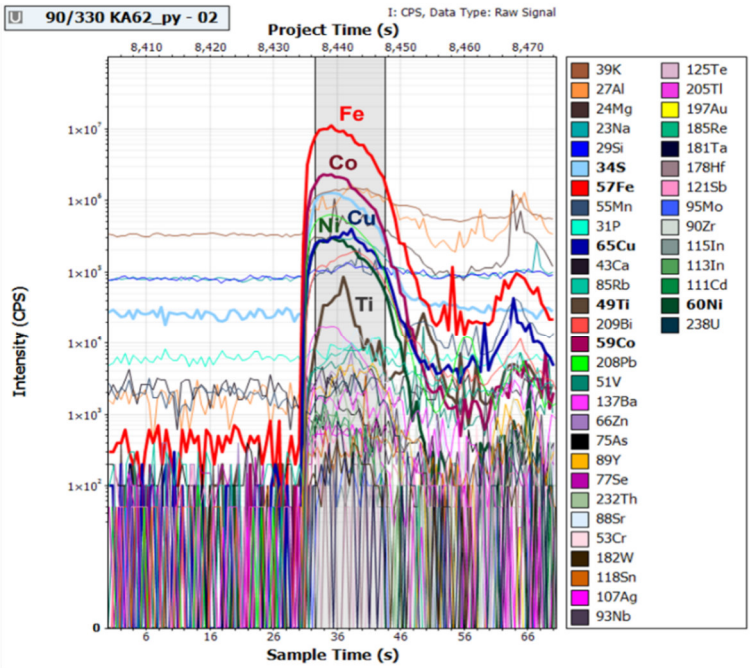


Figure 56 - LA-ICP-MS compositional pattern for pyrite sample KA62_py-02 from old tailings storage facility of the Kanmantoo mine, Australia. (source: Colombi et al., 2024)

Table 20 reports the correlation matrix for the pyrite dataset considering the most abundant detected elements. Complex geochemical association were identified, especially involving Cu, Zr, Ni, Bi, Zn, Ti, ad Mn as illustrade graphically in Figure 57.

*Table 20 - Correlation matrix for selected critical metals and trace elements measured in pyrite minerals (n = 7) in the old tailings storage facility of the Kanmantoo mine, Australia. (R values higher than 0.7 in **bold**)*

	^{90}Zr	^{209}Bi	^{66}Zn	^{65}Cu	^{60}Ni	^{59}Co	^{49}Ti	^{55}Mn
^{90}Zr	1							
^{209}Bi	**0.81**	1						
^{66}Zn	0.60	**0.80**	1					
^{65}Cu	**0.76**	0.32	0.07	1				
^{60}Ni	**0.99**	**0.75**	0.54	**0.75**	1			
^{59}Co	0.24	0.25	0.25	-0.01	0.35	1		
^{49}Ti	0.64	**0.97**	**0.82**	0.09	0.57	0.20	1	
^{55}Mn	0.31	**0.78**	0.53	-0.10	0.21	0.01	**0.87**	1

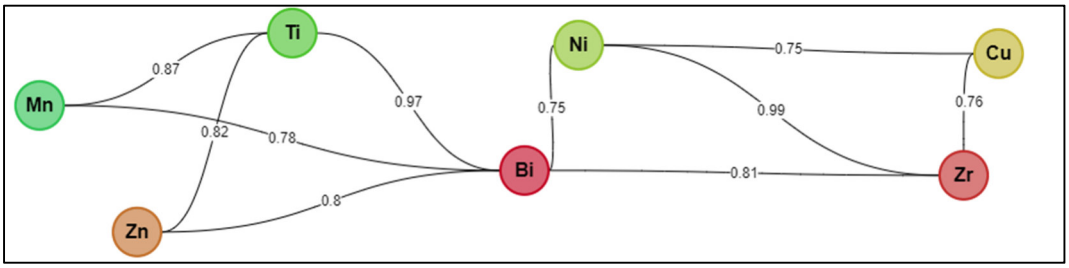


Figure 57 - Correlation diagram for elements having R > 0.7 measured in pyrite samples (n = 7) from the old tailings storage facility of the Kanmantoo mine, Australia (source: Colombi et al., 2024)

4.4 Geochemical considerations and critical metal tenor

Geochemical data collected for samples from the old tailings storage facility showed that materials were enriched in critical metals, as reported in the spider plot in Figure 58

The most enriched critical elements were Ag, As, Bi, Co, Cu, In, Mn, Se, Te, and W, most of them being more than 10 times higher than the average crustal abundance values (Rudnick & Gao, 2014).

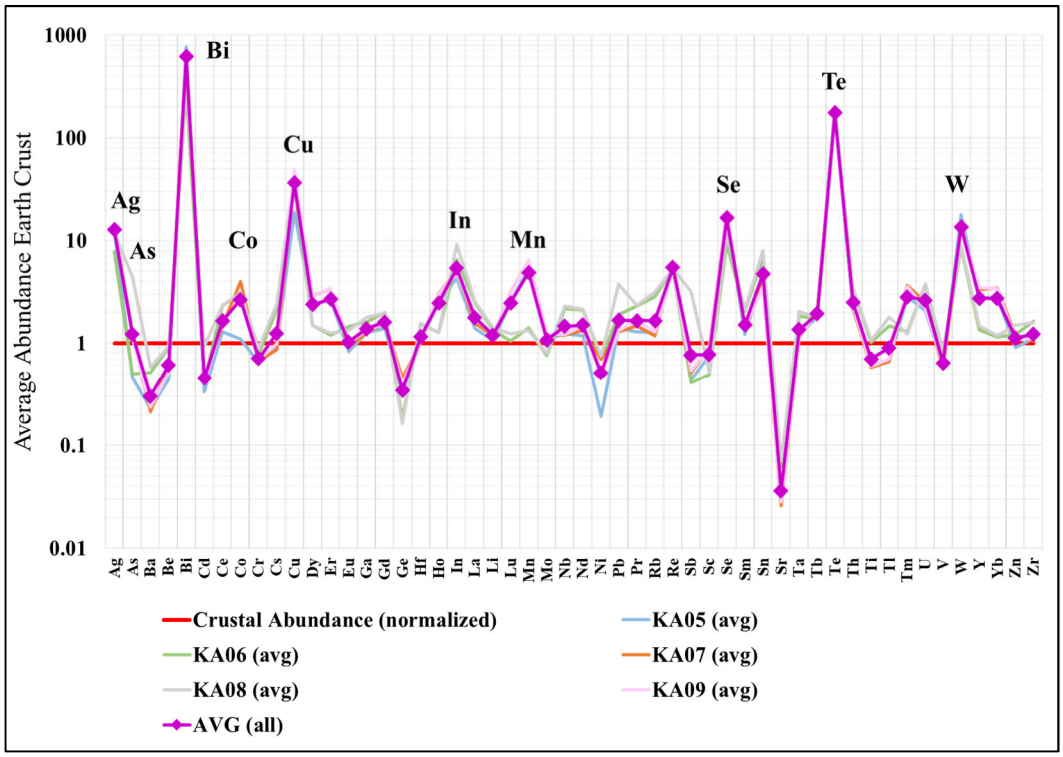


Figure 58 - Spider plot showing geochemistry summary statistic for old tailings storage facility samples from the Kanmantoo mine, Australia, normalised to the average crustal abundance values (Rudnick & Gao, 2014). (source: Colombi et al., 2024)

In Table 21 is reported a more detailed comparison of average measure values of critical and strategic elements, as listed by the Australian Government (Australian Government, 2024), with respective crustal abundance (Rudnick & Gao, 2014). The most enriched element was Bi, showing a concentration 618 times higher than the average abundance, followed by Te, which had a concentration 175 times higher. Among elements that were more than 10 times enriched, they were found Cu (x37), Se (x17), W (x14), and Ag (x13), while elements such as Re, In, Mn, Sn, Co, Nb, Ga, Ta, and As showed enrichment lower than 10 times, but higher than 1.

*Table 21 - Summary for critical and strategic elements values measured by geochemical analyses compared to crustal abundance concentrations for the old tailings storage facility of the Kanmantoo mine, Australia (n = 38). (In **bold** concentrations > 1x time higher than the average abundance;*: Rudnick & Gao, 2014; [1]: not included in the Australian critical elements list; [2]: included in the Australian strategic elements list).*

Elements	*Crustal abundance * (ppm)*	*Mean conc. (ppm)*	*Times higher than average crustal abundance*
Ag[1]	0.056	**1**	**13**
Al[2]	84,100	67,521	0.8
As	2.5	3	1.2
Be	1.9	1	0.6
Bi	0.18	**111**	**618**
Co	26.6	**71**	**2.7**
Cr	135	96	0.7
Cu[2]	27	**986**	**37**
Ga	16	22	1.4
Ge	1.3	0	0.3
Hf	3.7	4	1.2
In	0.05	**0.27**	**5**
Li	17	20	1
Mg	28,100	13,261	0.5
Mn	800	**3,902**	**5**
Mo	0.8	0.9	1
Nb	8	12	1.5
Ni	59	30	0.5
Re	0.000188	**0.0010**	**5**
Sb	0.2	0.2	0.8
Sc	21.9	17	0.8
Se	0.13	**2**	**17**
Sn[2]	1.7	**8.1**	**4.7**
Ta	0.7	**0.9**	**1.4**
Te	0.001	**0.175**	**175**
Ti	4,300	3,025	0.7
V	138	89	0.6
W	1	**14**	**14**
Zn[2]	72	81	1.1
Zr	132	161	1.2

In addition, REEs concentrations were compared to their average crustal concentrations, as reported in Table 22. No significant enrichment was found for these critical elements in the samples collected in the old tailings basin of the Kanmantoo mine, never exceeding 3 times the average crustal abundance

Table 22 - Summary for REEs values measured by geochemical analyses compared to crustal abundance concentrations for the old tailings storage facility of the Kanmantoo mine, Australia (n = 38). (: Rudnick & Gao, 2014).*

Elements	*Crustal abundance * (ppm)*	*Mean conc. (ppm)*	*Times higher than average crustal abundance*
Ce	43	71.1	1.7
Dy	3.6	8.6	2.4
Er	2.1	5.7	2.7
Eu	1.1	1.1	1.0
Gd	3.7	6.0	1.6
Ho	0.8	1.9	2.5
La	20	36	1.8
Lu	0.3	0.7	2.5
Nd	20	30	1.5
Pr	4.9	8.2	1.7
Sm	3.9	5.9	1.5
Tb	0.6	1.2	1.9
Tm	0.3	0.8	2.8

4.5 Final Remarks

The old tailings storage facility in the Kanmantoo mine was sampled, collecting 38 tailings samples from 5 hand-augered drill-holes, reaching a maximum depth of 5.9 m.

Geochemical analyses of the tailings material highlighted relevant concentrations of Cu, Co, Bi and Mn. According to chemical assays, six samples containing the highest values of measured elements were chosen for detailed mineralogical analyses using XRPD and MLA.

MLA analyses showed that samples collected in the old tailings storage facility contained mainly garnet, quartz, biotite and chlorite, with minor phases including magnetite, muscovite-illite, andalusite, jarosite, staurolite, goethite, mixed-layer clay, pyrite, chalcocyanite and hematite.

Detailed mineral chemistry measurements were realised by LA-ICP-MS, highlighting that the garnets were characterised by enrichment in critical elements such as Mn, Zr, Bi, Ti, and a suite of REEs, in particular La, Ce, Pr, and Nd. By contrast, pyrite minerals were found to be endowed with Ni, Co, and Cu

According to the collected data, some consideration regarding possible further questions to be targeted and possible reprocessing options for the studied materials could be deployed.

Experimental reprocessing testing may be oriented to high-intensity magnetic separation on garnets to understand if Zr could be recovered as a by-product of garnet concentration (Bhima Rao R, Singh D, & Mishra B., 2024). Considering the association of Ti and REEs with garnet in the tailings samples, heavy mineral sand, such as staurolite and andalusite, could represent a further exploration target for the site (Mudd & Jowitt, 2016). In addition, garnet may also be considered as an unconventional source of REEs (Klimpel et al., 2021).

For some samples, Mineralogical analyses reported relevant concentrations of biotite minerals (sample KA62, 25 wt%), which could represent a host mineral for Rb. Even if Rb is not considered at the moment a critical element, it would be recovered by leaching reprocessing, followed by ion exchange, preserving biotite for possible secondary uses (Zhengwei Han et al., 2023).

Although the presented data showed low pyrite content, it showed a p80 in the range of 11 μm – 50 μm, which is possibly suitable for conventional flotation reprocessing in case of proven economical convenience (Whitworth, Forbes, et al., 2022).

From an environmental standpoint, the old tailings storage facility in the Kanamantoo mine was characterised by a relevant presence of As, which may be further characterised by sequential extractions and leaching tests to better understand mobilisation of dangerous heavy metals, quantifying the acid metalliferous drainage potential of the basin (Ruiz-Sánchez, Tapia, & Lapidus, 2023). Additionally, it would be relevant to consider geo-environmental properties of the tailings materials and possible presence of hazardous metals in

the leachate, by applying standard environmental tests such as the Synthetic Precipitation Leaching Procedure (SPLP) (U.S. Environmental Protection Agency (USEPA), 2025) or standardised chemical extraction methods, like the Toxicity Characteristic Leaching Procedure (TCLP) (U.S. Environmental Protection Agency (USEPA), 2025).

Part II. Potential recovery of mine waste: 3 Italian case studies

Chapter 5

5. Case study 1: Traversella Mine, Piedmont, Italy

Part of the work presented in this chapter has been previously published in the following works:

Baldassarre, G., Fiorucci, A., & Marini, P. (2024). Recovery of Critical Raw Materials from Abandoned Mine Wastes: Some Potential Case Studies in Northwest Italy. *Materials Proceedings, 15*(1), 77. (Baldassarre, Fiorucci, & Marini, 2024)

Baldassarre, G., Mori De Oliveira, C., Fiorucci, A., Bellopede, R., & Marini, P. (2025). Exploring the Recovery Potential of Critical and Strategic Raw Materials from Traversella Mine (Piedmont, Italy) Waste: A Comparison of Laboratory-Scale Separation Techniques. *Mining, 5*(2), 21. (Baldassarre, Mori De Oliveira, Fiorucci, Bellopede, & Marini, 2025)

5.1 Site Description and Geological Setting

The Traversella mine is located about 60km north of Turin, Piedmont, and 20km from Ivrea, Turin, Piedmont. The mine is situated on the left bank of the Bersella River, within the Chiusella Valley and took its name from the closest village of Traversella. The Traversella's deposit can be considered a polymetallic Fe-Cu-W pyro-metasomatic skarn deposit, with accessory Mo, As, Sb, Bi, Au, and U (Turi & Zucchetti, 1978). The origin of the deposit is related to the intrusion of the granodioritic Traversella pluton in the local Sesia-Lanzo geological unit, characterised by micaschists and gneisses, around 30 Ma (Nimis, Costa, & Guastoni, 2014). The deposit is characterised by two types of skarn phenomena (Costa, Dino, Benna, & Rossetti, 2019; Respino, 2024):

- *Prograde skarn:* It occurs at the closest contact with the dioritic rock, is created at a high temperature, and is characterised by a nearly total replacement of the original local carbonatic rocks. At this stage, minerals such as garnet and diopside are deposited thanks to metasomatic reactions between the magma and the pre-existing rocks. Magnetite orebodies can be considered as an iron-rich variety of prograde skarn (Costa et al., 2019).
- *Retrograde skarn:* it is associated with the circulation of fluids resulting in hydration of the prograde skarn, with the formation of minerals, such as talc, amphiboles, carbonates, chlorite, and scheelite. Also, sulphides (pyrite, chalcopyrite, pyrrhotite and arsenopyrite) can be deposited at this stage (Costa et al., 2019).

The magnetite ore bodies, which were exploited during the operational period of the mine, are generally aligned in a North-South direction and are typically located at the external contact boundary between the skarn and the country rocks (Figure 59) (Costa et al., 2019; Nimis et al., 2014).

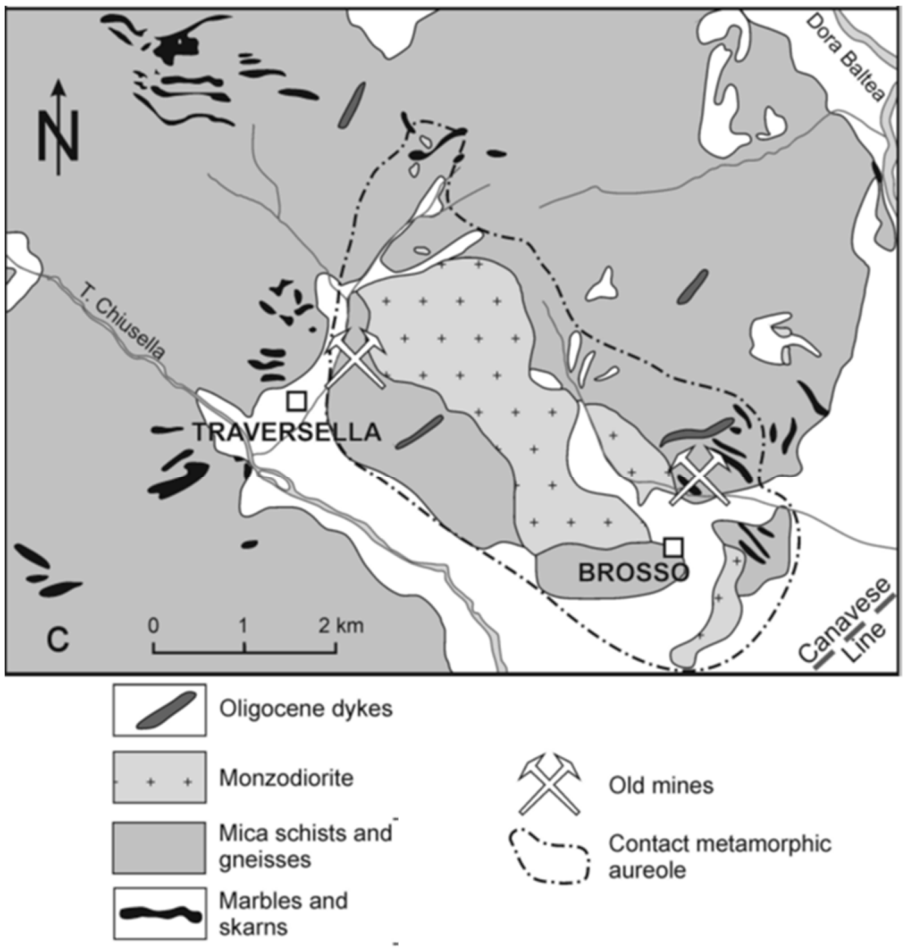


Figure 59 - Geological map of the Traversella area (readapted from Nimis, 2014)

The Traversella ore bodies are mainly characterised by the presence of magnetite, associated with other accessory minerals (pyrite, chalcopyrite, pyrrhotite, galena, sphalerite, arsenopyrite, and bismuthinite). Significant local concentrations of scheelite associated with the magnetite ore bodies have been reported in the literature (Respino, 2024; Zucchetti, 1966). Scheelite occurrences are mainly located around the magnetite ore bodies, particularly at the base of those closest to limestone masses, but also at the edges of some ferrous ore bodies (Respino, 2024).

5.1.1 Historical mining activities in the area

The iron ore richness of Traversella was probably well known to local populations starting from the pre-Roman period. During the Roman period, historical evidence shows that the ore bodies were well known and needed to support the local economy and weapons production. The local mines had been, since ancient times, a major source of wealth for the region, enough to be considered an Emperor's property and not a private citizen's asset. In the early Middle Ages, the Traversella mines were controlled by local noble families before falling under the control of the Dukes of Savoy in 1386. Historical records

confirm that the mine had been active throughout the 17th Century (Respino, 2024).

The industrial history of the Traversella mining district truly began in the early 1700s, following the discovery of new mineralised deposits in the area. As a consequence, about 340,000 metric tons of ore were extracted between 1723 and 1824 (Costa et al., 2019; «Le miniere di ferro di Traversella e Brosso», 2025). In the first decades of the 1800s, many mining operations were active in the district, which exploited ore bodies in an uncoordinated and chaotic approach, resulting in several incidents and rock mass collapses, since the excavation activities were taking place mainly in underground conditions. In this period, more than 80 single mining operations, run by 11 companies, could be counted, and the production reached more than 7800 metric tons of iron ore in 1835 (Respino, 2024).

In the late 1800s, local authorities decided to deeply regulate the mining activities in the area by entrusting the mine planning and technological innovation responsibilities to renowned engineers and technicians of the time, to improve the work conditions and productivity of the site. Among others, Quintino Sella, in 1855, designed and patented a rotating electromagnetic sorter for the separation of magnetite minerals and the recovery of copper minerals that were nearly impossible to achieve by manual sorting (Costa et al., 2019; Respino, 2024).

Due to anti-economic conditions, the mine was closed in 1884. The mining activity resumed at a later time in 1914, following several exploration campaigns led by the state-owned company FIAT, which identified new valuable ore bodies for exploitation. During the Italian autarkic period (1935-1943), mining activities intensified, and infrastructural improvements were made, including the construction of a ropeway for concentrate transportation. In addition, shaking tables and flotation cells were introduced in the mineral processing plant, enabling the recovery of heavy minerals such as scheelite and uraninite along with sulphide minerals from the treated run-of-mine material (Respino, 2024).

After World War II, mining activities were restored, applying planned and productive underground exploitation techniques, such as the room-and-pillar method. Additionally, operations targeted deeper mineralised orebodies containing residual scheelite, allanite, and uraninite minerals (Respino, 2024; Zucchetti, 1966). Accordingly, the production reached more than 2000 metric tons of iron ore concentrate, about 250 tons of pyrite, 60 tons of chalcopyrite, and 2 tons of scheelite in 1949. In the last years of activity (1960-1965), the production of the mine was 100 metric tons per day of iron ore with a 30% grade of Fe, having an hourly output stream of 6 metric tons of iron minerals at 65 ÷ 68% Fe_3O_4 concentrate grade from the dressing plant. Moreover, the average yearly production of scheelite was about 0.75 metric tons, having a 60% WO_3 grade, and 0.25 tons/year of heavy radioactive minerals, such as allanite and uraninite (Respino, 2024; Zucchetti, 1961, 1962). Geochemical studies conducted on scheelite samples collected from the orebodies during underground operations by Matteucci (1966) showed that Light Rare Earth Elements (LREEs) and Heavy Rare Earth Elements (HREEs) amounts were respectively 1036 ppm (min 101 ppm, max 2125 ppm) and 144 ppm (min 30 ppm, max 208 ppm).

Due to poor economic returns on mining activities and costly operational conditions of the Traversella mine, the excavation operations were interrupted in 1969, and the mine was permanently closed in 1971. (Costa et al., 2019; Nimis et al., 2014; Respino, 2024)

5.1.2 Mine waste accumulation areas

According to the ISPRA official mine waste national database, updated in 2022, mine waste accumulation areas are reported in the locality of Fornello di Traversella, Piedmont, Italy. The type of waste reported is classified as "*chaotic dumps*", potentially containing As, Cd, Co, Mn, Ni, Pb, Cu, V, and cyanide, and rated as having a "*high*" associated ecological and sanitary risk. No further information is reported in terms of spatial coordinates, volumes or position of the dump sites (Serra & Andrisani, 2022). In addition, minor works published in journals of mineral collectors reported the presence of dumping areas (Gruppo Mineralogico Valchiusella, 2004).

The potential mine waste dump area was reconstructed according to historical documents and photographs of the area publicly available and preserved at the Traversella Mine Museum (Museo della Miniera di Traversella, *Via Fornello Ex Chioso, 10080, Traversella, TO, Italy; website: https://mmttraversella.it/*).

Preliminary satellite image observation was performed in order to explore the vegetation coverage of the selected area. Sentinel-2 multispectral images were considered to obtain a Normalised Difference Vegetation Index (NDVI) map for the evaluation of the vegetation coverage of the area.

Following on-site inspections conducted in November 2023, the GPS coordinates of mine waste dump accumulation areas were recorded and mapped (Table 23, Figure 60).

Table 23 - Mine waste dump names and positions according to on-site inspections in the Traversella mine area.

Name	X (UTM 32N)	Y (UTM 32N)	Type	Sampling
Casette	403046	5040703	Waste Rock	No
Riondello	403086	5040546	Waste Rock	No
Piano Svedesi	403053	5040559	Waste Rock	Yes
Quota 913	402884	5040942	Waste Rock	No

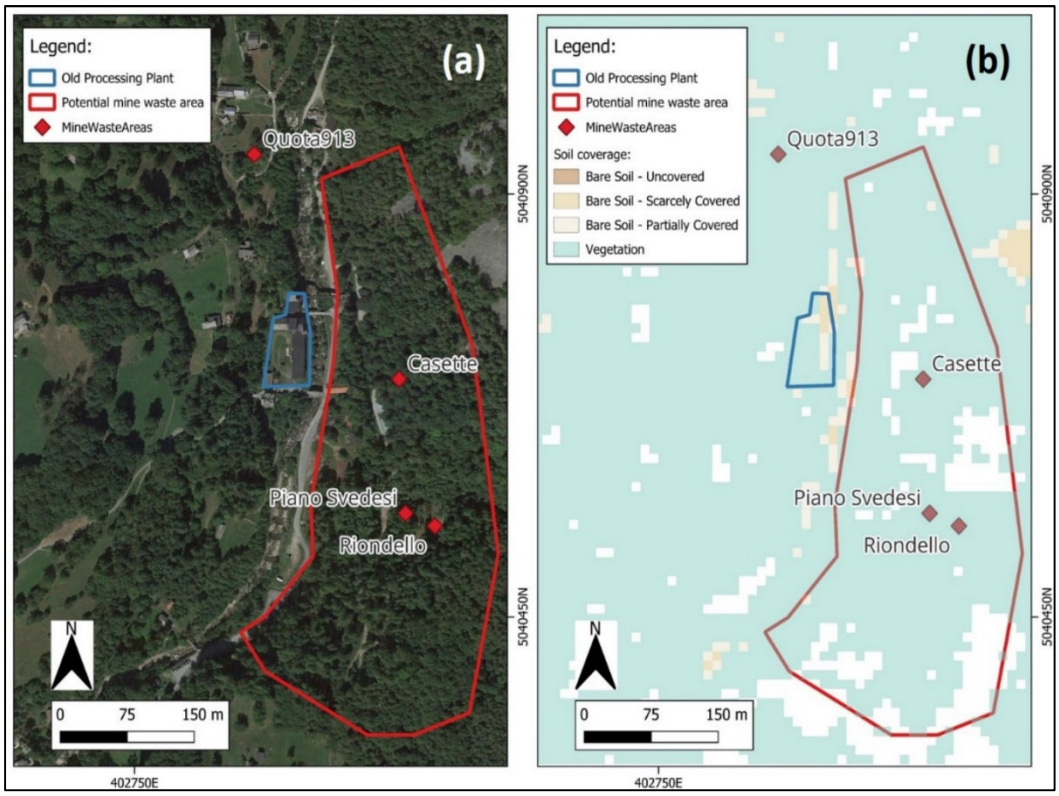


*Figure 60 – (**a**) Position of potential mine waste area around Traversella mine (red line), Traversella mine's old processing plant (blue line), and position of proven mine waste dump piles (red diamonds); (**b**) NDVI soil coverage layer and mine waste areas dump positions (source: Google Satellite Image. Coordinate system: WGS84/UTM Zone 32N)*

All the mine waste dumps recorded were located in highly vegetated areas, and at the time of the inspection, they were covered by a dense forest that had grown over the piles and limited the accessibility of the waste piles. This has made the sampling of the identified piles difficult and, sometimes, impossible. The most accessible point proved to be "*Piano Svedesi*", as it is located near existing road tracks and in a position where vegetation is relatively sparse.

5.2 Sampling strategy

Hand-picking sampling was realised for the "*Piano Svedesi*" waste rock dump, as it was an easily accessible area. According to the site characteristics, a grid-point sampling approach was adopted to collect representative samples from the waste pile. It consisted of a 9m wide and 3m high grid, with a total of 9 rectangular elements (Figure 61a). About 3 kg of material was collected from each grid element, carefully selecting appropriate portions according to the field characteristics of the material (Figure 61b). The reconstituted sample weighed approximately 30 kg.

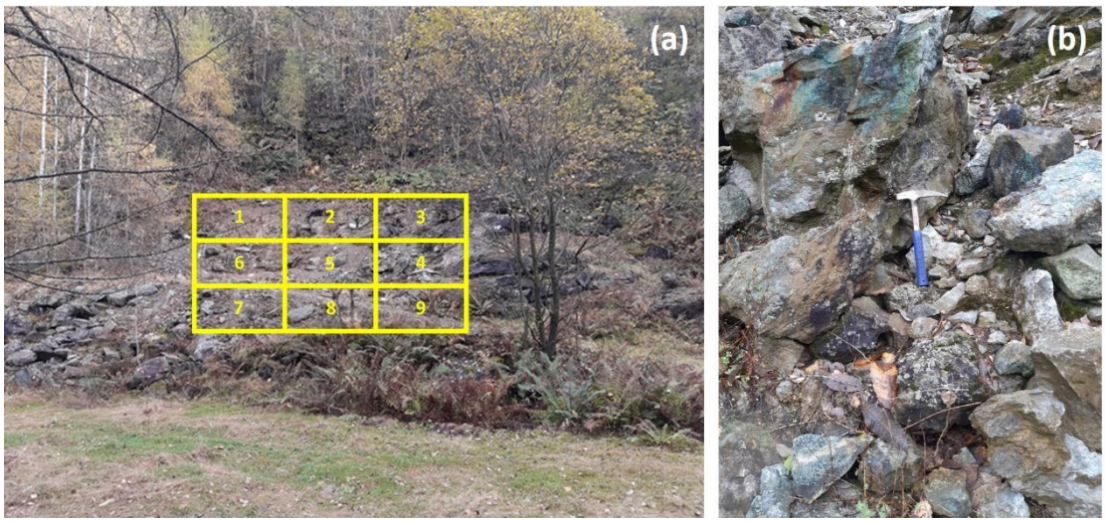


Figure 61 - (a) Photograph of "Piano Svedesi", Traversella mine, sampling point showing the 3 × 3 elements grid; (b) Zoomed photograph of sampling section #4 (source: Baldassarre et al., 2025)

5.3 Mineralogical and chemical characterisation

The initial characterisation of the material collected in the "*Piano Svedesi*" area was performed to understand the chemical and mineralogical features of the material using the following methodologies:

- OM – (***Par. 2.4.1***)
- SEM-EDS – (***Par. 2.4.2***)
- MLA – (***Par. 2.4.3***)
- XRPD – (***Par. 2.4.4***)
- HH-XRF – (***Par. 2.5.2***)
- ICP-MS – (***Par. 2.5.2***)

This approach provided detailed information for chemical and structural attributes for evaluating the material's potential for processing and recovery of valuable minerals.

5.3.1 Bulk sample characterisation results

The collected samples were characterised by having decimetric dimensions and showed a surficial oxidative mineralisation, while the internal sections exhibited a grey matrix interspersed with black veins (Figure 62).

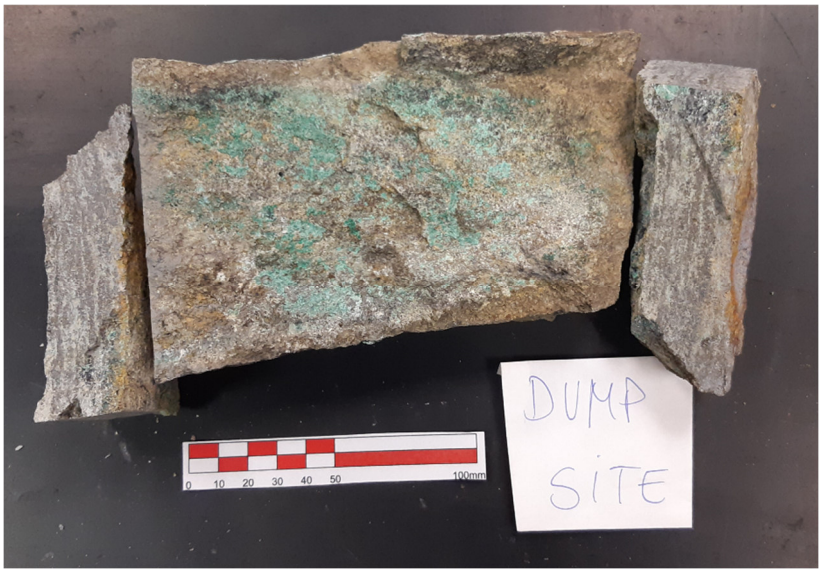


Figure 62 – Detail of a waste rock fragment collected in "Piano Svedesi" waste rock dump site in the Traversella mine area (source: Baldassarre et al., 2025)

5.3.1.1 Optical microscopy characterisation

Normal and polarised transmitted light was used to perform petrographic observation and identify the mineral structures and species. The images acquired from thin sections observation in transmitted light, parallel and polarised, are shown in Figure 63 (mineral abbreviations according to Warr (2021)).

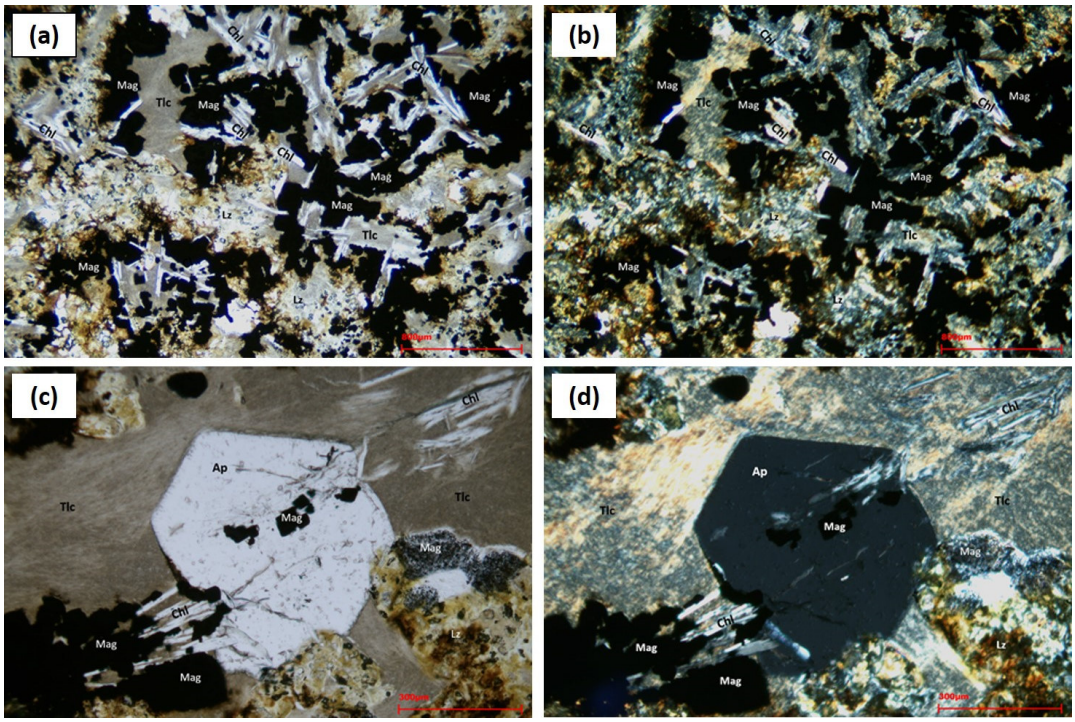


Figure 63 - Optical microscopy images of thin section in parallel transmitted light (PL) and cross-polarised light (XPL) from Traversella mine waste rock samples: (a) Thin Section #1, PL; (b) Thin Section #2, XPL; (c) Thin Section #2, PL; (d) Thin Section #2, XPL. Identified minerals: Ap – Apatite, Mag – Magnetite, Tlc – Talc, Chl – Chlorite, Lz – Lizardite. (source: Baldassarre et al., 2025)

The sample appeared highly heterogeneous, characterised by a matrix of silicate minerals such as talc and lizardite, interspersed with chlorite crystals. The mineralisation was characterised by opaque magnetite crystals showing a regular cubic shape. In some cases, magnetite grains were included in apatite grains.

In Figure 64 (mineral abbreviations according to Warr (2021)) is reported the petrographical detail of a visible feature detectable in the bulk sample (See Chapter 5.3.1)

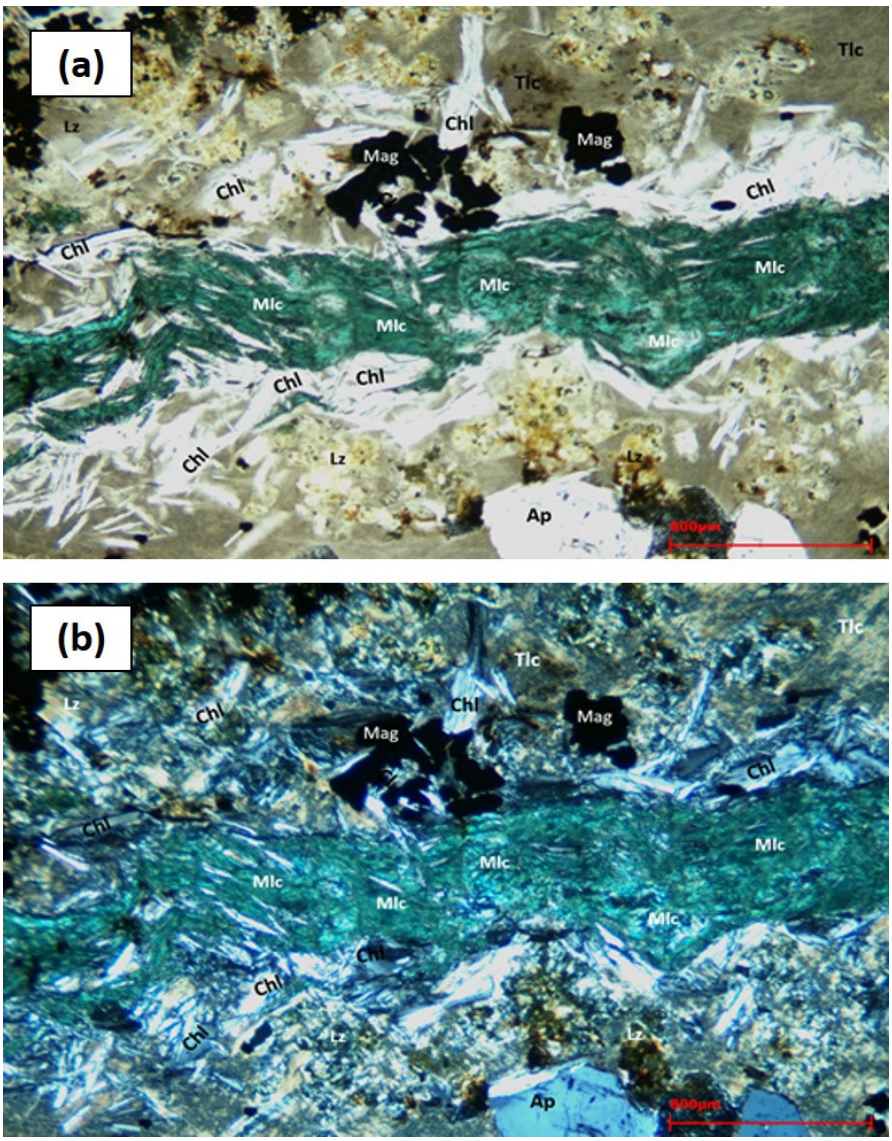


Figure 64 – Optical microscopy images of thin sections in parallel transmitted light (PL) and cross-polarised light (XPL) from Traversella mine waste rock samples: (a) Thin Section #3, PL; (b) Thin Section #3, XPL. Identified minerals: Ap – apatite, Mag – magnetite, Tlc – talc, Chl – chlorite, Lz – lizardite, Mlc – malachite. (source: Baldassarre et al., 2025)

5.3.1.2 XRPD characterisation results

X-ray diffraction analyses were performed on a representative portion of the initial sampled material after subsampling and milling according to the previous paragraph. Figure 65 shows the XRPD spectrum of the bulk material, while Table 24 shows the representative peak positions of the identified mineral phases.

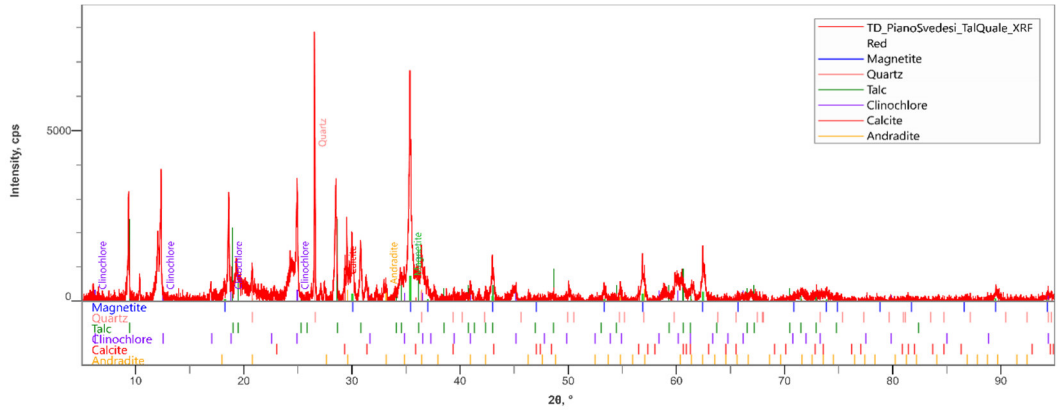


Figure 65 - XRPD spectrum for the bulk sample material sampled in Piano Svedesi area, Traversella mine.

Table 24 - Identified mineral phases for the "Piano Svedesi" bulk sample, Traversella mine.

Mineral Phase	Peak Positions (2θ, °)
Amphibole	10.48, 28.47, 33.09
Andradite	29.60, 33.19, 57.10
Calcite	29.41, 47.53, 48.52
Clinochlore	6.20, 12.42, 24.99
Magnetite	30.15, 35.51, 62.68
Quartz	20.86, 26.64, 50.15
Talc	9.45, 19.54, 28.60

Seven mineral phases were detected in the Piano Svedesi mine waste bulk sample, in particular: amphibole, andradite, calcite, clinochlore, magnetite, quartz and talc.

5.3.1.3 HH-XRF characterisation

HH-XRF analyses were performed to investigate the chemical assays of the samples, considering major elements and the detectable minor elements according to the equipment's range of detection and calibrations. Table 25 shows the measured values of 39 elements.

Table 25 - HH-XRF chemical assays for Piano Svedesi bulk sample, Traversella mine.

Element							
Ag (ppm)	**Al (%)**	**As (ppm)**	**Ba (ppm)**	**Ca (%)**	**Cd (ppm)**	**Ce (ppm)**	**Co (ppm)**
< 1.6	1.8±0.1	149±5.7	< 22	3.96± 0.01	< 2.0	< 21	< 210
Cr (ppm)	**Cu (%)**	**Eu (ppm)**	**Fe (%)**	**Gd (ppm)**	**Hg (ppm)**	**K (ppm)**	**La (ppm)**
< 37	1.10±0.01	< 354	16.9±0.02	< 632	< 0.2	334±13	< 16
Mg (%)	**Mn (ppm)**	**Nb (ppm)**	**Nd (ppm)**	**Ni (ppm)**	**P (%)**	**Pb (ppm)**	**S (%)**
11.4±0.5	1235±25	5±1.5	< 15	< 155	< 0.46	18±3.7	0.26± 0.01
Sb (ppm)	**Se (ppm)**	**Si (%)**	**Sn (ppm)**	**Sr (ppm)**	**Th (ppm)**	**Ti (ppm)**	**Tl (ppm)**
8.4±3.1	< 2.3	17.3±0.1	14±1.6	28±1.5	< 3.0	544±85	< 5.0
U (ppm)	**V (ppm)**	**W (ppm)**	**Y (ppm)**	**Zn (ppm)**	**Zr (ppm)**		
31±2.9	< 18	96±10	8.3±0.9	45±7.7	82±2		

Si and Fe were the most abundant elements, respectively, grading 17.3% and 16.9%. Considering the other major elements, Mg was detected in significant concentration (11.4%), while Ca and Al showed a lower grade of 3.96% and 1.8% respectively. S was measured to have a concentration of 0.26%.

Regarding critical and strategic elements assays, Cu was detected as the most abundant, with a concentration of 1.1%. Mn, Ti, As, and W were detected in traces, showing concentrations of 0.1%, 544 ppm, 149 ppm, and 96 ppm, respectively. In addition, Zn and Pb were assayed at 45 ppm and 18 ppm

5.3.1.4 ICP-MS characterisation

ICP-MS data were considered in order to have a more comprehensive geochemical characterisation of the collected sample. Notably, it was considered crucial to have a detailed characterisation of REEs and other critical elements. Table 26 shows the recorded geochemical assays.

Table 26 - ICP-MS geochemical assays for Piano Svedesi bulk sample, Traversella mine (: ALS ME-MS81 method)*

Element									
Ag (ppm)	**Al (%)**	**As (ppm)**	**Ba* (ppm)**	**Be (ppm)**	**Bi (ppm)**	**Ca (%)**	**Cd (ppm)**	**Ce* (ppm)**	**Co (ppm)**
0.8	1.4	140.5	16.0	1.36	0.21	3.40	0.21	7.90	91.7
Cr* (ppm)	**Cs (ppm)**	**Cu (%)**	**Dy* (ppm)**	**Er* (ppm)**	**Eu* (ppm)**	**Fe (%)**	**Ga* (ppm)**	**Gd* (ppm)**	**Ge (ppm)**
19.0	1.40	0.95	1.50	1.3	0.29	18.2	5.7	1.1	0.06
Hf* (ppm)	**Ho* (ppm)**	**In (ppm)**	**K (ppm)**	**La* (ppm)**	**Li (ppm)**	**Lu* (ppm)**	**Mg (%)**	**Mn (ppm)**	**Mo (ppm)**
1.6	0.4	0.8	300	5.5	6.4	0.3	13.3	1100	0.7
Nb* (ppm)	**Nd (ppm)**	**Ni (ppm)**	**P (ppm)**	**Pb (ppm)**	**Pr (ppm)**	**Rb* (ppm)**	**S (%)**	**Sb (ppm)**	**Sc* (ppm)**
4.04	4.4	16.8	590	3.5	1.08	5.6	0.14	8.85	2.2
Se (ppm)	**Sm* (ppm)**	**Sn* (ppm)**	**Sr* (ppm)**	**Ta* (ppm)**	**Te (ppm)**	**Tb* (ppm)**	**Th* (ppm)**	**Ti* (ppm)**	**Tl (ppm)**
1	0.92	12.2	25.7	0.5	< 0.05	0.21	2.06	700	0.2
U* (ppm)	**V* (ppm)**	**W* (ppm)**	**Y* (ppm)**	**Yb* (ppm)**	**Zn (ppm)**	**Zr (ppm)**		**∑ LREE (ppm)**	**∑ HREE (ppm)**
14.95	17	86	14.9	1.79	49	66		20.1	20.4

The reported data shows that Fe reported a grade of 18.15%, Al 1.42% and Mg 13.3%. Cu was present at a concentration of 0.95%, with Ni at 16.8ppm, Co at 91.7 ppm, and Zn at 49 ppm. As reached a concentration of 140.5 ppm, while

heavy elements such as U and Th graded 14.95 and 2.06 ppm, respectively. The total amount of REE is 40.5 ppm.

5.3.2 Geochemical, mineralogical and environmental considerations

Mineralogical and chemical characterisations performed on the collected samples in the Piano Svedesi mine waste dump can be considered in accordance with previous geological studies highlighting the characteristics of the Traversella orebodies described by Costa et al. (2019) and Nimis et al. (2014).
According to the collected chemical data, some considerations can be exploited regarding the abundance of critical, strategic and economic elements. A spider-plot (Figure 66) was plotted to identify the most concentrated elements compared to the average abundance of the Earth's crust (Rudnick & Gao, 2014).

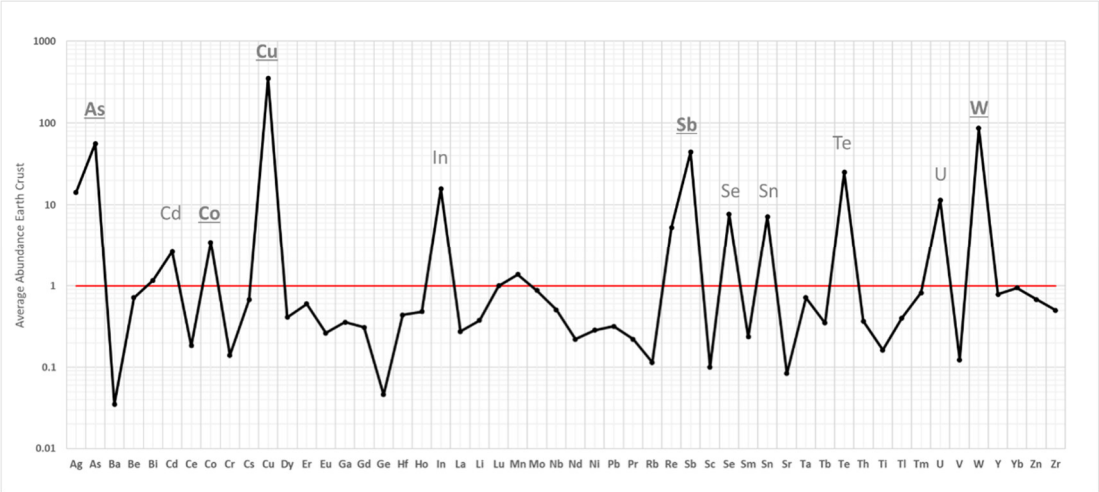


Figure 66 - Spider-plot for the geochemical summary of Piano Svedesi samples, Traversella mine, normalized against average abundance of elements in the Earth's crust by Rudnick & Gao, 2014

Piano Svedesi bulk sample showed to be relatively enriched in critical elements such as As, Co, Sb, and W, being more than 10 times higher than the average abundance. In addition, Cu was the most enriched strategic element, recording a concentration more than 100 times higher than the average. Other economically important elements exceeding 10 clarks included Cd, In, Se, Sn, Te, and U.

From an environmental point of view, the geochemical data obtained by ICP-MS analyses were compared to limits of metallic elements, Columns A (sites for public, private, and residential green use) and Column B (sites for commercial and industrial use), Table 1, Annexe 5 of the Law Decree 152/2006 (Italian Republic, 2006). The values were normalised against the Column A values, as shown in Figure 67.

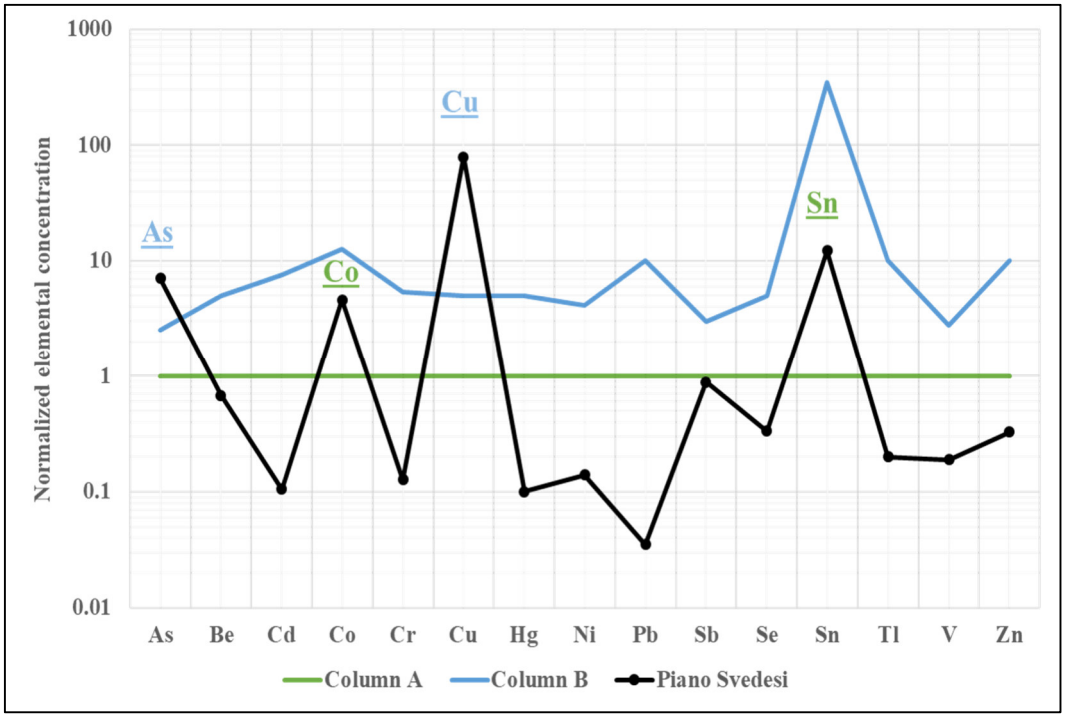


Figure 67 - Spider plot comparing Piano Svedesi, Traversella mine, elemental concentration with the normalised metallic element limits established by Legislative Decree 152/2006. Green: elements exceeding Column A; Blue: elements exceeding Column B

The bulk sample collected in the Piano Svedesi area showed exceeding values for soil quality limits for green use for Co and Sn, with concentrations of 91.7 ppm (Column A limit: 20 ppm) and 12.2 ppm (Column A limit: 1 ppm). In addition, As and Cu concentrations exceeded the Column B limits with values of 140.5 ppm (Limit Col. B: 50 ppm) and 9500 ppm (Limit Col. B: 600 ppm), respectively.

5.4 Lab-scale processing trials

In general, mineralogical and chemical characterisation of the material guided the selection of the processing steps. Target minerals were identified, and subsequently, a suitable recovery option was considered.

Preliminary tests on representative material were performed by sieving the comminution products and obtaining 3 size classes (> 0.250 mm, 0.250-0.125 mm, and < 0.125 mm) to perform free-grain size firstly qualitatively using optical macroscope observation, and subsequently using SEM images and MLA.

Particle size class 0.250-0.125mm was selected as being suitable for dry magnetic separation and gravity separation equipment. The finer size class <0.125 mm was considered only for wet magnetic separation trials.

Separation tests were performed in batch mode, and mass balances were considered in particular for separation processes.

The processing activities performed on the Piano Svedesi mine waste sample collected can be listed as follows:

- Jaw crushing – (***Par. 2.6.3.1, Par 2.6.3.2);***
- Rod milling – (***Par. 2.6.3.3***);
- Sieving – (***Par. 2.6.2***);
- Dry magnetic separation using a LIMS – (***Par. 2.6.4.1***);
- Wet magnetic separation using a WHIMS – (***Par. 2.6.4.2***);
- Gravity separation using a ST – (***Par. 2.6.5.1***);

In particular, 4 different lab-scale processing configurations were considered and evaluated, as summarised in Table 27.

Table 27 - Summary of processing trials performed on Piano Svedesi mine waste material, Traversella mine.

Test	Size Class (mm)	Condition	Equipment(s)
A	0.250-0.125	Dry	LIMS
B	0.250-0.125	Wet	ST
C	0.250-0.125	Dry, Wet	LIMS, ST
D	< 0.125	Wet	WHIMS

Mineralogy and chemical assays of the output materials were defined using XRPD and HH-XRF, considering a representative sub-sample of each concentrate obtained. Accordingly, Y (***Equation 1***), R (***Equation 2***), and ER (***Equation 3***) for selected target elements were calculated in order to evaluate the separation quality (***Par. 2.6.6***).

5.4.1 Crushing, grinding, and sieving

Crushing and grinding operations were realised according to the scheme reported in Figure 68. The processes were selected in order to progressively reduce the grain size of the material and obtain size classes suitable for the next phase of separation, and according to the requirements of each separation equipment.

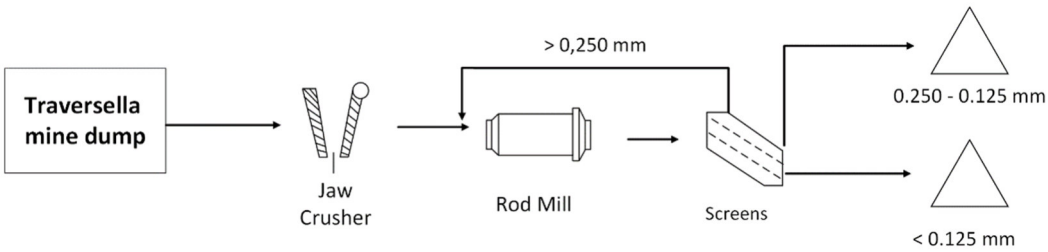


Figure 68 - Size reduction procedure for obtaining size fractions suitable for lab-scale processing trials of waste rock samples from Traversella mine.

After crushing and milling, sieving was performed to obtain three granulometric classes. Weight fractions obtained after milling are reported in Table 28.

Table 28 - Weight fractions for the obtained size classes after crushing, milling, and sieving, of waste rock samples from Traversella mine.

Size Class (mm)	Mass Rate (%)
>0.250	5.6
0.125–0.250	42.3
<0.125	52.1

Size classes 0.250-0.125 mm and < 0.125 mm were selected as the feeding material for separation tests. These size classes were further investigated to better define mineralogical and chemical characteristics. In particular, for size class 0.250-0.125 mm, the individuation and investigation of target minerals was performed to confirm the selection of the most suitable feeding material.

5.4.2 Feeding material characterisation – Size class 0.250-0.125 mm

5.4.2.1 Mineralogical characterisation – Size class 0.250-0.125 mm

Preliminary mineralogical characterisation on size class 0.250-0.125 mm was realised using XRPD (***Par. 2.4.4***). The acquired spectrum is reported in Figure 69.

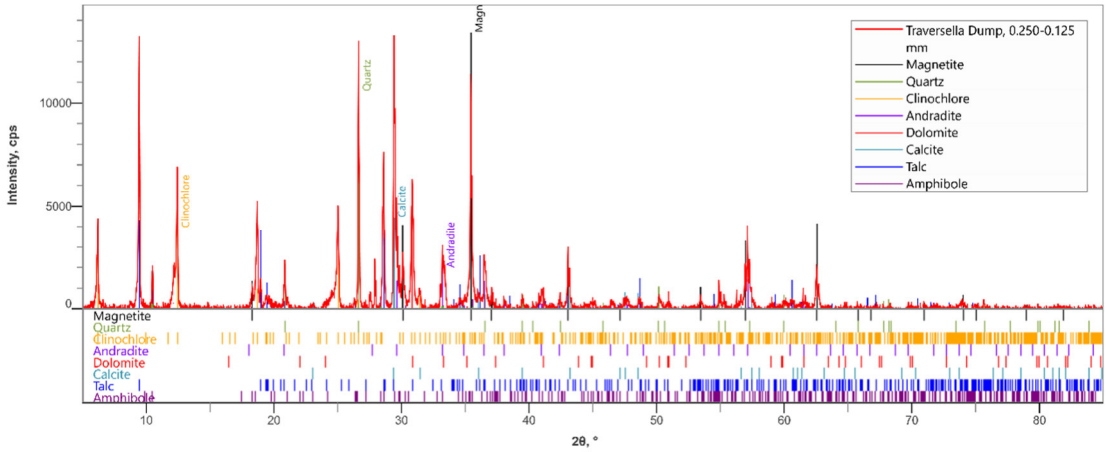


Figure 69 - XRPD spectrum for feeding material 0.250-0.125 mm size class obtained after comminution and sieving of waste rock samples from Traversella mine.

In Table 29, the identified mineral phases, according to the performed qualitative analysis.

Table 29 - XRPD mineral phases for 0.250-0.125 mm material obtained after comminution and sieving of waste rock samples from Traversella mine.

Mineral Phase	Peak Positions (2θ, °)
Amphibole	10.48, 28.47, 33.09
Andradite	29.60, 33.19, 57.10
Calcite	29.41, 47.53, 48.52
Clinochlore	6.20, 12.42, 24.99
Dolomite	30.87, 41.06, 50.94
Magnetite	30.15, 35.51, 62.68
Quartz	20.86, 26.64, 50.15
Talc	9.45, 19.54, 28.60

Eight mineral phases were recorded, being these comparable to the initial bulk material sampled in the field.

Following XRPD, SEM-EDS (***Par. 2.4.2***) and MLA (***Par. 2.4.3***) analyses were performed to better refine the mineralogical composition of the material, improving data that are challenging to detect only by X-ray mineralogical analyses.

Figure 70 shows an example of a BSE image and its colour masking automatically obtained by the MLA system.

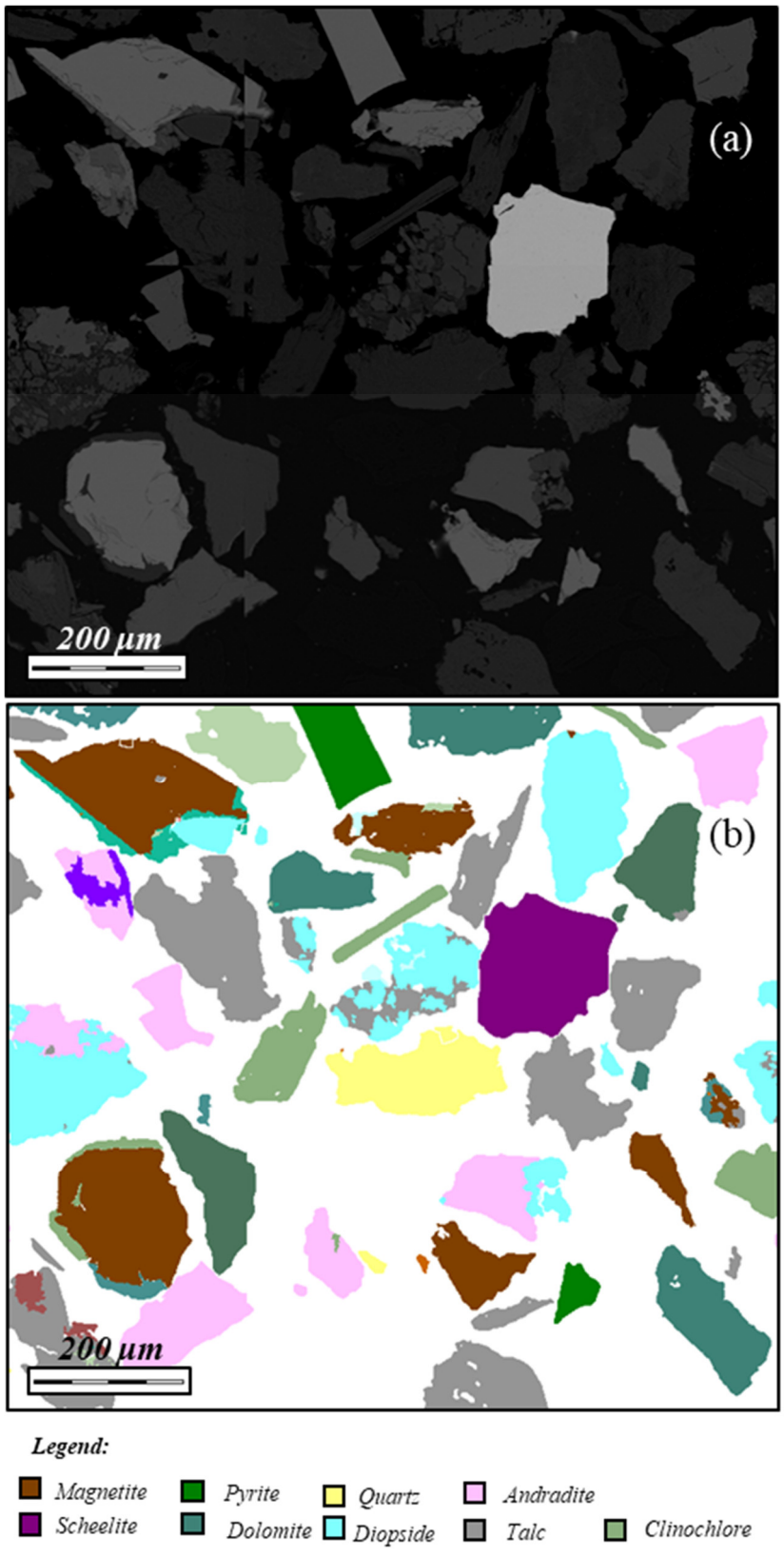


Figure 70 - (a) SEM-BSE image for sample 0.250-0.125mm obtained after comminution and sieving of waste rock samples from Traversella mine; (b) Mineralogy image for the same sample as determined by MLA.

MLA modal mineralogy results for size class 0.250-0.125 mm material are shown in Figure 71. Full data reported in ***Appendix C.1.***

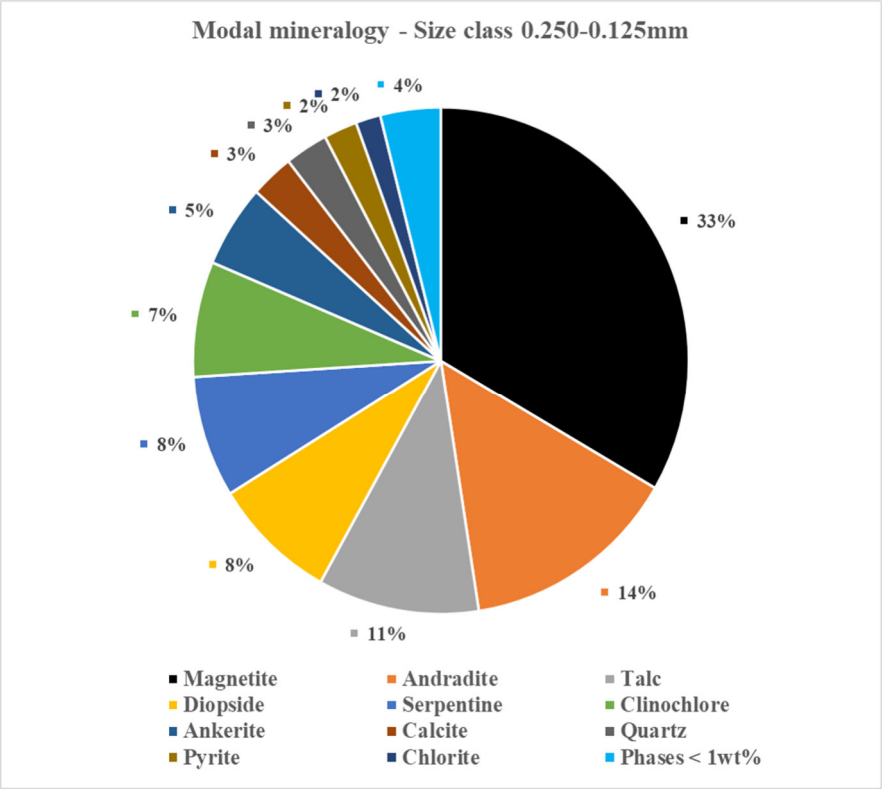
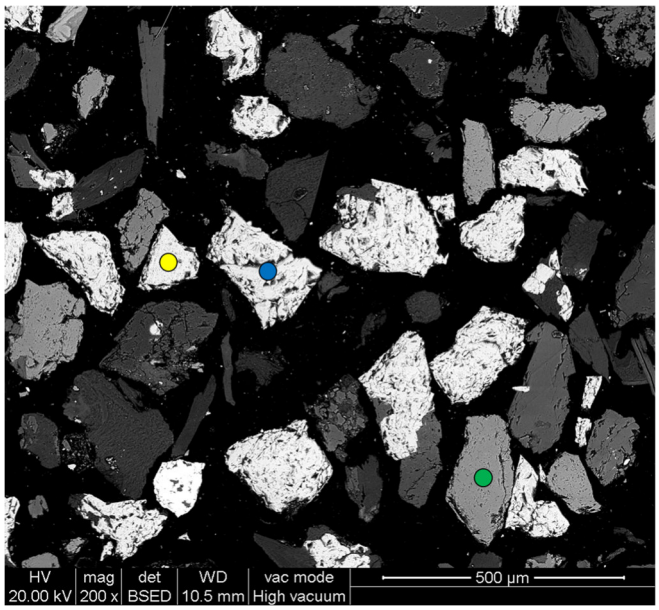


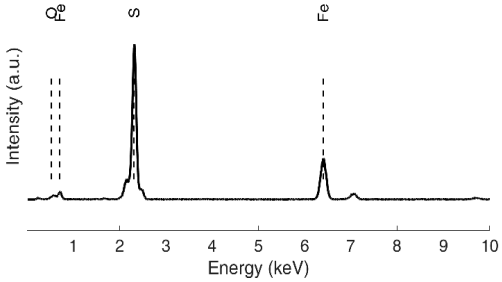
Figure 71 – Modal mineralogy pie chart for size class 0.250-0.125 mm obtained after comminution and sieving of waste rock samples from Traversella mine.

Size class 0.250-0.125mm was primarily characterised by the presence of magnetite (33.4 wt%) and andradite (14.2 wt%). The third most abundant mineral is talc (10.5 wt%). Minor phases include diopside (8.1 wt%), serpentine (7.8 wt%), clinochlore (7.4 wt%), ankerite (5.3 wt%), calcite (2.8 wt%), quartz (7.8 wt%), pyrite (2.2 wt%) and chlorite (1.6 wt%). Among the phases having a weight fraction below 1% (3.9 wt% of the total), apatite, ilmenite, sphalerite, scheelite, chalcopyrite, and scheelite are the most remarkable minerals.

Figure 72 shows a BSE image and some EDS spectra collected on an epoxy-mounted portion of the 0.250-0.125 mm size class.

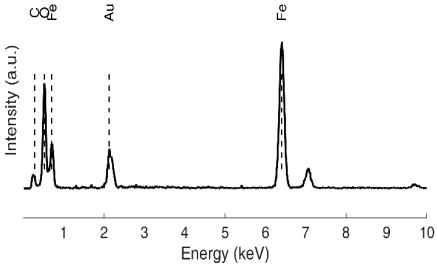


(**a**)



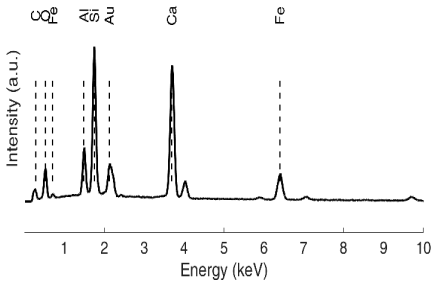
Fe (%)	S (%)
50.2	49.5

(**b**)



Fe (%)	O (%)
79.7	20.3

(**c**)



Al (%)	Ca (%)	Fe (%)	O (%)	Si (%)
8.0	31.2	16.9	20.7	23.2

(**d**)

Figure 72 - (a) SEM-BSE image from epoxy-mounted samples of 0.125–0.250 mm material obtained after comminution and sieving of waste rock samples from Traversella mine (yellow dot: pyrite grain; blue dot: magnetite grain; green dot: gangue mineral grain); (b) EDS spectrum and quantification for pyrite (yellow dot); (c) EDS spectrum and quantification for magnetite (blue dot); (d) EDS spectrum and quantification for silicate gangue mineral (green dot) (source: Baldassarre et al., 2025)

The collected SEM-EDS information showed the presence of several grains containing heavy elements, as indicated by the increased brightness of the BSE images, which can be related to a greater atomic number average of the elements contained in the single mineral grain (Krinsley, Pye, Jr, & Tovey, 1998). Magnetite was the most abundant metal-bearing mineral identified, appearing in single grains and being occasionally associated with other gangue minerals. Additionally, pyrite grains were identified as a minor phase. Gangue minerals were generally represented by silicates. Scheelite was identified as a CRM bearing mineral according to the MLA data presented in Figure 70.

In more detail, mineral associations of the selected valuable minerals were evaluated according to MLA data, as shown in Figure 73 and Figure 74.

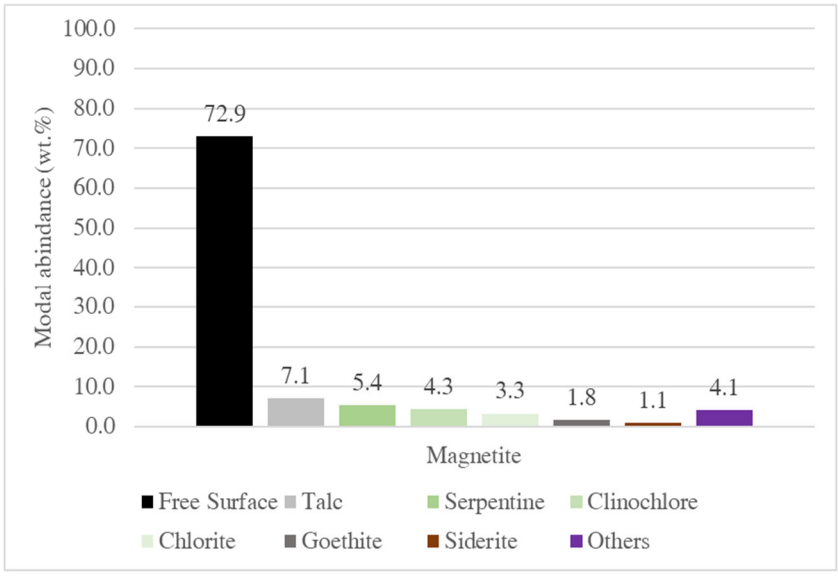


Figure 73 - Magnetite mineral association in the 0.250-0.125mm size class obtained after comminution and sieving of waste rock samples from Traversella mine.

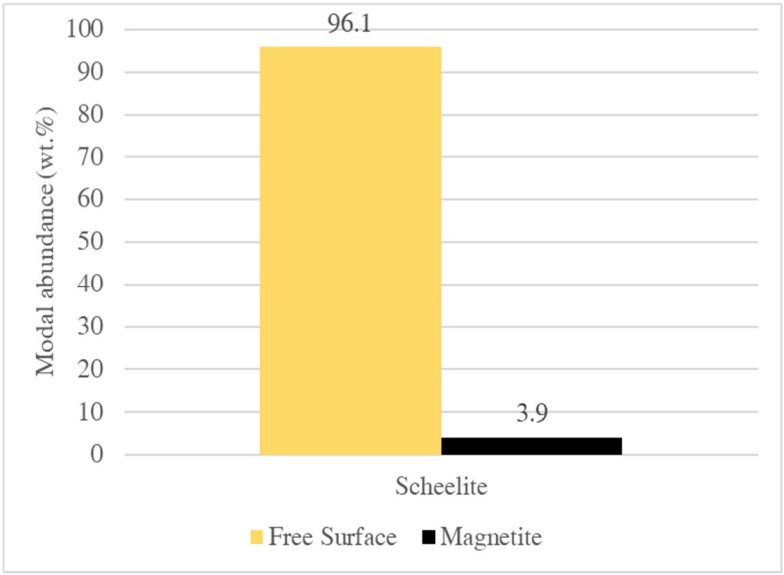


Figure 74 - Scheelite mineral association in the 0.250-0.125mm size class obtained after comminution and sieving of waste rock samples from Traversella mine.

Magnetite resulted in having a free surface for 72.2% of the total amount of considered grains. When locked to other mineral phases, magnetite tended to associate with talc (7.1%), serpentine (5.4%), clinochlore (3.3%), goethite (1.8%), and siderite (1.1%). On the other side, scheelite appeared as nearly totally free (96.1%), and the only associated mineral recorded was magnetite for 3.9%.

5.4.2.2 Free grain size and liberation analysis using Matlab image processing and MLA – Size Class 0.250-0.125 mm

BSE images acquired from 0.250-0.125mm materials were selected as input images for the semi-automated procedure for free-grain size determination and liberated grain size distribution (***Par. 2.4.2.1***). The areas associated with valuable grains were manually selected according to the magnetite grains present in the original (Figure 75a), producing two different black and white binary masks: the first represented the total magnetite minerals' areas (Figure 75b), while the second represented the gangue inclusions' areas of the first image (Figure 75c).

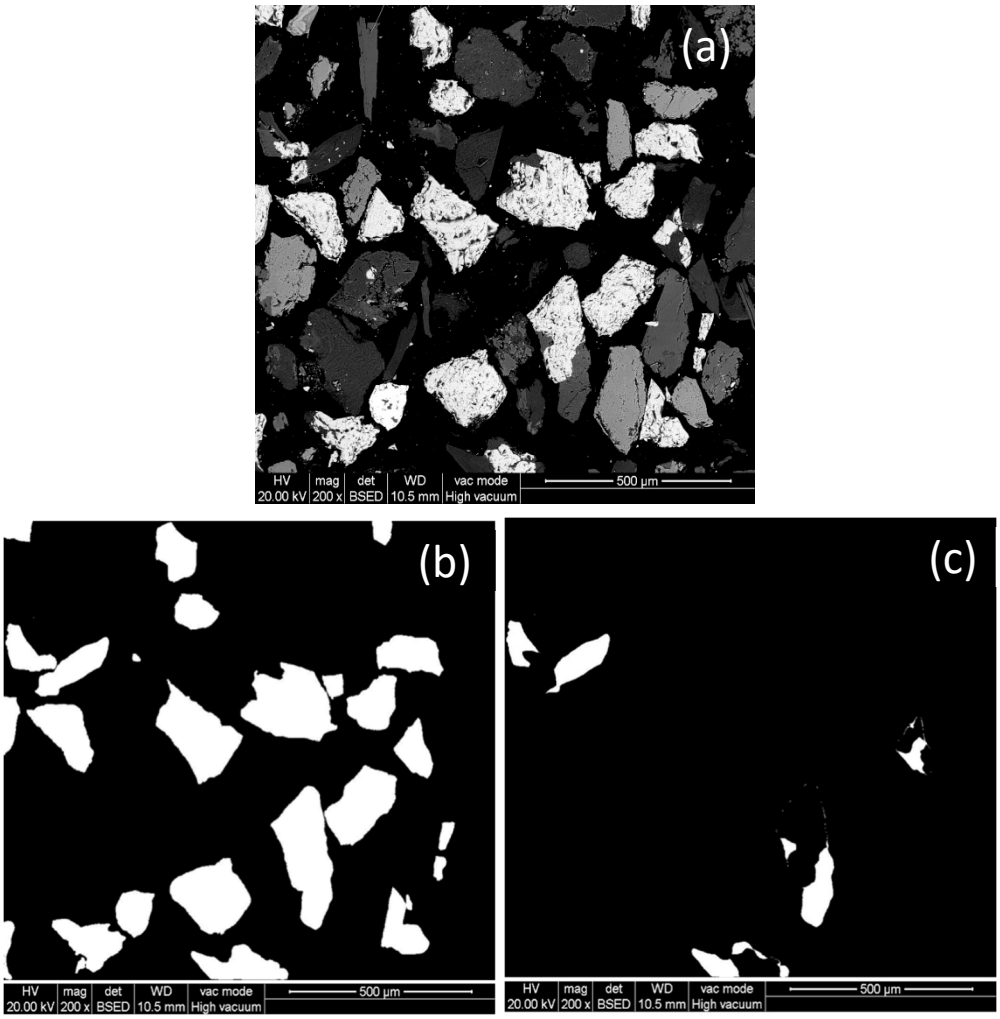


Figure 75 - (a) SEM-BSE image from epoxy-mounted samples of the size class 0.25–0.125 mm obtained after comminution and sieving of waste rock samples from Traversella mine; (b) binary mask for magnetite grains; and (c) binary mask for gangue minerals associated with magnetite grains. (source: Baldassarre et al., 2025)

The obtained binary masks were processed using the MATLAB script coded (***Appendix C.2***), which was designed to automatically calculate grain-by-grain liberation of magnetite grains.

The script calculated the total area of each grain, determined the magnetite area by subtracting the area of gangue minerals from the magnetite grains' mask. Subsequently, it quantified the proportion of magnetite area in each grain to assess the overlap percentage of these areas. Single grains were categorised into three classes based on the following thresholds: liberated grains (≥80% magnetite area), middling grains (<80% and ≥30% magnetite area), and locked grains (<30% magnetite area). In addition, the script calculated the granulometric distribution of magnetite grains using the equivalent diameter derived from the grain-by-grain analysis. Overall, three different BSE images were considered for this quantitative evaluation, considering 84 magnetite grains.

Grain-by-grain overlapping areas evaluation results are shown in Figure 76, indicating the areas assigned to magnetite or gangue minerals. Additional data re reported in ***Appendix C.3***, ***Appendix C.4***, and ***Appendix C.5***.

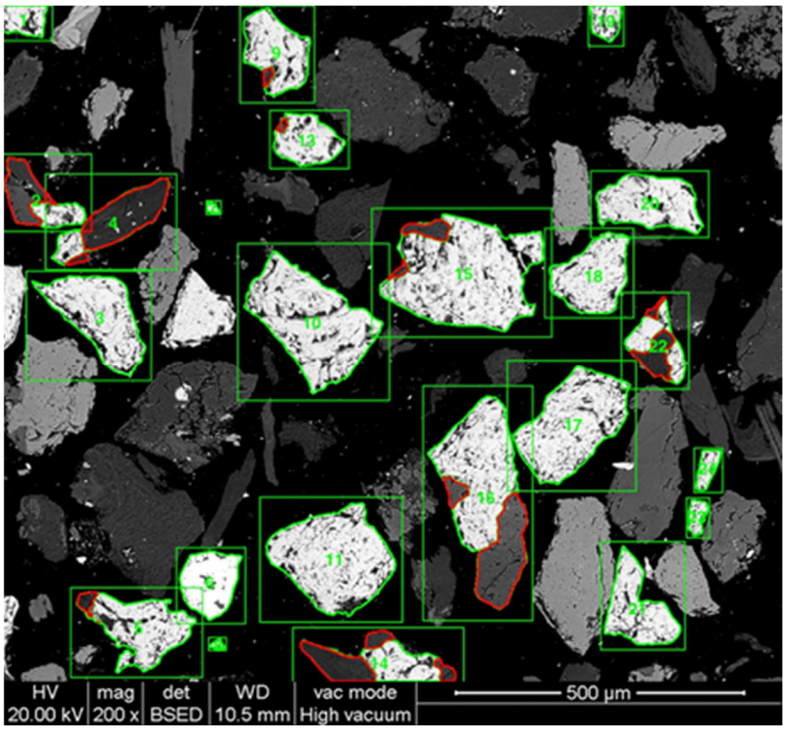


Figure 76 - TD_BSE2 specimen BSE image of 0.250–0.125 mm material, obtained after comminution and sieving of waste rock samples from Traversella mine, with grain contours overlapping (green contours: magnetite; red contours: gangue) (source: Baldassarre et al., 2025)

Liberation analysis for magnetite in the 0.250–0.125 mm size class is reported in Figure 77.

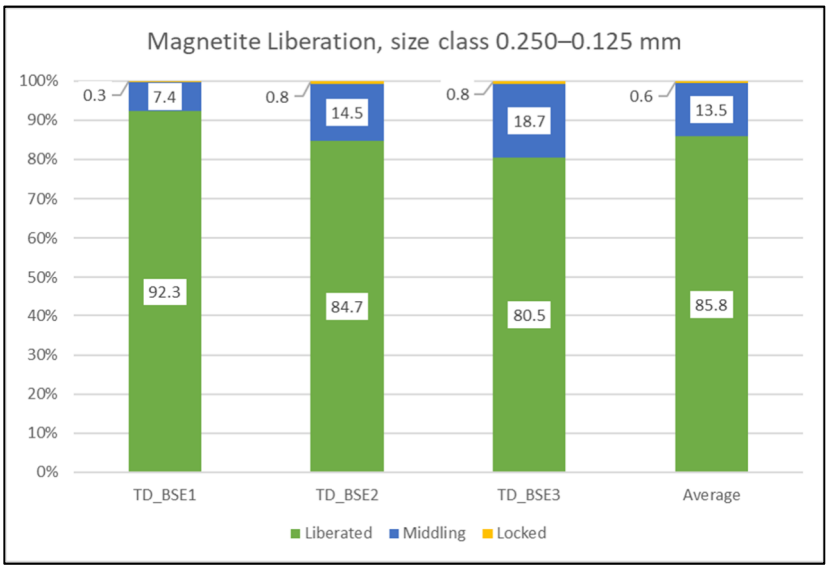


Figure 77 - Liberation characteristics of magnetite in size class 0.250–0.125 mm material after comminution and sieving of mine waste rocks from Traversella mine obtained from BSE image fields TD_BSE1, TD_BSE2, and TD_BSE3, and average liberation values. (source: Baldassarre et al., 2025)

On average, magnetite grains were 85.8% liberated (range 80.5–92.3%), with middling grains accounting for 13.5% (range 7.4–18.7%). Locked magnetite grains were negligible, averaging 0.6% (range 0.3–0.8%).

The free-grain size was evaluated according to the equivalent diameter particle size distribution extrapolated from the identified areas of liberated magnetite grains (Figure 78). According to the particle size distribution curves obtained, p80 and p50 were calculated for each considered image field, as reported in Table 30.

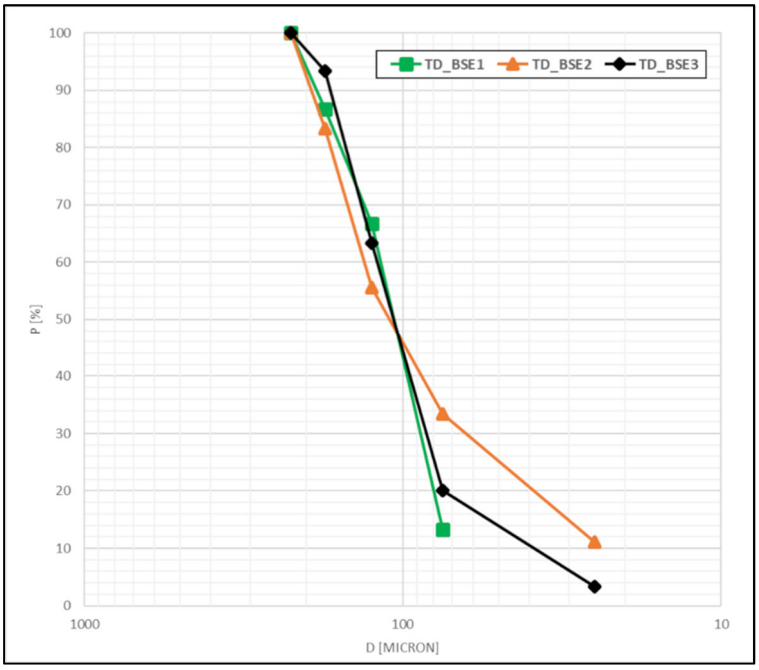


Figure 78 - Calculated particle size distribution curves for magnetite free-grains, according to their equivalent diameter from image analyses, for size class 0.250–0.125 mm material after comminution and sieving of mine waste rocks from Traversella mine (source: Baldassarre et al., 2025)

Table 30 – Particle size distribution percentiles calculated from magnetite liberated free-grain size analysis for size class 0.250–0.125 mm material after comminution and sieving of mine waste rocks from Traversella mine

Percentile	***TD-BSE1***	***TD-BSE2***	***TD-BSE3***	***Mean***
p80 (mm)	0.158	0.169	0.153	**0.160**
p50 (mm)	0.109	0.113	0.110	**0.111**

For p80, values ranged between 0.153 mm and 0.169 mm, with a mean value of 0.160 mm. p50 values ranged from 0.109 mm to 0.113 mm, having a mean of 0.111 mm.

MLA analyses were performed on the same size fraction in order to obtain more detailed information regarding liberation grade, mineral associations and particle size distribution of target minerals before separation tests. Particle size distribution of target minerals, such as magnetite and scheelite, was extrapolated from the MLA dataset, as shown in Figure 79 and Table 31.

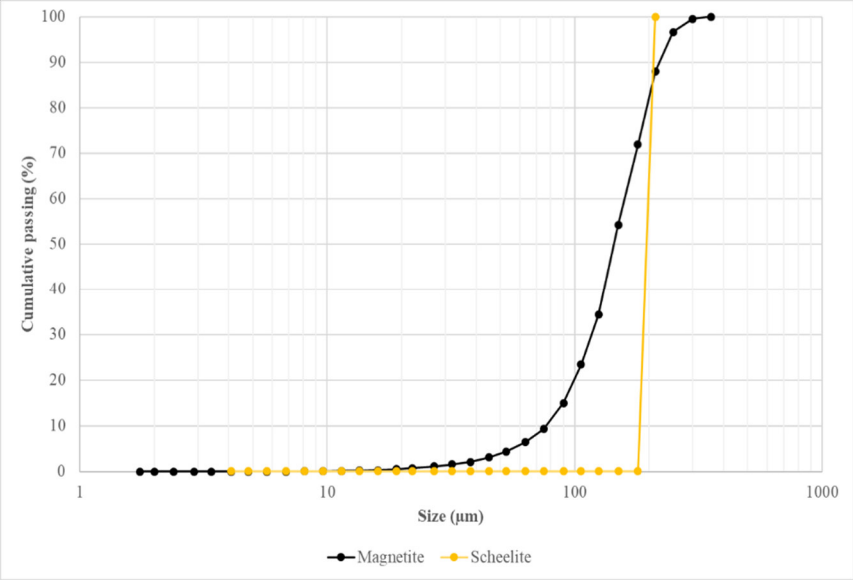


Figure 79 - Particle size distribution for magnetite and scheelite from the 0.250-0.125mm size class after comminution and sieving of mine waste rocks from Traversella mine

Table 31 - Particle size distribution percentiles calculated from magnetite and scheelite particle size distribution curves for the 0.250-0.125mm size class material after comminution and sieving of mine waste rocks from Traversella mine

Percentile	*Magnetite*	*Scheelite*
p80 (mm)	0.196	0.206
p50 (µm)	0.145	---

Magnetite showed a p80 of 0.196 mm and a p50 of 0.145 mm. For scheelite, the quality of available data made possible the only calculation of the p80 percentile, showing an extrapolated value of 0.206 mm.

Liberation analyses according to MLA data for magnetite and scheelite identified in the 0.250–0.125 mm size class are reported in Figure 80.

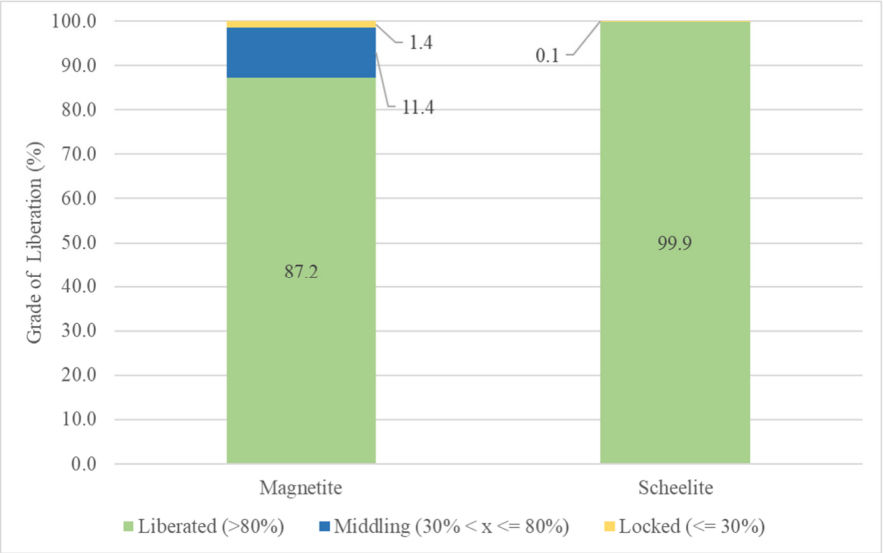


Figure 80 - Liberation analysis for magnetite and scheelite grains contained in the 0.250-0.125mm size class material obtained after comminution and sieving of mine waste rock samples from Traversella mine.

Magnetite resulted in a liberated form for 87.2%, having middling phases of about 11.4% and only 1.4% of locked grain. Additionally, scheelite grains resulted in full liberation for this size class.

Table 32 shows the number of grains considered for the Matlab semi-automated method and MLA, and the corresponding calculated data for liberation, and particle size distribution of liberated samples

Table 32 - Comparison of liberation grade and particle size distribution percentiles calculation for magnetite grains contained in the 0.250-0.125mm size class material obtained after comminution and sieving of mine waste rock samples from Traversella mine, according to the Matlab script processing of SEM-BSE images and MLA system

Parameters	***Matlab script***	***MLA***
Considered grains (n.)	84	5,263
Liberation grade (%)	85.8	87.2
p80 (mm)	0.160	0.196
p50 (mm)	0.111	0.145

Liberation analysis results for magnetite grains obtained by SEM-BSE images processed by a MATLAB script, and MLA are comparable, having a liberation grade of 85.5 % and 87.2 %. The consistency of the MLA data is ensured by the large number of grains analysed (5,263), which was made possible by the extended BSE map built by the system. By contrast, the MATLAB image processing script produced a comparable estimation of the magnetite liberation grade; however, as a semi-automated procedure, it considered only 84 grains as the initial dataset. Regarding particle size distribution percentiles, semi-automated methods showed a lower dimension for p80 and p50, respectively 0.160 mm and

0.111 mm, when compared to the ones calculated from MLA data (p80 = 0.196 mm, p80 = 0.145 mm).

In general, the proposed MATLAB-based liberation analysis method could be considered a potential alternative to more expensive automated mineralogical techniques, particularly for liberation analysis and free grain size determination on selected target minerals. However, MLA remains a highly reliable analytical tool due to the large number of grains it analyses and its ability to provide extensive information also on gangue and accessory minerals.

To conclude, two main target minerals were identified in the 0.250–0.125 mm size fraction of the material obtained after crushing, milling, and sieving of the initial waste rock sample: magnetite and scheelite. According to MLA analyses, magnetite was liberated at a grade of 87.2% at a p80 of 0.196 mm, while scheelite appeared to be completely liberated at a p80 of 0.205 mm. Consequently, this size fraction was selected as suitable for further lab-scale processing trials using magnetic and gravity separation.

5.4.2.3 Chemical characterisation – Size class 0.250-0.125 mm

HH-XRF analyses were performed to acquire chemical assays and define the grade of the material before separation tests. Resulting XRF assays are reported in Table 33.

Table 33 - HH-XRF assays for the 0.250-0.125 mm size class material obtained after comminution and sieving of mine waste rock samples from Traversella mine

Element							
Ag (ppm)	**Al (%)**	**As (ppm)**	**Ba (ppm)**	**Ca (%)**	**Cd (ppm)**	**Ce (ppm)**	**Co (ppm)**
< 1.0	1.9±0.1	152±4	< 12	7.5±0.01	4.7±1	< 11	< 143
Cr (ppm)	**Cu (%)**	**Eu (ppm)**	**Fe (%)**	**Gd (ppm)**	**Hg (ppm)**	**K (ppm)**	**La (ppm)**
< 20	1.26±0.01	< 202	18.3±0.02	< 353	< 0.1	815±16	< 8.7
Mg (%)	**Mn (ppm)**	**Nb (ppm)**	**Nd (ppm)**	**Ni (ppm)**	**P (%)**	**Pb (ppm)**	**S (%)**
10.2±0.5	2697±37	3.2±0.9	< 19	< 155	< 0.31	128±4.4	0.69±0.01
Sb (ppm)	**Se (ppm)**	**Si (%)**	**Sn (ppm)**	**Sr (ppm)**	**Th (ppm)**	**Ti (ppm)**	**Tl (ppm)**
7.6±1.9	< 1.8	15.7±0.1	23±1.0	26±1.2	< 4.0	469±94	< 5.0

U (ppm)	V (ppm)	W (ppm)	Y (ppm)	Zn (ppm)	Zr (ppm)
40±2.0	< 10	204±13	9.7±0.7	581±9.4	44±2

Based on the mineralogical data collected, Fe, Cu, and W were identified as the primary target elements before separation. Fe was the most abundant, with an assay of 18.3%, while copper graded at 1.23%. Tungsten was present at a concentration of 204 ppm. These three elements were considered for the calculation of R and ER after separation trials.

5.4.3 Feeding material characterisation – Size Class < 0.125 mm

5.4.3.1 Mineralogical characterisation – Size class < 0.125mm

Mineralogical characterisation on size class <0.125mm material was performed by XRPD qualitative analysis. The acquired data are reported in Figure 81 and Table 34.

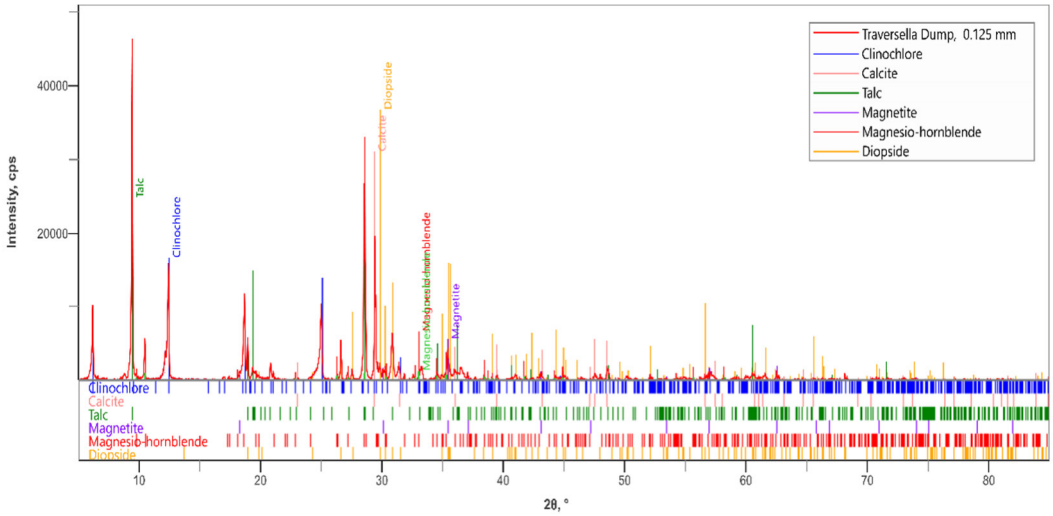


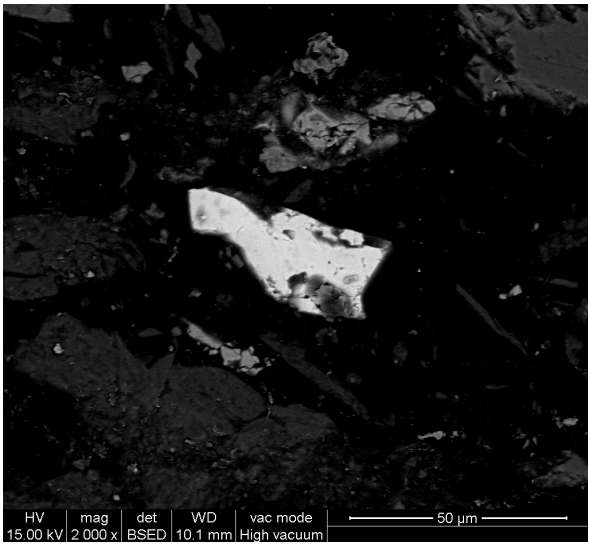
Figure 81 – XRPD spectrum for size class < 0.125 mm material 0.250-0.125mm size class material obtained after comminution and sieving of mine waste rock samples from Traversella mine.

Table 34 - XRPD mineral phases for size class < 0.125 mm material obtained after comminution and sieving of mine waste rock samples from Traversella mine

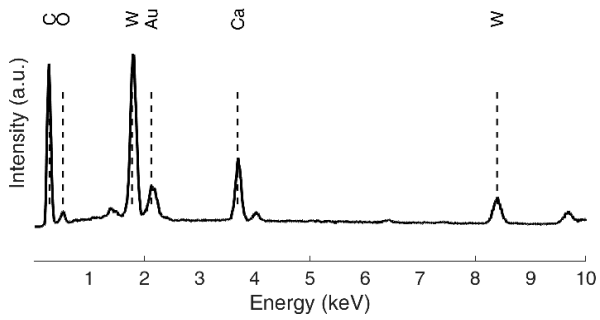
Mineral Phase	Peak Positions (2θ, °)
Calcite	29.41, 47.53, 48.52
Clinochlore	6.20, 12.42, 24.99
Diopside	29.83, 35.49, 35.64
Lizardite	12.22, 24.54, 35.91
Magnetite	30.15, 35.51, 62.68
Talc	9.45, 19.54, 28.60

The < 0.125mm size class material was characterised by six main mineral phases. Talc resulted in having the most intense peak. Andradite and quartz were not detected, while diopside resulted as the emerging phase for this size class. Magnetite was considered the only identifiable target mineral.

Figure 82a and Figure 83a show BSE images, obtained by SEM-EDS analyses, of minor mineral grains detected in the samples.



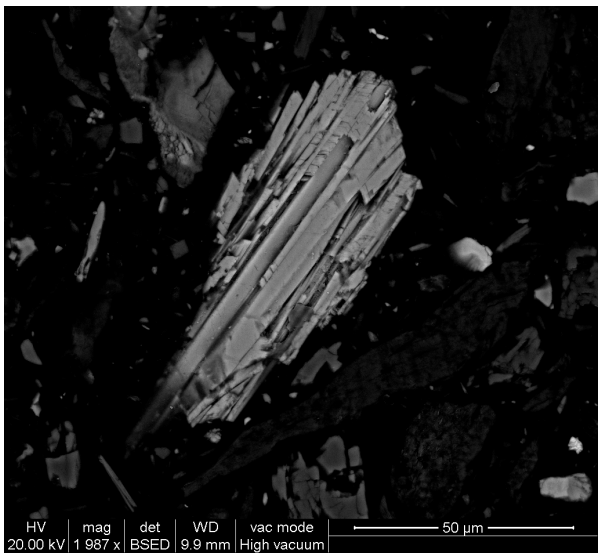
(a)



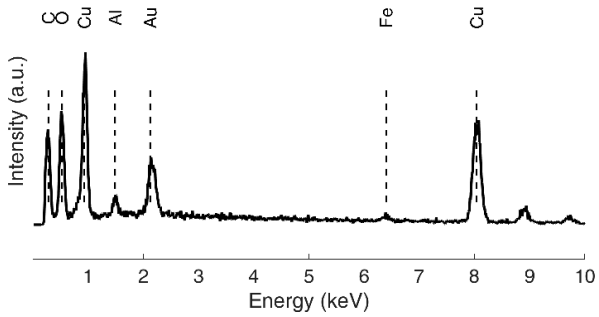
C (%)	Ca (%)	O (%)	W (%)
52.4	6.0	3.7	37.9

(b)

Figure 82 - (a) SEM-BSE image of scheelite grain from size class < 0.125 mm material obtained after comminution and sieving of mine waste rock samples from Traversella mine; (b) EDS Spectrum and quantitative chemical analysis (source: Baldassarre et al., 2025)



(**a**)



Al (%)	C (%)	Cu (%)	O (%)
1.5	38.2	41.7	18.6

(**b**)

Figure 83 - (a) SEM-BSE image of a malachite grain from size class<0.125 mm obtained after comminution and sieving of mine waste rock samples from Traversella mine; (b) ESD spectrum and quantitative chemical analysis (source: Baldassarre et al., 2025)

Analytical data confirmed the presence of CRMs-bearing minerals such as scheelite, observed as sparse single grains having a diameter of about 30µm. These grains were characterised by a high brightness in the BSE images and relevant W content, as indicated in the EDS spectrum (Figure 82b). Malachite was also detected, being the most abundant Cu-bearing mineral in this sample (Figure 83b)

5.4.3.2 Chemical characterisation – Size class < 0.125 mm

HH-XRF analyses were performed to acquire chemical assays and define the grade of the material before separation tests on size class < 0.125mm. Resulting XRF assays are reported in Table 35.

Table 35 - HH-XRF assays for size class <0.125 mm obtained after comminution and sieving of mine waste rock samples from Traversella mine.

Element							
Ag (ppm)	**Al (%)**	**As (ppm)**	**Ba (ppm)**	**Ca (%)**	**Cd (ppm)**	**Ce (ppm)**	**Co (ppm)**
< 0.9	1.4±0.1	141±4	< 12	7.6±0.01	< 1.1	< 12	< 105
Cr (ppm)	**Cu (%)**	**Eu (ppm)**	**Fe (%)**	**Gd (ppm)**	**Hg (ppm)**	**K (ppm)**	**La (ppm)**
< 16	0.90±0.01	< 194	14.0±0.02	< 342	< 0.1	893±16	14±6
Mg (%)	**Mn (ppm)**	**Nb (ppm)**	**Nd (ppm)**	**Ni (ppm)**	**P (%)**	**Pb (ppm)**	**S (%)**
8.9±0.5	2392±34	4.2±0.8	< 13	< 155	< 0.25	111±3.7	0.69±0.01
Sb (ppm)	**Se (ppm)**	**Si (%)**	**Sn (ppm)**	**Sr (ppm)**	**Th (ppm)**	**Ti (ppm)**	**Tl (ppm)**
7.4±1.7	< 1.5	15.9±0.1	21±1	45±1.2	< 4.0	462±86	< 5.0
U (ppm)	**V (ppm)**	**W (ppm)**	**Y (ppm)**	**Zn (ppm)**	**Zr (ppm)**		
33±1.7	< 8	188±11	8.6±0.6	294±7.4	33±2		

Fe, Cu, and W were identified as the primary target elements to consider before separation, as suggested by mineralogical phases identified in this size fraction.

Fe is characterised by a concentration of 14.0%, while Cu reported a concentration of 0.9 %, and W reported a 188ppm concentration. These three elements were considered for the calculation of R and ER after lab-scale separation trials.

5.4.4 Test A – Dry magnetic separation using LIMS

Dry magnetic separation lab-scale tests using a LIMS were performed using 1kg of 0.250-0.125mm size class material as feed, according to the flowsheet reported in Figure 84.

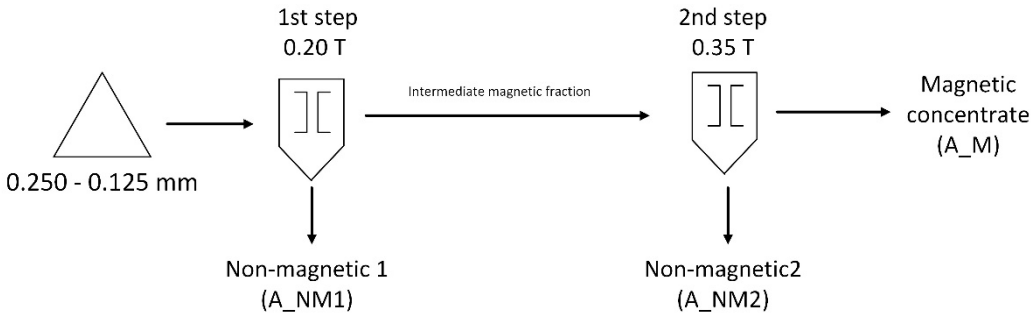


Figure 84 – Separation Test A flowsheet: dry magnetic separation using LIMS on size class 0.250-0.125 mm material obtained after comminution and sieving of mine waste rock samples from Traversella mine.

The material was processed in two steps at different magnetic field intensities, in order to recover the ferromagnetic mineral fractions contained in the feeding material, such as magnetite (Nzeh & Popoola, 2024), and to evaluate the content of valuable elements in the non-magnetic output. Three output materials were obtained:

- A_NM1: non-magnetic material after the application of a 0.20 T magnetic field;
- A_NM2: non-magnetic material after processing of the intermediate magnetic fraction at 0.20 T, applying a 0.35 T magnetic field;
- A_M: final magnetic concentrate.

Table 36 summarises yield, mineralogical and chemical data collected after Test A separation trials.

Table 36 - Yield, HH-XRF assays, and mineral phases identified by XRPD after separation Test A performed on waste rock samples from Traversella mine.

Output	*Yield* (%)	Fe (%)	W (ppm)	Cu (%)	Mineral phases detected*
A_NM1	67.5	7.6	218	0.8	Adr, Amp, Cal, Clc, Dol, Lz, Qz, Tlc;
A_NM2	5.7	12.3	280	0.9	Adr, Amp, Clc, Dol, Mag, Qz, Tlc;
A_M	26.8	66.2	47	0.6	Clc, Mag, Tlc.

Adr: andradite; Amp: amphibole; Cal: calcite; Clc: clinochlore; Di: diopside; Dol: dolomite; Lz: lizardite; Mag: magnetite; Qz: quartz; Tlc: talc. (abbreviations according to Warr (2021)).

Test A produced a magnetic concentrate (A_M) having a yield of 26.8%, characterised by a high grade of Fe (66.2%), and a low concentration of W (47 ppm). Mineralogical analyses identified magnetite as the main mineral phase in this fraction, associated with residual gangue minerals such as clinochlore and magnetite. The non-magnetic products (A_NM1, A_NM2), accounted in total for 73.2% of the mass yield of the process. A_NM1 was the most abundant, resulting

in 67.5%. Both non-magnetic outputs contained significantly lower grades of Fe, 7.6% for A_NM1 and 12.3% for A_NM2. In contrast, A_NM1 and A_NM2 showed a higher content of W, being respectively 218 pp and 280 pm. The mineralogy of the non-magnetic outputs was characterised by the presence of andradite, amphibole, calcite, and dolomite. Cu grade remained relatively constant across the Test A outputs, ranging between 0.6% and 0.9%.

Following the characterisation of the concentrates, ER was calculated as reported in Table 37.

Table 37 - ER values for separation concentrates calculated after separation Test A performed on waste rock samples from Traversella mine.

Output	ER_{Fe}	ER_{W}	ER_{Cu}
A_NM1	0.3	1.2	1.1
A_NM2	0.5	1.6	1.3
A_M	2.8	0.3	0.8

Test A produced a magnetic concentrate (A_M) having an enrichment in Fe grade of 2.8. Lower ER values were calculated for W and Cu, being 0.3 and 0.8, respectively. The non-magnetic outputs (A_NM1 and A_NM2) showed similar enrichment values, with ER ranging between 1.2 and 1.6 for W, and between 1.1 and 1.3 for Cu. Fe was scarcely concentrated in products A_NM1 and A_NM2, showing an ER of 0.3 and 0.5, respectively.

Table 38 reports the R values calculated according to measured mass balance and chemical assays (Table 36).

Table 38 - Recovery rates for selected target elements calculated after separation Test A performed on waste rock samples from Traversella mine.

Output	R_{Fe} (%)	R_{W} (%)	R_{Cu} (%)
A_NM1	21.6	83.7	72.3
A_NM2	3.0	9.1	7.2
A_M	75.4	7.2	20.5

Test A achieved a recovery rate of 75.4% for Fe in the magnetic product A_M, showing a partial recovery of Cu (20.5%) and low recovery of W (7.2%). The majority of W and Cu were recovered in the A_NM1 concentrate, showing recovery rates of 83.7% and 72.3%, respectively. The A_NM2 concentrate showed the poorest recovery rates for any of the considered target elements. In total, non-magnetic fractions, A_NM1 and A_NM2, recovered 92.8% of the available W.

5.4.5 Test B – Gravity separation using ST

Gravity separation lab-scale tests were realised using 1kg of 0.250-0.125mm size class material. This test was conducted in wet conditions using an ST, according to the scheme in Figure 85.

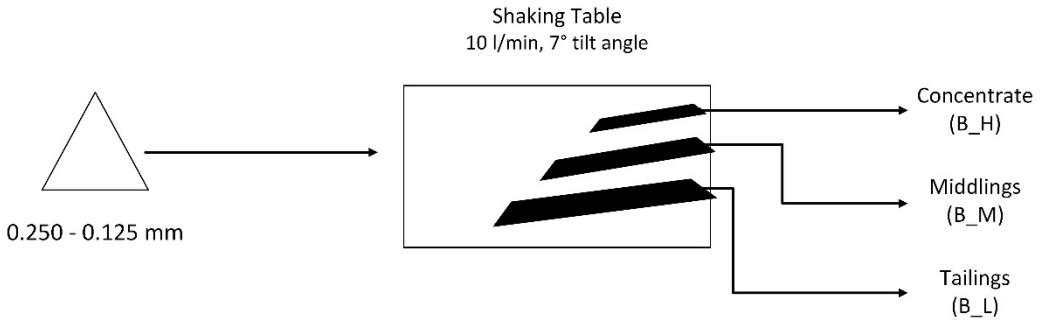


Figure 85 – Separation Test B flowsheet, gravity separation using ST on size class 0.125-0.250 mm material obtained after comminution and sieving of mine waste rock samples from Traversella mine.

The material was processed in order to recover the heavier fraction of the feeding material, such as magnetite and scheelite (Nzeh, Popoola, Okanigbe, Adeosun, & Adeleke, 2023), focusing on the concentrate fraction obtained by ST processing. Three output materials were obtained:

- B_H: heavy concentrate;
- B_M: middling product;
- B_L: light-tailings product.

Yield, chemical and mineralogical data collected after Test B trials are reported in Table 39.

Table 39 - Yield, HH-XRF assays, and mineral phases identified by XRPD after separation Test B performed on waste rock samples from Traversella mine.

Output	*Yield (%)*	Fe (%)	W (ppm)	Cu (%)	Mineral phases detected*
B_H	12.1	67.6	1289	0.3	Adr, Clc, Mag, Qz, Tlc
B_M	55.3	22.2	256	0.8	Adr, Amp, Cal, Clc, Di, Dol, Mag, Qz, Tlc
B_L	32.6	12.3	119	1.1	Adr, Amp, Cal, Clc, Di, Dol, Qz, Tlc

Adr: andradite; Amp: amphibole; Cal: calcite; Clc: clinochlore; Di: diopside; Dol: dolomite; Lz: lizardite; Mag: magnetite; Qz: quartz; Tlc: talc. (abbreviations according to Warr, (2021)).

Gravity separation processing Test B performed by ST produced a heavy concentrate (B_H) having a 12.1% yield, characterised by high 67.7 % Fe and 1289ppm W. The mineral phases contained in this concentrate were magnetite and andradite, with the presence of associated gangue minerals such as clinochlore, talc, and quartz, while scheelite was not identified in this concentrate. The intermediate material (B_M) represented the 55.3% of the output stream, showing

22.2% Fe grade and 256 ppm W grade; its mineralogical composition included silicates, carbonates, and magnetite. Light output material (B_L) accounted for 32.6% of the yield, assaying a lower Fe grade (12.3%) and a W concentration of 119 ppm. By contrast, it showed the highest Cu grade (1.1%) among the ST outputs. Mineral phases identified in B_L included amphibole, talc, carbonates, and andradite.

ER values were calculated according to chemical assay data (Table 39) and are shown in Table 40.

Table 40 - ER values for separation concentrates calculated after separation Test B performed on waste rock samples from Traversella mine.

Output	ER_{Fe}	ER_{W}	ER_{Cu}
B_H	2.8	3.8	0.4
B_M	0.9	0.8	1.0
B_L	0.5	0.4	1.3

Gravimetry separation performed in Test B produced a remarkable enrichment of W (3.8) and Fe (2.8) in the concentrate B_H. B_M middling product showed no significant enrichment in any of the target elements considered. The light product (ST-L) reported a weak concentration of Cu (1.3), while it did not report any enrichment in Fe and W, with an ER of 0.5 and 0.4, respectively.

R values calculated according to measured yield and chemical assays (Table 39), are listed in Table 41.

Table 41 - Recovery rates for selected target elements calculated after separation Test B performed on waste rock samples from Traversella mine

Output	R_{Fe} (%)	R_{W} (%)	R_{Cu} (%)
B_H	33.4	46.3	4.3
B_M	50.2	42.1	52.8
B_L	16.4	11.6	42.9

Test B recovered 46.3% of W and 33.4% of Fe in the B_H product. The middling concentrate (B_M) showed the highest recovery rates for Fe and Cu at 50.2% and 52.8%, respectively, while W recovery in this fraction was calculated at 42.1%. The light output fraction (B_L) recovered 42.9% of available Cu; in this fraction, Fe and W were characterised by the lowest recovery rates, being 16.4% and 11.6%, respectively.

5.4.6 Comparison of separation performances for Test A and Test B

In Test A, the 0.250–0.125 mm size class was tested using a dry magnetic separator (LIMS) to concentrate magnetic minerals and evaluate the potential enrichment of CRM-bearing minerals in the non-magnetic stream. While in Test

B, gravimetric separation using an ST was performed to explore a processing strategy for the recovery of magnetite and scheelite according to their high specific gravity.

Figure 86 shows a comparison between the grade of selected target elements, their recovery rates and the associated ER (only when >1) for any of the Test A and Test B output products.

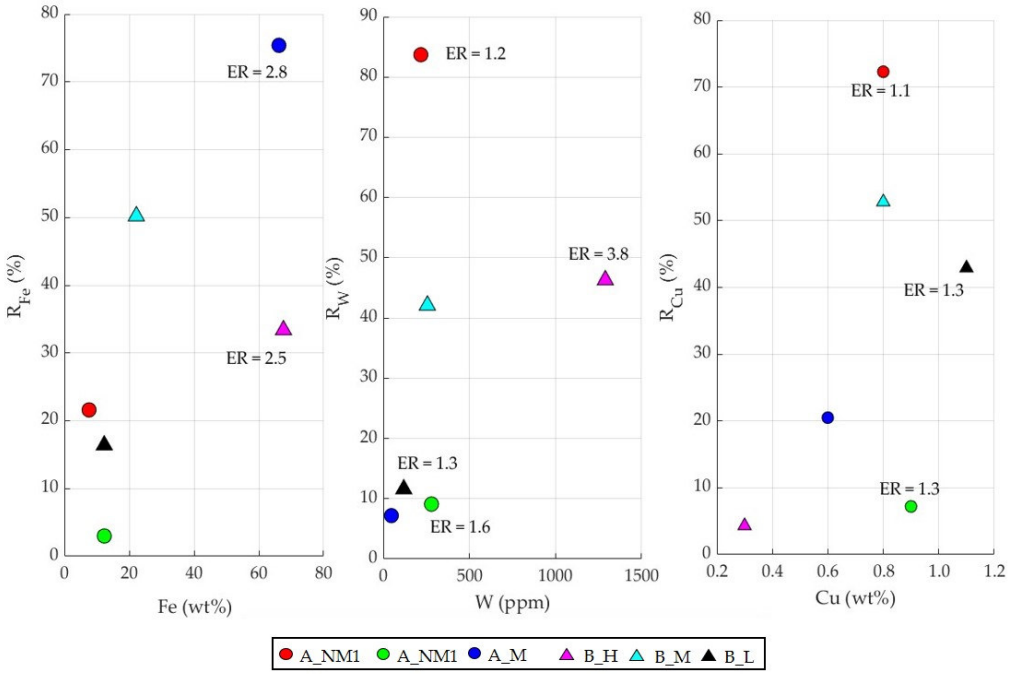


Figure 86 - Metal grade of target elements (Fe, W, Cu) plotted as a function of recovery rate of each output product after separation trials, Test A and Test B, performed on waste rock samples from Traversella mine. ER is reported only for values >1, assuming a reached concentration after separation. (source: Baldassarre et al., 2025)

Dry magnetic separation Test A produced a magnetic concentrate (A_M) having a Fe grade of 66.2% and recovering about 75% of the available Fe from the feed material, with an associated enrichment ratio of 2.8. The non-magnetic product obtained (A_NM1) led to an 85% recovery of W, a weak enrichment of 1.2, and a product grade of 208ppm. Additionally, the same A_NM1 product, Fe grade was reduced from 18.2% of the feed to 7.6%. Regarding Cu, more than 75% was recovered in the A_NM1 product, having no remarkable enrichment (ER=1.1).

Gravity separation Test B produced a heavy concentrate (B_H) assaying 67.6% of Fe and 1289 ppm of W, achieving a remarkable enrichment of both elements (ER_{Fe} = 2.5, ER_W = 3.8), but resulting in limited recovery rates (R_{Fe} = 33.4%, R_W = 46.3%). Middling product B_M showed no enrichment of any of the target elements considered, but reached a 50.2% recovery of Fe, 42.1% of W, and 58.8% of Cu. Moreover, a slight enrichment in W (1.3) and Cu (1.3) was reached in the light fraction B_L.

Overall, both Test A and Test B succeeded in recovering target minerals, but were poorly capable of efficiently separating magnetite and scheelite in distinct output streams and concentrating them at the same time. This highlighted the need for a blended test combining magnetic and gravity separation methods, having the final goal of obtaining a concentration and separation of valuable minerals, trying to direct magnetite and scheelite into clearly distinct output streams.

5.4.7 Test C – Dry magnetic separation (LIMS) and gravity separation (ST)

According to the data collected after Test A and Test B, a combined separation procedure was designed to consider the recovery of separate and concentrated products of Fe and W. Figure 87 shows the flowsheet of Test C processing trials, using a combined separation procedure using LIMS and ST.

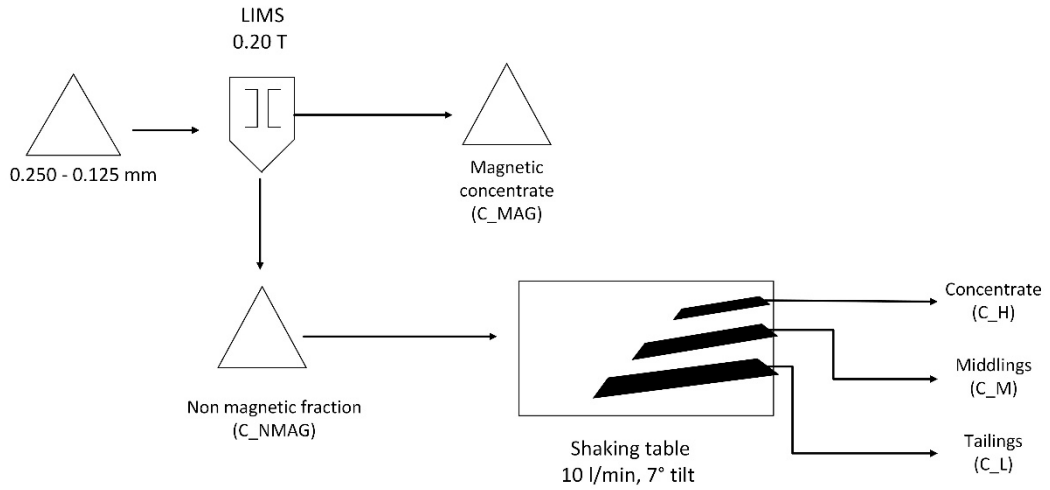


Figure 87 - Test C flowsheet, combined dry magnetic and gravity separation using LIMS and ST on size class 0.125-0.250 mm material obtained after comminution and sieving of mine waste rock samples from Traversella mine.

A mass of 1kg of the feed material was processed to firstly recover the magnetic fraction contained in the 0.250-0.125mm size class material, such as magnetite minerals, and consequently recover the non-magnetic fraction containing unconcentrated heavier CRM-bearing minerals, such as scheelite. The output fractions obtained by blended LIMS and ST processing are listed as follows:

- C_MG: magnetic concentrate after dry magnetic separation applying a 0.2 T magnetic field;
- C_NM: non-magnetic fraction after LIMS at 0.2 T magnetic field, used as feeding material for ST;
- C_H: heavy concentrate after ST on C_NMAG fraction;
- C_M: middling product after ST on C_NMAG fraction;
- C_L: light-tailings product after ST on C_NMAG fraction.

Yield, chemical and mineralogical data collected after Test C are reported in Table 42.

Table 42 – Total yield (Y_{tot}), relative yield to LIMS (Y_{LIMS}) and ST (Y_{ST}), and HH-XRF assays after Test C performed on waste rock samples from Traversella mine.

	Output	Y_{tot} (%)	Y_{LIMS} (%)	Fe (%)	W (ppm)	Cu (%)	Mineral phases detected*
LIMS	C_MG	38.1	38.1	78.4	40	0.56	Clc, Mag, Tlc.
	C_NM	61.9	61.9	10.4	333	0.84	Adr, Amp, Cal, Clc, Dol, Lz, Qz, Tlc;
	Output	**Y_{tot} (%)**	**Y_{ST} (%)**	**Fe (%)**	**W (ppm)**	**Cu (%)**	**Mineral phases detected***
ST	C_H	7.8	12.6	29.7	1604	0.87	Adr, Amp, Clc, Py, Sch, Tlc
	C_M	51.6	83.3	7.8	156	0.83	Adr, Amp, Ank, Cal, Clc, Crd, Di, Qz, Tlc
	C_L	2.5	4.1	3.7	30	0.95	Bt, Clc, Dck, Hbl, Qz, Tlc

Adr: andradite; Amp: amphibole; Ank: ankerite; Bt: biotite; Cal: calcite; Clc: clinochlore; Crd: cordierite; Di: diopside; Dck: dickite; Dol: dolomite; Hbl: hornblende; Lz: lizardite; Mag: magnetite; Py: pyrite; Qz: quartz; Sch: scheelite; Tlc: talc. Abbreviations according to Warr (2021)

First step LIMS processing produced a magnetic concentrate (C_MG) yielding 38.1% of the total introduced material, characterised by a Fe grade of 78.4%, a W grade of 40 ppm and a Cu grade of 0.56 %. The mineralogy of this output is mainly characterised by magnetite, with the presence of residual gangue minerals such as clinochlore and talc. In contrast, the non-magnetic product (C_NM) had a 61.9 % yield, showing a Fe grade of 10.4%, a 333 ppm W grade and a Cu grade of 0.84 %. The minerals contained in this fraction are andradite, quartz, talc, with minor amphibole, calcite, dolomite, and lizardite.

Second step ST separation on C_NM material produced a heavy output material C_H containing 29.7 % Fe, 0.87 % Cu and 1604 ppm of W. This fraction yielded 7.8 % of the total Test C process, and 12.6 % yield if considering only the ST test, containing CRM-bearing mineral scheelite along with andradite, pyrite, and residual gangue mineral such as amphibole, clinochlore, and talc.

The middling product C_M was the most abundant among the Test C output, having a total yield of 51.6 % (83.3 % if relative only to ST), but showed low

concentration of Fe, W, and Cu, being 7.8 %, 156 ppm and 0.83 % respectively, containing mainly gangue minerals and residual andradite.

Finally, the light tailings fraction had a residual yield of 2.5% of the total mass balance (4.1 % relative to ST), containing 3.7 % of Fe, 30 ppm of W, and 0.95 % of Cu, being characterised by the presence of only gangue minerals.

According to the measured metal assays, ER was calculated for each output material and reported in Table 43.

Table 43 – ER values calculated after combined LIMS and ST separation Test C performed on waste rock samples from Traversella mine.

Separation	***Output***	ER_{Fe}	ER_{W}	ER_{Cu}
LIMS	C_MG	2.2	0.2	0.8
	C_NM	0.3	1.5	1.2
	Output	ER_{Fe}	ER_{W}	ER_{Cu}
ST	C_H	0.8	7.2	1.2
	C_M	0.2	0.7	1.1
	C_L	0.1	0.1	1.3

Magnetic product C_MAG successfully enriched Fe, with an ER = 2.2. Cu was also enriched in this fraction, while W showed a lower ER of only 0.2. The LIMS non-magnetic fraction (ST feeding material), C_NM, is characterised by a slight enrichment in W (1.5) and Cu (1.2), but not in Fe (0.4).

The ST heavy product, C_H, remarkably enriched W with ER = 7.2, with a weak enrichment of Cu (1.2) and no enrichment for Fe, showing an ER of 0.8. The middling product C_M and the light fraction C_L showed no significant enrichment for any of the considered elements.

Recovery rates were calculated for the obtained materials and listed in Table 44.

Table 44 – Recovery rates for selected target elements after separation Test C performed on waste rock samples from Traversella mine.

Separation	***Output***	R_{Fe} (%)	R_{W} (%)	R_{Cu} (%)
LIMS	C_MG	82.2	6.9	29.1
	C_NM	17.8	93.0	71.3
	Output	R_{Fe} (%)	R_{W} (%)	R_{Cu} (%)
ST	C_H	6.4	56.4	9.3
	C_M	11.1	36.3	58.7
	C_L	0.3	0.3	3.3

Test C's LIMS stage resulted in high recoveries of Fe (82.2%) in the C_MG fraction, and lower recoveries of Cu and W, being 29.1% and 15.0%, respectively. The non-magnetic product, C_NM, delivered a nearly total recovery of 93.0% for W, a relevant recovery for Cu (71.3%), while only 17.8% of Fe was recovered in this fraction, serving also as ST feeding material.

The gravity separation heavy product, C_H, recovered 56.4% of W, while Fe and Cu recovery were minimal, at 6.4 % and 9.3 % respectively. The middling product, C_M, accounted for low recoveries for Fe (11.1%), residual recovery of W (36.3%), and a consistent recovery of Cu (58.7%). At last, C_L light-tailings material showed negligible recoveries: 0.3% for Fe, 0.3% for W, and 3.3% for Cu.

5.4.8 Test D – Wet magnetic separation using WHIMS

Wet magnetic separation tests were performed on 1kg of the finer crushing and comminution product (< 0.125 mm) using WHIMS, according to the flowsheet reported in Figure 88.

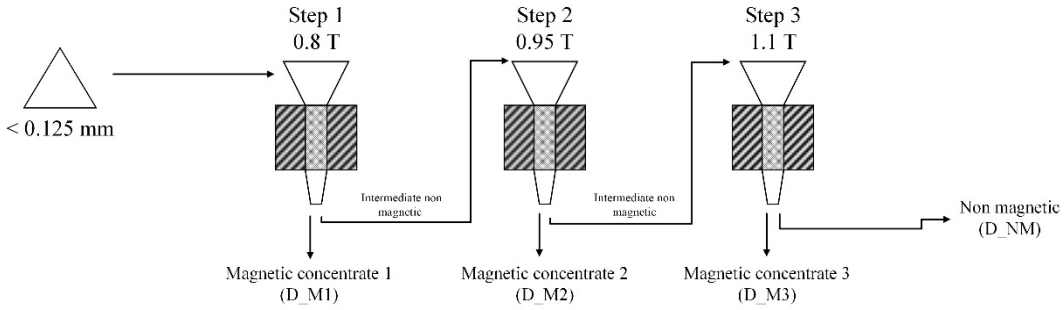


Figure 88 - Test D flowsheet, wet magnetic separation using WHIMS on size class <0.125 mm material obtained after comminution and sieving of mine waste rock samples from Traversella mine.

Material was processed to recover magnetic materials, such as magnetite, contained in this material and check whether the non-magnetic fraction could host valuable elements. Separation output materials resulting from Test D were labelled as follows:

- D_M1: magnetic concentrate after separation at 0.8T;
- D_M2: magnetic concentrate after separation at 0.95T obtained after processing non-magnetic material obtained from Step 1;
- D_M3: magnetic concentrate after separation at 1.10T obtained after processing non-magnetic material obtained from Step 2;
- D_NM: non-magnetic material after Step 3.

Table 45 shows yield, mineralogical and chemical data collected after Test D separation trials.

Table 45 - Yield, HH-XRF assays, and mineral phases identified by XRPD after separation Test D performed on waste rock samples from Traversella mine.

Output	Yield (%)	Fe (%)	W (ppm)	Cu (%)	Mineral phases detected*
D_M1	37.9	32.2	217	0.9	Adr, Amp, Cal, Clc, Dol, Lz, Mag, Qz, Tlc
D_M2	9.1	11.5	276	1.0	Adr, Cal, Clc, Dol, Lz, Mag, Qz, Tlc
D_M3	7.5	8.2	134	1.1	Adr, Cal, Clc, Dol, Lz, Mag, Qz, Tlc
D_NM	45.5	4.4	72	1.0	Cal, Clc, Dol, Lz, Mag, Qz, Tlc.

Output	Yield (%)	Fe (%)	W (ppm)	Cu (%)	Mineral phases detected*

:Adr: andradite; Amp: amphibole; Cal: calcite; Clc: clinochlore; Di: diopside; Dol: dolomite; Lz: lizardite; Mag: magnetite; Qz: quartz; Tlc: talc. Abbreviations according to Warr, (2021).

D_M1, D_M2, and D_M3 magnetic fractions showed a decreasing Fe assay as the applied magnetic field increased, showing concentrations of 32.2%, 11.5%, and 8.2% respectively. These magnetic products accounted for 54.5% of the total yield, with D_M1 being the most abundant at 37.9% yield. W concentrations in the magnetic products ranged between 134 ppm and 276 ppm. The mineralogy of magnetic fractions included magnetite, andradite, and carbonates like calcite and dolomite. The final non-magnetic product D_NM represented 45.5% of the yield, with low Fe and W concentrations of 4.4% and 72ppm, respectively. The mineralogical composition of the non-magnetic fraction was characterised by quartz, talc, calcite, and dolomite. Cu concentration remained constant for both magnetic and non-magnetic products, ranging between 0.9% and 1.1%.

ER values were calculated according to chemical assay data (Table 45) and are shown in Table 46.

Table 46 - ER values calculated after separation Test D performed on waste rock samples from Traversella mine.

Output	ER_{Fe}	ER_{W}	ER_{Cu}
D_M1	2.0	1.0	1.4
D_M2	0.7	1.0	1.8
D_M3	0.5	1.1	0.9
D_NM	0.3	1.0	0.5

In Test D concentrates, D_M1 had the highest enrichment value for Fe (2.0) and a moderate enrichment of Cu (1.4). Cu was concentrated by 1.4 and 1.8 times, respectively, in D_M1 and D_M2 products. D_NM Non-magnetic concentrate was characterised by depletion in Fe (0.3) and Cu (0.5), but W remained unconcentrated (1.0). In general, W was not concentrated in any of the output materials, maintaining this ER constant to a value of 1.0-1.1.

R values calculated according to measured yield and chemical assays (Table 45) are listed in Table 47.

Table 47 - Recovery rates for selected target elements calculated after separation Test D performed on waste rock samples from Traversella mine.

Output	R_{Fe} (%)	R_{W} (%)	R_{Cu} (%)
D_M1	77.0	54.8	36.8
D_M2	6.6	16.7	9.4
D_M3	3.9	6.7	8.3
D_NM	12.5	21.8	45.4

First magnetic concentrate D_M1 recovered most of the available Fe, with a recovery rate of 77.0%. In addition, a 54.8% recovery for W and a 36.8% recovery for Cu were calculated. The magnetic concentrates, D_M2 and D_M3, obtained from higher magnetic fields showed low recovery rates for all the target elements considered. The final non-magnetic product D_NM recovered 45.4% of the total available Cu, while Fe and W were recovered with low rates in this fraction.

5.5 Final Remarks

Waste rock piles were identified in a vegetated area surrounding the abandoned Traversella mine's adits. The most accessible site, Piano Svedesi, was sampled according to an imaginary 9x9 grid, yielding about 30kg of mine waste material. This material was subsequently subsampled for mineralogical (OM and XRPD) and chemical characterisation (HH-XRF and ICP-MS). The principal mineral phases identified included amphibole, andradite, calcite, clinochlore, magnetite, quartz and talc.

Chemical analyses revealed anomalies of CRM relative to average crustal abundances, in particular As, Co, Cu, Sb, and W. Moreover, four elements exceeded environmental thresholds for soil as defined by Italian Laws. Specifically, As and Cu were above limits for industrial soils, while Co and Sb failed the thresholds for agricultural soils.

To evaluate the recovery of CRM from the sampled waste material, laboratory-scale physical treatments were designed and tested. Following crushing and milling, two size fractions (0.250-0.125 mm and <0.125 mm) were selected for further characterisation (XRD, SEM-EDS, MLA, and HH_XRF) and processing: In both size classes, magnetite, scheelite and Cu-bearing minerals were identified as valuable target phases with Fe, W and Cu as target elements. Liberation was achieved in the 0.250-0.125mm fraction, with 87% for magnetite and 99.2% for scheelite.

Four separation trials were conducted, employing dry magnetic separation (LIMS), wet magnetic separation (WHIMS), and gravity separation (ST). Mineralogy and chemical grades of target elements were determined (XRPD and HH-XRF) for both concentrate and tailings materials. Separation performance was assessed by calculating Y, ER and R for any output material.

Among the investigated trials, Test C was the most effective, combining LIMS and ST on the non-magnetic fraction of the 0.250-0.125mm size class. This approach produced a final magnetic concentrate recovering 82.2% of Fe, with an enrichment ratio of 2.2 and a final Fe grade of 78.4%. Furthermore, the heavy concentrate obtained by gravity separation recovered 56.4% of W, achieving an enrichment ratio of 7.2 and an overall W grade of 1604 ppm.

Overall, lab-scale preliminary tests showed a technically feasible concentration of valuable minerals that should be further contextualised for market and cost considerations, as well as scaling-up possibilities and evaluation of process parameters.

Chapter 6

6. Case Study 2: Libiola Mine, Liguria, Italy

Part of the work presented in this chapter has been previously published in the following works:

Baldassarre, G., Fiorucci, A., & Marini, P. (2024). Recovery of Critical Raw Materials from Abandoned Mine Wastes: Some Potential Case Studies in Northwest Italy. *Materials Proceedings, 15*(1), 77. (Baldassarre et al., 2024)

6.1 Site description

6.1.1 Geological setting and historical mining activities

The Libiola mine, located about 8km North-East of the town of Sestri Levante, province of Genoa, Liguria. It extends over an area of about 4 km^2 in the Gromolo Creek basin, with elevations ranging between 42 m and a maximum of 402 m a.s.l. (Marescotti & Carbone, 2003; Marescotti et al., 2008) (Figure 89). The Libiola's Fe-Cu ore deposit can be classified as a strata-bound volcanic massive sulphide deposit (VMS). It occurs in massive lenses associated with pillow basalts and also as a sparse mineralisation, associated with serpentinitic rocks (Buccheri et al., 2018). In detail, Buccheri et al. (Buccheri et al., 2018) reported that three different types of mineralisations can be identified in the Libiola mining district:

- Strata-bound and lenticular bodies hosted in basaltic rocks containing massive pyrite-chalcopyrite mineralisations;
- Stock-work veins (pyrite and chalcopyrite) hosted in pillow lavas
- Scattered pyrite mineralisation hosted in basaltic and serpentinitic rocks, associated with serpentine, chlorite and magnetite matrix.

Pyrite and chalcopyrite were reported as primary minerals; secondary minerals are represented by sphalerite, pyrrhotite, marcasite, hematite, mackinawite, magnetite, cubanite, and gold, while quartz and carbonates are defined as accessory gangue minerals (Buccheri et al., 2018; Dinelli, Lucchini, Fabbri, & Cortecci, 2001; Marescotti & Carbone, 2003; Marescotti et al., 2008; Marini, Saldi, Cipolli, Ottonello, & Zuccolini, 2003).

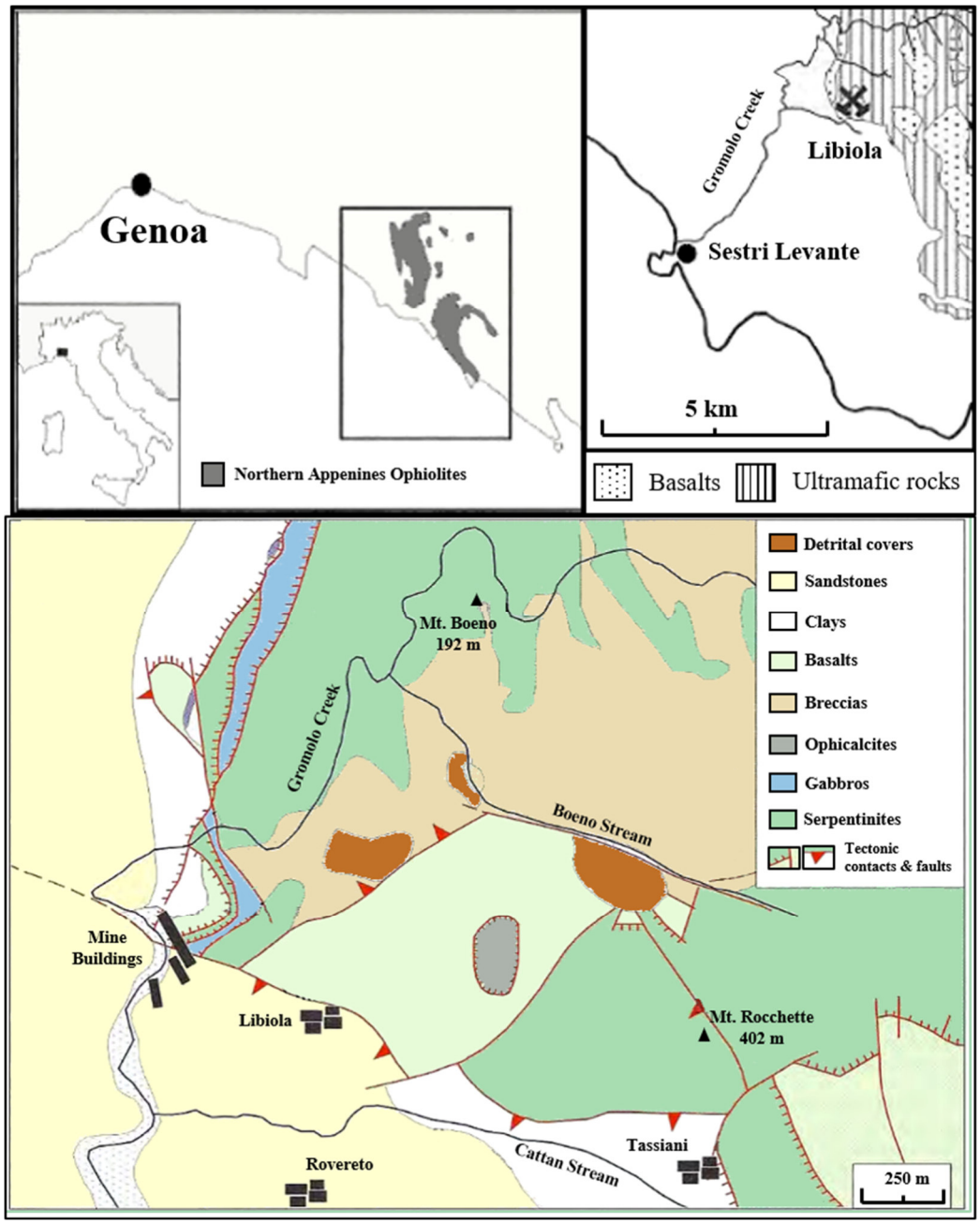


Figure 89 - Geological setting of the Libiola mine area, with details regarding local lithologies, surface water streams and villages (adapted and modified after Marescotti et al., 2003)

Archaeological mining tools recovered in the Libiola mine areas were dated to around 2500-3500 B.C., indicating that it was a well-known source of copper since the Bronze Age and one of the most ancient copper mines in Western Europe (Buccheri et al., 2018). The local pre-Roman population (the Ligurians) used to build their weapons for fighting Roman conquerors, showing that the mine had a relevant importance also during the Roman Period (Buccheri et al., 2018). Modern exploitation activities in the area started to develop between 1840 and 1860, when the Savoian government financed the first industrial-scale exploitation of the Libiola deposit. This included the construction of processing plants and the

development of mining infrastructures, reaching 25,000 metric tons of copper-bearing sulphides in 1899 (Buccheri et al., 2018; Dacquino, 2025). The mine reached its peak production at the beginning of the 20th Century, with historical records accounting for approximately 35,000 metric tons of iron and copper minerals in 1905, and decreasing to 12,000 tons in 1927 (Dacquino, 2025; Marini et al., 2003). During World War II, the mine remained active as it was classified as a "war industry" (Dacquino, 2025). In the post-bellic period, the mine lease was transferred to the Società Anonima Magnesifera Italiana (M.I.S.A.), which reached a production of about 35,200 metric tons of run-of-mine material, having 1.8% Cu grade and 13.6% of S, exploiting also lower quality disseminated mineralisations (Dacquino, 2025; Marescotti & Carbone, 2003). In 1955, mining activity faced a severe crisis, leading to the transfer of the mine lease to Montecatini Society. The mine was definitely closed and abandoned in 1962 (Buccheri et al., 2018; Dacquino, 2025).

During its operational lifespan, the mine was exploited through three open pits and a network of over 30 km of underground excavations. This network included 18 tunnels distributed within 250 m from the ground surface as well as 30 vertical shafts and numerous connecting shafts, as reported in Figure 90. (Dacquino, 2025; Marescotti et al., 2010, 2008; Marescotti, Carbone, Comodi, Frondini, & Lucchetti, 2012; Marescotti & Carbone, 2003)

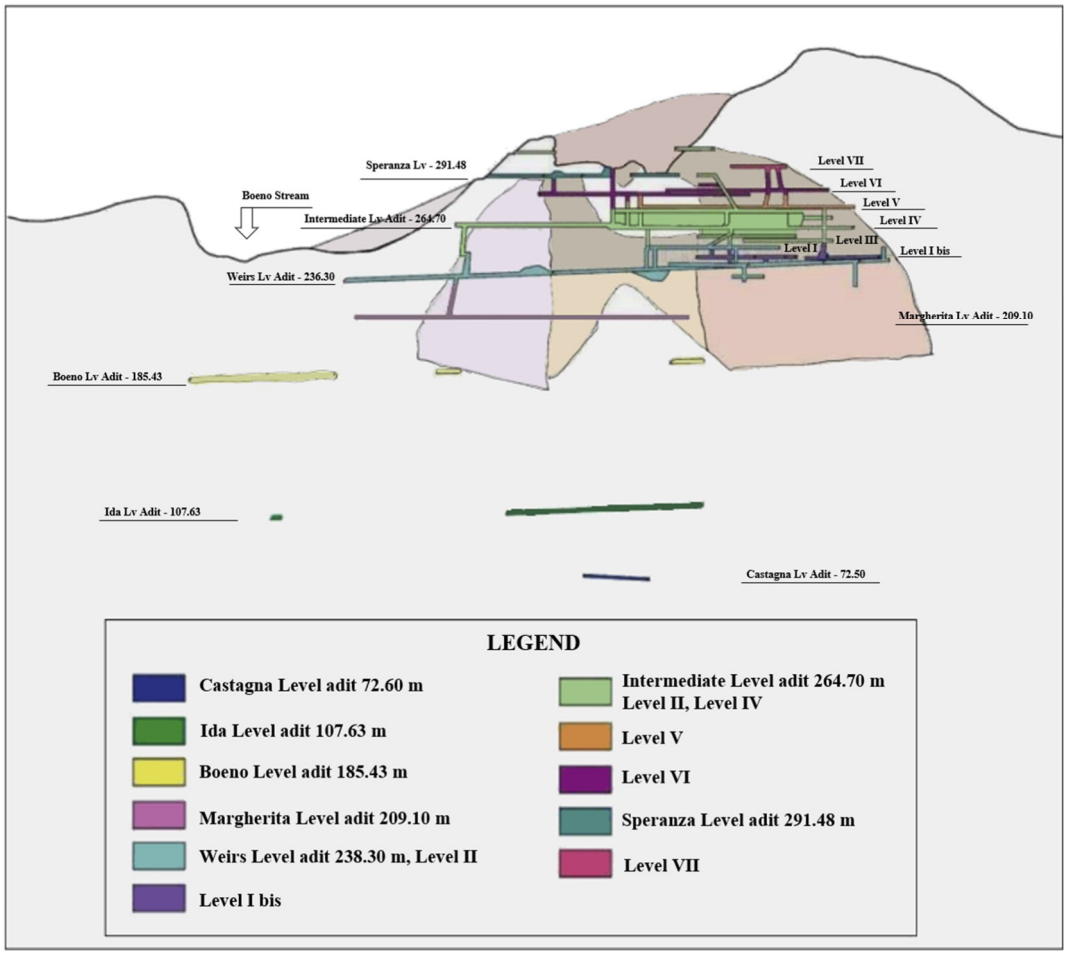


Figure 90 - Libiola Mine scheme, showing open pit area (dark pink) and underground works (adapted and modified after Marescotti et al, 2003)

Libiola is considered one of the most important copper mines in Italy, producing about 1 Mt of Fe-Cu ore with an average grade ranging between 7% and 14% of copper (Buccheri et al., 2018; Dacquino, 2025; Marescotti et al., 2010; Marescotti & Carbone, 2003; Marini et al., 2003)

6.1.2 Mine waste dumps

During mining operations, waste rocks were accumulated in five piles near tunnels, adits and open-pit exploitation areas, while tailings from processing operations were stocked in small dumps with no dedicated basins. The total extension surface is about 500,000 m^2 (Buccheri et al., 2018; Carbone et al., 2005; Cortecci, Boschetti, Dinelli, & Cabella, 2008; Marescotti et al., 2010, 2008; Marini et al., 2003).

The piles are characterised by a poorly sorted material (Figure 91), classified as a gravel having a p80 ranging between 9 and 70 mm (Marescotti et al., 2008). Dumps contain mineralised materials (pyrite and chalcopyrite) and gangue rocks (basalts and serpentinites), heterogeneously distributed in vertical and horizontal directions according to the former excavation techniques used during operations (Buccheri et al., 2018; Marini et al., 2003). The abandoned mine voids and the dumped materials present relevant environmental pollution problems due to Acid Mine Drainage (AMD) and Acid Rock Drainage (ARD) phenomena, which are heavily affecting surrounding soils and water streams (Carbone et al., 2005; Dinelli et al., 2001; Dinelli & Tateo, 2002; Marescotti et al., 2010, 2008).

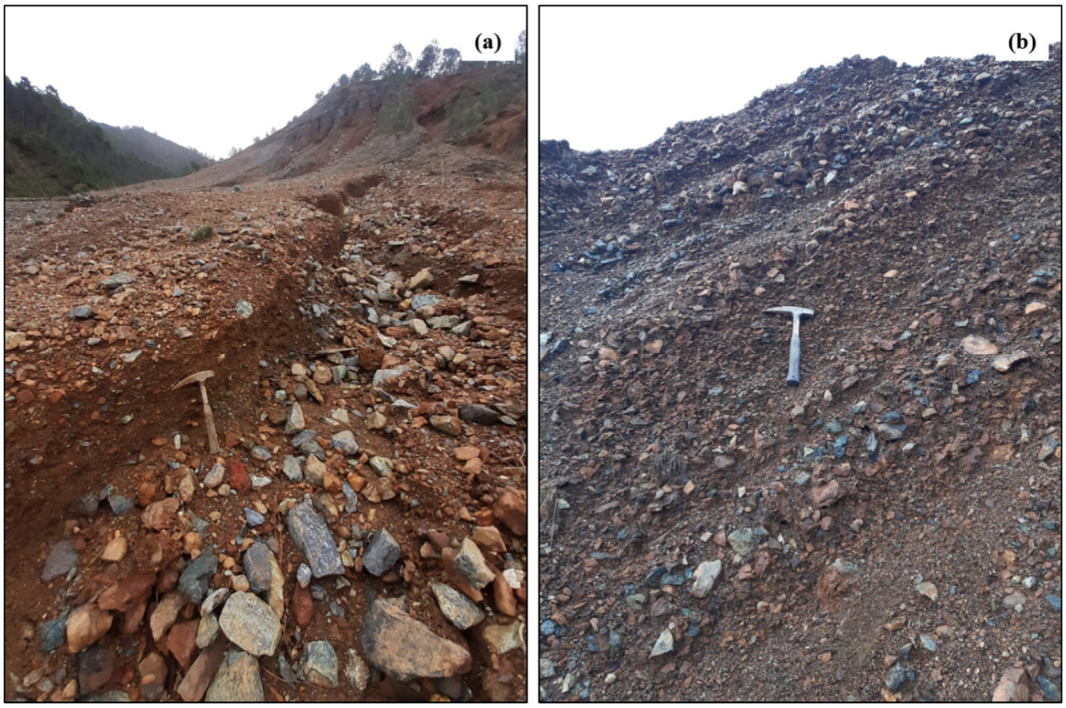


Figure 91 - (a) Poorly sorted and eroded material from North mine waste dump, Libiola mine; (b) Detail of mine waste accumulation strata in the South dump, Libiola mine (Photo credits: G. Baldassarre, 2024)

Some authors characterised the dumped materials, mainly located in the northern areas of the mine, using qualitative and quantitative methodologies for mineralogical and geochemical determinations (Buccheri et al., 2018; Marescotti et al., 2010, 2008; Marescotti & Carbone, 2003), performing surface sampling campaigns. These previous studies showed the presence of about 50% of gangue minerals (serpentine, plagioclase, magnetite, chlorite, augite, clay minerals, albite, quartz), 8% of primary sulphides (pyrite and chalcopyrite), about 40% of secondary minerals (Fe-oxyhydroxides and Fe-oxides, generated from the weathering of primary and sulphide minerals), and about 2% of other mineral species. Geochemical analyses showed the presence of 10 mg/kg of copper and relevant heavy metals concentration in the material collected from the dump bodies (Marescotti et al., 2008). Marescotti et al., (2003, 2010) also proposed a geostatistical distribution model for mapping the distribution of the main pollutants on the surface of mining waste heaps.

According to the ISPRA official mine waste national database, updated in 2022, mine waste accumulation areas are reported in four different localities in the Libiola Area. The type of waste reported is classified as "*Waste dumps*", potentially containing Co, Cr, Cu, Zn, and are rated as having a "*medium-high*" associated ecological and sanitary risk (Serra & Andrisani, 2022). No data were found in the literature regarding the volumetric distribution of the mine waste dumps in the case-study area.

The indicative positions of the mine waste dumps, according to the ISPRA official database, are reported in Table 48.

Figure 92 shows the considered mine waste areas in this study, the reconstructed perimeters after field inspections and the soil coverage of the considered areas.

Table 48 - Libiola mine waste dump positions and type description according to ISPRA national mine waste database (ISPRA, 2022)

Name (ISPRA)	***X (UTM 32N)***	***Y (UTM 32N)***	***Type***	***Considered in this study***	***Assigned name (this study)***
Libiola 1	535515	4905260	Waste dump	Yes	*Margherita dump*
Libiola 2	535463	4905385	Waste dump	Yes	*South dump*
Libiola 3	535715	4905785	Waste dump	Yes	*North dump*
Libiola 4	535304	4906300	Waste dump	No	-

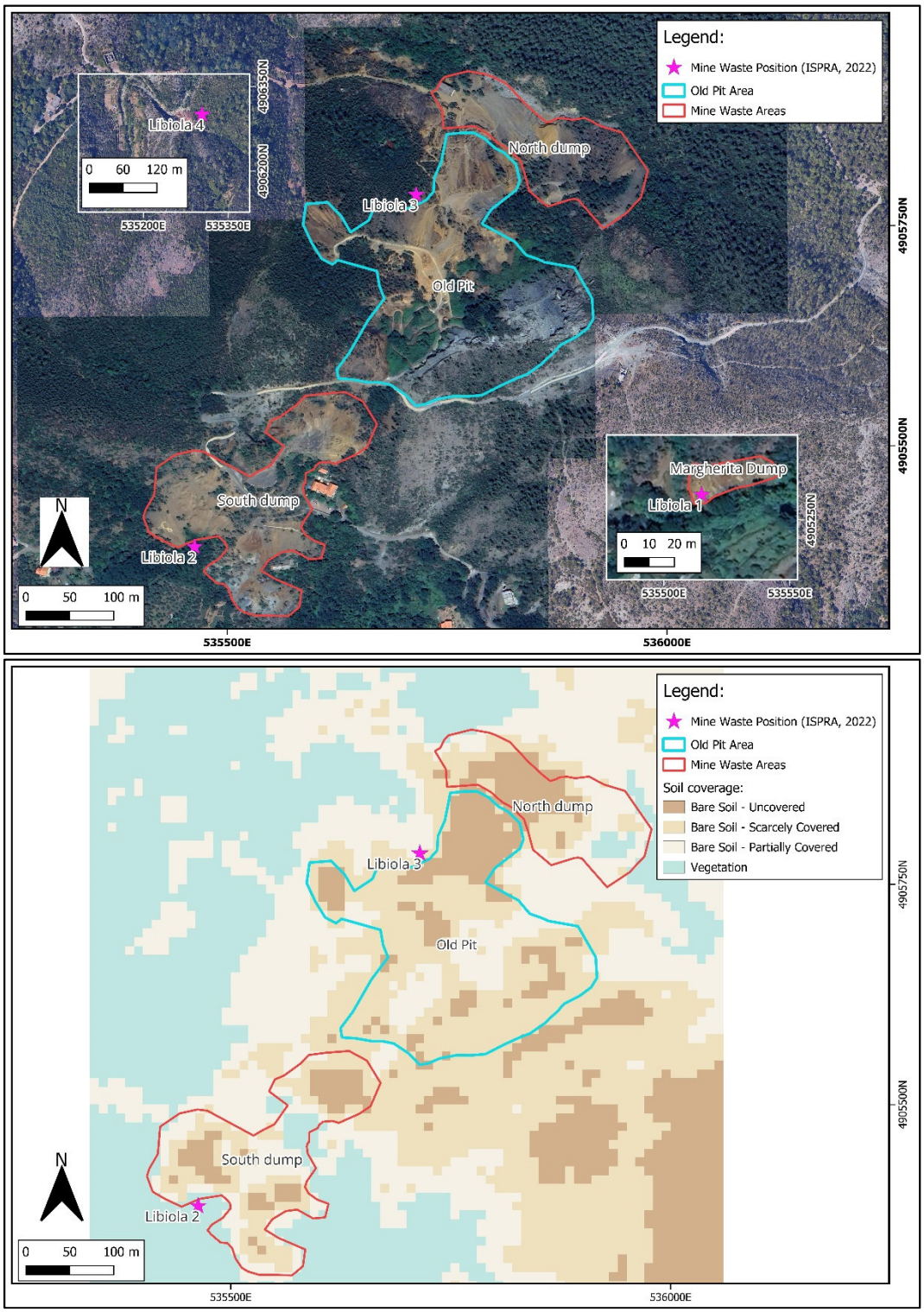


Figure 92 - (Top) Position of mine waste in the Libiola mine area according to ISPRA database (ISPRA, 2022) (magenta stars), old pit area (blue line), and perimeter of mine waste dumps considered in this study (red line); (Bottom) NDVI soil coverage layer and considered mine waste areas (source: Google Satellite Image. Coordinate system: WGS84/UTM Zone 32N)

The reported mine waste areas were located in the surroundings of the old mine adits and open pit zones. Field inspections confirmed that the study areas closely matched the mine waste sites indicated by the ISPRA database (Serra & Andrisani, 2022).

The soil coverage in the investigated area, primarily the North and South dumps due to their relevant surface extension, was characterised by either bare ground or sparse vegetation, highlighting easy accessibility of the selected locations.

Figure 93 illustrates the condition of the mine waste piles observed during the field inspections conducted as a part of this study.

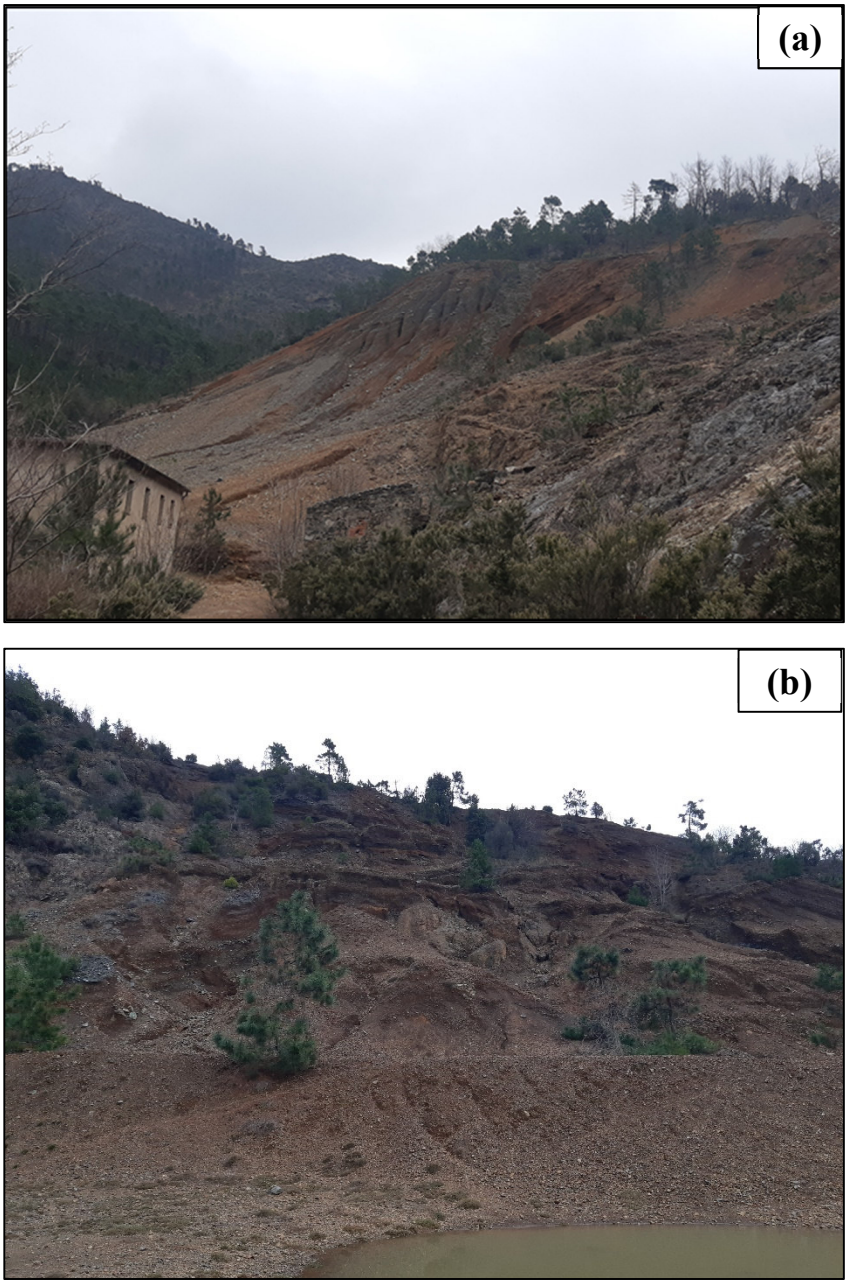


Figure 93 - (a) Panoramic view of North mine waste dump, Libiola mine; (b) Panoramic view of South mine waste dump, Libiola mine (Photo credits: G. Baldassarre, 2023(a), 2024 (b))

Based on the accessibility and field conditions of the selected areas, geophysical surveys and sampling activities were carried out, as described in the following paragraphs.

6.2 ERT geophysical survey results

Geophysical surveys were performed according to the procedure described in ***Par. 2.3.2***.

Three ERT geophysical survey lines were performed to investigate mine waste thickness across the Libiola mine waste areas selected. The collocation of these lines was determined by site accessibility, slope gradient, and the availability of field equipment.

Table 49 provides information about each ERT line deployed in the study area.

Table 49 - Libiola mine waste dumps ERT data acquisition parameters

Line	*Zone*	*Length (m)*	*Spacing (m)*	*Orientation*
ERT 1	South dump	50	2	NE-SW, aligned to slope
ERT 2	South dump	50	2	NW-SE, transversal to slope
ERT 3	North dump	50	2	E-W, oblique to slope (45°)

ERT 1 was positioned longitudinally along the maximum slope gradient of the South dump, potentially reflecting the bedrock slope profile and the downslope variations in thickness and stratification due to gravitational processes.

ERT 2 was oriented perpendicularly to ERT 1 and, as a result, transversely to the slope gradient. This orientation was selected for the reveal of possible lateral heterogeneities of the thickness and distribution of the material, such as the accumulation of the waste rock material according to preferential patterns.

In addition, ERT 3 was located in the North dump site and oriented approximately 45° to the slope. This configuration was chosen to compensate for the inability to deploy an additional ERT wire parallel to the slope due to the steep and unstable conditions of the waste heap's slope (Figure 93a). This oblique configuration was intended to provide a reliable representation of the waste thickness to identify the underlying bedrock slope profile.

Figure 94 shows the positioning of the described ERT lines within the mine waste dumps considered in this study.

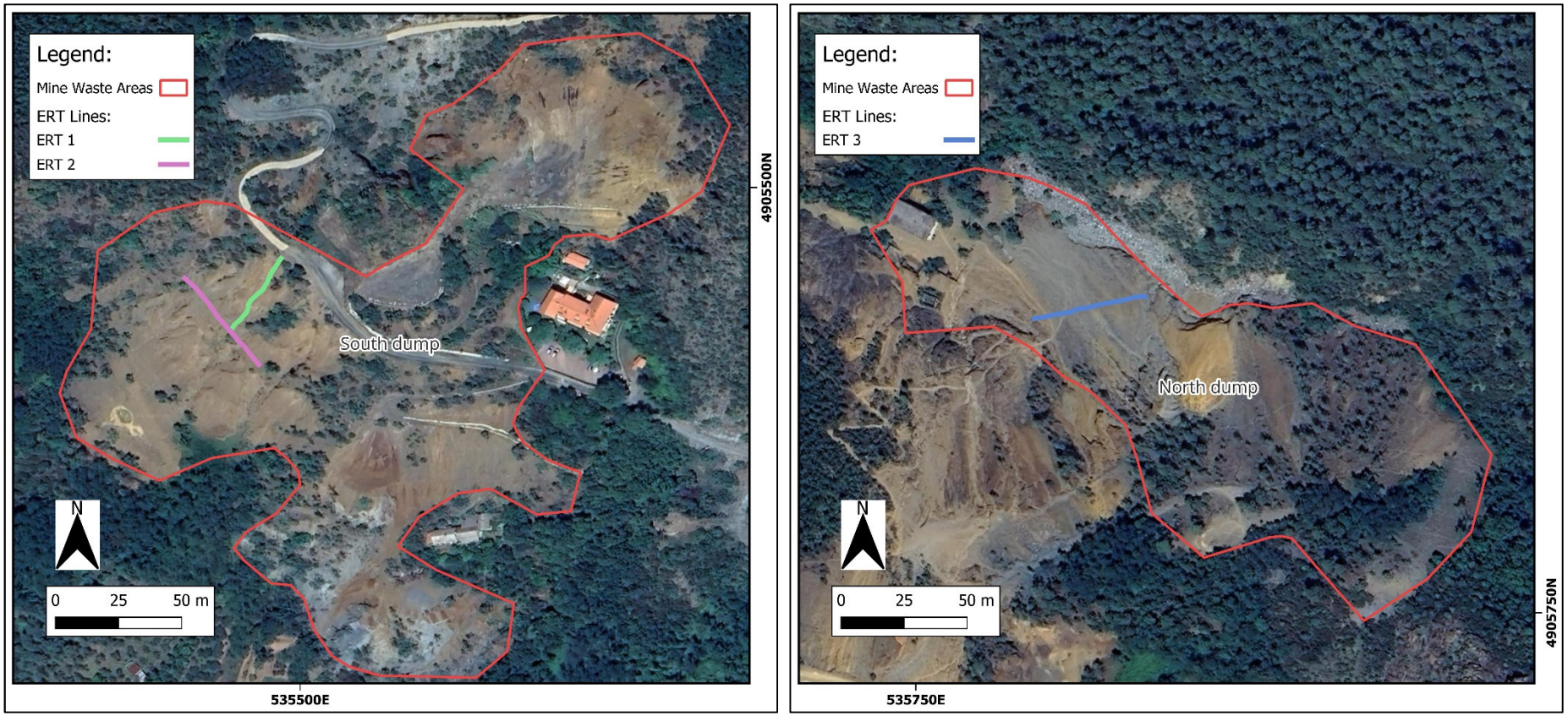


Figure 94 - (Left) ERT lines location on the South mine waste dump, Libiola mine; (Right) ERT line realised on the North mine waste dump, Libiola mine (source: Google Satellite Image. Coordinate system: WGS84/UTM Zone 32N)

From ERT1 results, shown in Figure 95, resistivity appeared to be relatively homogeneous, ranging between 200 and 235 Ωm, confirming that the acquisition line is positioned on a mine waste accumulation profile. The resolution towards the end of the line (South-West direction) is lower, resulting in a lack of sufficient detail for more robust interpretation. The overall thickness of the deposited mine waste material was estimated to be up to 5 m.

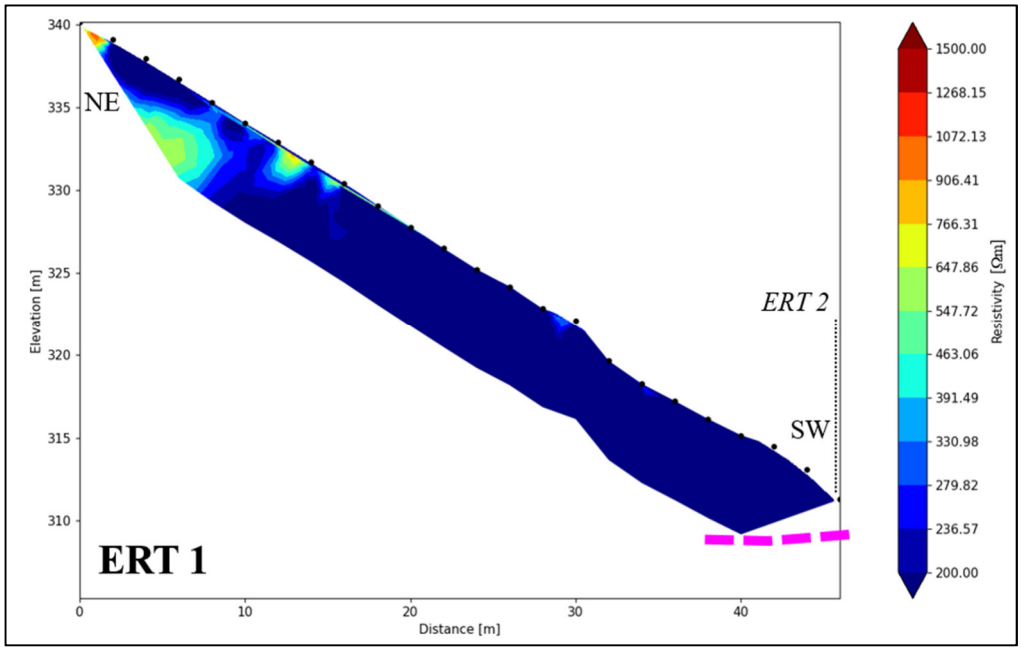


Figure 95 – ERT1 2D resistivity inversion profile realised on the South mine waste dump, Libiola mine. (Pink line: evaluated mine waste boundary) (Image Courtesy: C.Colombero)

Figure 96 reports the resistivity inversion profile obtained from ERT 2.

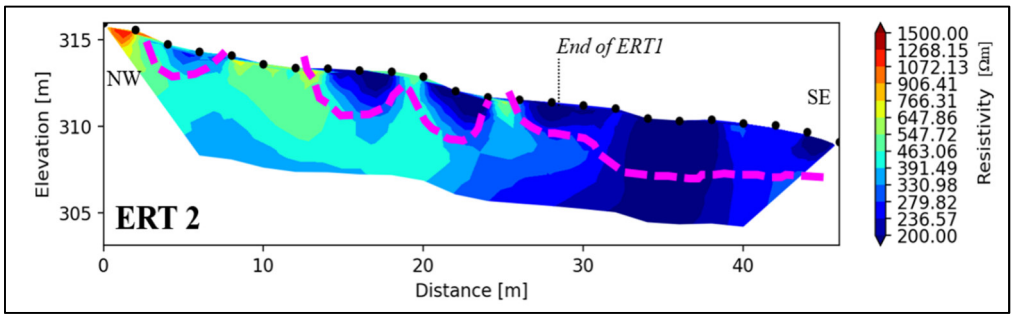


Figure 96 – ERT2 2D resistivity inversion profile realised on the South mine waste dump, Libiola mine. (Pink line: evaluated mine waste boundary) (Image courtesy: C. Colombero)

In the ERT2 profile, defined clusters with similar resistivity properties were identified. The highlighted pockets (Figure 96) appeared to correspond to mine waste material deposited in depressions within the fractured bedrock slope (resistivity < 350 Ωm). Following the South-East direction, resistivity globally decreased, possibly relating to an increased waste thickness and a higher degree of material saturation, likely due to highly conductive waters. Based on the

variability of the observed profile, an average thickness of approximately 3.5m was assumed.

ERT 3 resistivity inversion profile is shown in Figure 97.

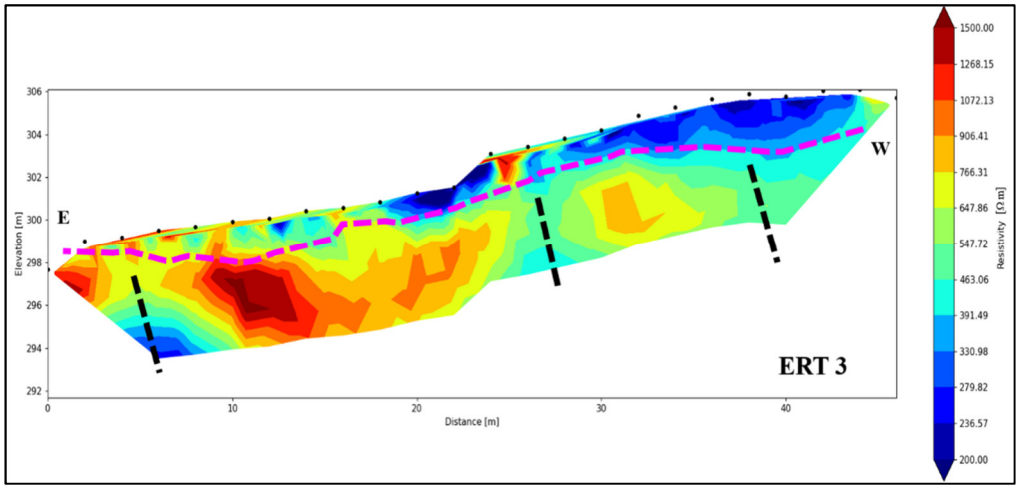


Figure 97 - ERT3 2D resistivity inversion profile realized on the North mine waste dump, Libiola mine. (Pink line: evaluated mine waste boundary; Black line: bedrock) (Image courtesy: C. Colombero)

According to the reported results, a distinct difference in the resistivity properties of the investigated materials was evident between 1.5 and 3.0m depth of the profile. This layer showed a progressive increase in thickness towards the East-West direction. At approximately 10m along the profile, an underground void was detected, associated with high resistivity values (> 1500 Ωm). Beneath the identified mine waste layer, the material showed characteristics comparable with water-saturated conditions, indicated by resistivity values ranging between 400 and 500 Ωm. To conclude, the average thickness of the mine waste material in the North dump was estimated to be around 2.5m.

6.2.1 Mine waste volume estimation results

Mine waste volumes were estimated by combining thicknesses with mapped projected areas, as described in ***Par. 2.3.2.1***.

Table 50 shows the results of the volume estimations.

Table 50 – Volume estimation resume for Libiola mine waste area, considering indicated and inferred volumes

Volume type	*Zone*	*Projected Area [m²]*	*Thickness estimation Mean (min-max) [m]*	*Volume estimation Mean (min-max) [m³]*
Indicated	*North*	*18,900*	*2.25 (1.5-3.0)*	*45,525 (28,350 - 56,700)*
	South	*29,900*	*4.25 (3.5-5.0)*	*127,075 (104,650 - 149,500)*
	North + South	48,800	3.25 (1.5-5.0)	169,600 (133,000 - 206,200)
Inferred	All (excluding North and South dumps)	451,200	3.25 (1.5-5.0)	1,466,400 (676,800 - 2,256,000)
Indicated + Inferred	**All**	**500,000***	**3.25** (1.5-5.0)	**1,636,000** (809,800 - 2,462,200)

**Mine waste area extension estimated by Buccheri et al., 2018; Carbone et al., 2005; Cortecci et al., 2008; Marescotti et al., 2008, 2010; Marini et al., 2003*

For the indicated volumes, corresponding to the North and South dumps, estimated volumes were 42,525 m³ (min 28,350 – max 56,700 m³) and 127,075 m³ (104,650–149,500 m³), respectively. Considering both mine waste dumps, this corresponded to 169,600 m³, considering a mean thickness of 3.25 m (min 1.5 – max 5.0 m). For the remaining area of about 451,200 m², the mean estimated inferred volume was 1,466,400 m³ (min 676,800 – max 2,256,000 m³), considering an average thickness of 3.25 m. The total indicated and inferred volume reached 1,636,000 m³, on average.

The calculated volumes were affected by different uncertainties, such as the complexity of the study area, which restricted the deployment of ERT lines, limited spatial coverage and reduced the level of achievable detail. Additionally, thickness values derived from ERT profiles interpretation were averaged across the entire study area, resulting in highly approximate volume estimates. Furthermore, the considered areas were calculated based only on projected surfaces from satellite images, which likely underestimated the true extent by neglecting the steep slopes that characterise the mine waste dumps in the Libiola area. Consequently, the estimated volumes should be considered mostly reliable

for the directly investigated areas and purely indicative for the areas lacking ground-truth validation.

6.3 Sampling strategy

Sampling was realised by hand-picking. Each sampling point consisted of a vertical or horizontal series of smaller sampling areas, where a 20cm-deep trench was excavated, depending on ground conditions. Material was collected to ensure equal representativeness of the fractions. For each of the three identified sampling sectors, an aliquot of material was collected using a shovel, resulting in a total collected sample of 5-8 kg. The material was stored in plastic bags for further laboratory determinations.

Before material collection, HH-XRF measurements were performed in each sampling sector to obtain an average value across the three identified sectors (HH-XRF results in section 6.4). Figure 98 shows a sampling procedure applied at a selected point.

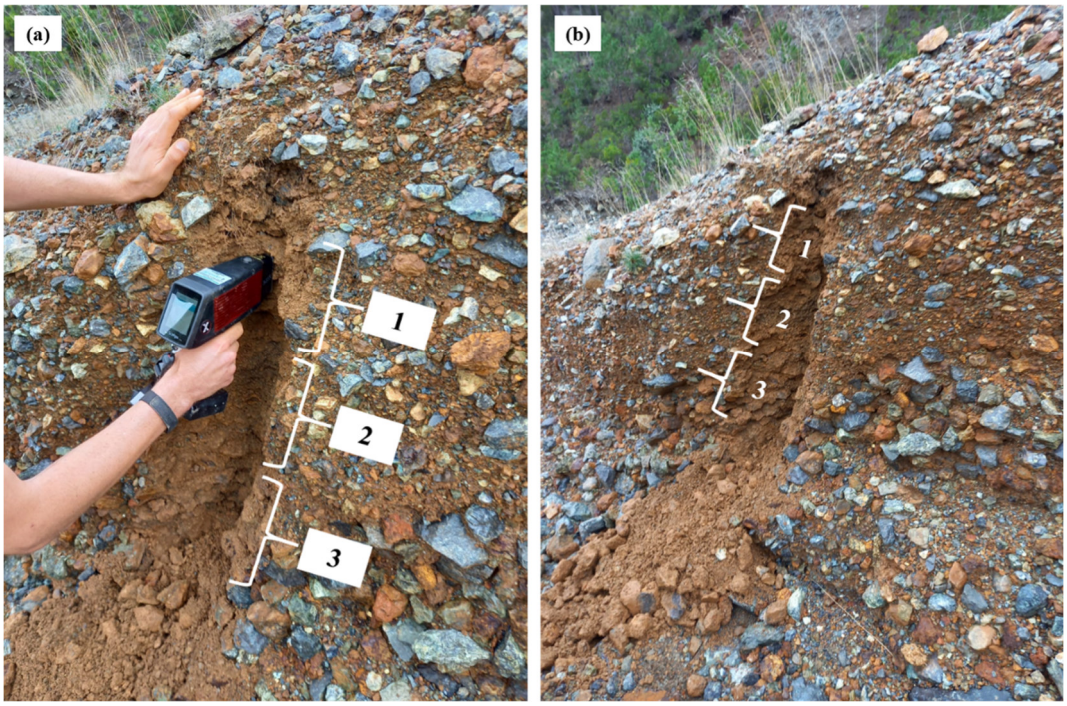


Figure 98 - (a) HH-XRF field measurements, according to 3 identified sectors; (b) Sampling vertical trench showing the three sectors forming the total amount of material collected. Sampling point LN8, North mine waste dump, Libiola mine (Photo credits: G. Baldassarre, 2024)

In total, 10 samples were collected from the North dump, 12 from the South dump and 1 from the Margherita dump site. Figure 99 shows the location of the sampled points, while further details are reported in ***Appendix D.1***. Samples were labelled using the following abbreviations:

- LN##: North dump, with progressive numbers;
- LS##: South dump, with progressive numbers;
- LM1: Margherita dump;

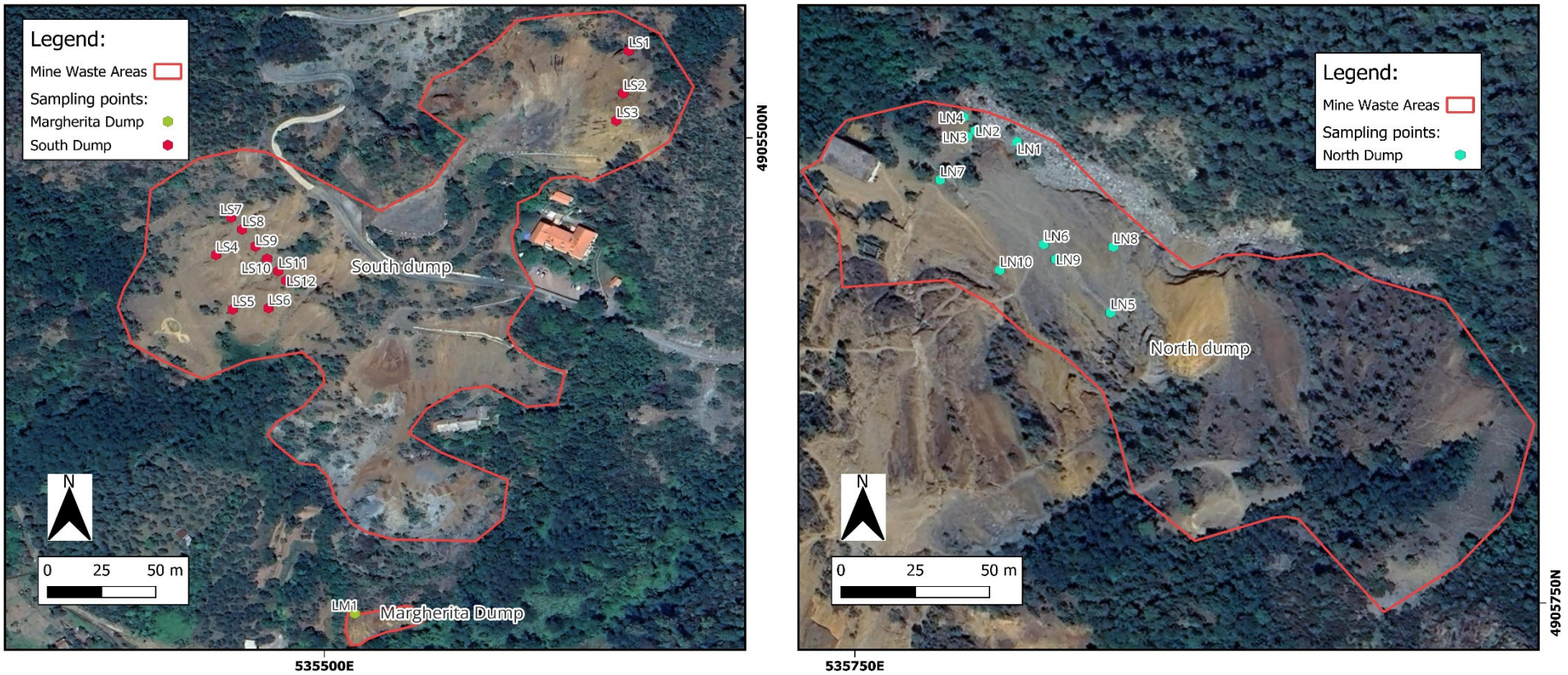


Figure 99 - (Left) Sampling points location on the South and Margherita mine waste dumps, Libiola mine; (Right) Sampling points location on the North mine waste dump, Libiola mine (source: Google Satellite Image. Coordinate system: WGS84/UTM Zone 32N).

The spatial distribution of the samples was adapted based on safety conditions and accessibility of the study areas. The steep slopes characterising the waste piles limited the possibility of achieving a homogeneous surficial distribution of sampling points. In total, over 100kg of material was collected during this sampling campaign.

6.4 Chemical and mineralogical characterisation

The initial characterisation of the material collected in the Libiola mine waste dumps was performed to define chemical and mineralogical features of the material using the following methodologies:

- HH-XRF – (***Par. 2.5.2***)
- ICP-MS – (***Par. 2.5.3***)
- XRPD – (***Par. 2.4.4***)

This approach provided detailed information for chemical and mineralogical attributes and for evaluating the material's potential for the selection of a proper reprocessing methodology aiming at the recovery of critical and strategic metals.

6.4.1 Chemical characterisation results

6.4.1.1 HH-XRF field characterisation results

HH-XRF analyses were performed to investigate chemical assays of the collected samples, considering major elements and the detectable minor elements according to the equipment detection and calibration limit. Table 51 shows the measured ranges of values collected during field sampling for the North and South waste dumps. The full results table is reported in ***Appendix D.2***.

*Table 51 - Summary statistics for HH-XRF results for selected detected elements after field measurements on Libiola North and South mine waste dumps (n = 22). *The LOD/2 rule was applied to values below the detection limit*

	Major Elements							
	Al (%)	***Ca (%)***	***Fe (%)***	***K (%)***	***Mg (%)***	***Mn (ppm)***	***Si (%)***	***Ti (%)***
North dump (n=10)								
Max	6.0	2.5	22.9	1.55	8.6	1,604	15.3	0.9
Min	2.3	1.3	8.4	0.01	1.8	673	10.4	0.3
Mean	3.6	2.0	15.8	0.28	5.4	1,137	13.2	0.6
Median	3.4	2.0	15.0	0.10	6.1	1,143	13.2	0.6
South dump (n=12)								
Max	5.3	2.4	31.2	2.25	7.7	1,480	14.2	0.8
Min	2.6	0.9	8.5	0.02	3.9	857	10.3	0.3
Mean	3.8	1.7	16.2	0.36	5.8	1,129	12.9	0.6
Median	4.2	1.7	13.3	0.21	5.7	1,079	13.1	0.7

	Minor Elements							
	Ag* ***(ppm)***	***As**** ***(ppm)***	***Cd*** ***(ppm)***	***Co**** ***(ppm)***	***Cr*** ***(ppm)***	***Cu*** ***(ppm)***	***Mo*** ***(ppm)***	***Nb**** ***(ppm)***
North dump (n=10)								
Max	16.0	14	11	313	1,222	20,264	38	8.3
Min	0.4	1	1	178	298	46	1	0.7
Mean	4.1	4	2	246	657	4,443	12	3.7
Median	2.8	3	1	246	553	2,516	11	3.2
South dump (n=12)								
Max	6.4	5	13	642	1,525	31,496	18	6.5
Min	0.4	1	1	342	218	703	3	0.6
Mean	1.8	2	2	492	858	6,562	7	3.1
Median	0.7	2	1	492	931	2,507	5	3.4
	Ni ***(ppm)***	***P**** ***(%)***	***Pb*** ***(ppm)***	***Rb*** ***(ppm)***	***S*** ***(%)***	***Se*** ***(ppm)***	***Sn*** ***(ppm)***	***Sr*** ***(ppm)***
North dump (n=10)								
Max	930	0.46	114	26	12.5	45.0	31	56.0
Min	78	0.08	6	3	0.1	0.5	1	0.4
Mean	431	0.19	37	12	3.1	10.6	9	16.4
Median	295	0.15	29	11	0.9	7.5	3	9.6
South dump (n=12)								
Max	1,151	0.83	62	33	13.4	20.0	8	45.0
Min	55	0.08	10	4	0.4	0.5	1	0.6
Mean	513	0.26	26	14	4.1	6.9	3	11.1
Median	410	0.18	20	10	1.7	4.6	1	5.7
	Tl ***(ppm)***	***U*** ***(ppm)***	***V*** ***(ppm)***	***Y*** ***(ppm)***	***Zn*** ***(ppm)***	***Zr*** ***(ppm)***		
North dump (n=10)								
Max	9	24	244	29	1,901	363		
Min	1	3	91	8	56	97		
Mean	5	13	142	18	503	211		
Median	5	13	109	18	223	180		
South dump (n=12)								
Max	9	40	226	32	4,552	220		
Min	2	6	49	1	58	77		
Mean	4	16	144	18	661	150		
Median	4	12	160	16	352	151		

North dump major-elements content was dominated by Fe and Si, having mean concentrations of 15.8% (min 8.4% - max 22.9 %) and 13.2% (min 10.4% - max 15.3%), respectively. Other major elements detected were Mg (5.4%, min 1.8% - max 8.6%), Al (3.6%, min 2.3% - max 6.0%), while Ca assayed 2.0% (min 1.3% - max 2.5%) on average. Ti was assayed at 0.6% (min 0.3% - max 0.9%), while K and Mn were the least abundant, having concentrations of 0.3% (min 0.01% - max 1.55%) and 1,137 ppm (min 673 ppm – max 1,604 ppm), respectively.

Regarding minor elements, in particular strategic and critical metals, Cu was the most abundant, with an average concentration of 4,443 ppm, ranging between

a minimum concentration of 46 ppm to a maximum of 20,264 ppm. Co concentrations ranged between 178 and 313 ppm, with an average value of 246 ppm; however, cobalt determination by HH-XRF was affected by several readings below the detection limits (***Appendix D.2***), which were treated as half of the detection limit value. Moreover, Ni and V showed concentrations of 431 ppm (min 78 ppm – max 930 ppm) and 142 ppm (min 91 ppm – max 244 ppm), respectively

Regarding other minor metals, Cr and Zr showed concentrations of 657 ppm (min 298 ppm – max 1222 ppm) and 211 ppm (min 97 ppm – max 363 ppm), respectively, while Zn was assayed at an average value of 503 ppm (min 56 ppm – max 1901 ppm). For detectable non-metals, S showed concentrations ranging between 0.1 % and 12.5%, with an average assay of 3.1%.

For the South dump, the most abundant major elements were Fe and Si, with concentrations of 16.2% (min 8.5% – max 31.2%) and 12.9% (min 10.3% – max 14.3%), respectively. Determinations for other major elements showed a mean concentration of 5.8% (min 3.9% - max 7.7%) for Mg, 3.8% (min 2.6% - max 5.3%) for Al, and 1.7% (min 0.9% - max 2.4%) for Ca. In addition, Ti was detected at a concentration of 0.6% (min 0.3% - max 0.8%) on average, while K and Mn were the least abundant, having mean grades of 0.4% (min 0.02% - max 2.25%) and 1,129 ppm (min 857 ppm – max 1,480 ppm), respectively.

Cu was the most abundant critical and strategic metal, assaying on average 6,562 ppm, ranging between a minimum grade of 703 ppm and a maximum concentration of 31,496 ppm. Co showed a mean concentration of 492 ppm (min 342 ppm – max 642 ppm), according to half of the detection limit values considered (***Appendix D.2***). Additionally, Ni and V were present at mean concentrations of 513 ppm (min 55 ppm – max 1,151 ppm) and 144 ppm (min 49 ppm – max 226 ppm), respectively

Other base metals, Zn assayed on average 661 ppm (min 58ppm – max 4,552 ppm), and V showed a 144 ppm (min 49 ppm - max 226 ppm) mean concentration. For non-metals, S was characterised by a mean grade of 4.1%, ranging between a minimum concentration of 0.4% and a maximum concentration of 13.4%.

Table 52 shows the HH-XRF results for the sample collected in the Margherita mine waste dump area. Full data are reported in ***Appendix D.2.***

Table 52 - HH-XRF results for major elements and selected minor elements from Libiola Margherita mine waste dump sample (LM1).

Margherita Dump (n = 1)							
Major Elements							
Al (%)	***Ca (%)***	***Fe (%)***	***K (%)***	***Mg (%)***	***Mn (ppm)***	***Si (%)***	***Ti (%)***
3.3 ± 0.1	1.1 ± 0.03	26.4 ± 0.03	0.22 ± 0.03	7.1 ± 0.6	1,651 ± 72	11.9 ± 0.1	0.35 ± 0.1
Minor Elements							
Ag (ppm)	***As (ppm)***	***Cd (ppm)***	***Co (ppm)***	***Cr (ppm)***	***Cu (ppm)***	***Mo (ppm)***	***Nb (ppm)***
< 1.0	76 ± 4.8	6.1 ± 0.9	< 222	1,047 ± 27	6,303 ± 37	8 ± 1	< 1.6
Ni (ppm)	***P (%)***	***Pb (ppm)***	***Rb (ppm)***	***S (%)***	***Se (ppm)***	***Sn (ppm)***	***Sr (ppm)***
790 ± 20	< 0.4	166 ± 6	19 ± 1.3	1.8 ± 0.02	< 2	242 ± 2.3	< 1.6
Tl (ppm)	***U (ppm)***	***V (ppm)***	***Y (ppm)***	***Zn (ppm)***	***Zr (ppm)***		
< 4	28 ± 2.4	124 ± 16	5 ±16	1,898 ± 28	116 ± 2.5		

The most abundant major elements are Fe and Si, showing concentrations of 26.4% and 11.9%, respectively. Other major elements determination included Mg (7.1%) and Al (3.3%), with Ca assaying 1.1%. In addition, Ti and Mn were detected at concentrations of 0.35% and 1651 ppm, respectively.

Again, Cu resulted the most abundant critical and strategic metals, having a concentration of 6,303 ppm, while Ni and V assayed 790 ppm and 124 ppm, respectively. Co determination fell under the detection limit, having an estimated LOD of 222 ppm.

Regarding base metals detected, Zn was measured having a concentration of 1,898 ppm. Cr graded 1,047 ppm, while lower concentrations of Sn (242 ppm) and Pb (166 ppm) were detected. S concentration was 19 %.

In general, HH-XRF results showed comparable concentrations of minor and major elements from the different mine waste dumps considered. Regarding the most abundant critical and strategic metal, Cu, the maximum average concentration was found in the South dump (6,562 ppm), while the North dump showed a slightly lower mean concentration of 4,443 ppm. For Margherita dump, a punctual Cu concentration of 6,303 ppm was recorded.

6.4.1.2 ICP-MS characterisation results

ICP-MS analyses were performed to define a more detailed geochemical characterisation while validating the on-field HH-XRF measurements. In particular, ICP-MS provided assays of those elements that fall below the detection limits of HH-XRF. Statistical results of geochemical assays, considering a selected set of elements, are summarised in Table 53. The full ICP-MS data are reported in ***Appendix D.3*** and ***Appendix D.4***.

*Table 53 - ICP-MS summary statistics for selected elements for Libiola North and South dumps (*ALS ME-MS81 method)*

	Ag (ppm)	***As (ppm)***	***Cd (ppm)***	***Co (ppm)***	***Cr (ppm)***	***Cu (ppm)***	***In (ppm)***	***Mo (ppm)***
North dump (n = 10)								
Max	13.9	26.6	9.4	125	1,865	17,861	0.48	40.0
Min	0.1	0.2	0.1	22	303	55	0.03	0.6
Mean	3.4	11.6	2.0	67	837	4,397	0.22	12.0
Median	1.9	10.8	0.8	70	595	2,780	0.22	10.5
South dump (n = 12)								
Max	6.1	9.4	12.6	373	2,010	26,145	0.70	18.9
Min	0.6	1.7	0.1	41	206	773	0.10	2.8
Mean	2.4	4.8	1.9	113	873	6,101	0.23	6.7
Median	1.8	4.3	0.9	77	681	3,015	0.17	5.0

	Ni (ppm)	***Pb (ppm)***	***Re (ppm)***	***Sb (ppm)***	***Se (ppm)***	***Sn (ppm)***	***U (ppm)***	***V (ppm)***
North dump (n = 10)								
Max	828	92.2	0.050	3.00	38.0	18.4	5.8	321
Min	95	1.9	0.002	0.05	1.0	1.3	0.5	154
Mean	386	25.5	0.014	0.89	11.5	7.6	1.7	221
Median	245	14.6	0.005	0.62	9.5	5.0	1.0	201
South dump (n = 12)								
Max	1,080	34.2	0.024	1.06	27.0	5.4	7.8	319
Min	66	6.5	0.002	0.14	2.0	2.3	1.0	111
Mean	448	13.2	0.009	0.41	9.5	3.3	2.9	212
Median	363	10.7	0.008	0.33	5.5	2.9	2.6	227

	Y (ppm)	***Zn (ppm)***	***∑LREE* (ppm)***	***∑HREE* (ppm)***
North dump (n = 10)				
Max	40.8	2,140	40	64
Min	18.5	99	13	28
Mean	28.3	560	23	41
Median	27.2	266	22	40
South dump (n = 12)				
Max	44.1	4,630	49	70
Min	14.7	88	9	19
Mean	28.1	707	30	44
Median	25.7	409	28	40

For the North dump, Cu was measured as the most abundant critical and strategic element, assaying on average 4,397 ppm (min 55 ppm – max 17,861 ppm). Among other elements of interest, Ni graded on average 386 ppm (min 95 ppm – max 828 ppm) while V had a mean concentration of 221 ppm (min 154 ppm – max 321 ppm). Co was detected in trace amounts being having a mean concentration of 67 ppm (min 22 ppm – max 125 ppm). As had an average assay of 11.6 ppm, with a minimum value of 0.1 ppm and a maximum of 13.9 ppm. REEs were present in relatively low concentrations, with LREEs and HREEs concentrations being 23 ppm and 41 ppm, respectively. Among base metals, Zn

showed an average grade of 560 ppm (min 99 ppm – max 2,140 ppm), and Cr was assayed at 837 ppm on average.

South dump showed a slightly higher average concentration of Cu, being 6,101 ppm and ranging between a minimum value of 773 ppm and a maximum of 26,145 ppm. Moreover, Ni graded on average 448 ppm (min 66 ppm – max 1080 ppm), and V was assayed at a mean value of 212 ppm (min 111 ppm – max 319 ppm). Co showed an average concentration of 113 ppm (min 41 ppm – max 373 ppm), and the As concentration was on average 4.8 ppm (min 1.7 – max 9.4). LREEs and HREEs assayed on average 30 ppm (min 9 ppm – max 49 ppm) and 44 ppm (min 19 ppm – max 70 ppm), respectively. For base metals, Zn had a measured concentration of 707 ppm (min 88 ppm – max 4,630 ppm) and Cr graded on average 873 ppm (min 206 ppm – max 2010 ppm).

Table 54 shows ICP-MS results for selected elements after characterization of the sample collected in the Margherita dump.

Table 54 - ICP-MS results for selected elements for Libiola Margherita mine waste dump sample LM1 (: ALS ME-MS81 method).*

Margherita dump (n = 1)							
Ag (ppm)	***As (ppm)***	***Cd (ppm)***	***Co (ppm)***	***Cr (ppm)***	***Cu (ppm)***	***In (ppm)***	***Mo (ppm)***
2.0	106	4.8	37	1,215	6,030	0.24	11.2
Ni (ppm)	***Pb (ppm)***	***Re (ppm)***	***Sb (ppm)***	***Se (ppm)***	***Sn (ppm)***	***U (ppm)***	***V (ppm)***
682	154	0.014	28	6	207	1.2	153
Y (ppm)	***Zn (ppm)***	***∑LREE* (ppm)***	***∑HREE* (ppm)***				
14.4	2,020	17	22				

For Margherita dump, the most abundant critical metal was Cu, having a concentration of 6,030 ppm. Ni assayed 682 ppm in this area, while Co showed a trace concentration of 37 ppm. Zn concentration reached 2,020 ppm, while Cr was measured at a concentration of 1,215 ppm. LREEs and HREEs were 17 ppm and 22 ppm, respectively.

In general, ICP-MS confirmed that Cu was the most abundant critical and strategic metal within mine waste areas in the Libiola mine, reaching a maximum concentration of 26,145 ppm in the South dump, and having average values among the sampled mine waste areas ranging between 4,397 ppm (North dump) and 6,101 ppm (South dump), and being 6,030 ppm in the Margherita dump. ICP-MS results gave a more precise determination for Co, confirming trace concentrations, ranging between 67 ppm (North dump) and 113 ppm (South dump), and 37 ppm for Margherita dump sample.

6.4.1.3 Comparison of HH-XRF and ICP-MS results

HH-XRF field results were compared to ICP-MS determination in order to validate the collected information from the field. Selected elements were

considered, in particular, potential target recovery elements for the Libiola mine waste areas, such as Cu, Ni, Co, and Zn.

Figure 100 shows XY plots comparing chemical results for Cu.

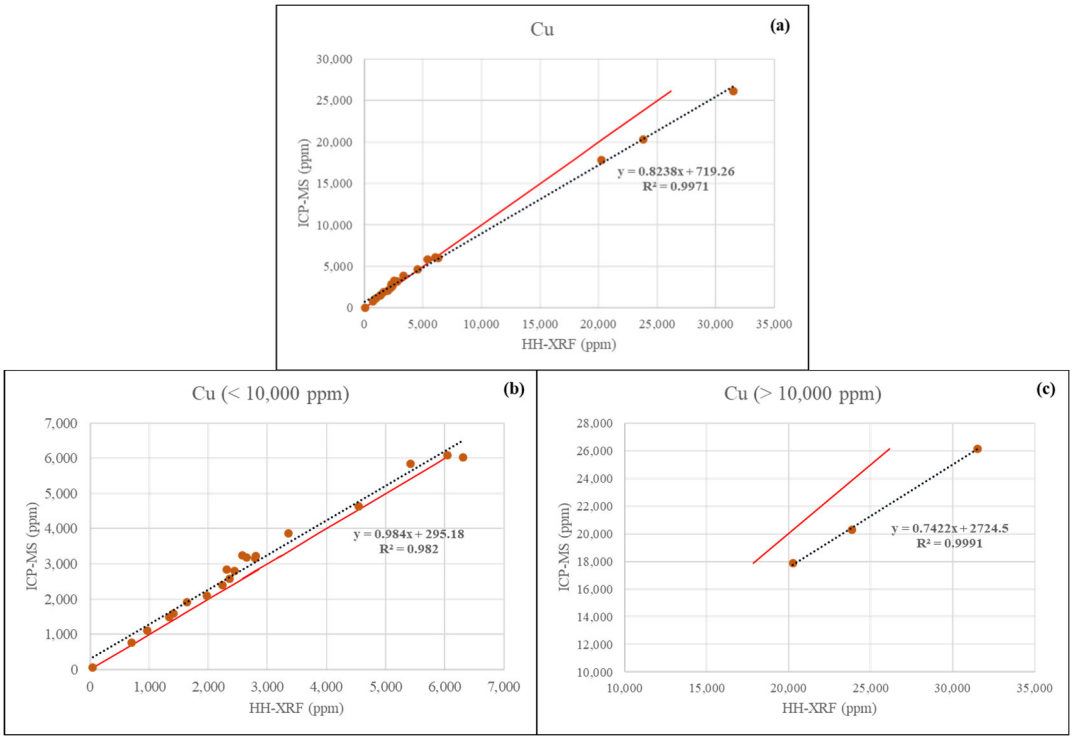


Figure 100 - (a) Comparison of HH-XRF and ICP-MS data for Cu considering the entire dataset of acquisitions of Libiola waste rock samples, (b) Data comparison for concentrations < 10,000 ppm; (c) Data comparison for concentrations > 10,000 ppm. Red line: x = y = ICP-MS values

According to the graphs, HH-XRF and ICP-MS datasets have a good correlation, indicating comparable determinations. Considering the entire dataset (Figure 100a), the angular coefficient of the interpolating line is around 0.8, showing that HH-XRF values were slightly overestimated when compared to ICP-MS data. In addition, a different behaviour of the dataset can be observed, considering a concentration of 10,000 ppm as a pivot point. For concentrations below this value, as reported in Figure 100b, the data resulted in an almost overlapping distribution, with the angular coefficient of the correlation line being slightly below 1 (0.98). It demonstrated that HH-XRF values are, in general, slightly higher than ICP-MS values. By contrast, Figure 100c shows that for values > 10,000 ppm, HH-XRF markedly overestimated Cu concentrations when compared to ICP-MS determinations.

Figure 101(a-c) shows chemical determinations comparison for Ni, Co and Zn.

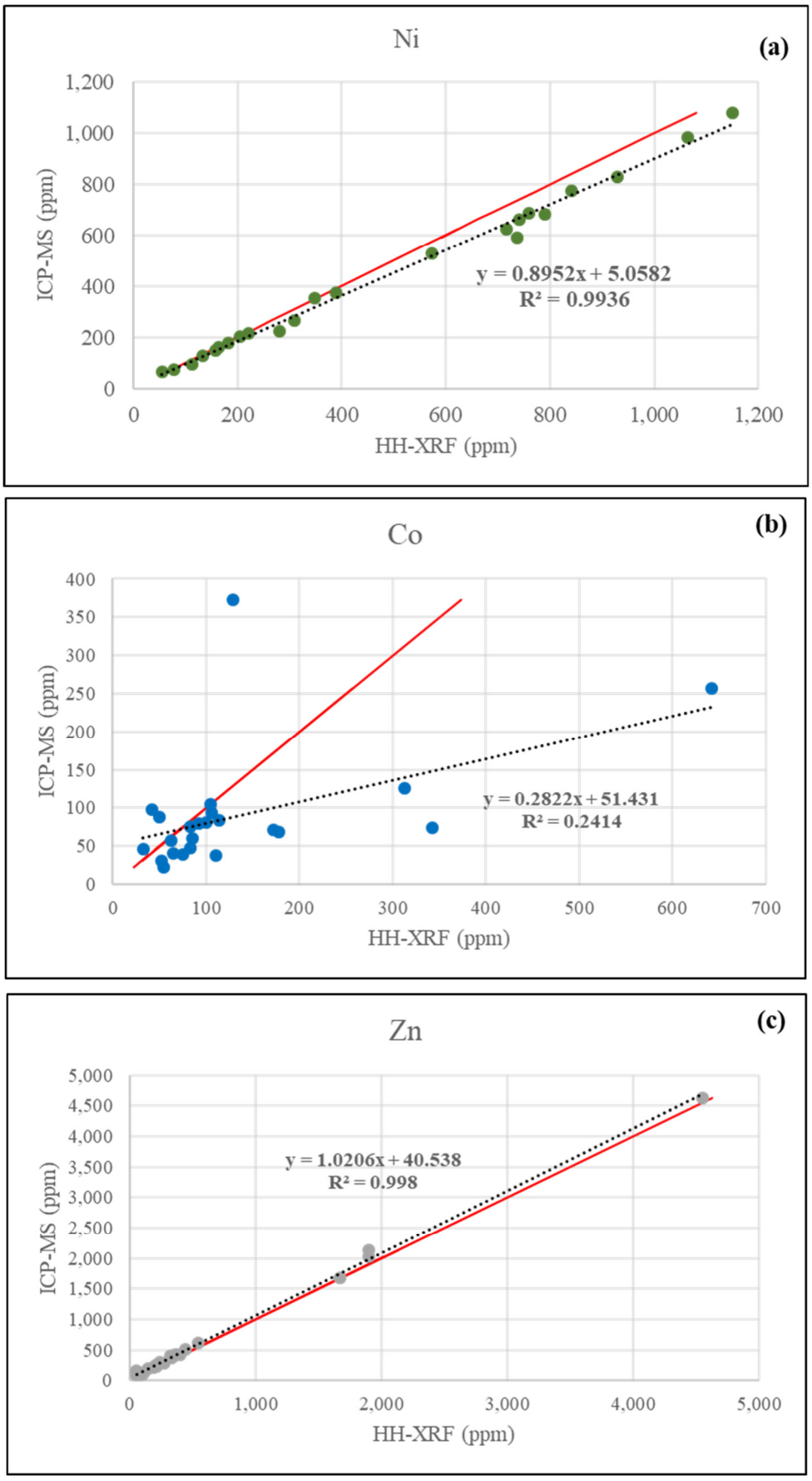


Figure 101 - Comparison of HH-XRF and ICP-MS for selected element acquisitions regarding considered Libiola waste rock samples : (a) Ni, (b) Co, (c) Zn. Red line: x = y = ICP-MS values

For Ni (Figure 101a), HH-XRF and ICP-MS chemical assays had a good correlation when compared to each other. The angular coefficient of the linear interpolating line was calculated to be lower than 1 (0.89), indicating a slight overestimation of HH-XRF data if compared to ICP-MS data. In general, the trend between the difference between the two methods is increasing with higher values, considering a changing behaviour for values above 250 ppm.

Regarding Co, HH-XRF and ICP-MS were poorly correlated (Figure 101b). HH-XRF assays were deeply overestimating values if compared to ICP-MS, according to the angular coefficient being 0.28. This trend was due to the difficulties in having HH-XRF reading over LOD, as described in paragraph 6.4.1.1. In this case, ICP-MS data should be considered more reliable and field determinations using HH-XRF should be considered purely indicative for this element.

Zn chemical assays comparison (Figure 13c) showed a nearly perfect linear correlation between HH-XRF and ICP-MS data. In addition, the angular coefficient of the interpolating line was 1.02, resulting in an almost negligible underestimation of HH-XRF data if compared to ICP-MS assays. Overall, there were no clear trends with varying concentration, highlighting the stability of measurements of Zn for the two proposed methods.

Finally, according to the comparison described, HH-XRF field measurements provided reliable data for a fast and streamlined method aiming at assessing quantities and variability of critical and strategic elements among mine waste areas surrounding the Libiola mine.

6.4.2 Mineralogical characterisation results

XRPD analyses were performed on selected samples collected in the mine waste areas considered in this study.

Figure 102 shows quantitative determinations for selected samples collected in North, South and Margherita Dump, while full data are reported in ***Appendix D.5***.

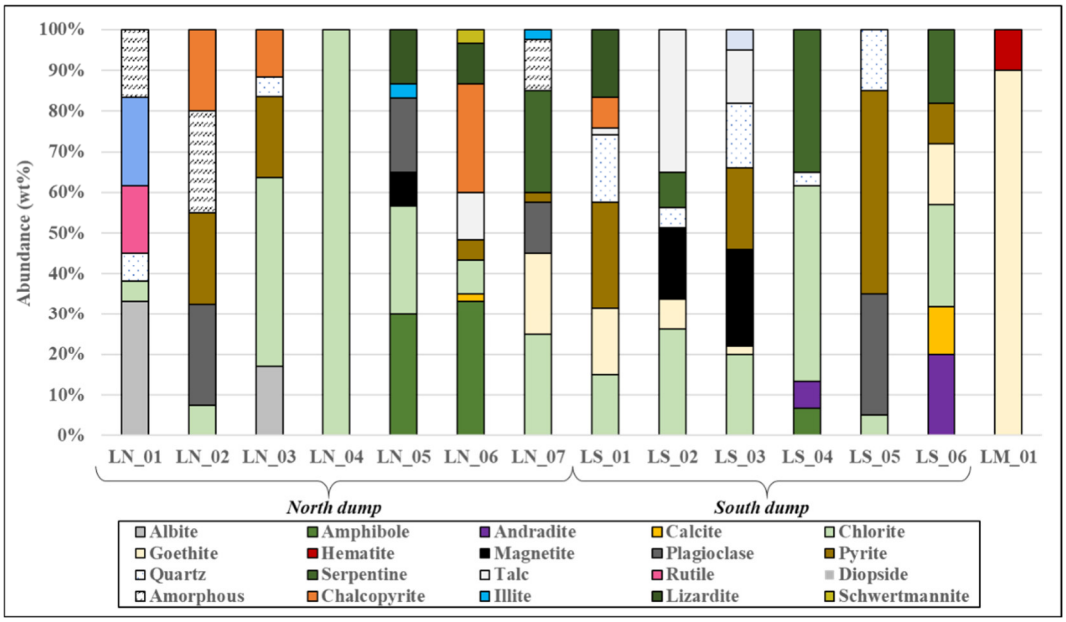


Figure 102 - Quantitative XRPD mineralogical determination for selected samples from Libiola North dump (n = 7), South dump (n = 6), and Margherita dump (n = 1). (Data courtesy: C. Carbone and G. Specchia)

According to XRPD analyses performed, common minerals detected in North and South dumps were chlorite, serpentine, lizardite, talc, quartz, magnetite, pyrite, chalcopyrite, and goethite. Calcite, schwertmannite, illite, albite, diopside, amphibole, and rutile were additionally detected in the sample coming from the North dump, while gypsum is the only additional mineral detected in the South dump. Margherita dump sample was mostly composed of goethite with a minor concentration of hematite.

Figure 103 shows the average concentration of mineral phases for the North Dump. For this area, minerals related to host rocks were identified to be prevalent, having a high concentration of chlorite (31.3%), amphibole (9.0%), plagioclase (8.0%), rutile (2%), and talc (1.7%). Regarding ore minerals detected, the most abundant was chalcopyrite, having an average concentration of 8.3%, while pyrite showed a lower concentration of 7.1%. Other phases included oxidised minerals, such as goethite (2.9%) and schwertmannite (0.5%).

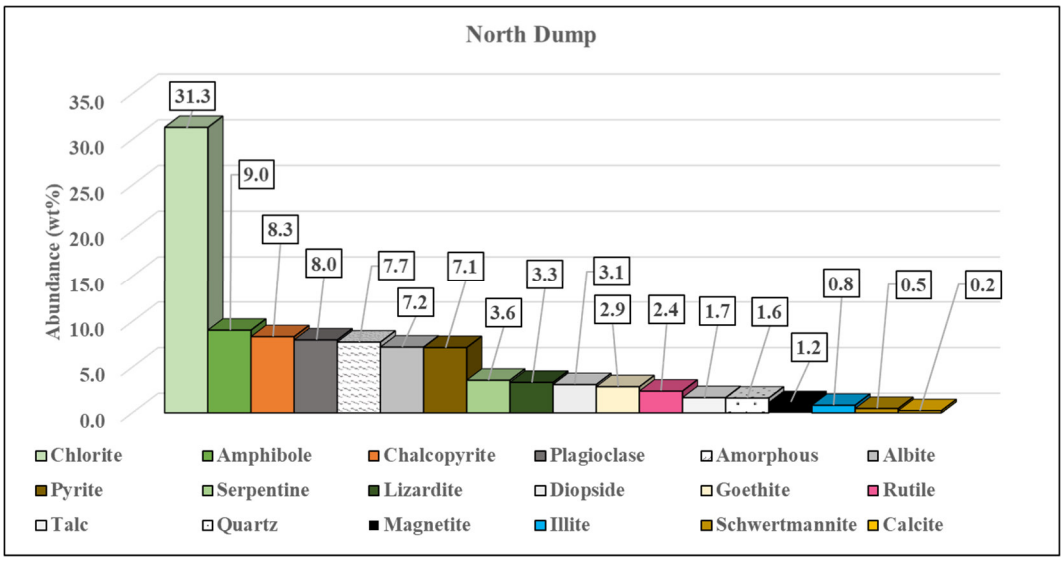


Figure 103 - Average mineral abundance for Libiola North dump, from XRPD data (Data courtesy:C.Carbone and G. Specchia)

Figure 104 reports average values of mineral phases detected in samples coming from the South dump. Minerals related to host rocks were chlorite (20.4%), talc (16.6%), magnetite (13.8%), and quartz (12.6%), with minor presence of lizardite (5.6%), serpentine (2.9%), and gypsum (1.7%). Regarding ore minerals, pyrite was the most abundant (15.3%), while chalcopyrite was residual, having an average concentration of 2.5%. The only oxidised mineral detected was goethite, having an average concentration of 8.7%.

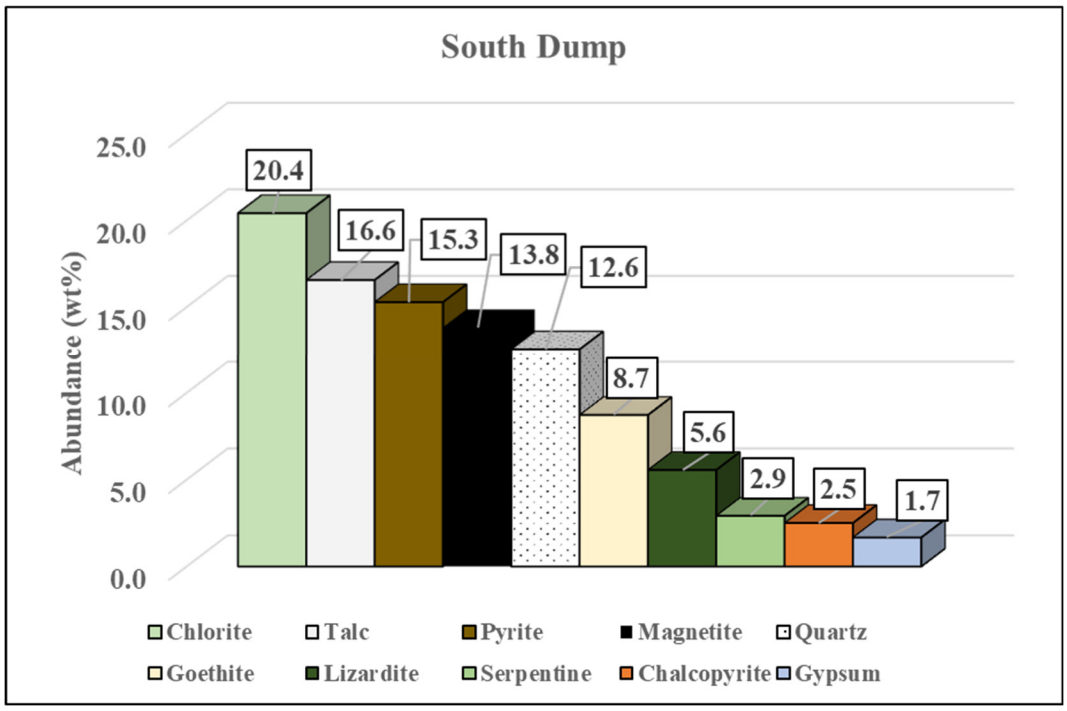


Figure 104 - Average mineral abundance for Libiola South Dump from XRPD data (Data courtesy: C. Carbone and G. Specchia)

6.5 Geochemical, mineralogical and environmental considerations

Geochemical and mineralogical characterisations performed showed results in accordance with previous detailed studies performed in the area, especially in the North dump area (Dinelli et al., 2001; Marescotti et al., 2010, 2008; Marescotti & Carbone, 2003). Less data was available in the literature regarding the South dump. Data produced in this study showed that the main geochemical and mineralogical features can be comparable with the North dump characteristics, but showed a higher average content of Cu and a slightly different presence of ore minerals, such as prevalent pyrite and minor chalcopyrite.

According to the collected geochemical data, considerations regarding the abundance of critical, strategic and economic elements are shown in the spider plot in Figure 105, compared to the normalised average abundance of elements by Rudnick & Gao (2014).

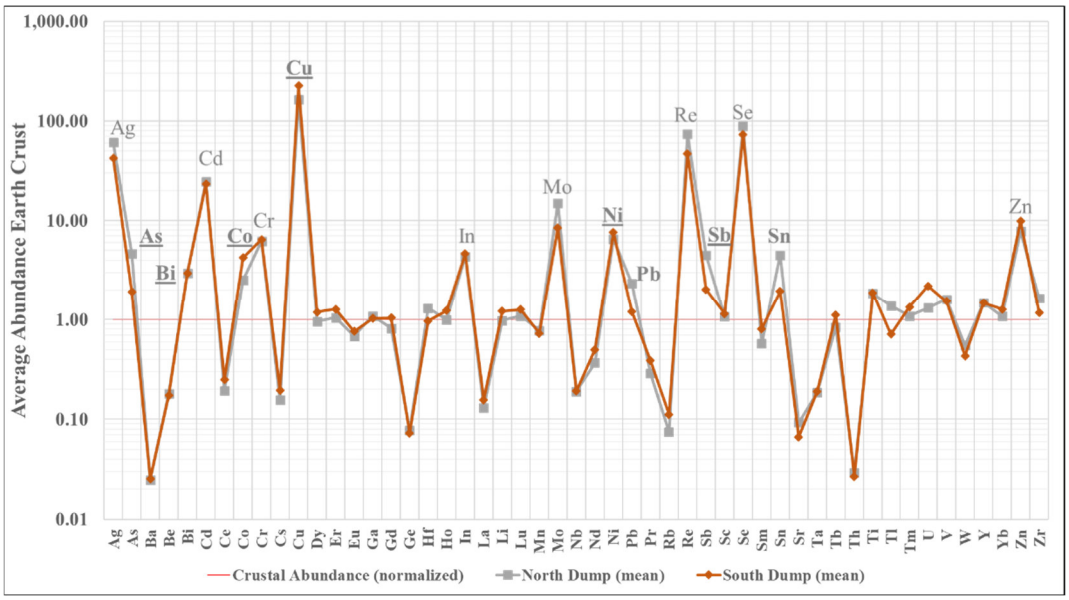


Figure 105 - Spider plot for the geochemical summary of Libiola North and South dumps samples, with mean values normalised against the average abundance of elements in the Earth's crust by Rudnick & Gao, 2014.

North and South mine waste dumps resulted in being relatively enriched in elements such as Ag, Cd, Cu, Mo, Re, and Se, being generally 10 times higher than the average crustal abundance.

Table 55 shows in more detail the summary statistics of the critical and strategic metals' mean concentration compared to the average crustal abundance. The most enriched CRMs and SRMs for the studied sites is Cu with a concentration 163 to 226 times higher than average crustal abundance. Other considered CRMs and SRMs, such as As, Bi, Co, Ga, Hf, Ni, Sb, Sc, V and HREEs, resulted in higher abundances than the average crustal concentrations, but none of them exceeded the 10 times threshold.

*Table 55 - Summary statistics for mean concentrations from ICP-MS analyses of critical and strategic metals from the Libiola North and South dumps compared to crustal abundance. In bold concentration at least 1x time higher than crustal abundance *(Rudnick & Gao, 2014)*

Critical and strategic element	Crustal abundance* (ppm)	***North dump (n = 10)***		***South dump (n = 12)***	
		Mean conc. (ppm)	*Times higher than average crustal abundance*	*Mean conc. (ppm)*	*Times higher than average crustal abundance*
As	2.5	**11.6**	***4.6***	**4.8**	***1.9***
Be	1.9	0.3	*0.2*	0.3	*0.2*
Bi	0.18	**0.5**	***3.0***	**0.5**	***3.0***
Co	26.6	**66.8**	***2.5***	**112.5**	***4.2***
Cu	27	**4,397**	***163***	**6,101**	***226***
Ga	16	**17**	***1.1***	16	*1.0*
Ge	1.3	0.1	*0.1*	0.1	*0.1*
Hf	3.7	**4.8**	***1.3***	3.6	*1.0*
Li	17	17	*1.0*	**21**	***1.2***
Mn	800	621	*0.8*	581	*0.7*
Nb	8	1.5	*0.2*	1.5	*0.2*
Ni	59	**386**	***6.5***	**448**	***7.6***
Sb	0.2	**0.9**	***4.5***	**0.4**	***2.0***
Sc	21.9	**23.4**	***1.1***	**25.0**	***1.1***
Sr	320	29.7	*0.1*	21.3	*0.1*
Ta	0.7	0.1	*0.2*	0.1	*0.2*
V	138	**220.9**	***1.6***	**211.9**	***1.5***
W	1	0.6	*0.6*	0.4	*0.4*
LREEs	92.9	21.8	*0.2*	27.9	*0.3*
HREEs	32.3	**40.3**	***1.3***	**40.4**	***1.3***

Considering other base and valuable metals, reported in Table 56, several elements resulted enriched more than 10 times the average crustal abundance. Regarding precious and base metals, Ag resulted enriched more than 30 times for both considered areas, Cd was measured to be concentrated by more than 20 times, while Mo was found to be 15 times higher only in the North dump. Other considered elements, such as Se showed an enrichment between 73.1 and 88.5, and Re showed values 47.0 times higher in the South dump, and 73.9 times in the North dump.

*Table 56 - Summary statistics for mean concentrations from ICP-MS analyses of base and valuable metals from the Libiola North and South dumps. In bold concentration at least 10x times higher than crustal abundance *(Rudnick & Gao, 2014)*

Element	Crustal abundance* (ppm)	***North dump (n = 10)***		***South dump (n = 12)***	
		Mean conc. (ppm)	*Times higher than average crustal abundance*	*Mean conc. (ppm)*	*Times higher than average crustal abundance*
Ag	0.056	**3.4**	**60.6**	**2.4**	**42.5**
Cd	0.08	**2**	**24.6**	**1.9**	**23.4**
Cr	135	837	6.2	873	6.5
In	0.05	0.22	4.4	0.2	4.6
Mo	0.8	**12**	**15.0**	6.7	8.4
Pb	11	26	2.3	13.2	1.2

Element	Crustal abundance* (ppm)	*North dump (n = 10)*		*South dump (n = 12)*	
		Mean conc. (ppm)	*Times higher than average crustal abundance*	*Mean conc. (ppm)*	*Times higher than average crustal abundance*
Re	0.000188	**0.0139**	**73.9**	**0.0088**	**47.0**
Se	0.13	**12**	**88.5**	**9.5**	**73.1**
Sn	1.7	8	4.5	3.3	1.9
Zn	72	560	7.8	707	9.8

From an environmental perspective, geochemical assays measured by ICP-MS were compared to Italian Law Decree 152/2006 (Italian Republic, 2006) metallic elements limits for soils in public, private and residential green use (Column A) and commercial and industrial use (Column B). Mean values were normalised against Column A values, as reported in Figure 106.

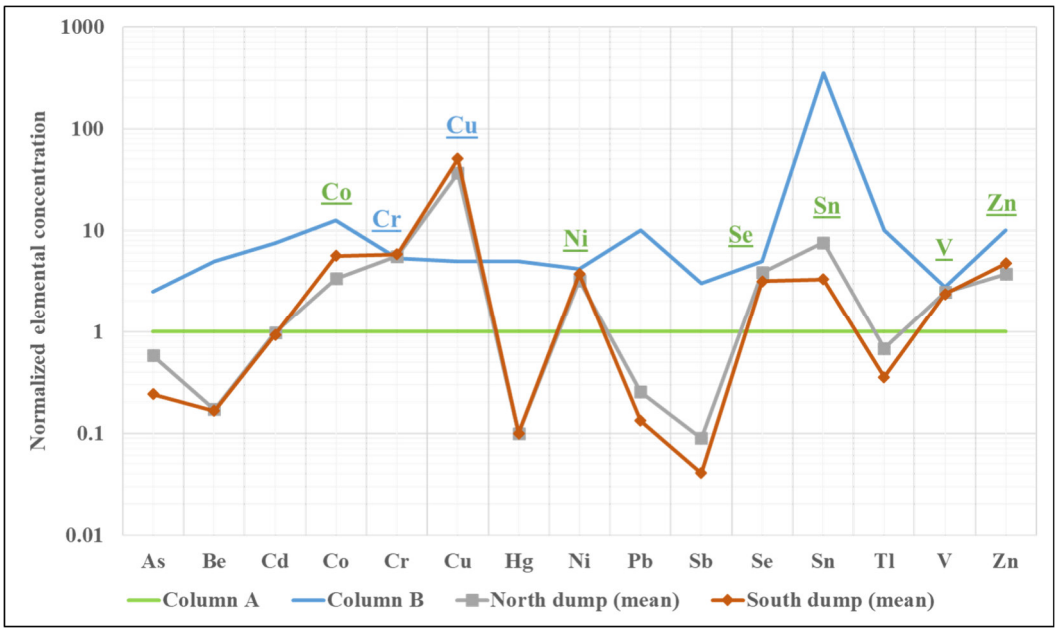


Figure 106 - Spider plot comparing Libiola North and South dumps mean elemental concentration with the normalised metallic element limits set by Legislative Decree 152/2006. Green: elements exceeding Column A; Blue: elements exceeding Column B.

Average metal contents measured in the Libiola mine waste dumps showed values above Column A law limits for Co, Ni, Se, Sn, V, and Zn. In addition, Cr and Cu exceeded Column B limits for both North and South dumps. The presented data showed that Libiola mine waste dumps could also be considered as an environmental liability left after the closure of the mine, for which reclamation actions should be considered.

6.6 Lab-scale processing trials

Geochemical and mineralogical characterisation of the Libiola mine waste dumps gave useful insights for the design of possible processing options aiming at the recovery of critical and strategic metals contained. According to the presented data, on average, the most abundant critical element detected was Cu, and it was considered the main target element for the reprocessing procedure. This metal was measured in variable concentrations among the collected samples and associated with a heterogeneous mineralogy, and was often associated with oxidised secondary minerals among the dataset. In addition, considering the initial conditions of the waste material, which is characterised by an average p80 from 9 mm to 70 mm (Marescotti et al., 2008) and the need for size reduction of samples, posed clear challenges to physical separation options, suggesting that hydrometallurgical reprocessing could be a viable option to be evaluated in terms of efficiency in recovering the selected target element. Two different leaching methodologies were tested and compared.

The reprocessing lab-scale testing consisted of the following activities:

- Size reduction for reaching a p80 < 0.075 mm (following procedure described in ***Par. 2.5.1***);
- Glycine alkaline leaching (***Par. 2.6.7.1***);
- Sulphuric acid leaching (***Par. 2.6.7.2***);

Table 57 shows the list of selected samples for testing and the details regarding the leaching time steps performed for each batch.

Table 57 – List of selected samples from Libiola mine waste and the batch testing time applied for each leaching test.

Sample	***Glycine leaching (h)***	***Sulphuric acid leaching (h)***
LN7	0.5 – 2 – 4 – 6 – 24 – 168	2
LN9	0.5 – 2 – 4 – 6 – 24	2
LS1	0.5 – 2 – 4 – 6 – 24 – 168	2
LS3	0.5 – 2 – 4 – 6 – 24 – 168	2
LS4	0.5 – 2 – 4 – 6 – 24	2

Reprocessing outcomes were evaluated using HH-XRF on the residual solid fractions after leaching, while leaching liquors were analysed by ICP-OES (***Par. 2.5.4***). The estimated recovery of target elements was calculated according to ***Equation 4*** and ***Equation 5*** described in ***Par. 2.6.8***.

6.6.1 Chemical and mineralogical characterisation of samples before leaching

Initial Cu and Fe assays were obtained by HH-XRF analysis realised on the same bulk sub-sample before leaching, while XRPD analyses provided mineralogical features for the same samples. Table 58 shows HH-XRF assays for the selected target minerals and main mineralogical phases detected by XRPD analyses.

Table 58 - HH-XRF results for target elements and main detected minerals by XRPD on selected samples from Libiola mine waste dumps before leaching tests.

Sample	*Cu (ppm)*	*Fe (ppm)*	*Detected minerals**
LN7	20,508 ± 65	232,034 ± 259	Chl, Gth, Ilt, Pl, Py, Srp
LN9	3,887 ± 24	144,326 ± 169	Lz, Chl
LS1	22,595 ± 72	269,354 ± 274	Ccp, Chl, Gth, Lz, Py, Qz, Tlc
LS3	30,858 ± 88	314,426 ± 310	Chl, Gp, Gth, Mag, Py, Qz, Tlc
LS4	4,769 ± 25	109,724 ± 152	Amp, Adr, Chl, Qz, Srp

**Mineral abbreviations according to Warr (2021): Amp: Amphibole, Adr: Andradite, Ccp: Chalcopyrite, Chl: Chlorite, Gp: Gypsum, Gth: Goethite, Ilt: Illite, Lz: Lizardite, Mag: Magnetite, Pl: Plagioclase, Py: pyrite, Qz: quartz, Srp: Serpentine, Tlc: Talc*

6.6.2 Leaching test results

6.6.2.1 pH variation during glycine leaching

During glycine leaching tests, pH was measured at the beginning of each test and at the end of each batch after the programmed leaching time. Figure 107 reports measured pH values for each time step.

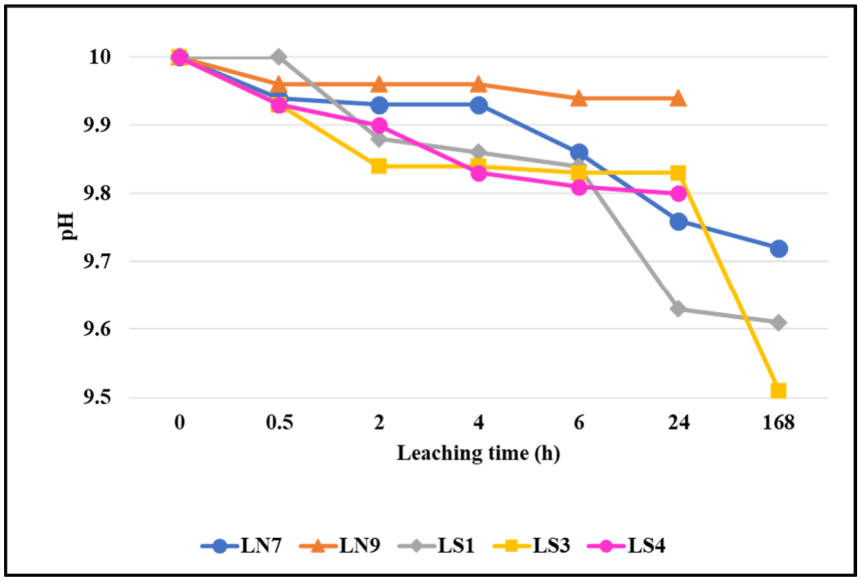
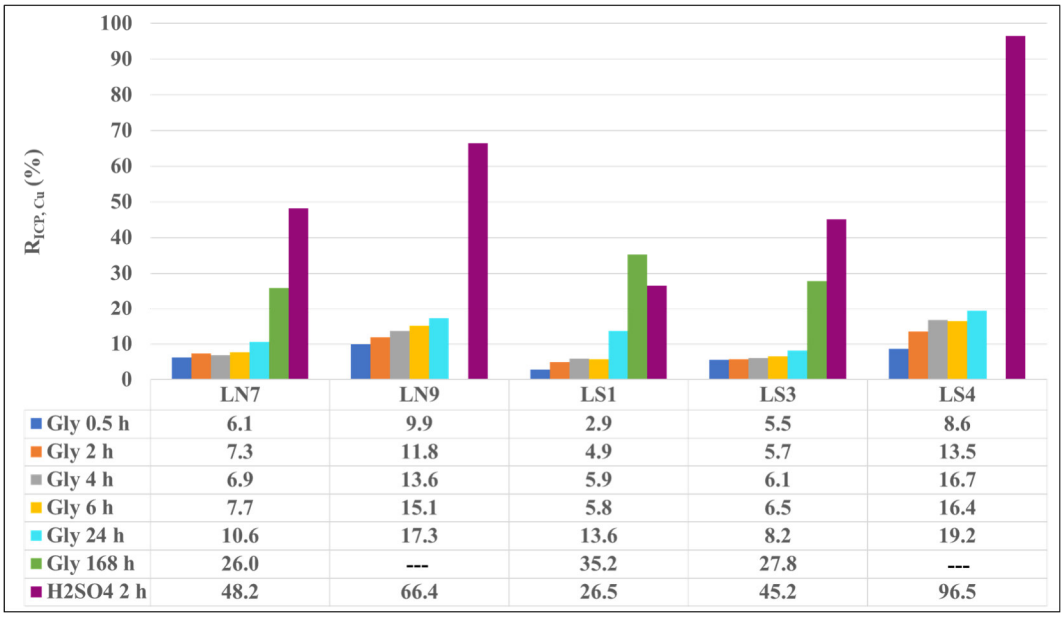


Figure 107 - pH values variation over glycine leaching time for Libiola mine waste samples.

According to the performed measurements, a general trend in decreasing pH can be observed over the considered leaching times and samples. In most cases, after 24h, the pH variation reached the most consistent variation. For samples that were tested until 168 h (7 days) leaching time, the variation appeared to be aligned with the decreasing trend, especially for sample LS3, which showed a pH drop to 9.5.

6.6.2.2 Post-leaching characterisations and metal recovery evaluation

Post-leaching leachate solutions were analysed by ICP-OES for quantification of Cu and Fe, and metal recoveries (R_{ICP}) were calculated according to the described formula (***Equation 4***). Figure 108 shows the calculated R_{ICP} values for each tested sample for glycine leaching at different times and for sulphuric acid after 2 hours. Full data are reported in the ***Appendix D.6***.



	LN7	LN9	LS1	LS3	LS4
Gly 0.5 h	6.1	9.9	2.9	5.5	8.6
Gly 2 h	7.3	11.8	4.9	5.7	13.5
Gly 4 h	6.9	13.6	5.9	6.1	16.7
Gly 6 h	7.7	15.1	5.8	6.5	16.4
Gly 24 h	10.6	17.3	13.6	8.2	19.2
Gly 168 h	26.0	---	35.2	27.8	---
H2SO4 2 h	48.2	66.4	26.5	45.2	96.5

Figure 108 - R_{ICP} calculated values for Cu after glycine leaching (Gly) and sulphuric acid leaching (H_2SO_4), for each of the tested Libiola mine waste samples .

According to the graph, Cu recovery by glycine leaching reached its maximum value after 168h for samples LN7 (26.0%), LS1 (35.2%), and LS3 (27.8%), while after 24 h, sample LN9 reached 17.3% recovery, and LS4 had an overall 19.2% Cu recovery, according to ICP-OES measurements. Sulphuric acid leaching produced, in general, higher recoveries of Cu, being 48.2 % for LN7, 66.4% for LN9, 45.2% for LS3 and 96.5% for LS4. Only for sample LS1, Cu recovery after 168h of glycine leaching was higher than the sulphuric acid leaching recovery rate (26.5%).

In Figure 109, glycine recovery values are plotted as a function of leaching time.

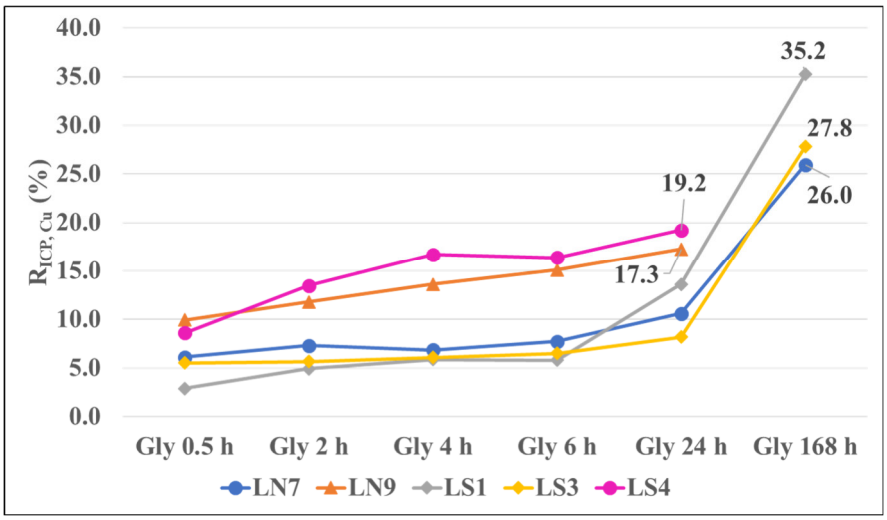


Figure 109 - R_{ICP} values for Cu as a function of glycine leaching time for the tested Libiola mine waste samples.

According to the graph, an increasing trend in Cu recovery over time was observed for the entire dataset. For samples LN7 and LS3, recovery values remained nearly constant during the first 24 hours, reaching a maximum recovery of about 10%. Between 24h and 168h, recovery progressively increased, reaching the maximum recovery.

Sample LS1 showed a nearly constant recovery up to 6 hours, followed by a sharp increase after 24 hours. After 168h, recovery was almost doubled, reaching its maximum value.

Samples LN9 and LS4 displayed different behaviours over time. In particular, LN9 was characterised by a steady increase in recovery during leaching time, but most of the achieved recovery was reached in the first 6 hours, resulting in a residual recovery in between 6 and 24 hours of leaching time. In contrast, sample LS4 reached nearly maximum recovery values just after 4h leaching, showing no great increase after reaching 24h.

Overall, glycine leaching resulted in low copper recoveries, leaving most of the estimated mass of metal in the residual solid.

In Figure 110, R_{ICP} values calculated for Fe associated with maximum glycine leaching time were compared to the values obtained after sulphuric acid leaching, highlighting the leaching selectivity of the proposed methods.

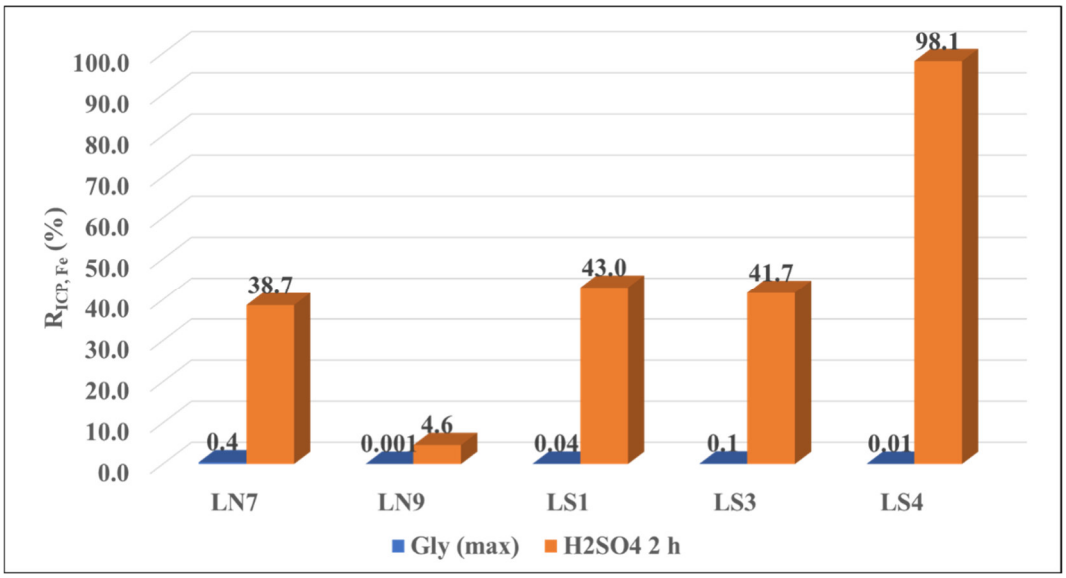


Figure 110 - Comparison of R_{ICP} values for Fe, considering the maximum glycine leaching time and sulphuric acid leaching for Libiola mine waste samples.

Fe recovery appeared to be nearly absent after glycine leaching, always being lower 0.5%. On the other hand, sulphuric acid leaching extracted most of the available iron in samples LN7, LS1, LS3 and LS4, showing a poor selectivity on the target metal Cu, even if associated to higher Cu recoveries (Figure 108). Sample LN9 was characterised by a low Fe recovery, probably related to its mineralogy being mostly composed of silicate minerals, such as lizardite and chlorite.

6.6.2.3 R_{ICP} and R_{XRF} metal recovery comparison

R_{XRF}, as defined by ***Equation 5***, values were calculated after HH-XRF chemical characterisation of residual solids (full data reported in ***Appendix D.7***) and were compared to R_{ICP} values calculated after ICP-OES on leachate solutions, as reported in Figure 111.

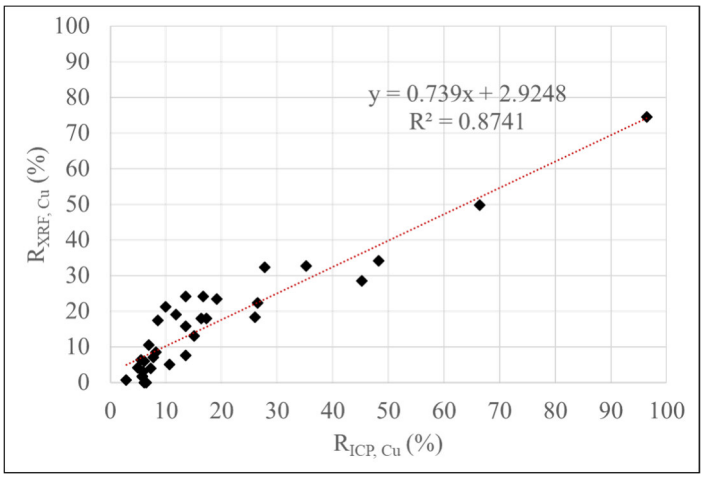


Figure 111 - Comparison of R_{ICP} and R_{XRF} values for Cu, obtained after post-leaching characterization of Libiola mine waste samples

R_{XRF} values showed a good correlation with R_{ICP}. Recovery calculated from HH-XRF results leads to an underestimation of the effective recovery, proven by an angular coefficient of the interpolation line lower than 1. This trend could be attributed to the intrinsic differences in the analytical methods used. In particular, ICP-OES is a calibrated methodology able to detect very low amounts of the target elements, having good sensitivity. On the other hand, HH-XRF showed fewer stable readings and difficulties in determining small differences in the concentration of the analysed sample. Therefore, it resulted in being an effective method for a fast and easy-to-use method in the lab for a preliminary determination of the metal recovery after leaching, needing a data validation for lower differences in concentration after leaching.

6.7 Final remarks

Relevant mine waste dumps are present in the surroundings of the abandoned Libiola copper mine. These dumps are mapped in the ISPRA mine waste database and were known in the academic literature. The study areas were mainly free of vegetation according to NDVI analyses, and they were identified as the North dump and the South dump.

ERT geophysical surveys were performed to determine the thickness of the accumulated mine waste materials for a preliminary determination of total indicated volumes, which were evaluated to be in the range 133,000-206,200 m^3. Moreover, the total estimation, including the inferred quantities, resulted in around 1.6 Mm^3, on average.

A sampling campaign was conducted on the accessible mine waste dumps, resulting in a total of 22 samples collected. The collected materials were characterised by HH-XRF, ICP-MS and XRPD. Quantitative mineralogical analyses showed the presence of different mineral phases in the two considered dumps, showing the presence of gangue and oxidised mineral phases, and residual ore minerals such as pyrite and chalcopyrite.

Chemical analyses showed that Cu was the most abundant CRM, having an overall average concentration between 0,44% and 0,65% and a relative abundance more than 100 times higher than the average crustal abundance. Furthermore, 8 heavy metals were found to be in concentrations exceeding environmental thresholds fixed by Italian Laws, being in particular Co, Ni, Se, Sn, V and Zn for agricultural soils limit, while Cu and Cr being over the industrial soils limit.

Hydrometallurgical reprocessing was selected to assess the possibility of recovering Cu from the analysed material. Five samples were crushed and milled until reaching a p80 < 75 μm. Leaching tests include the use of alkaline pH and glycine, an eco-friendly amino acid. Further, a sulphuric acid leaching test was also performed on the samples for results comparison.

Glycine leaching recovered a maximum of 35.2% of Cu, highlighting a limited efficiency in recovering the relevant amount of this metal contained in the samples, but limiting recovery of Fe in the leaching solution. By contrast, sulphuric acid leaching resulted in higher Cu recoveries for most of the considered samples, showing better performances when compared to innovative green leaching methodologies, but resulting also in relevant amounts of Fe in the leachate solutions.

These findings provided a basis for assessing preliminary possibilities to recover CRMs from Libiola's waste rocks. However, the need for energy-demanding crushing and milling to achieve very fine particles before hydrometallurgical treatment, combined with limited recoveries using environmentally friendly reagents, may pose constraints for larger-scale reprocessing operations. On the other hand, the higher Cu recovery obtained using sulphuric acid leaching could be considered a promising alternative. This method

could reduce the need for fine grinding, enhancing the economic viability of well-known extraction methods such as heap leaching. At the same time, the enhanced environmental risks associated with the use of strong acids and regulatory constraints should be carefully considered in the possibility of potential full-scale applications.

Chapter 7

7. Case Study 3: Fenice-Capanne, Tuscany, Italy

7.1 Site description

7.1.1 Geological setting and historical mining activities

Fenice Capanne mine is located 5 km south-east of the town of Massa Marittima (Grosseto, Tuscany) in the "Colline Metallifere" region. The mining area is situated between the localities of Poggio al Guardone and Poggio ai Frati, and it extends following a North-South oriented 4.5km long strip until the locality of Pesta del Campiglione (Gilli, 1984).

According to Mascaro et al. (2001), the lithologies present in the areas can be grouped as follows:

- Monticiano − Roccastrada Unit, containing anhydrites, phyllites and siliciclastic formations.
- Tuscan Nappe Unit, comprising anhydrites, limestones and marly limestones
- Ophiolitic Unit, including carbonatitic and phyllitic flysch.
- Neoautochtonus Unit, composed of lacustrine and marine sediments.

The area is characterised by several north-south trending faults with a dip angle of 45-50° in the East direction, extending over a length of about 3 km. These structures were responsible for the overlapping of flysch over phyllites. The Fenice Capanne ore body is constituted by mineralised lodes hosted in the phyllite formations or at the contact between phyllitic schists and cavernous limestones (Figure 112) (Gilli, 1984).

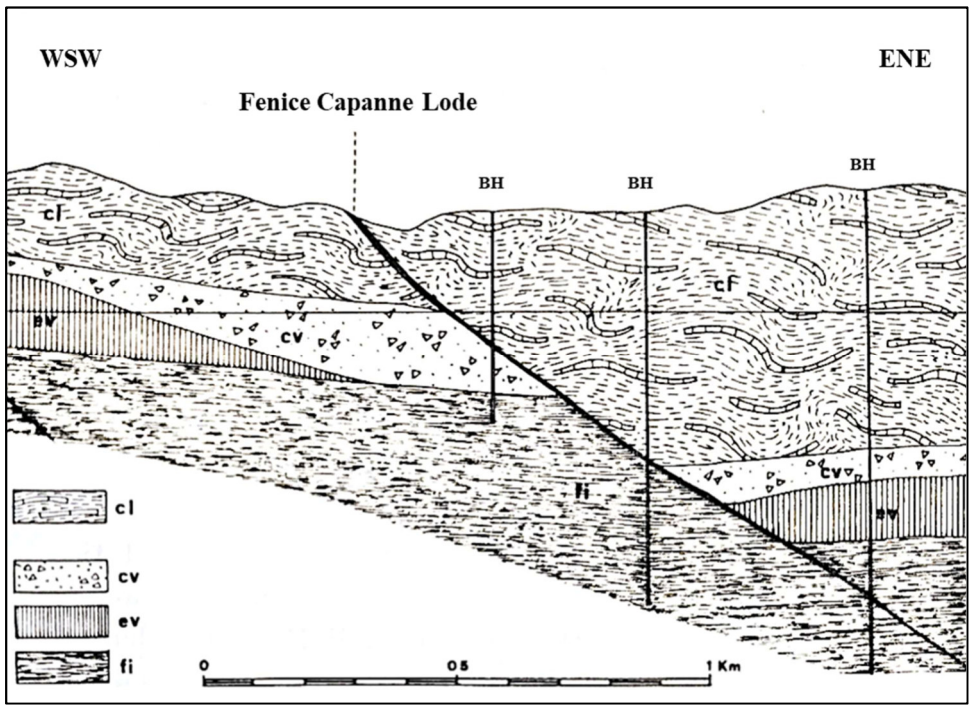


Figure 112 - Geological section sketch of the Fenice Capanne Lode. Legend: cl - Flysch; cv - Cavernous limestone; ev - Anhydrites; fi - Phyllites with anhydrite intercalations; BH - Exploration boreholes. (modified after Arisi Rota et al., 1971)

The Fenice Capanne deposit can be classified as a Cu, Pb, Zn and Ag polymetallic hydrothermal sulphide ore body. The mineralisation distribution is not uniform along the lode; as a result, authors divided it into two main sectors: the Central-Northern and the Southern sectors (Arisi Rota et al., 1971; Gilli, 1984; Mascaro, Benvenuti, Corsini, Costagliola, Lattanzi, Parrini, et al., 2001).

The Central-Northern sector is characterised by a higher metamorphic grade determined by the presence of a skarn containing epidote, hedembergite, quartz and carbonates, while the ore minerals are mainly represented by pyrite and chalcopyrite having a Cu grade ranging between 0.3% and 8%, sulfosalts, and traces of sphalerite, galena, bismutite, arsenopyrite and pyrrhotite. Gangue minerals are represented by prevalent quartz, calcite, siderite, chlorite and sericite.

The Southern sector is characterised by a mixed sulphide mineralisation, being pyrite-chalcopyrite occurrences replaced by galena and coarse-grained sphalerite with a 1÷4.5% Pb + Zn grade and a Cu grade of about 0.3%. Gangue minerals in this sector are quartz and calcedony with minor zinc oxides (Gilli, 1984; Mascaro, Benvenuti, Corsini, Costagliola, Lattanzi, Parrini, et al., 2001).

Historically, the Fenice Capanne mine is part of the wider mining district of Massa Marittima, in Southern Tuscany. In the whole area, mining activities, although in intermittent phases, had been present since Etruscan times. In the Middle Ages, mining activity reached its most active period, leaving behind several small-scale shafts and roasting residues in the area between Serabottini and Fenice-Capanne lodes. Between the 1500s and the early 1900s, the mining industry in the area was in a quiescent period, characterised by small operations for local raw materials needs. Starting from the first half of the 19th Century,

thanks to the modern industrial revolution, mining operations resumed at an industrial scale in the Fenice Capanne area. As stated by Arisi Rota et al. (1971), the copper-enriched part of the lode (Central-Northern sector) was entirely exploited until level 100 m.a.s.l., and some attempts to proceed at greater depths were discouraged by heavy water inflows. By contrast, the Southern sector was actively exploited, feeding the flotation plant with a run-of-mine having a total 6% Zn+Pb+Cu grade with prevalent sphalerite, associated with 12% pyrite content and associated with accessory metals such as Ag and Cd.

From the 1970s, the mine entered its declining phase. After a property change, from Montecatini to EGAM and then to SOLMINE in 1973, which led to a renewed industrial and mining plan, uncertainties persisted due to its limited mixed Pb-Zn sulphides resources, considered sub-economical for the mineral market of that period. Consequently, the mine was downgraded to a marginal production site characterised by small and intermittent production phases (Polvani, 2020).

The production activity ceased in 1985, when the site was definitively declared economically unviable with the subsequent abandonment of the underground operations and processing facilities (Benvenuti et al., 1999; Mascaro, Benvenuti, Corsini, Costagliola, Lattanzi, Morelli, et al., 2001; Pistolesi, 2024; Polvani, 2020).

7.1.1.1 The mineral processing plants

Despite complex industrial and economic circumstances, SOLMINE equipped the mine with a modern beneficiation plant designed to improve ore recovery and concentration, replacing the old mineral processing facilities operated from 1953 to 1978. The old plant consisted of a single processing line for the separation of mixed sulphides, having an overall recovery of 43 % for chalcopyrite, 72% for galena, 63% for sphalerite, and 37% for pyrite. The final discharged tailings contained, on average, 1.23 % of Zn, 0.12 % Pb, 0.14% Cu, 2.5% S and 6.34% of Fe (Gilli, 1984).

According to Gilli (1984), the mineralogical inhomogeneity of the mined horizons oriented the design of the new beneficiation plant to produce pyrite, chalcopyrite, sphalerite, and galena concentrates starting from two different types of feeding materials: chalcopyrite-pyrite ore from the Central-North sector and mixed sulphide ore extracted in the Southern sector.

Linea 2000, activated in March 1984, was the line dedicated to the beneficiation of mixed sulphide ore, having a nominal capacity of 650 t/day and including crushing, screening, grinding, flotation, thickening, filtration stages and a final storage facility for concentrates. The crushing and screening section was operated for 10 hours per day, producing a −16+0.200 mm material used as grinding feed, and a finer fraction < 200 μm sent to thickeners. Grinding was performed in two stages, firstly using a bar mill for a controlled size reduction, and secondly using two ball mills operating in parallel for obtaining a finer product. Subsequently, a series of hydrocyclones classified the ground material, obtaining an overpassing fraction having a p80 = 104 μm, sent to the flotation

stage. The froth flotation sector (Figure 113) consisted of two main circuits: the galena-chalcopyrite and the sphalerite-pyrite. Galena and chalcopyrite were floated using zinc sulphate and sodium thiosulphate as sphalerite and pyrite depressants, xanthate as a collector, and frothers, then additionally separated in a dedicated circuit using sodium cyanide at pH 9.5-10.0 as chalcopyrite depressant. Sphalerite was floated after activation with copper sulphate, while pyrite was depressed with quick lime, reaching a pH of 10. Residual gangue and pyrite minerals were sent to the tailings impoundment. All concentrates were filtered using rotary vacuum filters, obtaining a moisture content lower than 10%. Chalcopyrite and galena concentrates produced by *Linea 2000* processing unit contained up to 200 g/t and 1100 g/t of Ag, respectively. In the operational regime, this sector achieved 66.2% recovery for chalcopyrite, 76.1% for galena, 61.5% for sphalerite, and 64% for pyrite, significantly improving the products' grade compared to the old processing plant (Gilli, 1984).

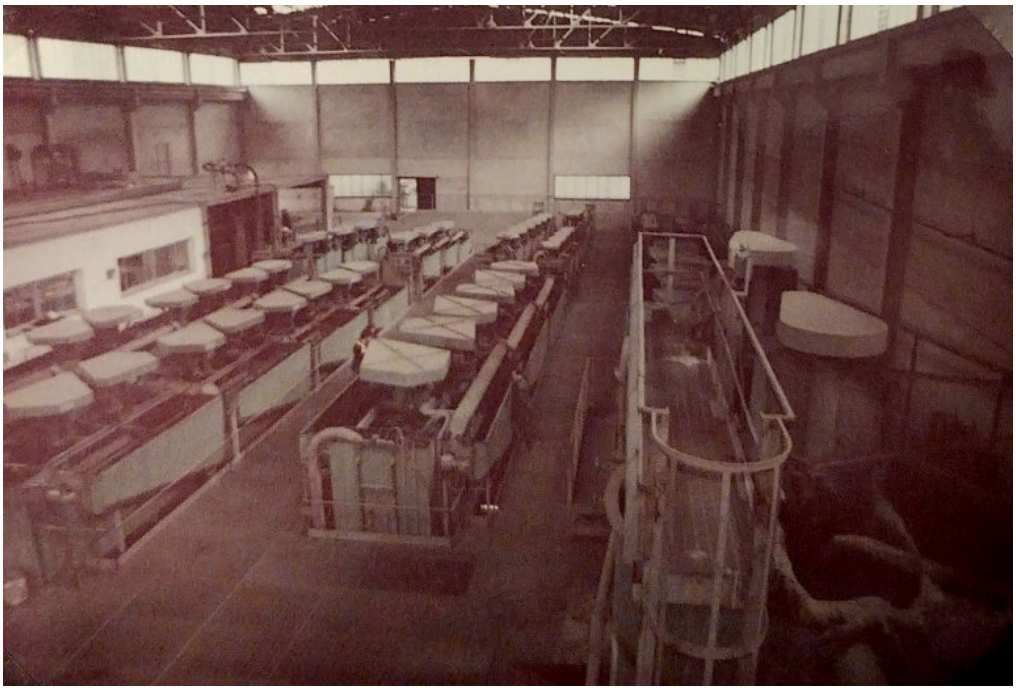


Figure 113 – "Linea 2000" flotation cells in the Fenice Capanne mineral processing plant (1984). (Photo credits: M. Gilli, 1984)

In parallel*, Linea 1000* was activated in July 1983 and was the line dedicated to chalcopyrite-pyrite ore (average grades: 8% S, 1÷1.5% Cu). This processing plant was designed to have a nominal capacity of 1550 tons per day, consisting of a crushing and screening sector configuration similar to *Linea 2000* but with different operational parameters for grinding and flotation sectors. The grinding sector (Figure 114) consisted of a sequential bar mill-ball mill scheme with a final classification performed by hydrocyclones, producing a material having p80 = 80 μm, before flotation. The froth flotation sector operated a selective separation of chalcopyrite and pyrite. Chalcopyrite was recovered using xanthate as a collector, frothers and quick lime as a temporary suppressant for pyrite and pH modifier for

obtaining values around 11.5. Pyrite was then recovered from gangue minerals by adding small quantities of xanthate for its activation and flotation. In total, the chalcopyrite circuit consisted of 4 rougher cells and 2 scavenger and cleaner series of cells, while the pyrite circuit had 3 rougher cells followed by 7 rougher and cleaner cells. The obtained concentrates were sent to thickeners, then vacuum filtered on rotary filters, and finally sent to stockpiling areas. This beneficiation line was capable of having a 60 t/h throughput while obtaining a 94% recovery of Cu and 88% recovery of S. Materials sent to tailing ponds had a residual 0.06% Cu grade and 1.21% S grade (Gilli, 1984).

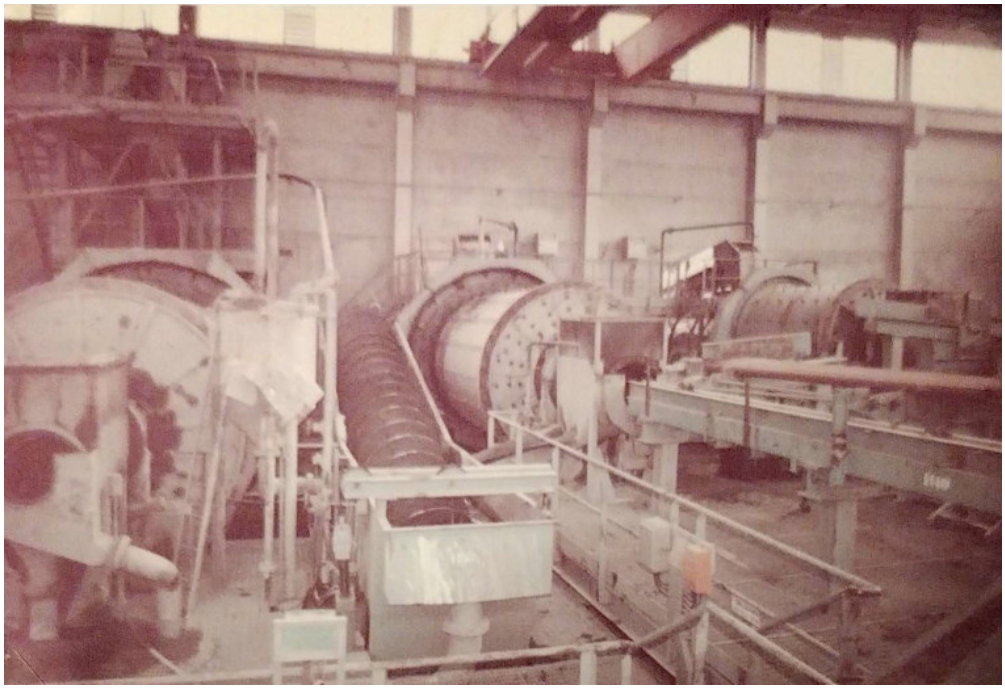


Figure 114 - "Linea 1000" grinding mills in the Fenice Capanne processing plant (1984). (Photo credits: M. Gilli, 1984)

Overall, the two lines were characterised by an average loss of 2÷3% of the total production. Process water originated from the mine's drainage tunnel located at +101 m level, delivering a flow of about 300 l/s. Mine water was pumped to a tank located at a higher elevation than the plant, allowing it to flow by gravity to the processing plant. The plant water consumption was estimated to be around 20 m^3/h; no water recirculation was implemented, and end-of-process water was sent to settling and treatment ponds before discharge (Gilli, 1984).

7.1.2 Mine waste dumps and tailings storage facilities

Fenice Capanne's mining activities left different types of mining and industrial waste in the surrounding areas. According to Benvenuti et al. (1999) and Mascaro et al. (2001), waste accumulated in the area can be classified as follows:

- Roasting heaps: produced between 1888 and 1930 from low-grade ore (< 4% Cu);
- Waste rocks: accumulated in 15-20 m high heaps, and partially revegetated.
- Tailings: accumulated in 5 different tailings storage facilities (TSFs) basins.

The oldest TSF was in use between 1950 and 1956, where tailings were discharged unconfined onto pre-existing roasting heaps, creating erosion channels and accumulation of fine-grained materials up to 3m thick. The more recent TSFs are represented by Basin 1 and Basin 2, realised by culverting the Fosso dei Noni beneath the two TSFs. Basin 1 operated from 1957 to 1964, while Basin 2 was active between 1964 and 1982. These are the largest basins over the site, covering an area of approximately 500×150 m and reaching a depth of about 30m, with an estimated volume of material contained of about 0.85 Mm^3. Basins 3 and 4 are the most recent and smallest of the area, used during the last operational phase of the plant (1982-1984). Each is about 10m deep and occupies an area of about 100×60 m (Benvenuti et al., 1999; Mascaro, Benvenuti, Corsini, Costagliola, Lattanzi, Parrini, et al., 2001).

According to the ISPRA official mine waste national database from 2022, for the Fenice Capanne, two mine waste accumulation areas were reported (Table 59). The types of waste reported are "*Settling Ponds*" and "*Waste dumps*", potentially containing As, Cd, Mn, Pb, Cu, and Zn for the first, and Sb, Ag, As, Co, Cr, Mn, Ni, Pb, Cu, Se, and Zn for the second. The sanitary risk associated with this waste was classified as "*Low*" (Serra & Andrisani, 2022).

Figure 115 shows the aerial view and location of the waste rock dump, roasting dump, and tailings basins for the Fenice Capanne mine and the soil coverage of the area.

Table 59 – Fenice Capanne mine waste accumulation areas position and classification according to ISPRA national mine waste database (ISPRA, 2022)

Name (ISPRA)	**X (*Gauss Boaga West*)**	**Y (*Gauss Boaga West*)**	**Type**
Fenice Capanne Bacini	1656231	4763856	Settling ponds
Fenice Capanne Roste Antiche	1656251	4764083	Waste dumps

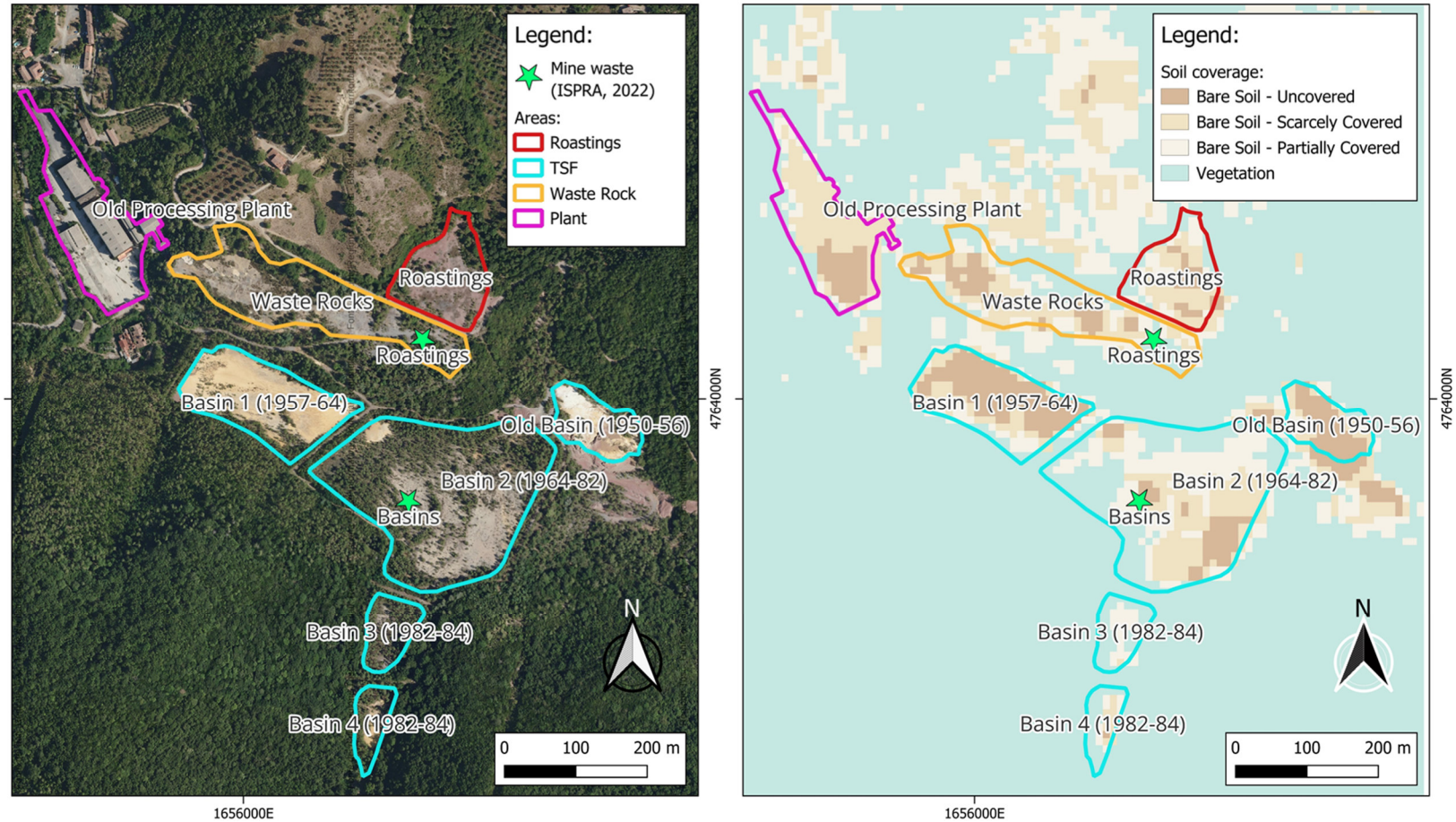


Figure 115 - (Left) Position of mine waste accumulation areas around Fenice Capanne mine according to ISPRA database (ISPRA, 2022) and other authors (Benvenuti et al., 1999, Mascaro et al., 2001); (Right) NDVI soil coverage layer and considered mine waste areas (Source: Google Satellite Image. Coordinate System: Gauss Boaga West).

Some authors conducted a sampling and characterisation campaign in the late 1990s to assess environmental risks associated with the abandoned waste in the areas and the potential acid generation (Benvenuti et al., 1999; Mascaro, Benvenuti, Corsini, Costagliola, Lattanzi, Morelli, et al., 2001, 2001). Tailings and roasting residues were systematically sampled to capture their spatial variability. Mineralogical and geochemical analyses were performed to determine heavy metals content such as Fe, As, Bi, Cu, Mn, Pb, and Zn, to evaluate the potential environmental limit of metals. Mineralogical phases found in tailings samples were sulphides, especially pyrite and arsenopyrite, oxides and silicates associated with secondary minerals originated from weathering processes. Additionally, roastings were characterised by iron oxides and other oxidised phases resulting from the roasting of sulfide ores.

Geochemical characterisation revealed relevant concentrations of heavy metals, such as Pb, Zn, and As. The fine-grained materials found in TSFs showed elevated leachability and low buffering capacity, highlighting their possible acid generation associated with an elevated mobility of metals, causing potential groundwater and surface water contamination (Mascaro, Benvenuti, Corsini, Costagliola, Lattanzi, Parrini, et al., 2001).

Protano and Riccobono (2002) studied that stream waters in the surrounding areas of the mine were characterised by unusually high concentrations of REEs, due to rainwater leaching of the oldest TSF, which was characterised by a higher presence of iron oxides. These phenomena were associated with the acid drainage of waste piles, which enhanced the mobility of REEs from Fe-rich minerals, posing environmental concerns regarding the long-term management of the roasting piles. Moreover, Pignattelli et al. (2012) confirmed heavy contamination of soils around mine waste areas in the Fenice Capanne area, identifying autochthonous plant species growing on the roasting piles able to potentially stabilise heavy metals and reduce further potential metal mobilisation in the waste dumps.

Since 2009, Eni Rewind S.p.A. has been legally responsible for the securing and environmental rehabilitation of the Fenice Capanne mine waste dumps, in accordance with governmental and local authorities agreements (Eni Rewind S.p.A., 2025).

Other studies or information related to large-scale environmental restoration or specific characterisation actions of mine waste aiming at recovering valuable metals were not found in the literature.

7.2 Tailings and roasting samples

Samples used in this work were probably collected in the 1980s in the Fenice Capanne mine site and were preserved in the historical repository of mining samples of the Department of Environmental, Land and Infrastructures Engineering (DIATI).

According to the archive information recovered, samples were collected in the two inactive TSFs at that time, corresponding to the previously described Basin 1 and Basin 2, in the Old Basin and from roasting heaps. In total, 20 samples were considered, re-labelling them with nomenclature from FC1 to FC20. Samples in good preservation status and having clear cataloguing information were considered for this study. Table 60 summarises the number of samples considered and their reported provenance.

Table 60 - Historical samples from Fenice Capanne mine waste accumulation areas considered in this study.

Samples	Area
FC1, FC2, FC4, FC5, FC7	Basin 1
FC9, FC10, FC11, FC12, FC13	Basin 2
FC15	Old Basin
FC20	Roasting
Total n. of samples	
12	

7.3 Chemical and mineralogical characterisation

The samples considered from the Fenice Capanne mine waste dumps were analysed to define chemical and mineralogical features according to the following methodologies:

- HH-XRF – (***Par. 2.5.2***)
- ICP-MS – (***Par. 2.5.3***)
- XRPD – (***Par. 2.4.4***)

This characterisation aimed to evaluate the content of CRMs and SRMs in the waste material and address possible lab-scale reprocessing options for assessing the recovery of valuable metals contained.

7.3.1 Chemical characterisation results

7.3.1.1 HH-XRF characterisation results

HH-XRF analyses were performed to obtain chemical assays of major and trace elements according to the capabilities and calibrations of the available

equipment. Table 61 shows the summary statistics of detected elements in the considered tailings samples. Full result tables are available in ***Appendix E.1***.

*Table 61 - HH-XRF summary statistic for selected major and minor elements for Fenice Capanne tailings samples (n=11). *The LOD/2 rule was applied to values below the detection limit*

	Major Elements							
	Al (%)	***Ca (%)***	***Fe (%)***	***K (%)***	***Mg (%)***	***Mn (ppm)***	***Si (%)***	***Ti (%)***
Max	4.8	6.0	7.6	3.0	1.0	1.0	26.8	0.3
Min	2.4	0.4	5.0	1.5	0.2	0.1	16.2	0.1
Mean	3.3	2.5	6.3	2.5	0.6	0.6	23.0	0.2
Median	3.3	0.7	6.6	2.6	0.5	0.7	24.9	0.2
	Minor Elements							
	Ag* (ppm)	***As (ppm)***	***Bi (ppm)***	***Cd* (ppm)***	***Co* (ppm)***	***Cr (ppm)***	***Cu (ppm)***	***Mo (ppm)***
Max	16.0	845	298	79	216	120	8,245	1.6
Min	0.4	162	18	0.5	21	33	243	0.7
Mean	6.0	394	93	15	44	71	2,495	0.9
Median	3.0	339	43	8	28	74	496	0.8
	Nb* (ppm)	***Ni (ppm)***	***P* (ppm)***	***Pb (ppm)***	***Rb (ppm)***	***S (%)***	***Sb (ppm)***	***Se* (ppm)***
Max	9.2	87	3,687	5,353	249	5.8	79	7
Min	4.0	39	467	121	67	1.6	19	1
Mean	5.6	66	1,622	1,191	169	3.4	46	2
Median	4.7	68	796	848	105	3.3	41	2
	Sn (ppm)	***Sr (ppm)***	***Tl (ppm)***	***U (ppm)***	***V (ppm)***	***Y (ppm)***	***Zn (ppm)***	***Zr (ppm)***
Max	10	392	14	13	106	19	21,831	105
Min	1.1	49	2	1	27	8	518	48
Mean	3.6	150	7	5	65	13	9,645	64
Median	1.1	98	8	4	63	14	11,139	56

For Fenice Capanne tailings, Si was the most abundant major element, showing a mean concentration of 23.0% (min 16.2% – max 26.8%). Fe and Al were characterised by lower concentrations, being on average 6.3% (min 5.0% – max 7.6%) and 3.3% (min 2.4% – max 4.8%). Other detected major elements were Ca (2.5%, min 0.4 – max 6.0%), K (2.5%, min 1.5% – max 3.0%), and Mg (0.6%, min 0.2% – max 1.0%). Ti and Mn were the least abundant, having a mean concentration of 0.2% (min 0.1 – max 0.3) and 0.6% (min 0.1 – max 1.0%), respectively.

Regarding minor elements, in particular strategic and critical metals, Cu resulted in the most abundant, having an average concentration of 2,495 ppm (min 243 ppm – max 8,245 ppm). Among others, As showed mean concentrations of 394 ppm, ranging between a minimum assay of 162 ppm to a maximum of 845 ppm, while Bi was assayed on average 93 ppm (min 18 ppm – max 298 ppm). Other critical metals were assayed in traces, such as Ni (66 ppm, 39 ppm – 87 ppm), Sb (46 ppm, 19 ppm – 79 ppm), Co (44 ppm, 21 ppm – 216 ppm), and V (65 ppm, 27 ppm – 106 ppm).

Other minor metals detected in high concentrations were Zn and Pb. The first showed an average concentration of 9,645 ppm, ranging between a minimum 512 ppm and a maximum of 21,831 ppm, while the second had a mean assay of 1,191 ppm, in a range between 121 ppm and 5,353 ppm. For detectable non-metals, S assayed on average 3.4 % (min 1.6 % – max 5.8%), while P had a mean concentration of 1,622 ppm (min 467 ppm – 3,687 ppm). Regarding precious metals, Ag was assayed at a mean concentration of 6.0 ppm (min 0.4 ppm – max 16.0 ppm).

Table 62 shows HH-XRF results for the sample from roasting heaps in the Fenice Capanne area.

Table 62 - HH-XRF results for major elements and selected minor elements from Fenice Capanne roasting sample FC20.

Fenice Capanne Roastings (n = 1)

Major Elements							
Al (%)	***Ca (%)***	***Fe (%)***	***Mg (%)***	***K (%)***	***Mn (ppm)***	***Si (%)***	***Ti (ppm)***
2.3 ± 0.1	0.4 ± 0.01	13.5 ± 0.01	< 0.2	1.1 ± 0.1	302 ± 16	26.2 ± 0.1	943 ± 96
Minor Elements							
Ag (ppm)	***As (ppm)***	***Bi (ppm)***	***Cd (ppm)***	***Co (ppm)***	***Cr (ppm)***	***Cu (ppm)***	***Mo (ppm)***
48 ± 1	741 ± 17	566 ± 9	< 1.3	< 148	< 19	2,925 ± 22	< 5.6
Nb (ppm)	***Ni (ppm)***	***P (%)***	***Pb (ppm)***	***Rb (ppm)***	***S (%)***	***Sb (ppm)***	***Se (ppm)***
20 ± 2	37 ± 7	< 0.4	2,062 ± 13	65 ± 2	1.2 ± 0.02	78 ± 2	< 3
Sn (ppm)	***Sr (ppm)***	***Tl (ppm)***	***U (ppm)***	***V (ppm)***	***Y (ppm)***	***Zn (ppm)***	***Zr (ppm)***
15 ± 1	97 ± 2	< 10	< 3.6	55 ± 6.5	463 ± 10	913 ± 10	7,677 ± 12

The most abundant major elements detected in the sample were Si and Fe, having concentrations of 26.2 % and 13.5%. respectively. Other major elements detected were Al (2.3%), K (1.1%), Ca (0.4%), Ti (943 ppm), and Mn (302 ppm).

Regarding critical and strategic metals, Cu was found in a concentration of 2,925 ppm, while As assayed 741 ppm, and Bi assayed 566 ppm. Other critical elements were found in traces, in particular Sb (78 ppm), V (55 ppm), Ni (37 ppm), and Nb (20 ppm). Other minor elements detected with higher concentrations were Zr (7,677 ppm), Pb (2,060 ppm), Zn (913 ppm), and Y (463 ppm). Precious metals such as Ag had a concentration of 48 ppm. For detectable non-metals, S showed a concentration of 1.2%, while P remained under the determination limit (< 0.4 %).

7.3.1.2 ICP-MS characterisation methods

ICP-MS analyses were performed to obtain more details for the determination of CRMs, SRMs and trace elements. This characterisation was also performed to validate HH-XRF assays and implement those elements that were non-detectable or fell below detection limits. In Table 63, the summary statistics for selected elements in Fenice Capanne tailings samples are reported. Full data are available in ***Appendix E.2*** and ***Appendix E.3***.

Table 63 - ICP-MS summary statistics for selected elements for Fenice Capanne tailings samples (n = 11). (: ALS ME-MS81 method; [a]: Values exceeding upper LOD were considered without any modification)*

	Ag (ppm)	***As (ppm)***	***Bi (ppm)***	***Cd (ppm)***	***Co (ppm)***	***Cr (ppm)***	***Cu (ppm)***	***In (ppm)***
Max	17	829	272	69	34	113	8,320	0.53
Min	1.7	215	6	0.5	7	49	271	0.03
Mean	7.5	457	69	14	23	76	2,498	0.17
Median	4.5	452	23	8	24	73	537	0.08
	Mo (ppm)	***Ni (ppm)***	***Pb (ppm)***	***Sb (ppm)***	***Sc* (ppm)***	***Se (ppm)***	***Te (ppm)***	***Tl (ppm)***
Max	1.7	67	4,960	81	15.9	5.0	0.4	6.8
Min	0.7	17	123	17	5.8	2.0	0.05	1.5
Mean	1.2	53	1,184	44	9.0	3.1	0.2	2.8
Median	1.1	57	916	36	7.8	2.0	0.1	1.8
	W* (ppm)	***Zn[a] (ppm)***	***Y* (ppm)***	***∑LREE* (ppm)***	***∑HREE* (ppm)***			
Max	25	10,000	22	145	37			
Min	5	532	9	46	15			
Mean	13	7,351	15	82	25			
Median	11	10,000	14	68	23			

Considering critical and strategic elements, Fenice Capanne tailings showed a high concentration of Cu, having an average concentration of 2,498 ppm (min 271 ppm – max 8,320 ppm), while As had a mean concentration of 457 ppm (min 215 – max 829 ppm). Other critical elements such as Co, Ni, Sb, Sc, W, LREE, and HREE had trace concentrations.

Pb and Zn were confirmed to be the most concentrated base metals, having an average concentration of 1,184 ppm (min 123 ppm – max 4,960 ppm) and 7,351 ppm (min 532 – max 10,000 ppm), respectively. Zn determination by ICP-MS was limited to 10,000 ppm, and 7 samples out of 11 exceeded this value (***Appendix E.2***). Precious metals such as Ag, showed an average assay of 7.5 ppm, ranging between a minimum of 1.7 ppm and a maximum of 17 ppm.

Table 64 reports ICP-MS results for the roasting dump sample from Fenice-Capanne mine.

Table 64 - ICP-MS results for selected elements for Fenice Capanne roastings dump sample FC20 (: ALS ME-MS81 method)*

Ag (ppm)	***As (ppm)***	***Bi (ppm)***	***Cd (ppm)***	***Co (ppm)***	***Cr (ppm)***	***Cu (ppm)***	***In (ppm)***
27.6	718	486	0.71	6.5	21	2,820	1.13
Mo (ppm)	***Ni (ppm)***	***Pb (ppm)***	***Sb (ppm)***	***Sc* (ppm)***	***Se (ppm)***	***Te (ppm)***	***Tl (ppm)***
0.51	16.4	1,960	73.1	3	7	0.82	4.7
W* (ppm)	***Zn (ppm)***	***Zr* (ppm)***	***Y* (ppm)***	***∑LREE* (ppm)***	***∑HREE* (ppm)***		
60.4	900	8,030	510	40	513		

The roasting sample exhibited relevant concentrations of critical and strategic raw materials, including Cu (2,820 ppm), As (718 ppm), Bi (486 ppm), and Y (510 ppm). Y contributed to being the most abundant among HREEs (513 ppm). The concentration of other base metals reached 1,960 ppm for Pb, while Zn showed a concentration of 900 ppm. Moreover, Zr had a very high concentration reaching 8,030 ppm, and Ag assayed 27.6 ppm.

7.3.1.3 Comparison of HH-XRF and ICP-MS results

HH-XRF results were compared to ICP-MS assays to assess the reliability of the method. Selected elements were considered for this comparison, in particular, potential recovery target elements from Fenice Capanne mine waste areas. As a result, Cu, Zn, Pb, As, Bi, and Sb were selected for this assessment.

Figure 116(a-f) shows XY plots comparing chemical results for the selected elements.

HH-XRF and ICP-MS datasets for Cu (Figure 116a) showed a good correlation, indicating highly comparable chemical determinations. In detail, the angular coefficient of the interpolating line is nearly equal to 1 (0.985), indicating that HH-XRF determinations were almost equal to ICP-MS determinations with negligible differences. A similar trend was observed for Zn (Figure 116e), where the linear correlation was confirmed, along with close values between HH-XRF and ICP-MS. The comparison for this element was performed only for ICP-MS determinations below the upper LOD of 10,000 ppm.

Figure 116c shows that for Pb, a good correlation of values was found, especially for concentrations up to 2,000 ppm. For higher assays, HH-XRF showed a slight overestimation for this element. Nevertheless, the angular coefficient of the interpolating line showed a value of around 0.92, indicating strongly comparable results between the two methods.

For less concentrated elements, such as As, Bi, and Sb, slight differences in chemical determination were observed. Figure 116b shows that for As the overall correlation is good between HH-XRF and ICP-MS, having an R^2 of about 0.93 but an angular coefficient of 0.86, resulting in an underestimation of the HH-XRF determination if compared with ICP-MS. Regarding Bi (Figure 116d), the datasets showed a good linear correlation but exhibited a systematic HH-XRF overestimation of the assay when compared to ICP-MS. To conclude, Figure 116f

reports the comparison for Sb, for which a good correlation was observed, while HH-XRF results slightly overestimated the ICP-MS assays.

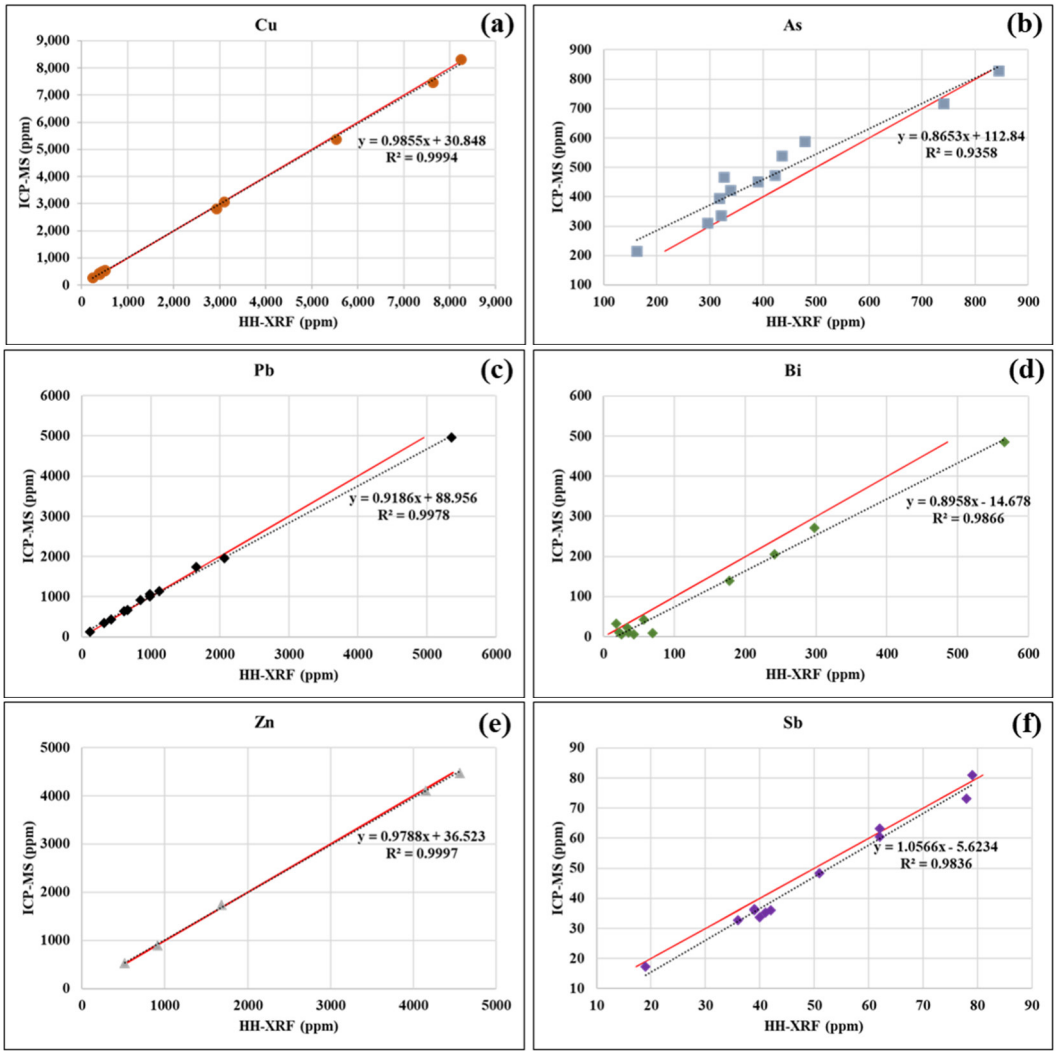


Figure 116 - Comparison of HH-XRF and ICP-MS assays of Fenice Capanne tailings samples for: (a) Cu, (b) As, (c) Pb, (d) Bi, (e) Zn, (f) Sb. Red line: x=y=ICP-MS values.

In general, HH-XRF measurements showed a good reliability in providing chemical determinations both for highly concentrated elements and for trace elements considered.

7.3.2 Mineralogical characterisation results

XRPD analyses were performed for the determination of the main mineralogical features of the material from Fenice Capanne tailings and roasting heaps.

As reported in Figure 117 and Table 65, Fenice Capanne tailings mineralogy was characterised by the dominant presence of quartz (mean 47.4 %, min 19.1 % – max 71.4 %), gypsum (11.1%, 0.1 % – 21.6 %), muscovite (10.7 %, 0% – 31.9 %), clinochlore (10.7 %, 0 % – 27.6 %), sanidine (9.4%, 0 % – 18 %), and pyrite (3.6%, 1 % – 8.8%). Other phases included kaolinite, calcite, and other minor phases. Full data are reported in ***Appendix E.4***.

Waste material from the roasting heaps was characterised by three main phases, being quartz (57.7%), diopside (31.2%), and hematite (11.1%), as reported in Figure 117 and ***Appendix E.4***.

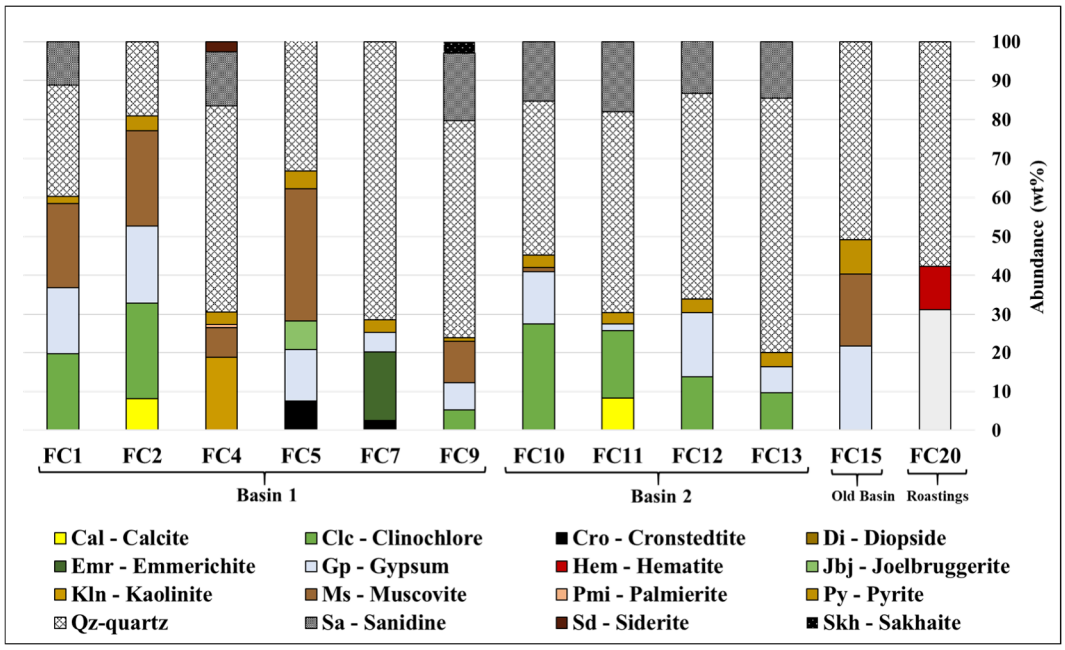


Figure 117 - Quantitative XRPD mineralogical determination for samples from Fenice Capanne accumulation areas (n = 12).

Table 65 – Summary statistics for XRPD mineral phase abundances for Fenice Capanne tailings samples (n = 11).

Mineral (wt%)	Min	Max	Mean
Quartz	19.1	71.4	47.4
Gypsum	0.1	21.6	11.1
Muscovite	b.d.l.	33.9	10.7
Clinochlore	b.d.l.	27.6	10.7
Sanidine	b.d.l.	18	9.4
Pyrite	1	8.8	3.6

Mineral (wt%)	Min	Max	Mean
Kaolinite	b.d.l.	18.6	1.7
Emmerichite	b.d.l.	17.7	1.6
Calcite	b.d.l.	8.3	1.5
Cronstedtite	b.d.l.	7.5	0.9
Joelbruggerite	b.d.l.	7.6	0.7
Sakhaite	b.d.l.	2.9	0.3
Siderite	b.d.l.	2.6	0.2
Palmierite	b.d.l.	1.2	0.1

7.4 Geohemical, mineralogical, and environmental considerations

Geochemical and mineralogical analyses performed produced results comparable with those found in the literature, both for tailings and roasting waste materials. (Benvenuti et al., 1999; Mascaro, Benvenuti, Corsini, Costagliola, Lattanzi, Morelli, et al., 2001; Mascaro, Benvenuti, Corsini, Costagliola, Lattanzi, Parrini, et al., 2001).

From the acquired geochemical data, relative enrichment and abundance information of economically important, critical and strategic raw materials can be extrapolated, as shown in the spider plot reported in Figure 118.

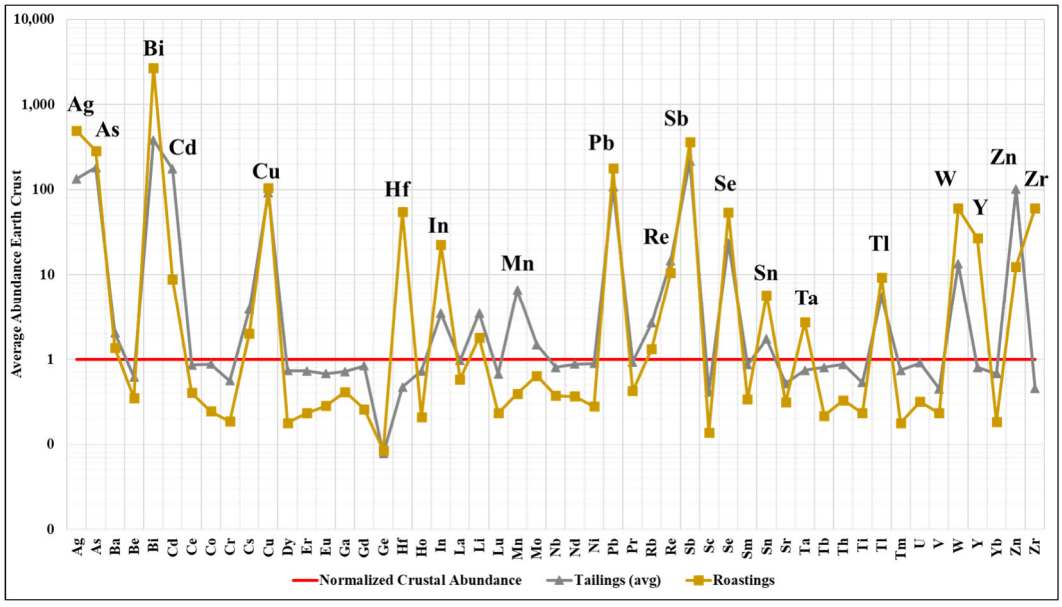


Figure 118 – Spider plot showing geochemistry summary statistic for Fenice Capanne tailings and roastings samples compared to the average crustal abundance values by Rudnick & Gao, 2014

Fenice Capanne tailings resulted in being relatively enriched in elements such as Ag, As, Bi, Cd, Cu, Pb, Re, Sb, Se, W, and Zn, having concentrations at least 10 times higher than the average crustal abundance. Similarly, roastings showed

enrichment in several elements, having relevant enrichment in Ag, As, Bi, Cu, Hf, In, Pb, Re, Sb, Se, Tl, W, Y, Zn, and Zr.

Table 66 reports a more detailed comparison of critical and strategic raw materials assays with the average crustal abundance of elements. For tailings, the most enriched critical element is Bi, reaching 384 times more its Earth's crust concentration, followed by Sb (x219) and As (x183). Cu showed a concentration 93 times higher than crustal abundance, while other considered CRMs, such as W, Li and Mn, exhibited slight enrichments up to 13 times more.

On the other side, roasting waste assays showed that Bi was the most enriched element, with 2,700 times higher than average concentration, while Sb was 366 times more concentrated, and As exceeded by 287 times the average crustal abundance. Another enriched critical element is Cu, having an enrichment of 106 times higher than average. Other elements presenting remarkable enrichments are: W (x60), Hf (x55), and HREEs (x16, mostly attributed to Y concentration).

*Table 66 – Critical and strategic raw materials summary from ICP-MS values compared to crustal abundance concentrations for Fenice Capanne tailings and roasting samples. In bold concentration at least 1x time higher than the average abundance. * (Rudnick & Gao, 2014)*

Critical and strategic element	Crustal abundance* (ppm)	***Tailings (n = 11)***		***Roasting (n = 1)***	
		Mean conc. (ppm)	*Times higher than average crustal abundance*	*Conc. (ppm)*	*Times higher than average crustal abundance*
As	2.5	**457**	***183***	**718**	***287***
Be	1.9	1.2	*0.6*	0.7	*0.4*
Bi	0.18	**69**	***384***	**486**	***2,700***
Co	26.6	23	*0.9*	6.5	*0.2*
Cu	27	**2,498**	***93***	**2,820**	***104***
Ga	16	11.4	*0.7*	6.6	*0.4*
Ge	1.3	0.1	*0.1*	0.11	*0.1*
Hf	3.7	1.7	*0.5*	**202**	***55***
Li	17	**59**	***4***	**31**	***1.8***
Mn	800	**5,269**	*7*	314	*0.4*
Nb	8	6.4	*0.8*	2.97	*0.4*
Ni	59	53	*0.9*	16	*0.3*
Sb	0.2	**44**	***219***	**73**	***366***
Sc	21.9	9	*0.4*	3	*0.1*
Sr	320	166	*0.5*	100	*0.3*
Ta	0.7	0.5	*0.7*	1.9	*3*
V	138	62	*0.4*	32	*0.2*
W	1	**13**	***13***	**60**	***60***
LREEs	92.9	82	*0.9*	40	*0.4*
HREEs	32.3	25	*0.8*	**513**	***16***

The same enrichment comparison was also performed for other base metals and valuable elements contained in the waste materials. As shown in Table 67, several metals were enriched by more than 10 times compared to crustal abundance. In particular, for tailings, the metals exceeding Earth's crustal abundances by 100 or more were Cd (x176), Ag (x134), Zn (x134), and Pb (x108). By contrast, roastings exhibited enrichments higher than 100 times only

for Ag (x493) and Pb (x178). Other elements showed moderate enrichments, for example In, Re, and Se.

*Table 67 – Crustal abundance comparison of base and valuable metals from Fenice Capanne tailings and roasting samples. In bold concentrations at least x10 times higher than average crustal abundance. *(Rudnick & Gao, 2014)*

Element	Crustal abundance* (ppm)	***Tailings (n = 11)***		***Roastings (n = 1)***	
		Mean conc. (ppm)	*Times higher than average crustal abundance*	*Conc. (ppm)*	*Times higher than average crustal abundance*
Ag	0.056	**7.5**	***134***	**28**	***493***
Cd	0.08	**14.1**	***176***	0.71	*9*
In	0.05	0.2	*3*	**1.1**	***23***
Pb	11	**1,185**	***108***	**1,960**	***178***
Re	0.000188	**0.003**	***16***	**0.002**	***11***
Se	0.13	**3**	***24***	**7**	***54***
Sn	1.7	2.9	*2*	10	*6*
Tl	0.5	2.8	*5.6*	4.7	*9.4*
Zn	72	**9,645**	***134***	**900**	***13***
Zr	93	59.5	*0.6*	**8,030**	***86***

The geochemical data collected were also assessed to understand possible environmental contamination related to the presence of mine waste. Chemical assays were compared to Italian Law Decree 152/2006 (Italian Republic, 2006) limits for metallic elements in agricultural and industrial soils (Column A and Column B). In Figure 119, chemical data were normalised against law limits are graphed in order to underline any exceeding value.

Tailings' average assays showed concentration exceeding Column A values for Cd, Co, Se, and Tl, while As, Cu, Pb, Sb, and Zn were higher than Column B limits. Similarly, roasting waste piles are characterised by a concentration of Se, Sn, Tl, and Zn exceeding limits for agricultural soils (Col.A), additionally having As, Cu, Pb, and Sb being higher than industrial soils limits (Col.B), as described by the law. To conclude, mine wastes accumulated in the Fenice Capanne area were associated with heavy metals environmental pollution, as also reported by other authors (Pignattelli et al., 2012).

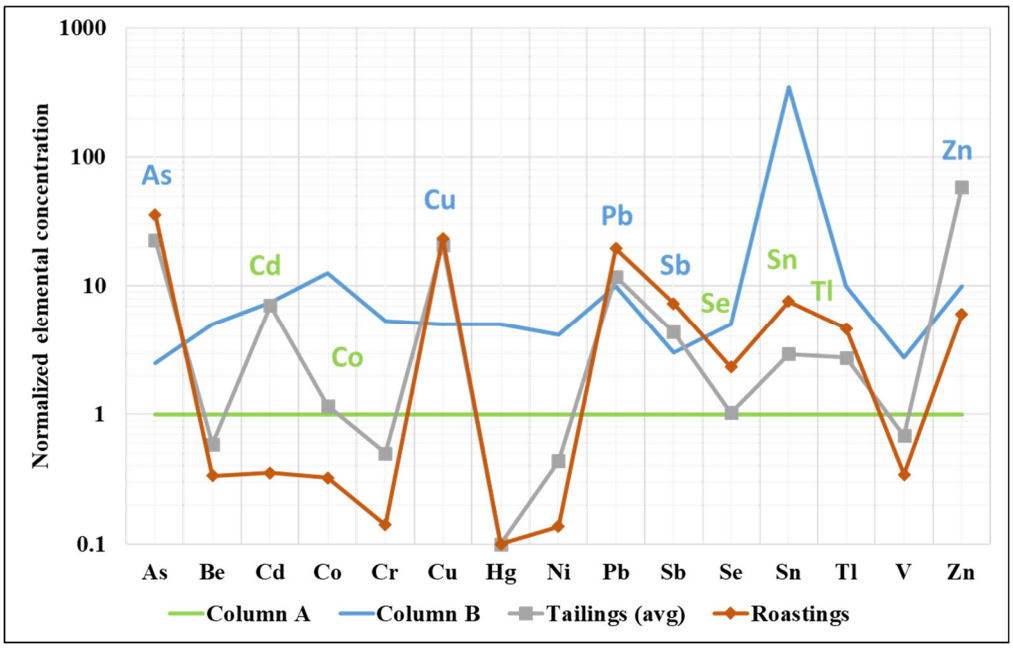


Figure 119 – Spider plot comparing Fenice Capanne tailings and roasting elemental concentrations to the Italian Law Decree 152/2006 limit for soil contamination. Green: elements exceeding Column A; Blue: elements exceeding Column B.

7.5 Lab-scale processing trials

Preliminary geochemical and mineralogical characterisation of the considered samples highlighted the presence of relevant concentrations of critical and valuable metals in the Fenice Capanne tailings samples, especially Co and Zn. A selected subgroup of samples was collected from the initial bulk material, based on their target element concentrations. According to mineralogical data, samples were mainly composed of gangue minerals (quartz, muscovite, clinochlore), secondary minerals (Siderite), and residual metal-bearing minerals such as pyrite. In addition, very fine particle dimensions of the material were considered penalising factors for a possible physical processing. In fact, hydrometallurgical processing was selected and tested in order to understand any possible recovery of valuable metals without any preliminary pretreatment of the material.

Two different leaching methodologies were tested and compared, as follows:

- Glycine alkaline leaching (***Par. 2.6.7.1***);
- Sulphuric acid leaching (***Par. 2.6.7.2***);

Table 68 shows the list of samples considered for leaching tests and the leaching times applied for each leaching test mode.

Table 68 - List of selected samples from Fenice Capanne tailings, leaching mode and leaching times applied.

Sample	***Glycine leaching (h)***	***Sulphuric acid leaching (h)***
FC2	0.5 – 2 – 4 – 6 – 24 – 168	2
FC4	0.5 – 2 – 4 – 6 – 24	2
FC5	0.5 – 2 – 4 – 6 – 24 – 168	2
FC10	0.5 – 2 – 4 – 6 – 24 – 168	2
FC15	0.5 – 2 – 4 – 6 – 24	2

Recovery of target elements after leaching tests was evaluated using ICP-OES (***Par. 2.5.4***) for the characterisation of dissolved metals in the leaching liquors, while solid residues were assayed by HH-XRF. Recovery rates were calculated according to ***Equation 4*** and ***Equation 5*** described in ***Par. 2.6.8***.

In addition, materials were characterised before and after leaching according to the following methodologies:

- PSD – (***Par. 2.6.2***)
- HH-XRF – (***Par. 2.5.2***)
- XRPD – (***Par. 2.4.4***)
- SEM-EDS – (***Par. 2.4.2***)
- MLA – (***Par. 2.4.3***)

7.5.1 Sample characterisation before leaching

7.5.1.1 Particle Size Distribution results

Particle size distribution of the selected sample is reported in Figure 120. The overall dimension of the analysed material is very fine, with a p80 ranging between 34 and 69 µm, as reported in Table 69.

According to the observed data, no further physical reduction was needed before leaching tests, being the material was in a range of granulometry suitable for chemical reprocessing.

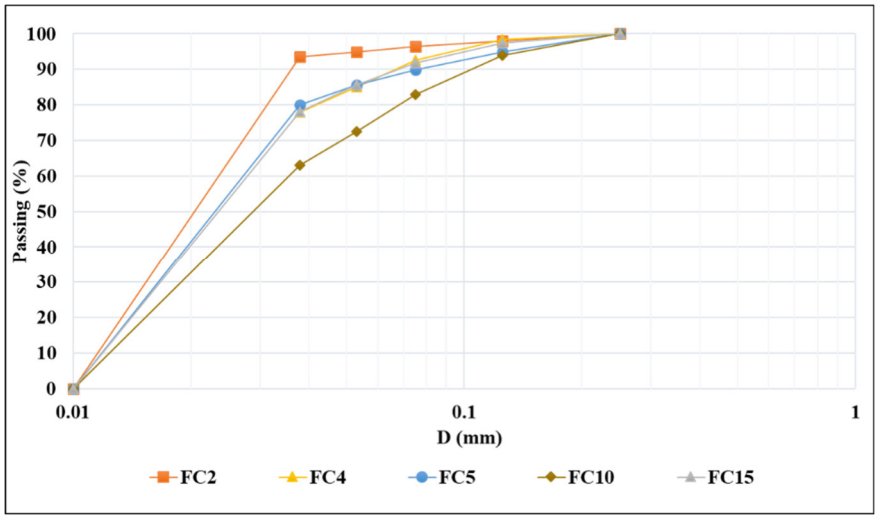


Figure 120 - PSD of tailings sample from Fenice Capanne mine selected for leaching tests

Table 69 - P80 values for tailings samples from Fenice Capanne mine

Sample	p80 (µm)
FC2	34
FC4	42
FC5	38
FC10	69
FC15	41

7.5.1.2 HH-XRF and XRPD results

Chemical assays of the selected samples regarding Cu, Zn, and Fe were assayed by HH-XRF, and the main mineralogical phases detected for each sample using XRPD were reported and summarised in Table 70.

Table 70 - HH-XRF results for target elements and main detected minerals by XRPD on selected samples from Fenice Capanne mine waste dumps before leaching tests

Sample	*Cu (ppm)*	*Zn (ppm)*	*Fe (ppm)*	*Detected minerals**
FC2	8,660 ± 34	3,981 ± 19	77,928 ± 148	Clc, Ms, Gp, Qz, Cal, Py
FC4	626 ± 10	10,693 ± 28	56,079 ± 116	Qz, Kln, Sa, Ms, Py, Sd, Pmi, Gp
FC5	7,108 ± 30	10,896 ± 30	72,322 ± 140	Ms, Qz, Gp, Jbj, Cro, Py
FC10	523 ± 10	14,983 ± 34	65,989 ± 127	Qz, Clc, Sa, Gp, Py, Ms
FC15	3,045 ± 20	21,134 ± 40	58,297 ± 120	Qz, Py, Gp

**Mineral abbreviations according to Warr (2021): Cal: Calcite; Clc: Clinochlore; Cro: Cronstedite; Gp: Gypsum; Jbj: Joelbruggerite; Kln: Kaolinite; Ms: Muscovite; Pmi: Palmierite; Py: Pyrite; Qz: Quartz; Sa: Sanidino; Sd: Siderite*

7.5.1.3 SEM-EDS results

A more detailed characterisation of the samples was performed by SEM-EDS for detecting minor mineral phases and to understand the morphology of the metal-bearing grains contained in the tailings samples.

The majority of the grains are composed of quartz, having irregular shapes and not well-defined morphological features (Figure 121a). Moreover, some pyrite and sphalerite grains were characterised by greater dimensions than the gangue and by a more defined morphology. In particular, as shown in Figure 121d, pyrite showed a cubic shape, being remarkably notable from the surrounding material and confirming its crystalline morphology.

Additionally, SEM-EDS images confirmed that the average dimension of the grains is very fine, with a homogeneous size distribution (Figure 121a,c). Some exceptions are represented by chalcopyrite (Figure 121e), sphalerite (Figure 121d) and pyrite (Figure 121b) grains that, in some cases, showed a greater size.

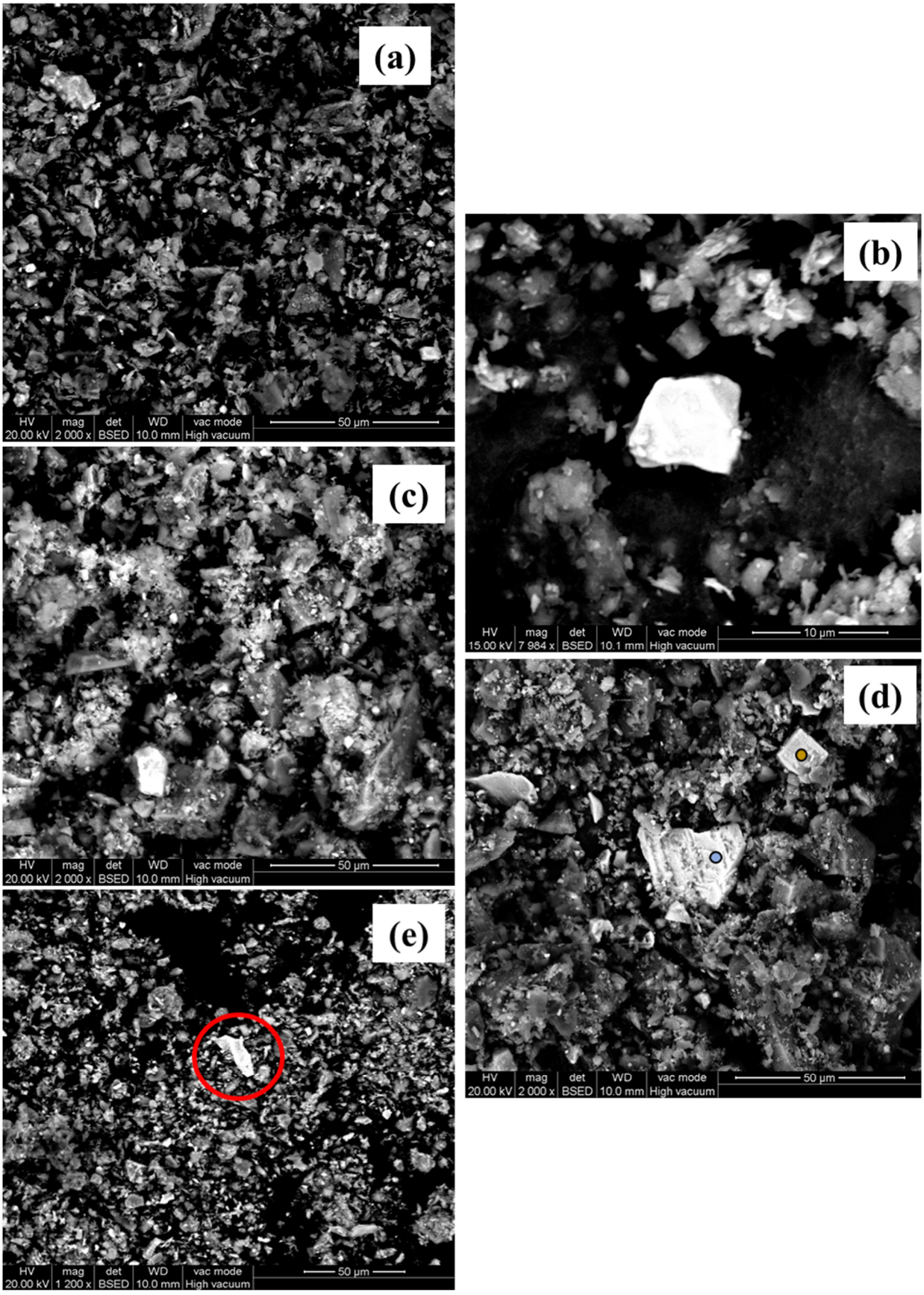


Figure 121 - SEM BSE images of tailings sample from Fenice Capanne: (a) FC2 sample full frame BSE image; (b) BSE image of pyrite grain from sample FC2; (c) FC10 sample full frame BSE image; (d) BSE image of pyrite (brown dot) and sphalerite (blue dot) grains from sample FC15; (e) FC5 full frame BSE image, with a chalcopyrite grain (red circle).

7.5.1.4 MLA results

Advanced mineralogical analyses were performed on sample FC15 to obtain more details regarding minor phases quantification, mineral association, and particle size distribution of target metal-bearing minerals.

Modal mineralogy of the sample is reported in Figure 122, while full data are reported in ***Appendix E.5***.

Mineralogy is characterised by a prevalent presence of gangue minerals, such as quartz (56.7%), plagioclase (14.5%) and K-feldspar (7.4%). Pyrite and sphalerite are present in abundances of 7.2% and 1.7%, respectively. In addition, chalcopyrite was present in minor concentrations of 0.6%.

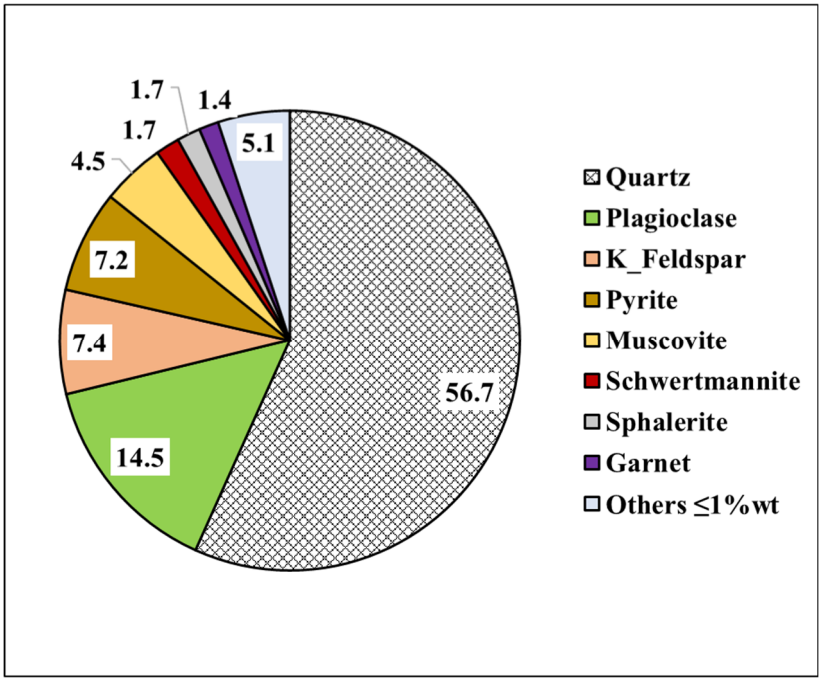


Figure 122 - Modal mineralogy pie chart for Fenice Capanne tailings sample FC15

Mineral associations of metal-bearing minerals are reported in Figure 123. The three considered minerals were lightly associated with plagioclase, schwertmannite, and quartz, but in general were mostly liberated when considering their available surface. In particular, chalcopyrite had 79.7% of free surface, sphalerite 80.9%, and pyrite 75.1%.

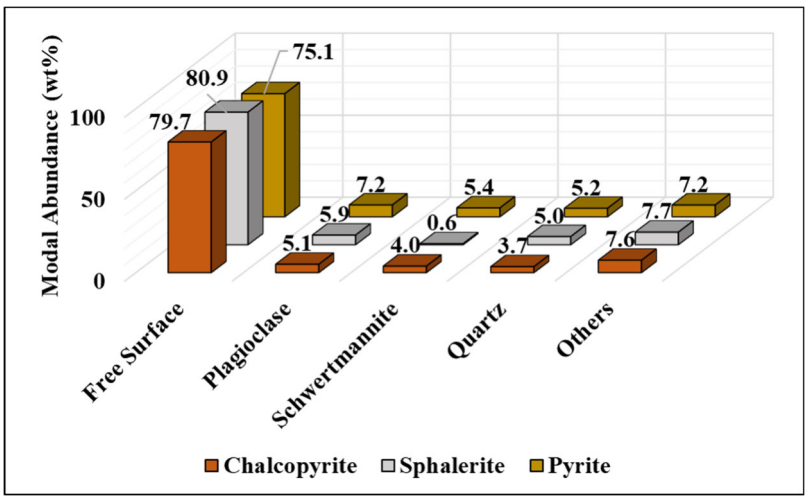


Figure 123 - Mineral association of metal-bearing minerals in Fenice Capanne tailings sample FC15

Considered minerals showed very fine granulometry, confirming the information collected from SEM-EDS images. Figure 124 reports the particle size distribution curves for pyrite, sphalerite, and chalcopyrite. P80 values, shown in Table 71, were 15µm for sphalerite, 17 µm for pyrite, and 18 µm for chalcopyrite.

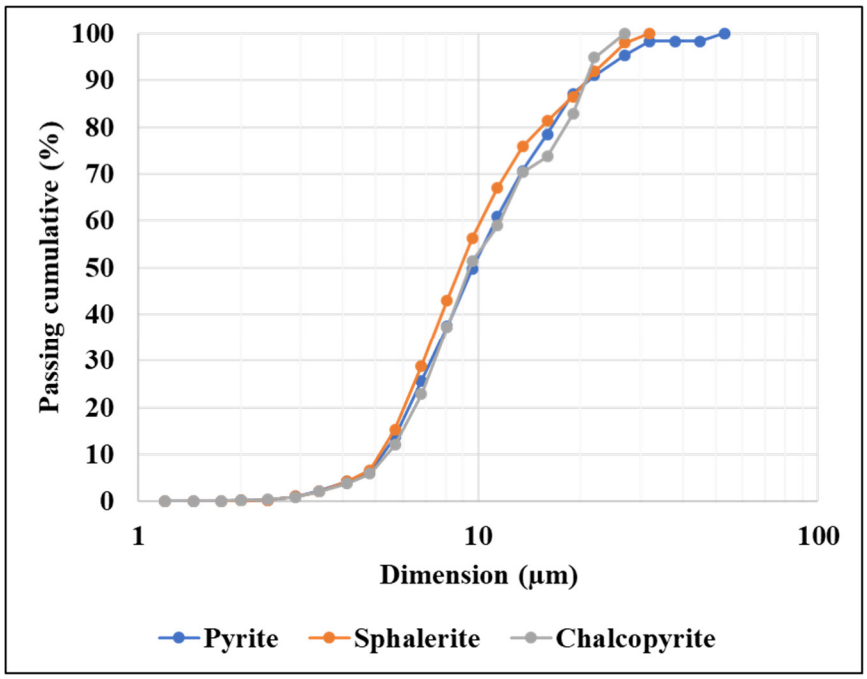


Figure 124 - Particle size distribution of metal-bearing minerals detected in Fenice Capanne tailings sample FC15

Table 71 - p80 values for metal-bearing minerals in Fenice Capanne tailings sample FC15

Sample	p80 (µm)
Pyrite	17
Sphalerite	15
Chalcopyrite	18

7.5.2 Leaching test results

7.5.2.1 pH variation during glycine leaching

Monitoring of pH values was performed at the beginning and at the end of each glycine leaching test performed. Figure 125 shows the pH values measured and their variation over time. In general, a decreasing trend could be outlined for all the performed tests. The reduction appeared to be constant, with the most remarkable decrease in pH for samples that were leached for 7 days (168h). Moreover, the difference in pH after 24 h and 168 h is residual, if compared to the variation in the first 24h. Sample FC5 recorded the lowest pH after 168h of 9.23, while the pH decrease of the other samples was limited to 9.5.

This evidence confirmed that the reaction was maintained at optimal pH in order to enhance the chelating properties of glycine on calcophile elements.

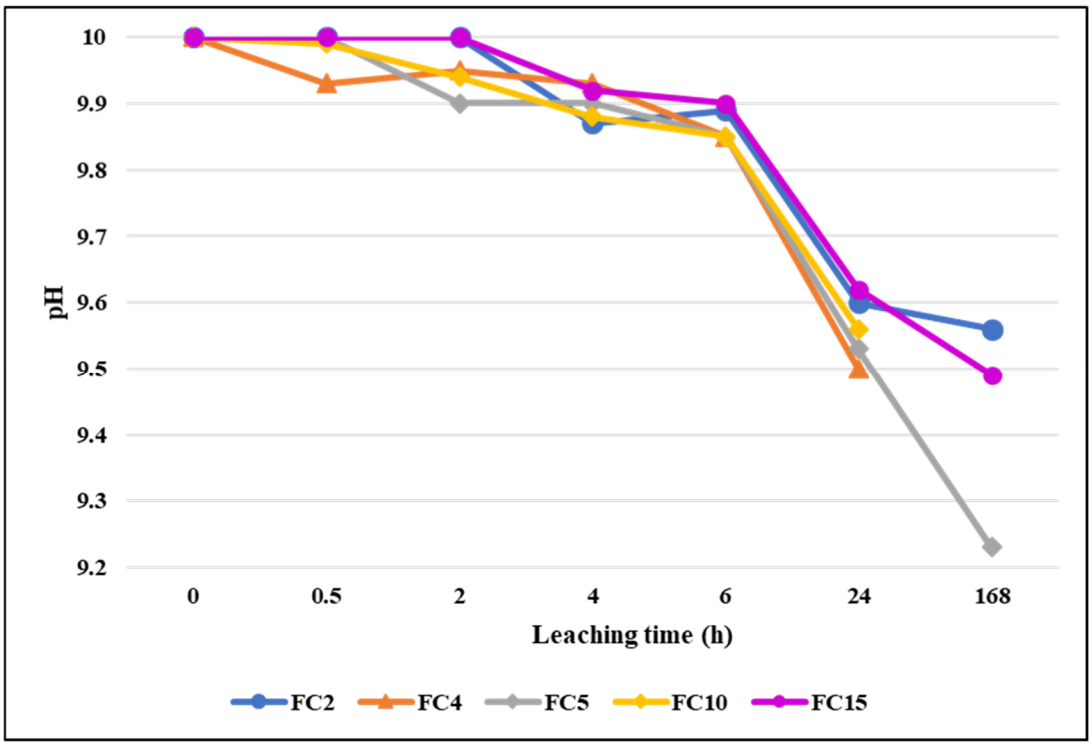
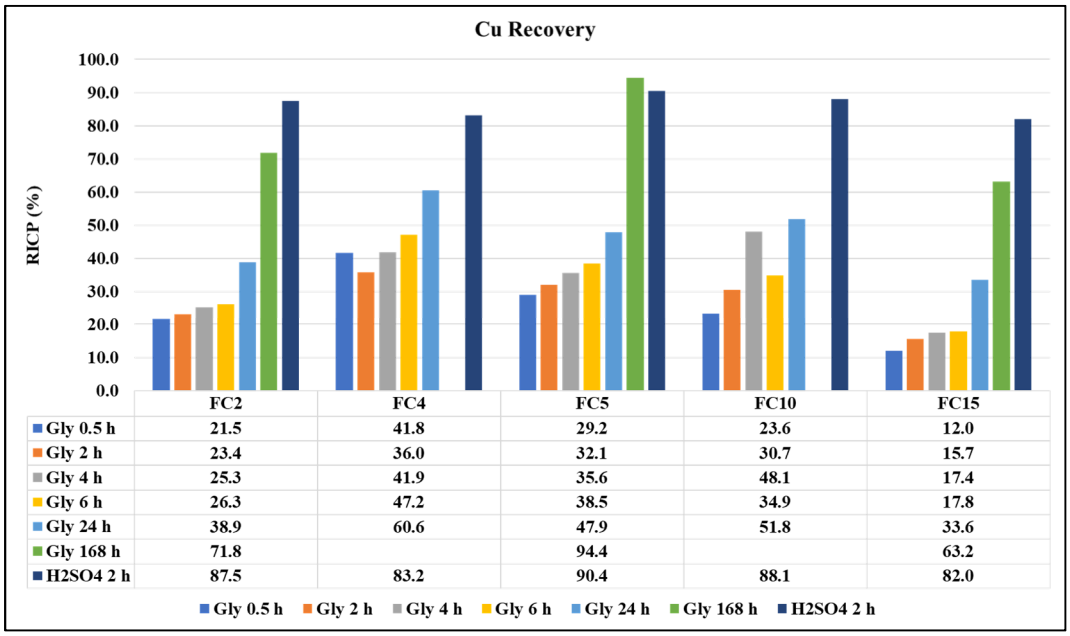


Figure 125 - pH values variation over glycine leaching time for Fenice Capanne tailings samples.

7.5.2.2 Post-leaching characterisation of leachate solutions and R_{ICP} evaluation

Leachate solutions were analysed using ICP-OES for the determination of Cu, Zn, and Fe concentrations. Metal recoveries (R_{ICP}) were calculated according to the formula described in previous paragraphs (***Equation 4***, ***Par. 2.6.8***). Figure 126 shows R_{ICP} values calculated after leaching and chemical characterisation of leachate solutions. Full data are reported in ***Appendix E.6***.

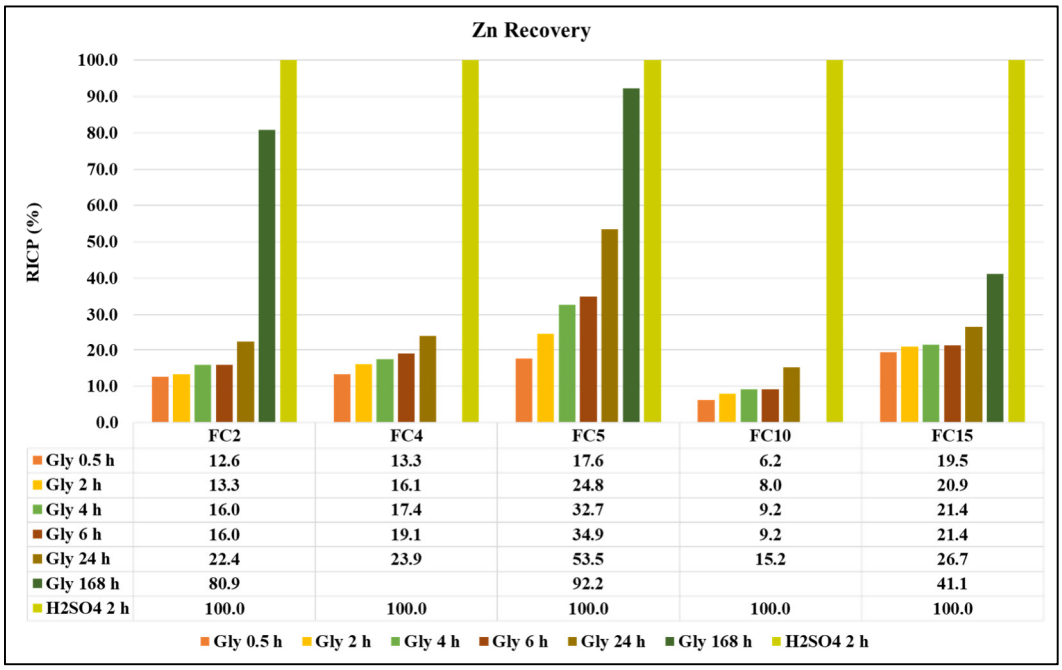


	FC2	FC4	FC5	FC10	FC15
Gly 0.5 h	21.5	41.8	29.2	23.6	12.0
Gly 2 h	23.4	36.0	32.1	30.7	15.7
Gly 4 h	25.3	41.9	35.6	48.1	17.4
Gly 6 h	26.3	47.2	38.5	34.9	17.8
Gly 24 h	38.9	60.6	47.9	51.8	33.6
Gly 168 h	71.8		94.4		63.2
H2SO4 2 h	87.5	83.2	90.4	88.1	82.0

Figure 126 - R_{ICP} calculated values for Cu after glycine leaching (Gly) and sulphuric acid leaching (H_2SO_4), for each of the tested Fenice Capanne tailings sample.

According to the shown data, Cu recovery after glycine leaching reached the highest rates after 168h leaching time, in particular for samples FC5 (94.4%%), FC2 (71.8%), and FC15 (63.2%), while after 24h leaching time, consistent recoveries were also achieved for sample FC4 (60.6%) and FC10 (51.8%). Sulphuric acid leaching produced an overall recovery higher than 80% for all the conducted results, and usually higher than the maximum recovery achieved by glycine leaching. Only for sample FC5, glycine leaching reached a higher recovery of Cu (94.4% after 168h) than sulphuric acid leaching (90.4% after 2h). Overall, glycine leaching produced relevant Cu recoveries if compared to sulphuric acid.

In Figure 127, R_{ICP} values calculated for Zn are reported (full data in ***Appendix E.6***).



	FC2	FC4	FC5	FC10	FC15
Gly 0.5 h	12.6	13.3	17.6	6.2	19.5
Gly 2 h	13.3	16.1	24.8	8.0	20.9
Gly 4 h	16.0	17.4	32.7	9.2	21.4
Gly 6 h	16.0	19.1	34.9	9.2	21.4
Gly 24 h	22.4	23.9	53.5	15.2	26.7
Gly 168 h	80.9		92.2		41.1
H2SO4 2 h	100.0	100.0	100.0	100.0	100.0

Figure 127 - R_{ICP} calculated values for Zn after glycine leaching (Gly) and sulphuric acid leaching (H_2SO_4), for each of the tested Fenice Capanne tailings sample

Zinc was successfully recovered after glycine leaching, especially for samples treated for 168h, such as FC5 (92.2%), FC2 (80.9%), and FC15 (41.1%). By contrast, samples with leaching times limited to 24h showed a residual Zn recovery that reached 23.9% for sample FC4 and 15.2% for FC10. Sulphuric acid leaching demonstrated a 100% recovery of Zn for all the tested samples.

R_{ICP} values for Zn and Cu were plotted as a function of glycine leaching time, as reported in Figure 128, showing similar trends in the recovery of metals over time. In detail, Cu recovery showed a steep increase in the first 0.5h for all the samples, when the reaction kinetics were arguably more active. The process efficiency tended to stabilise until 6h with no relevant improvement in the recovery. Recovery slightly increased at 24h leaching time, while a residual increase was obtained before reaching the maximum values at 168h. Similarly, Zn had a steady recovery up to 24h, while most of the increase was obtained at 168h.

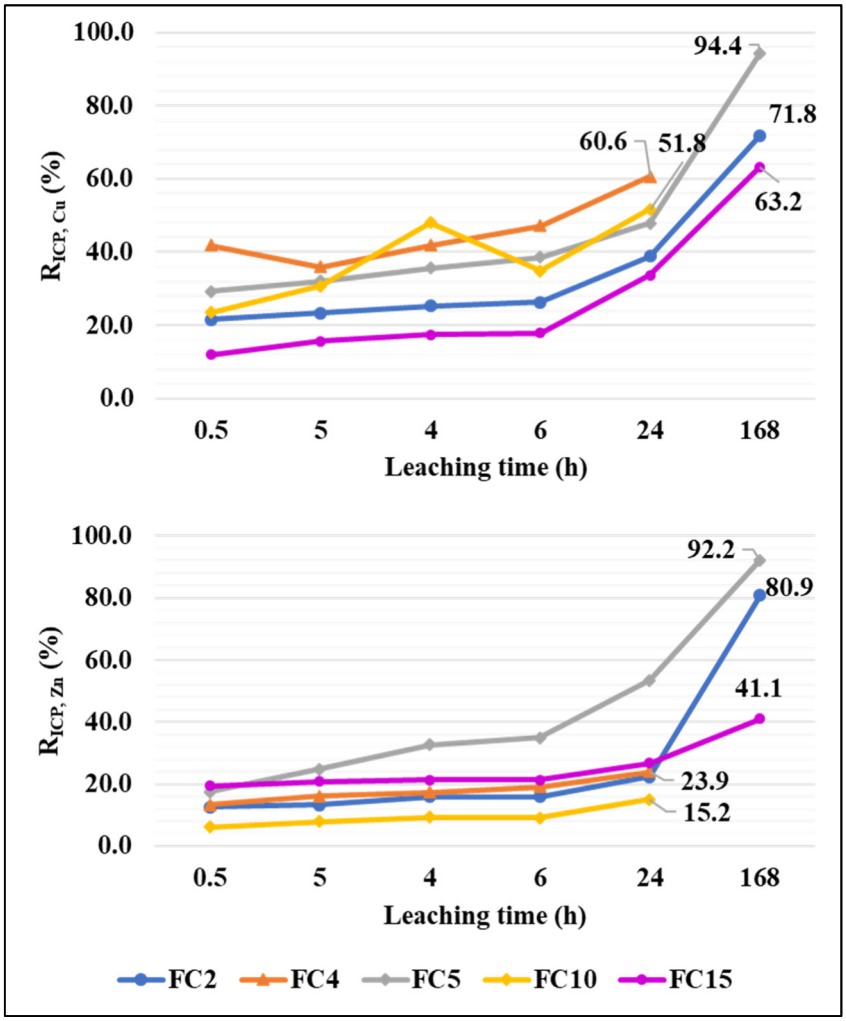


Figure 128 -R_{ICP} values for Cu (top) and Zn (bottom) as a function of glycine leaching time for Fenice Capanne tailings samples

As mentioned in previous lines, sulphuric acid showed higher recoveries for Cu and Zn for a shorter reaction time of 2h, but with a lower selectivity with respect to Fe. As a result, R_{ICP} values obtained after glycine leaching and sulphuric acid leaching were compared, as reported in Figure 129.

Fe recovery was measured to be very limited after glycine leaching, being absent for samples FC4 and FC10, while samples that had reacted for 168h showed extremely low values between 0.2% and 0.5%. By contrast, sulphuric acid leaching extracted most of the available Fe in the samples, showing poor selectivity on target Cu and Zn, even if associated with very high recovery rates (Figure 126, Figure 127).

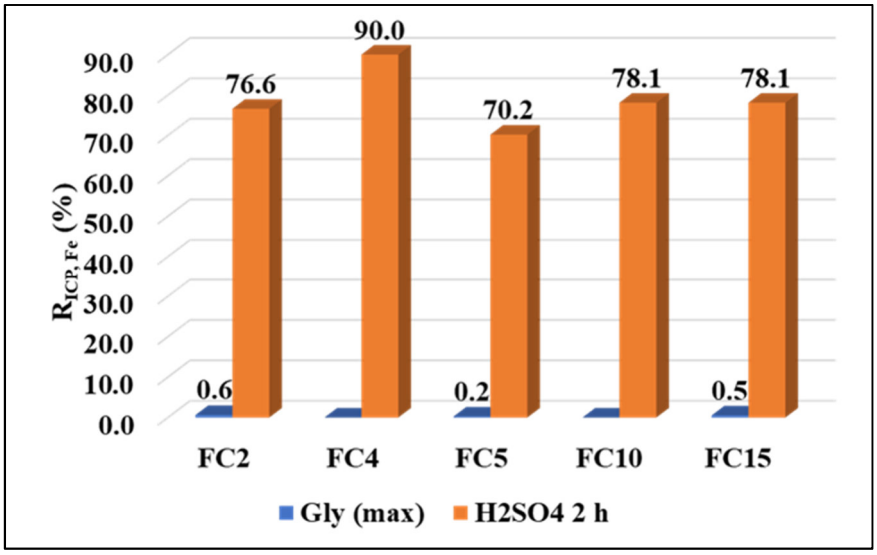


Figure 129 - Comparison of R_{ICP} values for Fe, considering the maximum glycine leaching time and sulphuric acid leaching for the considered Fenice Capanne tailings samples.

7.5.2.3 Solid residues characterisation after leaching

Solid residues collected after leaching tests were characterised using XRPD, while HH-XRF assays were collected for recovery rate (R_{XRF}) determination, according to ***Equation 5*** (***Par. 2.6.8***).

XRPD qualitative characterisation was performed on samples treated with glycine for the longest times (FC2, FC5, and FC15 – 168h; FC4 and FC10 – 24h), along with solid residues collected after sulphuric acid leaching tests.

As reported in Table 72, the main mineralogical phases detected in samples processed using glycine did not show significant differences when compared to pre-leaching samples. The only exception is related to gypsum, which was no longer detected after glycine leaching, possibly due to its dissolution during the tests. By contrast, solid residues characterised after sulphuric acid leaching showed reduced pyrite peak intensity. In addition, samples FC2 and FC5 showed the presence of gypsum as a new phase, probably related to the interaction between sulphuric acid and calcite detected in the original bulk sample.

Regarding metal recovery (R_{XRF}), Table 72 reports the calculated values according to HH-XRF determinations, while complete HH-XRF and R_{XRF} data are available in ***Annexe E.7***.

According to the calculated data, recovery rates for Cu resulted in being relevant for those samples that were treated using glycine solutions for 168h, while for Zn results were variable, in particular for sample FC2 ($R_{XRF, Cu}$: 69.9%, $R_{XRF, Zn}$: 22.7%), FC5 ($R_{XRF, Cu}$: 70.9%, $R_{XRF, Zn}$: 65.3%), and FC15 ($R_{XRF, Cu}$: 61.1%, $R_{XRF, Zn}$: 11.6%). In addition, samples treated for 24h with glycine showed consistent Cu recoveries (FC4: 58.5%; FC10: 44.9%), but poor Zn recoveries (FC4: 14.9%, FC10: 11.6%). By contrast, sulphuric acid leaching showed nearly total recovery of Zn across all considered samples. Cu recoveries showed greater

values for any of the samples, with restrained differences compared to the maximum performances of glycine leaching.

R_{XRF} values calculated for Fe showed that glycine leaching was the most selective leaching method, compared to high extraction and a lower amount of metal was measured in the solid residues.

Table 72 - RXRF values and detected mineral phases from solid residues after glycine (max time) and sulphuric acid leaching performed on Fenice Capanne tailings samples.

Sample	***Leaching mode***	***Leaching time (h)***	$R_{XRF, Cu}$ ***(%)***	$R_{XRF, Zn}$ ***(%)***	$R_{XRF, Fe}$ ***(%)***	***Detected minerals****
FC2	Glycine	168	69.9	22.7	-	Qz, Py, Cal, Ms, Clc
	H_2SO_4	2	74.7	87.0	50.9	Qz, Gp, Py, Ms
FC4	Glycine	24	58.5	14.9	-	Qz, Py, Ms, Sd
	H_2SO_4	2	91.7	96.6	77.9	Qz, Py, Sa, Ms
FC5	Glycine	168	70.9	65.3	-	Qz, Cal, Py, Sa, Ms
	H_2SO_4	2	72.8	93.6	46.8	Qz, Gp, Py, Sa, Ms
FC10	Glycine	24	44.9	11.6	1.5	Qz, Clc, Py, Sa, Sd, Ms
	H_2SO_4	2	89.7	96.0	76.1	Qz, Clc, Sa, Py, Ms
FC15	Glycine	168	61.1	34.3	3.1	Qz, Py
	H_2SO_4	2	71.1	84.2	58.0	Qz, Py

**Mineral abbreviations according to Warr (2021): Cal: Calcite; Clc: Clinochlore; Gp: Gypsum; Ms: Muscovite; Py: Pyrite; Qz: Quartz; Sa: Sanidino; Sd: Siderite*

7.5.2.4 R_{ICP} and R_{XRF} metal recovery comparison

R_{ICP} and R_{XRF} values were compared to define any correlation related to the two different formulas applied for target metal recovery evaluation. The two main elements compared were Cu and Zn, as shown in Figure 130.

R_{XRF} values showed, in general, a good correlation with R_{ICP} values for both of the considered elements. By contrast, the angular coefficients of the interpolating lines were, for both elements, lower than 1, indicating a general underestimation of R_{XRF} values compared to R_{ICP} ones.

In more detail, calculated recoveries for Cu appeared to be better distributed, maintaining linearity at higher values, confirming that HH-XRF provided fast and reliable data for metal assays. The RICP and RXRF comparison for Zn showed a poorly distributed set of variables, highlighting the fluctuating HH-XRF readings when assaying solid residue fractions.

To conclude, R_{ICP} is correlated to ICP-OES measurements, which are characterised by higher sensitivity and a linear response, providing more stable quantification of dissolved elements in the leachate solutions, while R_{XRF} values is affected by a more variable response due to HH-XRF measurements being affected by a higher variability such as sample matrix, measurement geometry,

and the response related to single analysed element. The relative enrichment phenomenon could be attributed to this evidence, for which the depletion of an element in the solid fraction could result in an apparent enrichment of residual elements in the solid fraction after leaching.

In general, HH-XRF could be considered a valid and fast characterisation methodology, providing a good approximation of real chemical assays.

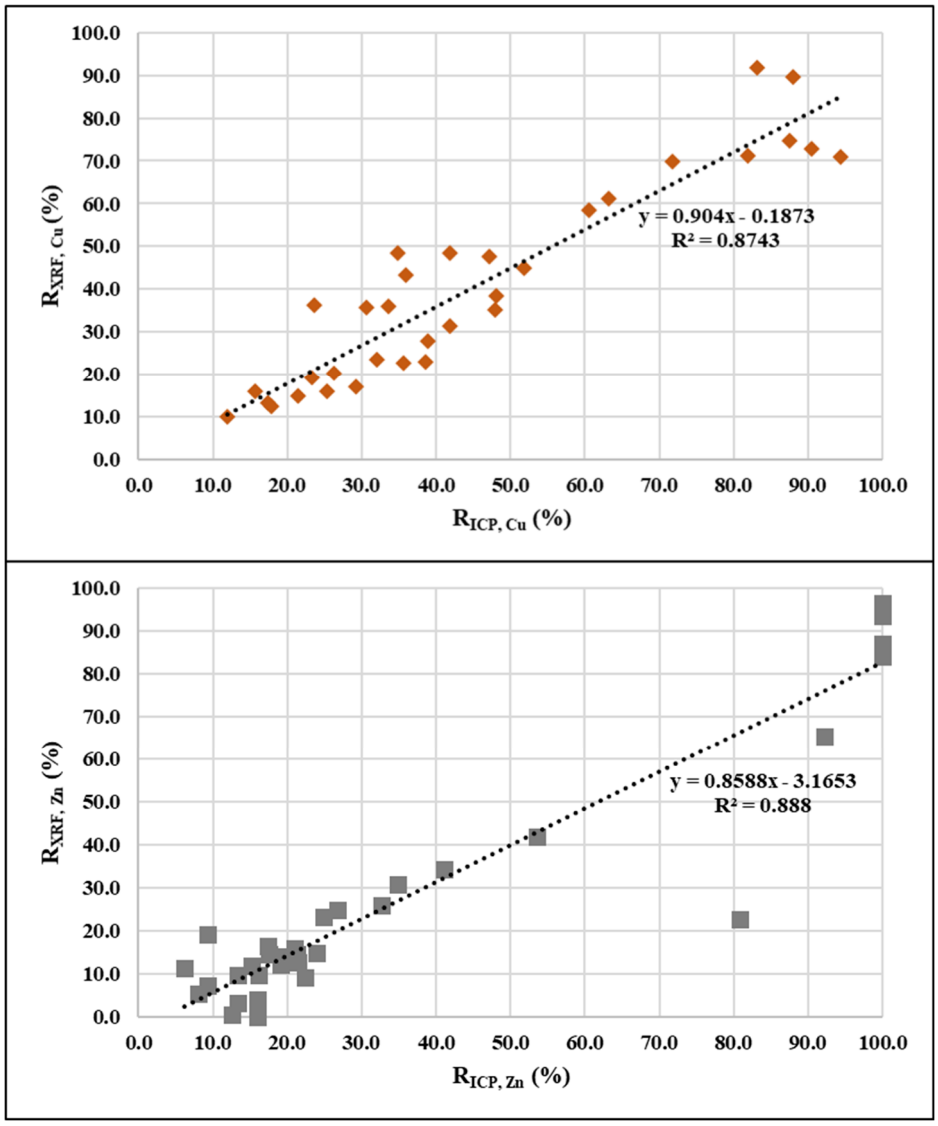


Figure 130 - Comparison of R_{ICP} and R_{XRF} values for Cu (top) and Zn (bottom), obtained after post-leaching characterisation of Fenice Capanne tailings samples.

7.6 Final Remarks

Mining operation in the Fenice Capanne area left a significant quantity of extractive and processing waste. This waste was known and mapped in the ISPRA official mine waste database and can be classified as roasting and tailings. Tailings were produced as a by-product of the flotation processing plant in which chalcopyrite, pyrite, sphalerite, and galena were separated. This waste was discharged from the 1950s to the 1980s in four different basins. Roasting heaps are older and were produced from low-grade ore and stored close to the old processing plants. According to satellite images and NDVI analyses, these areas are mainly free of vegetation and potentially accessible for detailed sampling campaigns.

Twelve historical tailings and roasting samples collected in the Fenice Capanne mine were found in the repository of mining samples of the Department of Environmental, Land and Infrastructures Engineering (DIATI) and were considered for chemical (HH-XRF and ICP-MS) and mineralogical (XRPD) determination.

Mineralogy of tailings samples was characterised by prevalent gangue minerals, such as quartz and sanidine, minor muscovite and clinochlore, while valuable minerals detected were mainly pyrite and chalcopyrite. Roasting samples were instead characterised mainly by quartz, diopside and minor hematite.

Geochemical analyses revealed that the most abundant critical raw materials were Cu and As, with mean concentrations of 2.498 ppm and 457 ppm, respectively, and a relative abundance exceeding that of the average crustal abundance by more than 100 times. In addition, high concentrations of base metals were found in the samples, including Zn and Pb, with mean assays of 9,645 ppm and 1,185 ppm, respectively, and an average of 7.5 ppm of Ag.

Roasting samples were characterised by elevated concentrations of Cu (2,820 ppm), As (718 ppm), and Bi (486 ppm), regarding critical raw materials, while other metals were found in relevant concentrations, especially Zr (8,030 ppm), Pb (1,960 ppm), and Zn (960 ppm).

For both types of analysed waste, 10 metals were found to be at concentrations above the limits imposed by the Italian Environmental Law, in particular As, Cu, Pb, Sb, and Zn, which exceeded the industrial soil limits.

The possibility of recovering valuable metals, such as Cu and Zn, from tailings was assessed through hydrometallurgical reprocessing using green chemicals, such as glycine. Sulphuric acid leaching was also considered as a benchmark for leaching metals. A sub-set of samples was characterised before leaching tests, showing a very fine particle size distribution of the material (p80 in the range of 64 to 34 μm), indicating no need for additional physical treatments.

Glycine leaching showed significant recoveries of Cu, ranging between 63.2 % and 94.4% for 168h leaching time, and in the range 51.8 − 60.6% for 24h leaching tests. Moreover, Zn showed relevant recoveries only for longer leaching times in the range of 41.1 – 92.2%, while poor results were obtained for 24h leaching. Glycine leaching showed competitive results if compared to sulphuric

acid leaching, especially for its selectivity on target metals with negligible extraction of Fe in the liquid solutions.

The results provided by processing tests showed that glycine leaching can provide a promising recovery rate of metals and high selectivity of valuable metals on a lab-scale, without any pretreatment of tailings materials. Although the processing requires longer processing times compared to conventional leaching methods, it should be considered that this could be counterbalanced by simple operational parameters such as atmospheric pressure and ambient temperature, associated with minimal environmental impacts related to applied reagents. Further investigation should be addressed on the optimisation and bench test of this hydrometallurgical method, including process scalability and reaction kinetics, highlighting the potential of glycine leaching as a sustainable alternative for recovering critical, strategic and valuable metals from mine waste and tailings.

Part III. Conclusions and Future Developments

Chapter 8

8. Conclusions

8.1 General aspects of the research

This research focused on the need to systematically assess mining waste deposits as a potential secondary source of CRMs and SRMs in Italy, by developing and applying a data-driven methodological approach.

The proposed methodology consisted of the collection of industrial and historical data, design of sampling campaign, mineralogical and geochemical characterisation, and preliminary laboratory-scale processing trials applied to selected case studies.

International guiding case studies were included in the dissertation to establish benchmark methodologies and top-notch procedures applied to mine waste management and prospectivity, while selected Italian case studies were employed to test the applicability, adaptability and limitations of the framework under heterogeneous and specific conditions, such as data availability, industrial history, geological context and type of mine waste.

The combination of different types of collected information and data, including mine waste composition and the applicability of recovery procedures, demonstrated that the potential recovery of valuable raw materials from mine waste requires an integrated evaluation that should consider information such as waste quantities estimation, definition of physical characteristics, metal distribution study, host minerals identification, liberation characteristics, and suitability to mineral processing or hydrometallurgical recovery approaches.

8.2 International reference examples and their methodological relevance

The proposed international case studies played a crucial role in the definition of the methodological approach proposed in this study, serving as benchmarks for large-scale screening through a national mine waste database and detailed site-specific characterisation of mine waste facilities.

Data extrapolation from the Finnish mine waste database showed the importance of different aspects of mine waste databases:

- Organised, structured and detailed dataset helps for the preliminary identification and prioritisation of sites with mine waste dumps containing valuable, critical and strategic raw materials.
- The introduction of the Economically Important-Equivalent Ton (t_{EIeq}) unit highlighted the importance of introducing tools for an evaluation supporting the preliminary estimated economic value.
- The application of a multi-parameter decision matrix helped in supporting that economic parameters need to be combined with the environmental risk associated with mine waste for a more complete prioritisation hierarchy.

Further actions should be focused on the production of more site-specific and detailed information to apply internationally recognised models for resource estimation, such as the UNFC framework, and detailed economic evaluation for those sites that exhibited a higher priority of actions.

From a site-specific perspective, the old tailings storage facility in the Kanmantoo mine, Australia, provided an applied example of secondary prospectivity of mine waste, paying particular attention to some key aspects:

- Proper sampling techniques provide the first evidence of variability and peculiarities of tailings materials, being useful for guiding more detailed characterisations.
- Detailed mineralogical and geochemical analyses are crucial for the choice of potential recovery solutions for mine waste materials.
- Statistically sound and advanced analytical techniques enable the identification of critical metals-hosting minerals.
- Critical elements can occur in accessory minerals that are not being targeted by previous extraction processes.
- The Australian case study served as a methodological bridge for transforming site and waste material characterisation into crucial information for practical recovery actions, although the environmental and regulatory context is not directly comparable with the Italian case studies subsequently considered.

Overall, the international guiding case studies provided a structured and transferable framework for adapting a methodology to the Italian context according to methodological robustness and reference practices.

8.3 Methodological application on the Italian case studies

The designed methodology was applied to three selected case studies in Italy (Traversella, Libiola, and Fenice-Capanne) and provided a practical validation of its applicability and reproducibility for different sites and mine waste typologies produced from different historical industrial processes.

The application of the framework highlighted the importance of data collection for some general purposes:

- Gathering existing scientific and technical literature is crucial for reconstructing the industrial history of the site and understanding the technologies that produced the mine waste stream in the areas under study.
- Identification of mine waste accumulation areas is needed for selecting appropriate field characterisation campaigns, considering the condition of the site, such as vegetation coverage and accessibility.
- The combined use of on-field chemical analyses and detailed geochemical and mineralogical characterisation provides a valid set of information useful for defining the distribution of valuable and critical elements embedded in the waste material.
- Definition of potential recovery solutions is tailored for site-specific materials characteristics.

The performed laboratory-scale recovery trials represented a crucial validation step of the methodology, allowing the assessment of applicable processing techniques for each of the considered sites:

- Mine waste material found in Traversella “Piano Svedesi” is partially accessible due to vegetation covering the area and needs a combination of physical treatments, including crushing, grinding and sieving with magnetic and gravity separation, for achieving a preliminary concentration of magnetite and scheelite from waste rocks.
- Steep and oxidised waste rock dumps in the Libiola site showed high Cu grades associated with highly weathered and oxidised minerals, which required a preliminary fine comminution before hydrometallurgical treatments using sulphuric acid leaching. A trade-off between physical pre-treatment and recovery efficiency should be carefully considered along with potential environmental restoration of

the site. Considerations regarding the environmental and regulatory feasibility of strong-acid use should be carefully implemented

- Fine-grained tailings materials from the Fenice Capanne can undertake direct hydrometallurgical processing without any preliminary physical treatment. Glycine leaching showed high selectivity and competitive recovery rate for target metals like Cu and Zn, enabling the future possibility to study on a wider scale the applicability of environmentally friendly processes for recovering CRMs.

The outcomes provided by the Italian case studies, reported in Table 73, confirmed that mine waste valorisation requires a site-specific and detailed knowledge of the waste materials, which should be carefully assessed for the definition of a technically feasible alternative for mine waste recovery.

Table 73 - Main outcomes from the methodology application to Italian case studies. N.a.: nat available; WR: waste rock; TL: tailings; RT: roastings

Case Study	***Type***	***Accessibility /vegetation***	***CRM/ SRM***	**Volume**	**Env. impact**	***Treatment and Recovery (R)***
Traversella	WR (boulders)	Partial due to vegetation	W (90 ppm)	n.a.	Light	Physical R=56%, 1600 ppm W
Libiola	WR (coarse gravel)	Partial due to steep slopes, sparse vegetation	Cu (5250 ppm)	~1.6 Mm^3	Heavy	Physical & Hydromet. Up to 97% Cu recovery with H_2SO_4 leaching
Fenice Capanne	TL, RT (fine sand)	Very good, no vegetation	Cu (2500ppm)	~1.0 Mm^3	Heavy	Hydromet. Up to 94% Cu recovery with glycine leaching

Overall, the results show that the proposed methodology can provide a structured pathway for moving from conceptual considerations to practical and technically viable recovery options, useful for guiding decision-makers and institutions in supporting a more sustainable and strategic mine waste management.

8.4 Limitations and future developments

From a site-scale perspective, the main limitations and further developments can be related to the following aspects:

- Representativity of sampling campaigns related to the high variability of mine waste deposits, considering only surficial sampling or not evenly distributed sampling points.
- The restricted or declined accessibility of mine waste areas limited the overall characterisation of the waste bodies in terms of volumes and area extension.
- Recovery trials were conducted mainly on a laboratory scale and should be considered as preliminary recovery actions. Bench and pilot scale testing should be developed in more detail and analysed for their economic viability, especially for those sites presenting reduced need for physical pre-treatment and promising recovery results, like Fenice Capanne tailings.
- Economic assessments and viability, related to resource estimation, industrial validation or piloting of reprocessing solutions, are crucial aspects to be considered for further advancements, but are beyond the scope of this work.
- The proposed methodological framework provided the base for a wider operational applicability, for the collection of site information that can be categorised in a more structured classification system.

8.5 Environmental restoration and resource recovery: a synergic action

Environmental reclamation opportunities should be considered along with processing arrangements aimed at recovering mine waste. These complementary strategies may create opportunities for the environmental restoration of post-mining or poorly managed liabilities.

The integration of resource recovery and land rehabilitation objectives is needed for sustaining the overall feasibility and acceptance of mine waste recovery projects. The Italian contexts, in particular, are characterised by mine waste deposit characterized by moderate or small quantities of waste, but associated with environmental liabilities. The sole resource recovery could be limited in terms of feasibility if the environmental conditions are neglected.

A key solution for the successful management of mine waste deposits should be designed considering a synergic approach between environmental reclamation and resource recovery actions. This could lead to a double outcome: the recovery of critical and strategic raw materials could drive the overall consideration, while reclamation procedures tailored to site-specific conditions have to be considered

for a full restoration of portions of lands heavily affected by poorly managed mining liabilities in historical times.

References

Abaka-Wood, G. B., Zanin, M., Addai-Mensah, J., & Skinner, W. (2019a). Recovery of rare earth elements minerals from iron oxide–silicate rich tailings – Part 1: Magnetic separation. *Minerals Engineering*, *136*, 50–61. https://doi.org/10.1016/J.MINENG.2019.02.026

Abaka-Wood, G. B., Zanin, M., Addai-Mensah, J., & Skinner, W. (2019b). Recovery of rare earth elements minerals from iron oxide–silicate rich tailings – Part 2: Froth flotation separation. *Minerals Engineering*, *142*, 105888. https://doi.org/10.1016/j.mineng.2019.105888

Abdale, L., & Trimmer, L. M. I. (2023). Italy [advance release]. In *U.S. Geological Survey Minerals Yearbook 2017-2018*: *Vol. III*. *Area Reports—International, U.S. Geological Survey Minerals Yearbook 2017-2018* (p. 23.1-23.6). Reston, VA, United States: U.S. Geological Survey. https://doi.org/10.3133/mybvIII

Agnew, M. K. (1998). *The formation of hardpans within tailings as possible inhibitors of acid mine drainage, contaminant release and dusting* (PhD Thesis). University of Adelaide.

Ait-Khouia, Y., Benzaazoua, M., & Demers, I. (2021). Environmental desulfurization of mine wastes using various mineral processing techniques: Recent advances and opportunities. *Minerals Engineering*, *174*, 107225. https://doi.org/10.1016/j.mineng.2021.107225

ALS Global. (2025). ALSGlobal.com. Recuperato 18 settembre 2025, da https://www.alsglobal.com/en/

Amar, H., Benzaazoua, M., Elghali, A., Hakkou, R., & Taha, Y. (2022). Waste rock reprocessing to enhance the sustainability of phosphate reserves: A critical review. *Journal of Cleaner Production*, *381*, 135151. https://doi.org/10.1016/j.jclepro.2022.135151

Amar, H., Benzaazoua, M., Elghali, A., Taha, Y., El Ghorfi, M., Krause, A., & Hakkou, R. (2023). Mine waste rock reprocessing using sensor-based sorting (SBS): Novel approach toward circular economy in phosphate mining. *Minerals Engineering*, *204*, 108415. https://doi.org/10.1016/j.mineng.2023.108415

Anawar, H., Hossain, Z., Santa-Regina, I., Strezov, V., & Akter, F. (2019). *Phytomining of Valuable Metals/Metalloids from Mining Wastes, Tailings and Contaminated Soils*. 109–125. https://doi.org/10.1201/9780429279072-8

Araya, N., Kraslawski, A., & Cisternas, L. A. (2020). Towards mine tailings valorization: Recovery of critical materials from Chilean mine tailings. *Journal of Cleaner Production*, *263*, 121555. https://doi.org/10.1016/j.jclepro.2020.121555

Arbon, H. (2011). *Bismuth distribution in the Cu-Au mineralisation of the Kanmantoo deposit, South Australia* (B.Sc. Honours Thesis). University of Adelaide, Australia.

Arendt, R., Muhl, M., Bach, V., & Finkbeiner, M. (2020). Criticality assessment of abiotic resource use for Europe– application of the SCARCE method. *Resources Policy*, *67*, 101650. https://doi.org/10.1016/j.resourpol.2020.101650

Arisi Rota, F., Brondi, A., Dessau, G., Franzini, M., Monte Amiata S.m.p.a., Stabilimento minerario del Siele S.p.A., … Vighi, L. (1971). I giacimenti minerari. In *Rendiconti della Società Italiana di Mineralogia e Petrologia*: *Vol. 27. La Toscana Meridionale—Fondamenti geologico-minerari per una prospettiva di valorizzazione delle risorse naturali* (Speciale, pp. 357–539). Milano: Museo Civico di Storia Naturale.

Aristone, O., & Loreto, A. D. (2016). Questions from the Underground Promotion Policies for Decommissioned Small and Medium Miningsites in Italy. *Journal of Engineering and Architecture*, *4*(2). https://doi.org/10.15640/jea.v4n2a4

Australian Government. (2024, febbraio 20). Australia's Critical Minerals List and Strategic Materials List [Government Website]. Recuperato 12 giugno 2025, da https://www.industry.gov.au/publications/australias-critical-minerals-list-and-strategic-materials-list

Baldassarre, G., Fiorucci, A., & Marini, P. (2024). Recovery of Critical Raw Materials from Abandoned Mine Wastes: Some Potential Case Studies in Northwest Italy. *RawMat 2023*, 77. MDPI. https://doi.org/10.3390/materproc2023015077

Baldassarre, G., Mori De Oliveira, C., Fiorucci, A., Bellopede, R., & Marini, P. (2025). Exploring the Recovery Potential of Critical and Strategic Raw Materials from Traversella Mine (Piedmont, Italy) Waste: A Comparison of Laboratory-Scale Separation Techniques. *Mining*, *5*(2), 21. https://doi.org/10.3390/mining5020021

Barragán-Mantilla, S. P., Gascó, G., Almendros, P., & Méndez, A. (2024). Insights into the use of green leaching systems based on glycine for the

selective recovery of copper. *Minerals Engineering*, *206*, 108534. https://doi.org/10.1016/j.mineng.2023.108534

Belperio, A. P., Preiss, W. V., Fairclough, M. C., Gatehouse, C. G., Gum, J., Hough, J., & Burtt, A. (1998). Tectonic and metallogenic framework of the Cambrian Stansbury Basin Kanmantoo Trough, South Australia. *AGSO Journal of Australian Geology and Geophysics*, *17*, 183–200.

Benvenuti, M., Mascaro, I., Corsini, F., Costagliola, P., Parrini, P., Lattanzi, P., & Giuseppe, T. (1999). Environmental problems related to sulfide mining in Tuscany. *Environmental Problems Related to Sulfide Mining in Tuscany*, *534*, 29–45.

Berthet, E., Lavalley, J., Anquetil-Deck, C., Ballesteros, F., Stadler, K., Soytas, U., … Laurent, A. (2024). Assessing the social and environmental impacts of critical mineral supply chains for the energy transition in Europe. *Global Environmental Change*, *86*, 102841. https://doi.org/10.1016/j.gloenvcha.2024.102841

Bhima Rao R, Singh D, & Mishra B. (2024). RECOVERY OF RARE EARTH BEARING PLACER HEAVY MINERALS BY JUDICIOUS COMBINATIONS OF GRAVITY, MAGNETIC AND FLOTATION. In *F. Kongoli, L. Andric, K. Aravossis, V. Chanturiya, I. Chatjigeorgiou, D. Fuerstenau, C. Kavalopoulos, C. O'Connor, V. Panayotov, J. Rubinstein (Eds.), Sustainable Industrial Processing Summit Volume 2 Anastassakis Intl. Symp / Mineral Processing* (pp. 255–270). Montreal, Canada: FLOGEN Star Outreach.

Blannin, R., Frenzel, M., Tolosana-Delgado, R., & Gutzmer, J. (2022). Towards a sampling protocol for the resource assessment of critical raw materials in

tailings storage facilities. *Journal of Geochemical Exploration*, *236*, 106974. https://doi.org/10.1016/J.GEXPLO.2022.106974

Blengini, G. A., Nuss, P., Dewulf, J., Nita, V., Peirò, L. T., Vidal-Legaz, B., … Ciupagea, C. (2017). EU methodology for critical raw materials assessment: Policy needs and proposed solutions for incremental improvements. *Resources Policy*, *53*, 12–19. https://doi.org/10.1016/j.resourpol.2017.05.008

Boliden Group. (2025a). Smelters—Boliden Harjavalta [Corporate Web Site]. Recuperato 12 settembre 2025, da Boliden website: https://www.boliden.com/operations/smelters/boliden-harjavalta/

Boliden Group. (2025b). Smelters—Boliden Kokkola [Corporate Web Site]. Recuperato 12 settembre 2025, da Boliden website: https://www.boliden.com/operations/smelters/boliden-kokkola/

Both, R. A. (1990). Kanmantoo Trough geology and mineral deposits. In *Geology of the Mineral Deposits of Australia and Papua New Guinea* (pp. 1195–1203). Melbourne: The Australasian Institute of Mining and Metallurgy.

Buccheri, G., Andras, P., Vajda, E., Midula, P., Melichová, Z., & Dirner, V. (2018). Soil contamination by heavy metals at Libiola abandoned copper mine, Italy. *Acta Montanistica Slovaca*, *23*, 337–345.

Burtt, A. C. (2008). Kanmantoo Trough. In *South Australian mineral explorers guide* (p. (Chapter 8) 1-20).

Carbone, C., Di Benedetto, F., Marescotti, P., Martinelli, A., Sangregorio, C., Cipriani, C., … Romanelli, M. (2005). Genetic evolution of nanocrystalline Fe oxide and oxyhydroxide assemblages from the Libiola mine (eastern Liguria, Italy): Structural and microstructural investigations.

European Journal of Mineralogy, *17*(5), 785–795. https://doi.org/10.1127/0935-1221/2005/0017-0785

Colombi, F., Jackson, L., Baldassarre, G., & Parbhakar-Fox, A. (2024). *Secondary prospectivity of South Australia's mine waste: Kanmantoo Cu, Au and Ag mine* (Departmental Publication - Geological Survey Geoscience Publication Fasc. 2024/00036; p. 178). Geological Survey of South Australia. Recuperato da Geological Survey of South Australia website: https://pid.sarig.sa.gov.au/document/mesac134

Colombi, F., Silvester, E., Holland, A., Baldwin, D., MacRae, C., Wilson, N., … Lawrence, S. (2025). Arsenic speciation and mobility in gold mining-impacted riverine sediments from the Loddon River catchment in Victoria, Australia. *Applied Geochemistry*, *193*, 106582. https://doi.org/10.1016/j.apgeochem.2025.106582

Correia, V., Falck, E., & Komac, M. (2024). Invisible Mining: Addressing EU Raw Material Challenges Through Technological Innovation. *Intereconomics*, *59*(6), 344–351. https://doi.org/10.2478/ie-2024-0067

Cortecci, G., Boschetti, T., Dinelli, E., & Cabella, R. (2008). Sulphur isotopes, trace elements and mineral stability diagrams of waters from the abandoned Fe-Cu mines of Libiola and Vigonzano (Northern Apennines, Italy). *Water, Air, and Soil Pollution*, *192*(1–4), 85–103. https://doi.org/10.1007/S11270-008-9637-8

Costa, E., Dino, G. A., Benna, P., & Rossetti, P. (2019). The Traversella Mining Site as Piemonte Geosite. *Geoheritage*, *11*(1), 55–70. https://doi.org/10.1007/s12371-017-0271-y

Crane, R. A., & Sapsford, D. J. (2018). Towards Greener Lixiviants in Value Recovery from Mine Wastes: Efficacy of Organic Acids for the

Dissolution of Copper and Arsenic from Legacy Mine Tailings. *Minerals*, *8*(9), 383. https://doi.org/10.3390/min8090383

Dacquino, C. (2025). Miniera di Libiola. Recuperato 27 ottobre 2025, da Le miniere italiane dal 1870 al 2024 website: https://sites.google.com/view/miniere-italia/regioni/liguria/minerali-del-rame/miniera-di-libiola

Dacquino, C. (2026). Evoluzione temporale dell'attività estrattiva. Recuperato 16 gennaio 2026, da Le miniere italiane dal 1870 al 2024 website: https://sites.google.com/view/miniere-italia/analisi-dei-dati/evoluzione-temporale-dellattivit%C3%A0-estrattiva

Das, S. K., Kundu, T., Dash, N., & Angadi, S. I. (2023). Separation behavior of Falcon concentrator for the recovery of ultrafine scheelite particles from the gold mine tailings. *Separation and Purification Technology*, *309*, 123065. https://doi.org/10.1016/j.seppur.2022.123065

Davoise, D., & Méndez, A. (2025). Advances in the Development of Hydrometallurgical Processes in Acidic and Alkaline Environments for the Extraction of Copper from Tailings Deposit. *Minerals*, *15*(6), 550. https://doi.org/10.3390/min15060550

De Oliveira, D., Silva, T., Morais, I., & Fernandes, J. (2025). Chemical and Mineralogical Characterization of Waste from Abandoned Copper and Manganese Mines in the Iberian Pyrite Belt, Portugal: A First Step Towards the Waste-to-Value Recycling Process. *Minerals*, *15*(1), 58. https://doi.org/10.3390/min15010058

Deiana, C., & Giua, L. (2023). This site is closed! The effect of decommissioning mining waste facilities on mortality in the long run. *Journal of*

Environmental Economics and Management, *119*, 102797. https://doi.org/10.1016/j.jeem.2023.102797

Deng, Z., Oraby, E. A., & Eksteen, J. J. (2020). Cu adsorption behaviours onto chelating resins from glycine-cyanide solutions: Isotherms, kinetics and regeneration studies. *Separation and Purification Technology*, *236*, 116280. https://doi.org/10.1016/j.seppur.2019.116280

Dhiman, S., Singh, A. D., Kour, J., Bhardwaj, T., Tikoria, R., Kumar, D., … Bhardwaj, R. (2024). Phytomining: An Innovative Technique for Sustainable Recovery of Valuable Metals/Metalloids from Agro-industrial and Mining Wastes. In D. B. Pal, A. K. Rai, & S. Siddiqui (A c. Di), *Sustainable Clean Energy Production Using Waste Biomass* (pp. 101–127). Singapore: Springer Nature Singapore. https://doi.org/10.1007/978-981-97-0840-6_5

Dinelli, E., Lucchini, F., Fabbri, M., & Cortecci, G. (2001). Metal distribution and environmental problems related to sulfide oxidation in the Libiola copper mine area (Ligurian Apennines, Italy). *Journal of Geochemical Exploration*, *74*(1), 141–152. https://doi.org/10.1016/S0375-6742(01)00180-7

Dinelli, E., & Tateo, F. (2002). Different types of fine-grained sediments associated with acid mine drainage in the Libiola Fe–Cu mine area (Ligurian Apennines, Italy). *Applied Geochemistry*, *17*(8), 1081–1092. https://doi.org/10.1016/S0883-2927(02)00009-4

Dold, B. (2020). Sourcing of critical elements and industrial minerals from mine waste – The final evolutionary step back to sustainability of humankind? *Journal of Geochemical Exploration*, *219*, 106638. https://doi.org/10.1016/j.gexplo.2020.106638

Draslovka. (2025, dicembre 9). From Tailings to Value: Reprocessing Mining Waste for Profit, Sustainability, and Extended Mine Life [Corporate Web Site]. Recuperato 15 gennaio 2026, da Draslovka website: https://www.draslovka.com/from-tailings-to-value-reprocessing-mining-waste-for-profit-sustainability-and-extended-mine-life-67

Eerola, T., Solismaa, S., Karlsson, T., & Hokka, J. (2024). *Environmental and social governance issues of the Otanmäki (Finland) ilmenite tailings remining project* (Open File Research Report Fasc. 56/2024; p. 22). Espoo: GTK - Geological Survey of Finland.

Eksteen, J. J., Oraby, E. A., & Tanda, B. C. (2017). A conceptual process for copper extraction from chalcopyrite in alkaline glycinate solutions. *Minerals Engineering*, *108*, 53–66. https://doi.org/10.1016/j.mineng.2017.02.001

Eni Rewind S.p.A. (2025). Colline Metallifere—Gli interventi di messa in sicurezza e bonifica dei siti ex minerari in Toscana [Corporate Web Site]. Recuperato 17 novembre 2025, da Eni.com website: https://www.eni.com/enirewind/it-IT/bonifiche/progetti-bonifica-colline-metallifere.html

European Commission. (2019). *Going climate-neutral by 2050: A strategic long-term vision for a prosperous, modern, competitive and climate-neutral EU economy*. Luxembourg: Publications Office of the European Union.

European Commission. A Green Deal Industrial Plan for the Net-Zero Age. , Pub. L. No. 52023DC0062, COM/2023/62 final COM(2023) 62 final 21 (2023).

European Commission. Regulation (EU) 2024/1252 of the European Parliament and of the Council of 11 April 2024 establishing a framework for ensuring

a secure and sustainable supply of critical raw materials and amending Regulations (EU) No 168/2013, (EU) 2018/858, (EU) 2018/1724 and (EU) 2019/1020. , Pub. L. No. 32024R1252, 2024/1252 Regulation (EU) 2024/1252 (2023).

European Commission. (2023c). *Study on the critical raw materials for the EU 2023: Final report.* LU: Publications Office. Recuperato da https://data.europa.eu/doi/10.2873/725585

European Commission. Directorate General for Internal Market, Industry, Entrepreneurship and SMEs. (2017). *Methodology for establishing the EU list of critical raw materials: Guidelines.* LU: Publications Office. Recuperato da https://data.europa.eu/doi/10.2873/769526

European Union. (2023). Critical Raw Materials Act [Institutional]. Recuperato 1 ottobre 2026, da Internal Market, Industry, Entrepreneurship and SMEs website: https://single-market-economy.ec.europa.eu/sectors/raw-materials/areas-specific-interest/critical-raw-materials/critical-raw-materials-act_en

European Union. (2025a). Critical Raw Materials [Institutional]. Recuperato 1 ottobre 2026, da Critical raw materials website: https://single-market-economy.ec.europa.eu/sectors/raw-materials/areas-specific-interest/critical-raw-materials_en

European Union. (2025b). Selected strategic projects [Institutional]. Recuperato 1 ottobre 2026, da Internal Market, Industry, Entrepreneurship and SMEs website: https://single-market-economy.ec.europa.eu/sectors/raw-materials/areas-specific-interest/critical-raw-materials/strategic-projects-under-crma/selected-projects_en

Falagán, C., Grail, B. M., & Johnson, D. B. (2017). New approaches for extracting and recovering metals from mine tailings. *Minerals Engineering*, *106*, 71–78. https://doi.org/10.1016/J.MINENG.2016.10.008

Feichtinger, G., & Posch, W. (2025). Evaluation of European Critical Raw Material Assessments under Energy Transition Considerations: Applications and Prospects. *Circular Economy and Sustainability*, *5*(3), 2057–2131. https://doi.org/10.1007/s43615-024-00493-0

Fereydouni, H., Naseri, T., & Mousavi, S. M. (2025). Synergistic recovery of Pr, Eu, and Ce from gold mine tailings using bioleaching and oxalic acid pretreatment. *Scientific Reports*, *15*. https://doi.org/10.1038/s41598-025-88594-0

Ferri-Moreno, I., Barquero-Peralbo, J. I., Andreu-Sánchez, O., Higueras, P., Roca-Pérez, L., García-Lorenzo, M. L., & Esbrí, J. M. (2023). Categorization of Mining Materials for Restoration Projects by Means of Pollution Indices and Bioassays. *Minerals*, *13*(4), 492. https://doi.org/10.3390/min13040492

Focke, D., Schmidt Mumm, A., Tedesco, A., Seifert, T., & Bradey, R. (2009). Pressure, temperature and fluid composition variation of the mineralizing system at the Kanmantoo Cu-Au deposit: Combining fluid inclusion analysis with Ti in quartz thermometry. *Journal of Geochemical Exploration*, *101*(2).

Foden, J., Sandiford, M., Dougherty-Page, J., & Williams, I. (1999). Geochemistry and geochronology of the Rathjen Gneiss: Implications for the early tectonic evolution of the Delamerian Orogen. *Australian Journal of Earth Sciences*, *46*(3), 377–389. https://doi.org/10.1046/j.1440-0952.1999.00712.x

Fojtíková, L., Pekarčíková, K., Sousedíková, R., Vaněk, M., & Dvořáček, J. (2025). Determinants of critical raw material imports: The case of the European Union and China. *Mineral Economics*. https://doi.org/10.1007/s13563-025-00528-4

Fomchenko, N., & Muravyov, M. (2020). Sequential Bioleaching of Pyritic Tailings and Ferric Leaching of Nonferrous Slags as a Method for Metal Recovery from Mining and Metallurgical Wastes. *Minerals*, *10*, 1097. https://doi.org/10.3390/min10121097

Gilli, M. (1984). *Relazione sull'impianto di trattamento della miniera Fenice-Capanne*. Politecnico di Torino. Placement report, Politecnico di Torino.

Grant, D. C., Goudie, D. J., Shaffer, M., & Sylvester, P. (2016). A single-step trans-vertical epoxy preparation method for maximising throughput of iron-ore samples via SEM-MLA analysis. *Transactions of the Institutions of Mining and Metallurgy, Section B: Applied Earth Science*, *125*(1), 57–62. https://doi.org/10.1080/03717453.2015.1104056

Gruppo Mineralogico Valchiusella. (2004). La scheelite di Traversella. Recuperato 18 marzo 2025, da https://drive.google.com/file/d/12BfddB_jgQJmxDyz7516QEqH-TZPlk6o/view

GTK. (2024). *Mineral Deposit Database of Finland* (Versione (Not published)) [Digital map database, Electronic resource]. Espoo: Geological Survey of Finland.

Gu, Y. (2003). Automated Scanning Electron Microscope Based Mineral Liberation Analysis An Introduction to JKMRC/FEI Mineral Liberation Analyser. *Journal of Minerals and Materials Characterization and Engineering*, *02*(01), 33–41. https://doi.org/10.4236/jmmce.2003.21003

Guglietta, D., Belardi, G., Cappai, G., Casentini, B., Godeas, A., Milia, S., … Trapasso, F. (2020). Toward a Multidisciplinary Strategy for the Classification and Reuse of Iron and Manganese Mining Wastes. *Chemistry Journal of Moldova*, *15*(1), 21–30. https://doi.org/10.19261/cjm.2019.650

Gum, J. C. (1998). *The sedimentology, sequence stratigraphy and mineralization of the Silverton Subgroup, South Australia* (PhD Thesis). University of South Australia, Australia.

Hammerli, J., Spandler, C., & Oliver, N. H. S. (2016). Element redistribution and mobility during upper crustal metamorphism of metasedimentary rocks: An example from the eastern Mount Lofty Ranges, South Australia. *Contributions to Mineralogy and Petrology*, *171*(4), 36. https://doi.org/10.1007/s00410-016-1239-7

Han, Z., Golev, A., & Edraki, M. (2021). A Review of Tungsten Resources and Potential Extraction from Mine Waste. *Minerals 2021, Vol. 11, Page 701*, *11*(7), 701. https://doi.org/10.3390/MIN11070701

Hillgrove Resources. (2020). *Kanmantoo Copper Mine—Program for Environment Protection & Rehabilitation—Main Report* (Mineral Company Report - Mining Environmental Program Fasc. PEPR 4738257; p. 269). Recuperato da https://catalog.sarig.sa.gov.au/document/mesac29321

Hillgrove Resources. (2025). Kanmantoo Underground [Corporate Web Site]. Recuperato 5 maggio 2025, da Hillgrove Resources website: https://hillgroveresources.com.au/projects/kanmantoo-underground

Hofmann, M., Hofmann, H., Hagelüken, C., & Hool, A. (2018). Critical raw materials: A perspective from the materials science community.

Sustainable Materials and Technologies, *17*, e00074. https://doi.org/10.1016/j.susmat.2018.e00074

Hool, A., Helbig, C., & Wierink, G. (2024). Challenges and opportunities of the European Critical Raw Materials Act. *Mineral Economics*, *37*(3), 661–668. https://doi.org/10.1007/s13563-023-00394-y

ISPRA, I. S. per la P. e la R. A. (2025a). *Approvato il Programma Nazionale di Esplorazione Mineraria* [Comunicato Stampa]. Roma: Ufficio Stampa ISPRA. Recuperato da https://www.isprambiente.gov.it/files2025/area-stampa/comunicati-stampa/comunicato-programma-nazionale-esplorazione.pdf

ISPRA, I. S. per la P. e la R. A. (2025b). *Programma Nazionale di Esplorazione* [Guideline]. Roma: ISPRA - Istituto Superiore per la Protezione e la Ricerca Ambientale. Recuperato da https://www.isprambiente.gov.it/files2025/attivita/pne_finale

Italian Republic. (2006). *Legislative Decree of 3 April 2006, No. 152. Environmental Regulations*. Repubblica Italiana. Recuperato da https://www.normattiva.it/uri-res/N2Ls?urn:nir:stato:decreto.legislativo:2006-04-03;152

Jamett, I., Carrasco, P., Olmos, M., & Hernández, P. (2022). Glycine/Glutamate: "Green" Alternatives to Recover Metals from Minerals/Residues—Review of Current Research. *Minerals*, *13*(1), 22. https://doi.org/10.3390/min13010022

Jamieson, H. E., Walker, S. R., & Parsons, M. B. (2015). Mineralogical characterization of mine waste. *Applied Geochemistry*, *57*, 85–105. https://doi.org/10.1016/j.apgeochem.2014.12.014

Jenks, G. F. (1967). The Data Model Concept in Statistical Mapping. *International Yearbook of Cartography*, *7*, 186–190.

Kabekkodu, S. N., Dosen, A., & Blanton, T. N. (2024). PDF-5+: A comprehensive Powder Diffraction File™ for materials characterization. *Powder Diffraction*, *39*(2), 47–59. https://doi.org/10.1017/S0885715624000150

Kannan, S. G., Fleming, M., Hirwa, J., Castillo, E., & Eggert, R. (2025). Critical materials and manufacturing: Comparing China, the European Union, Japan, and the United States. *Resources, Conservation & Recycling Advances*, *25*, 200250. https://doi.org/10.1016/j.rcradv.2025.200250

Karlsson, T., Hokka, J., Kauppila, P., Tornivaara, A., & Baldassarre, G. (2024, settembre 17). *Potential of Critical Raw Materials in Closed Finnish Mine Waste Sites: A Preliminary Review*. 9. Halifax, Nova Scotia, Canada: Canadian Institute of Mining, Metallurgy and Petroleum.

Kikis, C., Thalassinos, G., & Antoniadis, V. (2024). Soil Phytomining: Recent Developments—A Review. *Soil Systems*. https://doi.org/10.3390/soilsystems8010008

Kinnunen, P., Karhu, M., Yli-Rantala, E., Kivikytö-Reponen, P., & Mäkinen, J. (2022). A review of circular economy strategies for mine tailings. *Cleaner Engineering and Technology*, *8*, 100499. https://doi.org/10.1016/j.clet.2022.100499

Klimpel, F., Bau, M., & Graupner, T. (2021). Potential of garnet sand as an unconventional resource of the critical high-technology metals scandium and rare earth elements. *Scientific Reports*, *11*(1), 5306. https://doi.org/10.1038/s41598-021-84614-x

Krinsley, D. H., Pye, K., Jr, S. B., & Tovey, N. K. (1998). *Backscattered Scanning Electron Microscopy and Image Analysis of Sediments and Sedimentary Rocks*. Cambridge University Press. https://doi.org/10.1017/CBO9780511628894

Le miniere di ferro di Traversella e Brosso. (2025). Recuperato 5 marzo 2025, da Le Miniere Italiane dal 1870 al 2019 website: https://sites.google.com/view/miniere-italia/regioni/piemonte/metalliferi/miniere-di-ferro-di-traversella-e-brosso

Leskelä, T., Hokka, J., & Karlsson, T. (2025). Geostatistical modelling of mine tailings and comparative analysis of sampling methodologies: A case study of the Otanmäki ilmenite tailings storage facility project. *Journal of Geochemical Exploration*, *274*, 107759. https://doi.org/10.1016/j.gexplo.2025.107759

Lewicka, E., Guzik, K., & Galos, K. (2021). On the Possibilities of Critical Raw Materials Production from the EU's Primary Sources. *Resources*, *10*(5), 50. https://doi.org/10.3390/resources10050050

Li, H., Deng, Z., Oraby, E., & Eksteen, J. (2023). Amino acids as lixiviants for metals extraction from natural and secondary resources with emphasis on glycine: A literature review. *Hydrometallurgy*, *216*, 106008. https://doi.org/10.1016/j.hydromet.2022.106008

Li, Y., Lv, J., Li, Z., Zhou, Y., & Qin, L. (2024). A Novel Technology for the Recovery and Separation of Cassiterite- and Iron-Containing Minerals from Tin-Containing Tailing. *Minerals*, *14*(10), 1058. https://doi.org/10.3390/min14101058

Løvik, A. N., Hagelüken, C., & Wäger, P. (2018). Improving supply security of critical metals: Current developments and research in the EU. *Sustainable*

Materials and Technologies, *15*, 9–18. https://doi.org/10.1016/j.susmat.2018.01.003

Lucarini, M., Carta, R., Fumanti, F., Martarelli, L., & Serra, M. (2020). The Italian Database GeMMA: from monitoring production to cataloguing mining wastes, a starting point for recovering critical raw materials from abandoned mines? Raw materials in Italy: A general overview. In *European Geologist* (Vol. 49). Recuperato da https://eurogeologists.eu/lucarini-the-italian-database-gemma-from-monitoring-production-to-cataloguing-mining-wastes-a-starting-point-for-recovering-critical-raw-materials-from-abandoned-mines/

Lucarini, M., Fumanti, F., Martarelli, L., & Serra, M. (2023). Policymaking and geosciences: The case of Critical Raw Materials in Italy. *European Geologist*, *56*, 32–38. https://doi.org/10.5281/zenodo.10463593

Luino, F., Bonetto, S., Bono, B., Comina, C., Little, W. W., Porfido, S., … Turconi, L. (2024). Marl Mining Activity and Negative Repercussions for Two Hillside Villages (Northern Italy). *Geosciences*, *14*(7), 181. https://doi.org/10.3390/geosciences14070181

Lyons, N. (2012). *Evidence for magmatic hydrothermal mineralisation at Kanmantoo Copper deposit, South Australia* (B.Sc. Honours Thesis). University of Adelaide, Australia.

Mäkinen, J., Salo, M., Khoshkhoo, M., Sundkvist, J., & Kinnunen, P. (2020). Bioleaching of cobalt from sulfide mining tailings; a mini-pilot study. *Hydrometallurgy*. https://doi.org/10.1016/j.hydromet.2020.105418

Maltais, A., Canales, N., & Larsen, R. K. (2026). Challenges in Balancing Sustainability, Competitiveness and Geopolitics in Critical Mineral Supply

Chains. *Business Strategy and the Environment*, *35*(1), 790–802. https://doi.org/10.1002/bse.70213

Maltrana, V., & Morales, J. (2023). The Use of Acid Leaching to Recover Metals from Tailings: A Review. *Metals*, *13*(11), 1862. https://doi.org/10.3390/met13111862

Marescotti, P., Azzali, E., Servida, D., Carbone, C., Grieco, G., Capitani, L. D., & Lucchetti, G. (2010). Mineralogical and geochemical spatial analyses of a waste-rock dump at the Libiola Fe–Cu sulphide mine (Eastern Liguria, Italy). *Environmental Earth Sciences*, *61*(1), 187–199. https://doi.org/10.1007/s12665-009-0335-7

Marescotti, P., & Carbone, C. (2003). La miniera dismessa di Libiola (Sestri Levante, Liguria Orientale): Studio mineralogico sui processi di alterazione di solfuri di Fe e Cu e valutazione del loro impatto ambientale. *GEAM - Geoingegneria Ambientale e Mineraria*, *109*, 45–53.

Marescotti, P., Carbone, C., Capitani, L. D., Grieco, G., Lucchetti, G., & Servida, D. (2008). Mineralogical and geochemical characterisation of open-air tailing and waste-rock dumps from the Libiola Fe-Cu sulphide mine (Eastern Liguria, Italy). *Environmental Geology*, *53*(8), 1613–1626. https://doi.org/10.1007/s00254-007-0769-8

Marescotti, P., Carbone, C., Comodi, P., Frondini, F., & Lucchetti, G. (2012). Mineralogical and chemical evolution of ochreous precipitates from the Libiola Fe–Cu-sulfide mine (Eastern Liguria, Italy). *Applied Geochemistry*, *27*(3), 577–589. https://doi.org/10.1016/j.apgeochem.2011.12.024

Marini, L., Saldi, G., Cipolli, F., Ottonello, G., & Zuccolini, M. V. (2003). Geochemistry of water discharges from the Libiola mine, Italy.

Geochemical Journal, *37*, 199–216. https://doi.org/10.2343/geochemj.37.199

Mascaro, I., Benvenuti, M., Corsini, F., Costagliola, P., Lattanzi, P., Morelli, F., … Tanelli, G. (2001). Impatto ambientale nell'area mineraria (Cu, Pb, Zn) abbandonata di Fenice Capanne—Prima parte. *Siti Contaminati*, 20–22.

Mascaro, I., Benvenuti, M., Corsini, F., Costagliola, P., Lattanzi, P., Parrini, P., & Tanelli, G. (2001). Mine wastes at the polymetallic deposit of Fenice Capanne (southern Tuscany, Italy). Mineralogy, geochemistry, and environmental impact. *Environmental Geology*, *41*(3–4), 417–429. https://doi.org/10.1007/S002540100408/METRICS

Masindi, V., Foteinis, S., Renforth, P., Ndiritu, J., Maree, J. P., Tekere, M., & Chatzisymeon, E. (2022). Challenges and avenues for acid mine drainage treatment, beneficiation, and valorisation in circular economy: A review. *Ecological Engineering*, *183*, 106740. https://doi.org/10.1016/j.ecoleng.2022.106740

Matteucci, E. (1966). Tenori e distribuzione degli elementi del gruppo delle Terre rare nella Scheelite di Traversella. *Symposium Internazionale Sui Giacimenti Minerari delle Alpi*, *2*, 689–704. Trento, Italia: Arti Grafiche «Saturnia» - Trento.

Medina-Díaz, H., Lopez-Bellido, F., Alonso-Azcárate, J., Fernández-Morales, F., & Rodríguez, L. (2024). Can rare earth elements be recovered from abandoned mine tailings by means of electrokinetic-assisted phytoextraction? *Environmental Science and Pollution Research International*, *31*, 26747–26759. https://doi.org/10.1007/s11356-024-32759-3

Mohammed, T., Bezuidenhout, G. A., Oraby, E. A., & Eksteen, J. J. (2024). Sequential Separation of Cobalt, Copper, and Nickel from Alkaline Glycinate Solutions Using Solvent Extraction. *Journal of Sustainable Metallurgy*, *10*(4), 2455–2468. https://doi.org/10.1007/s40831-024-00920-4

Mokhlis, H., Drissi Daoudi, R., & Azzi, M. (2021). Study of the electrochemical behavior of printed circuit boards (PCBs) leaching solutions using glycine and copper recovery by electrodeposition from leachate solutions. *Materials Today: Proceedings*, *37*, 3973–3979. https://doi.org/10.1016/j.matpr.2020.09.765

Montana, F., Cellura, M., Di Silvestre, M. L., Longo, S., Luu, L. Q., Riva Sanseverino, E., & Sciumè, G. (2024). Assessing Critical Raw Materials and Their Supply Risk in Energy Technologies—A Literature Review. *Energies*, *18*(1), 86. https://doi.org/10.3390/en18010086

Mudd, G. M., & Jowitt, S. M. (2016). Rare earth elements from heavy mineral sands: Assessing the potential of a forgotten resource. *Applied Earth Science*, *125*(3), 107–113. https://doi.org/10.1080/03717453.2016.1194955

Mulenshi, J., Khavari, P., Chelgani, S. C., & Rosenkranz, J. (2019). Characterization and Beneficiation Options for Tungsten Recovery from Yxsjöberg Historical Ore Tailings. *Processes*, *7*(12), 895. https://doi.org/10.3390/pr7120895

Na, H., Eom, Y., Yoo, K., & Diaz Alorro, R. (2024). A review on the reprocessing of sulfide tailings for resource recovery and AMD prevention using mineral processing methods. *Minerals Engineering*, *218*, 109025. https://doi.org/10.1016/j.mineng.2024.109025

Nascimento, S. C., Parbhakar-Fox, A., Cracknell, M. J., Cooke, D. R., Miller, C. B., & Heng, W. X. (2023). Geochemical, mineralogical, and geophysical methods to establish the geoenvironmental characteristics of the King River delta, Queenstown, Western Tasmania. *Applied Geochemistry*, *159*, 105820. https://doi.org/10.1016/j.apgeochem.2023.105820

Nassar, N. T., Graedel, T. E., & Harper, E. M. (2015). By-product metals are technologically essential but have problematic supply. *Science Advances*, *1*(3). https://doi.org/10.1126/sciadv.1400180

Neutrog Australia Pty Ltd. (2025). Neutrog Biological Fertilisers [Corporate Web Site]. Recuperato 1 maggio 2025, da Neutrog Biological Fertilisers website: https://neutrog.com.au/about/

Nguyen, T., Won, S., Ha, M.-G., Nguyen, D., & Kang, H. (2021). Bioleaching for environmental remediation of toxic metals and metalloids: A review on soils, sediments, and mine tailings. *Chemosphere*, *282*, 131108. https://doi.org/10.1016/j.chemosphere.2021.131108

Nimis, P., Costa, L. D., & Guastoni, A. (2014). Cobaltite-rich mineralization in the iron skarn deposit of Traversella (Western Alps, Italy). *Mineralogical Magazine*, *78*(1), 11–27. https://doi.org/10.1180/minmag.2014.078.1.02

Norilsk Nickel Harjavalta Oy. (2025). Nornickel Harjavalta [Corporate Web Site]. Recuperato 17 dicembre 2025, da Nornickel Harjavalta website: https://www.nornickel.fi/en-gb/nornickel-harjavalta

Nzeh, N. S., & Popoola, P. A. (2024). Physical beneficiation of heavy minerals – Part 2: A state of the art literature review on magnetic and electrostatic concentration techniques. *Heliyon*, *10*(11), e32201. https://doi.org/10.1016/J.HELIYON.2024.E32201

Nzeh, N. S., Popoola, P., Okanigbe, D., Adeosun, S., & Adeleke, A. (2023). Physical beneficiation of heavy minerals – Part 1: A state of the art literature review on gravity concentration techniques. *Heliyon*, *9*(8), e18919. https://doi.org/10.1016/J.HELIYON.2023.E18919

Oliver, N. H. S., Dipple, G. M., Cartwright, I., & Schiller, J. (1998). Fluid flow and metasomatism in the genesis of the amphibolites-facies, pelite-hosted Kanmantoo copper deposit, South Australia. *American Journal of Science*, *298*(3), 181–218. https://doi.org/10.2475/ajs.298.3.181

Omori, M. (2021a). Powder X-ray Diffraction Basic Course Second installment: Selection of equipment configuration to obtain high-quality data. *Rigaku Journal*, *37*(1).

Omori, M. (2021b). *Powder X-ray Diffraction Basic Course Third Installment: Sample preparation and measurement conditions to obtain high-quality data*. *37*(2), 8.

Otanmäki Mine Oy. (2025). Ilmenite project—Recovering ilmenite from tailings sand [Corporate Web Site]. Recuperato 12 settembre 2025, da Otanmäki Mine website: https://www.otanmaki.fi/en/ilmenite-project/

Parbhakar-Fox, A., Edraki, M., Walters, S., & Bradshaw, D. (2011). Development of a textural index for the prediction of acid rock drainage. *Minerals Engineering*, *24*(12), 1277–1287. https://doi.org/10.1016/j.mineng.2011.04.019

Parbhakar-Fox, A., Fox, N., Hill, R., Ferguson, T., & Maynard, B. (2018). Improved mine waste characterisation through static blended test work. *Minerals Engineering*, *116*, 132–142. https://doi.org/10.1016/J.MINENG.2017.09.011

Parker, A. J. (1986). Tectonic development and metallogeny of the Kanmantoo Trough in South Australia. *Ore Geology Reviews*, *1*(2–4), 203–212. https://doi.org/10.1016/0169-1368(86)90009-0

Pignattelli, S., Colzi, I., Buccianti, A., Cecchi, L., Arnetoli, M., Monnanni, R., … Gonnelli, C. (2012). Exploring element accumulation patterns of a metal excluder plant naturally colonizing a highly contaminated soil. *Journal of Hazardous Materials*, *227*, 362–369. https://doi.org/10.1016/j.jhazmat.2012.05.075

Pistolesi, C. (2024). *L'età delle miniere—Il declino dell'industria mineraria nell'Italia repubblicana*. Arcidosso (GR), Italia: Effigi Edizioni.

Pollock, M. V., Spry, P. G., Tott, K. A., Koenig, A., Both, R. A., & Ogierman, J. (2018). The origin of the sediment-hosted Kanmantoo Cu-Au deposit, South Australia: Mineralogical considerations. *Ore Geology Reviews*, *95*, 94–117. https://doi.org/10.1016/j.oregeorev.2018.02.017

Polvani, S. (2020). *Fabbrica e territorio: Il lavoro, le lotte, le imprese nell'alta Maremma*. Firenze: Regione Toscana, Consiglio regionale.

Protano, G., & Riccobono, F. (2002). High contents of rare earth elements (REEs) in stream waters of a Cu–Pb–Zn mining area. *Environmental Pollution*, *117*(3), 499–514. https://doi.org/10.1016/S0269-7491(01)00173-7

Rabe, W., Kostka, G., & Smith Stegen, K. (2017). China's supply of critical raw materials: Risks for Europe's solar and wind industries? *Energy Policy*, *101*, 692–699. https://doi.org/10.1016/j.enpol.2016.09.019

Remigio, A. C., Chaney, R., Baker, A., Edraki, M., Erskine, P., Echevarria, G., & Van Der Ent, A. (2020). Phytoextraction of high value elements and contaminants from mining and mineral wastes: Opportunities and

limitations. *Plant and Soil*, *449*, 11–37. https://doi.org/10.1007/s11104-020-04487-3

Respino, D. (2024). *Traversella—Miniere, minatori, minerali* (First). Torino, Italia: Giove Editrice s.r.l.

Riekkola-Vanhanen, M. (2013). Talvivaara mining company – From a project to a mine. *Minerals Engineering*, *48*, 2–9. https://doi.org/10.1016/j.mineng.2013.04.018

Roberto, F., & Schippers, A. (2022). Progress in bioleaching: Part B, applications of microbial processes by the minerals industries. *Applied Microbiology and Biotechnology*, *106*, 5913–5928. https://doi.org/10.1007/s00253-022-12085-9

Rosario-Beltré, A. J., Sánchez-España, J., Rodríguez-Gómez, V., Fernández-Naranjo, F. J., Bellido-Martín, E., Adánez-Sanjuán, P., & Arranz-González, J. C. (2023). Critical Raw Materials recovery potential from Spanish mine wastes: A national-scale preliminary assessment. *Journal of Cleaner Production*, *407*, 137163. https://doi.org/10.1016/j.jclepro.2023.137163

Rudnick, R. L., & Gao, S. (2014). Composition of the Continental Crust. In *Treatise on Geochemistry* (pp. 1–51). Elsevier. https://doi.org/10.1016/B978-0-08-095975-7.00301-6

Ruiz-Sánchez, A., Tapia, J. C. J., & Lapidus, G. T. (2023). Evaluation of acid mine drainage (AMD) from tailings and their valorization by copper recovery. *Minerals Engineering*, *191*, 107979. https://doi.org/10.1016/j.mineng.2022.107979

Santillán-Saldivar, J., Cimprich, A., Shaikh, N., Laratte, B., Young, S. B., & Sonnemann, G. (2021). How recycling mitigates supply risks of critical

raw materials: Extension of the geopolitical supply risk methodology applied to information and communication technologies in the European Union. *Resources, Conservation and Recycling*, *164*, 105108. https://doi.org/10.1016/j.resconrec.2020.105108

Sarker, S. K., Haque, N., Bhuiyan, M., Bruckard, W., & Pramanik, B. K. (2022). Recovery of strategically important critical minerals from mine tailings. *Journal of Environmental Chemical Engineering*, *10*(3), 107622. https://doi.org/10.1016/j.jece.2022.107622

Schiller, J. C. (2000). *Structural geology, metamorphism and origin of the Kanmantoo Copper deposit, South Australia* (PhD Thesis). University of Adelaide, Adelaide.

Schmidt Mumm, A., Tedesco, A., & Focke, D. (2009). Application of Ti-in-quartz thermometry to Au and Cu–Au mineralising systems. *Journal of Geochemical Exploration*, *101*(1), 93. https://doi.org/10.1016/j.gexplo.2008.11.014

SciAps.com. (2025). Recuperato 18 settembre 2025, da https://www.sciaps.com/

Scotti, A., Silvani, V., Juárez, N., Godeas, A., & Ubaldini, S. (2022). The Role of Mycorrhizal-Assisted Phytomining in the Recovery of Raw Materials from Mine Wastes. *Metals*. https://doi.org/10.3390/met12111828

Seccombe, P. K., Spry, P. G., Both, R. A., Jones, M. T., & Schiller, J. C. (1985). Base metal mineralization in the Kanmantoo Group, South Australia; a regional sulfur isotope study. *Economic Geology*, *80*(7), 1824–1841. https://doi.org/10.2113/gsecongeo.80.7.1824

Sedda, L., De Giudici, G., Fancello, D., Podda, F., & Naitza, S. (2023). Unlocking Strategic and Critical Raw Materials: Assessment of Zinc and REEs Enrichment in Tailings and Zn-Carbonate in a Historical Mining Area

(Montevecchio, SW Sardinia). *Minerals*, *14*(1), 3. https://doi.org/10.3390/min14010003

Serra, M., & Andrisani, M. G. (2017). *Inventario nazionale delle strutture di deposito di rifiuti estrattivi, chiuse o abbandonate, di tipo A. Rapporto di aggiornamento 2017* (Fasc. GEO 2017/RA/01; p. 33). Roma: ISPRA - Istituto Superiore per la Protezione e la Ricerca Ambientale. Recuperato da ISPRA - Istituto Superiore per la Protezione e la Ricerca Ambientale website: https://www.isprambiente.gov.it/files/miniere/Inventario_Aggiornamento_2017.pdf

Serra, M., & Andrisani, M. G. (2022). *Inventario nazionale delle strutture di deposito di rifiuti estrattivi, chiuse o abbandonate, di tipo A. Rapporto di aggiornamento 2022* (Fasc. 378/2022; p. 49). Roma: ISPRA - Istituto Superiore per la Protezione e la Ricerca Ambientale. Recuperato da ISPRA - Istituto Superiore per la Protezione e la Ricerca Ambientale website: https://www.isprambiente.gov.it/files2023/pubblicazioni/rapporti/rapporto-inventario-strutture-deposito-rev-3782022.pdf

Sesini, M., Zwickl-Bernhard, S., Münchmeyer, M., & Hobbs, B. F. (2025). Market dynamics and power risks in green technology materials: Platinum under the EU 2030 hydrogen target. *Applied Energy*, *383*, 125262. https://doi.org/10.1016/j.apenergy.2024.125262

Sokić, M., Marković, B., Stanković, S., Kamberović, Ž., Štrbac, N., Manojlović, V., & Petronijević, N. (2019). Kinetics of Chalcopyrite Leaching by Hydrogen Peroxide in Sulfuric Acid. *Metals*, *9*(11), 1173. https://doi.org/10.3390/met9111173

Solomon, M., & Groves, D. I. (1994). *The geology and origin of Australia's mineral deposits*. Oxfod: Clarendon Press.

Spry, P. G., Schiller, J. C., & Both, R. A. (1988). Structure and metamorphic setting of base metal mineralisation in the Kanmantoo Group, South Australia. *Australasian Institute of Mining and Metallurgy Proceedings*, *293*, 57–65.

Stander, H.-M., & Broadhurst, J. L. (2021). Understanding the Opportunities, Barriers, and Enablers for the Commercialization and Transfer of Technologies for Mine Waste Valorization: A Case Study of Coal Processing Wastes in South Africa. *Resources*, *10*(4), 35. https://doi.org/10.3390/resources10040035

Takahashi, G. (2015). *Sample preparation for X-ray fluorescence analysis*. *31*(1), 5.

Tedesco, A. (2009). *Late-stage orogenic model for Cu-Au mineralisation at Kanmantoo Mine: New insights from titanium in quartz geothermometry, fluid inclusions and geochemical modelling* (B.Sc. Honours Thesis). University of Adelaide, Australia.

Thomson, B. P. (1975). Kanmantoo Trough-regional geology and comments on mineralization. In *Economic Geology of Australia and Papua New Guinea, vol. 1* (pp. 555–560). Melbourne: The Australasian Institute of Mining and Metallurgy.

TOMRA Mining. (2023). TOMRA Mining's XRT ore sorting technology delivers value and sustainability at Mt Carbine Tungsten mine [Corporate Web Site]. Recuperato 15 gennaio 2026, da TOMRA website: https://www.tomra.com/mining/media-center/customer-stories/mt-carbine-tungsten-mine

Toteff, S. (1999). *Cambrian Sediment-hosted Exhalative Base Metal Mineralisation, Kanmantoo Trough, South Australia* (Report of Investigation Fasc. RI 057; p. 41). Government of South Australia. Recuperato da Government of South Australia website: https://pid.sarig.sa.gov.au/document/2018d037115

Trimmer, L. M. I. (2024). Italy [advance release]. In *U.S. Geological Survey Minerals Yearbook 2019*: *Vol. III. Area Reports—International, U.S. Geological Survey Minerals Yearbook 2019* (p. 23.1-23.6). Reston, VA, United States: U.S. Geological Survey. https://doi.org/10.3133/mybvIII

Turi, B., & Zucchetti, S. (1978). Indagine isotopica sui processi minerogenetici nel giacimento di Traversella (Torino). *Geoingegneria Ambientale e Mineraria*, *15*, 42–53.

U. S. Geological Survey. (2024). *Mineral commodity summaries 2024* (p. 212). https://doi.org/10.3133/mcs2024

United Nations. (2020). *United Nations Framework Classification for Resources: Update 2019*. Geneva: United Nations. https://doi.org/10.18356/44105e2b-en

U.S. Environmental Protection Agency (USEPA). (2025). *SW-846 Test Method 1311: Toxicity Characteristic Leaching Procedure*. U.S. Environmental Protection Agency. Recuperato da https://www.epa.gov/hw-sw846/sw-846-test-method-1312-synthetic-precipitation-leaching-procedure

Valenta, R. K., Lèbre, É., Antonio, C., Franks, D. M., Jokovic, V., Micklethwaite, S., … Yahyaei, M. (2023). Decarbonisation to drive dramatic increase in mining waste–Options for reduction. *Resources, Conservation and Recycling*, *190*, 106859. https://doi.org/10.1016/J.RESCONREC.2022.106859

Verwoerd, P. J., & Clergorn, J. H. (A c. Di). (1975). Kanmantoo copper orebody. In *Economic geology of Australia and Papua New Guinea 1* (pp. 560–565). Melbourne: The Australasian Institute of Mining and Metallurgy.

Wallace, L. (2021, novembre). *Australia's next copper mine*. Presentato al South Australian Exploration and Mining Conference (SAEMC).

Warr, L. N. (2021). IMA–CNMNC approved mineral symbols. *Mineralogical Magazine*, *85*(3), 291–320. https://doi.org/10.1180/mgm.2021.43

Whitworth, A. J., Forbes, E., Verster, I., Jokovic, V., Awatey, B., & Parbhakar-Fox, A. (2022). Review on advances in mineral processing technologies suitable for critical metal recovery from mining and processing wastes. *Cleaner Engineering and Technology*, *7*, 100451. https://doi.org/10.1016/J.CLET.2022.100451

Whitworth, A. J., Vaughan, J., Southam, G., Van Der Ent, A., Nkrumah, P. N., Ma, X., & Parbhakar-Fox, A. (2022). Review on metal extraction technologies suitable for critical metal recovery from mining and processing wastes. *Minerals Engineering*, *182*, 107537. https://doi.org/10.1016/j.mineng.2022.107537

Wills, B. A., & Finch, J. A. (2015). Wills' mineral processing technology: An introduction to the practical aspects of ore treatment and mineral recovery. In *Wills' Mineral Processing Technology: An Introduction to the Practical Aspects of Ore Treatment and Mineral Recovery*. Elsevier Inc. Recuperato da http://www.sciencedirect.com:5070/book/9780080970530/wills-mineral-processing-technology

Wilson, G. L. (2009). *Structural setting and timing of the Kanmantoo Cu-Au deposit, Callington, SA* (B.Sc. Honours Thesis). University of Adelaide, Australia.

Zhang, S. E., Bourdeau, J. E., Nwaila, G. T., & Ghorbani, Y. (2023). Emerging criticality: Unraveling shifting dynamics of the EU's critical raw materials and their implications on Canada and South Africa. *Resources Policy*, *86*, 104247. https://doi.org/10.1016/j.resourpol.2023.104247

Zhengwei Han, Wei Ran, Jing Li, Afsar Khan, Hui Zhong, & Zhiguo He. (2023). Efficient Leaching of Rubidium from Biotite by Ion Exchange without Destroying the Lamellar Crystal Structure. *ACS Sustainable Chemistry & Engineering*, *11*(24), 8822–8835. https://doi.org/10.1021/acssuschemeng.3c00441

Žibret, G., Lemiere, B., Mendez, A.-M., Cormio, C., Sinnett, D., Cleall, P., … Carvalho, M. T. (2020). National Mineral Waste Databases as an Information Source for Assessing Material Recovery Potential from Mine Waste, Tailings and Metallurgical Waste. *Minerals*, *10*(5). https://doi.org/10.3390/min10050446

Zucchetti, S. (1961). Uranium-bearing bodies in the ore deposits of Traversella (Italy). *Economic Geology*, *56*(8), 1469–1471. https://doi.org/10.2113/GSECONGEO.56.8.1469

Zucchetti, S. (1962). Su una zona uranifera con allanite nel deposito di Traversella. *Rendiconti della Società Mineralogica Italiana*, *18, 293*. Pavia.

Zucchetti, S. (1966). Studi sul giacimento di Traversella (Torino). I corpi mineralizzati a scheelite. *Symposium Internazionale sui Giacimenti Minerari delle Alpi*, *2*, 939–960.

A. Appendix A

This appendix material is referred to in ***Chapter 3***.

A.1. Calculated tEI,eq values according to chemical assays reported in the METSO-GTK database

Mine Site	Q_t [t]	Commodity/ Mineral	C_c [ppm]	$Q_t * C_c$ [t]	EI_c	$t_{EI,eq,i}$	$\Sigma t_{EI,eq}$
Aijala	1,980,000	Cu	1,200	2,376	4	9,504	**57,024**
		Zn	5,000	9,900	4.8	47,520	
Hällinmäki	4,200,000	Co	50	210	6.8	1,428	**11,046**
		Cu	310	1,302	4	5,208	
		Ni	100	420	5.7	2,394	
		Zn	100	420	4.8	2,016	
Korsnäs	850,000	LREE La	7,000	5,950	2.9	17,255	**28,125**
		HREE Eu	57	48	3.3	160	
		Pb	3,000	2,550	4.2	10,710	
Hitura	15,000,000	Cu	980	14,700	4	58,800	**479,010**
		Ni	2,140	32,100	5.7	182,970	
		Zn	100	1,500	4.8	7,200	
		Cr	2,130	31,950	7.2	230,040	
Pyhäsalmi 1	10,000,000	Baryte	50,000	500,000	3.5	1,750,000	**1,935,883**
		Cu	680	6,800	4	27,200	
		Au	0.3	3	2.4	7	
		Ag	6	60	4.6	276	
		Zn	3,300	33,000	4.8	158,400	
Pyhäsalmi 2	4,000,000	Cu	600	2,400	4	9,600	**34,560**
		Zn	1,300	5,200	4.8	24,960	
Pyhäsalmi 3	6,000,000	Sb	50	300	5.4	1,620	**115,649**
		As	406	2,436	2.9	7,064	

Mine Site	Q_t [t]	Commodity/ Mineral	C_c [ppm]	$Q_t * C_c$ [t]	EI_c	$t_{EI,eq,i}$	$\Sigma t_{EI,eq}$
		Cd	6.9	41	4.1	170	
		Cr	43	258	7.2	1,858	
		Co	92	552	6.8	3,754	
		Cu	1,236	7,416	4.0	29,664	
		Pb	118	708	4.2	2,974	
		Mo	10	60	6.7	402	
		Ni	20	120	5.7	684	
		V	46	276	3.9	1,076	
		Zn	2,305	13,830	4.8	66,384	
Pyhäsalmi (Aggregate 1,2,3)	20,000,000	Baryte	-	500,000	3.5	1,750,000	**2,086,093**
		Au	-	3	2.4	7	
		Ag	-	60	4.6	276	
		Sb	-	300	5.4	1,620	
		As	-	2,436	2.9	7,064	
		Cd	-	41	4.1	170	
		Cr	-	258	7.2	1,858	
		Co	-	552	6.8	3,754	
		Cu	-	16,616	4	66,464	
		Pb	-	708	4.2	2,974	
		Mo	-	60	6.7	402	
		Ni	-	120	5.7	684	
		V	-	276	3.9	1,076	
		Zn	-	52,030	4.8	249,744	
Luikonlahti	14,300,000	As	100	1,430	2.9	4,147	**361,590**

Mine Site	Q_t [t]	Commodity/ Mineral	C_c [ppm]	$Q_t * C_c$ [t]	EI_c	$t_{EI,eq,i}$	$\Sigma t_{EI,eq}$
		Co	600	8,580	6.8	58,344	
		Ni	520	7,436	5.7	42,385	
		Zn	2,000	28,600	4.8	137,280	
		Cr	1,160	16,588	7.2	119,434	
Enonkoski	6,600,000	Sb	18	119	5.4	641	**156,783**
		As	20	132	2.9	383	
		Cd	2	13	4.1	54	
		Cr	800	5,280	7.2	38,016	
		Co	100	660	6.8	4,488	
		Cu	600	3,960	4	15,840	
		Pb	48	317	4.2	1,331	
		Ni	2,300	15,180	5.7	86,526	
		Zn	300	1,980	4.8	9,504	
Hammaslahti	5,300,000	Cd	3	16	4.1	65.19	**35,056**
		Cr	28	148	7.2	1,068	
		Co	55	292	6.8	1,982	
		Cu	762	4,039	4	16,154	
		Au	0.06	0.3	2.4	0.8	
		Pb	30	159	4.2	668	
		Mn	305	1,617	6.9	11,154	
		Ni	15	79.5	5.7	453	
		Se	13	69	4.8	330	
		Ag	1.97	10	4.6	48	
		Zn	123	652	4.8	3,132	

Mine Site	Q_t [t]	Commodity/ Mineral	C_c [ppm]	$Q_t * C_c$ [t]	EI_c	$t_{EI,eq,i}$	$\Sigma t_{EI,eq}$
Haveri	1,400,000	As	157	220	2.9	637	**9,431**
		Co	142	199	6.8	1,352	
		Cu	934	1,308	4	5,230	
		Au	1.13	1.6	2.4	3.8	
		Ni	131	183	5.7	1,045	
		Ag	3	4.2	4.6	19	
		Zn	170	238	4.8	1,142	
Kotalahti	9,400,000	As	3	28	2.9	82	**200,867**
		Cr	1,100	10,340	7.2	74,448	
		Co	30	282	6.8	1,918	
		Cu	330	3,102	4	12,408	
		Au	0.024	0.2	2.4	0.5	
		Pb	60	564	4.2	2,369	
		Mn	1,100	10,340	6.9	71,346	
		Mo	10	94	6.7	630	
		Ni	610	5,734	5.7	32,683	
		Ag	0.44	4	4.6	19	
		Zn	110	1,034	4.8	4,963	
Kylmäkoski	650,000	Co	100	65	6.8	442	**8,053**
		Cu	430	280	4	1,118	
		Au	0.02	0.013	2.4	0.03	
		Ni	910	592	5.7	3,372	
		Ag	0.4	0.26	4.6	1.2	
		Zn	1,000	650	4.8	3,120	

Mine Site	Q_t [t]	Commodity/ Mineral	C_c [ppm]	$Q_t * C_c$ [t]	EI_c	$t_{EI,eq,i}$	$\Sigma t_{EI,eq}$
Makola	380,000	Co	1,100	418	6.8	2,842	**6,416**
		Ni	1,650	627	5.7	3,574	
Mätäsvaara	1,000,000	Co	285	285	6.8	1,938	**3,814**
		Mo	280	280	6.7	1,876	
Orijärvi	1,000,000	Co	30	30	6.8	204	**48,684**
		Cu	1,800	1,800	4	7,200	
		Au	0.1	0.1	2.4	0.24	
		Pb	2,500	2,500	4.2	10,500	
		Ag	13	13	4.6	60	
		Zn	6,400	6,400	4.8	30,720	
Otanmäki	11,800,000	Co	200	2,360	6.8	16,048	**11,245,400**
		Cu	100	1,180	4	4,720	
		Mn	80,000	944,000	6.9	6,513,600	
		Ni	200	2,360	5.7	13,452	
		Ti	73,000	861,400	5.4	4,651,560	
		V	1,000	11,800	3.9	46,020	
Outokumpu	1,000,000	Co	600	600	6.8	4,080	**14,925**
		Cu	1,430	1,430	4	5,720	
		Au	0.059	0.059	2.4	0.14	
		Se	5.9	5.9	4.8	28	
		Ag	2.06	2.06	4.6	9.5	
		Zn	1,060	1,060	4.8	5,088	
Raajärvi	2,900,000	Co	130	377	6.8	2,564	**2,107,641**
		Cu	180	522	4	2,088	

Mine Site	Q_t [t]	Commodity/ Mineral	C_c [ppm]	$Q_t * C_c$ [t]	EI_c	$t_{EI,eq,i}$	$\Sigma t_{EI,eq}$
		Fe ore	100,000	290,000	7.2	2,088,000	
		Ni	130	377	5.7	2,149	
		V	1,000	2,900	3.9	11,310	
		Zn	110	319	4.8	1,531	
Rautuvaara 1	7,060,000	As	20	141	2.9	409	**103,146**
		Co	110	777	6.8	5,281	
		Cu	1,300	9,178	4	36,712	
		Mn	1,200	8,472	6.9	58,457	
		Ni	40	282	5.7	1610	
		Zn	20	141	4.8	678	
Rautuvaara 2	2,470,000	As	140	346	2.9	1,003	**44,067**
		Co	160	395	6.8	2,687	
		Cu	900	2,223	4	8,892	
		Mn	1,600	3,952	6.9	27,269	
		Ni	190	469	5.7	2,675	
		Zn	130	321	4.8	1,541	
Rautuvaara (Aggregated 1,2)	9,530,000	As	-	487	2.9	1,412	**147,213**
		Co	-	1,172	6.8	7,968	
		Cu	-	11,401	4	45,604	
		Mn	-	12,424	6.9	85,725	
		Ni	-	752	5.7	4,284	
		Zn	-	462	4.8	2,219	
Vihanti	13,700,000	Cu	800	10,960	4	43,840	**220,946**
		Au	0.14	1.9	2.4	4.6	

Mine Site	Q_t [t]	Commodity/ Mineral	C_c [ppm]	$Q_t * C_c$ [t]	EI_c	$t_{EI,eq,i}$	$\Sigma t_{EI,eq}$
		Pb	900	12,330	4.2	51,786	
		Ag	5.9	81	4.6	372	
		Zn	1,900	26,030	4.8	124,944	
Virtasalmi	4,200,000	Co	50	210	6.8	1,428	**11,404**
		Cu	310	1,302	4	5,208	
		Au	0.03	0.13	2.4	0.3	
		Pb	20	84	4.2	352	
		Ni	100	420	5.7	2,394	
		Ag	0.3	1.26	4.6	5.8	
		Zn	100	420	4.8	2,016	
Vuonos	9,000,000	Co	700	6,300	6.8	42,840	**421,012**
		Cu	1,900	17,100	4	68,400	
		Au	0.03	0.3	2.4	0.6	
		Mn	400	3,600	6.9	24,840	
		Ni	1,000	9,000	5.7	51,300	
		Se	7	63	4.8	302	
		Ag	1.2	10.8	4.6	50	
		Zn	5,400	48,600	4.8	233,280	
Ylöjärvi	2,800,000	Co	50	140	6.8	952	**9,942**
		Cu	210	588	4	2,352	
		Pb	20	56	4.2	235	
		Ag	5.7	16	4.6	73	
		W	155	434	8.7	3,776	
		Zn	190	532	4.8	2,554	

A.2. Calculated economic values in Finnish mine waste sites

Mine Site	Commodity	Comm. Q.ty [t]	Price [US$/ton]	Value [MUS$]	EV [MUS$]
Aijala	Cu	2,376	9,790	23.3	**51**
	Zn	9,900	2,850	28.2	
Hällinmäki	Co	210	35,274	7.4	**31**
	Cu	1,302	9,790	12.8	
	Ni	420	22,000	9.2	
	Zn	420	2,850	1.2	
Korsnäs	LREE La	5,950	2,570	15.3	**22**
	HREE Eu	48	27,000	1.3	
	Pb	2,550	2,185	5.6	
Hitura	Cu	14,700	9,790	143.9	**1,242**
	Ni	32,100	22,000	706.2	
	Zn	1,500	2,850	4.3	
	Cr	31,950	12,125	387.4	
Pyhäsalmi 1	Baryte	500,000	150	75.0	**464**
	Cu	6,800	9,790	66.6	
	Au	3	61,086,330	183.3	
	Ag	60	752,326	45.1	
	Zn	33,000	2,850	94.1	
Pyhäsalmi 2	Cu	2,400	9,790	23.5	**38**
	Zn	5,200	2,850	14.8	
Pyhäsalmi 3	Sb	300	12,346	3.7	**206**
	As	2,436	4,409	10.7	
	Cd	41	4,100	0.17	
	Cr	258	12,125	3.13	
	Co	552	35,274	19.47	
	Cu	7,416	9,790	72.60	
	Pb	708	2,185	1.55	
	Mo	60	55,600	3.34	
	Ni	120	22,000	2.64	
	V	276	178,000	49.13	
	Zn	13,830	2,850	39.42	
Pyhäsalmi (Aggregated 1, 2, 3)	Baryte	500,000	150	75.00	**708**
	Au	3	61,086,330	183.3	
	Ag	60	752,326	45.1	
	Sb	300	12,346	3.7	
	As	2,436	4,409	10.7	
	Cd	41	4,100	0.2	
	Cr	258	12,125	3.1	
	Co	552	35,274	19.5	
	Cu	16,616	9,790	162.7	
	Pb	708	2,185	1.6	

Mine Site	Commodity	Comm. Q.ty [t]	Price [US$/ton]	Value [MUS$]	EV [MUS$]
	Mo	60	55,600	3.3	
	Ni	120	22,000	2.6	
	V	276	178,000	49.1	
	Zn	52,030	2,850	148.3	
Luikonlahti	As	1,430	4,409	6.31	**755**
	Co	8,580	35,274	302.7	
	Ni	7,436	22,000	163.6	
	Zn	28,600	2,850	81.5	
	Cr	16,588	12,125	201.1	
Enonkoski	Sb	119	12,346	1.47	**468**
	As	132	4,409	0.58	
	Cd	13	4,100	0.05	
	Cr	5,280	12,125	64.0	
	Co	660	35,274	23.3	
	Cu	3,960	9,790	38.8	
	Pb	316.8	2,185	0.7	
	Ni	15,180	22,000	334.0	
	Zn	1,980	2,850	5.6	
Hammaslahti	Cd	16	4,100	0.07	**84**
	Cr	148	12,125	1.80	
	Co	292	35,274	10.28	
	Cu	4,039	9,790	39.54	
	Au	0.32	61,086,330	19.43	
	Pb	159	2,185	0.35	
	Mn	1,617	5	0.01	
	Ni	80	22,000	1.75	
	Se	69	19,000	1.31	
	Ag	10	752,326	7.86	
	Zn	652	2,850	1.86	
Haveri	As	220	4,409	1.0	**125**
	Co	199	35,274	7.0	
	Cu	1,308	9,790	12.8	
	Au	1.6	61,086,330	96.6	
	Ni	183	22,000	4.0	
	Ag	4	752,326	3.2	
	Zn	238	2,850	0.7	
Kotalahti	As	28	4,409	0.1	**318**
	Cr	10,340	12,125	125.4	
	Co	282	35,274	10.0	
	Cu	3,102	9,790	30.4	
	Au	0.2	61,086,330	13.8	
	Pb	564	2,185	1.2	
	Mn	10,340	5	0.05	

Mine Site	Commodity	Comm. Q.ty [t]	Price [US$/ton]	Value [MUS $]	EV [MUS $]
	Mo	94	55,600	5.2	
	Ni	5,734	22,000	126.2	
	Ag	4.1	752,326	3.1	
	Zn	1,034	2,850	3.0	
Kylmäkoski	Co	65	35,274	2.3	**21**
	Cu	280	9,790	2.7	
	Au	0.01	61,086,330	0.8	
	Ni	592	22,000	13.0	
	Ag	0.26	752,326	0.2	
	Zn	650	2,850	1.9	
Makola	Co	418	35,274	14.7	**29**
	Ni	627	22,000	13.8	
Mätäsvaara	Co	285	35,274	10.0	**26**
	Mo	280	55,600	15.6	
Orijärvi	Co	30	35,274	1.1	**58**
	Cu	1,800	9,790	17.6	
	Au	0.1	61,086,330	6.1	
	Pb	2,500	2,185	5.5	
	Ag	13	752,326	9.8	
	Zn	6,400	2,850	18.2	
Otanmäki	Co	2,360	35,274	83.3	**2,562**
	Cu	1,180	97,90	11.6	
	Mn	944,000	5	4.7	
	Ni	2,360	22,000	51.9	
	Ti	861,400	360	310.0	
	V	11,800	178,000	2,100	
Outokumpu	Co	600	35,274	21.2	**44**
	Cu	1,430	9,790	14.0	
	Au	0.059	61,086,330	3.6	
	Se	5.9	19,000	0.1	
	Ag	2.1	752,326	1.6	
	Zn	1,060	2,850	3.0	
Raajärvi	Co	377	35,274	13.3	**576**
	Cu	522	9,790	5.1	
	Fe ore	290,000	110	31.9	
	Ni	377	22,000	8.3	
	V	2,900	178,000	516.2	
	Zn	319	2,850	0.9	
Rautuvaara 1	As	141	4,409	0.6	**125**
	Co	777	35,274	27.4	
	Cu	9,178	9,790	89.9	
	Mn	8,472	5	0.04	
	Ni	282	22,000	6.2	

Mine Site	Commodity	Comm. Q.ty [t]	Price [US$/ton]	Value [MUS$]	EV [MUS$]
	Zn	141	2,850	0.4	
Rautuvaara 2	As	346	4,409	1.5	**49**
	Co	395	35,274	14.0	
	Cu	2,223	9,790	21.8	
	Mn	3,952	5	0.02	
	Ni	469	22,000	10.3	
	Zn	321	2,850	0.92	
Rautuvaara (Aggregate 1,2)	As	487	4,409	2.2	**173**
	Co	1,172	35,274	41.3	
	Cu	11,401	9,790	111.6	
	Mn	12,424	5	0.1	
	Ni	752	22,000	16.5	
	Zn	462	2,850	1.3	
Vihanti	Cu	10,960	9,790	107.3	**386**
	Au	1.9	61,086,330	117.2	
	Pb	12,330	2,185	26.9	
	Ag	81	752,326	60.8	
	Zn	26,030	2,850	74.2	
Virtasalmi	Co	210	35,274	7.4	**39**
	Cu	1,302	9,790	12.8	
	Au	0.126	61,086,330	7.7	
	Pb	84	2,185	0.2	
	Ni	420	22,000	9.2	
	Ag	1.3	752,326	1.0	
	Zn	420	2850	1.2	
Vuonos	Co	6,300	35,274	222.2	**752**
	Cu	17,100	9,790	167.4	
	Au	0.27	61,086,330	16.5	
	Mn	3,600	5	0.02	
	Ni	9,000	22,000	198.0	
	Se	63	19,000	1.2	
	Ag	11	752,326	8.1	
	Zn	48,600	2,850	138.5	
Ylöjärvi	Co	140	35,274	4.9	**42**
	Cu	588	9,790	5.8	
	Pb	56	2,185	0.12	
	Ag	16	752,326	12.0	
	W	434	40,000	17.4	
	Zn	532	2,850	1.5	

B. Appendix B

This appendix material is referred to in ***Chapter 4***.

B.1. List, depth and location of collected samples from old TSF, Kanmantoo

Sample ID	*Hole ID*	*Longitude (WGS84)*	*Latitude (WGS84)*	*Depth from (m)*	*Depth to (m)*
KA33	KA05	139.0047	-35.08	0	1.3
KA34	KA05	139.0047	-35.08	1.3	2.2
KA35	KA05	139.0047	-35.08	2.2	2.7
KA36	KA05	139.0047	-35.08	2.7	2.9
KA37	KA05	139.0047	-35.08	2.9	3.2
KA38	KA05	139.0047	-35.08	3.2	3.5
KA39	KA05	139.0047	-35.08	3.5	4.3
KA40	KA05	139.0047	-35.08	4.3	4.7
KA41	KA05	139.0047	-35.08	4.7	4.9
KA42	KA05	139.0047	-35.08	4.9	5.7
KA43	KA05	139.0047	-35.08	5.7	5.9
KA45	KA06	138.9997	-35.0808	0	1.9
KA46	KA06	138.9997	-35.0808	1.9	2.2
KA47	KA06	138.9997	-35.0808	2.2	2.7
KA48	KA06	138.9997	-35.0808	2.7	4.1
KA49	KA06	138.9997	-35.0808	4.1	4.2
KA50	KA07	139.0019	-35.0827	0	1.7
KA51	KA07	139.0019	-35.0827	1.7	1.9
KA52	KA07	139.0019	-35.0827	1.9	2.5
KA53	KA07	139.0019	-35.0827	2.5	3
KA54	KA07	139.0019	-35.0827	3	3.5
KA55	KA07	139.0019	-35.0827	3.5	4
KA56	KA07	139.0019	-35.0827	4	4.4
KA57	KA07	139.0019	-35.0827	4.4	4.6
KA58	KA07	139.0019	-35.0827	4.6	4.8
KA59	KA07	139.0019	-35.0827	4.8	5.6
KA61	KA08	138.9981	-35.0828	0	0.8
KA62	KA08	138.9981	-35.0828	0.8	1.5
KA63	KA08	138.9981	-35.0828	1.5	2
KA64	KA08	138.9981	-35.0828	2	2.5
KA65	KA09	139.0022	-35.0827	0	2.1
KA66	KA09	139.0022	-35.0827	2.1	2.4
KA67	KA09	139.0022	-35.0827	2.4	2.7
KA68	KA09	139.0022	-35.0827	2.7	2.8
KA69	KA09	139.0022	-35.0827	2.8	3.4
KA70	KA09	139.0022	-35.0827	3.4	3.7
KA71	KA09	139.0022	-35.0827	3.7	4.2
KA72	KA09	139.0022	-35.0827	4.2	5.3

C. Appendix C

This appendix material is referred to in ***Chapter 5.***

C.1. MLA modal mineralogy results for 0.250-0.125mm size class - Traversella

Mineral	***wt.%***
Magnetite	33.4
Andradite	14.2
Talc	10.5
Diopside	8.1
Serpentine	7.8
Clinochlore	7.4
Ankerite	5.3
Calcite	2.8
Quartz	2.8
Pyrite	2.2
Chlorite	1.6
Phases < 1 wt%	**3.9**
Goethite	0.81
Amphibole	0.81
Siderite	0.49
Spertiniite	0.33
Brucite	0.28
Biotite	0.19
Plagioclase	0.18
Apatite	0.15
Ilmenite	0.13
K_Feldspar	0.12
Muscovite	0.12
Dolomite	0.10
Jarosite	0.06
Sphalerite	0.04
Fluorite	0.03
Scheelite	0.03
Chalcopyrite	0.02
Galena	0.01
Rutile	0.01
Titanite	0.01
Epidote	0.01
Barite	0.01

C.2. Matlab script for semi-automated liberation analysis based on SEM-BSE images

```
% --------- INPUT SECTION - START -------------
% Analysis name input
analysisName = input('Enter the name of the analysis: ', 's');
analysisName = regexprep(analysisName, '[^\w]', '_');

% Display the entered analysis name
disp(['Analysis Name: ', analysisName]);

% Open a file selection dialog for the BW_values_input.mat
file
fprintf('\n');
display('Select the BW masks input file')

[bwFileName, bwFilePath] = uigetfile('*.mat', 'Select the
BW_values_input.mat file');
if isequal(bwFileName, 0)
    error('No file selected. Please select the
BW_values_input.mat file.');
end
bwFullPath = fullfile(bwFilePath, bwFileName);

% Open Selection dialog windows for selecting the BSE image
file
fprintf('\n');
display('Select the BSE original image')

[bseFileName, bseFilePath] = uigetfile({'*.tif;*.png;*.jpg',
'Image Files (*.tif, *.png, *.jpg)'}, 'Select the BSE image
file');
if isequal(bseFileName, 0)
    error('No file selected. Please select the BSE image
file.');
end
bseFullPath = fullfile(bseFilePath, bseFileName);

% Input pixel size in microns
fprintf('\n');
pixelSize = input('Enter the pixel size in pixel/microns
[px/um]: ');


% Load the maskedImage and BW MATLAB files
load(bwFullPath);

% Load the original BSE image (grayscale or color)
originalBSEImg = imread(bseFullPath);
```

```
    % Confirmation messages
    disp(['Loaded BW values from: ', bwFullPath]);
    disp(['Loaded BSE image from: ', bseFullPath]);
    fprintf('\n');
    disp(['Pixel size set to: ', num2str(pixelSize), ' [px/um]']);
    fprintf('\n');

    % Select the output folder
    outputFolder = uigetdir('', 'Select the output folder for the
files');

    % No folder selected message
    if isequal(outputFolder, 0)
        error('No folder selected. Please run the script again and
select a folder.');
        fprintf('\n');
    end



    % Set Liberated percentage Threshold
    Lib_thr = 80 ;

    % Set Middling percentage Threshold
    Mid_thr = 30 ;

    %Set the dimensions in [um] for the free-grain size
determination.
    Sieve_series = fliplr(25:50:225);

    % Load the binary images
    maskGrains = BW_totalMag_gangue;  % Grains mask (binary image)
- To be created Manually with Segment Image Matlab Tool
    maskGangue = BW_interlock_gangue;    % Gangue mask (binary
image) - To be created Manually with Segment Image Matlab Tool

    % Minimum grain area threshold (in pixels)
    minArea = 10;
    % Scaling factor for bounding box
    scaleFactor = 1.1;

    % --------- INPUT SECTION - END -------------%

    % --------- GRAIN MASKING SECTION - START -------------%


    % Label each connected component in the grain mask
    [labeledGrains, numGrains] = bwlabel(maskGrains);

    % Get properties for each grain
    grainProps = regionprops(labeledGrains, 'BoundingBox', 'Area',
'EquivDiameter','MajorAxisLength','Centroid');
```

```
    % Initialize the results table
    overlapData = [];
    libGrainsData = [];
    EqDiam = [];


    % Overlap area image creation
    figure (001);
    set(gcf,  'Name',  ['Valuable  Grains  -  ',  analysisName],
'NumberTitle', 'off');

    imshow(originalBSEImg);
    title(['Valuable  Grains  -  ',  analysisName],  'FontWeight',
'bold');

    hold on;

    % Single grain processing
    for k = 1:numGrains
        % Area calculation for single grain
        grainArea = grainProps(k).Area;
        EqDiam_px = grainProps(k).EquivDiameter;
        MajAx_px = grainProps(k).MajorAxisLength;
        centroid = grainProps(k).Centroid;

        %Filter grains with area smaller than threshold
        if grainArea < minArea
        continue;
        end

        % Create a binary mask for the current grain only
        singleGrainMask = (labeledGrains == k);

        % Get the bounding box for the current grain
        boundingBox = grainProps(k).BoundingBox;

        % Calculate new bounding box with enlarged size
        x = boundingBox(1);
        y = boundingBox(2);
        width = boundingBox(3);
        height = boundingBox(4);

        % Enlarge the bounding box
        newWidth = round(width * scaleFactor);
        newHeight = round(height * scaleFactor);

        % Recalculate the position to keep it centered
        newX = round(max(1, x - (newWidth - width) / 2));
        newY = round(max(1, y - (newHeight - height) / 2));

        % Ensure the box doesn't go outside the image
        newWidth = min(newWidth, size(maskGrains, 2) - newX + 1);
```

```
        newHeight = min(newHeight, size(maskGrains, 1) - newY +
1);

        % Create the new bounding box with enlarged size
        enlargedBoundingBox = [newX, newY, newWidth, newHeight];

        % Crop the same region from the binary mask
        croppedGrainMask          =          imcrop(singleGrainMask,
enlargedBoundingBox);

        % Fill holes in the binary mask
        filledGrainMask = imfill(croppedGrainMask, "holes");

        % Now calculate the overlap with the valuable mineral mask
        croppedGangueMask            =            imcrop(maskGangue,
enlargedBoundingBox);

        % Fill holes in the magnetite mask
        filledGangueMask = imfill(croppedGangueMask, "holes");

        % --------- GRAIN MASKING SECTION – END -------------%

        %--------- CALCULATION SECTION - START ----------%

        % Calculate the area of valuable mineral in the grain
(valuable mineral area = total - gangue)
        ValMinArea = grainArea - sum(croppedGangueMask(:));

        % Calculate the overlap percentage
        overlapPercentage = (ValMinArea/grainArea) * 100;

        % Store the data for the current grain (grain number,
overlap percentage, total valuable mineral area, and grain area)
        overlapData = [overlapData; k, grainArea, ValMinArea,
overlapPercentage];

        if overlapPercentage >= Lib_thr


              EqDiam = EqDiam_px/pixelSize;
              MajAx = MajAx_px/pixelSize;


            libGrainsData = [libGrainsData; k, EqDiam, MajAx];
        end


        %--------- CALCULATION SECTION - END ----------%

        %--------- PLOTTING SECTION - START ----------%

        % Plot the bounding box of the grain (in green)
```

```
        rectangle('Position',   enlargedBoundingBox,   'EdgeColor',
'g', 'LineWidth', 1);

        % Highlight the valuable grain perimeter in green
        gangueBoundary      =      bwperim(croppedGrainMask      &
~croppedGangueMask);
        [yVal, xVal] = find(gangueBoundary);
        xVal = xVal + newX - 1;
        yVal = yVal + newY - 1;
        plot(xVal, yVal, 'g.', 'MarkerSize', 5);

        % Highlight the gangue perimeter in red
        ValBoundary = bwperim(croppedGangueMask);
        [yGangue, xGangue] = find(ValBoundary);
        xGangue = xGangue + newX - 1;
        yGangue = yGangue + newY - 1;
        plot(xGangue, yGangue, 'r.', 'MarkerSize', 5);

        % Add the grain identification number
        text(centroid(1), centroid(2), num2str(k), 'Color', 'g',
'FontSize',   14,   'FontWeight',   'bold',   'HorizontalAlignment',
'center', 'VerticalAlignment', 'middle');



    end

    % Add the legend
    hold on;
    h1 = plot(NaN, NaN, 'g.', 'MarkerSize', 5); % Green dot for
valuable areas contour
    h2 = plot(NaN, NaN, 'r.', 'MarkerSize', 5); % Red dot for
gangue areas contour
    legend([h1,  h2],  {'Green  Contour  (Grain)',  'Red  Contour
(Gangue)'}, 'Location', 'NorthEastOutside', 'FontWeight', 'bold');

    outputImageFile1   =   fullfile(outputFolder,   ['GrainMasks_',
analysisName, '.jpg']);

    saveas(gcf, outputImageFile1);

    % Display a confirmation message
    disp(['Figure 1 saved as ', outputImageFile1]);
    fprintf('\n');

        %--------- PLOTTING SECTION - END ----------%


    %-------- Categoirization Section - START -------%
```

```
    overlapTable    =    array2table(overlapData,    'VariableNames',
{'Grain  #',  'Total  Grain  Area  [px]',  'Valuable  Mineral  Area
[px]','Overlap Percentage'});
    overlapping_percentage = overlapTable{:, 4};
    categories = strings(size(overlapping_percentage));


    categories(overlapping_percentage >= Lib_thr) = "Liberated";
    categories(overlapping_percentage       <       Lib_thr       &
overlapping_percentage >= Mid_thr) = "Middling";
    categories(overlapping_percentage < Mid_thr) = "Locked";

    overlap_Table_with_categories          =          [overlapTable,
table(categories)];


    overlap_Table_with_categories.Properties.VariableNames{end}   =
'Liberation Category';



    disp("Grains' List with liberation Categories")
    disp(overlap_Table_with_categories);
    fprintf('\n');

    %Convert the equivalent diameter data to a table
    libGrainsData_table         =         array2table(libGrainsData,
'VariableNames', {'Grain #', 'EqDiam [um]', 'Major Axis [um]'});
    disp("Liberated Grains - Equivalent diameter in microns")
    disp(libGrainsData_table);
    fprintf('\n');

    %-------- Categoirization Section - END -------%


    %-------- Liberation Analysis Section - START -------%


    magnetiteArea = overlapTable{:, 3};
    overlapPercentage = overlapTable{:, 4};

    % Calculate total magnetite area for each category
    totalMagnetiteLiberated_A                                          =
sum(magnetiteArea(overlapPercentage >= Lib_thr));
    totalMagnetiteMiddling_A  =  sum(magnetiteArea(overlapPercentage
>= Mid_thr & overlapPercentage < Lib_thr));
    totalMagnetiteLocked_A = sum(magnetiteArea(overlapPercentage <
Mid_thr));
    totalMagnetite_A = sum(magnetiteArea(:));

    %Liberation Ratio calculation
    Lib_ratio = (totalMagnetiteLiberated_A / totalMagnetite_A);
    Mid_ratio = (totalMagnetiteMiddling_A / totalMagnetite_A );
```

```
    Lock_ratio = (totalMagnetiteLocked_A / totalMagnetite_A );

    Lib_ratio_data = [Lib_ratio, Mid_ratio, Lock_ratio];

    % Calculate percentages for each category
    percentages = 100 * Lib_ratio_data;

    % Create labels with percentages
    labels = {
        sprintf('Liberated (%.2f%%)', percentages(1)),
        sprintf('Middling (%.2f%%)', percentages(2)),
        sprintf('Locked (%.2f%%)', percentages(3))
    };

    % Plot pie chart
    figure (002);
    set(gcf, 'Name', ['Liberation Analysis on Valuable Mineral
phase - ', analysisName], 'NumberTitle', 'off');


    h = pie(Lib_ratio_data);

    % Add percentages to the segments
    for i = 1:2:length(h) % Pie chart text handles are in odd
positions
        h(i+1).String = sprintf('%.1f%%', percentages((i+1)/2));
    end

    legend({'Liberated', 'Middling', 'Locked'}, 'Location',
'southoutside', 'Orientation', 'horizontal');

    title(['Liberation Analysis on Valuable Mineral phase - ',
analysisName], 'FontWeight', 'bold');


    outputImageFile2                                              =
fullfile(outputFolder,['LiberationPie_',analysisName,'.jpg']);

    saveas(gcf, outputImageFile2);

    % Display a confirmation message
    disp(['Figure 2 saved as ', outputImageFile2]);
    fprintf('\n');

    %-------- Liberation Analysis Section - END -------%

    %-------- Free-Grain Size Analysis Section - START -------%

    %Create the Equivalent Diagram Vector

    EqDiam = libGrainsData(:, 2);

    % Initialize cumulative passing percentages
```

```
    Cumulative_percent = zeros(size(Sieve_series));

    % Calculate cumulative passing frequence
    for i = 1:length(Sieve_series)
        Cumulative_percent(i) = (sum(EqDiam <= Sieve_series(i)) /
length(EqDiam)) * 100;
    end

    Sieve_series(Sieve_series == 0) = 1e-6;

    % Define target passing percentages
    targetPassing = [10, 50, 80];

    % Initialize array to store d10, d50, and d80
    dValues = zeros(size(targetPassing));

    % Linear interpolation for d10, d50, and d80
    for j = 1:length(targetPassing)
        % Interpolate the sieve size at the specified cumulative
percentage
        dValues(j) = interp1(Cumulative_percent, Sieve_series,
targetPassing(j));
    end

    % Display the results
    fprintf("Free-grain size results\n");
    fprintf('d10: %.2f μm\n', dValues(1));
    fprintf('d50: %.2f μm\n', dValues(2));
    fprintf('d80: %.2f μm\n', dValues(3));
    fprintf('\n');

    % Plot the cumulative passing curve with markers for d10, d50,
and d80
    figure(003);
    set(gcf, 'Name', ['Free Grains (Cumulative Passing) - ',
analysisName], 'NumberTitle', 'off');

    semilogx(Sieve_series, Cumulative_percent, '-o', 'LineWidth',
1.5, 'MarkerSize', 8);
    hold on;

    % Add markers and label for d10, d50, and d80 on the curve
    semilogx(dValues, targetPassing, 'rx', 'MarkerSize', 10,
'LineWidth', 2);

    for j = 1:length(targetPassing)
        text(dValues(j), targetPassing(j), sprintf('d%d = %.2f
μm', targetPassing(j), dValues(j)), 'VerticalAlignment', 'bottom',
'HorizontalAlignment', 'right', 'FontWeight', 'bold');
    end

    xlabel('Sieve Size (\mum)', 'FontWeight', 'bold');
    ylabel('Cumulative Passing (%)', 'FontWeight', 'bold');
```

```
    title(['Free Grains (Cumulative Passing) - ', analysisName],
'FontWeight', 'bold');

    grid on;

    outputImageFile3 = fullfile(outputFolder,['FreeGrain_Curve_',
analysisName, '.jpg']);
    saveas(gcf, outputImageFile3);

    % Confirmation message
    disp(['Figure 3 saved as ', outputImageFile3]);

    %-------------- OUTPUT FILE CREATION - START ---------------%
    % Create a table with the data
    granulometricTable           =           table(Sieve_series',
Cumulative_percent','VariableNames',        {'Sieve_Size_microns',
'Cumulative_Passing_Percentage'});
    librationTable = table(Lib_ratio_data(1), Lib_ratio_data(2),
Lib_ratio_data(3), 'VariableNames', {'Liberated [%]', 'Middling
[%]', 'Locked [%]'});

    % Specify output file name
    outputFileName1                                                =
fullfile(outputFolder,['FreeGrainSizeCurve_',analysisName,'.xls'])
;
    outputFileName2                                                =
fullfile(outputFolder,['LiberatedGrainsDiameters_',analysisName,'.
xls']);
    outputFileName3                                                =
fullfile(outputFolder,['LiberationCategories_',analysisName,'.xls'
]);
    outputFileName4                                                =
fullfile(outputFolder,['TotalLiberation_',analysisName,'.xls']);
    fprintf('\n');

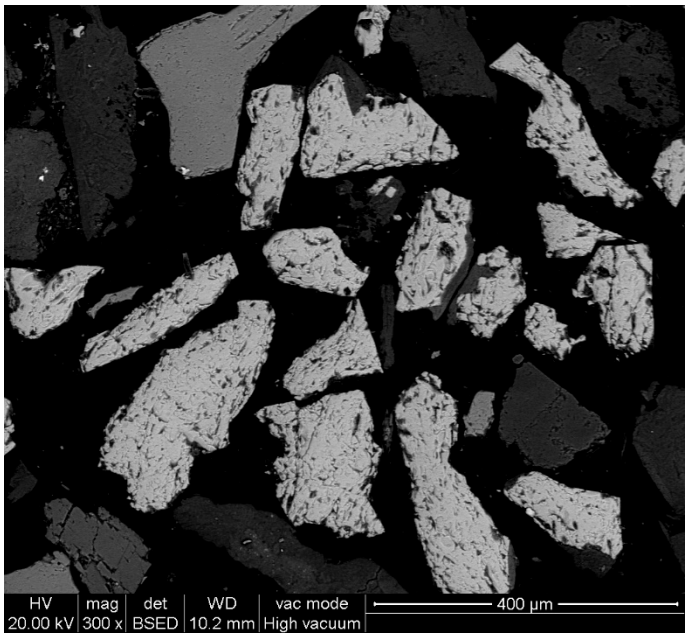

    % Write the table to an Excel file

    writetable(granulometricTable, outputFileName1);
    writetable(libGrainsData_table, outputFileName2);
    writetable(overlap_Table_with_categories, outputFileName3);
    writetable(librationTable,outputFileName4);

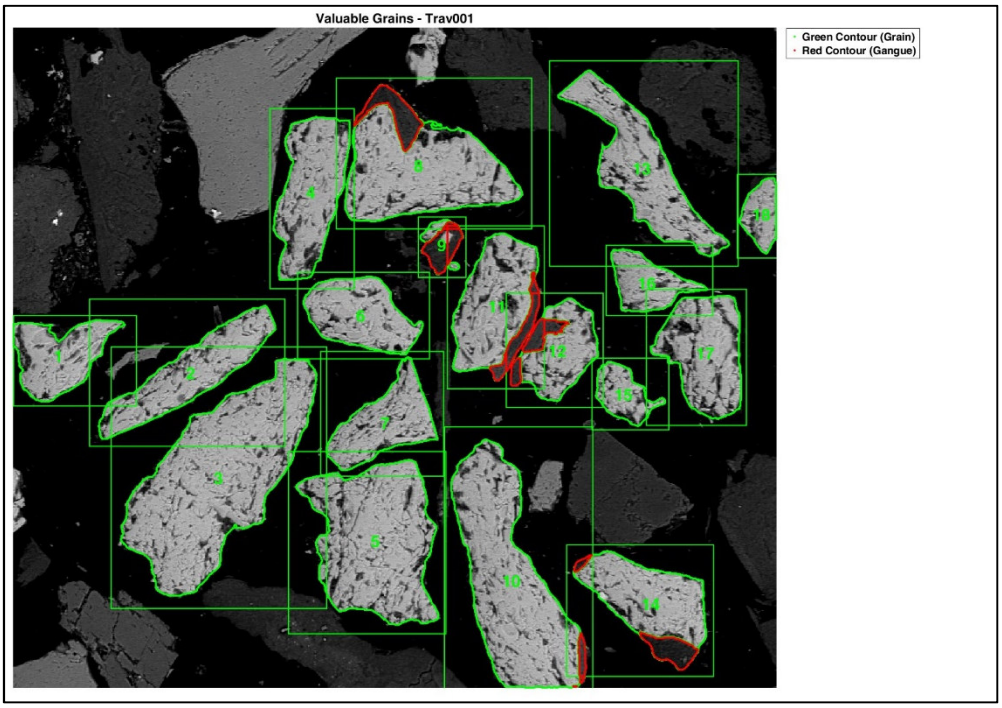
    % Display a confirmation message
    disp(['Output files will be saved in: ', outputFolder]);
    fprintf('\n');
    disp(['Data successfully saved to ', outputFileName1]);
    disp(['Data successfully saved to ', outputFileName2]);
    disp(['Data successfully saved to ', outputFileName3]);
    disp(['Data successfully saved to ', outputFileName4]);
```

C.3. Image processing TD_BSE1 – 0.250-0.125mm size class - Traversella

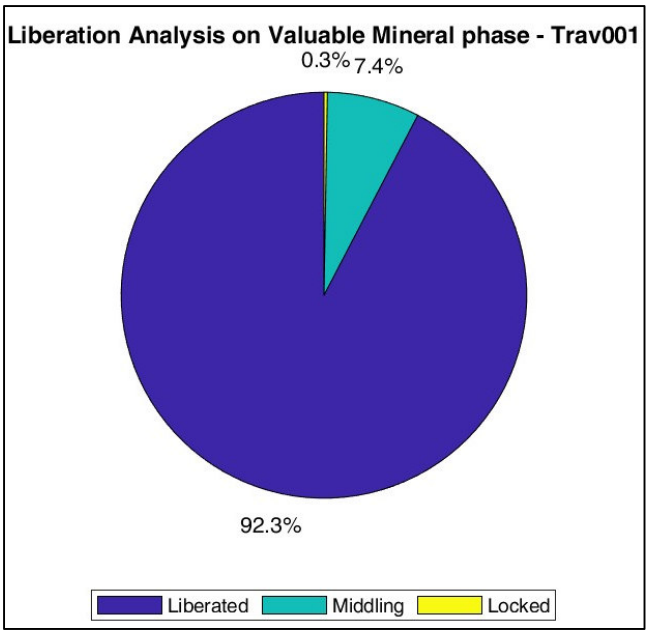
Original TD_BSE1 Image



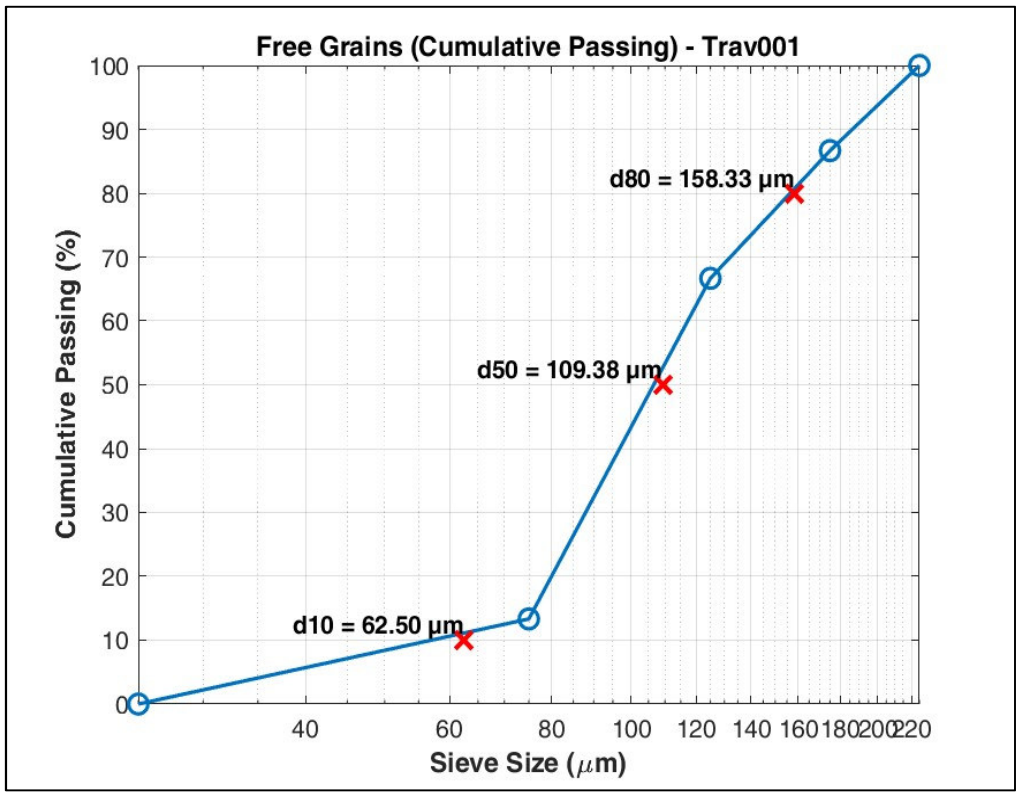
Post-processed TD_BSE1 image



Liberation pie-chart (TD_BSE1)

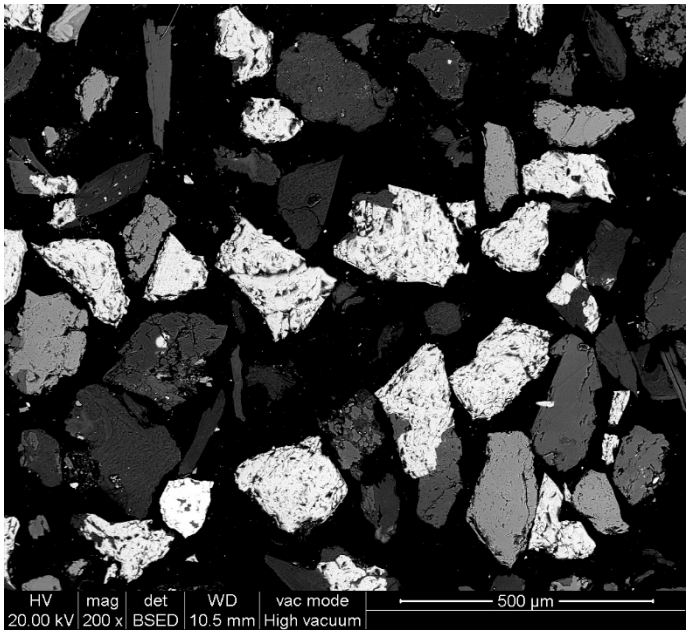


Free-grain size PSD curve, showing d10, d20, d80 percentiles (TD_BSE1)

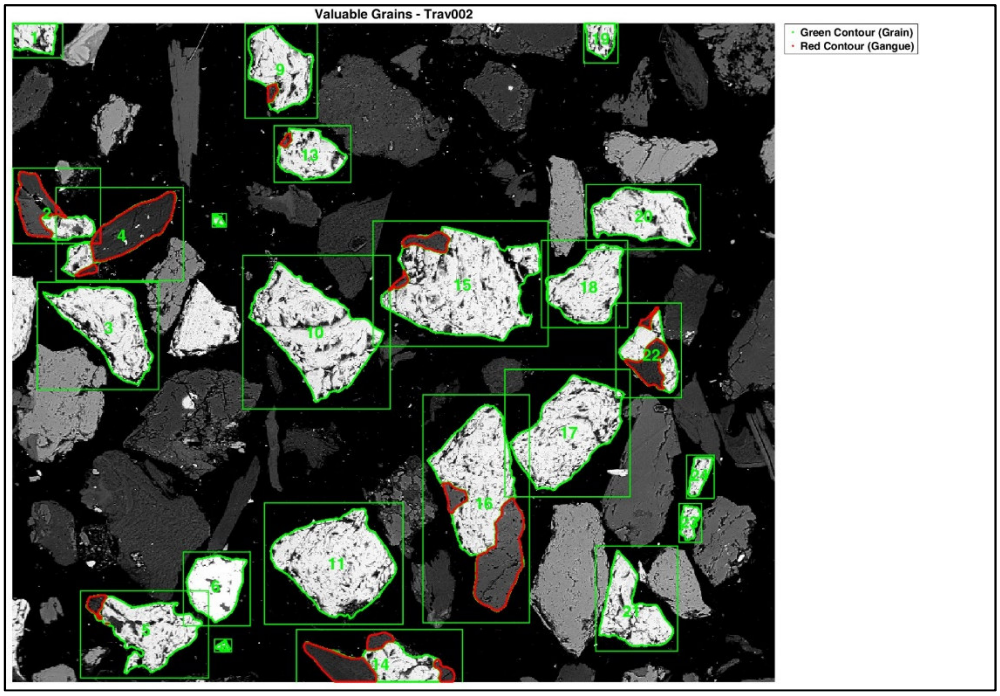


C.4. Image TD_BSE2 - 0.250-0.125mm size class - Traversella

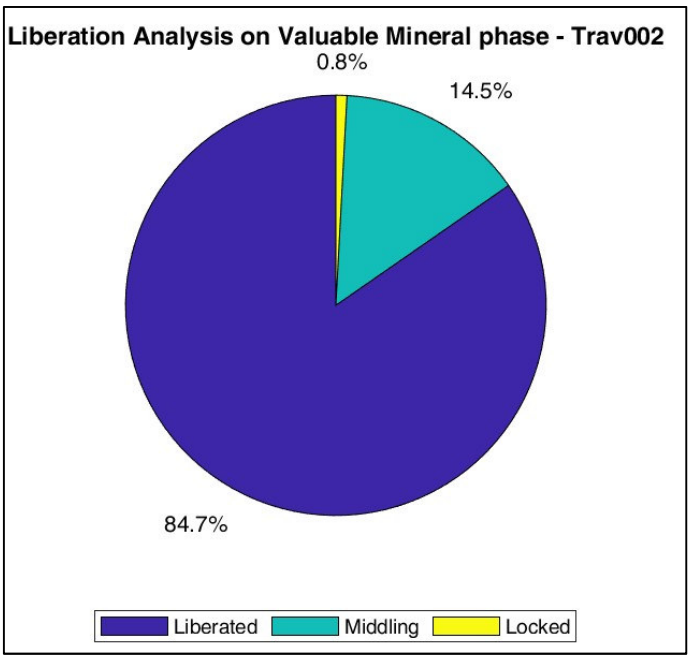
Original TD_BSE2 Image



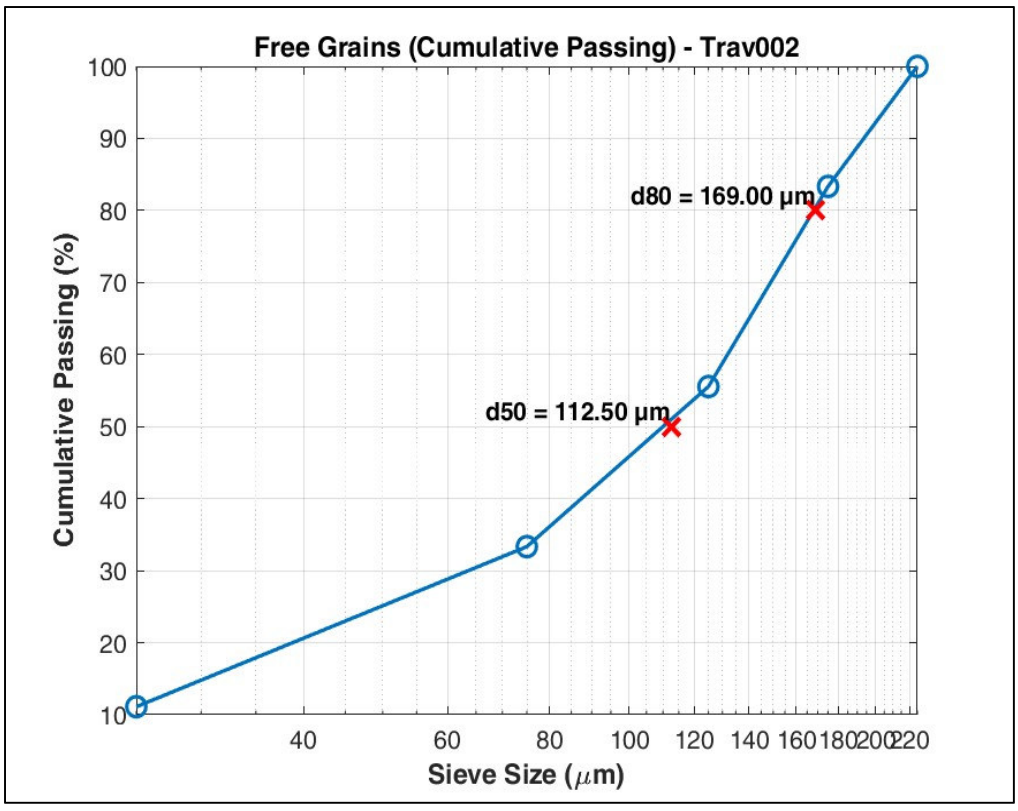
Post-processed TD_BSE2 image



Liberation pie-chart (TD_BSE2)

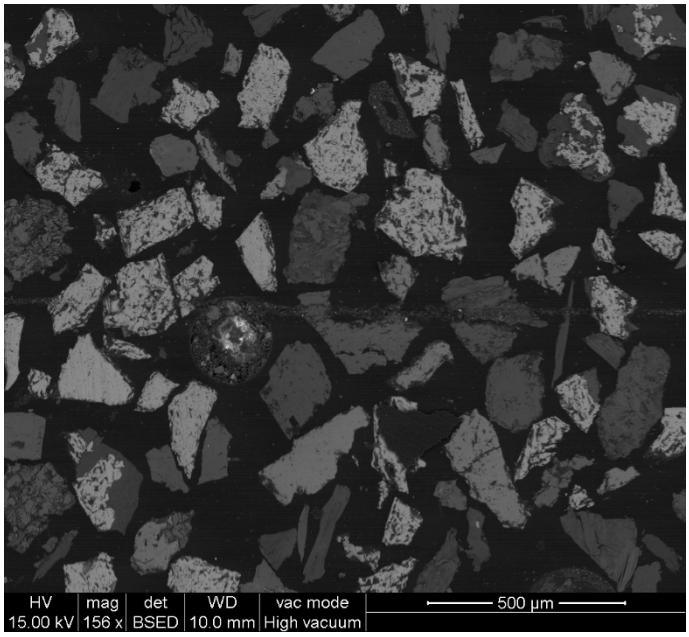


Free-grain size PSD curve, showing d10, d20, d80 percentiles (TD_BSE2)

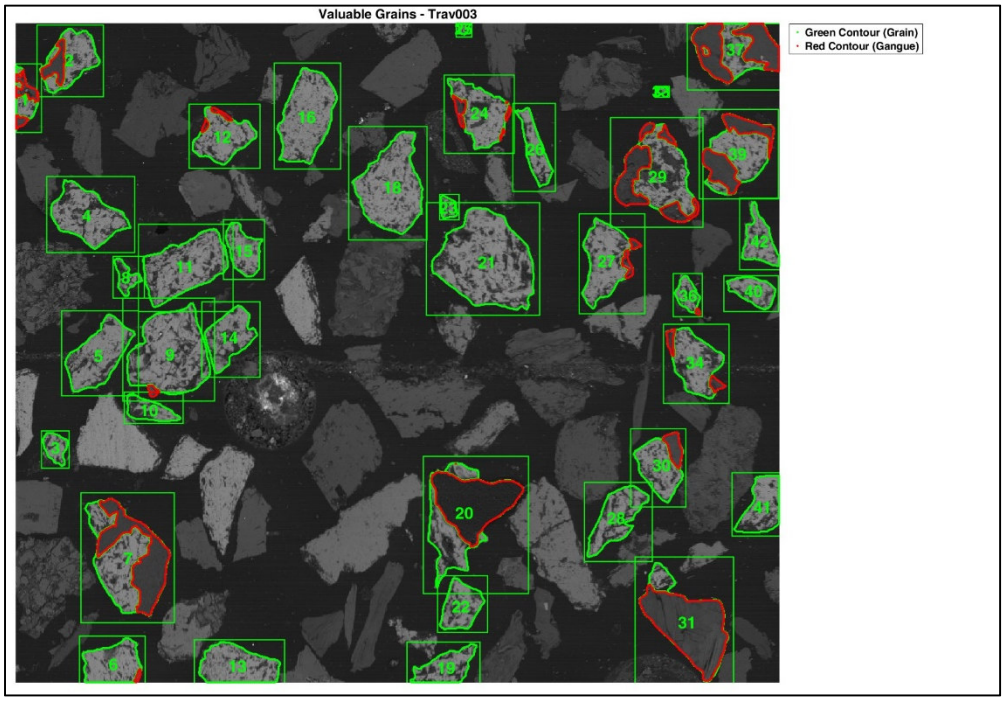


C.5. Image TD_BSE3 - 0.250-0.125mm size class - Traversella

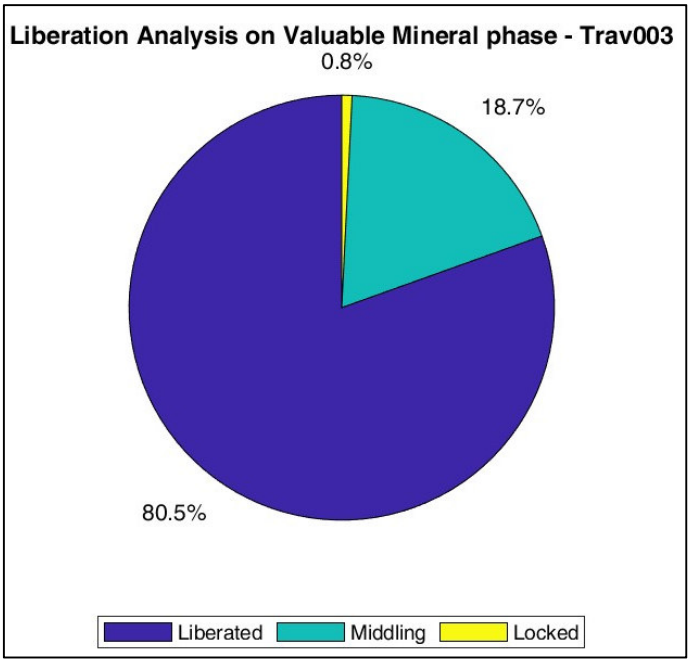
Original TD_BSE3 Image



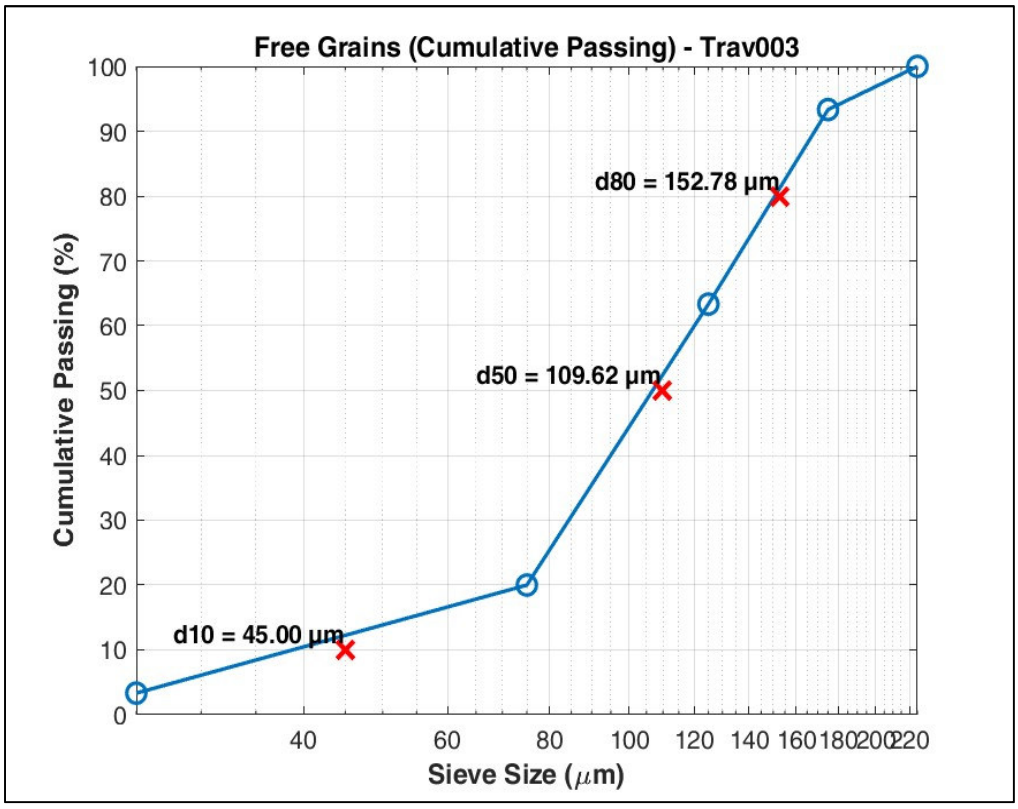
Post-processed TD_BSE3 image



Liberation pie-chart (TD_BSE3)



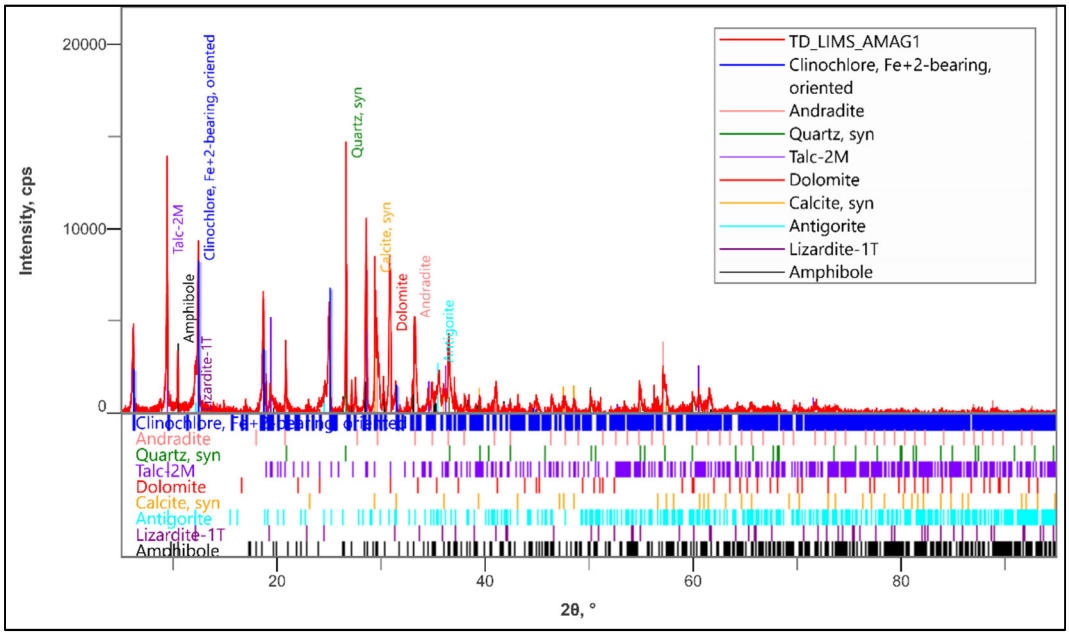
Free-grain size PSD curve, showing d10, d20, d80 percentiles (TD_BSE3)



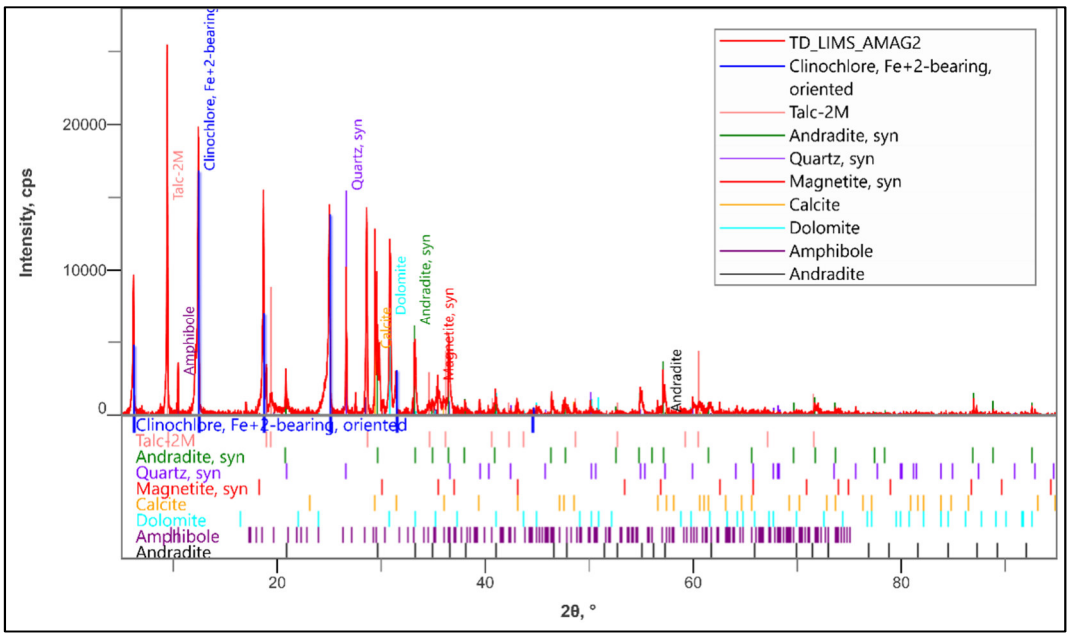
C.6. XRPD Spectra – Output materialsTest A, Test B, Test C, Test D - Traversella

Test A

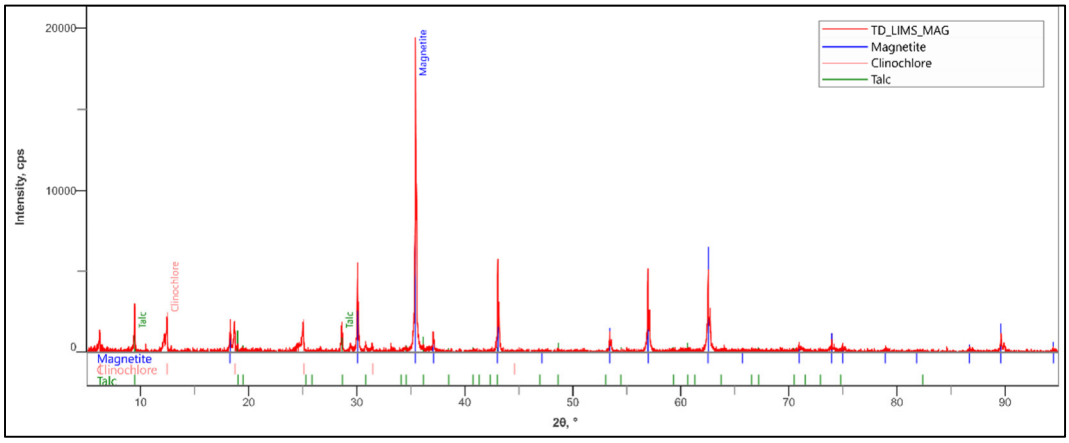
Sample A_NM1



Sample A_NM2

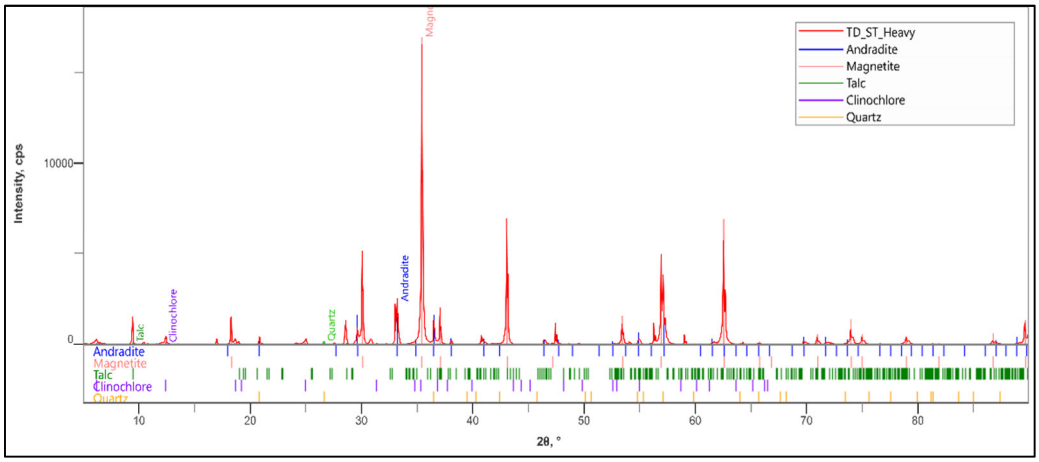


Sample A_M

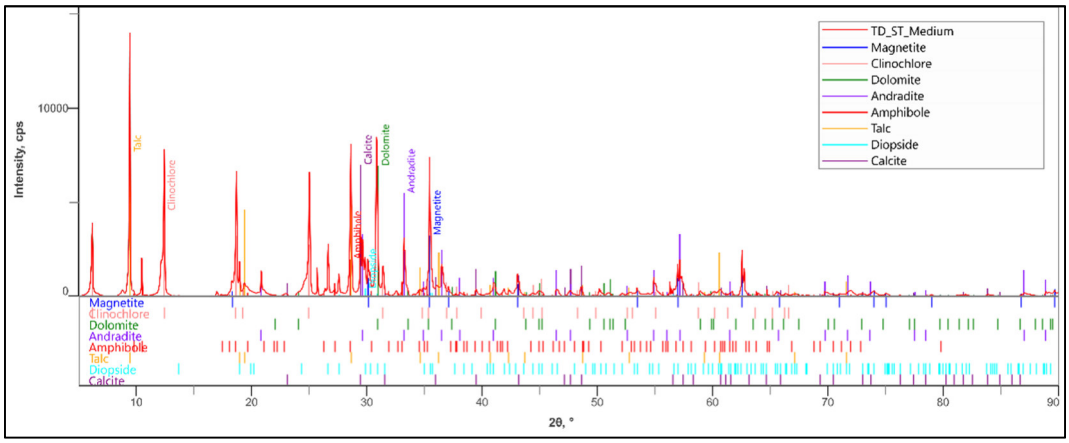

TD_LIMS_MAG
Magnetite
Clinochlore
Talc
Intensity, cps
20000
10000
0
Talc
Clinochlore
Talc
Magnetite
Magnetite
Clinochlore
Talc
10
20
30
40
50
60
70
80
90
2θ, °

Test B

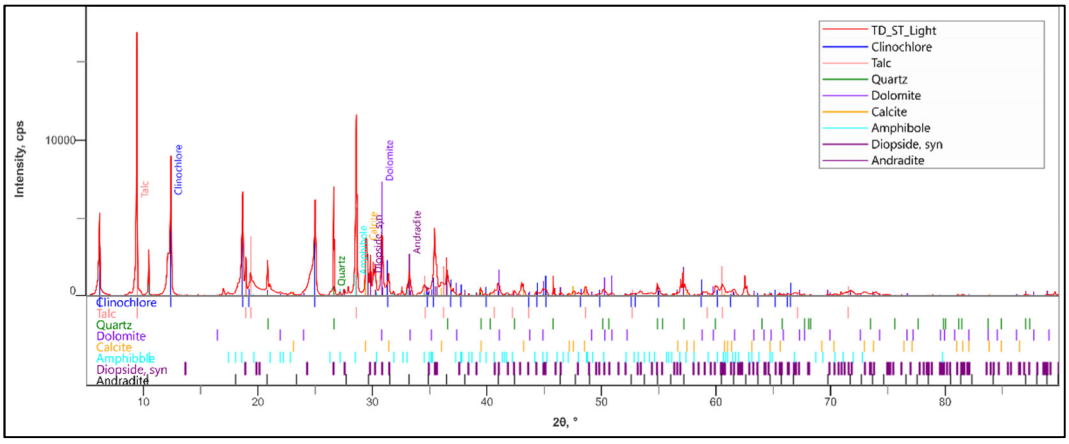
Sample B_H



Sample B_M

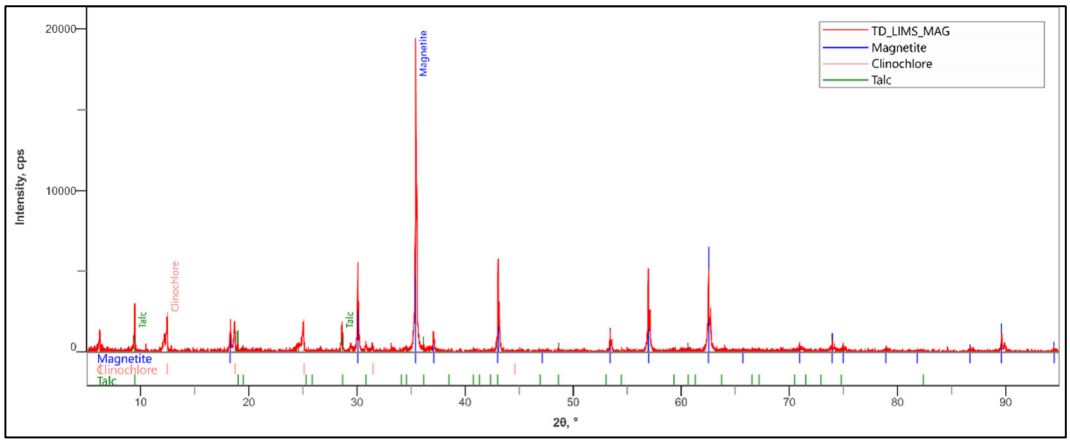


Sample B_L

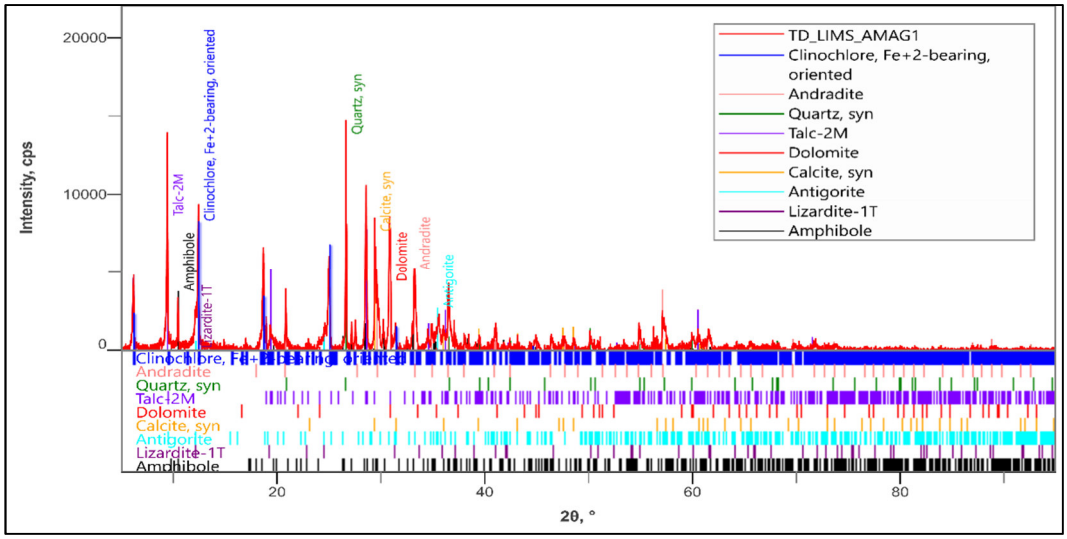


Test C

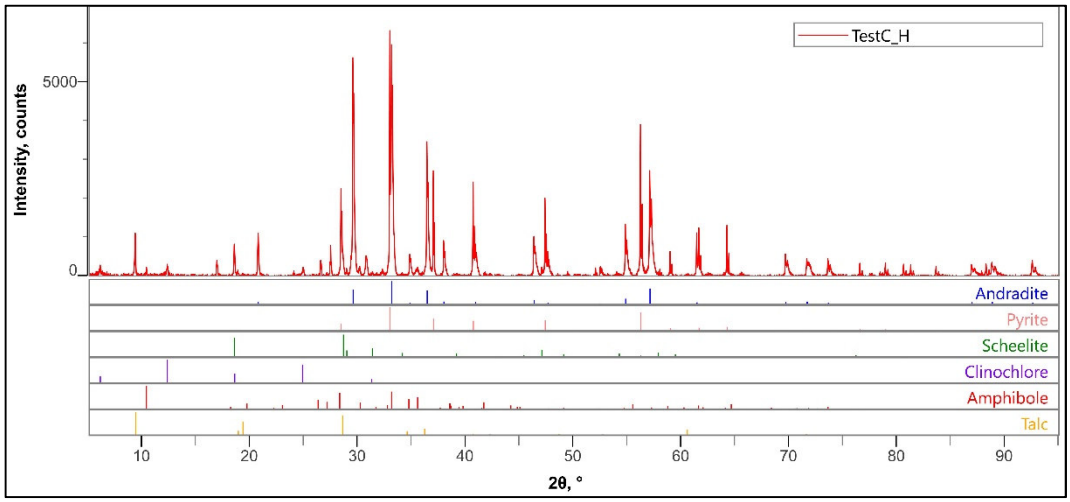
Sample C_MG



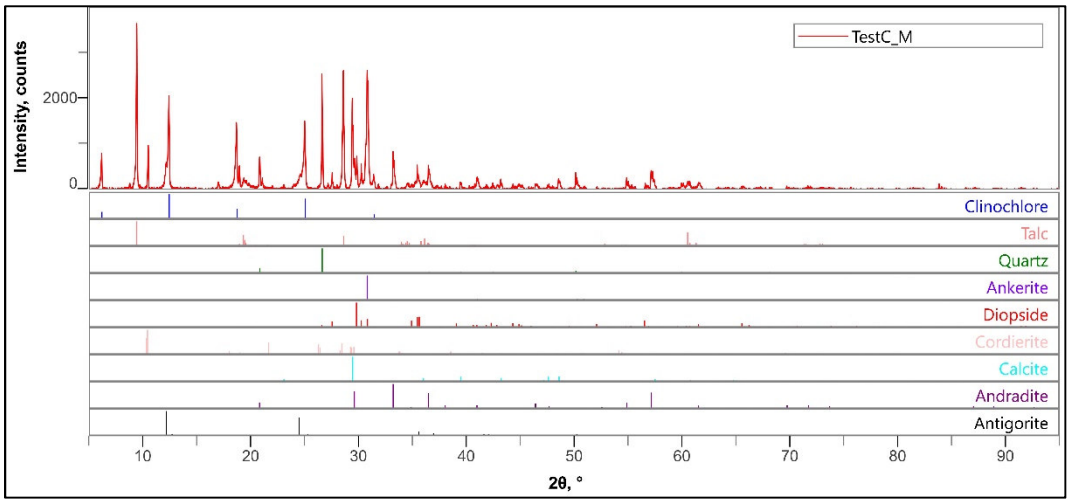
Sample C_NM



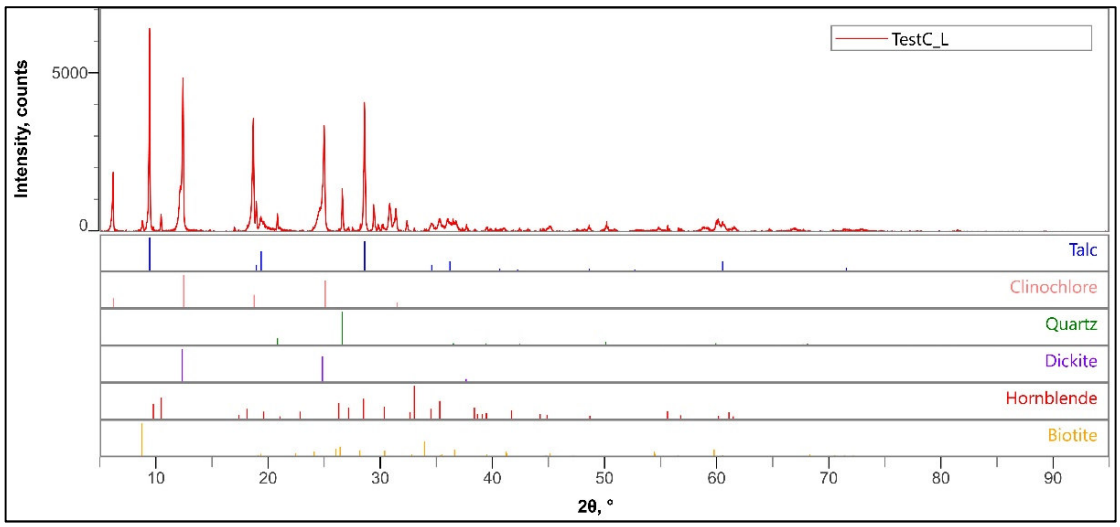
Sample C_H



Sample C_M

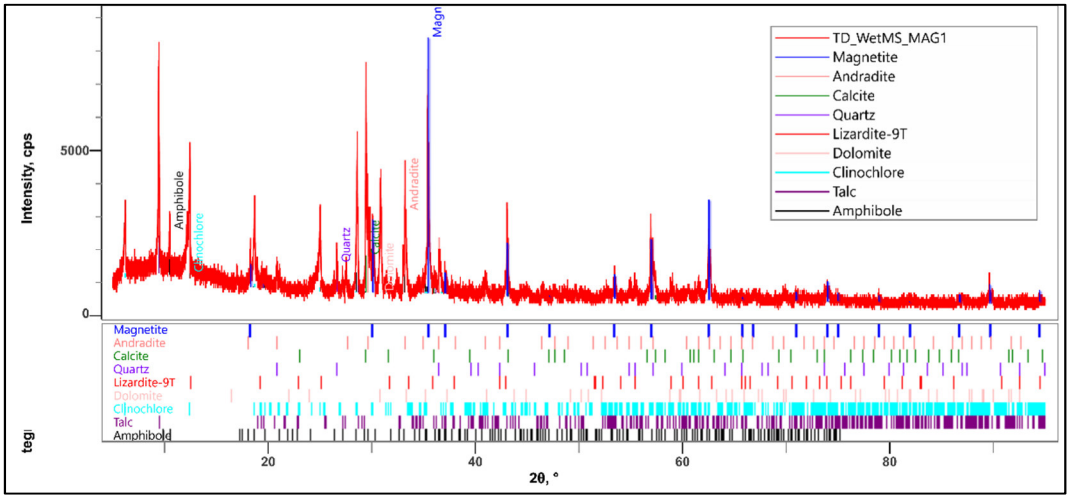


Sample C_L

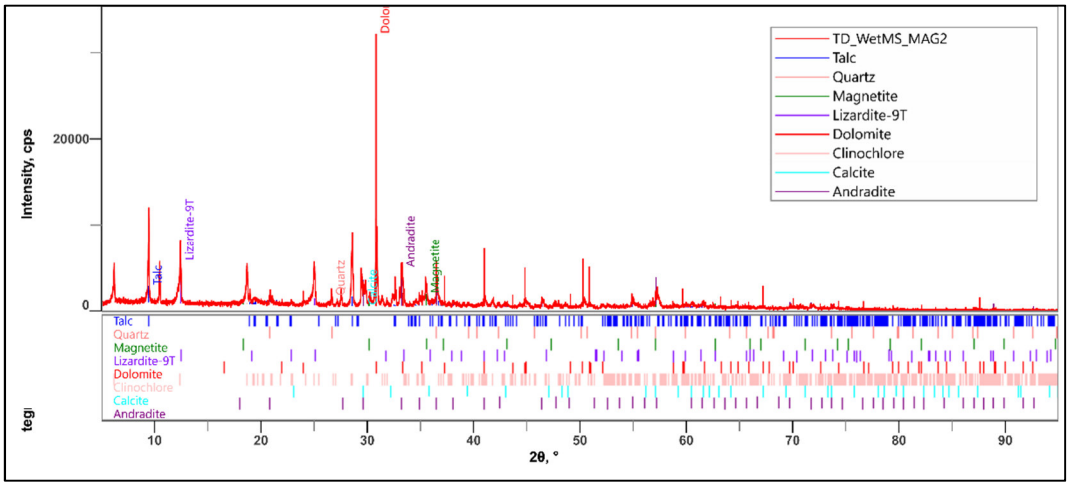


Test D

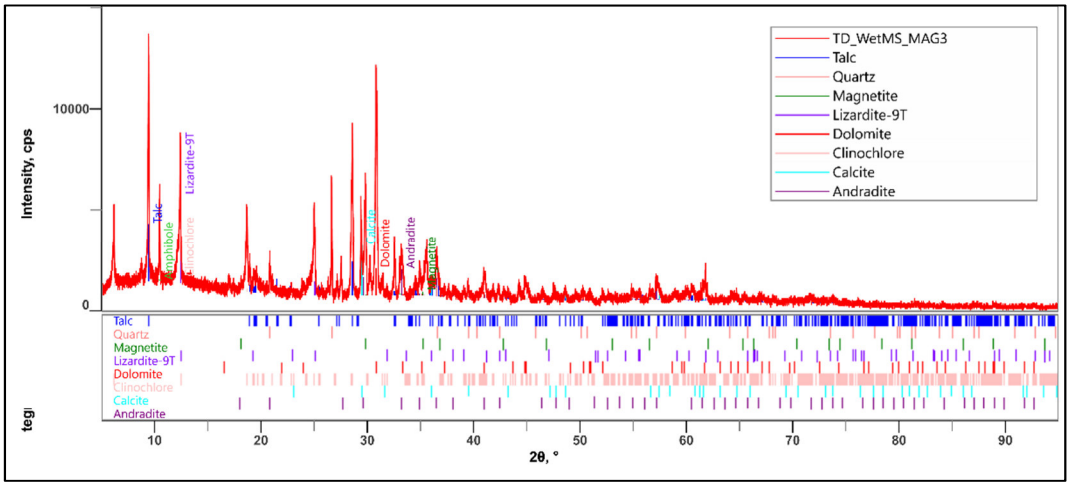
Sample D_M1



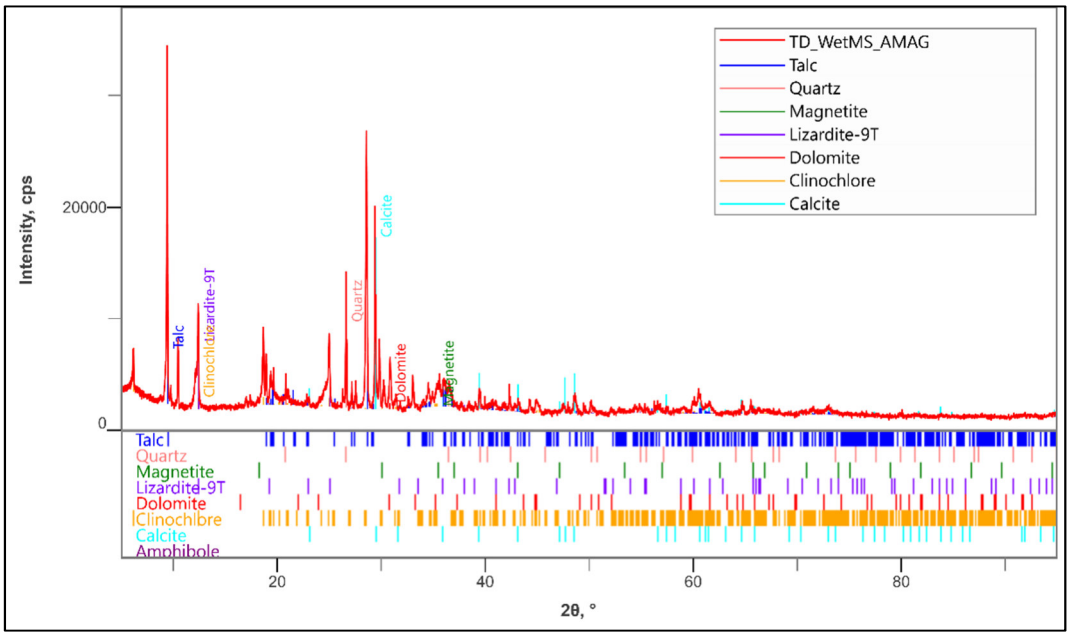
Sample D_M2



Sample D_M3



Sample D_NM


TD_WetMS_AMAG
Talc
Quartz
Magnetite
Lizardite-9T
Dolomite
Clinochlore
Calcite
Intensity, cps
20000
0
Talc
Clinochlore
Lizardite-9T
Quartz
Calcite
Dolomite
Magnetite
Talc
Quartz
Magnetite
Lizardite-9T
Dolomite
Clinochlore
Calcite
Amphibole
20
40
60
80
2θ, °

D. Appendix D

This appendix material is referred to in ***Chapter 6.***

D.1. List and location of sampling points - Libiola

Sample ID	*Type*	*Sampling Zone*	*East_WGS84*	*North_WGS84*
LN1	Waste Rock	North Dump	9.448896	44.305576
LN2	Waste Rock	North Dump	9.448719	44.305612
LN3	Waste Rock	North Dump	9.448685	44.305593
LN4	Waste Rock	North Dump	9.44867	44.305655
LN5	Waste Rock	North Dump	9.449285	44.305037
LN6	Waste Rock	North Dump	9.449006	44.305253
LN7	Waste Rock	North Dump	9.44857	44.305458
LN8	Waste Rock	North Dump	9.44929808	44.30524391
LN9	Waste Rock	North Dump	9.44905588	44.30520598
LN10	Waste Rock	North Dump	9.44881988	44.30517267
LS1	Waste Rock	South Dump	9.446812	44.302258
LS2	Waste Rock	South Dump	9.44678	44.302074
LS3	Waste Rock	South Dump	9.446738	44.301956
LS4	Waste Rock	South Dump	9.444418	44.301384
LS5	Waste Rock	South Dump	9.444512	44.301148
LS6	Waste Rock	South Dump	9.44472	44.301153
LS7	Waste Rock	South Dump	9.44450664	44.30154551
LS8	Waste Rock	South Dump	9.44457064	44.30149341
LS9	Waste Rock	South Dump	9.44464641	44.3014201
LS10	Waste Rock	South Dump	9.44471363	44.30136611
LS11	Waste Rock	South Dump	9.44477784	44.30131281
LS12	Waste Rock	South Dump	9.44482377	44.30127177
LM1	Waste Rock	Margherita Dump	9.44521	44.29983

D.2. HH-XRF results from field survey – Libiola North, South and Margherita dumps (values in ppm)

Sample_ID	*Mg*	*Mg +/-*	*Al*	*Al +/-*	*Si*	*Si +/-*	*P*	*P +/-*	*S*	*S +/-*	*K*	*K +/-*	*Ca*	*Ca +/-*
LM1	71435	6085	33209	944	119144	993	ND	< 3950	18713	266	2199	294	10664	283
LN1	17634	3886	31071	732	153035	895	ND	< 2619	9452	181	1216	167	23345	58
LN2	21489	4340	40078	873	134973	912	ND	< 3273	27735	279	3214	250	17958	55
LN3	31572	3835	44308	816	129207	791	ND	< 2343	36278	277	15514	368	23163	57
LN4	73414	4618	59672	944	104143	760	ND	< 2249	ND	< 1670	790	149	13258	235
LN5	77884	3831	28865	597	137094	713	ND	< 1600	3244	802	793	101	20546	44
LN6	64814	3912	22567	575	146293	765	ND	< 1992	9195	155	ND	< 157	24664	51
LN7	57463	4827	35541	840	125805	872	ND	< 3469	124569	544	2024	230	17969	59
LN8	74915	5653	33149	884	119844	933	ND	< 6821	2542	145	607	404	18204	56
LN9	86036	4883	31130	748	128514	838	ND	< 4421	2529	128	ND	< 386	19207	51
LN10	38805	3804	35088	719	140941	799	4569	2778	98156	433	3479	339	23964	60
LS1	56605	5438	53375	1084	102930	886	8345	2811	134152	616	ND	< 372	14588	339
LS2	56778	5549	40249	975	128494	994	ND	< 3910	32308	327	ND	< 365	10628	46
LS3	58049	5624	31442	915	141958	1040	6913	2964	127731	622	ND	< 381	19204	68
LS4	67358	4056	26032	620	126058	733	ND	< 2042	16697	189	545	119	23610	51
LS5	61876	4270	26198	665	131795	793	ND	< 2546	116538	477	2225	191	9041	176
LS6	41361	3312	47648	727	131922	690	ND	< 1520	16805	176	22519	359	19831	46
LS7	62422	4736	44948	878	127254	861	ND	< 4594	5734	154	3382	388	13308	441
LS8	77337	4056	28733	622	136790	745	ND	< 2890	6311	135	1977	236	14799	364
LS9	51375	4297	43173	812	113390	769	ND	< 4219	4086	133	2473	336	21948	559
LS10	74164	4411	29779	683	133789	801	ND	< 3534	16739	202	1140	249	13008	383
LS11	54430	4254	45157	823	130617	814	ND	< 3774	9306	168	4018	354	21218	513
LS12	38897	3485	44689	719	137925	734	ND	< 3096	8194	145	4109	291	22098	48

Sample_ID	*Ti*	*Ti +/-*	*V*	*V +/-*	*Cr*	*Cr +/-*	*Mn*	*Mn +/-*	*Fe*	*Fe +/-*	*Co*	*Co +/-*	*Ni*	*Ni +/-*
LM1	3488	104	124	16	1047	27	1651	72	264161	250	ND	< 222	112	11
LN1	8368	135	188	15	492	22	871	36	155243	190	ND	< 110	205	13
LN2	8749	140	192	17	603	29	1164	48	196902	218	ND	< 151	158	11
LN3	8660	144	179	14	349	19	1121	39	141719	186	ND	< 105	134	11
LN4	8909	131	244	16	298	19	1604	42	135593	168	ND	< 101	759	13
LN5	4951	110	104	8.4	939	19	1079	32	83756	132	178	45	741	14
LN6	4176	107	91	9.1	930	26	959	35	105521	153	313	57	309	16
LN7	4314	130	107	13	503	28	1347	53	226547	257	ND	< 167	717	18
LN8	3428	102	111	28	820	25	1355	109	228709	232	ND	< 345	930	17
LN9	3876	103	98	20	1222	28	1192	83	144584	176	ND	< 212	280	13
LN10	6334	140	107	20	418	34	673	62	157661	209	ND	< 201	78	15
LS1	8092	157	179	21	241	31	1455	59	281673	292	642	138	55	14
LS2	7879	136	226	22	218	31	1078	57	258492	255	ND	< 210	183	18
LS3	4100	138	101	17	1198	35	857	68	312230	317	ND	< 257	842	15
LS4	3718	102	83	9	1371	27	861	34	105281	151	ND	< 83	737	17
LS5	4399	84	49	8.2	852	27	1019	42	167250	210	ND	< 124	165	9.6
LS6	8083	138	186	9.9	294	13	971	31	84648	138	ND	< 65	573	15
LS7	6899	121	150	26	1041	54	1304	85	156051	182	ND	< 228	1151	16
LS8	3468	95	88	14	1525	29	1079	60	97046	139	342	89	348	12
LS9	6995	120	215	26	776	45	1480	74	136710	169	ND	< 185	1065	17
LS10	3692	100	87	17	1332	28	1208	69	124940	162	ND	< 166	390	13
LS11	7304	125	170	23	1010	46	1270	69	129611	166	ND	< 171	221	10
LS12	8274	134	190	19	441	27	965	56	92833	141	ND	< 129	430	24

Sample_ID	*Cu*	*Cu +/-*	*Zn*	*Zn +/-*	*As*	*As +/-*	*Se*	*Se +/-*	*Rb*	*Rb +/-*	*Sr*	*Sr +/-*	*Y*	*Y +/-*
LM1	6303	37	1898	28	76	4.8	ND	< 2.2	19	1.3	ND	< 1.6	5	0.8
LN1	968	16	56	3.7	14	1.8	15	1.2	9.7	0.7	56	1.3	21	0.7
LN2	2790	34	1901	23	8.4	2.4	13	1.4	18	1	25	1.2	18	0.8
LN3	1336	19	270	6.7	4.6	1.5	3.2	0.9	26	0.9	23	0.9	26	0.8
LN4	46	5.3	89	3.9	ND	< 1.5	ND	< 1.0	7.8	0.6	ND	< 0.8	29	0.7
LN5	1975	20	151	4.4	ND	< 1.2	ND	< 1.0	2.9	0.4	16	0.7	18	0.5
LN6	5417	26	105	4.4	ND	< 1.5	3	0.8	3.5	0.5	3.2	0.6	14	0.5
LN7	20264	65	1672	22	6.5	3	45	2.2	19	1.1	ND	< 1.3	12	0.8
LN8	6046	35	237	15	ND	< 5.6	11	2.8	14	1.9	ND	< 2.5	7.9	1.3
LN9	3350	65	209	12	ND	< 3.4	6.6	1.9	4.1	1.1	ND	< 1.8	10	1
LN10	2241	46	337	14	ND	< 4.8	8.4	2	12	1.3	38	2	21	1.3
LS1	23839	75	117	7.7	ND	< 3.4	20	2	30	1.3	ND	< 1.2	14	0.9
LS2	2577	38	58	5.7	ND	< 3.1	15	1.8	17	1.2	ND	< 1.2	11	0.8
LS3	31496	90	187	11	ND	< 3.7	16	2.2	20	1.4	ND	< 1.6	ND	< 1.2
LS4	4538	24	215	5.7	ND	< 1.6	4.6	0.8	4	0.5	19	0.8	16	0.6
LS5	2361	28	4552	23	ND	< 2.7	9.4	1.2	11	0.8	7.7	0.8	15	0.7
LS6	703	12	380	6.9	5	1.2	ND	< 0.9	33	0.9	24	0.8	32	0.7
LS7	2798	59	326	15	ND	< 3.5	ND	< 2.6	9.4	1.3	ND	< 1.8	16	1.2
LS8	2437	41	444	13	ND	< 2.5	4.6	1.4	6.5	0.9	6	1	12	0.8
LS9	1412	33	342	13	ND	< 3.2	ND	< 2.0	9.5	1.2	5.4	1.2	28	1.3
LS10	2309	43	399	13	ND	< 3.1	5.9	1.6	8.1	1	2.2	1.1	12	0.9
LS11	1638	35	362	13	ND	< 3.3	2.3	1.5	11	1.1	21	1.5	24	1.2
LS12	2640	45	549	15	ND	< 2.8	2.6	1.3	7.9	0.9	45	1.7	30	1.2

Sample_ID	*Zr*	*Zr +/-*	*Nb*	*Nb +/-*	*Mo*	*Mo +/-*	*Ag*	*Ag +/-*	*Cd*	*Cd +/-*	*Sn*	*Sn +/-*	*Sb*	*Sb +/-*
LM1	116	2.5	ND	< 1.6	8	1	ND	< 1.0	6.1	0.9	242	2.3	32	2.1
LN1	363	2.9	4.9	0.8	7.8	0.8	5.1	0.7	ND	< 1.2	17	1	ND	< 2.8
LN2	313	3	ND	< 1.4	38	1.2	7	0.7	11	0.9	23	1	ND	< 2.7
LN3	318	2.7	6	0.8	17	0.9	2.2	0.6	ND	< 1.1	4.6	0.8	ND	< 2.6
LN4	202	2.2	6	0.8	1.3	0.7	ND	< 0.8	ND	< 1.0	ND	< 1.2	ND	< 2.5
LN5	119	1.7	3.8	0.7	2.6	0.6	ND	< 0.8	ND	< 1.0	2.3	0.8	ND	< 2.4
LN6	157	2	2.1	0.7	2.3	0.6	ND	< 0.8	ND	< 1.1	ND	< 1.2	ND	< 2.5
LN7	156	2.6	2.6	0.9	13	0.9	16	0.8	6	0.9	31	1.1	ND	< 3.0
LN8	150	2.5	ND	< 2.7	17	1.8	3.4	1.1	ND	< 2.0	13	1.7	ND	< 4.7
LN9	97	1.9	ND	< 2.2	9.3	1.4	1.7	1	ND	< 1.8	ND	< 2.0	ND	< 4.2
LN10	232	2.6	8.3	1.4	12	1.5	4.3	1.1	ND	< 2.0	ND	< 2.2	ND	< 4.5
LS1	220	3.1	6.5	1	18	1	6.4	0.8	ND	< 1.4	7.3	1	ND	< 9.0
LS2	162	2.7	ND	< 1.6	7.4	1	ND	< 1.0	ND	< 1.3	6.5	0.9	ND	< 9.0
LS3	195	3.2	ND	< 1.7	12	1.1	6.3	0.9	ND	< 1.5	7.6	1.1	ND	< 9.0
LS4	111	1.8	ND	< 1.1	4.8	0.6	ND	< 0.8	ND	< 1.0	2.4	0.8	ND	< 9.0
LS5	151	2.3	3.4	0.8	3.4	0.7	3	0.6	13	0.9	8.4	0.9	ND	< 9.0
LS6	190	2	5.5	0.7	4.2	0.6	ND	< 0.8	ND	< 1.0	ND	< 1.1	ND	< 9.0
LS7	129	2	ND	< 2.3	5	1.3	ND	< 1.4	ND	< 1.8	ND	< 2.0	ND	< 4.2
LS8	77	1.6	2	1.2	2.8	1	1.3	0.9	ND	< 1.6	ND	< 1.9	ND	< 3.9
LS9	148	2	3.4	1.4	3.7	1.2	ND	< 1.4	ND	< 1.8	ND	< 2.0	ND	< 4.2
LS10	86	1.7	3.5	1.2	5.5	1.1	ND	< 1.4	ND	< 1.7	ND	< 2.0	ND	< 4.1
LS11	150	2	4	1.3	7.8	1.2	ND	< 1.4	ND	< 1.8	ND	< 2.0	ND	< 4.2
LS12	177	1.9	5.7	1.3	5.5	1.1	ND	< 1.3	ND	< 1.7	ND	< 1.9	ND	< 3.9

Sample_ID	*Ba*	*Ba +/-*	*La*	*La +/-*	*Ce*	*Ce +/-*	*Pr*	*Pr +/-*	*Nd*	*Nd +/-*	*Sm*	*Sm +/-*	*Eu*	*Eu +/-*
LM1	ND	< 12	ND	< 9.2	ND	< 12	ND	< 25	ND	< 13	ND	< 22	ND	< 218
LN1	ND	< 15	ND	< 11	ND	< 14	ND	< 28	ND	< 22	ND	< 24	ND	< 242
LN2	ND	< 13	ND	< 9.6	ND	< 12	ND	< 25	ND	< 17	25	15	ND	< 216
LN3	ND	< 13	ND	< 9.9	ND	< 13	ND	< 26	ND	< 14	ND	< 23	ND	< 214
LN4	ND	< 14	ND	< 10	ND	< 13	ND	< 26	ND	< 21	ND	< 23	ND	< 207
LN5	ND	< 14	ND	< 10	ND	< 13	ND	< 26	ND	< 17	ND	< 23	ND	< 200
LN6	ND	< 14	ND	< 10	ND	< 13	ND	< 26	ND	< 18	ND	< 23	ND	< 209
LN7	ND	< 12	ND	< 9.3	ND	< 12	ND	< 24	ND	< 13	ND	< 23	ND	< 227
LN8	ND	< 20	ND	< 15	ND	< 20	ND	< 40	ND	< 14	ND	< 37	ND	< 342
LN9	ND	< 21	ND	< 16	ND	< 20	ND	< 41	ND	< 33	ND	< 37	ND	< 321
LN10	ND	< 20	ND	< 15	ND	< 19	ND	< 39	ND	< 32	ND	< 36	ND	< 330
LS1	ND	< 27	ND	< 13	ND	< 15	ND	< 24	ND	< 27	ND	< 30	ND	< 227
LS2	ND	< 27	ND	< 13	ND	< 15	ND	< 24	ND	< 27	ND	< 30	ND	< 221
LS3	ND	< 27	ND	< 13	ND	< 15	ND	< 24	ND	< 27	ND	< 30	ND	< 239
LS4	ND	< 27	ND	< 13	ND	< 15	ND	< 24	ND	< 27	ND	< 30	ND	< 202
LS5	ND	< 27	ND	< 13	ND	< 15	ND	< 24	ND	< 27	ND	< 30	ND	< 205
LS6	ND	< 27	ND	< 13	ND	< 15	ND	< 24	ND	< 27	ND	< 30	ND	< 197
LS7	ND	< 21	ND	< 16	ND	< 21	ND	< 42	ND	< 33	ND	< 38	ND	< 331
LS8	ND	< 21	ND	< 16	ND	< 21	ND	< 42	ND	< 33	ND	< 37	ND	< 308
LS9	ND	< 21	ND	< 16	ND	< 20	ND	< 41	ND	< 33	ND	< 37	ND	< 320
LS10	ND	< 22	17	11	ND	< 21	ND	< 42	ND	< 34	ND	< 38	ND	< 323
LS11	ND	< 22	ND	< 16	ND	< 21	ND	< 42	ND	< 33	ND	< 38	ND	< 323
LS12	ND	< 21	ND	< 16	ND	< 21	ND	< 41	ND	< 14	ND	< 37	ND	< 310

Sample_ID	*Gd*	*Gd +/-*	*Hg*	*Hg +/-*	*Tl*	*Tl +/-*	*Pb*	*Pb +/-*	*U*	*U +/-*
LM1	ND	< 379	ND	< 0.1	ND	< 4.1	166	6.3	28	2.4
LN1	ND	< 430	ND	< 1	5.6	1.6	41	2.6	11	1.2
LN2	ND	< 378	ND	< 1	ND	< 2.8	68	3.5	19	1.7
LN3	ND	< 372	ND	< 1	8.8	1.6	26	2.2	16	1.4
LN4	ND	< 363	ND	< 1	4	1.3	14	1.8	11	1.1
LN5	ND	< 343	ND	< 0.1	2.6	1.1	5.6	1.3	3.3	0.8
LN6	ND	< 363	ND	< 0.1	5.3	1.3	9.3	1.6	5.8	0.9
LN7	ND	< 397	ND	< 0.1	5.7	2.3	114	4.6	24	1.9
LN8	ND	< 603	ND	< 0.1	ND	< 5.0	32	6	21	3.6
LN9	ND	< 549	ND	< 0.1	ND	< 3.9	8.9	3.5	6.4	2.1
LN10	ND	< 572	ND	< 0.1	7.3	3	50	4.9	15	2.4
LS1	ND	< 393	ND	< 1	ND	< 3.4	62	4.1	40	2.4
LS2	ND	< 386	ND	< 1	ND	< 3.0	35	3.6	24	2.2
LS3	ND	< 419	ND	< 1	ND	< 3.9	39	4.3	29	2.7
LS4	ND	< 348	ND	< 1	5.3	1.3	12	1.6	7.5	1
LS5	ND	< 351	ND	< 1	9.2	1.8	41	2.7	16	1.4
LS6	ND	< 339	ND	< 1	4.5	1.2	23	1.7	6.7	1
LS7	ND	< 577	ND	< 0.1	ND	< 4.1	13	3.8	12	2.4
LS8	ND	< 530	ND	< 0.1	3.6	2	9.9	2.5	5.5	1.5
LS9	ND	< 560	ND	< 0.1	4.1	2.4	21	3.5	20	2.3
LS10	ND	< 569	ND	< 0.1	6.3	2.4	19	3.3	9.9	1.9
LS11	ND	< 564	ND	< 0.1	6.5	2.5	19	3.3	11	2
LS12	ND	< 532	ND	< 0.1	5.1	2.2	15	2.8	7.9	1.7

D.3. ICP-MS results – Libiola North (LN), South (LS) and Margherita (LM) dumps (ALS ME-MS61 method)

Sample	*Ag (ppm)*	*Al (%)*	*As (ppm)*	*Ba (ppm)*	*Be (ppm)*	*Bi (ppm)*	*Ca (%)*	*Cd (ppm)*	*Ce (ppm)*	*Co (ppm)*	*Cr (ppm)*	*Cs (ppm)*	*Cu (ppm)*	*Fe (%)*
LN1	3.75	5.26	22.7	10	0.32	0.42	2.59	1.34	5.06	22.4	378	0.16	1,115	15.05
LN2	5.74	5.59	26.6	30	0.36	0.39	1.74	9.4	9.6	38.8	396	0.32	3,160	19.25
LN3	1.76	6.89	12	20	0.44	0.22	2.26	1.34	10.35	31.3	241	0.71	1,495	14.55
LN4	0.07	9.05	0.2	10	0.23	0.01	0.81	0.14	12.5	88.6	195	0.32	54.8	13.75
LN5	0.36	4.93	0.9	<10	0.37	0.07	2.9	0.51	10.35	69	714	0.38	2,090	8.82
LN6	0.56	3.66	1.5	<10	0.24	0.12	3.01	0.29	4.17	125	772	0.26	5,850	11.15
LN7	13.9	4	18.6	10	0.62	2.23	1.53	4.71	6.6	47.5	276	0.2	17,861	22.4
LN8	1.6	3.31	18.4	10	0.23	0.59	2.07	0.35	5.42	71.6	622	0.18	6,080	22.8
LN9	2.02	3.76	5.8	<10	0.22	0.54	2.35	0.46	6.71	93.3	1,070	0.25	3,860	14.9
LN10	4.16	4.92	9.5	10	0.41	0.75	2.02	1.12	8.91	80.5	325	0.22	2,400	17.9
LS1	6.13	5.68	8.1	<10	0.09	2.72	0.64	0.34	15.5	257	138	0.26	20,274	27
LS2	1.93	5.17	7	10	0.09	0.59	0.93	0.08	7.21	105	144	0.26	3,250	24.7
LS3	5.99	2.14	5.7	10	0.12	2.2	1.29	0.81	3.48	373	604	0.2	26,145	29.5
LS4	0.63	3.99	1.7	10	0.28	0.06	3.09	1.16	8.44	98.2	691	0.23	4,640	11.85
LS5	3.39	2.94	9.4	20	0.24	0.25	0.75	12.55	5.25	57.7	480	0.36	2,570	19.25
LS6	1.92	7.83	7.1	30	0.92	0.02	2.52	1.17	13.95	45.4	211	0.84	773	9.12
LS7	1	6.26	2.4	10	0.29	0.09	0.89	0.69	12.4	84.3	610	0.34	3,230	15.5
LS8	2.52	3.63	2.3	20	0.25	0.08	1.27	1.28	7.31	74.6	1,115	0.26	2,790	10.15
LS9	0.66	7.38	2.7	10	0.39	0.05	1.57	0.83	15.15	79.4	429	0.6	1,595	14.75
LS0	1.39	3.9	3	10	0.29	0.17	0.92	0.83	7.35	74.9	1,100	0.28	2,850	13.65
LS11	1.66	6.93	4.9	10	0.42	0.09	1.49	0.97	13.5	59.6	494	0.45	1,915	13.5
LS12	1.35	7.9	3.6	20	0.6	0.07	2.58	1.74	14.75	40.9	308	0.48	3,180	9.91
LM1	2.04	2.75	105.5	40	0.1	0.29	0.53	4.83	7.6	37.2	1,005	0.3	6,030	24.7

Sample	*Ga (ppm)*	*Ge (ppm)*	*Hf (ppm)*	*In (ppm)*	*K (%)*	*La (ppm)*	*Li (ppm)*	*Mg (%)*	*Mn (ppm)*	*Mo (ppm)*	*Na (%)*	*Nb (ppm)*	*Ni (ppm)*	*P (ppm)*
LN1	16.35	0.07	7.5	0.242	0.09	1.5	6.2	2.28	495	8.15	2.69	1.9	95	620
LN2	19.8	0.11	7.1	0.234	0.17	3.4	11.5	2.16	509	40	1.98	2.3	201	730
LN3	16.8	0.07	7.5	0.196	0.93	3.1	32	4.07	644	15.45	1.12	2.1	148	570
LN4	18.45	0.06	3.7	0.033	0.05	3.3	19.3	11.55	904	0.63	0.03	2.2	127.5	880
LN5	10.35	0.05	2.7	0.133	0.07	3	25.5	12.2	868	2.49	0.79	1.5	686	510
LN6	11.4	0.05	3.1	0.259	0.02	1.4	11.6	11.7	622	1.96	0.27	1.2	660	270
LN7	16.55	0.17	2.6	0.122	0.11	2.6	13.4	5.02	583	12.65	0.5	0.8	264	290
LN8	9.75	0.27	3.4	0.479	0.02	1.8	16.2	8.88	570	17.9	0.32	0.9	622	340
LN9	9.48	0.07	2.1	0.319	0.02	2.2	17.7	12.2	646	10.25	0.25	1	828	350
LN10	10.65	0.09	5.7	0.163	0.24	2.7	12.8	4.08	364	10.7	1.48	1.4	225	460
LS1	17.6	0.17	4.1	0.459	0.02	3.8	38.8	4.89	498	18.85	0.02	1.6	73.9	340
LS2	24.7	0.21	2	0.274	0.02	2.3	21.3	6.09	416	7.25	0.05	2	66.1	700
LS3	12	0.13	3.5	0.698	0.01	1	11.9	4.03	232	13.25	0.03	0.8	177.5	180
LS4	8.19	0.05	2.4	0.221	0.04	2.6	15.4	11.05	526	5.29	0.89	1	776	370
LS5	8.2	0.08	3.7	0.115	0.13	1.6	14.3	7.59	458	4.77	0.71	0.9	592	310
LS6	17.25	0.07	3.5	0.099	1.44	3.6	18	6.99	689	4.53	0.92	2.7	159.5	860
LS7	14.7	0.1	2	0.22	0.19	3.7	19.7	9.35	667	4.45	0.33	1.9	527	550
LS8	8.44	0.05	1.6	0.097	0.13	2.3	16.8	13.7	686	2.94	0.31	1	1,080	350
LS9	16.7	0.09	3	0.098	0.13	3.5	32.6	8.72	808	2.79	0.45	2.1	353	600
LS0	10.5	0.06	1.7	0.187	0.08	2.2	18	12.85	670	5.53	0.29	1.1	982	350
LS11	15.8	0.07	3	0.151	0.28	4.2	21.1	7.94	691	7.09	0.91	2.1	372	690
LS12	15.35	0.06	3.6	0.158	0.31	4.3	20.4	6.06	635	4.16	1.86	2.3	215	850
LM1	11	0.24	2.5	0.237	0.11	2.5	6.4	7.73	626	11.15	0.65	1.1	682	520

Sample	*Pb (ppm)*	*Rb (ppm)*	*Re (ppm)*	*S (%)*	*Sb (ppm)*	*Sc (ppm)*	*Se (ppm)*	*Sn (ppm)*	*Sr (ppm)*	*Ta (ppm)*	*Te (ppm)*	*Th (ppm)*	*Ti (%)*	*Tl (ppm)*
LN1	30.6	1.5	0.006	0.66	0.75	21.1	13	8.5	68	0.18	0.98	0.1	0.93	1.32
LN2	48.3	4.1	0.041	3.37	1.44	20.6	15	13.4	47.5	0.19	1.16	0.41	0.898	1.04
LN3	18.7	21.2	0.011	4.85	0.49	28.9	5	4.3	37.2	0.16	0.33	0.19	0.958	1.01
LN4	1.9	1.4	0.004	0.26	0.05	19.6	1	1.3	5.8	0.21	<0.05	0.1	1.08	0.03
LN5	2.9	1.5	<0.002	0.26	0.1	24.1	3	1.7	24	0.12	0.16	0.15	0.655	0.09
LN6	3.4	0.5	0.002	1.56	0.17	18.9	5	1.5	13.8	0.1	0.21	0.06	0.531	0.16
LN7	92.2	2.3	0.019	>10.0	3	13.2	38	19.8	14.5	0.07	3.22	0.09	0.405	1.24
LN8	10.4	0.6	<0.002	0.16	1.66	16.6	16	11.4	20.4	0.09	1.08	0.09	0.405	0.09
LN9	6.8	0.6	<0.002	0.17	0.49	19.3	10	4.3	11.6	0.09	0.91	0.09	0.46	0.13
LN10	40.2	4.7	0.05	>10.0	0.79	19.9	9	3.7	49.7	0.11	1.1	0.12	0.636	1.74
LS1	10.3	0.3	0.016	>10.0	0.54	22.2	27	3.5	4.2	0.14	1.57	0.1	0.766	0.34
LS2	11.1	0.6	0.007	3.84	0.38	21	19	3.5	6.5	0.15	0.82	0.08	0.904	0.59
LS3	13.4	0.7	0.024	>10.0	0.39	7.7	25	2.9	8.6	0.07	0.88	0.1	0.325	0.35
LS4	7.8	0.9	0.009	2.75	0.14	18.4	7	2.2	31.4	0.09	0.25	0.07	0.462	0.15
LS5	34.2	3	0.011	>10.0	1.06	12.8	10	8.9	22	0.07	0.66	0.07	0.383	0.54
LS6	24.4	20	0.005	2.93	0.9	36	2	2.7	34.5	0.2	<0.05	0.09	1.235	0.89
LS7	8	4.7	0.008	0.67	0.19	26.2	4	2.1	13.6	0.14	0.22	0.14	0.802	0.22
LS8	7.4	3.4	0.004	0.99	0.19	18.2	4	2.7	14.6	0.08	0.31	0.11	0.421	0.16
LS9	6.5	2.9	0.002	0.71	0.19	28.4	3	3.4	17.4	0.16	0.11	0.16	1.07	0.18
LS0	13.5	2.1	0.008	2.61	0.25	19.2	7	2.7	13.8	0.09	0.28	0.11	0.474	0.22
LS11	12.1	6.6	0.01	1.27	0.33	30.2	3	2.9	35.7	0.16	0.18	0.19	0.91	0.36
LS12	9.8	6.6	0.002	1.13	0.32	32.1	3	3.9	57	0.19	0.17	0.17	1.055	0.27
LM1	153.5	2.1	0.014	1.37	28.4	15.2	6	221	19.8	0.09	0.45	0.17	0.371	0.46

Sample	*U (ppm)*	*V (ppm)*	*W (ppm)*	*Y (ppm)*	*Zn (ppm)*	*Zr (ppm)*
LN1	0.4	249	0.1	27.4	160	324
LN2	1.1	229	0.4	28.2	2,140	289
LN3	6.2	248	0.1	35.2	279	315
LN4	0.7	280	0.1	32.5	99	145.5
LN5	0.5	165	0.1	22.5	204	101
LN6	0.5	136	0.2	18.9	111	122.5
LN7	1.8	185	0.1	19	1,675	112.5
LN8	0.8	129	0.1	18.2	308	151
LN9	0.8	148	0.1	17.3	252	80.1
LN10	3.3	164	<0.1	27	367	226
LS1	4.2	200	0.1	30.1	131	166.5
LS2	1.8	241	0.2	17.2	88	72.1
LS3	2	93	0.1	13.4	216	138.5
LS4	1.1	124	0.1	22	233	103.5
LS5	0.9	102	0.1	19.2	4,630	157
LS6	1.7	292	0.1	34.5	420	126.5
LS7	2.4	202	0.1	22.4	400	79.6
LS8	1.6	131	<0.1	14.4	513	58.8
LS9	7	264	0.1	34.6	385	119
LS0	1.8	147	<0.1	15.8	423	66.7
LS11	2.8	230	0.1	31.2	417	128.5
LS12	2.9	263	0.1	35.4	623	137.5
LM1	1.1	139	42.4	14.4	2,020	100

D.4. ICP-MS results – Libiola North (LN), South (LS) and Margherita (LM) dumps (ALS ME-MS81 method)

Sample	*Ba (ppm)*	*Ce (ppm)*	*Cr (ppm)*	*Cs (ppm)*	*Dy (ppm)*	*Er (ppm)*	*Eu (ppm)*	*Ga (ppm)*	*Gd (ppm)*	*Hf (ppm)*	*Ho (ppm)*	*La (ppm)*	*Lu (ppm)*	*Nb (ppm)*
LN1	9.8	6	567	0.18	3.07	2.04	0.63	21.7	2.6	8.01	0.69	1.9	0.33	2.04
LN2	24.2	9.5	623	0.31	3.38	2.11	0.77	23.4	2.83	7.11	0.71	3.4	0.32	2.12
LN3	22.3	10	374	0.63	4.3	2.72	1.26	20.4	3.76	7.33	0.99	2.9	0.43	2.05
LN4	8.7	14.4	303	0.46	6.26	4.06	0.96	23.4	5.86	4.9	1.43	4	0.61	2.26
LN5	7	9.7	1,110	0.43	3.8	2.4	0.79	12.8	3.55	2.83	0.85	2.8	0.34	1.42
LN6	6.2	4.6	1,450	0.26	2.73	1.82	0.44	13.8	2.06	3.75	0.58	1.4	0.27	1.3
LN7	5.6	7.6	482	0.22	2.62	1.77	0.59	21.9	2.03	3.11	0.6	3	0.26	0.88
LN8	15.3	5.7	1,075	0.18	2.18	1.37	0.54	12.2	1.92	3.67	0.47	1.8	0.2	0.86
LN9	5.3	6.8	1,865	0.22	2.71	1.62	0.58	11.4	2.57	2.29	0.57	2.2	0.2	0.95
LN10	8.9	8.7	520	0.22	3.34	2.03	0.93	13.3	3.1	5.38	0.75	2.7	0.31	1.36
LS1	4.5	15.6	206	0.24	4.18	2.65	0.7	21.7	4.16	4.51	0.91	4	0.37	1.54
LS2	5.3	7.3	216	0.3	3.5	2.64	0.36	27.4	2.92	3.64	0.83	2.2	0.42	1.75
LS3	11	3.4	1,175	0.19	1.16	0.76	0.21	14.2	1.08	3.21	0.28	0.9	0.13	0.72
LS4	9.4	8.4	1,245	0.21	3.78	1.96	0.82	10	3.34	2.47	0.76	2.6	0.26	0.96
LS5	20.8	5.1	705	0.36	2.12	1.29	0.55	9.8	1.87	3.46	0.48	1.5	0.2	0.74
LS6	30.7	16.7	325	0.98	7.05	4.22	1.86	20.2	6.44	4.9	1.54	4.6	0.63	2.47
LS7	9.3	12.2	928	0.29	3.99	2.75	0.73	17.1	3.8	2.99	0.92	3.7	0.4	1.57
LS8	7.3	7	2,010	0.25	2.65	1.64	0.57	10.6	2.42	2.4	0.59	2.2	0.24	0.92
LS9	7.4	16.8	657	0.73	7.85	4.62	1.04	21.8	6.94	3.88	1.61	3.9	0.59	2.07
LS0	8	7	1,940	0.24	2.69	1.68	0.55	11.9	2.41	2.3	0.61	2	0.24	0.89
LS11	8.5	13.4	655	0.44	5.94	3.79	1.14	16.1	4.87	4.07	1.33	4.6	0.53	2.29
LS12	16.8	15.2	408	0.46	6.62	4.13	1.5	16	5.85	5.05	1.53	5.4	0.55	2.47
LM1	35.2	6.5	1,215	0.24	2	1.3	0.42	11.6	1.78	2.74	0.42	2.2	0.18	1.16

Sample	*Nd (ppm)*	*Pr (ppm)*	*Rb (ppm)*	*Sc (ppm)*	*Sm (ppm)*	*Sn (ppm)*	*Sr (ppm)*	*Ta (ppm)*	*Tb (ppm)*	*Th (ppm)*	*Ti (%)*	*Tm (ppm)*	*U (ppm)*	*V (ppm)*
LN1	5.9	1.06	1.5	25.8	2	10	72.4	0.1	0.45	0.13	1.04	0.31	0.52	274
LN2	7.7	1.56	4.1	21.1	2.1	15.8	46.8	0.2	0.47	0.42	1.01	0.29	1.45	267
LN3	9.1	1.67	20	28.6	2.81	5.6	34.7	0.2	0.61	0.23	1.08	0.4	5.81	275
LN4	13.3	2.52	1.3	40.8	4.43	2.3	6.5	0.2	0.95	0.16	1.26	0.51	1.1	321
LN5	8.7	1.62	1.3	24.2	2.6	1.8	24	0.1	0.6	0.17	0.74	0.34	0.56	192
LN6	4.2	0.81	0.4	19.7	1.38	1.3	13.4	0.1	0.35	0.08	0.61	0.24	0.7	160
LN7	5.5	1.12	2.6	15.9	1.42	18.4	17.2	0.1	0.37	0.12	0.48	0.26	1.98	210
LN8	5	0.94	0.5	17.9	1.42	13.8	20.2	0.1	0.31	0.1	0.46	0.2	0.9	154
LN9	5.9	1.2	0.6	20.5	1.88	4.4	11.8	0.1	0.42	0.11	0.52	0.22	0.9	171
LN10	8.1	1.52	4.4	19.9	2.32	2.6	49.9	0.1	0.5	0.11	0.7	0.28	3.13	185
LS1	13.4	2.54	0.4	24.1	3.34	2.5	4.5	0.1	0.65	0.12	0.85	0.38	3.99	226
LS2	6.7	1.24	0.6	23.9	2.25	5	6.8	0.1	0.55	0.15	0.98	0.38	2.82	264
LS3	3.1	0.55	0.5	8.1	0.75	2.4	9.2	0.1	0.19	0.12	0.36	0.11	1.94	111
LS4	8	1.48	0.7	19.6	2.64	2.8	31	0.1	0.56	0.09	0.52	0.3	1.3	142
LS5	4.8	0.89	2.7	13.4	1.5	5.4	20.8	<0.1	0.35	0.07	0.41	0.19	0.95	114
LS6	16.6	3.09	34.9	43.1	5.16	2.4	32.3	0.2	1.1	0.17	1.35	0.62	2.62	319
LS7	10	2.18	4.9	28.1	3.06	2.3	13.1	0.1	0.63	0.18	0.9	0.38	2.48	228
LS8	6.2	1.12	3.6	19.2	1.89	2.6	14.4	0.1	0.41	0.1	0.47	0.23	1.64	149
LS9	17.4	3.18	3.1	35.3	6.24	4.2	19.2	0.1	1.19	0.22	1.18	0.58	7.84	301
LS0	6.1	1.24	1.8	20.1	2.1	3	13.2	0.1	0.41	0.11	0.53	0.25	1.96	163
LS11	12.7	2.49	6	32	4.05	3.3	34.2	0.3	0.92	0.22	0.98	0.5	3.06	245
LS12	15	2.83	6.8	33.4	4.76	3.7	56.3	0.2	1.1	0.25	1.08	0.58	3.73	281
LM1	5.4	1.05	2.4	18.2	1.62	207	19.5	1.7	0.32	0.15	0.41	0.17	1.16	153

Sample	*W (ppm)*	*Y (ppm)*	*Yb (ppm)*	*Zr (ppm)*
LN1	0.6	34.4	2.01	362
LN2	0.9	31.1	1.98	320
LN3	0.6	37.9	2.65	330
LN4	0.6	40.8	3.88	218
LN5	0.5	25.4	2.27	131
LN6	0.5	22	1.61	171
LN7	<0.5	23.5	1.58	139
LN8	0.6	19.9	1.26	163
LN9	0.6	18.5	1.48	102
LN10	0.5	29	1.78	240
LS1	0.5	31.9	2.37	199
LS2	0.6	24.8	2.59	159
LS3	0.5	14.7	0.83	155
LS4	<0.5	23.8	1.79	117
LS5	<0.5	20.1	1.16	159
LS6	0.6	44.1	4.04	206
LS7	0.7	26.6	2.63	135
LS8	<0.5	16.6	1.4	103
LS9	<0.5	42.9	3.78	170
LS0	<0.5	17.9	1.63	97
LS11	0.7	33.3	3.06	166
LS12	0.7	39.9	3.72	196
LM1	44.6	14.4	1.24	114

D.5. XRPD quantitative analyses results (values in wt%) - Libiola

Sample	*Ab*	*Amp*	*Adr*	*Cal*	*Ccp*	*Chl*	*Di*	*Gp*	*Gth*	*Hem*	*Ilt*	*Lz*	*Mag*	*Pl*	*Py*	*Qz*	*Srp*	*Swm*	*Tlc*	*Rt*	*Amorphous*
LN_01	33.3	-	-	-	-	5	21.67	-	-	-	-	-	-	-	-	6.67	-	-	-	16.67	16.67
LN_02	-	-	-	-	20	8	-	-	-	-	-	-	-	25	22.5	-	-	-	-	-	25
LN_03	17	-	-	-	12	47	-	-	-	-	-	-	-	-	20	5	-	-	-	-	-
LN_04	-	-	-	-	-	100	-	-	-	-	-	-	-	-	-	-	-	-	-	-	-
LN_05	-	30	-	-	-	26.7	-	-	-	-	3.4	13.3	8.3	18.3	-	-	-	-	-	-	-
LN_06	-	33.3	-	1.7	26.67	8.33	-	-	-	-	-	10	-	-	5	-	-	3.3	11.7	-	-
LN_07	-	-	-	-	-	25	-	-	20	-	2.5	-	-	12.5	2.5	-	25	-	-	-	12.5
LS_01	-	-	-	-	7.5	15.0	-	-	16.7	-	-	16.7	-	-	25.8	16.7	-	-	1.7	-	-
LS_02	-	-	-	-	-	26.25	-	-	7.5	-	-	-	17.5	-	-	5	8.75	-	35	-	-
LS_03	-	-	-	-	-	20	-	5	2	-	-	-	24	-	20	16	-	-	13	-	-
LS_04	-	6.67	6.67	-	-	48.3	-	-	-	-	-	-	-	-	-	3.33	35	-	-	-	-
LS_05	-	-	-	-	-	5	-	-	-	-	-	-	-	30	50	15	-	-	-	-	-
LS_06	-	-	20	12	-	25	-	-	15	-	-	-	-	-	10	-	18	-	-	-	-
LM_01	-	-	-	-	-	-	-	-	90	10	-	-	-	-	-	-	-	-	-	-	-

Mineral abbreviations according to Warr, 2021: Ab: Albite; Amp: Amphibole, Adr: Andradite, Cal: Calcite, Ccp: Chalcopyrite, Chl: Chlorite, Di: Diopside, Gp: Gypsum, Gth: Goethite, Hem: Hematite, Ilt: Illite, Lz: Lizardite, Mag: Magnetite, Pl: Plagioclase, Py: pyrite, Qz: quartz, Srp: Serpentine, Swm: Schwertmannite, Tlc: Talc, Rt: Rutile.

D.6. ICP-OES characterisation of leachate solutions and calculated R_{ICP} values - Libiola

Sample	*Leaching mode*	*Leaching time (h)*	*Cu (ppm)*	$R_{ICP, Cu}$ *(%)*	*Fe (ppm)*	$R_{ICP, Fe}$ *(%)*
LN7	Glycine	0.5	62	6.1	1.6	0.02
	Glycine	2	74	7.3	< 1	-
	Glycine	4	69	6.9	< 1	-
	Glycine	6	78	7.7	< 1	-
	Glycine	24	108	10.6	1.1	0.01
	Glycine	168	263	26.0	4.7	0.04
	H_2SO_4	2	489	48.2	4,329	38.7
LN9	Glycine	0.5	19.2	9.9	< 1	-
	Glycine	2	22.8	11.8	< 1	-
	Glycine	4	26.3	13.6	< 1	-
	Glycine	6	29.2	15.1	< 1	-
	Glycine	24	33.3	17.3	< 1	-
	H_2SO_4	2	33.3	66.4	346	4.6
LS1	Glycine	0.5	34	2.9	2.8	0.02
	Glycine	2	59	4.9	2.1	0.02
	Glycine	4	70	5.9	2.0	0.01
	Glycine	6	69	5.8	1.8	0.01
	Glycine	24	162	13.6	2.8	0.02
	Glycine	168	420	35.2	5.6	0.04
	H_2SO_4	2	316	26.5	5,811	43.0
LS3	Glycine	0.5	87	5.5	1.6	0.01
	Glycine	2	89	5.7	< 1	-
	Glycine	4	96	6.1	< 1	-
	Glycine	6	102	6.5	< 1	-
	Glycine	24	129	8.2	1.1	0.01
	Glycine	168	438	27.8	9.7	0.07
	H_2SO_4	2	711	45.2	6,152	41.7
LS4	Glycine	0.5	20	8.6	< 1	-
	Glycine	2	31	13.5	< 1	-
	Glycine	4	38	16.7	< 1	-
	Glycine	6	37	16.4	< 1	-
	Glycine	24	44	19.2	< 1	-
	H_2SO_4	2	219	96.5	5,811	98.1

D.7. HH-XRF characterisation of post-leaching solid residues and calculated R_{XRF} values - Libiola

Sample	*Leaching mode*	*Leaching time (h)*	*Cu (ppm)*	$R_{XRF, Cu}$ *(%)*	*Fe (ppm)*	$R_{XRF, Fe}$ *(%)*
LN7	Glycine	0.5	19,294	5.9	243,761	-
	Glycine	2	19,697	4.0	244,126	-
	Glycine	4	18,347	10.5	237,888	-
	Glycine	6	19,077	7.0	238,095	-
	Glycine	24	19,491	5.0	242,719	-
	Glycine	168	16,761	18.3	242,478	-
	H_2SO_4	2	13,521	34.1	193,364	16.7
LN9	Glycine	0.5	3,063	21.2	139,723	3.2
	Glycine	2	3,147	19.0	141,677	1.8
	Glycine	4	3,274	15.8	145,144	-
	Glycine	6	3,380	13.0	146,665	-
	Glycine	24	3,190	17.9	143,546	0.5
	H_2SO_4	2	1,950	49.8	147,282	-
LS1	Glycine	0.5	22,432	0.7	284,620	-
	Glycine	2	21,672	4.1	280,733	-
	Glycine	4	21,895	3.1	285,436	-
	Glycine	6	22,187	1.8	290,553	-
	Glycine	24	20,858	7.7	292,163	-
	Glycine	168	15,178	32.8	292,214	-
	H_2SO_4	2	17,555	22.3	241,220	10.4
LS3	Glycine	0.5	28,920	6.3	320,799	-
	Glycine	2	30,335	1.7	343,774	-
	Glycine	4	32,066	-	347,320	-
	Glycine	6	31,447	-	328,682	-
	Glycine	24	28,232	8.5	316,574	-
	Glycine	168	20,852	32.4	279,247	11.2
	H_2SO_4	2	22,052	28.5	272,438	13.4
LS4	Glycine	0.5	3,940	17.4	107,923	1.6
	Glycine	2	3,616	24.2	107,421	2.1
	Glycine	4	3,618	24.1	110,863	-
	Glycine	6	3,913	17.9	109,793	-
	Glycine	24	3,652	23.4	109,277	0.4
	H_2SO_4	2	1,217	74.5	76,309	30.5

E. Appendix E

This appendix material is referred to in ***Chapter 7.***

E.1. HH-XRF results for Fenice Capanne Tailings and Roasting samples (values in ppm, ND: Not Detected)

Sample_ID	*Mg*	*Mg +/-*	*Al*	*Al +/-*	*Si*	*Si +/-*	*P*	*P +/-*	*S*	*S +/-*	*K*	*K +/-*	*Ca*	*Ca +/-*
FC1	6971	1518	43566	710	173262	761	ND	< 1460	34160	241	28473	66	49406	76
FC2	9627	2773	48020	736	161524	737	ND	< 1517	36549	244	29022	66	57198	81
FC4	ND	< 2000	35163	568	242094	825	ND	< 913	15528	181	29655	66	7385	31
FC5	3404	536	37297	659	176132	749	ND	< 1591	44962	265	24655	61	51008	76
FC7	ND	< 2000	27691	513	267506	813	2613	633	31704	228	23315	57	3688	61
FC9	ND	< 2000	24440	513	229057	772	ND	< 934	24375	203	21821	54	22422	48
FC10	ND	< 2000	33451	593	249457	845	3687	791	35463	249	26672	64	4980	77
FC11	2168	450	26857	540	256145	810	ND	< 1090	32532	232	25745	60	60013	79
FC12	ND	< 2000	33715	588	251574	841	2761	754	31228	236	26369	63	7112	94
FC13	ND	< 2000	28612	534	262177	823	3401	705	26107	214	24056	58	5536	77
FC15	ND	< 2000	29010	535	258358	836	ND	< 957	57746	301	14880	48	4089	60
FC20	ND	< 2000	23131	601	262003	1022	ND	< 3900	12268	203	11315	49	4005	26

Sample_ID	*Ti*	*Ti +/-*	*V*	*V +/-*	*Cr*	*Cr +/-*	*Mn*	*Mn +/-*	*Fe*	*Fe +/-*	*Co*	*Co +/-*	*Ni*	*Ni +/-*
FC1	3190	47	98	5.3	77	8.8	5392	70	76216	146	ND	< 61	62	9.5
FC2	3259	47	106	5.3	91	9.1	5430	72	74536	145	ND	< 61	68	9.6
FC4	2705	42	86	4.8	62	7.4	838	27	66819	127	ND	< 51	85	8.7
FC5	1950	31	63	3.6	82	9.3	7818	91	68253	137	ND	< 63	79	9.6
FC7	1178	20	42	2.4	79	7	6786	52	49877	112	ND	< 48	68	8.4
FC9	1905	33	67	3.9	33	6.3	1599	35	58676	120	ND	< 46	39	8.1
FC10	1358	24	51	2.9	74	8.6	10206	65	66032	130	ND	< 57	87	9.2
FC11	2017	31	82	3.8	34	5.2	2533	43	52213	124	ND	< 42	42	8.8
FC12	1554	27	52	3.1	70	8.2	8426	90	67413	131	ND	< 56	67	9
FC13	1248	22	42	2.6	64	7.1	9787	97	54963	117	ND	< 49	79	8.6
FC15	723	16	27	2	120	9.4	7100	101	58345	123	216	51	55	9.2
FC20	943	96	55	6.5	ND	< 19	302	16	135537	185	ND	< 148	37	6.9

Sample_ID	*Cu*	*Cu +/-*	*Zn*	*Zn +/-*	*As*	*As +/-*	*Se*	*Se +/-*	*Rb*	*Rb +/-*	*Sr*	*Sr +/-*	*Y*	*Y +/-*
FC1	5524	27	3784	30	321	7.4	ND	< 1.5	177	2.1	233	2.4	14	0.9
FC2	7632	32	4561	20	391	7.6	ND	< 1.5	249	2.7	217	2.3	16	1
FC4	496	9.4	1178	13	339	6.7	ND	< 1.2	130	1.7	75	1.2	8.8	0.7
FC5	8245	33	12309	32	296	8.8	ND	< 1.7	148	2	235	2.5	19	1
FC7	384	8.7	12634	30	318	6	ND	< 1.2	98	1.5	61	1.1	14	0.7
FC9	378	8.2	1561	15	423	5.8	ND	< 1.0	97	1.4	157	1.7	7.5	0.6
FC10	511	10	15262	35	479	7.6	ND	< 1.4	113	1.7	57	1.1	18	0.8
FC11	447	8.9	476	7.4	162	3.3	ND	< 1.0	105	1.5	392	3.2	7.5	0.6
FC12	495	10	11139	30	436	6.7	ND	< 1.2	105	1.6	73	1.2	15	0.8
FC13	243	7.3	11799	29	327	5.2	ND	< 1.1	98	1.5	49	1	12	0.7
FC15	3093	21	21831	41	845	18	7.2	1.8	67	1.6	98	1.8	15	1.6
FC20	2925	22	913	9.9	741	17	ND	< 3.1	65	2	97	1.9	463	9.7

Sample_ID	*Zr*	*Zr +/-*	*Nb*	*Nb +/-*	*Mo*	*Mo +/-*	*Ag*	*Ag +/-*	*Cd*	*Cd +/-*	*Sn*	*Sn +/-*	*Sb*	*Sb +/-*
FC1	94	1.9	7	0.8	ND	< 0.8	13	0.6	7.7	0.8	10	0.8	62	2
FC2	105	2	7.8	0.8	1.6	0.6	16	0.7	6.8	0.7	8	0.8	51	1.9
FC4	61	1.6	4.6	0.7	1.1	0.5	2.9	0.5	ND	< 1.0	ND	< 1.1	39	1.7
FC5	81	1.9	9.2	0.8	ND	< 0.9	10	0.6	29	0.9	5.6	0.8	62	2
FC7	50	1.5	4	0.7	ND	< 0.8	3.3	0.5	11	0.7	ND	< 1.1	42	1.8
FC9	48	1.5	4.9	0.7	ND	< 0.7	ND	< 0.8	ND	< 1.0	2	0.7	36	1.7
FC10	60	1.7	4.4	0.8	ND	< 0.8	3.8	0.5	15	0.8	ND	< 1.1	41	1.8
FC11	54	1.7	4.6	0.7	ND	< 0.7	ND	< 0.7	ND	< 1.0	ND	< 1.1	19	1.6
FC12	56	1.6	6.1	0.7	ND	< 0.8	2.3	0.5	9	0.7	ND	< 1.1	39	1.8
FC13	49	1.5	4.7	0.7	ND	< 0.8	1.9	0.5	7.1	0.7	ND	< 1.1	40	1.8
FC15	50	1.7	4.5	0.9	ND	< 1.0	16	0.7	79	1.2	7.2	0.8	79	2.2
FC20	7677	12	20	2.4	ND	< 5.6	48	1	ND	< 1.3	15	0.9	78	2.3

Sample_ID	*Ba*	*Ba +/-*	*La*	*La +/-*	*Ce*	*Ce +/-*	*Pr*	*Pr +/-*	*Nd*	*Nd +/-*	*Sm*	*Sm +/-*	*Eu*	*Eu +/-*
FC1	1122	15	39	7.4	ND	< 14	ND	< 30	ND	< 22	ND	< 25	ND	< 225
FC2	1151	15	24	7.2	32	9.1	ND	< 29	ND	< 19	ND	< 24	ND	< 216
FC4	1078	14	13	6.9	ND	< 13	ND	< 28	ND	< 21	ND	< 23	ND	< 198
FC5	940	14	27	6.9	35	8.9	ND	< 28	ND	< 21	ND	< 23	ND	< 215
FC7	787	13	22	6.8	ND	< 13	ND	< 27	ND	< 21	ND	< 22	ND	< 204
FC9	780	13	ND	< 10	ND	< 13	ND	< 28	ND	< 21	ND	< 22	ND	< 202
FC10	741	13	27	6.7	ND	< 13	ND	< 27	ND	< 21	ND	< 22	ND	< 204
FC11	1082	14	22	6.8	ND	< 13	ND	< 28	ND	< 21	ND	< 22	ND	< 201
FC12	763	13	ND	< 10	ND	< 13	ND	< 28	ND	< 18	ND	< 23	ND	< 208
FC13	647	12	21	6.7	ND	< 13	ND	< 27	ND	< 20	ND	< 22	ND	< 201
FC15	668	12	ND	< 10	ND	< 13	ND	< 27	32	12	ND	< 23	ND	< 213
FC20	503	12	27	6.5	ND	< 13	ND	< 26	ND	< 21	ND	< 23	ND	< 218

Sample_ID	*Gd*	*Gd +/-*	*Hg*	*Hg +/-*	*Tl*	*Tl +/-*	*Pb*	*Pb +/-*	*Bi*	*Bi +/-*	*U*	*U +/-*
FC1	ND	< 407	ND	< 0.1	ND	< 5.1	1323	10	242	6	ND	< 2.6
FC2	ND	< 389	ND	< 0.1	12	3.3	1142	9.4	298	6.5	ND	< 2.9
FC4	ND	< 346	ND	< 0.1	ND	< 4.3	1178	8.7	42	3.9	9.4	1.5
FC5	ND	< 376	ND	< 0.1	14	4.2	1865	12	178	5.9	3.9	1.8
FC7	ND	< 350	ND	< 0.1	7.7	2.6	740	7	25	3.4	ND	< 1.9
FC9	ND	< 349	ND	< 0.1	ND	< 3.1	498	5.7	34	3.3	7.5	1.3
FC10	ND	< 349	ND	< 0.1	11	3	991	8.5	69	4.4	13	1.6
FC11	ND	< 346	ND	< 0.1	5.4	1.5	151	3.9	57	3.2	4.8	1.4
FC12	ND	< 358	ND	< 0.1	8.7	2.6	720	7.2	35	3.8	12	1.5
FC13	ND	< 342	ND	< 0.1	9.6	2.1	370	5.3	43	3.3	11	1.4
FC15	ND	< 372	ND	< 0.1	ND	< 12	5353	19	18	36	ND	< 2.3
FC20	ND	< 379	ND	< 0.1	ND	< 10	2062	13	566	9	ND	< 3.6

E.2. ICP-MS results – Fenice-Capanne tailings and roastings samples (ALS ME-MS61 method)

Sample	*Ag (ppm)*	*Al (%)*	*As (ppm)*	*Ba (ppm)*	*Be (ppm)*	*Bi (ppm)*	*Ca (%)*	*Cd (ppm)*	*Ce (ppm)*	*Co (ppm)*	*Cr (ppm)*	*Cs (ppm)*	*Cu (ppm)*	*Fe (%)*
FC1	13.1	5.84	337	140	1.74	206	5.04	7.01	57.5	22	67	18.7	5,370	6.78
FC2	17	7.06	452	130	2.06	272	5.52	6.42	65.9	24.1	78	27.5	7,480	7.02
FC4	5.05	4.14	423	210	1.11	11	0.64	9.63	35.1	23.8	71	5.63	537	5.21
FC5	11.3	5.02	311	110	1.68	139.5	4.96	25.5	52.2	33.8	57	12.2	8,320	6.55
FC7	3.98	3.03	395	140	0.79	6.66	0.61	9.38	26.6	26.8	55	3.61	397	4.88
FC9	2.84	3.1	473	270	0.72	22.6	2.04	0.61	20.3	7	39	3.41	454	5.61
FC10	4.45	3.74	588	170	1.12	9.72	0.8	13.25	31.4	30.9	49	3.71	543	6.52
FC11	1.7	3.55	215	200	0.97	42.6	4.52	0.52	27.1	14.9	41	4.41	509	5.21
FC12	3.83	3.64	540	130	1.1	10.3	1.05	7.84	31.2	23.6	48	3.77	521	6.79
FC13	2.62	3.3	467	220	0.94	6.39	0.8	5.89	27.1	28.2	43	2.95	271	5.73
FC15	16.9	3.13	829	60	0.72	32.7	0.89	68.6	30	22	85	4.93	3,080	5.76
FC20	27.6	2.19	718	620	0.67	486	0.28	0.71	18.35	6.5	21	4.27	2,820	13.15

Sample	Ga (ppm)	Ge (ppm)	Hf (ppm)	In (ppm)	K (%)	La (ppm)	Li (ppm)	Mg (%)	Mn (ppm)	Mo (ppm)	Na (%)	Nb (ppm)	Ni (ppm)	P (ppm)
FC1	16	0.11	0.6	0.438	2.97	29.9	52	1.07	4,600	1.45	0.04	8.6	50.6	330
FC2	19.15	0.14	0.7	0.526	3.26	34	56.1	1.41	4,670	1.74	0.03	9.7	55.5	340
FC4	10.7	0.09	0.5	0.052	2.63	17.8	68.2	0.63	5,470	1.07	0.02	5.7	65.1	260
FC5	12.75	0.13	0.6	0.379	2.64	25.9	50.8	0.93	5,330	1.33	0.03	7.5	57	310
FC7	7.42	0.08	0.4	0.033	2.31	13.6	67.2	0.43	6,130	0.98	0.02	4.1	63.3	210
FC9	7.72	0.1	0.4	0.078	2.36	9.5	55.2	0.36	1,320	0.92	0.02	4.5	17.4	220
FC10	9.44	0.1	0.5	0.062	2.72	15.8	56.3	0.53	9,140	0.85	0.02	5.4	67.3	250
FC11	8.19	0.09	0.4	0.115	2.57	13	52.6	0.58	2,390	0.69	0.03	4.6	27.3	190
FC12	8.94	0.1	0.3	0.067	2.63	15.4	56.8	0.51	6,420	1.41	0.02	5.3	53.9	250
FC13	8.09	0.08	0.4	0.041	2.5	13.4	58.1	0.47	7,700	0.92	0.02	4.5	59.9	200
FC15	8.63	0.09	0.2	0.108	1.42	13.6	76	0.35	4,790	1.66	0.01	3.1	60.8	220
FC20	6.37	0.11	190	1.13	1.17	11	30.6	0.1	314	0.51	0.02	2.7	16.4	110

Sample	Pb (ppm)	Rb (ppm)	Re (ppm)	S (%)	Sb (ppm)	Sc (ppm)	Se (ppm)	Sn (ppm)	Sr (ppm)	Ta (ppm)	Te (ppm)	Th (ppm)	Ti (%)	Tl (ppm)
FC1	1,140	188.5	0.003	3.95	63.2	11.6	5	5.3	250	0.7	0.32	5.16	0.28	5.11
FC2	1,010	231	0.004	4.41	48.4	13.8	5	6.1	239	0.69	0.4	6.05	0.312	6.79
FC4	1,065	124	0.003	2.99	36	8.2	2	1.7	70.3	0.42	0.05	3.4	0.205	1.81
FC5	1,745	154	0.004	5.13	60.5	9.9	5	4.3	255	0.57	0.3	4.55	0.247	4.33
FC7	663	100.5	0.002	3.13	36	5.8	2	1.1	62	0.32	0.05	2.54	0.151	1.48
FC9	433	105	0.002	2.25	32.8	5.5	2	1.4	165	0.36	0.08	2.73	0.153	1.6
FC10	916	121	<0.002	3.73	35.3	7	2	1.4	61.5	0.41	<0.05	3.34	0.187	1.74
FC11	123	110.5	0.002	3.69	17.3	6.1	2	2.2	412	0.37	0.23	3.08	0.153	1.95
FC12	635	115.5	<0.002	3.61	36.5	6.7	2	1.4	79.3	0.4	0.06	2.98	0.181	1.55
FC13	341	108	0.003	3.05	33.7	5.8	2	1.3	52.2	0.35	<0.05	2.8	0.158	1.5
FC15	4,960	69.8	0.003	5.28	81	5.3	5	3	100	0.29	0.1	1.84	0.116	2.57
FC20	1,960	65.8	0.002	0.78	73.1	1.8	7	7.6	96.5	2.25	0.82	1.48	0.088	4.66

Sample	*U (ppm)*	*V (ppm)*	*W (ppm)*	*Y (ppm)*	*Zn (ppm)*	*Zr (ppm)*
FC1	1.1	86	21.5	14.1	4,110	12.4
FC2	1.2	106	23.4	16	4,480	15.4
FC4	0.5	60	5.2	10.2	>10,000	12.1
FC5	1	72	18.6	15.8	>10,000	11.9
FC7	0.3	40	4.8	9.6	>10,000	8.7
FC9	0.5	39	8.8	6.4	1,740	10.3
FC10	0.5	48	5.3	10.9	>10,000	11.3
FC11	0.6	44	19.6	8	532	8.1
FC12	0.4	47	6.7	10.2	>10,000	7.6
FC13	0.4	40	5	8.9	>10,000	8.3
FC15	0.8	44	16.1	16.8	>10,000	3.2
FC20	0.2	31	57.8	490	900	>500

E.3. ICP-MS results – Fenice-Capanne tailings and roastings samples (ALS ME-MS81 method)

Sample	*Ba (ppm)*	*Ce (ppm)*	*Cr (ppm)*	*Cs (ppm)*	*Dy (ppm)*	*Er (ppm)*	*Eu (ppm)*	*Ga (ppm)*	*Gd (ppm)*	*Hf (ppm)*	*Ho (ppm)*	*La (ppm)*	*Lu (ppm)*	*Nb (ppm)*
FC1	1,090	57.3	88	17.05	3.18	1.89	1.06	17	3.97	2.37	0.67	30.9	0.26	9.92
FC2	1,125	65.4	102	24.2	4.08	2.15	1.12	19.8	4.59	2.51	0.77	34.1	0.3	10.5
FC4	837	34.2	94	5.41	2.42	1.4	0.7	11.8	2.85	1.75	0.54	18.3	0.19	6.42
FC5	1,020	52.7	75	12.15	3.45	1.95	1.04	14.1	4.37	1.94	0.82	27.9	0.27	8.54
FC7	833	28.6	73	3.66	2.02	1.39	0.51	8.4	2.39	1.42	0.47	15.4	0.14	4.66
FC9	892	20.5	49	3.51	1.76	0.98	0.47	8.1	1.55	1.46	0.33	10.7	0.14	5.11
FC10	903	30.7	66	3.71	2.5	1.43	0.68	10	2.87	1.78	0.51	16	0.2	5.9
FC11	1,160	27.7	55	4.25	1.77	1.24	0.55	8.9	2.34	1.56	0.39	15.1	0.16	5.24
FC12	912	29.3	62	3.47	2.14	1.46	0.57	9.5	2.75	1.78	0.52	15.4	0.21	5.81
FC13	749	25.8	53	2.79	2.09	1.12	0.51	8.4	2.17	1.5	0.42	13	0.15	5.02
FC15	632	31.6	113	4.77	3.54	1.77	0.97	9.6	4.05	1.1	0.72	14.7	0.19	3.46
FC20	618	17.4	25	4.02	0.64	0.49	0.31	6.6	0.96	202	0.16	11.6	0.07	2.97

Sample	Nd (ppm)	Pr (ppm)	Rb (ppm)	Sc (ppm)	Sm (ppm)	Sn (ppm)	Sr (ppm)	Ta (ppm)	Tb (ppm)	Th (ppm)	Ti (%)	Tm (ppm)	U (ppm)	V (ppm)
FC1	26.7	7.02	191.5	13	5.01	6.1	259	0.6	0.62	7.18	0.32	0.22	1.74	97
FC2	30.8	7.97	226	15.9	5.73	6.9	247	0.7	0.73	8.5	0.36	0.32	2.15	117
FC4	16	4.25	125	9.7	2.87	1.8	72	0.6	0.43	4.85	0.24	0.21	1.02	64
FC5	25.3	6.48	155	12.3	4.66	4.9	269	0.5	0.69	6.27	0.29	0.27	1.63	78
FC7	13.2	3.42	104	6.2	2.57	1.1	66.6	0.5	0.4	3.55	0.18	0.19	0.73	40
FC9	9.9	2.63	105.5	6.1	1.78	1.4	175	0.5	0.24	3.75	0.18	0.13	0.77	45
FC10	13.8	3.72	119.5	8.7	2.79	1.2	62.9	0.5	0.42	4.63	0.22	0.2	0.97	51
FC11	12.9	3.51	117.5	7.4	2.57	2.4	432	0.5	0.32	4.09	0.18	0.15	1.01	45
FC12	13.9	3.57	114.5	7.8	2.74	1.9	81.3	0.5	0.39	4.26	0.21	0.18	0.93	49
FC13	11.9	3.03	106	5.8	2.12	1.5	56.2	0.5	0.38	3.84	0.18	0.18	0.8	43
FC15	17.6	4.3	72.6	6.6	4.02	3.1	108.5	0.3	0.67	2.74	0.14	0.22	1.22	50
FC20	7.3	2.07	64.6	3	1.32	9.8	99.5	1.9	0.13	1.84	0.1	0.05	0.41	32

Sample	W (ppm)	Y (ppm)	Yb (ppm)	Zr (ppm)
FC1	23.6	18.6	1.62	81
FC2	24.7	21.6	1.97	93
FC4	5.6	14.2	1.16	61
FC5	20.8	20.7	1.45	70
FC7	4.9	12.8	1.02	46
FC9	10.6	8.8	0.84	49
FC10	5.3	14	1.22	59
FC11	23.3	10.8	1.01	49
FC12	7.4	13.4	1.39	56
FC13	5.3	11.6	1.03	54
FC15	16.4	20.9	1.4	37
FC20	60.4	510	0.35	8,030

E.4. XRPD quantitative analyses results (values in wt%) – Fenice-Capanne

Sample	*Cal*	*Clc*	*Cro*	*Di*	*Emr*	*Gp*	*Hem*	*Jbj*	*Kln*	*Ms*	*Pmi*	*Py*	*Qz*	*Sa*	*Sd*	*Skh*
FC1	-	19.7	-	-	-	17.1	-	-	-	21.7	-	1.8	28.5	11.2	-	-
FC2	8.1	24.8	-	-	-	19.7	-	-	-	24.6	-	3.7	19.1	-	-	-
FC4	-	-	-	-	-	0.1	-	-	18.6	7.6	1.2	3.1	52.9	13.9	2.6	-
FC5	-	-	7.5	-	-	13.3	-	7.6	-	33.9	-	4.5	33.4	-	-	-
FC7	-	-	2.5	-	17.7	4.9	-	-	-	-	-	3.5	71.4	-	-	-
FC9	-	5.2	-	-	-	7	-	-	-	10.6	-	1	55.9	17.4	-	2.9
FC10	-	27.6	-	-	-	13.4	-	-	-	1	-	3.2	39.6	15.2	-	-
FC11	8.3	17.3	-	-	-	2	-	-	-	-	-	2.8	51.6	18	-	-
FC12	-	13.7	-	-	-	16.8	-	-	-	-	-	3.5	52.7	13.4	-	-
FC13	-	9.6	-	-	-	6.7	-	-	-	-	-	3.7	65.5	14.5	-	-
FC15	-	-	-	-	-	21.6	-	-	-	18.7	-	8.8	50.8	-	-	-
FC20	-	-	-	31.2	-	-	11.1	-	-	-	-	-	57.7	-	-	-

Mineral abbreviations according to Warr (2021): Cal: Calcite; Clc: Clinochlore; Cro: Cronstedite; Di: Diopside; Emr: Emmerichite; Gp: Gypsum; Hem: Hematite; Jbj: Joelbruggerite; Jrs: Jarosite; Kln: Kaolinite; Ms: Muscovite; Pmi: Palmierite; Py: Pyrite; Qz: Quartz; Sa: Sanidine; Sd: Siderite; Skh: Sakhaite.

E.5. MLA modal mineralogy results for sample FC15, Fenice-Capanne

Mineral	***wt.%***
Quartz	56.71
Plagioclase	14.48
K_Feldspar	7.36
Pyrite	7.19
Muscovite	4.46
Schwertmannite	1.69
Sphalerite	1.65
Garnet	1.38
Phases ≤ 1 wt%	**5.05**
Amphibole	1.01
Chlorite	0.79
Chalcopyrite	0.63
Dolomite	0.31
FeMn-Carbonate	0.3
Galena	0.27
Biotite	0.26
FeOxide	0.26
Siderite	0.25
FeMnZn-carbonate	0.17
Gypsum	0.17
Ankerite	0.12
Arsenopyrite	0.1
Rutile	0.1
Talc	0.1
Fluorite	0.07
Chalcocite	0.03
Epidote	0.03
Tetrahedrite	0.03
Apatite	0.01
Barite	0.01
Calcite	0.01
Molybdenite	0.01
Monazite	0.01

E.6. ICP-OES characterisation of leachate solutions and calculated R_{ICP} values – Fenice-Capanne

Sample	*Leaching mode*	*Leaching time (h)*	*Cu (ppm)*	$R_{ICP, Cu}$ (%)	*Zn (ppm)*	$R_{ICP, Zn}$ (%)	*Fe (ppm)*	$R_{ICP, Fe}$ (%)
FC2	Glycine	0.5	93	21.5	25	12.6	< 1	-
	Glycine	2	101	23.4	267	13.3	< 1	-
	Glycine	4	110	25.3	32	16.0	< 1	-
	Glycine	6	114	26.3	32	16.0	< 1	-
	Glycine	24	168	38.9	45	22.4	2.9	0.1
	Glycine	168	311	71.8	161	80.9	24	0.6
	H_2SO_4	2	379	87.5	263	100	2,984	76.6
FC4	Glycine	0.5	13	41.8	71	13.3	< 1	-
	Glycine	2	11	36.0	86	16.1	< 1	-
	Glycine	4	13	41.9	93	17.4	< 1	-
	Glycine	6	15	47.2	102	19.1	< 1	-
	Glycine	24	19	60.6	128	23.9	1.1	0.1
	H_2SO_4	2	26	83.2	668	100	2,523	90.0
FC5	Glycine	0.5	104	29.2	96	17.6	< 1	-
	Glycine	2	114	32.1	135	24.8	< 1	-
	Glycine	4	127	35.6	178	32.7	< 1	-
	Glycine	6	137	38.5	190	34.9	< 1	-
	Glycine	24	170	47.9	291	53.5	< 1	-
	Glycine	168	335	94.4	502	92.2	8.7	0.2
	H_2SO_4	2	321	90.4	627	100	2,540	70.2
FC10	Glycine	0.5	6	23.6	47	6.2	< 1	-
	Glycine	2	8	30.7	60	8.0	< 1	-
	Glycine	4	13	48.1	69	9.2	< 1	-
	Glycine	6	9	34.9	69	9.2	< 1	-
	Glycine	24	14	51.8	114	15.2	1.3	0.1
	H_2SO_4	2	23	88.1	973	100	2,983	90.4
FC15	Glycine	0.5	18	12.0	206	19.5	< 1	-
	Glycine	2	24	15.7	221	20.9	< 1	-
	Glycine	4	27	17.4	227	21.4	< 1	-
	Glycine	6	27	17.8	226	21.4	< 1	-
	Glycine	24	51	33.6	282	26.7	3	0.1
	Glycine	168	96	63.2	435	41.1	14	0.5
	H_2SO_4	2	125	82.0	1266	100	2,276	100

E.7. HH-XRF characterisation of post-leaching solid residues and calculated R_{XRF} values – Fenice-Capanne

Sample	*Leaching mode*	*Leaching time (h)*	*Cu (ppm)*	$R_{XRF, Cu}$ *(%)*	*Zn (ppm)*	$R_{XRF, Zn}$ *(%)*	*Fe (ppm)*	$R_{XRF, Fe}$ *(%)*
FC2	Glycine	0.5	7,366	14.9	3,966	0.4	83,192	-
	Glycine	2	7,003	19.1	3,861	3.0	78,686	-
	Glycine	4	7,267	16.1	4,471	-	84,340	-
	Glycine	6	6,907	20.2	3,825	3.9	83,430	-
	Glycine	24	6,242	27.9	3,623	9.0	82,637	-
	Glycine	168	2,604	69.9	3,078	22.7	81,253	-
	H_2SO_4	2	2,194	74.7	516	87.0	38,262	50.9
FC4	Glycine	0.5	626	31.3	9,651	9.7	58,609	-
	Glycine	2	430	43.3	9,655	9.7	58,481	-
	Glycine	4	355	48.6	8,942	16.4	55,732	0.6
	Glycine	6	322	47.8	9,404	12.1	57,940	-
	Glycine	24	327	58.5	9,104	14.9	57,137	-
	H_2SO_4	2	260	91.7	361	96.6	12,417	77.9
FC5	Glycine	0.5	5,894	17.1	9,327	14.4	78,490	-
	Glycine	2	5,428	23.6	8,369	23.2	76,686	-
	Glycine	4	5,499	22.6	8,069	25.9	81,611	-
	Glycine	6	5,474	23.0	7,544	30.8	79,102	-
	Glycine	24	4,609	35.2	6,325	42.0	75,503	-
	Glycine	168	2,069	70.9	3,786	65.3	75,290	-
	H_2SO_4	2	1,936	72.8	697	93.6	38,469	46.8
FC10	Glycine	0.5	333	36.3	13,315	11.1	63,615	3.6
	Glycine	2	336	35.8	14,207	5.2	66,075	-
	Glycine	4	322	38.4	13,911	7.2	66,224	-
	Glycine	6	270	48.4	12,110	19.2	62,477	5.3
	Glycine	24	288	44.9	13,238	11.6	64,981	1.5
	H_2SO_4	2	54	89.7	598	96.0	15,748	76.1
FC15	Glycine	0.5	2,742	10.0	18,184	14.0	59,291	-
	Glycine	2	2,558	16.0	17,806	15.7	59,006	-
	Glycine	4	2,639	13.3	18,447	12.7	60,754	-
	Glycine	6	2,662	12.6	18,096	14.4	60,054	-
	Glycine	24	1,946	36.1	15,901	24.8	55,638	4.6
	Glycine	168	1,184	61.1	13,892	34.3	56,467	3.1
	H_2SO_4	2	879	71.1	3,344	84.2	24,469	58.0